DEVELOPMENT AND APPLICATION OF AN OPTIMISATION ARCHITECTURE WITH ADAPTIVE SWARM ALGORITHM FOR AIRFOIL AERODYNAMIC DESIGN

by

Manas Singh Khurana

Bachelor of Engineering (Aerospace) with Honours

A thesis submitted in fulfilment of the requirements for the degree of

Doctor of Philosophy

in the

School of Aerospace, Mechanical and Manufacturing Engineering

RMIT University

July 2011

Declaration of Authorship

I, **MANAS KHURANA**, declare that this thesis titled, **'Development and Application of an Optimisation Architecture with Adaptive Swarm Algorithm for Airfoil Aerodynamic Design'** and the work presented in it are my own. I confirm that:

- Except where due acknowledgement has been made, the work is that of myself alone;
- The work has not been submitted previously, in whole or in part, to qualify for any other academic award;
- The content of the thesis is the result of work which has been carried out since the official commencement date of the approved research program;
- Any editorial work, paid or unpaid, carried out by a third party has been acknowledged; and
- Ethics procedures and guidelines have been followed.

Signed: _____

Date: _____

Abstract

Khurana, Manas Singh, **Development and Application of an Optimisation Architecture with Adaptive Swarm Algorithm for Airfoil Aerodynamic Design**, PhD Thesis, RMIT University, July 2011, Australia

The development of a Multi-Mission Unmanned Aerial Vehicle (MM-UAV) is at the forefront of aerospace research and design. Present Unmanned Aerial Vehicles (UAVs) have issues and challenges of high acquisition costs and limited operating efficiency. Past airframe design efforts have focused on developing mission-specific systems. Hence, there exists a large fleet of UAVs in the military and civil sectors that are optimised for operation with restricted roles. Concurrently the optimal flight performances of the system are characterised by limited speed and altitude operating limits. Operators also endure high costs attributed with maintaining a large fleet of UAVs and are focusing on investing in flexible aerial systems.

The development of a robust platform has been identified as a design alternate to address the identified issues and challenges of a uni-mission system. A MM-UAV will provide the design flexibility in flight operation by wing morphing to conform to a wide-set of mission goals. Shape morphing will facilitate the development of mission-segment airfoils that will achieve optimal flight performance over extended speed and altitude flight domains. The MM-UAV will further address the issues of high acquisition costs as it will replace mission-specific UAVs in the fleet, while enhancing the operating flexibility that is made available to the operator.

The design of a MM-UAV is a multidisciplinary process. The research focuses on the aerodynamic design of mission-segment airfoils for the identified platform. Novel shape design processes using Evolutionary Algorithms (EA) and a surrogate-based management system are developed to address the identified issues and challenges of solution feasibility and computational efficiency associated with present methods. Feasibility refers to the optimality of the converged solution as a function of the defined objectives and constraints. Computational efficiency is a measure of the number of design iterations needed to achieve convergence to the theoretical optimum.

Airfoil design problems are characterised by a multi-modal solution topology. Present gradient-based optimisation methods do not converge to an optimal profile, hence solution feasibility is compromised. Population-based optimisation methods including the Genetic Algorithm (GA) have been used in the literature to address this issue. The GA can achieve solution feasibility, yet it is computationally time-intensive, hence efficiency is compromised.

Novel EAs are developed to address the identified shortcomings of present methods. A variant to the original Particle Swarm Optimisation algorithm (PSO) is presented. Novel mutation operators are implemented which facilitate the transition of the search particles toward a global solution. The methodology addresses the limited search performance of the original PSO algorithm for multi-modal problems, while maintaining acceptable computational efficiency for aerodynamic design applications.

Demonstration of the developed principles confirmed the merits of the proposed design approach. Airfoil optimisation for a low-speed flight profile achieved drag performance improvement that is

lower than a off-the-shelf shape designed for the intent role. Acceptable computational efficiency is achieved by restricting the optimisation phase to promising solution regions through the development of a novel, design variable search space mapping structure. The merit of the optimisation framework is further confirmed by transonic airfoil design for high-speed missions. The wave drag of the established optima is lower than the identified, off-the-shelf benchmark. Concurrently significant computational time-savings are achieved relative to the design methodologies present in the literature. A novel surrogate-assisted optimisation framework by the definition of an Artificial Neural Network with a pattern recognition model is developed to further improve the computational efficiency. This has the potential of enhancing the aerodynamic shape design process.

The measure of computational efficiency is critical in the development of an optimisation algorithm. Airfoil design simulations presented required 80% fewer design iterations to achieve convergence than the GA. Computational time-savings spanning days was achieved by the innovative algorithms developed relative to the GA. Hence, computational efficiency of the developed processes is confirmed. Aircraft shape design simulations involve three-dimensional configurations which require excessive computational effort due to the use of high-fidelity solvers for flow analysis in the optimisation process. It is anticipated that the confirmed computational efficiency performance of the design structure presented on two-dimensional cases will be transferable to three-dimensional shape design problems. It is further expected that the novel principles will be applicable for analysis within a multidisciplinary design structure for the development of a MM-UAV.

List of Publications

Journal

1. **Khurana M.S.** and Winarto H, Development and Validation of an Efficient Direct Numerical Optimisation Approach for Airfoil Shape Design, The Aeronautical Journal, Volume 114, No 1160, Pages 611-628, October 2010

Peer-Reviewed Conference Publications

1. **Khurana M.S.**, Winarto H and Sinha A.K., Airfoil Optimisation by Swarm Algorithm with Mutation and Artificial Neural Networks, Proceedings of the 47th AIAA Aerospace Sciences Meeting including The New Horizons Forum and Aerospace Exposition, Orlando, Florida, Jan. 5-8, 2009

2. **Khurana M.S.**, Winarto H and Sinha A.K., Application of Swarm Approach and Artificial Neural Networks for Airfoil Shape Optimization, Proceedings of the 12th AIAA /ISSMO Multidisciplinary Analysis and Optimization Conference, Victoria, British Columbia, Sep. 10-12, 2008

3. **Khurana M.S.**, Application of an Hybrid Optimization Approach in the Design of Long Endurance Airfoils, Proceedings of the 26th International Congress of the Aeronautical Sciences, Anchorage, Alaska, 2008 [**Recommended for Journal Publication**]

4. **Khurana M.S.**, Sinha A.K. and Winarto H, Multi Mission Re-Configurable UAV - Airfoil Optimisation through Swarm Approach and Low Fidelity Solver, Proceedings of the 23rd Bristol International Unmanned Air Vehicle Systems Conference, Bristol, United Kingdom, 2008 [**Recommended for Journal Publication**]

5. **Khurana M.S.**, Winarto H and Sinha A.K., Airfoil Geometry Parameterization Through Shape Optimizer and Computational Fluid Dynamics, Proceedings of the 46th AIAA Aerospace Sciences Meeting and Exhibit, Reno, Nevada, Jan. 7-10, 2008

6. **Khurana M.S.**, Sinha A.K. and Winarto H, Multi-Mission Re-Configurable Unmanned Aerial Vehicle - Airfoil Optimisation Architecture, Proceedings of the International Conference on Engineering Technology, Kuala Lumpur, Malaysia, 2007

7. **Khurana M.S.**, Sinha A.K. and Winarto H, Multi-Mission Re-Configurable UAV - Airfoil Shape Parameterisation Study, Proceedings of the 22nd International Unmanned Air Vehicle Systems Conference, Bristol 16th-18th April, 2007

8. **Khurana M.S.**, Sinha A.K. and Winarto H, Multi-Mission Re-Configurable UAV - Airfoil Analysis through Shape Transformation and Computational Fluid Dynamics, Proceedings of the Twelfth Australian International Aerospace Congress - Second Australasian Unmanned Air Vehicles Conference 21st March, 2007

Acknowledgements

I, **MANAS KHURANA**, sincerely thank and acknowledge the following:

- **My Parents - Gurcharan and Sushil Khurana**;
- **A/Prof. Hadi Winarto**, Thesis Supervisor: For his valuable supervisory guidance, advice, motivation and support throughout the research;
- **Robert Carrese**, RMIT Aerospace PhD Candidate: For his technical support in the field of shape optimisation;
- **Dr. Omar Ilaya**, RMIT Aerospace PhD: For his technical support on optimisation algorithms;
- **Dr. Gerhard Kranner**, Managing Director, Viscovery Software GmbH: For providing a complimentary copy of Viscovery5.0 for the duration of the PhD project and the technical support in the field of data mining for engineering applications;
- **Dr. Arvind Sinha**, Research Consultant: For his guidance and advice;
- **Victorian Partnership for Advanced Computing (VPAC)**: For providing supercomputing infrastructure and systems technical support to setup algorithms for analysis by parallel computing;
- **Clinton Hughes**, RMIT, Information Technology Services: For his assistance throughout the research program particularly during the concluding stages of the PhD; and
- **Andrew Ponnadurai**: Proof-reading.

Contents

Declaration of Authorship i

Abstract ii

List of Publications iv

Acknowledgements v

List of Figures xii

List of Tables xix

List of Algorithms xxii

Abbreviations xxiii

Symbols xxv

1 Introduction 1
- 1.1 Overview . . . 1
- 1.2 Background . . . 2
- 1.3 Design Application . . . 3
  - 1.3.1 Wing Morphing for RC-MM-UAV . . . 6
- 1.4 Motivation . . . 9
  - 1.4.1 Airfoil Shape Parameterisation . . . 10
  - 1.4.2 Fitness Function Solver . . . 11
  - 1.4.3 Optimisation Algorithm . . . 11
  - 1.4.4 Surrogate Modeling . . . 12
- 1.5 Scope of Research . . . 12
- 1.6 Thesis Contribution . . . 14
- 1.7 Thesis Structure . . . 15

2 Aerodynamic Design Optimisation Methodology 18
- 2.1 Overview . . . 18
- 2.2 Inverse Design . . . 19
- 2.3 Direct Design . . . 20
- 2.4 Review of Direct Design Process . . . 22
- 2.5 Airfoil Shape Parameterisation . . . 24
  - 2.5.1 Discrete Approach . . . 26

2.5.2 CAD Based Approach . . . 27
2.5.3 Analytical Approach . . . 29
2.5.4 Polynomial Functions . . . 29
2.6 Flow Solver . . . 35
2.6.1 Fully Potential Methods . . . 36
2.6.2 Euler Methods . . . 36
2.6.3 Navier-Stokes . . . 37
2.7 Optimisation Algorithms . . . 39
2.7.1 Gradient-Based Methods . . . 41
2.7.2 Adjoint Methods . . . 44
2.7.3 Evolutionary Algorithms - Global Search Methods . . . 47
2.7.3.1 Genetic Algorithms . . . 48
2.7.3.2 Simulated Annealing . . . 50
2.7.3.3 Ant Colony . . . 51
2.8 Summary . . . 52

3 Particle Swarm Optimisation 54
3.1 Overview . . . 54
3.1.1 PSO Structure Design-of-Experiments Study . . . 55
3.2 Particle Swarm Optimiser . . . 56
3.2.1 Local and Global-Based Particle Swarm Optimiser . . . 58
3.3 Variants to the Particle Swarm Optimiser . . . 61
3.4 Adaptive-Mutation Particle Swarm Optimiser . . . 63
3.4.1 Space Filling Design for Solution Initialisation . . . 64
3.4.2 Adaptive Inertia Weight . . . 67
3.4.3 Wall Boundary Conditions . . . 68
3.4.4 Adaptive Position Update Time-Variant Mutation . . . 69
3.4.5 Optimisation Termination . . . 72
3.5 Data Mining . . . 74
3.5.1 Self-Organising Maps . . . 74
3.5.2 Kohonen's Batch SOM . . . 79
3.5.2.1 Visualisation by Data Cluster . . . 81
3.5.2.2 Case Study One: 2D Test Problem . . . 82
3.5.2.3 Case Study Two: 3D Test Problem . . . 85
3.5.2.4 Case Study Three: Wing Weight Estimation . . . 88
3.6 AM-PSO Design of Experiments . . . 91
3.6.1 Numerical Test Validation with Pre-Defined Termination Definition . . . 91
3.6.1.1 Rosenbrock Function . . . 92
3.6.1.2 Additional Test Evaluation . . . 97
3.6.2 Numerical Test Validation with Extended Termination Definition . . . 104
3.6.2.1 AM-PSO Search Parameter Settings . . . 105
3.6.2.2 Simulation Results and Discussion . . . 107
3.7 Summary . . . 112

4 Aerodynamic Design Optimisation Architecture Development & Validation 114
4.1 Overview . . . 114
4.2 Geometrical Parameterisation Model . . . 115
4.2.1 Inverse Shape Fitting . . . 116
4.2.1.1 Inverse Shape Fitting Analysis by the Analytical Approach . . . 118
4.2.1.2 Inverse Shape Fitting Analysis by Polynomial-Based Functions . . . 124
4.2.1.3 Inverse Shape Fitting Analysis by the Polynomial-Based PARSEC-Modified Approach . . . 134
4.2.2 Design Variables Pre-Screening . . . 141

4.2.2.1 Solution Search Space . . . 143
4.2.2.2 Design Variables Measure of Importance . . . 148
4.3 Summary . . . 156

5 Flow Solver Validation for Airfoil Design Fitness Function Evaluation 157
5.1 Overview . . . 157
5.2 Flow Solver Definition . . . 158
5.3 Low-Fidelity Solver Validation . . . 160
5.4 Flow Analysis by a High-Fidelity Solver . . . 161
5.4.1 Review of One-Equation Turbulence Model Application . . . 162
5.4.2 Review of Computational Model Requirements . . . 163
5.4.3 High-Fidelity Flow Solver Validation at HALE Flight Envelope . . . 163
5.4.4 Angle-of-Attack Trimming Validation for HALE Airfoil Optimisation . . . 172
5.4.5 High-Fidelity Flow Solver Validation at Transonic Flight Envelope . . . 175
5.4.6 Angle-of-Attack Trimming Validation for Transonic Airfoil Optimisation . . . 182
5.5 Summary . . . 183

6 Aerodynamic Shape Optimisation by Direct Approach 185
6.1 Overview . . . 185
6.2 Limitations of the Stand-Alone Local Gradient-Based Method for HALE Airfoil Optimisation . . . 186
6.3 MM-UAV HALE Airfoil Design Definition . . . 193
6.3.1 Parallel Computing Set-Up . . . 193
6.3.2 HALE Airfoil Design Objective Function / Constraints Set-Up . . . 194
6.4 MM-UAV HALE Airfoil Optimisation by the AM-PSO Algorithm with a Low-Fidelity Solver . . . 196
6.4.1 MM-UAV HALE Single-Point Airfoil Optimisation . . . 198
6.4.2 MM-UAV HALE Multi-Point Airfoil Optimisation . . . 203
6.4.3 MM-UAV HALE Airfoil Optimisation by a Robust Design Approach . . . 211
6.5 Validation of AM-PSO Optimisation Results . . . 218
6.5.0.1 AM-PSO Single-point Design Solution Validation . . . 219
6.5.0.2 AM-PSO Multi-point Design Solution Validation . . . 222
6.5.0.3 Post-Processing of Optimisation Results Summary . . . 224
6.6 HALE Single-Point Airfoil Optimisation Architecture Set Up for Flow Analysis by a High-Fidelity Solver . . . 225
6.6.1 Airfoil Optimisation by the Stand-Alone AM-PSO Algorithm with FLUENT . 229
6.6.2 Optimisation by Hybrid AM-PSO & Gradient Method Algorithm . . . 238
6.7 Transonic Airfoil Design . . . 240
6.8 Transonic Single-Point Airfoil Optimisation Architecture Set Up for Flow Analysis by a High-Fidelity Solver . . . 242
6.9 Transonic Optimisation by Stand-Alone AM-PSO Algorithm . . . 247
6.10 Transonic Optimisation by Hybrid AM-PSO & Gradient Method Algorithm . . . 253
6.10.1 Transonic Optimisation by Hybrid AM-PSO & Gradient Method Algorithm: Measure of Computational Efficiency . . . 257
6.11 Summary . . . 259

7 Development of a Metamodel Assisted Optimisation Algorithm 261
7.1 Overview . . . 261
7.2 Introduction . . . 262
7.2.1 Implementation of a Surrogate Model in the DNO Structure . . . 263
7.3 Surrogate Model Type Review of Application . . . 264
7.3.1 Development and Integration Strategies of the Surrogate Model into the DNO Structure . . . 269
7.3.2 Review of Selected Surrogate Model Type for Airfoil Design . . . 274

7.3.3 Offline-training Global Based Artificial Neural Network . . . 275
7.3.4 Offline-training: Global Based Artificial Neural Network Development & Application for Airfoil Design . . . 280
7.3.5 Design Principles & Merits of an Online-Based Surrogate Model for Optimisation Simulations . . . 288
7.3.5.1 AM-PSO Based Online-training Surrogate Model Design Definition . 291
7.3.5.2 Design Definition & Demonstration of the AM-PSO Based Online Surrogate Model . . . 299
7.4 Summary . . . 315

8 Concluding Remarks **317**
8.1 Research Summary . . . 317
8.2 Contributions . . . 317
8.3 Future Research . . . 323

A Analytical Approach Shape Functions **327**
A.1 Hicks-Henne Functions . . . 327
A.2 NACA Functions . . . 328
A.3 Wagner Functions . . . 330
A.4 Bernstein Polynomials . . . 331
A.5 Legendre Polynomials . . . 332

B PSO Test Validation Fitness Contour Plots **333**
B.1 Rosenbrock Function: Fitness Distribution as a function of Particle Population & Maximum Velocity for $D = 10, 20, 30$ . . . 333
B.2 Ackley Function: Fitness Distribution as a function of Particle Population & Maximum Velocity for $D = 10, 20, 30$ . . . 334
B.3 Michalewics Function: Fitness Distribution as a function of Particle Population & Maximum Velocity for $D = 10, 20, 30$ . . . 335
B.4 Schwefel Function: Fitness Distribution as a function of Particle Population & Maximum Velocity for $D = 10, 20, 30$ . . . 336

C Demonstration of Swarm Search Process **337**
C.1 Ackley Function: Swarm Convergence to Minima Solution Region by the AM-PSO Algorithm . . . 337
C.2 Michalewics Function: Swarm Convergence to Minima Solution Region by the AM-PSO Algorithm . . . 338
C.3 Rosenbrock Function: Swarm Convergence to Minima Solution Region by the AM-PSO Algorithm . . . 339

D Impact of PARSEC Shape Variables by Visualisation on Airfoil Aerodynamics & Geometry **340**
D.1 PARSEC Variable: y_{te} . . . 340
D.2 PARSEC Variable: t_{eg} . . . 341
D.3 PARSEC Variable: t_{ew} . . . 341
D.4 PARSEC Variable: x_u . . . 342
D.5 PARSEC Variable: y_{xxu} . . . 343
D.6 PARSEC Variable: x_l . . . 343
D.7 PARSEC Variable: y_l . . . 344
D.8 PARSEC Variable: y_{xxl} . . . 345

E Airfoil Design Variables Solution Space Mapping **346**
E.1 PARSEC Solution Space Mapping at HALE Mach Numbers . . . 346

E.2 PARSEC Solution Space Mapping at Transonic Mach Numbers . . . 347
E.3 CST BPO2 Solution Space Mapping at HALE Mach Numbers . . . 348
E.4 CST BPO2 Solution Space Mapping at Transonic Mach Numbers . . . 349
E.5 CST BPO3 Solution Space Mapping at HALE Mach Numbers . . . 350
E.6 CST BPO3 Solution Space Mapping at Transonic Mach Numbers . . . 351
E.7 CST BPO4 Solution Space Mapping at HALE Mach Numbers . . . 352
E.8 CST BPO4 Solution Space Mapping at Transonic Mach Numbers . . . 353
E.9 CST BPO5 Solution Space Mapping at HALE Mach Numbers . . . 354
E.10 CST BPO5 Solution Space Mapping at Transonic Mach Numbers . . . 356

F Shape Variables Qualitative Measure of Sensitivity on Aerodynamics 358
F.1 PARSEC Sensitivity at HALE Flight Envelope - Aerodynamic Coefficients . . . 358
F.2 PARSEC Sensitivity at HALE Flight Envelope - Boundary Layer Transition . . . 360
F.3 PARSEC-Modified Sensitivity at Transonic Flight Envelope - Coefficient of Drag . . . 361
F.4 PARSEC-Modified Sensitivity at Transonic Flight Envelope - Shock Wave One . . . 362
F.5 PARSEC-Modified Sensitivity at Transonic Flight Envelope - Shock Wave Two . . . 363
F.6 PARSEC-Modified Sensitivity at Transonic Flight Envelope - Coefficient of Moment . 364
F.7 PARSEC-Modified Sensitivity at Transonic Flight Envelope - Minimum Coefficient of Pressure Airfoil Chord Location . . . 365

G Airfoil Shape Variables Quantitative Measure of Sensitivity on Aerodynamics 366
G.1 HALE Flight Performance - PARSEC Shape Function . . . 366
G.2 HALE Flight Performance - PARSEC Shape Function Contribution to c_d & $c_{l_{max}}$ . . . 366
G.3 HALE Flight Performance - PARSEC-Modified Shape Function . . . 366
G.4 Transonic Flight Performance - PARSEC-Modified Shape Function . . . 366

H Low-Fidelity Solver TSFOIL Validation for Transonic Design 371
H.1 TSFOIL Airfoil Node Population Convergence . . . 371

I Angle-of-Attack Trimming Analysis at Transonic Flight Envelope 372
I.1 RAE 2822 Angle-of-Attack Trimming Analysis . . . 372

J AoA by Trimming at Transonic Flight Envelope 373
J.1 Boxplot Representation of the Established c_l^T Distribution . . . 373
J.2 Histogram Representation of the Established c_l^T Distribution . . . 374

K Transonic Airfoil Design Aerodynamic Optimisation Analysis 375
K.1 Airfoil Optima & Equating Coefficient of Pressure by the PARSEC-Modified Reduced Modeling Shape Function & Hybrid Optimisation Approach . . . 375
K.2 Transonic Airfoil Design Convergence to Optima by PARSEC-Modified Reduced Modeling Shape Function & Hybrid Optimisation Approach . . . 376

L Online-Training ANN Model Development Performance Charts 377
L.1 Ackley Test Function . . . 377
L.1.1 ANN Function Approximation Model . . . 377
L.1.2 ANN Pattern Recognition Model . . . 379
L.2 Michalewics Test Function . . . 382
L.2.1 ANN Function Approximation Model . . . 382
L.2.2 ANN Pattern Recognition Model . . . 384
L.3 Schwefel Test Function . . . 387
L.3.1 ANN Function Approximation Model . . . 387
L.3.2 ANN Pattern Recognition Model . . . 389

Bibliography **392**

List of Figures

1.1 Mission Market Survey for Australian Military & Civil Sectors [1] . . . 5
1.2 Morphing Wing Configuration for Optimal Aerodynamic Mission Performance [2] . . . 8
1.3 RC-MM-UAV Design Concepts [1, 3–5] . . . 9

2.1 Airfoil Inverse Design Process . . . 19
2.2 Airfoil Direct Design Process . . . 21
2.3 Airfoil Parameterisation by Discrete Approach . . . 26
2.4 Definition of PARSEC Airfoil . . . 30
2.5 PARSEC Airfoil with Equating Shape Parameters . . . 31
2.6 Optimisation Solution Classification . . . 40
2.7 Objective Function Solution Representation . . . 41

3.1 Particle Swarm Neighborhood Topology Types . . . 59
3.2 Design of Experiments Space Filling . . . 67
3.3 Adaptive-Based Swarm Probability of Mutation . . . 70
3.4 SOM Structure Representation . . . 75
3.5 SOM Radius Neighborhood Function Representation . . . 77
3.6 Exponential Decay in Radius of Neighborhood about the BMU as a function of k . . . 78
3.7 Spring Oscillation Decay with Time . . . 82
3.8 SOM Representation of Spring Oscillation Decay with Time . . . 83
3.9 3D De Jong's Function . . . 85
3.10 3D De Jong's Function . . . 86
3.11 SOM Representation of Aircraft Wing Weight Estimation with Ten-Variables . . . 89
3.12 Rosenbrock Function . . . 92
3.13 Rosenbrock Function SOM Representation of v_{max} as a function of Dimension Search Space for S-PSO & AM-PSO . . . 93
3.14 Effect of Particle Population and Velocity on Fitness by the AM-PSO Algorithm . . . 94
3.15 Effect of Particle Population, Maximum Velocity & Dimensional Search Space on Rosenbrock Function Fitness by the AM-PSO Algorithm . . . 95
3.16 Ackley Function . . . 98
3.17 Michalewics Function . . . 98
3.18 Schwefel Function . . . 99
3.19 Ackley Function: SOM Representation of v_{max} as a function of Dimension Search Space for S-PSO & AM-PSO . . . 99
3.20 SOM Cluster Dimensional Space Fitness Mean & Standard Deviation Distribution; $m = 20, 40, 80$ & $v_{max} = [0.10, \cdots, 10.00]$ of x_{max} . . . 100
3.21 Michalewics Function: SOM Representation of v_{max} as a function of Dimension Search Space for S-PSO & AM-PSO . . . 101
3.22 Michalewics Function: SOM Cluster Fitness Mean & Standard Deviation Distribution; $m = 20, 40, 80$ & $v_{max} = [0.10, \cdots, 10.00]$ of x_{max} . . . 102
3.23 Schwefel Function: SOM Representation of v_{max} as a function of Dimension Search Space for S-PSO & AM-PSO . . . 102

3.24 Schwefel Function: SOM Cluster Fitness Mean & Standard Deviation Distribution; $m = 20, 40, 80$ & $v_{max} = [0.10, \cdots, 10.00]$ of x_{max} . . . 104
3.25 Effect of Wall Boundary Conditions on Solution Convergence . . . 107
3.26 Schwefel Function: Demonstration of Swarm Search Progress to Global Point . . . 109

4.1 Inverse Airfoil Shape Fitting . . . 117
4.2 Representation of Base & Target Airfoils for Evaluation of Wall Boundary Condition type by the Inverse Shape Fitting Approach with Hicks-Henne Shape Functions . . . 119
4.3 NASA LRN(1)-1007 Inverse Shape Fitting: Effect of Wall Boundary Condition Type on Objective Function . . . 119
4.4 Inverse Shape Fitting Fitness Distribution by the AM-PSO with Random Initialisation Wall Boundary Condition . . . 121
4.5 Inverse Shape Fitting Cumulative Fitness Distribution by the Line Search Method with Random Initialisation Wall Boundary Condition over Sixteen Target Airfoils . . . 122
4.6 Inverse Shape Fitting Fitness by Hicks-Henne Shape Function: Comparison of Uni & Hybrid Based Optimisation Process . . . 123
4.7 NLF(1)-0416 Airfoil Convergence by the CST Method . . . 124
4.8 NLF(1)-0416 Boxplot of Shape Convergence Error Distribution by the CST Method . 125
4.9 NLF(1)-0416 Inverse Airfoil Fitting with CST by AM-PSO & Kulfan Numerical Method 125
4.10 NLF(1)-0416 Airfoil Aerodynamic Convergence by the CST Method . . . 127
4.11 Base Airfoils for PARSEC Airfoil Definition . . . 130
4.12 Effect of r_{le} on Airfoil Geometry . . . 130
4.13 Effect of r_{le} on Airfoil Aerodynamics . . . 131
4.14 Effect of y_u on Airfoil Geometry . . . 131
4.15 Effect of y_u on Airfoil Aerodynamics . . . 132
4.16 Inverse Shape Fitting Fitness Distribution Comparison between Analytical & Polynomial Based Approach . . . 133
4.17 PARSEC-Modified Representation . . . 136
4.18 NLF Airfoil Representation by PARSEC & PARSEC-Modified Method . . . 137
4.19 Inverse Shape Fitting Fitness Distribution Comparison between Hicks-Henne, PARSEC & PARSEC-Modified Approach . . . 138
4.20 Inverse Shape Fitting by the PARSE-Modified Approach . . . 139
4.21 PARSEC-Modified Variables Solution Space Mapping for Airfoil Design at HALE Mach Numbers . . . 145
4.22 PARSEC-Modified Variables Solution Space Mapping for Airfoil Design at Transonic Mach Numbers . . . 147
4.23 PARSEC-Modified Variables Contribution to c_d & $c_{l_{max}}$ at HALE Flight Envelope . . 152
4.24 PARSEC-Modified Variables Contribution to Airfoil Aerodynamics at Transonic Flight Envelope; Mach=0.74, $R_n = 2.70 \times 10^6$ & $c_l = 0.733$ . . . 154
4.25 PARSEC-Modified Variables Contribution to $x/c_{shock\ 1}$ & $x/c_{shock\ 2}$ at Transonic Flight Envelope . . . 154

5.1 Effect of XFOIL Node Distribution on Aerodynamic Convergence at HALE Conditions; Mach=0.10, $R_n = 4.00 \times 10^6$ & $\alpha = 2°$ . . . 161
5.2 NLF(1)-0416 C-Type Computation Grid Domains . . . 164
5.3 NLF(1)-0416 CFD Computation Validation with Experiment [6] by the 4 Equation $k-\omega$ SST Transition Turbulence Model; $R_n = 4.0 \times 10^6$; $M_\infty = 0.10$ . . . 166
5.4 NLF(1)-0416 c_p CFD Computation Validation with Experiment [6] by the 4 Equation $k-\omega$ SST Transition Turbulence Model; $R_n = 4.0 \times 10^6$; $M_\infty = 0.10$ . . . 168
5.5 NLF(1)-0416 Aerodynamic Computation Comparison by $k-kl-\omega$ & $k-\omega$ SST Transition Models with Experiment [6]; $R_n = 4.0 \times 10^6$; $M_\infty = 0.10$ . . . 169
5.6 Comparison of NLF(1)-0416 Boundary Layer Transition (Laminar Flow) Location by Experiment [6] & $k-\omega$ SST Transition Turbulence Model (Mesh 3); $R_n = 4.0 \times 10^6$ & $M_\infty = 0.10$ . . . 171

5.7 Comparison of NLF(1)-0416 Boundary Layer Transition (Turbulent Flow) Location by Experiment [6] & $k-\omega$ SST Transition Turbulence Model (Mesh 3); $R_n = 4.0 \times 10^6$ & $M_\infty = 0.10$ . . . 171
5.8 NLF(1)-0416 Lift-Curve Slope Validation by α_{trim} Approach with Computational Domain Mesh Type 3 . . . 173
5.9 NLF(1)-0416 Aerodynamic Coefficients at Target α_{trim} with Computational Domain Mesh Type 3 . . . 174
5.10 Cell Aspect Ratio Representation around Computational Domain . . . 175
5.11 RAE 2822 Airfoil 29 by 29 Computational Domain . . . 176
5.12 RAE 2822 Airfoil 129 by 129 Computational Domain . . . 176
5.13 Boundary Layer Fluid Sub-domain Zones for Transition Modeling around RAE 2822 Airfoil . . . 177
5.14 c_p Computational Data Comparison with Experiment by $k-\omega$ SST Transition Turbulence Model with Mean Velocity for Flow Initialisation; M_∞=0.740, $\alpha = 3.19°$ & $R_n = 2.7 \times 10^6$ . . . 178
5.15 c_p Computational Data Comparison with Experiment by $k-\omega$ SST Transition Turbulence Model with FMG Flow Initialisation; M_∞=0.740, $\alpha = 3.19°$ & $R_n = 2.7 \times 10^6$ . . . 180
5.16 RAE 2822 Aerodynamic Performance Contours; $M_\infty = 0.740$, $\alpha = 2.87°$, $R_e = 2.7 \times 10^6$ & $c_l = 0.733$ . . . 181
5.17 Aerodynamic Coefficient Convergence History by the Mean Velocity & FMG Flow Initialisation Approach . . . 182
5.18 RAE 2822 c_p Convergence by α_{trim} Approach to Theoretical and Experimental Distribution; ($M_\infty = 0.740$, $R_e = 2.7 \times 10^6$) . . . 183

6.1 MM-UAV Mission Profile . . . 185
6.2 Airfoil Design by Gradient Method with NACA 0012 Base Airfoil . . . 187
6.3 Airfoil Design by Gradient Method with NLF(1)-0115 Base Airfoil . . . 188
6.4 Airfoil Design by Gradient Method with RAE 2822 Base Airfoil . . . 188
6.5 AM-PSO Swarm Initialisation about NACA 0012 Airfoil . . . 190
6.6 AM-PSO Airfoil at Convergence (Eqn. 6.1) with Disparate Swarm Initialisation Base Shapes . . . 192
6.7 HALE Single-Point Airfoil Optimisation Results by the AM-PSO Method with XFOIL 199
6.8 HALE Single-Point Airfoil Optimisation - Analysis of Solution Convergence by AM-PSO and XFOIL with PARSEC & PARSEC-Modified Variants . . . 202
6.9 HALE Multi-Point Airfoil Optimisation Results by the AM-PSO Method with XFOIL 204
6.10 HALE Multi-Point Airfoil Optimisation - Analysis of Solution Convergence by AM-PSO and XFOIL with PARSEC & PARSEC-Modified Variants . . . 210
6.11 Definition of Target Lift Coefficient Design Flight Points $\mathcal{N}$ for Airfoil Optimisation by the Robust Approach . . . 214
6.12 Airfoil Profile Comparison of the Multi-Point & Robust Design Approach Method with Baseline NLF(1)-0416 . . . 216
6.13 Airfoil Drag Polar Comparison of the Multi-Point & Robust Design Approach Method with Baseline NLF(1)-0416 at Mach=0.10 & $R_n = 4.0 \times 10^6$ . . . 217
6.14 Single-point AM-PSO Solution topology by SOMs . . . 219
6.15 HALE Single-point Solution topology Validation by SOMs . . . 221
6.16 Multi-Point HALE PARSEC-Modified Coefficients y_l & y_{xxl} by Disparate Optimisation Design Methods . . . 224
6.17 CST Solution Search Space Convergence for HALE Airfoil Design by the Single-Point Design Approach with AM-PSO & XFOIL . . . 226
6.18 Solution Search Space Convergence by Disparate Airfoil Shape Parameterisation Function Types as a Function of Swarm Population for HALE Airfoil Design with AM-PSO 227
6.19 Solution Search Space Convergence by Disparate Airfoil Shape Parameterisation Function Types as a Function of Swarm Population for HALE Airfoil Design with AM-PSO & Gradient Optimisation Methods . . . 228

6.20 NLF(1)-0416 c_p distribution with XFOIL & FLUENT at the estimated trimming-based α for $c_l^T \approx 0.40$ . . . 231
6.21 Probability of Mutation as a Function of Particle Extremity Distance Metric for HALE Airfoil Design with FLUENT & PARSEC-Modified Method with 13 Shape Variables . 232
6.22 Swarm Fitness Convergence for HALE Airfoil Design with FLUENT & PARSEC-Modified Method with 13 Shape Variables . . . 233
6.23 HALE Airfoil Design Boxplot Analysis of the Computed c_l^T of each Airfoil Modeled by a Particle in the Swarm . . . 234
6.24 HALE Airfoil Design Histogram Analysis of the $c_l^T = 0.40$ Distribution For Select Particles in the Swarm . . . 235
6.25 HALE Single-Point Optima Airfoil Profile by XFOIL & FLUENT in the DNO Structure 237
6.26 HALE FLUENT-Based Single-Point Airfoil Optima Profile at Convergence by the AM-PSO/Gradient Method with Variance in Shape Parameterisation Dimensionality Size . 240
6.27 Solution Search Space Convergence by Disparate Airfoil Shape Parameterisation Function Types as a Function of Swarm Population for Transonic Airfoil Design with AM-PSO 245
6.28 Solution Search Space Convergence by Disparate Airfoil Shape Parameterisation Function Types as a Function of Swarm Population for Transonic Airfoil Design with AM-PSO & Gradient Optimisation Methods . . . 246
6.29 Transonic Airfoil Optimisation at $c_l^T \approx 0.733$ by the Stand-Alone AM-PSO Algorithm with PARSEC-Modified Full & Reduced Design Variable Set . . . 249
6.30 Transonic Airfoil Design Swarm Personal Best Convergence toward Optima as a function of Search Iteration . . . 251
6.31 Transonic Airfoil Optimisation at $c_l^T \approx 0.733$ by the Stand-Alone AM-PSO & Hybrid Design Approach Method with PARSEC-Modified Full Design Variable Set . . . 254
6.32 Transonic Airfoil Design Convergence toward an Optima by the PARSEC-Modified Full Variable Set Modeling Approach . . . 256

7.1 Definition of Flow Solver Metamodel in the DNO Structure . . . 263
7.2 Benchmark Test Functions: Effect of Sampling Strategy on ANN Generalisation Convergence Errors . . . 278
7.3 Offline-Based Neural Network Structure for Airfoil Design . . . 281
7.4 Affect of Neural Network Structure on Lift Coefficient . . . 283
7.5 Affect of Neural Network Structure on Drag Coefficient . . . 283
7.6 Offline Training-based Neural Network Aerodynamic Coefficient Modelling Histogram of Errors . . . 285
7.7 Single-point Airfoil Optimisation by the AM-PSO with ANN developed by an Offline-training Approach . . . 286
7.8 Flowchart of the Design Process by the Direct & Surrogate-Based Fitness Evaluation Approach . . . 289
7.9 Optimisation by the AM-PSO Based Online Surrogate Model Development Approach for Fitness Evaluation . . . 292
7.10 Rosenbrock Function ANN Approximation Training Performance . . . 300
7.11 Rosenbrock Function ANN Approximation Training Error Histogram . . . 301
7.12 Rosenbrock Function ANN Approximation Regression Analysis . . . 302
7.13 Rosenbrock Function ANN Training Regression Curve & Error Performance . . . 303
7.14 Rosenbrock ANN Pattern Recognition Surrogate Model Development Training Performance . . . 306
7.15 General Representation of a Confusion Matrix . . . 306
7.16 Rosenbrock ANN Pattern Recognition Confusion Matrix Analysis . . . 308
7.17 Rosenbrock ANN Pattern Recognition Training Error Histogram . . . 309
7.18 Rosenbrock ANN Pattern Recognition Receiver Operating Characteristic . . . 311
7.19 Rosenbrock ANN Pattern Recognition Classification Ensemble Accuracy . . . 312

A.1 Airfoil Shape Parameterisation by the Hicks-Henne Approach . . . 328

A.2 Airfoil Shape Parameterisation by the NACA Functions . . . 329
A.3 Airfoil Shape Parameterisation by the Wagner Functions . . . 330
A.4 Airfoil Shape Parameterisation by the Bernstein Functions . . . 331
A.5 Airfoil Shape Parameterisation by the Legendre Functions . . . 332

B.1 Rosenbrock Function: Effect of Particle Population & Velocity on Fitness by the AMPSO Algorithm . . . 333
B.2 Ackley Function: Effect of Particle Population & Velocity on Fitness by the AMPSO Algorithm . . . 334
B.3 Michalewics Function: Effect of Particle Population & Velocity on Fitness by the AMPSO Algorithm . . . 335
B.4 Schwefel Function: Effect of Particle Population & Velocity on Fitness by the AMPSO Algorithm . . . 336

C.1 Ackley Function: Demonstration of Swarm Search Progress to Global Point . . . 337
C.2 Michalewics Function: Demonstration of Swarm Search Progress to Global Point . . . 338
C.3 Rosenbrock Function: Demonstration of Swarm Search Progress to Global Point . . . 339

D.1 Effect of y_{te} on Airfoil Geometry . . . 340
D.2 Effect of y_{te} on Airfoil Aerodynamics . . . 340
D.3 Effect of t_{eg} on Airfoil Geometry . . . 341
D.4 Effect of t_{eg} on Airfoil Aerodynamics . . . 341
D.5 Effect of t_{ew} on Airfoil Geometry . . . 341
D.6 Effect of t_{ew} on Airfoil Aerodynamics . . . 342
D.7 Effect of x_u on Airfoil Geometry . . . 342
D.8 Effect of x_u on Airfoil Aerodynamics . . . 342
D.9 Effect of y_{xxu} on Airfoil Geometry . . . 343
D.10 Effect of y_{xxu} on Airfoil Aerodynamics . . . 343
D.11 Effect of x_l on Airfoil Geometry . . . 343
D.12 Effect of x_l on Airfoil Aerodynamics . . . 344
D.13 Effect of y_l on Airfoil Geometry . . . 344
D.14 Effect of y_l on Airfoil Aerodynamics . . . 344
D.15 Effect of y_{xxl} on Airfoil Geometry . . . 345
D.16 Effect of y_{xxl} on Airfoil Aerodynamics . . . 345

E.1 PARSEC Variables Solution Space Mapping for Airfoil Design at HALE Mach Numbers 346
E.2 PARSEC Variables Solution Space Mapping for Airfoil Design at Transonic Mach Numbers . . . 347
E.3 CST BPO2 Variables Solution Space Mapping for Airfoil Design at HALE Mach Numbers 348
E.4 CST BPO2 Variables Solution Space Mapping for Airfoil Design at Transonic Mach Numbers . . . 349
E.5 CST BPO3 Variables Solution Space Mapping for Airfoil Design at HALE Mach Numbers 350
E.6 CST BPO3 Variables Solution Space Mapping for Airfoil Design at Transonic Mach Numbers . . . 351
E.7 CST BPO4 Variables Solution Space Mapping for Airfoil Design at HALE Mach Numbers 352
E.8 CST BPO4 Variables Solution Space Mapping for Airfoil Design at Transonic Mach Numbers . . . 353
E.9 CST BPO5 Variables Solution Space Mapping for Airfoil Design at HALE Mach Numbers 354
E.10 CST BPO5 Variables Solution Space Mapping for Airfoil Design at Transonic Mach Numbers . . . 356

F.1 Qualitative Representation of the Relationship of PARSEC Airfoil Design Variables on c_l, c_d & c_m . . . 359

F.2 Qualitative Representation of the Relationship of PARSEC Airfoil Design Variables on Airfoil Boundary Layer Transition . . . 360
F.3 PARSEC-Modified Variables Pre-Screening: Two-Way Interactions on Coefficient of Drag at Transonic Flight Envelope . . . 361
F.4 PARSEC-Modified Variables Pre-Screening: Impact of Two-Way Interactions on Airfoil Upper Surface Shock Wave One Chord Location at Transonic Flight Envelope . . . 362
F.5 PARSEC-Modified Variables Pre-Screening: Impact of Two-Way Interactions on Airfoil Upper Surface Shock Wave Two Chord Location at Transonic Flight Envelope . . . 363
F.6 Two-Way Interactions on Coefficient of Moment; $R_n = 2.76 \times 10^6$, Mach=0.74 & $c_l^T = 0.733$ . . . 364
F.7 Two-Way Interactions on Minimum c_p Airfoil Chord Location; $R_n = 2.76 \times 10^6$, Mach=0.74 & $c_l^T = 0.733$ . . . 365

G.1 PARSEC Variables Contribution to Airfoil Aerodynamics at HALE Flight Envelope . . . 367
G.2 PARSEC Variables Contribution to c_d & $c_{l_{max}}$ at HALE Flight Envelope . . . 368
G.3 PARSEC-Modified Variables Contribution to Airfoil Aerodynamics at HALE Flight Envelope . . . 369
G.4 PARSEC-Modified Variables Contribution to Airfoil Aerodynamics at Transonic Flight Envelope . . . 370

H.1 Effect of TSFOIL Node Distribution on Aerodynamic Convergence at Transonic Conditions; Mach=0.74, $R_n = 2.70 \times 10^6$ & $\alpha = 2°$ . . . 371

I.1 RAE 2822 Lift-Curve Slope Estimation by α_{trim} for c_l^T Estimation Approach . . . 372
I.2 RAE 2822 Aerodynamic Coefficients at Target Lift by α_{trim} Approach . . . 372

J.1 Transonic Airfoil Design Boxplot Analysis of the Computed c_l^T of each Airfoil Modeled by a Particle in the Swarm . . . 373
J.2 Transonic Airfoil Design Histogram Analysis of the $c_l^T = 0.733$ Distribution For Select Particles in the Swarm . . . 374

K.1 Transonic Airfoil Optimisation at $c_l^T \approx 0.733$ . . . 375
K.2 Transonic Airfoil Design Convergence toward an Optima by the PARSEC-Modified Reduced Variable Set Modeling Approach . . . 376

L.1 Ackley Function ANN Approximation Training Performance . . . 377
L.2 Ackley Function ANN Approximation Training Error Histogram . . . 378
L.3 Ackley Function ANN Approximation Regression Analysis . . . 378
L.4 Ackley Function ANN Training Regression Curve & Error Performance . . . 379
L.5 Ackley ANN Pattern Recognition Training Performance . . . 379
L.6 Ackley ANN Pattern Recognition Confusion Analysis . . . 380
L.7 Ackley ANN Pattern Recognition Training Error Histogram . . . 380
L.8 Ackley ANN Pattern Recognition Receiver Operating Characteristic . . . 381
L.9 Ackley ANN Pattern Recognition Classification Ensemble Accuracy . . . 381
L.10 Michalewics Function ANN Approximation Training Performance . . . 382
L.11 Michalewics Function ANN Approximation Training Error Histogram . . . 382
L.12 Michalewics Function ANN Approximation Regression Analysis . . . 383
L.13 Michalewics Function ANN Training Regression Curve & Error Performance . . . 384
L.14 Michalewics ANN Pattern Recognition Training Performance . . . 384
L.15 Michalewics ANN Pattern Recognition Confusion Analysis . . . 385
L.16 Michalewics ANN Pattern Recognition Training Error Histogram . . . 385
L.17 Michalewics ANN Pattern Recognition Receiver Operating Characteristic . . . 386
L.18 Michalewics ANN Pattern Recognition Classification Ensemble Accuracy . . . 386
L.19 Schwefel Function ANN Approximation Training Performance . . . 387
L.20 Schwefel Function ANN Approximation Training Error Histogram . . . 387

L.21 Schwefel Function ANN Approximation Regression Analysis 388
L.22 Schwefel Function ANN Training Regression Curve & Error Performance 389
L.23 Schwefel ANN Pattern Recognition Training Performance 389
L.24 Schwefel ANN Pattern Recognition Confusion Analysis 390
L.25 Schwefel ANN Pattern Recognition Training Error Histogram 390
L.26 Schwefel ANN Pattern Recognition Receiver Operating Characteristic 391
L.27 Schwefel ANN Pattern Recognition Classification Ensemble Accuracy 391

List of Tables

1.1 UAV Tier Classification Category [7] . . . 4
1.2 RC-MM-UAV Mission Classification [7] . . . 6
1.3 Flight Profile Mission Segment Requirements for Optimal Performance [2] . . . 7

3.1 Latin Hypercube Sample . . . 65
3.2 Benchmark Validation Test Functions . . . 91
3.3 PSO Variant Types & Test Validation Set-Up . . . 93
3.4 Rosenbrock Function: Fitness Evaluation Comparison by S-PSO, AIWPSO [8] & AM-PSO with Velocity at 0.10% of x_{max} . . . 96
3.5 Rosenbrock Function: Fitness Evaluation Comparison by S-PSO, AM-PSO & AIWPSO [8] Algorithms with Velocity at 100% of x_{max} . . . 97
3.6 Test Function Simulation Results . . . 111

4.1 Inverse Shape Fitting by the Analytical Approach Function Definition . . . 118
4.2 Effect of Wall Boundary Condition Type on Inverse Shape Fitting by the Hicks-Henne Functions . . . 120
4.3 PARSEC Airfoil Design Parameters . . . 128
4.4 PARSEC Airfoil Design Variable Definition Test Case Study . . . 129
4.5 PARSEC-Modified Airfoil Design Parameters . . . 135
4.6 Inverse Shape Fitting Measure of Accuracy of the PARSEC-Modified Approach by an Aerodynamic Convergence Analysis; $\alpha = 2°$, $R_n = 3.0 \times 10^6$ & Mach=0.50 . . . 140
4.7 Airfoil Category types for Solution Space Mapping . . . 144
4.8 PARSEC-Modified Solution Search Space for Airfoil Design at HALE Mach Numbers 146
4.9 PARSEC-Modified Solution Search Space for Airfoil Design at Transonic Mach Numbers 147
4.10 PARSEC-Modified Variables Contribution to c_d at HALE Flight Conditions; Mach=0.10, $R_n = 4.00 \times 10^6$, $\alpha = 2°$ & $c_{l_{max}}$ at Mach=0.10, $R_n = 3.00 \times 10^6$ & $\alpha = \alpha_{c_{l_{max}}}$ . . . 152
4.11 PARSEC-Modified Variables Contribution to $c_{d_{wave}}$ at Transonic Flight Envelope; Mach=0.74, $R_n = 2.70 \times 10^6$ & $c_l = 0.733$ . . . 153

5.1 NLF(1)-0416 Airfoil Validation with Experiment [6] by the 3 Equation $k - kl - \omega$ Transition Turbulence Model; $M_\infty = 0.10$, $\alpha = [-3°, \cdots, +10°]$ & $R_n = 4.0 \times 10^6$ . . . 164
5.2 NLF(1)-0416 Airfoil Validation with Experiment [6] by the 4 Equation $k - \omega$ SST Transition Turbulence Model; $M_\infty = 0.10$, $\alpha = [-3° - 10°]$ & $R_n = 4.0 \times 10^6$ . . . 165
5.3 RAE 2822 Computational Data Comparison with Experiment [9] by the $k - \omega$ SST Transition Turbulence Model with Mean Velocity for Flow Initialisation; M_∞=0.740, $\alpha = 3.19°$ & $R_n = 2.7 \times 10^6$ . . . 178
5.4 RAE 2822 Computational Data Comparison with Experiment [9] by $k-w$ SST Transition Turbulence Model with the FMG Initialisation Approach; M_∞=0.740, $\alpha = 3.19°$ & $R_n = 2.7 \times 10^6$ . . . 179

6.1 MM-UAV Mission Profile Aerodynamic Design Conditions . . . 186
6.2 Aerodynamics of Converged Shapes with Disparate Initial Starting points for HALE Airfoil Optimisation with Gradient Method . . . 189

6.3 Aerodynamics of Converged Shapes with Disparate Initial Starting points for HALE Airfoil Optimisation with Gradient Method, AM-PSO & Hybrid Optimisation Strategy 191
6.4 HALE Single-Point Airfoil Optimisation Objective Measure by the AM-PSO Method with XFOIL . . . 200
6.5 HALE Single-Point Airfoil Optimisation Constraints Measure by the AM-PSO Method with XFOIL . . . 200
6.6 HALE Multi-Point Airfoil Optimisation Objective Measure at Cruise $c_l^T = 0.40$ by the AM-PSO Method with XFOIL . . . 206
6.7 HALE Multi-Point Airfoil Optimisation Objective Measure at Climb $c_l^T = 1.00$ by the AM-PSO Method with XFOIL . . . 207
6.8 HALE Multi-Point Airfoil Optimisation Constraints Measure by the AM-PSO Method with XFOIL . . . 208
6.9 HALE Airfoil Optimisation Comparison of Constraints Measure by the AM-PSO Method with XFOIL & Full Set PARSEC-Modified Shape Function for Single, Multi & Robust Design Approach . . . 217
6.10 HALE Single-Point Airfoil Optimisation Objective Measure by the AM-PSO, AM-PSO Perturbation & Hybrid Optimisation Approach with XFOIL . . . 220
6.11 HALE Single-Point Airfoil Optimisation Constraints Measure by the AM-PSO, AM-PSO Perturbation & Hybrid Optimisation Approach with XFOIL . . . 220
6.12 HALE Multi-Point Airfoil Optimisation Objective Measure by the AM-PSO, AM-PSO Perturbation, Hybrid Optimisation & Perturbation of the Hybrid Approach with XFOIL at Cruise $c_l^T = 0.40$ . . . 222
6.13 HALE Multi-Point Airfoil Optimisation Constraints Measure by the AM-PSO, AM-PSO Perturbation, Hybrid Optimisation & Perturbation of the Hybrid Approach with XFOIL at Cruise $c_l^T = 0.40$ . . . 222
6.14 HALE Multi-Point Airfoil Optimisation Objective Measure by the AM-PSO, AM-PSO Perturbation, Hybrid Optimisation & Perturbation of the Hybrid Approach with XFOIL at Climb $c_l^T = 1.00$ . . . 223
6.15 Validation of the AoA Trimming Methodology by Performance Evaluation at $c_{l_{cruise}}$ of the NLF(1)-0416 Airfoil with Low and High-Fidelity Solvers . . . 230
6.16 HALE Single-Point Airfoil Optimisation Results by the AM-PSO Method with FLUENT 234
6.17 HALE Single-Point Airfoil Optimisation Convergence Assessment by the AM-PSO Method with FLUENT . . . 236
6.18 HALE FLUENT-Based Single-Point Airfoil Optimisation Aerodynamic Performance Definition by the AM-PSO & AM-PSO/Gradient Method . . . 238
6.19 HALE FLUENT-Based Single-Point Airfoil Optimisation Constraint Definition by the AM-PSO & AM-PSO/Gradient Method . . . 239
6.20 Transonic Single-Point Airfoil Optimisation Results by the AM-PSO Method with FLUENT . . . 248
6.21 Transonic Single-Point Airfoil Optimisation Convergence Assessment by the AM-PSO Method with FLUENT . . . 251
6.22 Transonic FLUENT-Based Single-Point Airfoil Optimisation Aerodynamic Performance by the AM-PSO & AM-PSO/Gradient Method . . . 253
6.23 Transonic Single-Point Airfoil Optimisation Convergence Assessment by the AM-PSO/GM Method with FLUENT . . . 258

7.1 Offline Training-based Optimal Neural Network Configuration for Lift and Drag Coefficient . . . 284
7.2 Offline Training-based Optima Airfoil Aerodynamics & Fitness . . . 287
7.3 Rosenbrock Function - ANN Pattern Recognition Classification Accuracy Measure by ROC Curve Representation . . . 311
7.4 Validation of the online-based ANN Training Methodology with AM-PSO Algorithm for Design Optimisation . . . 313

A.1 Convergence to Target Airfoil NACA 0012 by the Hicks-Henne Functions . . . 327

A.2 Convergence to Target Airfoil NACA 0012 by the NACA Shape Functions 328
A.3 Convergence to Target Airfoil NACA 0012 by the Wagner Functions 330
A.4 Convergence to Target Airfoil NACA 0012 by the Bernstein Polynomials 331
A.5 Convergence to Target Airfoil NACA 0012 by Legendre Polynomials 332

E.1 PARSEC Variables Solution Space Mapping for Airfoil Design at HALE Mach Numbers 347
E.2 PARSEC Variables Solution Space Mapping for Airfoil Design at Transonic Mach Numbers 348
E.3 CST BPO2 Variables Solution Space Mapping for Airfoil Design at HALE Mach Numbers 349
E.4 CST BPO2 Variables Solution Space Mapping for Airfoil Design at Transonic Mach Numbers 350
E.5 CST BPO3 Variables Solution Space Mapping for Airfoil Design at HALE Mach Numbers 351
E.6 CST BPO3 Variables Solution Space Mapping for Airfoil Design at Transonic Mach Numbers 352
E.7 CST BPO4 Variables Solution Space Mapping for Airfoil Design at HALE Mach Numbers 353
E.8 CST BPO4 Variables Solution Space Mapping for Airfoil Design at Transonic Mach Numbers 354
E.9 CST BPO5 Variables Solution Space Mapping for Airfoil Design at HALE Mach Numbers 355
E.10 CST BPO5 Variables Solution Space Mapping for Airfoil Design at Transonic Mach Numbers 357

L.1 Ackley Function - ANN Pattern Recognition Classification Accuracy Measure by ROC Curve Representation 381
L.2 Michalewics Function - ANN Pattern Recognition Classification Accuracy Measure by ROC Curve Representation 386
L.3 Schwefel Function - ANN Pattern Recognition Classification Accuracy Measure by ROC Curve Representation 391

List of Algorithms

1 Standard Optimisation by Gradient-Based Framework 42
2 Standard Global-Based PSO Algorithm 58
3 Standard Local-Based PSO Algorithm 59
4 AM-PSO Algorithm 73
5 Sequential SOM Training Algorithm 78
6 Batch SOM Training Algorithm 80
7 Online Artificial Neural Network Training based on AM-PSO Design Principles 293

Abbreviations

ACO	**A**nt **C**olony **O**ptimisation
AIW	**A**daptive **I**nertia **W**eight
AIWPSO	**A**daptive **I**nertia **W**eight **P**article **S**warm **O**ptimisation
AM-PSO	**A**daptive **M**utation - **P**article **S**warm **O**ptimisation
ANN	**A**rtificial **N**eural **N**etworks
AoA	**A**ngle-**o**f-**A**ttack
AUC	**A**rea **U**nder **C**urve
BB	**B**aldwin-**B**ath
BMU	**B**est **M**atching **U**nit
BP	**B**ernstein **P**olynomial
BPO	**B**ernstein **P**olynomial **O**rder
BWB	**B**lended **W**ing **B**ody
CFD	**C**omputational **F**luid **D**ynamics
D	**D**imension Size
DACE	**D**esign and **A**nalysis of **C**omputer **E**xperiments
DNO	**D**irect **N**umeric **O**ptimisation
DoE	**D**esign **o**f **E**xperiments
DTE	**D**ivergent **T**railing **E**dge
DV	**D**esign **V**ariable
EI	**E**xpected **I**mprovement
FMG	**F**ull **M**ulti **G**rid
FN	**F**alse **N**egative
FP	**F**alse **P**ositive
FPR	**F**alse **P**ositive **R**ate
HALE	**H**igh **A**ltitude **L**ong **E**ndurance
HAME	**H**igh **A**ltitude **M**edium **E**ndurance
IPE	**I**nexact **P**re-**E**valuation
IQR	**I**nter **Q**uartile **R**ange
ISR	**I**ntelligence **S**urveillance **R**econnaissance

LAME	**L**ow **A**ltitude **M**edium **E**ndurance
LRN	**L**ow **R**eynolds **N**umber
LSB	**L**aminar **S**eparation **B**ubble
MAME	**M**edium **A**ltitude **M**edium **E**ndurance
MDO	**M**ultidisciplinary **D**esign **O**ptimisation
MM-UAV	**M**ulti **M**ission - **U**nmanned **A**erial **V**ehicle
MSE	**M**ean **S**quared **E**rror
MTOW	**M**aximum **T**ake-**o**ff **W**eight
NACA	**N**ational **A**dvisory for **C**ommittee for **A**eronautics
NLF	**N**atural **L**aminar **F**low
NS	**N**avier-**S**tokes
OP	**O**ptimal **P**oint
PDE	**P**artial **D**ifferential **E**quation
PRS	**P**olynomial **R**esponse **S**urface
PS	**P**ressure **S**ide
PSO	**P**article **S**warm **O**ptimisation
RANS	**R**eynolds **A**verage **N**avier **S**tokes
RBF	**R**adial **B**asis **F**unction
RC	**R**e **C**onfigurable
RC-MM-UAV	**R**e **C**onfigurable - **M**ulti **M**ission - **U**nmanned **A**erial **V**ehicle
RLV	**R**eusable **L**aunch **V**ehicle
ROC	**R**eceiver **O**perating **C**haracteristic
SA	**S**palart-**A**llmaras
SEAD	**S**uppression of **E**nemy **A**ir **D**efense
SOM	**S**elf-**O**rganising-**M**ap
S-PSO	**S**tandard - **P**article **S**warm **O**ptimisation
SQP	**S**equential **Q**uadratic **P**rogramming
SS	**S**uction **S**ide
SST	**S**hear **S**tress **T**ransport
TE	**T**railing **E**dge
TN	**T**rue **N**egative
TP	**T**rue **P**ositive
TPR	**T**rue **P**ositive **R**ate
UAV	**U**nmanned **A**erial **V**ehicle
UCAV	**U**nmanned **C**ombat **A**erial **V**ehicle
VPAC	**V**ictorian **P**artnership for **A**dvanced **C**omputing

Symbols

A	Online-training Neural Network Data Points Archive	–
c	Airfoil Chord Length	m
c_1 & c_2	Stochastic Acceleration Terms	–
c_d	Coefficient of Drag	–
$c_{d_{wave}}$	Coefficient of Wave Drag	–
cj	Expected maximum cost to repair constraint j	–
c_l	Coefficient of Lift	–
c_{lmax}	Maximum Coefficient of Lift	–
$c_{lmax_{pen}}$	Maximum Coefficient of Lift Penalty	–
c_l^T	Target Coefficient of Lift	–
$c_{l_{pen}^T}$	Target Coefficient of Lift Penalty	–
c_m	Pitching-moment Coefficient	–
$c_m 0$	Pitching-moment Coefficient at Zero Lift	–
$c_{m0}pen$	Pitching-moment Coefficient at Zero Lift Penalty	–
c_p	Coefficient of Pressure	–
c_p^T	Target Coefficient of Pressure	–
$\frac{d_{cp}}{d_x}$	Pressure Gradient	–
$\frac{d_{cp}}{d_x pen}$	Pressure Gradient Penalty	–
$d_i(x)$	Elementary Effect	–
d_s	Euclidean Fitness Distance between two Extreme Particles	–
f_{ANN}	Estimated Fitness	–
f_p	Fitness as a result of Penalty	–
$F_{pbesti,max}$	Maximum Particle Personal Best Fitness in the Swarm	–
$F_{pbesti,min}$	Minimum Particle Personal Best Fitness in the Swarm	–
$f_{\text{Theoretical}}$	Theoretical Fitness	–
f_x	Position Vector Measure of Fitness	–
$f_{x_{\text{mutation}}}$	Mutation Position Vector Measure of Fitness	–
$\mathcal{J}_{min}$	Fitness Minimisation	–
k	Iteration	–

K	Constriction Factor	–
L/D	Aerodynamic Efficiency Factor; Lift-to-Drag Ratio	–
$lbest$	Local Best	–
M_∞	Mach Number	–
M_i	Control Points	–
m_{mich}	Michalewics Function - Steepness of the Solution Valleys	–
mr_i	Matrix of *random* Numbers for Each Particle i	–
n	Number of Design Variables	–
$\mathcal{N}$	Number of Sample Points	–
N	Ratio of True Negative to False Negative	–
$N^{'}$	Ratio of True Negative to False Positive	–
P	Ratio of True Positive to False Positive	–
$P^{'}$	Ratio of True Positive to False Negative	–
p	Discrete Number of Levels	–
$pbestg$	Global Best Fitness	–
$pbest_i$	Particle Personal Best Fitness	–
p_f	Personal Best Fitness Range	–
$p_\mathcal{Q}$	Artificial Neural Network Training Inputs	–
pr_M	Probability of Particle Mutation	–
P_t	Receiver Operating Characteristic - Probability Threshold	–
$\mathcal{Q}$	Artificial Neural Network Training Data Size	–
r	Number of Elementary Effects for Each Variable	–
R_n	Reynolds Number	–
$\mathcal{S}$	Design Search Space	–
t/c	thickness-to-chord	–
t/c_{pen}	thickness-to-chord Penalty	–
T/W	Thrust Loading	–
T_c	Confusion Matrix - Total Number of Data Entries	–
$t_\mathcal{Q}$	Artificial Neural Network Training Targets	–
v_i	Particle Velocity	–
v_{max}	Maximum Particle Velocity	–
w	Inertia Weight	–
W/S	Wing Loading	–
w_i	Objective Function Weights	–
x	Position Vector	–
x/c	Airfoil Chord Abscissa	m
X_0	Initial Experimental Design	–
x_i	Particle Position Vector	–

$x_{mutation}$	Mutation Position Vector	–
$x_{tr_{low}}$	Boundary Layer Transition Point Location on Airfoil Lower Surface	m
$x_{tr_{up}}$	Boundary Layer Transition Point Location on Airfoil Upper Surface	m
y/c	Airfoil Chord Ordinate	m
α	Angle-of-Attack	$\circ$
α_{AIW}	Inertia Weight Positive Constant	–
$\mathcal{E}$	Euclidean Neighborhood Distance Metric	–
ϵ_{end}	User-defined Tolerance Factor	–
ε	Histogram Error Measure	–
ϵ_{ANN}	Absolute Fitness Approximation Error	–
ϕ	Stratified Sampling Function	–
ϕ_{op}	Airfoil Operating Conditions for Variable Space Mapping	–
σ_t	Fitness Standard Deviation of the Swarm	–
η_{con}	Number of Constraints	–
λ_i	Design variable	–
λ_{T_i}	Target Airfoil	–
λ_{A_i}	Approximated Airfoil	–
$\Delta_{dist.}$	Airfoil Shape Disturbances	–
ω_M	Mutation Scalar Factor	–
y^+	Dimensionless Wall Distance	-
$\overline{z}$	Fitness Mean	–
σ_z	Fitness Standard Deviation	–

Dedicated to my father, ***Gurcharan Singh Khurana*** *- For his bravery & courage*

Chapter 1

Introduction

1.1 Overview

Aircraft design is a multi-disciplinary and complex process. The design principles require optimal integration of aerospace engineering sub-disciplines of aerodynamics, structures and materials, propulsion and associated areas to establish a functionally viable aircraft system. The design methodologies are concurrently applied, developed and optimised to attain a viable platform. A holistic systems-based approach is established to form an effective design methodology that conforms to user-defined requirements and design goals.

Research efforts in Aviation focus on addressing the following fundamental issues and challenges: **a)** Minimise the impact of aviation on greenhouse gas emissions, hence climate change; **b)** Improve aircraft fuel efficiency; and **c)** Mitigating noise pollution, especially around airports. An economy affected by recessions and/or increases in oil prices has a negative impact on profits for commercial carriers. Efficient airplane configurations will be less susceptible to global economic instabilities as aviation fuel prices are directly proportional to world peak oil production rates and by the direct influence of world political leaders to address economic events. A fuel efficient airplane configuration will reduce emissions, thus mitigating the aviation impact on the environment and the operating costs will further be minimised [10]. Research efforts examining alternate fuel types to minimise the impact of emissions on the environment and to further reduce fuel rate-of-burn are currently at the forefront of aerospace design and analysis. Hydrogen and bio-kerosene based fuel types were considered, but no substantial reduction in green-house gas emissions were observed [11]. Alternative fuel types are currently under research analysis [12].

Design development of an efficient aircraft configuration is the direct result of the shape optimisation process. In this thesis, novel aerodynamic shape optimisation algorithms are developed. The presented principles are valid for direct integration into a multidisciplinary design optimisation (MDO) framework. The design methodologies will facilitate a valid aircraft design process and address the identified issues and challenges within the Aviation industry.

1.2 Background

Shape optimisation is applied in various engineering designs as follows:

1. **Rail transportation**: There have been rapid advancements in the rail industry with the development of fast, bullet-trains. A streamlined nose profile contour is generated as a result of the shape optimisation process for drag minimisation purposes [13].

2. **Automotive**: The automotive industry applies shape optimisation particularly in the design of formula one racing cars. Shape optimisation algorithms are applied for the purposes of minimising drag and maximising downforce, at high-speeds and at turn maneuvers. Endplates are developed and attached to front and rear wings, with the aim of minimising induced drag. A compromise between generating sufficient downforce at corners, while directing adequate cool air to brakes and radiators at high speeds is a typical design constraint [14].

3. **Naval**: Shape optimisation principles are further applied in naval applications. The design development of a hydrofoil aims to minimise drag while maximising lift of the foil-strut configuration. Constraints on minimum transit speed and lifting mass performances are imposed [15]. The optimisation principles are developed to minimise noise due to turbulent flow over profile trailing-edge for stealth purposes. Typical constraints define minimum span length for lift purposes, with balance on low acoustic levels.

4. **Astronautics**: Shape optimisation is also applied in astronautical applications. The design development of a Reusable Launch Vehicle (RLV) require MDO algorithms to achieve optimal vehicle configuration. Design algorithms are used to develop insulation systems to maintain platform structural integrity due to high re-entry temperatures. They are further used to achieve a streamlined RLV design to avoid surface wall anomalies that may degrade aerodynamic performance and result in excessive wall thermal effects. Design methodologies are also applied to maintain vibrational loads at lift-off that are within the specified structural design thresholds. The successful design of the NASA space shuttle presents the validity of shape optimisation algorithms for RLV design applications within a MDO process [16].

5. **Aeronautics**

   (a) *Fixed Wing*: In fixed-wing platforms, aircraft aerodynamic efficiency is improved with novel wingtip devices. The flow turbulence at the wingtips mitigates lift generation and increases drag. The wingtip vortices create turbulence which propagate aft of the LE and inboard toward the wing root. A wingtip device shifts the vortex formation region away from the wing surface, as the center of the resulting vortex is restricted at the tip, toward the winglet [17]. The optimal configuration of the wingtip device is aircraft performance-based dependent. Shape optimisation algorithms are applied to formalise the profile of the winglet, hence improve the aerodynamic performance of the structure based on defined goals and requirements.

   (b) *Blended Wing Body*: The Blended Wing Body (BWB) concept is a direct result of an extensive shape optimisation process. The design concept provides superior aerodynamic

performance with enhanced fuel efficiency, which corresponds to extended range and endurance compared to conventional shaped platforms. The concept is viable for direct application in the design of Unmanned Aerial Vehicles (UAVs), as the performance of the platform is not restricted to the tolerances of a human pilot. The operating merits of a BWB concept can be exploited further to attain reduction in fuel burn, hence emissions levels. The application of numerical shape optimisation algorithms have been developed to address the motivating design goals [18].

(c) *Silent Aircraft Initiative*: Development of quiet aircrafts is also at the forefront of aerospace research and design. Shape optimisation principles are applied for aircraft noise reduction while conforming to defined constraints. Streamlined designs by a MDO design definition process are applied and integrated with acoustic design principles to maximise aerodynamic efficiency and minimise airframe noise. Engines are major noise sources and the following components attribute to the acoustic levels from the propulsion unit [19]: **a)** Jet noise, due to the mixing of the air stream between the core efflux, the bypass exhaust flow and the ambient freestream air; **b)** Fan noise, from the front and rear of the engine profile; **c)** Turbine noise, which is dominant at landing and is from the rearward section of the engine; **d)** Compressor noise, which is dominant at the frontal section of the engine and; **e)** Buzz-saw noise, which occurs when the tips of the fan blades are at a velocity near the speed of sound at take-off [19]. Engine manufacturers are continuously developing novel shape design algorithms to minimise the noise signature.

(d) *Rotary Wing*: In rotary wing designs, the blade profile is designed as a function of design objectives and constraints. High maneuver load factors require high static and dynamic lift coefficients, hence a blade airfoil with a high Mach divergence number is a design goal [20]. Stealth is maintained by shape optimisation algorithms that control rotor blade tip speed, with the result of reducing noise emissions to increase survivability. The constraints on skin profile contour angles are also imposed to control the extent of radar signal absorption and reflection. Shape optimisation algorithms have been developed to address the identified goals and performance constraints [21].

The presented application classes validate the merits of shape optimisation algorithms for configuration design and development. The proposed design methodology is extended in this thesis for airfoil aerodynamic design and optimisation for a MM-UAV platform.

1.3 Design Application

Unmanned aerial vehicle operations in the Australian civil sector has been restricted to atmospheric monitoring and aerial photography with mineral exploration emerging as a new sector [22]. From the defense view point, the Australian Defence Force's - AIR 7000 project Request-for-Proposal initiated market interest in the development of a Multi-Role UAV. The JP129 project was also initiated with the aim of developing a tactical UAV for Intelligence, Surveillance, Target Acquisition and Reconnaissance Capabilities. The AIR 7000 project was primarily initiated with the aim of replacing the AP-3C Orion whilst incorporating the added flexibility of High-Altitude Long Endurance Surveillance

sorties for Maritime Patrol and Response missions to Land and Electronic Surveillance Roles [23]. The operational envelope within which UAVs operate are wide requiring the need of designs with multi-rotary, multi-mission capabilities. A Tier of UAVs based on future operational requirements was identified such that a common classification based on operating performance metric could be established (Table 1.1) [22].

Category	**Designation**	**Max. Alt. [ft]**	**Radius [km]**	**Cruise Speed [kts]**	**Endurance [hrs]**
Tier I	Interim-Medium Alt. Endurance	15,000	250	60-100	5-24
Tier II	Medium Alt. Endurance	3,000-25,000	900	70	>24
Tier II Plus	High Alt. Endurance	65,000	5,000	350	42
Tier III Minus	Low Observable-High Alt. Endurance	45,000-65,000	800	300	12

TABLE 1.1: UAV Tier Classification Category [7]

The study by Wong [22] indicated the need to develop a multi-role platform for implementation within the Australian industry. A set of mission performance requirements of the platform are needed for the design exercise. The Australian market survey provided an overview of typical missions that would provide operational benefits when implemented within the Australian market sector. The results of the market survey are used as a case for the following: **a)** Identification of suitable missions within the civil and defense sectors; and **b)** Formulation of mission performance requirements that satisfy the proposed mission.

A sizing process was undertaken for each mission for weights calculations [7]. The design performance requirements of each mission in terms of range and endurance characteristics, operating speeds and altitudes, lift, cruise and maneuver roles were mapped onto a wing and thrust loading chart. The chart was then used to identify combinations of wing and thrust loading which adequately satisfies the proposed mission requirements. The wing-thrust loading combination provides the first indication of the trade-off in size of the platform in terms of wing area and thrust loading required to achieve the foreseen mission.

The maximum take-off weight (MTOW) is the aggregate weights of the UAV, fuel and payload. The combination of wing-thrust loading provides an initial estimate of MTOW based on the required wing area and maximum thrust requirements. The payload is dependent on mission requirements. A set of base line, off-the-shelf components, included navigation, avionics, sensory and communications systems that are common to each mission were identified and the individual component weights recorded. The mission specific payloads such as survivability systems to imagery equipment for weather monitoring and mineral exploration were identified. The combination of baseline and mission specific components provided the total payload mass estimate. The combination of fuel and empty mass were then calculated by using a series of empirical equations and charts. Statistical relationship exists between the structural weight of the UAV and fuel for a specified MTOW, with

the data correlated across various classes of civil and defense aircrafts [24, 25]. Given that MTOW was established from the matching chart, the ratio $\frac{M_{fuel}}{M_{empty}}$ for each mission was evaluated.

A sizing methodology was undertaken to compute the MTOW and wing area of each mission. The results are transformed into a design envelope to map the variances of MTOW and wing area for the proposed mission package (Fig. 1.1).

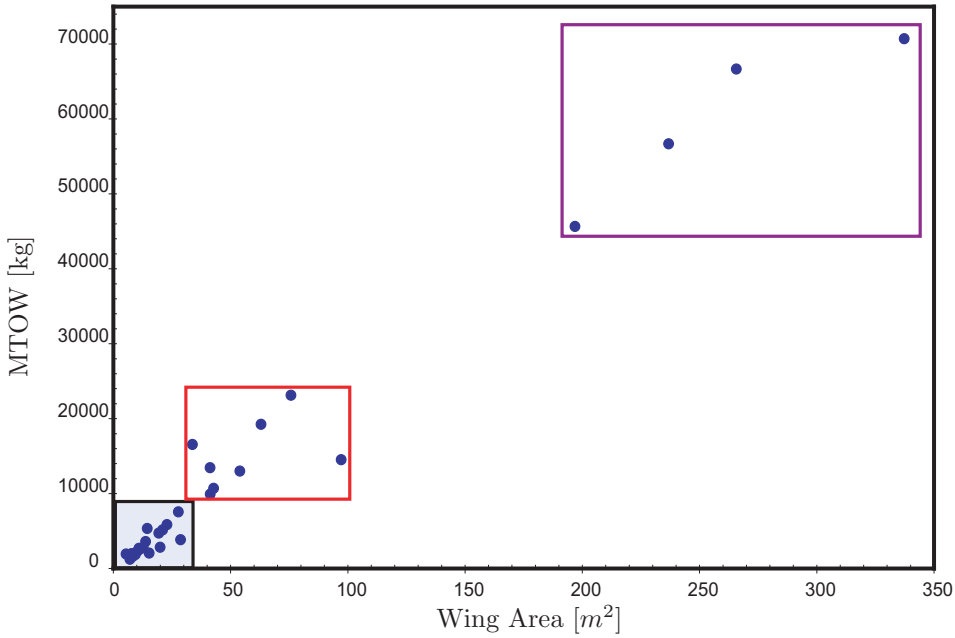

(a) RC-MM-UAV Mission Spectrum

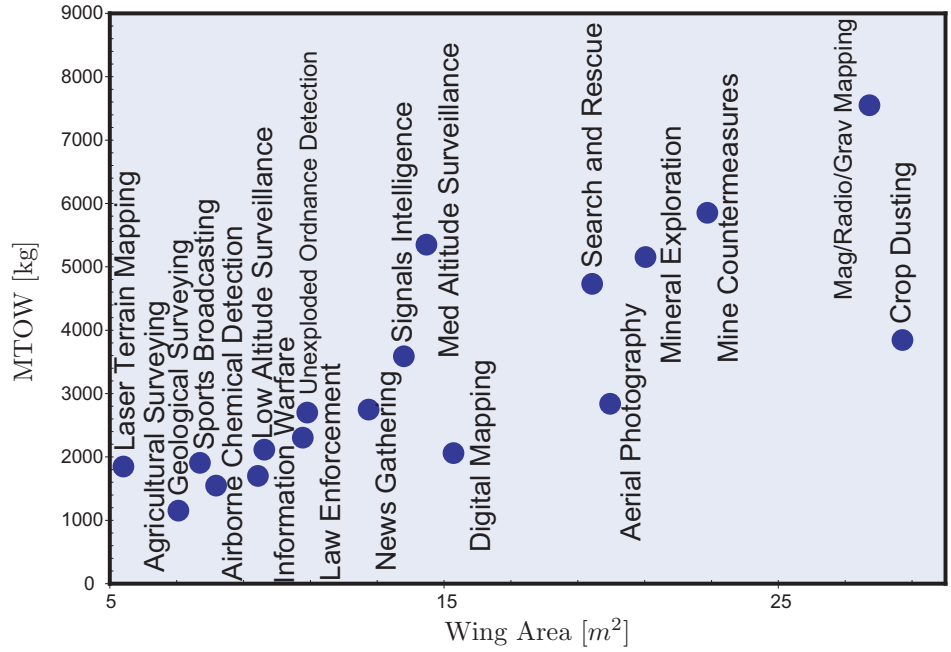

(b) RC-MM-UAV Mission Types for Restricted Design Envelope

FIGURE 1.1: Mission Market Survey for Australian Military & Civil Sectors [1]

The missions are sampled into three groups (Fig. 1.1(a)) as a function of MTOW and wing area. A large sample of missions from the market survey are in group one and are classified with a MTOW

range of $\approx 4,000 - 10,000kg$ with wing area interval $\approx 5 - 30m^2$ (Fig. 1.1(b)). The mission types in group one are detailed in Figure 1.1(b) for Australian military and civil sectors. The sizing of the missions is directly related to the design requirements. Crop dusting operations is at slow cruise Mach numbers (< 0.10) and low operating altitudes ($< 5,000ft$). A large wing area ($\approx 29m^2$) is required to satisfy the lift requirements at the defined flight conditions. The Magnetic, Radio and Gravity Mapping mission requires multiple sensor based systems for mission-specific payload types, hence a high MTOW (Fig. 1.1(b)). Laser terrain mapping has a low endurance constraint of 10 hours and range performance of 1,000 km with a cruise altitude at 20,000 ft. Mission specific payload consists of a Synthetic Aperture Radar and with low requirements for endurance and range, the MTOW is low (Fig. 1.1(b)). The missions are allocated into groupings of low altitude medium endurance (LAME), medium altitude medium endurance (MAME), high altitude long endurance (HALE) and UCAV based designs. The flight parameters of the missions in the design groups (Fig. 1.1(a)) are:

Requirement	**LAME**	**MAME**	**HALE**	**UCAV**
Cruise Speed (at mission Alt.)	< Mach 0.30	< Mach 0.30	Mach 0.30	Mach 0.60-0.80
Loiter Speed (at mission Alt.)	< Mach 0.30	< Mach 0.30	Mach 0.30	< Mach 0.50-0.60
Operational Altitude	< 10,000 ft	20,000 ft	40,000 ft	20,000 ft
Maximum Altitude	10,000 ft	30,000 ft	40,000 ft	30,000 ft
Payload Mass	100 kg	250 kg	350 kg	500 kg
Endurance	12 hr	24 hr	24 hr	4 hr
Range Radius	200 km	500 km	1000 km	1000 km

TABLE 1.2: RC-MM-UAV Mission Classification [7]

In this thesis, airfoil optimisation algorithms are developed and applied for airfoil design for a specific mission type from group one (Fig. 1.1(a)). The mission selected has segments of low and high speed operations for intelligence, surveillance and reconnaissance (ISR) and suppression of enemy air defense units (SEAD) sorties. Mission segment based airfoils are established by the novel shape design algorithm for the identified flight segments. The MM-UAV will have the design flexibility to operate at different flight conditions including speeds and altitudes with optimal performance as a result of the shape optimisation process.

1.3.1 Wing Morphing for RC-MM-UAV

Present unmanned aerial platforms apply fixed wing geometries and are mission specific designs. Unmanned platforms provide a cost and mission effective performance in comparison to manned systems as they can operate in remote and dangerous regions for extended period of time, without

endangering the crew. Present UAVs are designed for single missions which has resulted in a large inventory of UAVs with inherent 'issues and challenges' of operation and support [26]. Operators face high acquisition costs due to a large fleet of UAVs. Considering the envisaged future mission requirements, a single mission design concept is neither operationally nor cost effective. Hence, there is a demand by the industry to develop a robust UAV system. A multi-mission platform has been widely acknowledged worldwide both on civil and military fronts as a viable design concept to address the issues of uni-mission based platforms [26]. A Multi-Mission UAV is a viable solution to the demerits of a uni-mission based platform and will provide greater mission effectiveness.

There is a performance compromise between the different mission segments due to the restrictions in wing shape morphing. High dash speed maneuvers on HALE specific platforms is operationally infeasible. Flight operations exceeding the design intent is not viable. Platforms must have the flexibility to adapt to changes in mission objectives and goals for an overall efficient flight performance for all mission segments. The platform needs to address the variations in flight performances with speed and altitudes without compromising the efficiency of the system. The performance requirements at specific mission segments is defined in Table 1.3:

Mission Segment	**Altitude [ft]**	**Velocity/Mach Number**	**Performance Metric**
Take-off	Sea Level	$V = 0$ to V_{LO}	Minimise Time to Accelerate
Climb 1	Sea Level	$V_{Best\ ROC}$	$\uparrow ROC_{max}$
Climb 2	30,000	$V_{Best\ ROC}$	$\uparrow ROC_{max}$
Cruise 1	Sea Level	$V_{Best\ Range}$	$\uparrow (L/D)_{max}$
Cruise 2	30,000	$V_{Best\ Range}$	$\uparrow (L/D)_{max}$
Acceleration	30,000	$M = 0.50$	$\downarrow Drag_{min} \therefore \uparrow Acceleration_{max}$
Dash	30,000	V_{max}	$\uparrow V_{max}$
Endurance	40,000	$V_{Best\ Endurance}$	$\uparrow (L/D)_{max}$
Instantaneous Turn	Sea Level	$Corner\ Speed$	$\uparrow (Turn\ Rate)_{max}$
Sustained Turn	40,000	$V_{Best\ Turn\ Rate}$	$\uparrow (Turn\ Rate)_{max}$

TABLE 1.3: Flight Profile Mission Segment Requirements for Optimal Performance [2]

Each mission segment in Table 1.3, has specific goals that must be achieved in order to attain optimal flight performance. The morphing of wings will facilitate a multi-dimensional operational spectrum for a RC-MM-UAV. The platform will have the flexibility for optimal performance with flexibility in wing planform morphing. Variation of airfoil camber and thickness with span wing twist will address the performance requirements of a multi-mission flight profile. The development of a RC-MM-UAV will address these goals. Typical wing shape configurations for mission specific roles are presented in Figure 1.2.

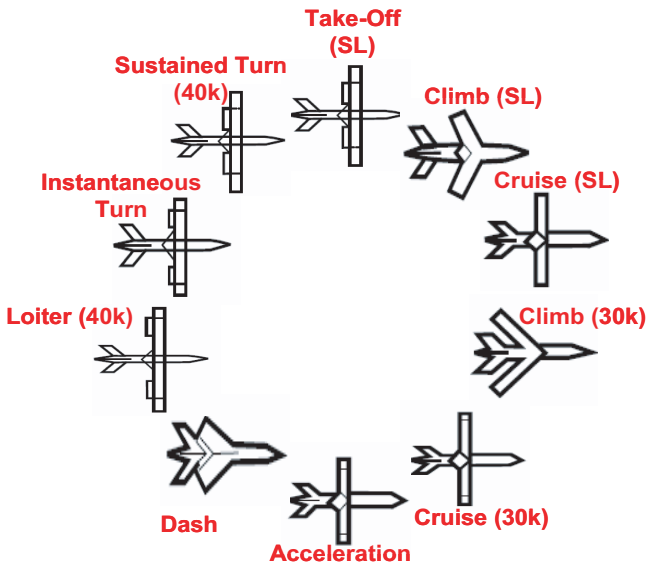

FIGURE 1.2: Morphing Wing Configuration for Optimal Aerodynamic Mission Performance [2]

Slow speed maneuvers at take-off and landing are achieved by application of high-lift devices for increased lift and drag performance in Figure 1.2. The wing area is increased accordingly to increase c_l by the extension of trailing edge wing flaps. High altitude, long endurance systems are optimised for slow speed operations to address excessive viscous drag at low Reynolds number operation. A HALE sortie in ISR role with extended endurance and range requirements, will require the maximisation of the aerodynamic efficiency factor, L/D. The airfoil/wing design process is defined accordingly and large aspect ratio wings will address the design goals. Quick dash segments at SEAD operations requires swept-back wings (Fig. 1.2), to delay the critical Mach number and address the demerits of the shock wave on drag. The disparity in aerodynamic performance goals and wing shape planforms at low and high Mach numbers for ISR and SEAD operations respectively is established in Table 1.3 and Figure 1.2. Instead of developing a uni-mission based UAV platform for low and high speed mission roles, a RC-MM-UAV platform with flexibility in payload and wing morphing is a viable alternate to address the issues and challenges of uni-mission based platforms [26].

To address the issues and challenges of current UAV systems, research efforts at RMIT University in partnership with the Technical University of Munich, have focused on the design development of a RC-MM-UAV for Australian mission requirements [1, 3–5, 7]. An automated sizing process was developed to independently size each mission based on specific mission goals and requirements. From the mission-specific W/S and T/W loadings, the wing size of each mission was defined. The initial UAV design concept is based on a reconfigurable (RC) concept to accomplish multiple mission requirements from the single platform. The proposed concept exhibits geometry flexibility in wing-span, aspect ratio and wing area, fuselage length, including payload arrangement with interchangeable bays, empennage size and also modification to the propulsion system in Figure 1.3(a).

The demerit of the proposed RC-MM-UAV concept is the complexity of the system and the operational challenges. Operators will experience issues and challenges in handling the interchangeable components. The RC concept necessitates new training processes and documentations to familiarise ground crew to maintenance and support within the RC structure. The costs associated with this

process is an issue for the operators [26]. The RC system will also require novel techniques in the handling of the RC components. The transportation and availability of the interchangeable components based on the mission requirements over vast distances is also a major issue.

To address the limitations of a RC platform, design iterations were simulated which resulted in a fixed fuselage and engine component [3, 4, 27]. The re-design concept was modeled with flexibility for high-speed operations with increased stealth for survivability based on military operations (Fig. 1.3(b)). A telescopic wing is applied to modify wing area and aspect ratio for the multi-mission flight envelope [3]. Ongoing research efforts have been focused on developing a robust planform configuration to address the operating intervals of range and endurance, hence fuel and MTOW requirements within a uni-based MM-UAV platform. Detachable payload bays to accommodate the disparity in mission specific equipment and variations in payload mass within the overall UAV planform is under investigation [4]. In this thesis, intelligent aerodynamic shape optimisation algorithms are developed for airfoil design at low-subsonic and transonic Mach numbers for the re-design of a MM-UAV platform in Figure 1.3(b).

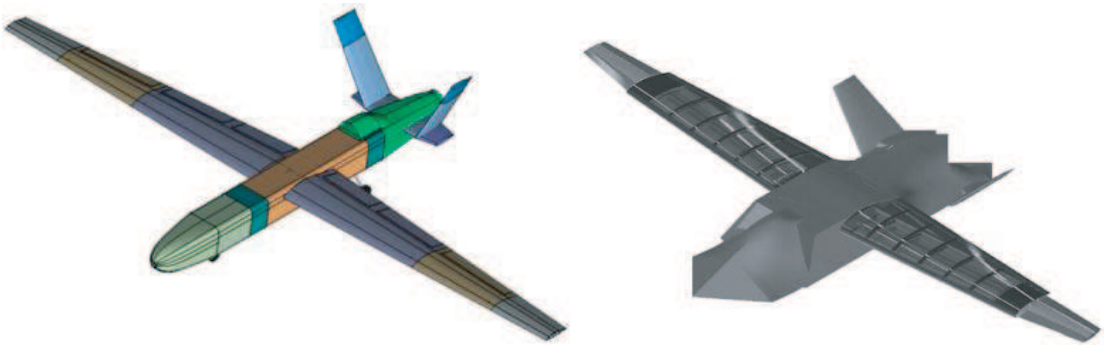

(a) Initial RC-MM-UAV Concept (b) Re-Design RC-MM-UAV Concept

FIGURE 1.3: RC-MM-UAV Design Concepts [1, 3–5]

1.4 Motivation

The goal of this research is to exploit the benefits of a UAV system with the development of a robust multi-mission platform to reduce costs and increase operating efficiency. The overall goal of this project is to support the design development of MM-UAV based on Australian industry requirements. The role of this thesis within the overall design project involves the development of intelligent shape optimisation algorithms for mission segment-based airfoils. A mission from the market survey is selected and applied as a case study in the design optimisation of airfoils. Novel design algorithms will be developed and applied to optimise the airfoil for select profile segments for the identified mission case study. The results of this thesis will facilitate future research work in the design of morphing concepts for airfoil shape change between the different mission segments. Hence, the results will facilitate continuous design development of a MM-UAV platform (Fig. 1.3(b)).

Novel planform configurations are conceptualised by a shape optimisation process. Regardless of aerial planform type from conventional configuration to the BWB model type, numerical design

optimisation algorithms are required for continuous design improvement. The motivating factor underlying aircraft design processes are governed by improvements to shape configurations to enhance fuel efficiency. The optimisation simulation has the potential for further improvements in fuel efficiency by the development of novel shape configurations, to address the user-defined objectives and constraints. Improvements in fuel efficiency involve a MDO design process that involves multiple engineering design disciplines. In aerospace applications, fuel efficiency is related to aerodynamics and weights. Hence, design improvements are related to the identified aerospace design disciplines. A MDO approach is required to attain a feasible shape configuration that maximises the operating efficiency.

The process of shape optimisation has issues and challenges that need to be addressed. Shape design comprises of three modules of study: **a)** Geometry shape parameterisation model; **b)** Computational fitness function solver; and **c)** Optimisation algorithm. The modules are integrated to formalise the design structure. The design modules need to be defined, developed and validated to facilitate acceptable shape design simulations. The analysis presented in this thesis will address these requirements. The success-of-validation of the design principles are applied to assess the feasibility of the proposed shape design process for direct application to a RC-MM-UAV.

1.4.1 Airfoil Shape Parameterisation

A. Effect of Shape Parameterisation on Design Optimisation
The effect of varying airfoil shape function and design variable population size on profile optimisation has not been comprehensively addressed in detail in the open literature. The impact of shape parameterisation function type on airfoil optimisation at low-to-high Mach numbers requires definition. If the shape function has limited flexibility, then a sub-optimal shape will be generated. If the design variable population size is increased to address this issue, the efficiency of the computational approach will be affected as the measuring location of the objective function has increased. Despite a theoretical increase in shape function flexibility, a sub-optimal shape can be generated if the optimisation algorithm has limitations for an extended dimensional search space. The number of variables for shape function type must be balanced with the design thresholds of the optimiser. Ideally, the optimiser must be developed and validated based on the required dimensional search space that maximises the flexibility of the parameterisation model. The scope of the search space resulting in a global optimal, as a function of shape function representation method and design variable population size is not *a-priori* knowledge and needs to be defined accordingly.

B. Solution Search Space Mapping
The intervals of the shape variables applied to parameterise the airfoil for design optimisation at HALE and transonic flight envelopes needs to be defined. The solution search space must be characterised by aerodynamically viable profiles that are representative of shapes which match the intent design goal. Hence, computational resources are not exhausted on simulating airfoil aerodynamics on profiles that are infeasible from the defined objective view point. The search limits of the design variables need to be mapped as a function of an airfoil performance metric. The shape coefficients are restricted to regions that are representative of airfoils that are similar to the defined design goal. The novel

methodology provides an innovative alternate relative to current processes applied in the literature, where designer intuition and experience is relied upon for the intent design study.

1.4.2 Fitness Function Solver

The suitability of applying variable-fidelity solvers for shape optimisation simulations must be defined. A comprehensive validation process must follow to evaluate the test domain and turbulence model type required to simulate the expected flow features at low and high Mach numbers. A boundary layer transition prediction model needs to be integrated into the design process to enhance the accuracy of the solver at low Mach numbers. A computational domain needs to be defined to further model the airfoil shock at transonic flight envelopes, hence to achieve a true estimate of the wave drag for high-speed airfoil design and optimisation.

The airfoil optimisation results by the integration of a high-fidelity solver in the design process needs to be compared with panel method solver results. The feasibility of applying computationally cheap, low-fidelity tools for airfoil design needs to be assessed.

1.4.3 Optimisation Algorithm

The structure of the optimisation model must be well-defined to facilitate efficient and solution valid search simulations. If the user-defined parameters in the search algorithm are ill-defined then a sub-optima result will be the output. At the initial stage, the optimisation architecture requires design verification to specify user-defined search parameters. The following issues and challenges needs to be addressed:

- **Search Population Size:** The population of the biological search agents in Evolutionary Algorithms (EA) based models has a direct influence on the rate-of-success of the optimisation method. If the population size is large, then a computationally time-intensive simulation will follow as each search agent is directly analysed by the flow solver. If the population size is small, then a sub-optimal result may be generated due to minimal solution diversity. The population size required for airfoil design simulations needs to be defined accordingly; and
- **Adaptive Mutation for Search Diversity:** To suppress the generation of sub-optimal airfoils as part of the design process, the optimisation algorithm applied must be robust and flexible to explore infinite airfoil class types. The robustness of the search process is enhanced by introducing diversity to the search process through mutation. The demerit is increased computational overheads as additional solver calls are required to assess the aerodynamics of the mutated population. The design development, validation and demonstration of a novel-mutation process with the aim of introducing search diversity, yet minimising the computational expense for airfoil design has not been addressed and will be developed accordingly.

The parameters are problem based and a design-of-experiment (DoE) analysis is needed to establish the structure of the optimisation methodology for airfoil design at HALE and transonic conditions.

1.4.4 Surrogate Modeling

To reduce the computational time to convergence for shape design problems, approximation methods to the fitness function solver are applied and are referred to as surrogate models. A generic framework for use of a valid surrogate model with evolutionary algorithms is a requirement. The computational time for data output by the surrogate model is negligible compared to the theoretical mathematical model. The prospects of minimising the computational time to convergence for design optimisation simulations are significant. A valid surrogate model is developed using an iterative training process. The methodology involves drawing training sample points from the theoretical model to generate a valid approximation tool. Training convergence is measured by an error distribution analysis to assess the magnitude of errors between theoretical and approximated outputs.

Surrogate models have been extensively applied in EA methods for engineering design applications. The development of a surrogate structure including the direct integration to an optimisation algorithm has the following issues and challenges that need to be addressed:

- Type of surrogate model;
- Type of approximation; (function versus pattern recognition model)
- Data points selection/sampling techniques;
- Process for partitioning data points into training and generalisation samples;
- Type of data training algorithms;
- Surrogate quality: Identification of error thresholds for valid design simulations;
- Online versus offline surrogate models; and
- Effect of errors on design optimisation

The sensitivity of the issues and challenges to facilitate the development of an accurate meta-model is problem dependent. The identified points have not been comprehensively addressed for airfoil design at HALE and transonic Mach numbers. As engineering design optimisation applications are characterised by time-consuming fitness function solvers, the issues and challenges need to be considered accordingly to continuously enhance the computational efficiency of the design optimisation process. The work presented in this thesis will develop an innovative structure to address these requirements. Concurrently the benefits of the surrogate-based design management system for optimisation simulations is assessed accordingly. The results will advance the current body-of-knowledge in the related field of study.

1.5 Scope of Research

Airfoil design may appear trivial as it has been extensively evaluated in the open literature. Based on a review of related works, the methodologies developed have design limitations. The computational time to convergence is excessive and the feasibility of the optimal shape has not been interrogated.

The measure-of-success of the developed approach can not be assessed. As a result the architecture to airfoil design process has not been optimised and there remains a design window that requires further development.

The principles developed in this thesis will be applicable for large scale, shape optimisation problems including 3D wing design, to fuselage topology configuration analysis, including engine nacelles and associated areas. The viability of the proposed design methods is confirmed on 2D shape design analysis. Hence, airfoil design is important as a means of assessing the potential practical value of the proposed optimisation method for application to real-world problems. A two-dimensional airfoil analysis provides an efficient design approach to facilitate rapid computational turn-over time. An exhaustive design of experiments (DoE) analysis is defined to develop and fine-tune the optimisation approach for valid shape design simulations. The novel design approach will be adaptable to airplane design configuration analysis.

The thesis addressed the following questions:

- What are the issues and challenges to airfoil design?
- How are these issues and challenges addressed?
- What issues and challenges are not being addressed?
- How can these issues and challenges be addressed? Specifically:
  - What design improvements are necessary to facilitate valid shape design simulations?
  - How does the development of a novel direct optimisation approach improve convergence to the solution?
  - Can the integration of an intelligent, robust, surrogate model to the optimisation architecture further improve convergence to the solution?

The objectives of the thesis are addressed through the modifications and extensions of the direct optimisation approach for airfoil design. Novel computational approaches are developed to address the demerits of the current design methods. The research identifies areas in the design optimisation approach that have potential for further design improvement. Hence, extensions to the current off-the-shelf optimisation algorithms are developed and validated, to address the research questions. Modifications to the optimisation approach are generic to ensure the computational tool is not restricted to a specific problem class type. The research primarily focuses on developing a black-box implementation of an optimisation approach that is valid across a MDO process. The developed optimisation approach is not applicable for all optimisation problem types as a function of design variable population size. Instead the merits of the developed approach is assessed on numerical benchmark functions and against published airfoil design simulation data in the literature. The validations assess the robustness and flexibility of the developed design approach over current systems and contributions to the current body of knowledge are identified. Accordingly the validation process identifies the limitations of the developed computational approach and avenue for further research work is identified.

The research was undertaken in the following segments.

1. The first segment outlined the development of a novel shape optimisation architecture to facilitate computationally efficient and aerodynamically feasible optimisation simulations. The proposed design architecture followed two distinct approaches:

   (i) Direct optimisation approach; and

   (ii) Surrogate-based optimisation methodology

   Contributions to the intended field of study are outlined with due consideration to the analysis reported in the open literature.

2. The second segment details the development, validation and application of the direct optimisation approach for airfoil design. The computational efficiency and feasibility of the solution is evaluated against published data to assess the measure-of-success of the defined thesis motivating factor (Sec. 1.4) - *the design merits of the outlined design approach, hence contribution to the intended field of study must outweigh the performance measures of computational efficiency and solution feasibility of the developed techniques reported in the open literature.*

3. The third segment focuses on the development, validation and application of an online surrogate-based optimisation algorithm. The analysis assesses the feasibility of the motivating factor with performance evaluation comparison to the direct design approach to address the design motivating factor (Sec. 1.4) - *developing a surrogate model to facilitate valid optimisation simulations for computationally intensive design problems*

The research objectives are sequentially addressed through a series of logical processes. Novel design methodologies are developed to address the identified limitations from a review of related works. Each section within the scope of this research has a sub-set of research questions, including issues and challenges that must addressed to answer the fundamental research questions. The contributions from each research section are integrated to define a novel airfoil aerodynamic shape design optimisation methodology. The developed process will contribute to the current body of knowledge.

1.6 Thesis Contribution

In this thesis, four original, system level-based contributions are made to the current body-of-knowledge. The sub-systems that characterise and map the defined contributions are:

1. **Adaptive-Mutation Particle Swarm Optimisation algorithm**
   A novel particle swarm optimisation (PSO) algorithm is developed that induces search diversity by mutation for convergence to an optima point.

2. **Definition of Airfoil Design Solution Search Space**

   (a) **Application and Development of a Variant, off-the-shelf Shape Parameterisation Function**
   A variant to the original PARSEC airfoil generator by Sobieczky [28] is developed to further increase the airfoil class types that can be parameterised relative to the original function.

(b) **Evaluation of Shape Parameterisation Function Validity**
Novel design test methodologies are developed to confirm the merits of the developed shape parameterisation model against the methods in the open literature.

(c) **Design Variables Pre-screening Analysis**
Test methods are applied to confirm and rank the importance of each airfoil shape variable in the parameterisation model and its impact on the design objective. Theoretically, the computational efficiency of the optimisation process will be enhanced by limiting the search space to important variables only relative to shape coefficients with minor influence.

(d) **Definition of Airfoil Solution Search Space Envelope for HALE and transonic Flight Designs**
The search intervals of the design variables are defined. The search envelope of the AM-PSO algorithm for airfoil design will be restricted to promising solution regions only. Theoretically, the defined methodology will enhance the computational efficiency of the design process as computational resources are not exhausted on modeling airfoils that are aerodynamically infeasible relative to the defined objectives.

3. **Validation of the Developed Optimisation Approach by Airfoil Design Simulations**
The theoretical principles of the sub-systems which define the airfoil design solution search space module is confirmed. Airfoil design simulations are performed at low and high Mach number flight envelopes with the defined optimisation structure.

(a) **Assessment of Airfoil Solution Search Space Convergence**
The airfoil shape parameterisation function type and the scope of the solution topology is varied in the airfoil design process. Confirmation of the solution landscape that corresponds to the true optima for the defined problem is verified accordingly.

(b) **Development of a Robust Airfoil Design Methodology**
In-lieu of a multi-point airfoil design approach within a single-objective design mainframe, a robust methodology is developed. The approach avoids the need to directly specify the flight points for optimisation. Instead, these are defined by the design algorithm during the optimisation cycle.

(c) **Data-mining for Optimisation Post-Processing**
Data mining techniques are applied to confirm the optimality of the converged point for the defined problem.

4. **Development of a Novel Surrogate-assisted Design Optimisation Methodology**

(a) **Online training-based Surrogate Algorithm Coupled to the AM-PSO Algorithm for Shape Design Simulations**
The computational efficiency of the design simulations is enhanced by the application of a surrogate model in the AM-PSO structure. The methodology approximates the fitness with negligible effort relative to solving the theoretical fitness function equations.

1.7 Thesis Structure

The thesis is structured in eight chapters:

1. In **Chapter One**, the process of shape optimisation and application to engineering processes are defined. The role of shape optimisation in aerospace disciplines is defined to substantiate the importance of the research field to the current body-of-knowledge. Application of the proposed shape design process developed in this thesis to a real-life design problem is defined. A summary of research contributions to the body-of-knowledge are summarised.

2. In **Chapter Two**, aerospace shape design principles are defined. The merits and demerits of each approach are outlined. A comprehensive survey of related works is established to identify the shape design methodologies that are reported in the open literature. The design limitations within the scope of this research are identified. An overview of the research window for further design analysis, hence contribution to the intended field of study is defined.

3. In **Chapter Three**, a novel variant of the original particle swarm optimisation algorithm is developed. The original PSO method was developed to duplicate the success of the Genetic Algorithm (GA) method in locating the global optima with fewer design iterations, hence reducing the computational time to convergence. Despite the theoretical merits, the PSO algorithm is sensitive to a multi-modal solution search topology and can converge at a sub-optima point. A novel Adaptive Mutation - Particle Swarm Optimisation (AM-PSO) method is developed and validated to address the identified limitations.

4. In **Chapter Four**, the sub-components for airfoil solution search space definition at low and transonic Mach numbers are developed and applied. The validity of the developed and disparate airfoil shape parameterisation function types in open literature is examined with the AM-PSO algorithm from *Chapter Three*. The solution search space is modeled by: **a)** Ranking of variable importance relative to the defined objective function; and **b)** Mapping the search intervals of the design variables. Theoretically, the defined processes will enhance the computational efficiency of the airfoil optimisation process.

5. In **Chapter Five**, the computational domain type required to facilitate valid aerodynamic performance computation, hence fitness function evaluations is defined. The turbulence model type required to model airfoil boundary layer transition points and surface shock at HALE and transonic flight envelopes respectively is defined. The accuracy of the developed computational domain type is verified with published experimental data. The mesh type which exhibits an acceptable balance between computational accuracy and efficiency is identified.

6. In **Chapter Six**, airfoil optimisation at HALE and transonic Mach numbers is presented for a MM-UAV mission case study. The developed optimisation structure from chapter four and the flow solver computational domain from chapter five are applied in the design process. The results are evaluated with design methods reported in the literature for the same problem type. The data comparative analysis will confirm the merits of the developed design approach.

7. In **Chapter Seven**, an online-surrogate assisted fitness function approximation model within an AM-PSO structure is presented with the aim of enhancing the computational efficiency of the design optimisation process. A comprehensive development process is presented to outline the principles of the novel approach. The principles of the design algorithm will be demonstrated on benchmark test functions and the results compared to published data. The performance comparative analysis between the developed and reported methods in the open literature are

summarised to confirm the viability of the developed approach. The contributions made to the current body-of-knowledge are summarised.

8. In **Chapter Eight**, a summary of research outcomes and contributions to the intended field-of-study are presented. The contributions are in direct relation to the outlined research motivation and project scope from Sections 1.4 and 1.5 respectively. The research roadmap to further progress on the work presented in this thesis will be identified.

Chapter 2

Aerodynamic Design Optimisation Methodology

2.1 Overview

Shape design originated by understanding the physics of flight, through the observations of birds in motion for various flight conditions. Designers attempted to model bird wing shape for planform design, through continuous shape modification and aerodynamic performance evaluation in wind tunnel at low Reynolds Numbers. The National Advisory Committee for Aeronautics (NACA) introduced a computational shape function, which was used to generate a series of airfoil geometries with varying thickness-to-chord and camber profiles [29]. The aerodynamics was established by wind tunnel tests that simulated flow at flight Reynolds numbers. The flight data was catalogued for designers to use as off-the-shelf shapes for future designs. The catalog was limited in operational coverage of flight domains lift, drag and moment. This limited the shape optimisation for the required flight phases. Airfoil performance is susceptible to shape changes and the 'cut-and-try' approach requires a high number of design modifications to establish an optimal shape and is economically unviable.

To address the issues and challenges of airfoil design to meet a wide domain of flight performance requirements, robust methodologies have been explored through the use of computer and mathematical modeling. Computational models simulating flow characteristics have been developed, with the introduction of the Eppler Airfoil Design and Analysis code [30]. In this approach, a conformal-mapping technique was used to generate airfoils and a panel method solver utilised to compute the potential flow coupled to a boundary-layer integral method for viscous drag. An arbitrary number of airfoils were analysed without expensive and time consuming wind tunnel experiments. Computer codes have been developed to facilitate airfoil design methodologies which are extendable to three-dimensional wing designs.

Airfoil design methods are classified into two categories: **a)** Inverse; and **b)** Direct approach. The merits and demerits of each process are identified for shape design application.

2.2 Inverse Design

In the inverse approach, the target/optimal coefficient of pressure c_p, performance for the mission requirements is defined and design algorithms are integrated to establish an airfoil shape which matches the defined target c_p in Figure 2.1.

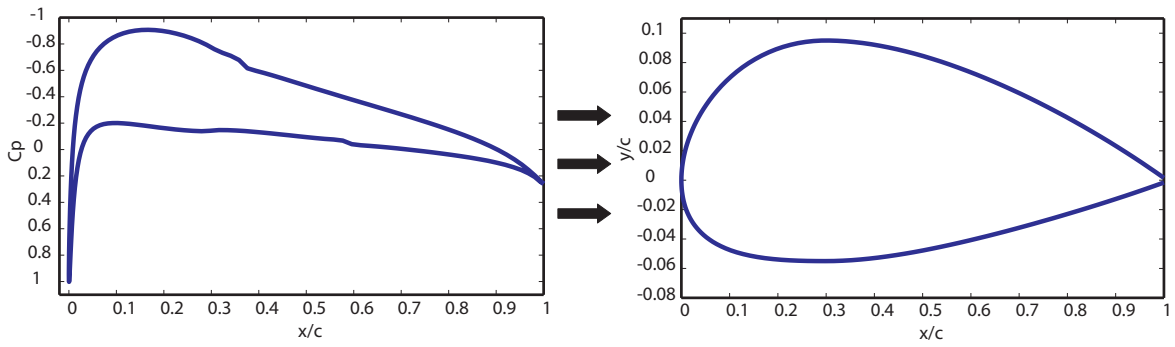

FIGURE 2.1: Airfoil Inverse Design Process

The optimisation problem is represented by a least square problem, where the target pressure distribution c_p^T, must match the computed c_p, along airfoil chord x/c_i (Eqn. 2.1). The objective function $\mathcal{J}$, is defined as:

$$\mathcal{J}_{min} = \sum_{i=1}^{M} \left| c_p(x/c_i) - c_p^T(x/c_i) \right| \tag{2.1}$$

The inverse approach is theoretically effective as designers have the flexibility to incorporate vital flow features based on pre-defined mission requirements. Long endurance performances require extended regions of laminar flow over the wing surface to minimise induced drag. The requirement is established in the inverse approach by specifying a c_p distribution, which extends the favorable adverse pressure gradient $\frac{dcp}{dx}$, downstream of the leading edge radius, to a specified airfoil chord station, x/c. Flow transition can also be delayed aft of airfoil leading edge, in the design process to attain extended laminar flow for HALE performances. The inverse approach can also control the shock wave at transonic Mach numbers. The c_p distribution is defined to delay the onset of shock wave, hence reduce the $c_{d_{wave}}$. Theoretically, the inverse approach has the merits of converging to the true optimal of a defined problem, as the aerodynamics of the desired solution are pre-defined.

Despite the theoretical advantages of the inverse approach, the method has limitations that must be considered. A major design challenge is the process of transforming the mission goals into a suitable pressure profile. 'The transformation of the desired boundary-layer characteristics into a pressure distribution is left to the imagination of the airfoil designer' [31]. Establishment of valid pressure profile does not guarantee an aerodynamically feasible shape. The generation of a 'fish-tail' airfoil with the upper and lower surfaces bisecting is a probable solution. The input velocity profile will require re-adjustment to address this issue. Experience in inverse design has demonstrated that the re-specification of the target pressure distribution is inevitable [32]. Depending on the degree-of-alteration, the resulting pressure profile will generate a compromised solution with the performance contrary to the initial design requirement.

An additional demerit is the non-application of geometrical constraints. The pressure distribution defines the required aerodynamic performances, but neglects geometry constraint application. Implementation of minimum wing volume through the specification of airfoil thickness-to-chord t/c, is essential in wing design for fuel / payload storage and wing structural spar requirements. The specification of an aerodynamic c_p profile, ignores structural geometrical constraints in the design process. Hence, an airfoil shape as a result of the inverse optimisation process may conform to the aerodynamic requirements, but may ignore shape contour constraints. In this case, the solution is not a true optimal.

Labrujere and Slooff [32] proposed that this limitation could be overcome by means of a hybrid direct-inverse approach. The design process required the definition of an airfoil region that conformed to the required geometrical requirement. The pressure distribution conforming to the required leading and trailing edge thicknesses was exactly specified and was static during the design process. The optimisation process would then design the c_p profile for the remaining airfoil profile accordingly. The hybrid search methodology has demonstrated that an optimal solution is not always achievable. By limiting the flexibility of the c_p design envelope as a function of airfoil chord, which is dependent on the severity of the static pressure profile for structural constraints, the generation of an aerodynamically feasible shape for the defined c_p performance becomes a design challenge. The issue is related to the originally defined design challenge of the inverse approach; desired performance definition does not guarantee an aerodynamically feasible airfoil shape. This issue is compounded further if the flexibility of c_p profile design envelope is restricted due to the integration of shape constraint by the proposed approach in [32].

Computationally, the robustness of the optimisation process in Equation 2.1, depends on the number of airfoil control points M_i, for x/c distribution. If M_i is high, then the optimisation algorithm will require higher flexibility and degree-of-freedom to compute $\mathcal{J}$, at each node i, thus affecting the robustness of the search algorithm. If M_i is low, then interpolation between control points will be required to generate the c_p profile. Airfoil shape is sensitive to the c_p definition. Interpolation of the pressure distribution will introduce 'noise' to the design process due to the errors in generalisation as induced by interpolation. The intended design merits of the c_p performance of the optimal profile will be diminished by this external factor. Hence, the solution will not reflect the intended performance benefits by the optimisation process due to the loss of shape generalisation by 'noise' in the design process. Thus, based on the limitations identified, the inverse approach is not viable for shape design and is not considered in this thesis.

2.3 Direct Design

Alternate approach to the inverse method for airfoil shape design is the direct computational approach in Figure 2.2. Airfoil shapes are intelligently and iteratively examined by an optimisation algorithm until convergence based on user-defined aerodynamics and constraints is achieved.

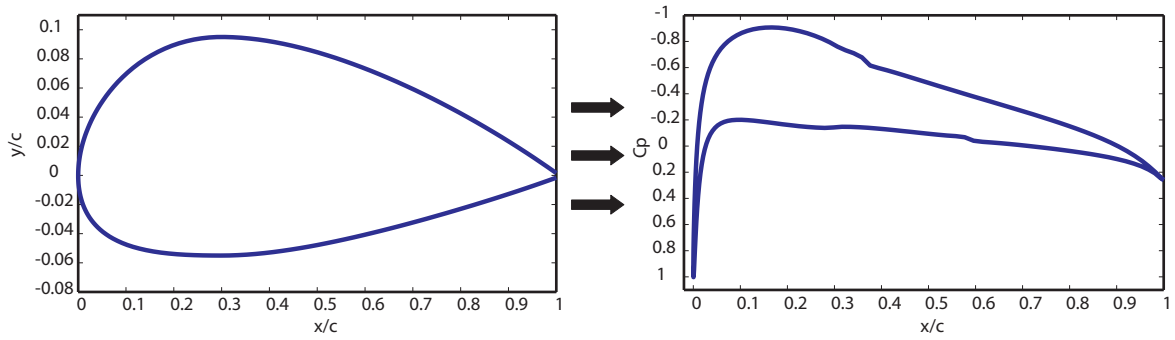

FIGURE 2.2: Airfoil Direct Design Process

The methodology is the integration of: **a)** Geometry shape parameterisation model to mathematically represent an arbitrary airfoil/wing, which is then integrated to a; **b)** Flow solver for aerodynamic analysis; and **c)** Optimisation algorithm based on directed evolutionary search analysis. The components operate in iteration to convergence based on defined objectives and constraints. The approach permits the integration of shape generation by the direct manipulation of the airfoil shape variables within the parameterisation function. The definition of the expected c_p profile at optimum conditions is neglected in the formulation of the direct approach. Thus, *a-priori* knowledge of the required operating profile for specific aerodynamic performance is not a requirement, hence avoiding the ambiguity of transforming the mission parameters to a pressure profile.

Shape constraints are applied by the design variables which act as parameters to the airfoil shape mathematical function, for geometry representation. The geometry parameterisation model applied must exhibit one-to-one geometry control, with a physical connection between shape variables and airfoil geometry parameters including nose radius, t/c, chord location of maximum t/c, camber and trailing edge wedge angles. The efficiency of the optimisation process is enhanced as the search limits of the design variables are restricted to shapes that satisfy geometry constraints.

Shape optimisation by the direct approach is defined by a set of shape variables x, that minimise (or maximise) an objective function $\mathcal{J}$, as computed by a validated computational algorithm $f(x)$, subject to constraints $g_i(x) \geq 0$ and/or $h_j(x) = 0$. Typical aerodynamic shape optimisation problems are in the form of drag minimisation, subject to a set of aerodynamic constraints including moment and/or adverse pressure gradients to control boundary layer flow transition. Geometric constraints are not explicitly applied to the problem. Instead, these are implicit and are defined by the search limits of the shape variables.

The mission objectives by the specified design requirements are transformed to a set of aerodynamic coefficients. The formulation of the objective function is simplified in comparison to the inverse approach. It is required from an optimisation algorithm perspective with $\mathcal{J}$, calculated globally and not locally, which is represented by the shape fit at each airfoil chord station M in Equation 2.1, by the inverse approach. A global objective function in the direct approach requires minimising the drag coefficient c_d, at cruise, with constraint on target lift coefficient c_l^T subject to a set of geometrical constraints including minimum t/c, bounded by a lower and upper limit t/c^L and t/c^U respectively.

Mathematically, the direct approach is defined as:

$$\begin{aligned} J_{min} &= c_d \\ \text{Subject to} : c_l &\geq c_l^T \\ : t/c^L &< t/c < t/c^U \end{aligned} \tag{2.2}$$

The feasibility of the optimal point is sensitive to the applied optimisation algorithm. A limited search model will examine shapes at local search solution topologies, resulting in a sub-optimal solution. The demerit of the DNO approach is the increased computational search process. Flow simulations for optimisation iterations are computationally intensive. With the integration of high-fidelity solvers in the optimisation loop, computational time required for convergence increases significantly. The use of parallel computing can partially alleviate this problem. The components in the DNO architecture make possible the use of parallel computing by allocating each search agent to a certain CPU in a cluster of processors. The direct search approach is effective for airfoil shape optimisation, if the search algorithm is robust and validated. The objective function mitigates ambiguity in relation to the mission objectives and is represented directly by both aerodynamic and geometrical parameters in Equation 2.2. The process of airfoil optimisation in this thesis will be based on the direct search approach. The modules in the applied design methodology need to be defined to ensure a feasible optimum solution is established.

2.4 Review of Direct Design Process

The DNO components are developed and validated to ensure a feasible optimisation simulation for the shape design process. Airfoil parameterisation model defines the solution space to the optimisation problem. The profile generator must model infinite airfoil class types for increased search flexibility. Aerodynamic solvers must be validated to compute flow features from shock development at transonic Mach numbers to laminar separation bubbles at low-speeds. Computational codes for high angle-of-attack flows for maximum lift at pre-stall angles-of-attack must be established accurately and is critical in numerical optimisation processes. The core of the optimisation process is governed by the search algorithm used. The optimiser type is developed and tuned for a valid search process and is problem dependent. This section investigates the techniques used in the DNO approach and the knowledge gained in the development process.

In the analysis by Barrett et al. [33] the performance of the direct and the inverse approach for airfoil shape optimisation at subsonic Mach numbers is evaluated. The analysis indicated that the inverse methodology is computationally more efficient in comparison to the direct approach. The conclusion is based on the efficiency of the computational process and the reduction in drag performance in comparison to a baseline NASA low-speed airfoil. The performance merits are a function of design variable population size and the resulting iteration count to convergence. The direct approach is modeled with 13 variables for airfoil parameterisation in comparison to 6, for c_p^T representation in the inverse method. Due to the increase in solution search space mapping area by the direct approach, the method is computationally intensive in comparison to the inverse method. The disparity in airfoil shapes and equating c_d performance across 5 simulations indicates that the

direct approach has not converged to valid solution region within the allocated maximum iteration count. Reduction in problem dimensionality by the inverse process resulted in a flexible exploration of the solution search space, hence as an efficient design process. A consistent magnitude of optimum c_d is noted over the five independent design simulations, hence indicating a greater degree-of-convergence in comparison to the direct approach [33].

The comparative analysis between the two design approaches in [33] has limitations. The validity of the integrated GA variant optimisation method for the defined problem dimension search space was not confirmed. Hence, if the search method is limited, then the direct design process will have issues including premature convergence to a local solution and/or an inefficient design process. The effect of varying parameterisation function type, hence the flexibility for airfoil representation was not assessed. A limited shape flexibility will result in convergence to a sub-optimum point. The optimality of the defined solutions by the direct method cannot be assessed with confidence.

Khurana et al. [34] showed that a hybrid design approach with the integration of a population-based search method and a gradient-based sequential quadratic programming (SQP) algorithm, facilitates convergence to a global point. The objectives of a current off-the-shelf airfoil designed by NASA were used to define the shape optimisation process, hence to confirm the viability of the developed design approach. The aerodynamic performance of the converged airfoil was superior to the benchmark test profile at the defined flight conditions. The feasibility of the solution was confirmed by the comparative analysis. The conclusions in [33] does not correlate to the findings in [34], as the merits of the direct design approach are confirmed by the evaluation of results relative to the published data by NASA for the validation case study.

Due to the identified issues and challenges of the inverse approach, research efforts are focused on further developing novel, direct-based design approaches. Based on the review of related works for the inverse and direct design approaches, the direct method is identified as a viable option for airfoil shape design. The methodology requires further design development with focus on: **a)** Design and validation of an efficient optimisation algorithm with due consideration to a hybrid-based design approach; and **b)** Validation of solution search space convergence with variations in airfoil shape parameterisation model types. The identified issues and challenges are addressed in this thesis.

The earliest reported aerodynamic shape optimisation analysis, originated in wing design by Hicks et al. [35]. Hicks integrated a fully potential, inviscid aerodynamics code, coupled with a conjugate gradient optimisation algorithm, based on the steepest descent direction of the objective function. Shape parameterisation was achieved by adding a series of sinusoidal curves (Hicks-Henne functions), to a baseline shape to generate a new geometry. Participating coefficients are design variable multipliers to the shape function, for generation of a new shape. The feasibility of the proposed methodology was examined over a series of test cases. These included efforts to: **a)** Reduce the shock drag with a constraint on wing volume; **b)** Increase of the aerodynamic efficiency factor of lift-to-drag ratio with an additional constraint on the lift coefficient; and **c)** Establish acceptable stall progression at low-speeds.

Hicks [35] supports the direct approach over the inverse method, as off-design conditions are automatically considered during the optimisation process. The study reported several recommendations, for numerical design techniques, including increased computational resources. It was concluded that

a detail mesh study is required, with minimal number of grid points, without compromising aerodynamic data for efficient optimisation. The convergence criteria needs close analysis to enhance the search process. Hicks reduced the velocity residuals for convergence from 10^{-5} to 10^{-4}, which accelerated computation for convergence, with negligible effect on the maximisation of the lift-drag ratio. The result was an issue with the optimiser, as a reliable partial gradient for search direction calculation was not achievable irrespective of the convergence threshold. The final recommended conclusion was based on the development of a flexible shape representation model. A limited geometry model does not confirm a global optimal solution and the search capabilities of the optimiser is limited by the deficiency of the shape model.

Research efforts for robust and efficient DNO structure development are based on the recommendations of Hicks et al. [35]. A survey of DNO components covers: **a)** Airfoil shape parameterisation; **b)** Validated flow solver; and **c)** Intelligent search optimisation algorithm.

2.5 Airfoil Shape Parameterisation

Aircraft components are classified in two configuration types [36]: **a)** Wing type cross-sections (airfoils) which are extruded to develop a 3D lifting surface (wing); and **b)** Body type cross-sections (fuselage bubble), which is distributed about the longitudinal axes to develop a 3D model (aircraft fuselage). In some cases, integration of two shape classes is required to develop a component. Nacelles can be defined with a set of airfoil sections that are circumferentially distributed about the object centerline and also by the physical transformation of the actual body-type about the component centerline.

A mathematical formulation is required to numerically represent aircraft shapes for design development and optimisation. The methodology requires flexible shape functions to arbitrary vary geometry features with minimal shape parameters. The shape representation framework becomes part of the overall optimisation tool, used to represent potential airfoils for analysis by the high-fidelity, computational fluid dynamics (CFD) flow solver. The choice of shape representation methodology for the aerodynamic design of aircraft components has a strong influence on the overall design optimisation cycle. A computationally intensive shape function will result in an inefficient optimisation architecture, due to the requirement of greater computational resources. Alternately, a computationally acceptable shape representation tool may have limited flexibility. This will affect the available solution design space, thus resulting in a combination of irregular and physically unrealistic shapes. The optimiser will have issues in locating a feasible optimum solution for the stipulated objectives and constrains and a false solution will be the result.

The methodology for airfoil shape representation has a major influence on the proposed optimisation cycle and must be valid to attain valid design simulations. The two main airfoil shape representation strategies include: **a)** Knowledge-Based; and **b)** Free-Form. In the knowledge-based design, an algebraic expression is applied to represent a series of sinusoidal curves, which are multipliers to the design coefficients to represent disparate airfoil shapes. Expressions directly related to airfoil geometry (including leading edge radius, maximum thickness, camber, trailing edge wedge angles) are developed and used as design variables in optimisation. In the free-form methodology,

the shape is represented by a linear combination of basis functions including splines. Control nodes represent key airfoil parameters and are design variables to the problem. A large node population ensures an extended solution space and the potential to represent disparate classes of geometries, at the expense of computation cost.

The shape parameterisation function must address the following:

- **Ease of Application:** Shape variables must be directly related to airfoil geometry;
- **Feasibility:** The shape function must be stable to mitigate the generation of undulating airfoil contours and provide realistic and smooth surfaces;
- **Efficiency:** Negligible computation expense in the generation of airfoil shapes;
- **Flexibility:** Acceptable design space through the utilisation of few shape variables to generate disparate classes of airfoils;
- **Robust:** Provide shape flexibility to control airfoil parameters including camber, chordwise location of maximum camber point, thickness-to-chord, maximum thickness-to-chord location, leading edge radius, trailing edge wedge angles, airfoil contour upper and lower crest curvatures;
- **Control:** Shape variables must provide control of airfoil curve to independently modify shape parameter/s and in the application of geometrical constraints for airfoil shape optimisation; and
- **Ease of Translation:** Shapes must maintain geometrical consistency when transformed from 2D to 3D plane

The following techniques are valid for airfoil representation:

- Discrete Approach;
- Conformal Mapping Shape Transformations;
- CAD Based Approach;
- Polynomial Surface Definitions;
- Cubic Spline;
- Orthogonal Basis Functions; and
- Analytical Approaches with linearly added shape functions to a reference base airfoil

Disparate shape representation types have been applied in the literature for design optimisation applications. The use of one method over the other is problem based, defined by the formulated objective function and in accordance to flow and geometric constraints, including optimiser type. The shape parameters are first defined to establish the advantages and demerits of select methods for use in airfoil shape optimisation.

2.5.1 Discrete Approach

The general form of airfoil shape representation is by the discrete approach. In the methodology, each wall-surface node boundary point is a design variable to the problem, over a defined chord length c, in Figure 2.3. Theoretically, the method will generate an infinite airfoil class type. The method is quick and easy to implement. The optimiser perturbs the control points to generate potential airfoil class types for analysis by the solver during the shape design process.

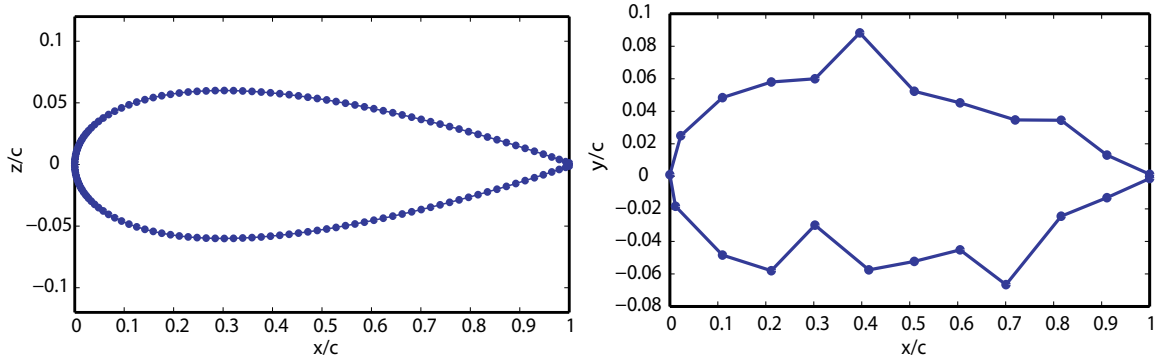

(a) Smooth Contour with Acceptable Control Node Population

(b) Undulating Contour with Minimal Control Node Population

FIGURE 2.3: Airfoil Parameterisation by Discrete Approach

The methodology has design limitations. The approach is unsuitable for numerical optimisation as there is no physical connection between wall-boundary points and airfoil aerodynamics and geometry. The application of shape constraints is a design issue. Controlling airfoil t/c and/or camber will require simultaneous manipulation of a set of discrete points. The location and the magnitude of the maximum thickness point is a geometrical constraint, governed by the spar location. Transforming the shape constraint into a discrete approach is a design issue. The methodology will require gradual perturbation of a population of node points to define the maximum and minimum airfoil crests and equating chord location on upper and lower surfaces respectively. The t/c of the profile and chord-location is achieved accordingly, but an excessive number of control points will be required. Curve interpolation will be required between the control points to generate the airfoil contour. Curve generalisation errors will result in airfoil surface irregularities and the aerodynamics of the profile will be ill-defined.

The discrete approach is further unsuitable from an optimisation perspective as a large population of control points are required to impose shape constraints. Considering airfoil representation by the discrete approach is defined with a conservative value of 40 nodes points, then the complexity of the dimensional search becomes prohibitive. With each node applied as a design variable, the combinatorial-permutation between node population will be intensive when integrated to evolutionary search algorithm. The optimiser will be required to independently adjust each control point for shape parameterisation and an inefficient search process will ensue.

Minimising node population will address the issue of a computationally intensive design process. The demerit is the generation of undulating airfoils in Figure 2.3(b). The design space during an optimisation cycle will be populated with airfoils with surface irregularities. Random shape generation

due to constraint violation and/or mutation for search diversity will result in ill-defined shapes with surface concavities (Fig. 2.3(b)), due to rapid contour deviations between adjoining control points [37]. The flow solver will have convergence issues due to high frequency shape oscillations. As airfoil surface is sensitive to sudden changes in geometry, generating airfoil contours by the discrete approach will result in sub-optimal solutions due to ill-defined outputs by the fitness function evaluator. The shapes by the discrete approach are also not viable for manufacturing purposes [38].

Research efforts to minimise the drawbacks of the discrete approach have been conducted. Samareh [39] reports that surface smoothness is achievable by implementing multi-point constraints on the design variables. Dynamic adjustments are set on the upper and lower bounds of the design variables, thus limiting node degree-of-freedom and avoiding non-smooth airfoils. Reducing the search limits of the variables does not address the large population size of the design variables. Even with a modest population, point-based shape alterations can cause rapid and drastic shape changes between consecutive nodes. The computational flow solver will encounter convergence problems for steady state flow simulations [37].

An alternate approach to address non-smooth shapes is by directly modifying the cost function as reported by Jameson et al. [40]. It is a function of the flow features of the shape and is modified during the descent process of the optimisation run, to guarantee a smooth shape for valid continuation of the search process. Jameson [40] maintains surface smoothness by replacing the cost with a smoothed value, which is calculated from a discrete approximation of the original cost, in the dimensional direction. A pre-defined smoothing parameter acts as a multiplier to the modified cost function approximation parameter. The magnitude of the smoothing parameter is user-defined and the effect of varying the size and general parameter selection guidelines is not clear. The proposed smoothing method by Jameson [40] is based on shape optimisation using the adjoint control theory. Despite the rapid convergence rate, the technique is unable to account for flow separation and can converge to local minima as reported by Namgoong [41], thus affecting the quality of the final solution. The application of the discrete approach for airfoil design optimisation is unsuitable and alternate shape parameterisation methods are required to address the identified issues.

2.5.2 CAD Based Approach

The discrete method indicates airfoil generation with minimal control points is a design requirement. The spline curve interpolation based methods have been applied to address the identified issues and challenges of the discrete approach for shape optimisation [42–46]. The shape nodes are strategically partitioned along airfoil chord to control camber and thicknesses distributions. It has been shown that a large population of control points, in excess of twenty are required to generate smooth shapes. Since the chord station of the control nodes is fixed and the degree-of-freedom restricted to $y-$axis, generation of undulating shapes which are aerodynamically unfeasible becomes a design issue.

Airfoil shape representation by a CAD based approach using Bezier curves, B-splines and Non-Uniform Rational B-Splines (NURBS) is an alternate to the discrete method. The functions apply control points, which act as multipliers to a set of defined weight terms, hence are manipulated to form variant airfoil class types. The number of control points required for shape representation is minimal in comparison to the discrete approach. The number of design variables required for airfoil

parameterisation is reduced significantly and the numerical optimisation process is enhanced as the size of the dimensional-search space is reduced. The proposed method have design limitations. Bezier curves parameterise the shape globally and perturbing one independent control point, collectively modifies the entire airfoil contour. Independent shape control for constraint applications is not possible. B-splines induce local surface modifications only [47], hence several additional control points are required to perform global shape modifications.

The NURBS approach has been applied to address the demerits of local and global-based geometry parameterisation methods associated with Bezier and B-splines formulations respectively. The method is an extension of the B-spline methodology, with the introduction of weight terms. These act as multipliers to the control points, hence manipulating the magnitude-of-shape-change, that can be induced by an independent node. The methodology facilitates changes that are local and global from a shape modification perspective. The flexibility of the shape function in increased. Node points are strategically positioned along airfoil chord to generate disparate airfoil types. Ghaly et al. [48] applied NURBS for a gas turbine blade design. An inverse shape-fitting study, indicated that an approximated shape to a pre-defined target profile was within the machining tolerance, using NURBS with only nine control points. The corresponding aerodynamic performance of the approximated profile was in agreement with the target profile, hence further validating the merits of the approximation profile.

The NURBS methodology has design limitations. Firstly, there are no set guidelines governing the magnitude of the weight terms. If the weights are ill-defined, then the solution search space will be affected with poor shape parameterisation, thus resulting in a sub-optimal shape. The chord-wise (x/c) location of the control points requires user definition. Generally two control points, one on upper and lower airfoil surface, at the leading edge are introduced to control nose camber and radii. An additional control point is applied at the maximum thickness point, to satisfy minimum shape volume constraint. The trailing edge ordinate is also fixed at $(0, 0)$. The chord-wise location of the remaining control points are arbitrarily defined. Painchaud-Ouellet et al. [49] performed transonic airfoil shape optimisation with NURBS using 13 control points, with two points fixed at the trailing edge. The remaining 11 control points have a degree-of-freedom in the x, y and z axes and the scope of the search space is increased to 33 design variables [49]. The corresponding solution topology for single and multi-point optimisation simulations was excessive. A local gradient based optimisation model was applied in the search process and the computational time to convergence was minimised with compromise on the optimality of the final shape. The computational time to convergence will be excessive if population based, global-search methods were applied since the measuring location of the objective in the solution topology, as a function of the dimensional search space is extreme.

Successful transonic airfoil optimisation simulations with evolutionary programming methods, coupled to a polynomial shape function and fewer than half the total number of design variables in [49] is presented by Namgoong [41]. Shape parameterisation methodology by the polynomial approach has one degree-of-freedom per design parameter. In comparison to the NURBS methodology, the scope of the problem is increased as each shape parameter is modeled with three degree-of-freedom, thus increasing the scope of the problem. The analysis by Namgoong [41] indicated that such a significant increase in search topology was not justified.

The NURBS methodology is also limited since it has no physical connection between the control points and airfoil aerodynamics. Kulfan [50] outlines that the parameterisation model must have an

intuitive geometric interpretation. The optimiser is able to exploit the relationship between airfoil geometry and aerodynamics, hence objective function, as a result of geometric perturbations. The optimisation simulation time to convergence is enhanced by this direct relationship. The NURBS methodology does not address this requirement.

2.5.3 Analytical Approach

The analytical approach has been applied for airfoil shape parameterisation [41, 51]. Methods include the Hicks-Henne [35], Wagner [52], Legendre, Bernstein, and NACA normal modes [29, 53]. The polynomials represent a series of sinusoidal curves over a specified chord length. The finite sum of closed shape functions are linearly added to a base airfoil to generate a new section. The design variables to the shape functions are multipliers and determine the contribution of each function to the final shape [39]. Mathematically the approach is represented as follows:

$$y(x/c, \lambda_i) = y(x/c)_{\text{base}} + \sum_{i=1}^{n} \lambda_i f(x/c) \tag{2.3}$$

Where:

λ_i	= Design variable
$y(x/c)_{\text{base}}$	= Ordinate of airfoil base section
n	= Number of Design Variables
$f(x/c)$	= Shape function along airfoil chord

The polynomial functions for the different methods examined in the thesis are presented in Appendix A. Results for a shape convergence simulation to a target NACA 0012 airfoil is presented (Appendix A). The magnitude of the design variables is computed by a least squares optimisation problem, by minimising the difference of the ordinates at each chord-station x/c, between target and approximated airfoil by the shape function. A comprehensive overview of the adopted test methodology applied to verify the feasibility of the analytical function approach for airfoil shape optimisation is presented in Chapter 4, Section 4.2.1.1.

2.5.4 Polynomial Functions

An example of the polynomial shape function is the PARSEC airfoil methodology by Sobieczky [28]. It is a sixth-order polynomial function applied to generate disparate airfoil class types and is similar to the NACA 4-digit generator. The methodology is characterised by eleven design coefficients in Figure 2.4(a), which control airfoil shape parameters including: **a**) Leading edge radius; **b**) Curvature of the upper and lower crests; **c**) Ordinates and abscissa of the upper and lower surfaces; **d**) Trailing edge ordinate thickness and location; and **e**) Trailing edge wedge angle.

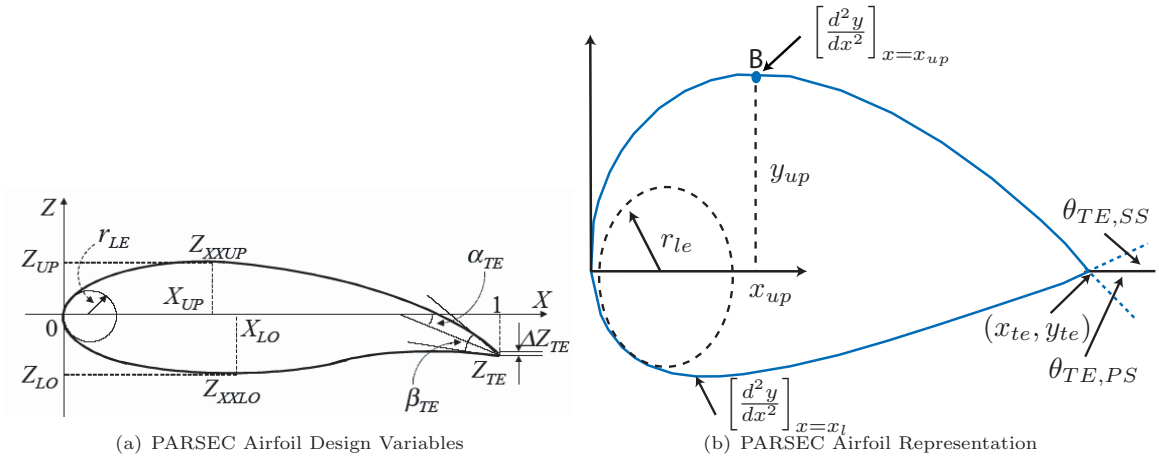

(a) PARSEC Airfoil Design Variables (b) PARSEC Airfoil Representation

FIGURE 2.4: Definition of PARSEC Airfoil

The polynomials applied for airfoil upper y_u and lower y_l, surfaces are:

$$y_u = \sum_{n=1}^{6} a_n x^{n-\frac{1}{2}} \tag{2.4}$$

$$y_l = \sum_{n=1}^{6} b_n x^{n-\frac{1}{2}} \tag{2.5}$$

Where: x = Chord location and a_n & b_n = Shape Coefficients for airfoil pressure (PS) and suction surfaces (SS), respectively.

Consider an airfoil with a LE at $(0, 0)$ and TE at $(1, 0)$ in Figure 2.4. The following boundary conditions apply for the design variables representing an arbitrary airfoil (Figs. 2.4(a) - 2.4(b)) in Equations 2.4 - 2.5:

$$y(1) = 0 \tag{2.6}$$

$$tan(\theta_{TE}, PS) = \left(\frac{dy}{dx}\right)_{x=1} = \sum_{n=1}^{6}(n-\frac{1}{2})a_n x_{te}^{n-\frac{3}{2}} \tag{2.7}$$

$$y(x_{up}) = y_{up} = \sum_{n=1}^{6} a_n x_{up}^{n-\frac{1}{2}} \tag{2.8}$$

$$0 = \left(\frac{dy}{dx}\right)_{x=x_{up}} = \sum_{n=1}^{6}(n-\frac{1}{2})a_n x_{up}^{n-\frac{3}{2}} \tag{2.9}$$

$$\left(\frac{d^2y}{dx^2}\right)_{x=x_{up}} = \sum_{n=1}^{6}(n-\frac{3}{2})(n-\frac{1}{2})a_n x_{up}^{n-\frac{5}{2}} \tag{2.10}$$

$$r_{le} = \left[\frac{\frac{d^2y}{dx^2}}{\left[1+\frac{dy^2}{dx}\right]^{\frac{3}{2}}}\right]_{x=x_{le}} = \frac{a_1^2}{2} \tag{2.11}$$

$$\therefore a_1 = \sqrt{2.r_{le}} \tag{2.12}$$

The coordinates x_{up} and y_{up} (Fig. 2.4(b)), represent the maximum thickness point of the airfoil. The second derivative of y, at point B, is the crest of the airfoil curvature and is mathematically

represented from Equation 2.4, for upper surface as:

$$y(x) = a\sqrt(x) + ax^{\frac{3}{2}} + ax^{\frac{5}{2}} + ax^{\frac{7}{2}} + ax^{\frac{9}{2}} + ax^{\frac{11}{2}} \tag{2.13}$$

$$y^{'}(x) = \frac{1}{2}\frac{a}{\sqrt{x}} + \frac{3}{2}a\sqrt{x} + \frac{5}{2}ax^{\frac{3}{2}} + \frac{7}{2}ax^{\frac{5}{2}} + \frac{9}{2}ax^{\frac{7}{2}} + \frac{11}{2}ax^{\frac{9}{2}} \tag{2.14}$$

$$y^{''}(x) = -\frac{1}{4}\frac{a}{x^{\frac{3}{2}}} + \frac{3}{4}\frac{a}{\sqrt{x}} + \frac{15}{4}a\sqrt{x} + \frac{35}{4}ax^{\frac{3}{2}} + \frac{63}{4}ax^{\frac{5}{2}} + \frac{99}{4}ax^{\frac{7}{2}} \tag{2.15}$$

From Equations 2.6 - 2.15, the coefficients a_n and b_n are computed by:

$$\begin{bmatrix} 1 & 1 & 1 & 1 & 1 \\ x_{up}^{\frac{3}{2}} & x_{up}^{\frac{5}{2}} & x_{up}^{\frac{7}{2}} & x_{up}^{\frac{9}{2}} & x_{up}^{\frac{11}{2}} \\ \frac{3}{2} & \frac{5}{2} & \frac{7}{2} & \frac{9}{2} & \frac{11}{2} \\ \frac{3}{2}x_{up}^{\frac{1}{2}} & \frac{5}{2}x_{up}^{\frac{3}{2}} & \frac{7}{2}x_{up}^{\frac{5}{2}} & \frac{9}{2}x_{up}^{\frac{7}{2}} & \frac{11}{2}x_{up}^{\frac{9}{2}} \\ \frac{3}{4}x_{up}^{\frac{1}{2}} & \frac{15}{4}x_{up}^{\frac{1}{2}} & \frac{35}{4}x_{up}^{\frac{3}{2}} & \frac{63}{4}x_{up}^{\frac{5}{2}} & \frac{99}{4}x_{up}^{\frac{7}{2}} \end{bmatrix} \begin{bmatrix} a_2 \\ a_3 \\ a_4 \\ a_5 \\ a_6 \end{bmatrix} = \begin{bmatrix} \left[y_{te} + (\frac{1}{2}.t_{te})\right] - a_1 \\ y_{up} - a_1.\sqrt{x_{up}} \\ tan(\theta_{TE}, PS) - \frac{1}{2}.a_1 \\ -\frac{1}{2}.\left(\frac{a_1}{\sqrt{x_{up}}}\right) \\ \frac{d^2y}{dx_{up}^2} + \frac{1}{4}.\left(\frac{a_1}{\sqrt{x_{up}^3}}\right) \end{bmatrix} \tag{2.16}$$

$$\begin{bmatrix} 1 & 1 & 1 & 1 & 1 \\ x_{l}^{\frac{3}{2}} & x_{l}^{\frac{5}{2}} & x_{l}^{\frac{7}{2}} & x_{l}^{\frac{9}{2}} & x_{l}^{\frac{11}{2}} \\ \frac{3}{2} & \frac{5}{2} & \frac{7}{2} & \frac{9}{2} & \frac{11}{2} \\ \frac{3}{2}x_{l}^{\frac{1}{2}} & \frac{5}{2}x_{l}^{\frac{3}{2}} & \frac{7}{2}x_{l}^{\frac{5}{2}} & \frac{9}{2}x_{l}^{\frac{7}{2}} & \frac{11}{2}x_{l}^{\frac{9}{2}} \\ \frac{3}{4}x_{l}^{\frac{1}{2}} & \frac{15}{4}x_{l}^{\frac{1}{2}} & \frac{35}{4}x_{l}^{\frac{3}{2}} & \frac{63}{4}x_{l}^{\frac{5}{2}} & \frac{99}{4}x_{l}^{\frac{7}{2}} \end{bmatrix} \begin{bmatrix} b_2 \\ b_3 \\ b_4 \\ b_5 \\ b_6 \end{bmatrix} = \begin{bmatrix} \left[y_{te} - (\frac{1}{2}.t_{te})\right] + a_1 \\ y_{l} + a_1.\sqrt{x_{l}} \\ tan(\theta_{TE}, SS) - \frac{1}{2}.a_1 \\ \frac{1}{2}.\left(\frac{a_1}{\sqrt{x_{l}}}\right) \\ \frac{d^2y}{dx_{l}^2} - \frac{1}{4}.\left(\frac{a_1}{\sqrt{x_{l}^3}}\right) \end{bmatrix} \tag{2.17}$$

An example of a PARSEC airfoil with corresponding shape parameters is presented in Figure 2.5.

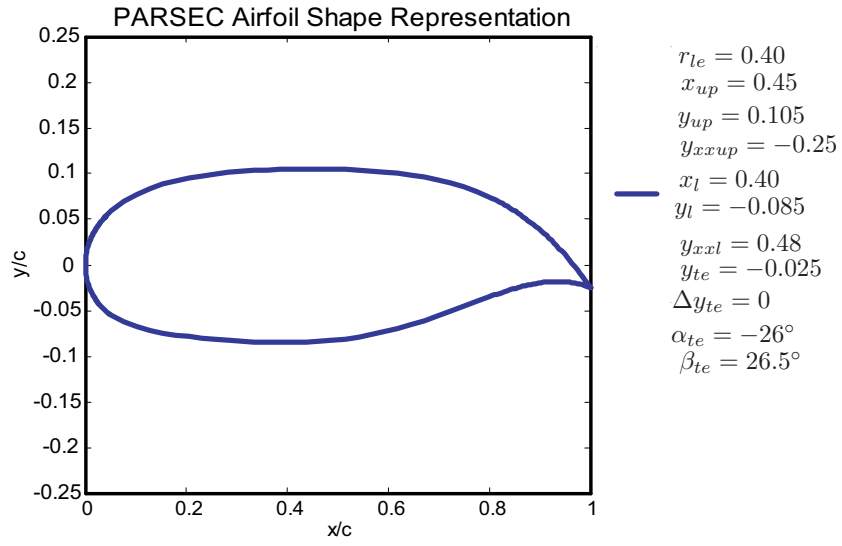

FIGURE 2.5: PARSEC Airfoil with Equating Shape Parameters

Theoretically the PARSEC method provides direct control over important airfoil shape features and is ideal for preliminary optimisation analysis. The method has been used in the design optimisation of transonic airfoils, thick airfoils for HALE operations and for low Reynolds number operations. Fuhrmann [54] applied the shape function to model an airfoil operating in the Martian atmosphere [54] at transonic speeds. Winnemoller and Dam [55] used a modified variant of the PARSEC method

for shape optimisation of thick airfoils at low subsonic Mach and Reynolds numbers [55]. Vavalle and Qin [56] applied the PARSEC formulation with a response surface-based optimisation structure for shape design at transonic Mach numbers. Jeong et al. [57] applied the PARSEC method coupled to a surrogate-based assisted meta-model to re-design a current off-the-shelf transonic airfoil.

Fuhrmann [54] modified the methodology by closing the trailing edge at a single point, since blunt and divergent trailing edge (DTE) shapes contributed significantly to drag at transonic Mach numbers. Thick trailing edges profiles were included in the analysis, but were fixed for ease of grid generation. The impact of t_{te} during the optimisation process on drag was reduced. The results indicated that x_u had a strong influence in the improvement of L/D and the magnitude-of-change, varied as a function of target c_l^T. The parameter y_{xxu} also influenced drag performance, hence L/D at transonic flight regimes [54]. The findings are consistent with the data reported by Jeong et al. [58].

Wind-turbine blades at low Reynolds and Mach numbers were designed with the PARSEC methodology by Winnemoller and Dam [55]. Thick airfoil was a requirement and the search limits for t/c and t_{te} were mapped accordingly. Since the PARSEC shape coefficients exhibit direct one-to-one geometry control, the search intervals for y_u, y_l and t_{te} were defined to control t/c and t_{te} respectively. Constraining the variables ensured the optimiser only examined shapes that conformed with user defined requirements. The search intervals for the remaining PARSEC coefficients were similarly mapped to ensure an acceptable design space with smooth and realistic airfoils. The optimum airfoil satisfied the t/c and t_{te} constraints since the search space was bounded with geometrically acceptable solutions. The PARSEC methodology coupled to a GA based optimisation model, showed that a blunt trailing edge airfoil was required for thick airfoil operating at subsonic speeds. The flexibility of the PARSEC shape coefficients allowed for direct control of shape geometry. The inclusion of a penalty to the objective function for shape constraint violated designs was not required with the PARSEC methodology which simplified the scope of the solution search space [55].

A response surface method was applied to optimise a 2D wing profile of a blended wing body aircraft and the transonic RAE 2822 airfoil using the PARSEC method by Vavalle and Qin [56]. The solution search space was reduced from eleven to nine variables for both test cases. The thickness at the trailing edge and y_{te} was set to zero, hence blunt trailing edge airfoils were not considered in the optimisation process. An off-the-shelf airfoil from a 2D blended wing body and the RAE 2822 airfoil were used as base airfoils and a least-square optimisation process applied to determine the corresponding PARSEC coefficients of the datum airfoils. The search intervals of the design variables were mapped as a pre-defined percentage of the PARSEC coefficient of the base airfoils. Geometry constraints were taken into consideration during the search interval mapping process. Since the PARSEC process provided direct control over profile thickness, the percentage multiplier to y_u for the base RAE 2822 airfoil was defined to ensure the minimum t/c of the potential airfoils examined during the shape optimisation process was not less than $t/c_{\text{RAE 2822}} = 0.121$. The upper limit of y_u is set to avoid sampling thicker airfoils in excess of $t/c > 0.1452$, which would be characterised by high compressibility drag. The shape optimisation simulations showed that the PARSEC methodology realised a 62% reduction in drag for the outer wing 2D profile in comparison to the original base section. Shape modification of the RAE 2822 airfoil, resulted in an airfoil generated by the PARSEC method, with drag reduction in excess of 47% in comparison to the base section. The flexibility of the

PARSEC method to achieve acceptable global solutions was verified. The results also indicated that the pre-processing of the shape variables had the further benefit of an efficient optimisation simulation as the solution search space was confined to regions with geometrically acceptable solutions. The application of penalty functions for shape-violated designs was avoided [56].

A Kriging-based optimisation method was developed and applied by Jeong et al. [57] in the re-design of a transonic airfoil with the PARSEC methodology. The total number of design variables was ten, with t_{te} set to zero such that only sharp trailing edge airfoils were considered. Shape optimisation with constraint on target lift c_l^T and airfoil cross-sectional area was implemented. The results indicated a shock-free profile with all constraints satisfied, in comparison to a base RAE 2822 airfoil. Drag reduction in excess of 16% was established and the aerodynamic efficiency (L/D) was enhanced. The flexibility of the PARSEC method to conform to stringent aerodynamic and geometry constraints was established. The analysis further evaluated the influence of each PARSEC shape variable on lift and drag at transonic Mach numbers with an analysis of variance (ANOVA) method. The results indicated that y_u and y_l had a dominant effect on c_l and c_d. The leading edge radius r_{le}, was computed with minimal impact. A pre-optimisation, sensitivity analysis was recommended to evaluate design variable impact on the solution search space. Shape optimisation with a reduced variable set by elimination of the least important coefficients was required for an efficient optimisation process. The scope of the solution search space was reduced, without compromising the flexibility of the shape function [57].

The original PARSEC method fitted a smooth curve between the maximum thickness point and the trailing edge, hence localised curvature changes at the trailing edge was not possible. The flexibility of the original PARSEC model [28] was extended with additional camber functions, including a modified trailing edge factor and an adaptive bump function by Klein and Sobieczky [59]. The total number of design variables increased from 11 to 14, with the inclusion of the proposed shape functions and the solution search space was enhanced. The modified PARSEC method was developed to represent various airfoil class types including the divergent trailing edge profiles for supercritical, high-speed performances to the highly-cambered sections for high-lift operations. Optimal airfoil profiles were a function of operating Mach and Reynolds numbers. The variant PARSEC method provided the design flexibility to model candidate airfoil shapes for optimisation over a wide-mission performance range spectrum [59].

A novel shape parameterisation method referred to as the class function / shape function transformation (CST) methodology was established by Kulfan [60]. The development focused on implementing a robust shape function model capable of generating disparate geometry types, with few design variables for efficient shape optimisation simulations. Unlike the PARSEC method, the CST function is not restricted to airfoil parameterisation. Instead, shape function transformations are implemented to model aerospace shape components including fuselage cross sections, rotor hubs and shrouds, engine nacelles, 3-dimensional aircraft wings, winglets, including pylons and struts. Theoretically, the CST method provides the design flexibility to model any airfoil class type, with acceptable accuracy.

The airfoil is mathematically represented by a combination of shape and class functions [60]. The shape functions are developed to represent arbitrary profiles as a function of geometry parameters. A mathematical equation is modeled to characterise the geometry for airfoil analysis. Shape functions

are developed from the fundamental geometry representation, as a function of profile parameters including leading edge radius, trailing edge angles and thickness distribution. Shape changes are applied by directly manipulating the corresponding parameters to control profile contour, while sustaining smooth and continuous shapes. Class functions are further applied and define airfoil shape type. Kulfan [60] developed several class functions for airfoil analysis including profiles with round nose and sharp aft body, to round nose / round aft body and sharp nose and aft body profiles. Class types are controlled by two user-defined parameters and the method theoretically provides an infinite set of profile types.

The order of the unit shape function influences airfoil contour at leading and trailing edge [60]. A unit function of one is decomposed into two component shape functions that scale the leading edge radius and the trailing edge angle. Scaling factors are applied which act as multipliers to each of the two component shape functions, hence controlling the relative magnitude of the leading edge radius and the trailing edge angle. A zero order unit shape function will generate a standard shape, representative of the particular class function type. Consider a class function with round nose and sharp trailing edge profile. A zero order unit function will result in a symmetrical airfoil with round nose and sharp aft body profile. The thickness distribution, including leading and trailing edge profiles is controlled by the order of the shape function [60].

The unit shape functions are based on the order of the Bernstein Polynomial (BP) [60]. The CST method provides a robust process, whereby the component shapes in the unit function are decomposed by the order of the BP. The first and last component shape functions will represent the leading edge radius and the trailing edge angle respectively for an arbitrarily defined BP order. The in-between component functions are referred to as 'shaping-terms' and additional corrections by Kulfan [50] are imposed to parameterise cambered sections that do not directly affect the leading and trailing edge regions. By increasing the order of the BP, the CST method provides a systematic approach to represent disparate airfoil family types. Theoretically, the method exhibits an acceptable design flexibility to facilitate a shape parameterisation model for airfoil design applications.

The feasibility of the CST method in comparison to the discrete and the B-Spline approach was evaluated for shape optimisation by the adjoint-based approach in [61]. Inverse and direct shape design applications were applied in the evaluation process. The computed c_p profile was evaluated against the user-defined benchmark performance by the inverse approach. An increase in the BP order resulted in the established pressure profile closely matching the intended target for the CST methodology. The shock wave modeled was in agreement to the target profile. A BP of order 11 was required to model the variation in pressure profile at the airfoil leading edge with acceptable convergence. Comparatively, a BP of order five, seven and nine did not exhibit acceptable pressure convergence. The physical airfoil shape convergence with variation in BP order, indicated a miss-match between target and computed profiles was isolated about the leading edge for selected wing stations. Acceptable airfoil shape convergence, irrespective of the order of the BP functions, was not achieved and limitations in solution accuracy were concluded. Irrespective of the shape and c_p profile miss-match, the CST method presented the best results in comparison to the B-spline and the discrete approach for the same design variable population size [61].

Shape optimisation by the direct approach was further examined to verify the feasibility of the CST method for two and three-dimension shape design by Mousavi et al. [61]. The objective was defined

with the requirement of minimising a weighted sum of c_d, with constraint on c_t^T and minimum wing thickness. Reduction in drag was comparable to the performance achieved by the discrete, B-spline and the Hicks-Henne shape functions for a 2D analysis. An increase in CST BP order was required to minimise wave drag by reducing shock at the tip for a 3D swept wing design. Comparably, the method did not achieve acceptable shock reduction at the root, hence drag was not reduced significantly. The discrete approach yielded lower drag performance in comparison [61].

To further verify the feasibility of the CST method, an optimisation case-study for a rectangular wing with NACA 0012 cross-sections was defined [61]. Drag performance of the optimal wing, at transonic Mach numbers and at a low angle-of-attack was established. The optimal profile is shock-free at all span stations in comparison to the base wing, modeled with symmetrical NACA 0012 profiles. The findings indicated that the measure of feasibility of the CST method was problem dependent and must be assessed accordingly due to the disparity in results for swept and planar rectangular wings.

The CST method was further applied in the design optimisation of a 2D airfoil and a 3D wing using the Tranair++ optimisation architecture developed by Boeing in [62]. A single-point problem was defined based on the cruise conditions of the RAE 2822 airfoil at transonic Mach number with constraints on c_l^T and thickness distribution. The BP order was systematically increased and the defined optimisation process in Tranair++, was applied and optimal drag performance was computed. Low drag is achieved at a BP of order six which asymptotes up to BP of order twelve, with variations restricted to one drag count. The asymptotic trend in drag performance highlighted the convergence of the solution search space at BP order six, for the design conditions examined. The CST method facilitated the evaluation of the search space due to the systematic increase of the design variables.

The solution search space convergence from 2D airfoil analysis was applied for 3D wing design, with cross-section profiles modeled by the BP functions in [62]. The application of geometry constraints for nose leading edge radius, trailing edge angle, including spar thickness and location were directly imposed on the corresponding CST shape coefficients. The flexibility for shape control, which was an identified design requirement of a parameterisation model, can be applied for wing-shape design. The optimisation process resulted in a drag reduction of 20 counts. The pressure isobars of the optimal shape indicated a smooth and 'clean' c_p performance. It was assumed that a further increase in BP order for wing spanwise modeling, will have a negligible effect on drag [62]. From the analysis, it was evident that a sensitivity analysis is required to determine the scope of the solution search space, as a function of the shape parameterisation model applied for the design cycle.

2.6 Flow Solver

The fitness of the objective function for aerodynamic shape optimisation simulations is calculated from the flow solver. The output must be of consistent accuracy for an acceptable optimisation. Solver types include: **a)** Fully potential; **b)** Coupled boundary-layer; **c)** Euler; and **d)** Viscous Navier-Stokes. The merits and demerits must be considered for integration into an optimisation architecture.

2.6.1 Fully Potential Methods

The fully potential methods are used to describe inviscid, irrotational, compressible flow, thus are valid at high Mach numbers. Irrotational conditions impose constant entropy, thus flow is considered isentropic instead of satisfying the Rankine-Hugoniot relation [37]. A constant entropy results in overestimation of the wave drag and it over predicts the shock location to be too far aft, hence overestimating lift [37]. The degree-of-severity of the overestimated coefficients has an influence on the optimisation process. Consider design optimisation of a transonic airfoil, where the objective is to minimise wave drag. If the full-potential solver overestimates the drag coefficient to be proportionally greater than the over predicted lift, then the search model will be guided away from shapes with strong shocks. This is presumed to be the case in the work by Obayashi et al. [63]. Quagliarella et al. [64] uses the method in the minimisation of the wave drag for single-element airfoils, under the assumption that the main contributor to drag at the transonic region is due to the development of a weak shock and not viscosity in the boundary layer. Alternately, accurate aerodynamic data prediction through the use of numerical relations is established by Klopfer et al. [65] where empirical functions are used to estimate the Rankine-Hugoniot relation for flows across shocks with full-potential methods.

2.6.2 Euler Methods

Euler methods represent rotational, compressible flow and neglect viscous effects. The solver is used for flows at low α, where the flow is attached and the boundary layer is thin. The demerit is the additional computational time expense for flow simulations, in comparison to full-potential methods, which is not acceptable for an iterative optimisation cycle. Iollo et al. [66] performed design optimisation of a supercritical airfoil at Mach 0.75 based on the assumption of attached flow. The computational time penalty was addressed by using a pseudo-time scheme of Ta'asan [67]. The proposed algorithm, calculates the gradient of the search direction. It solves the minimisation of the objective function along the hypersurface defined by the state, co-state and design equations, instead on the intersection of the state and co-state region of traditional gradient methods. Namgoong [41] addresses the issue of additional computational time, in the design optimisation and computation of wave drag for transonic airfoils. This is carried out by using the Euler methods, distributing the optimisation on a parallel computing cluster. Huyse et al. [68] applied unstructured grids for single and multi-point airfoil optimisation. It was concluded that viscous effects need to be integrated to establish accurate pressure distributions.

Fully-potential and Euler methods consider inviscid flowfield with wall surface viscosity computed by coupling empirical functions, to establish regions of laminar and turbulent flows. Boundary-layer parameters including displacement and momentum thickness and shape factor are calculated from flow velocity profiles. Empirical methods determine the extent of laminar and turbulent regions, including the onset of flow transition and eventual flow separation. Hence, viscous drag due to the development of a boundary layer is established. Quagliarella et al. [64] used a coupled method in the design optimisation of high-lift, multi-element airfoils by modeling the inviscid region using Euler equations and integral compressible boundary layer equations to establish viscous flow. Thus, viscous drag due to the development of complex flow features such as flow separation, on wall surface as a result of high-lift flows was accounted for by the coupling method.

De Sousa et al. [69] integrated a potential method with a boundary-layer code for flow simulation, in the design optimisation of airfoils at low Reynolds and Mach numbers. The potential flow was calculated based on panel discretisation with source and vortex singularities implemented to determine the aerodynamic coefficients and a boundary layer integral formulation for laminar-turbulent transition point estimation and the onset of flow separation. The proposed design architecture was appropriate for the set problem, due to flight operations at low Reynolds and Mach numbers, where the effects of viscosity are significant [69].

2.6.3 Navier-Stokes

Viscous/inviscid interactions are critical at low Reynolds numbers. Navier-Stokes solvers are used as it considers the viscous effects in the entire flow region and solve the Reynolds Average Navier Stokes (RANS) equations of the flow. The RANS equations coupled with turbulence modeling are applied to compute the flow features at HALE and transonic Mach numbers. In laminar flow for HALE airfoils, a Laminar Separation Bubble (LSB), due to adverse pressure gradients in the boundary layer are formed at low lift coefficients and the wall viscous effects are dominant. The surface boundary layer mesh must be well-defined and turbulence modeling applied accordingly to accurately model the viscous drag. At low α, the LSB can lead to a sudden and rapid loss of lift. An adaptive wall surface mesh is applied to concentrate the cells at regions exhibiting adverse/fluctuating flow residuals due to the formation of a LSB and/or dominant viscous effects. The magnitude of the Reynolds number and flow angle-of-attack, affect the position of the LSB, which influences flow transition to turbulence. The formation of turbulence creates a large momentum transport normal to the shear layer, with the flow re-attaching to the surface further downstream, thus closing the bubble. The size of the LSB affects the magnitude of the pressure drag by displacing the outer inviscid flow, thus reducing suction over the forward section and decreasing the pressure recovery at the aft region of the airfoil. Panel method solvers with an integrated coupled boundary-layer integral method, are not reliable in identifying the development and break-up of a LSB, hence pressure drag. At transonic Mach numbers, the shock wave increases wave drag and can result in flow transition to sudden and rapid separation.

Sophisticated RANS with turbulence modeling and coupled to a valid wall surface mesh have been defined to model the complicated flow patterns, including the generation of a LSB in [70, 71] and validated [70–74]. Chaouat [70] developed a model to numerically predict flow past airfoils at high angle-of-attack by solving the transport equations on the individual Reynolds stresses, in particular turbulent normal wall stress, which is critical in high-lift flows. Windte et al. [72] examined the effectiveness of a RANS model in predicting the aerodynamics of a low-Reynolds number airfoil, operating at typical Micro-Aerial Vehicle (MAVs) flight regime (Re=6×10^4). At these conditions, the onset of flow transition across a LSB is evident in the experimental process. Computationally, the onset of transition is identified by using an approximate envelope method that is the bases of the Linear-Stability Theory (LST).

In the analysis by Hellsten [75] the importance of a boundary layer under adverse pressure gradients, wakes and mixing layers is identified as critical flow features in the development of a turbulence model. Specifically the interaction of a boundary layer with surface wake, influences the maximum lift coefficient of multi-element airfoils at high-lifts. Original turbulence models incorrectly model

the gradual spread of wakes due to unphysical sharp edges of the turbulent regions, thus incorrectly computing the maximum lift coefficient of multi-element airfoils. The original $\kappa-\omega$ turbulence model of Menter [76] is modified by Hellsten [75] by calibrating the diffusive terms through numerical computations and validations. Test problems including plane channel flows, plane far wakes and mixing of layers in multi-element airfoils are tested and validated with acceptable accuracy relative to published experimental data.

Windte et al. [77] examined the effectiveness of a RANS model in predicting the aerodynamics of a low-Reynolds number airfoil, operating at typical Micro-Aerial Vehicle (MAVs) flight regime (6×10^4). At these conditions, the onset of flow transition across a LSB is evident in the experimental process. Computationally, the onset of transition is identified by using the LST method. The integral flow parameters are computed using boundary layer equations, to establish flow shape parameter and Reynolds number based on the momentum thickness. The approximate envelope is built from XFOIL [78] and the e^N - method used to calculate the amplification rate of the flow instabilities. The amplification rate is integrated to the established N-factor envelope and transition location predicted by comparison to the critical N-factor. Simulations indicated acceptable measurement of the LSB and aerodynamic coefficient agreement relative to experimental data [77], with Menter's two equation turbulence model [76]. Simulations using XFOIL as a direct flow solver, predicted a thin LSB in comparison to theoretical experimental data, which is attributed to the prediction of the transition point that is slightly upstream of the measured location from the experimental data. An alternate approach for transition prediction was proposed by Stock [79]. The pressure distribution from the RANS solver can be used to compute the velocity profile with a boundary layer method. Windte et al. [77] observed that available boundary layer methods cannot accurately model the laminar separated flows, for low Reynolds number flight associated with MAV operations.

Choi et al. [73] used a one-equation, Spalart-Allmaras turbulence model to predict the aerodynamic characteristics of an elliptical airfoil at Reynolds numbers between 2.48×10^6 and 3.91×10^6 with freestream Mach numbers in the subsonic to transonic range. A boundary layer transition prediction methodology was not used and the flow was assumed to be fully turbulent. Computational results were compared against published experimental data for a NACA 0012 profile to validate solver set-up. Acceptable aerodynamic agreement for lift, drag and moment was observed at a Reynolds number of 3.91×10^6 and Mach 0.30, where wave drag was not an issue. At transonic speeds with Mach 0.80 and with a lower Reynolds number of 3.00×10^6, drag due to viscosity became significant together with wave drag. A fully turbulent flowfield was one of the reasons why poor drag convergence in comparison to experimental data was observed. Choi et al. [73] attributed this to the over predicted reverse-pressure region aft of the shock wave. At lower Reynolds and Mach numbers, acceptable coverage of the leading-edge LSB including flow separation at the trailing edge was established in comparison to experimental solutions. In this case, a comparison between solver and experimental data was limited to pressure coefficient distribution. The potential flow theory adequately provided acceptable lift accuracy and is unaffected by the presence of a viscous boundary layer. The drag and moment forces are influenced by the properties of the boundary layer at lower Reynolds number. Convergence of the aerodynamic coefficients toward experimental data was not presented. The affect of a fully turbulent flow condition and corresponding influence on drag and moment in comparison to experimental solutions was not established from the analysis.

Kern [74] validates a one-equation Baldwin-Bath (BB), Spalart-Allmaras (SA) and a two-equation Shear Stress Transport (SST) turbulence models, to predict high-lift flows on multi-element airfoils. Turbulence modeling often over-predicts the c_{lmax} and the AoA at c_{lmax}. Even with fine grids, the reading of stall characteristics with one and two equation turbulence models is a design challenge. In the simulations by Kern [74], lift trends up to stall AoA, including the α at c_{lmax} were adequately modeled by the three turbulence models. Correlation of post-stall lift and pressure coefficients were not accurate in all models. The BB and SST models provided similar lift trends as the experiment in the post-stall AoA range, with the SA model indicating the worst convergence, with an error in excess of 14%. The validation process indicated that the SST model is superior to one-equation models in predicting post-stall airfoil leading edge suction including flow separation and re-attachment. The leading edge flap suction is modeled more adequately with the BB model than the SST, but the SST indicated acceptable convergence to experiment for suction on the trailing edge flap. It is recognised that the onset of flow transition should be modeled to improve solver accuracy and is critical to accurately predict c_{lmax} and the α at c_{lmax} [74].

2.7 Optimisation Algorithms

The DNO architecture requires the development of an intelligent search operator for airfoil shape design. The process uses the inputs of the geometrical shape function to represent the airfoil and a flow solver to establish the aerodynamic coefficients. The search mechanisms in the optimisation algorithm operate iteratively to guide the search to the optimal point. An efficient optimisation algorithm must be capable of providing a global solution with acceptable computational resources. In aerodynamic design, time-consuming flow solvers are used to model the complicated flow features for fitness evaluations (Sec. 2.6). The application of an efficient search algorithm capable of generating a global solution with acceptable computational resources is a requirement for iterative based optimisation simulations.

The optimiser type applied will influence the computational resources required to convergence and the feasibility of the established solution. Search algorithms are problem based and must be defined accordingly. Optimiser types for shape design include: **a)** Gradient-Based; **b)** Adjoint-Based; and **c)** Evolutionary Algorithms. Optimisation problems are governed by user-defined objectives and constraints. Constraints include equality and inequality terms which may conflict with the objective function. The constraints are often nonlinear and the optimiser is required to solve a set of nonlinear constraints to establish the minimum of a nonlinear objective function. The search topology will consist of multiple local minima and a robust search process becomes a requirement.

In airfoil design, a decrease in profile drag may conflict with the user-defined geometry constraints, hence resulting in a multi-modal search topology. The optimiser type applied must adapt the search process to mitigate conflicting design issues between constraints and objectives. The search principles, including the merits and demerits of the optimiser type must be considered for direct application into airfoil design at HALE and transonic Mach number flight conditions.

Mathematically, the optimisation process is defined in the form:

$$\begin{aligned} \underset{x \in \mathbb{R}^n}{\text{minimise}} \quad & f(x) \\ \text{subject to} \quad & c_i(x) = 0,\ i = 1, \cdots, n_e \\ & d_j(x) \geq 0,\ j = 1, \cdots, n_i \end{aligned}$$

Where:

Variables	$: x \in \mathbb{R}^n$
Objective Function	$: f:\ \mathbb{R}^n \rightarrow \mathbb{R}$
Equality Constraint	$: c_i : \mathbb{R}^n \rightarrow \mathbb{R}$
Inequality Constraint	$: d_j : \mathbb{R}^n \rightarrow \mathbb{R}$
Feasible Search Set	$: \mathcal{D} = \{x \in \mathbb{R}^n \ \lvert c_i(x) = 0,\ d_j(x) \geq 0\}$

The solution in an optimisation problem may be classified as global minimum, local minimum or local minima as shown in Figure 2.6.

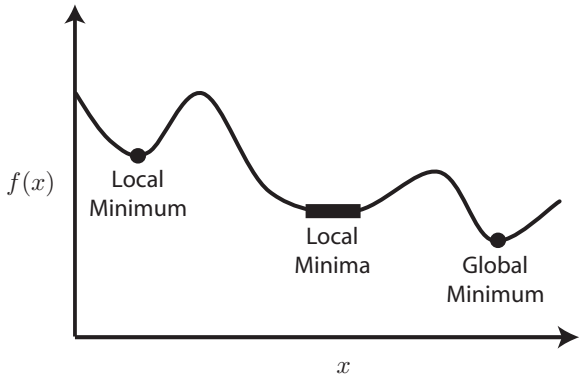

FIGURE 2.6: Optimisation Solution Classification

Where:

Global Minimum	: A point x^*satisfying $f(x^*) \leq\ f(x)\ \forall x \in \mathbb{R}$
Local Minimum	: A neighborhood $\mathcal{N}$ of x^*exists such that $f(x^*) <\ f(x)\ \forall x \in \mathcal{N}$
Local Minima	: A neighborhood $\mathcal{N}$ of x^*exists such that $f(x^*) \leq\ f(x)\ \forall x \in \mathcal{N}$

The objective function is defined as convex (Fig. 2.7(a)) or non-convex (Fig. 2.7(b)). In convex designs, there is a *unique* optimum to the design problem. In non-convex problems, there exists multiple minima topologies and a flexible search method is required to locate the true solution.

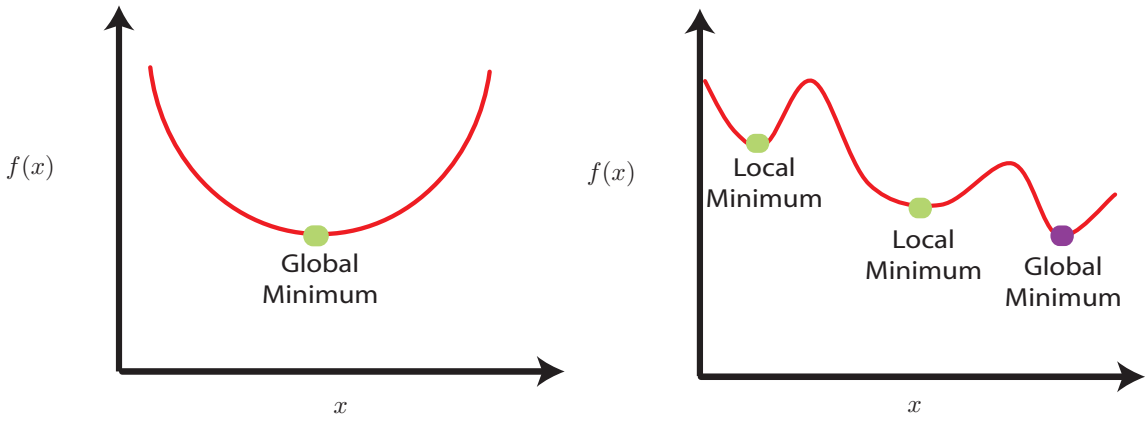

(a) Convex Objective Function

(b) Non-convex Objective Function

FIGURE 2.7: Objective Function Solution Representation

Disparate optimisation algorithm types can be applied to minimise (or maximise) $f(x)$ and include:

2.7.1 Gradient-Based Methods

Gradient-Based methods (GM), have been widely used for aerodynamic shape optimisation problems. The algorithm computes the sensitivity of the fitness derivative by perturbing the design variables, to guide the search toward an global optima. The objective function is iteratively minimised by modifying the direction of the gradient vector toward a solution. Consider an arbitrary airfoil shape $f(x)$, defined by a series of design parameters a_i and shape functions b_i in Equation 2.18:

$$f(x) = \sum_{i=1}^{n} a_i.b_i(x) \tag{2.18}$$

The objective function $\mathcal{J}$, is a function of the design parameters such that:

$$\delta\mathcal{J} = \sum_{i=1}^{n} \frac{\partial\mathcal{J}}{\partial a_i}\delta a_i \tag{2.19}$$

Where:

$$\frac{\partial\mathcal{J}}{\partial a_i} \text{ is the gradient vector}$$

The objective $\mathcal{J}$, which is a function of the shape parameters a_i, is selected as the drag coefficient or the maximisation of L/D. The sensitivities are calculated by [80]:

$$\frac{\partial\mathcal{J}}{\partial a_i} \approx \frac{\mathcal{J}(a_i + \delta a_i) - \mathcal{J}(a_i)}{\delta a_i} \tag{2.20}$$

The change in $\mathcal{J}$ is by the continuous and iterative flow calculations with variations in a_i. Independent flow analysis is needed to estimate gradient, hence search direction for each design variable. The computational costs become prohibitive for a large dimensional search space.

The gradient vector computes the search direction to improve $\mathcal{J}$. The gradient establishes the search direction S, at iteration k, which is multiplied by a scalar step length β_k, to update the search

direction at $k+1$ in Equation 2.21.

$$S_{k+1} = S_k + \beta_k . \Delta f(x^{(k)}) \tag{2.21}$$

The computation of S, is dependent on first or second order methods. First order methods apply $\Delta f(x^{(k)})$ to calculate S, while second-order methods use both $\Delta f(x^{(k)})$ and the Hessian matrix, which is the second derivative of $\delta \mathcal{J}$, to establish the search direction. The line search methodology is applied to obtain the gradient of the objective function at each iteration k, through a higher order Quasi-Newton method [53] for GM-based simulations in the thesis. The algorithm uses the partial derivative of the objective function $\Delta f(x^{(*)})$ and the approximations to the Hessian H, is based on the Quasi-Newton method [53]:

$$\Delta f(x^{(*)}) = Hx^* + c \approx 0 \tag{2.22}$$

Where:

$$\begin{aligned} x^* &= \text{Optimal Solution} \\ c &= \text{Constant Vector} \\ H &= -x^{*-1}c \end{aligned}$$

The gradient of the objective function by the perturbation of design variables is obtained with a finite differences method, to refine the search toward a minima. The line search algorithm applies a pre-defined scalar step length a_k, to direct the search p_k, with a decreasing objective function, after each iteration x_k. The iterative process is based on Wolfes method which operates along the line $x_k + a_k . p_k$, until convergence. The line search algorithm and the search mode are expressed as follows [53]:

$$x_{k+1} = x_k + a_k . p_k \tag{2.23}$$

$$p_k = -H_k^{-1} . \Delta f(x_k) \tag{2.24}$$

The Pseudocode of the GM method is summarised in Algorithm 1:

Algorithm 1 Standard Optimisation by Gradient-Based Framework

1: Define Search Initialisation point x_0 at iterate $k = 0$
2: **while** no convergence **do**
3: $\quad x_{k+1} = x_k + \alpha_k p_k$
4: $\quad k \leftarrow k + 1$
5: **end while**

The GM process is classified as sequential or transformation based. Sequential based are applied to simplify nonlinear problems by linearising the objective function and constraints. The linear approximation is only valid in the neighborhood of the specified starting point and the norm of the search vector used to guide the algorithm must be constrained to avoid search patterns in unfeasible regions (i.e. non-linear topologies). The search vector is further constrained by restricting the maximum allowable perturbations of the design variables, or the move limits. These limits must be well defined and adaptive to the search process. If the variable perturbations are extreme, then the

search will oscillate and experience convergence difficulties since it will violate the identified linearisation neighborhood and search non-linearisation regions. If the perturbations are limited, then a slow convergence will result which is computationally not viable with a time intensive fitness function evaluator.

The transformation based methodology introduces a penalty to the objective function, to shift nonlinear optimisation problems into an unconstrained problem. During the search process, if the stipulated constraints are violated, a penalty is added to the objective (for function minimisation) to avoid search processes in unfeasible regions. The severity of the penalty will influence the search patterns of the optimiser. Thus, an acceptable penalty function is required to establish an optimal solution that conform to defined constraints.

A global solution by a GM analysis is achieved if the objective and constraints are differentiable and convex (Fig. 2.7(a)). In engineering design applications this condition is not true and the process of validating the search topology is a design issue. In general, the GM method will converge to a local solution about the starting point. The sensitivity of the search process is directly related to the feasibility of the starting point. To ensure solution viability, the optimisation process is initiated with random starting points to confirm solution convergence. The GM method is not computationally viable nor robust. The demerits of the GM method include: **a)** Convergence to a local solution for an ill-defined starting point; **b)** Computational efficiency is influenced by the methodology applied to compute the gradient of the objective and constraints functions; and **c)** Gradient calculation is sensitive to search space noise.

The use of GM is problem dependent. It has been shown that aerodynamic optimisation problems are non-smooth or non-convex [41, 81] and the use of GM will have issues and challenges. Shape design problems are nonlinear and exhibit discontinuous derivatives for objective and constraint functions, hence limiting the use of GM for airfoil shape optimisation. A GM method with an ill-defined starting point, will generate a local optimum in the neighborhood of the search initialisation point. The application of constraints further complicates the search process. Sequential quadratic programming methods have been developed to handle objective constraints. Equality and inequality constraints are handled in the same manner as objectives (i.e. reduced for minimisation functions). The Jacobean matrix is calculated for both the constraints and the objectives. If the objective function can no longer be improved, without deteriorating the constraint values, the search will stagnate and prematurely terminate.

Namgoong [41] examined the use of GM in the design optimisation of transonic airfoils with variations in solution starting point, for wave drag minimisation. Drag reduction was directly related to variations in base airfoils, thus indicating a local optimal about the starting point with a multi-modal solution topology. The results indicated disparate solutions with respect to initial base airfoils. The solution search space was characterised by a highly non-linear and discontinuous topology, with several combinations of design variables not having a feasible solution. A multi-modal design space with numerous local minima was not conducive to feasible design optimisation simulations by the GM approach.

Gallarat [42] evaluated the performance of three GM tools in the design optimisation of an airfoil for morphing aircraft. It is acknowledged that the proposed method does not guarantee a global optimum.

Khurana et al. [82] established the solution space to HALE airfoil designs, to be highly multi-modal. Despite integrating a current off-the-shelf HALE airfoil for search initialisation, aerodynamic performance improvement in comparison to the baseline shape was minimal. It was concluded that GM provides a local solution about the starting point and not the true global optima.

It has also been shown that the solution search space for an objective function at multiple flight conditions is complex and multi-modal due to the non-linearity within the different objective components. Gradient based methods are not valid and novel search strategies are required. The merits and demerits of the different optimiser types must be considered for airfoil shape design to address the limitations of the GM approach.

2.7.2 Adjoint Methods

Post Hicks and Henne, advancements in gradient methods by the adjoint formulation [80, 83, 84] have been used for shape optimisation. Since aerodynamic optimisation problems require a large design variable population size, the application of finite difference schemes is not viable. Optimisation strategies using a mathematical control of systems governed by the partial differential equations (PDE), have been developed to address the demerits of finite differences approach [85]. An adjoint method was formulated where the flow equations are applied to compute the gradient of the objective function by Jameson [85]. As the methodology did not apply the shape coefficients for gradient computation, the computational costs were minimised. The methodology facilitated a design optimisation with a large design variable population size for shape parameterisation flexibility, than the finite differences method. The computational effort for design iteration is the time required to solve the flow equations.

The adjoint approach is independent of the number of design variables. The methodology is suited for the design optimisation for problems with an extended search space, with a large design variable population size. The design optimisation of shock-free airfoils at transonic conditions is sensitive to small surface perturbations. High Mach number flow shape designs require a greater number of shape variables to minimise and/or eliminate the onset of shock. The adjoint approach facilitates the implementation of additional shape variables for subtle geometry changes, hence shock minimisation.

The shape of the airfoil is a primary design structure that controls the lift generated by manipulating the flow. In the adjoint approach, the airfoil a, is modified to manipulate the flow equations R, for an optimal design. The objective is defined by cost $\mathcal{J} = c_d$, which is an integral of flow variables w over airfoil a. Shape modifications are performed to reduce c_d, hence vary cost $\delta\mathcal{J}$. The flow variables of the shape are computed from the flow equation $R(w, a)$. A modified shape ∂a with $\delta\mathcal{J}$, is a function of δa, which is established by the flow PDE of δR. The finite difference approach solves δw to compute $\delta\mathcal{J}$, which results in a high computational turn-over time if the vector w is large. The adjoint approach does not directly solve δw due to the introduction of a Lagrange multiplier which has the effect of eliminating the calculation of δw from the gradient computation of $\mathcal{J}$, with respect to an arbitrary number of design variables [86].

The gradient of the objective function is related to the state (flow) equations. Relating the cost function $\mathcal{J}$, to the drag coefficient, as a function of flow field variables (w) and airfoil geometry a,

the cost function is described as [80]:

$$\mathcal{J} = \mathcal{J}(w, a) \tag{2.25}$$

The cost function is modified, due to shape perturbation a by [83]:

$$\delta\mathcal{J} = \left[\frac{\partial\mathcal{J}^T}{\partial w}\right]_I \delta w + \left[\frac{\partial\mathcal{J}^T}{\partial a}\right]_{II} \delta a \tag{2.26}$$

Where the subscripts I and II denote to the change in δw in the flow field and shape perturbation δa respectively.

The governing flow equation R, is modeled as a function of w and a, in the flow field domain D as:

$$R(w, a) = 0 \tag{2.27}$$

Hence, δw is computed from [83]:

$$\delta R = \left[\frac{\partial R}{\partial w}\right]_I \delta w + \left[\frac{\partial R}{\partial a}\right]_{II} \delta a = 0 \tag{2.28}$$

The finite difference approach computes δw (Eqn. 2.28) and substitutes into Equation 2.26 to establish $\mathcal{J}$. The computational costs becomes excessive for geometry parameterisation with a large dimension search space.

In the adjoint approach [80, 83, 84] the direct computation of δw is not required. Since the change in δR is zero, a Lagrange multiplier ψ, is introduced. The variation in δR is subtracted from $\delta\mathcal{J}$. The variant of Equation 2.26 by the adjoint approach becomes [83]:

$$\begin{aligned}\delta\mathcal{J} &= \frac{\partial\mathcal{J}^T}{\partial w}\delta w + \frac{\partial\mathcal{J}^T}{\partial a}\delta a - \psi^T\left(\left[\frac{\partial R}{\partial w}\right]\delta w + \left[\frac{\partial R}{\partial a}\right]\delta a\right) \\ &= \left\{\frac{\partial\mathcal{J}^T}{\partial w} - \psi^T\left[\frac{\partial R}{\partial w}\right]\right\}_I \delta w + \left\{\frac{\partial\mathcal{J}^T}{\partial a} - \psi^T\left[\frac{\partial R}{\partial a}\right]\right\}_{II} \delta a\end{aligned} \tag{2.29}$$

Where ψ is applied to satisfy the adjoint equation [83]:

$$\left[\frac{\partial R^T}{\partial w}\right]\psi = \frac{\partial\mathcal{J}}{\partial w} \tag{2.30}$$

The first term in Equation 2.29 is eliminated and $\delta\mathcal{J}$ is defined as [83]:

$$\delta\mathcal{J} = \mathcal{G}^{\mathcal{T}}\delta a \tag{2.31}$$

Where [83]:

$$\mathcal{G} = \left[\frac{\partial\mathcal{J}^T}{\partial a}\right] - \psi^T\left[\frac{\partial R}{\partial a}\right] \tag{2.32}$$

The benefits of the adjoint approach is evident in Equation 2.31. The function is independent of ∂a. The gradient $\mathcal{G}$ is computed without additional solver evaluations with respect to the number of design variables [84]. The gradient vector $\mathcal{G}$ in Equation 2.32 is used to establish the search direction

improvement, which is based on the steepest descent method by [84]:

$$\delta a = -\lambda \mathcal{G} \tag{2.33}$$

Where the parameter $+\lambda$, is user-defined and small enough to facilitate a variation in $\delta \mathcal{J}$ toward solution improvement such that [84]:

$$\delta \mathcal{J} = -\lambda \mathcal{G}^T \mathcal{G} < 0 \tag{2.34}$$

Specified constraints are integrated into the design problem to establish a gradient that conforms to the set design requirements. Hence, constraint satisfied solutions can be achieved by the select optimisation algorithm which include robust non-linear search processes including quasi-Newton methods or sequential quadratic programming (SQP) approaches, for design problems with linear and non-linear constraints [84].

The adjoint approach will theoretically result in an efficient computational design process. The defined control theory is used to evaluate the gradient by solving a single adjoint equation that is directly related to the computational resources needed to solve the flow equations. The merits of the adjoint approach are further related to the method type used to solve the fundamental PDE equations. The two adjoint categories include the *continuous* and *discrete* methods. Kim [84] acknowledges that the *discrete* approach will theoretically output gradients that are of an acceptable match to the exact finite-difference gradients method. The *continuous* adjoint system has a form that is independent of the scheme applied to solve the flow field equations. Kim [84] refers to the study by Nadarajah and Jameson [87], where a gradient performance comparison between the two approaches is examined. It is concluded that there is no distinct benefit in using either method due to the trade-offs between the complexity of the discretisation of the adjoint equations, including the accuracy of the output estimates of the gradient and the overall computational expense needed by the respective approach for convergence to the optimum.

The adjoint approach for accurate gradient estimation is problem dependent [84]. Verification studies by Burgreen and Baysal [88] confirmed the advantages of the *discrete* approach for wing shape optimisation using structured grids. Anderson and Venkatakrishnan [89] validated the merits of the *continuous* approach for CFD problems with unstructured grids.

The integration of the steepest descent method (Eqn. 2.34) for shape optimisation simulations within an adjoint formulation has drawbacks. Premature convergence to a local minimum is an issue due to the limitations of the steepest descent approach, hence a well-defined starting point is a requirement. Additionally, the adjoint method requires the derivation of an entirely new system of partial differential equations in terms of non-physical adjoint variables and the specification of the corresponding boundary conditions [41]. It has also been shown that the accuracy of the *continuous* adjoint process depends on the discretisation scheme, which must be as close as possible to that used for the discretisation of the state equations [90].

The application of the adjoint approach for shape optimisation problems with multiple constraints will require independent adjoint equations to solve the gradient for each constraint. The theoretical merits of computational time benefits are diminished as the number of constraints imposed on the design problem is increased. The integration of a GM optimisation algorithm within an adjoint approach is not justified due to the identified limitations of a gradient search process based on the

steepest descent method. Hence, aerodynamic design methodologies with stochastic optimisation algorithms are explored instead to address the identified limitations.

2.7.3 Evolutionary Algorithms - Global Search Methods

Evolutionary algorithms, also referred to as global search methods, have been developed to mimic the process of natural evolution. Theoretically, EAs have the advantage of yielding global optima by overcoming the limitations of the deterministic gradient-based search methods. The technique represent the process of reproduction, mutation, recombination and selection based on the biological evolution. Candidate solutions to the optimisation problem are characterised by a set of search agents or sample population, which evolve in the search environment to achieve an acceptable solution to the objective function. The search operators iterate until an optimal solution is established. The method is computationally demanding in comparison to local methods as the individual search agents need to be evaluated by the fitness function. This leads to a time consuming search process for CFD applications and the use of parallel processing becomes a requirement.

The EA based methods do not require the definition of a scalar step length λ for shape perturbation, unlike GM and adjoint based algorithms. Instead, adaptive functions based on the collective search behavior of the population are applied to intelligently control the magnitude of λ. The step length varies in accordance to the nature of the solution topology as mapped by the search population during the design evolution stage. The size of λ is set to balance between a global or local search process. The ambiguity of specifying a valid λ based on designer experience or intuition or as a result of time-intensive, design-of-experiments study is avoided. The methodology also does not require a user-defined starting point. Instead, the search is initiated by a random generation of sample shapes. The issue and challenges associated with defining an acceptable search initialisation point is avoided.

The issue of generating a local, sub-optimal solution by gradient-based algorithms is due to reduced solution diversity from an ill-poised starting point and by the incorrect definition of λ. The implementation of EA based methods enhances the search diversity and the probability of convergence to the true optima is increased. Biological operators including reproduction, mutation and recombination of the strongest (low fitness cost) solutions are applied to increase diversity. Due to the population based search principles of EAs, the methodology is computationally time-intensive. The algorithm is adaptable to computation by parallel computing and accelerated simulations are achievable.

The EA design optimisation methodology is ideal for multi-modal and discontinuous search topologies. An assumption of a smooth and continuous solution space to achieve a search process to an acceptable optimal is not necessary unlike local design methods. The algorithm is applicable for engineering design problems. The fundamental search principles within the EA methodology guide the search through the solution topology until convergence is achieved based on a user-defined termination criteria.

Widely used methods include genetic algorithms (GA) [91], simulated annealing (SA) [92], ant colony (AC) [93] and particle swarm optimisation (PSO) [94]. The GA, SA and AC are effective for design optimisations, but are computationally intensive due to the implementation of time-exhaustive

search operators such as crossovers and mutations. The biological operators for search diversity have the demerit of increasing the number of fitness function solver calls. The PSO methodology was initially developed without mutation operators to maintain acceptable computational resources. The drawback was a reduction is solver robustness and sub-optimal solutions were generated for high-dimensional search spaces. Research efforts have focused on developing intelligent algorithms for acceptable solution diversity, hence enhancing the feasibility of the solution. An acceptable balance between fitness computation overheads and solution validity are the goals in the development of a robust EA model. The identified requirements have been partially addressed by the GA, SA, AC and PSO methods, but there are pending issues and challenges which need to be addressed.

2.7.3.1 Genetic Algorithms

The GA has been widely applied in aerodynamic shape optimisation problems. Huang et al. [95] used a real-coded GA for airfoil flow optimisation using a two-jet control system. Due to the multi-modal nature of the search domain, modifications to the base GA were executed to improve the local search capabilities. A series of operators were developed to accelerate convergence by explicitly updating the search boundaries and adding search control methodologies to reduce the probability to premature convergence. The analysis confirmed that regardless of the theoretical search capabilities of the optimiser, the robustness of the algorithm must be evaluated for the proposed design problem. The use of an off-the-shelf GA for shape optimisation without search parameter tuning for specific design applications will result in a sub-optimal solution. The limitations of the search method need to be identified and addressed before simulating a design optimisation process, especially if computationally demanding function evaluators are integrated into the design cycle.

Holst et al. [96] used a real-number encoding methodology to represent genes for airfoil shape design space definition. The applied method eliminated the requirement of converting binary representations of the design variables to linear numbers, thus reducing CPU time. The performance of GA is evaluated by airfoil direct and inverse design process with constrained lift for drag minimisation at transonic speeds. The developed GA method converges to an acceptable airfoil shape, but the validity of the solution was not verified.

Namgoong [41] showed that the presence of a shock wave affects the discontinuity and multi-modality of the design space, thus GM was unsuitable in the design optimisation of transonic airfoils. To address the shortcoming, a GA was used to yield superior solutions in comparison [97]. A binary-coding GA was used to represent the design variables and a tournament selection methodology to select the 'fittest' particles for survival at each generation. A crossover operator was used to develop new strings by combining the two parent strings to form two child designs, based on a user-defined crossover rule. Single and multi-objective optimisations in the form of aerodynamic only and the combination of aerodynamic and strain energy models, required to morph the airfoil were examined respectively with the proposed GA. Drag minimisation at three disparate target lift coefficients was individually examined for a single-point / single-objective design. In total 134,400 XFOIL function calls were required for solution convergence. A multi-point optimisation was further examined. The objective function was in the form of a weighted sum of the drag coefficient at the three lift coefficients as examined in the single-point design. A compromised solution for drag which compensated for

performances at three different flight conditions was established and 403,200 XFOIL simulations were executed. The analysis was further extended to a multi-objective process with the introduction of a strain energy function together with the minimisation of drag at disparate flight conditions. Consequently, the total number of function calls increased significantly and was in excess of one million for a complete multi-objective simulation [97].

The number of function calls for single-point optimisation was excessive in [41, 97]. This was attributed to the underlying workings of the GA search operators and the relaxed termination condition which was introduced to mitigate premature convergence. Even though parallel computing addresses the heavy computational overheads, the need to maintain an acceptable function evaluation count, without compromising the global optima, requires further design consideration. This will be of greater importance for multi-objective analysis, where additional functional calls are required at each simulation to account for the disparate objectives. With the introduction of an additional objective, the complexity of the search topology increases. A relaxed termination criterion would result in a global solution, at the expense of computation time. The results by Namgoong [41] indicated that the operating principles of the search algorithm needed to be tuned to address the issue of high computation time associated with single and multi objective design optimisation simulations, without compromising the feasibility of the solution. The developed algorithms in the thesis address this requirement (Chapter 3).

In the analysis by Winnemller et al. [98], a hybrid search methodology was proposed. The gradient search tool was combined with the GA of Holst [96] for the multi-objective design optimisation of thick airfoils with a viscous Navier-Stokes solver. The objectives required maximising airfoil lift-to-drag and the moment of inertia with geometry shape constraints [98]. The proposed methodology initially applied the gradient based method for a single objective problem, focusing primarily on maximising the lift-to-drag ratio of the airfoil. Since the objectives were contradictory, a constraint on the minimum allowable aerodynamic efficiency was formulated to avoid airfoils with high moment of inertia and drag. The solution of the GM was then applied as an input to the GA for a multi-objective optimisation analysis. The results indicated the development of blunt trailing edge airfoils. Due to the multi-objective formulation, the solutions to the Pareto front were used to select a shape with acceptable compromise between aerodynamic and structural efficiency. The viability of applying a hybrid search methodology with the combination of local and global search models was presented. It was proposed that a local search methodology would provide solution improvements where the degree-of-enhancement was problem and search model based, only if the outputs of the global method were used as inputs to the GM search algorithm [98].

In the analysis by Quagliarella et al. [99], a standard GA and a GM based on the hill-climbing approach were applied for airfoil shape design. Two hybrid methodologies were proposed and demonstrated. The population set of the GA data at each generation was used as an input to the local method with the following distribution: **a)** The entire solution population is used as an input to the GM; and **b)** Intermediate selection process determines a subset of elements from the population that will be analysed in GM. The hybrid architecture used the standard GA operators of selection, crossover and mutation, to initiate the optimisation followed by a GM analysis on the chosen individuals. The results indicated that a hybrid search approach resulted in a drag reduction of 0.7% in

comparison to a stand-alone GA simulation for constrained airfoil design optimisation at transonic speeds.

The effect of varying the optimisation algorithm based hybrid search operators and the maximum iteration count for search termination on drag was not defined in [99]. The operators would influence the search properties and the sensitivity of the selected parameters was unknown. An adaptive approach would suffice which varies the distribution set through the search process, instead of fixing the search coefficients to pre-defined values. The variables are also problem dependent and no reasoning was provided on the selection process. The optimality of the output solution can not be confirmed. The identified issues are addressed in the development of a novel search algorithm in Chapter 3 of the thesis.

2.7.3.2 Simulated Annealing

Simulated annealing is based on the annealing process of materials in metallurgy, where the specimens are heated to a maximum temperature, followed by a cooling process to its natural state. The heating process causes the atoms to disperse from their initial state and the local minimum of the internal energy, to higher energy levels. As the metal cools, the atoms rearrange to regions with a minimum energy configuration. The position of the atom in the metal is the solution to the problem and is modified based on a defined cooling schedule. The rate-of-cooling, forces the atoms to shift to regions with lower internal energy than their initial position, thus reducing the objective function (for minimisation problems).

Simulated annealing has been widely used for aerodynamic shape optimisation problems. Wang et al. [100] developed a parallel SA algorithm for airfoil inverse design at transonic Mach numbers. The objective function was in the form of a least squares definition that required minimising the Euclidean distance between target and approximated pressure profile over the defined airfoil chord length (Eqn. 2.1). An unsteady Navier-Stokes solver was used to compute the two-dimensional viscous flow features and the search operators of the algorithm were distributed into multiple processors to accelerate the optimisation process. The change in energy due to the movement of atoms as part of the cooling process was computed by each processor in accordance to an algebraic cooling schedule. The processor with the best solution was identified and applied to develop a new sub-chain of solutions for the following iteration. The inverse design solution search space is multi-modal and the optimisation process established a global optima with acceptable convergence between target and computed pressure profiles. The implementation of parallel computing resulted in an almost linear speedup, as the number of processors increased from a single machine to 24 CPUs [100].

The inverse design analysis presented is limited from the view point of examining the flexibility of the SA method for aerodynamic shape design applications. The target pressure coefficient was defined based on an off-the-shelf airfoil and the existence of a physically realisable shape was *a-priori* knowledge. Thus, a well-defined SA would converge to the pre-defined solution. In true design optimisation scenarios, the required pressure profile is defined with no indication on the nature of the final contour profile. Airfoil designs further require shape constraints which complicate the search topology with multiple local solutions. The robustness of the proposed SA method must be evaluated on these test cases. The analysis is simplified by selecting a pressure profile with a known solution

in-lieu of shape constraints. It was accepted that the performance measure of the SA method must be extended to an inverse constrained design problem with the specification of an arbitrarily defined pressure profile [100]. The flexibility of the SA method for complex design problems can be evaluated.

In the analysis by Wang et al. [101], the efficiency and speedup of SA over a series of aerodynamic shape optimisation problems was examined. The inverse design methodology was adopted for high-speed internal flow design processes. Euler and Navier-Stokes equations were used to compute the flowfield at high Mach numbers. Parallel processing was applied to speed-up computations. The shape optimisation problem focused on the design of a diffuser through an inverse process, hence a least-squares minimisation problem was formulated. Due to a high Mach number operating environment and with the development of shock waves, the objective function was considered non-smooth. The problem was ideal to test the flexibility of SA. The results indicated acceptable pressure convergence, in comparison to specified target profile. Significant computational speed-up was attained with a distributed computing structure [101].

The analysis presented in [100, 101] are preliminary as the efficiency of the method depends on the number of the design variables. The search agent sample size was limited to four predictors and the measuring location of the objective function was minimal in [101]. The problems examined were also unconstrained [101], thus further simplifying the search domain. The feasibility of the SA algorithm for aerodynamic shape optimisation needs to be established for problems with larger variable populations. The robustness of the search pattern due to the implication of linear and non-linear constraints requires further investigation.

Based on the overview of the SA algorithm, it is evident that the process is adaptable to computation by parallel computing. In time-intensive aerodynamic shape optimisation simulations, there exists a potential for significant time saving. The method has been applied across a wide spectrum of aerodynamic design case studies. The affect of varying the user-defined search parameters has not been covered. The sensitivity of the search process with variations in annealing schedule type is not addressed. It has been identified that the definition of a problem-based annealing schedule will require significant computational time investment [102]. The viability of the final solution can not be assessed with confidence as a generic-based annealing schedule is applied in [100, 101], instead of a problem-specific method. The SA models investigated do not facilitate the application of biological search operators to avoid convergence to a sub-optimal point. To increase search diversity for airfoil direct design processes, the optimisation algorithm must introduce randomness in an intelligent and adaptive manner as a function of search iteration, which are not addressed in [100, 101]. As the search topology for engineering design disciplines is multi-modal with finite local solutions, the implementation of novel search operators including crossovers and/or mutation is necessary.

2.7.3.3 Ant Colony

Aerodynamic shape optimisation problems have been solved by Fainekos and Giannakoglou [103] with the Ant Colony Optimisation algorithm (ACO) [104]. The method is inspired from the social behavior of animals, where it is recognised that certain mammals exhibit poor individual social system in comparison to their collective behavior, when operating in a large groups. The analogy is related to a swarm of fish, birds or bees operating in teams to solve their problem; locating the optimal path

to a food source. The species apply a communication media to share information with the rest of the swarm and by distributing the search activities, complex search models are solved efficiently. The social movement of animals inspired the development of an optimisation architecture that duplicates the behavior of ant colonies [104].

The ACO methodology provides a promising avenue for further research in the development of robust, population based optimisation methods. The motivation is based on the swarm theory with inspiration from the social behavior of animals in nature operating in large groups/teams. The ACO process is further adaptable to computation by parallel computing with each ant processed concurrently on a specific computing node. In time-intensive aerodynamic design simulations with high-fidelity solvers, the computational time for fitness function evaluations will be reduced significantly with the integration of the ACO in a parallel computing architecture. The thesis will focus on the development of a novel swarm-based optimisation method based on the governing principles of the ACO process.

2.8 Summary

A comprehensive overview into the principles of airfoil shape design optimisation was presented. A review of related works was undertaken to identify the current body-of-knowledge. The direct design method will be applied in the thesis for airfoil shape design. The design approach has been successfully applied in the literature (Sec. 2.4). The identified methodology has issues and challenges that will be addressed to facilitate a valid optimisation structure.

The airfoil shape design modules that require definition include:

1. **Geometry shape parameterisation model**
   An overview of the merits and demerits of several airfoil shape parameterisation model types was identified. From the survey of related works, it is acknowledged that the scope of the search topology as a function of design variable population size and parameterisation function type is problem specific and needs to be defined accordingly.

2. **Fitness function flow solver**
   The definition of a valid computational domain is needed to obtain an accurate measure of the aerodynamic coefficients, hence magnitude of the fitness function. A test performance is required to validate a computational domain with published experimental data to facilitate airfoil shape design at the defined flight conditions. (Chapter 5).

3. **Optimisation algorithm**
   The merits and demerits of disparate optimisation algorithm types was considered. Evolutionary algorithms need to be integrated into the design process to facilitate design convergence to an acceptable global optimal for airfoil design simulations. Current off-the-shelf design algorithms are characterised by limited search performances and are computationally intensive. From the literature review, the definition of a novel variant to the original particle swarm optimisation algorithm was proposed to address the defined issues and challenges. The proposed modifications will be defined in Chapter 3.

The design requirements identified will be addressed in the thesis. The findings will contribute to the current body-of-knowledge.

Chapter 3

Particle Swarm Optimisation

3.1 Overview

An heuristic methodology inspired from the notion of 'collective intelligence' in biological populations, is the Particle Swarm Optimiser by Kennedy et al. [94]. The method is developed to address the demerits of a time-exhaustive search process of the GA (Sec. 2.7.3.1) and the limited search capabilities of the SA (Sec. 2.7.3.2). Similar to the ACO structure (Sec. 2.7.3.3), the solution is represented by a particle in a swarm, as part of a socio-cognitive process to establish a feasible solution. A physical analogy is a swarm of birds operating in large groups to locate a food source. The birds apply personal memory gained during the search experience and an information sharing approach to solve the problem. The search principles are based on an constructive cooperation amongst the individuals and not the survival of the fittest through crossover and tournament selection processes as in GA. The nature of the search terrain is assimilated through the communication between the agents. The search agents continue to navigate until a consensus in regards to the feasibility of the final point. In collective search patterns, this is as a result of the population of particles converging to a common point/region in the search volume.

The PSO method provides a simple and efficient process for design optimisation and is ideal for continuous variable problems. Variants of the algorithm have been applied across disparate optimisation case studies including electromagnetic design [105], computer science [106], medical physics [107], finance [108] and sports engineering [109]. In the sections to follow, the following terms are used to define the workings of the PSO structure:

- **Particle / Agent:** Each search member in the swarm is referred to as the particle or agent (based on the analogy of a flock of bees / birds). The particle operates independently with the search principle of accelerating toward personal best and to the overall best solution in the swarm. The search process is continuously adapted to facilitate solution improvement due to the collective search behavior of the swarm and based on personal search experiences;
- **Particle Position:** Represents the solution to the problem. The position is an array of coordinates for an D-dimensional search space;

- **Particle Velocity:** Represents the speed at which the particles navigate about in the search space. The velocity limits must be within acceptable tolerances to ensure convergence at a global minima search region and to further mitigate the over-shooting of the particles outside of the defined search envelope due to excessive speeds. The velocity magnitudes are problem based and are defined for airfoil shape design in this chapter;
- **Fitness:** The magnitude of the objective from the user-defined function;
- **Personal Best:** The personal best solution found of an individual particle during the search history; and
- **Global Best:** The overall best solution located by a particle in the swarm during the search history

3.1.1 PSO Structure Design-of-Experiments Study

The PSO structure must be well-defined to facilitate efficient and solution valid search simulations. If the user-defined parameters are ill-defined then a sub-optimal point will be the result. The PSO parameters are problem based and must be defined accordingly for the specific problem. In this chapter, the following concepts will be discussed as part of the PSO development process:

- **Search Population Size:** The population size of the biological search agents in EA based models influences the rate-of-success of the optimisation method. If the population size is significant, then a computationally time-intensive simulation will follow as each search agent is directly analysed by the flow solver. If the population size is limited, then a sub-optimum result will be generated due to minimal solution diversity. The size of the search population must be well-defined to address the conflicting requirements;
- **Adaptive Mutation for Search Diversity:** Design development, validation and demonstration of the novel-mutation process to introduce search diversity;
- **Scalar Step Length:** Magnitude of minimum and maximum scalar step lengths for shape generation during the iterative search process;
- **Wall Boundary Conditions:** The search agents can violate the defined solution envelope during the iterative process. Wall boundary conditions are applied to re-instate the search agents back into the search domain. The feasibility of several wall boundary condition treatment methods, for airfoil shape design is assessed;
- **Measure of Convergence:** Premature optimisation convergence of the search process will result in a sub-optimum solution. Novel measures are defined to define the measure of convergence for EA based models; and
- **Test Validation:** The feasibility of the developed optimisation algorithm including robustness is evaluated. Benchmark mathematical functions, with *a-priori* knowledge of the theoretical solution are applied in the validation process. The verification process provides avenue for further design improvements to fine-tune the design process to attain acceptable solutions.

The DoE analysis will provide an avenue for the development of an airfoil design-specific PSO model, which has not yet been addressed. As the DoE process involves a comprehensive experimental process, the output data will be extensive. To best represent the trade-offs and the relationship between the user-defined variables and the search performance of the algorithm, a data mining technique in the form of Self-Organising Maps (SOM) is applied. The methodology will qualitatively represent the results for ease-of-interpretation, hence facilitating the definition of a valid PSO design algorithm for the intended field of study. In this chapter, a comprehensive analysis addressing the identified requirements is discussed. The results will significantly contribute to the current body-of-knowledge.

3.2 Particle Swarm Optimiser

Unconstrained optimisation is in the form of D-dimensional minimisation problem as $f(x), x = [x_1, x_2, ..., x_D]$. The dimensional size is proportional to the mapping area of the objective function. As D increases the mapping region required by the optimiser in search of potential solution increases. The use of GM algorithms becomes an issue, as a 'well-defined' starting point is required to avoid local search patterns about a sub-optimal region. Since the nature of the objective function is unknown, definition of an acceptable solution initialisation point is a design challenge.

The search agents evaluate the solution topology. Consider an i^{th} member of the population, represented by position $x_i^D = [x_i^1, x_i^2, ..., x_i^D]$ and velocity $v_i^D = [v_i^1, v_i^2, ..., v_i^D]$, in the solution search space. The information sharing process among the particles leads to a velocity update rule, which is applied to modify the positioning of the particles for the next search iteration. The position of each particle is updated by considering the collective search patterns of the swarm with consideration to $pbest_i$ and particle position with $pbest_g$. Randomness in terms of external noise is introduced to the velocity update rule for search diversity. The position of each particle for the iteration that follows is modified by the velocity function in Equation 3.1.

Unlike GM, a PSO does not require the gradient information of the objective function to establish the search direction. The algorithm is adaptable to standard programming languages with primitive mathematical operators. The method also does not require an initial starting point as the initial swarm is randomly generated. An iterative search process follows which updates the position and velocity of the search agents based on personal and global search patterns of the particle and swarm respectively. The ambiguity of selecting an acceptable search starting point, a trait in GM structures is not a design issue.

The design variables represent the dimensional positioning of the particles and are stored in a position vector x_i^D. The PSO operators update the velocity v_i^D at iteration k, as:

$$v_i^D(k) = K[v_i^D(k-1) + c_1 r_1(pbest_i^D - x_i^D(k-1)) + c_2 r_2(pbestg - x_i^D(k-1))] \tag{3.1}$$

Where:

x_i^D =Position Vector;

v_i^D =Randomly generated velocity of the particles at search initialisation;

$pbest_i^D$ =Best solution achieved by the particle and represented by vector $pbest_i^D = [pbest_i^1, pbest_i^2, ..., pbest_i^D]$;

$pbestg$ =Global best solution collectively achieved by the swarm;

c_1 & c_2 =Stochastic acceleration terms that pull each particle toward $pbest_i^D$ and $pbestg$ positions respectively;

r_1 & r_2 =Random numbers in the uniform range [0,1]; and

K =Constriction factor introduced by Shi and Eberhart [110] and applied as an inertia weight term to balance global and local search capabilities of the particles. A large weight factor promotes global search patterns and a small value facilitates a local search process. Shi and Eberhart [110] propose K as:

$$K = \frac{2}{\left|2 - \varphi - \sqrt{\varphi^2 - 4\varphi}\right|}, \varphi = c_1 + c_2, \varphi > 4 \tag{3.2}$$

Through empirical studies, Shi and Eberhart performed test experiments over benchmark test functions and proposed c_1 and $c_2 = 2.05$, thus $\varphi = 4.10$ and $K = 0.729$ [111].

The update of position vector at iteration k is:

$$x_i^D(k) = x_i^D(k-1) + v_i^D(k) \tag{3.3}$$

The equations 3.1 - 3.3 have the effect of accelerating the particles toward the weighted sum of the personal and global best with an element of randomness. The iterative search process continues until the maximum number of user-defined iterations is achieved and convergence is assumed.

The Pseudocode of the standard global-based PSO algorithm is summarised in Algorithm 2:

Algorithm 2 Standard Global-Based PSO Algorithm

for all particles i **do**
    Initialise position $x_i^D(k)$ randomly in the dimensional search space
    $v_i^D(k) = 0$
end for
while termination criteria not satisfied **do**
    k=0
    for all particles i **do**
        Evaluate fitness of each particle in the swarm
        Set personal best $pbest_i^D(k)$ as the best position located by the particle so far
        Set global best $pbestg(k)$ as the best position located by the swarm so far
    end for
    for all particles i **do**
        Update velocity of the particles by:
        $v_i^D(k+1) = w \cdot v_i^D(k) + c_1 \cdot r_1 \cdot [pbest_i^D(k) - x_i^D(k)] + c_2 \cdot r_2 \cdot [pbestg(k) - x_i^D(k)]$
        Update position of the particles by:
        $x_i^D(k+1) = x_i^D(k) + v_i^D(k)$
        Evaluate fitness of the new position
        Update personal best position
        Update global best position
    end for
    k=k+1
end while

3.2.1 Local and Global-Based Particle Swarm Optimiser

There are two forms of the PSO method and include: **a)** Global-based *pbestg*, (Alg. 2); and **b)** Local-based *lbest*, (Alg. 3). The difference in the two models is influenced by the neighborhood structure corresponding to the location of the global best solution of the swarm. In the two methods, the personal and global best position of the particles, as a function the physical size of the search topology govern the search movement of each particle. In the global-based model, particle movement is a balance between previous personal best and the global best within the swarm. Hence, each particle's search in influenced by the best position located by any search member in the swarm population. In the local-based model, each particle is guided toward personal best and by the best particle in a user-restricted neighborhood envelope. The movement is limited by a user-defined search window of the adjacent search members only, instead of the overall swarm as in global-based models.

There exists a number of communication topology types (Fig. 3.1), for application with varying results [112]. The commonly applied local-based method is the ring model which connects each particle to only two other particles in the swarm (Fig. 3.1(b)). In the global method, each particle is interlinked to each other (Fig. 3.1(a)), hence information of the overall best solution established by the entire swarm population at iteration k is available. The fundamental equations which define the velocity (Eqn. 3.1) and position (Eqn. 3.3) of the search particles in the two methods follows the defined process from Section 3.2.

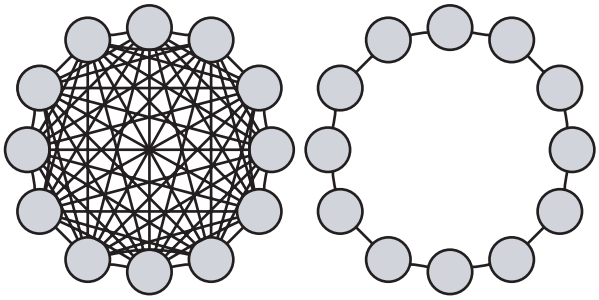

(a) The Global-Best Topology (b) The Local-Best Topology

FIGURE 3.1: Particle Swarm Neighborhood Topology Types

The Pseudocode of the standard local-based *lbest*, PSO algorithm is summarised in Algorithm 3:

Algorithm 3 Standard Local-Based PSO Algorithm

for all particles i **do**
    Initialise position $x_i^D(k)$ randomly in the dimensional search space
    $v_i^D(k) = 0$
end for
Partition swarm into n neighborhoods with equal number of particles
while termination criteria not satisfied **do**
    k=0
    for all particles i **do**
        Evaluate fitness in the defined neighborhood
        Establish leader $lbest_i^D(k)$ from each neighborhood
    end for
    for all particles i **do**
        Update velocity from the identified leader of each neighborhood:
        $v_i^D(k+1) = w \cdot v_i^D(k) + c_1 \cdot r_1 \cdot [pbest_i^D(k) - x_i^D(k)] + c_2 \cdot r_2 \cdot [pbestg(k) - x_i^D(k)]$
        Update position of the particles by:
        $x_i^D(k+1) = x_i^D(k) + v_i^D(k)$
        Evaluate fitness of the new position
        Update personal best position
    end for
    k=k+1
end while

In the global-based model accelerated convergence is theoretically achieved with the probability of convergence to a local optima increased [112]. Global based methods exhibit accelerated convergence to a valid search space region during the initial stages of the optimisation [112]. The search process is sensitive to oscillation about a minima valley (for minimisation problems), due to limited search diversity and randomness in the search process. The best fitness by the local-based model will exceed the global based model due to the simulation of additional fitness function evaluations, particularly for multi-modal test problems [112]. The additional function evaluations implies a computationally heavy search process, but increases the probability of converging to a valid solution.

In the local-based model, slower convergence is anticipated but is offset by acceptable search exploration capabilities. The application of the local-based PSO model has design issues and challenges.

The definition of an acceptable *local neighborhood topology*, for inter-communication between the particles is problem-based and must be defined accordingly. There are no set guidelines that govern the requirements of an acceptable communication topology type for problem-specific applications. The communication topology structure must be arbitrarily defined and does not guarantee and optimal set-up. It can be defined with greater degree-of-confidence by an extensive DoE analysis. The analysis is not viable if the fitness function evaluator is computationally intensive. The application of an extensive DoE analysis to finalise a feasible neighborhood structure is not viable for airfoil optimisation with RANS equations as the fitness function evaluator. The application of a viable communication structure is a design challenge.

Bratton and Kennedy [112] stated that the disadvantage of the local-best model (Alg. 3), is in the slower convergence rate relative to the global-based model (Alg. 2). If the global best solution is found, then the additional fitness function evaluations is a demerit. Alternately, if the swarm has converged upon a suboptimal location, then the slower convergence is a direct result of the additional search iterations required to escape the local solution region. In this case, the merits of the local-based model is evident. Despite the merits of the local method in converging to a true solution, the methodology is not ideal for all test problems [112]. The global method will result in accelerated convergence than the local-based method for unimodal problems due to the lack of multi-modal valleys in the solution topology. Even for complex multi-modal test problems, the global search method is preferable in comparison to the local-based process, if the global-based algorithm is well-defined and set-up specifically to the intended design problem [112].

Direct performance comparison between the global and local based PSO model must be evaluated to verify the performance measure between the two methods [112]. While the accelerated performance of the global model may indicate superior search performance, the feasibility of the optimal point governs the overall success of the proposed test algorithm. Hence, a comprehensive test validation study is required with *a-priori* knowledge of the theoretical solution to verify success. Comparison between the number of fitness function evaluations to convergence and the optimality of the converged point must be used in the performance comparative analysis.

The issues relating to the acceptable definition of a user-defined neighborhood communication topology is significant. Even if the topology layout type is identified by a DoE analysis, the correct combination of the interlinks between the communicating particles is a design challenge. If the layout and/or the interlinks between the communicating particles are ill-defined, the search process will: **a)** Not converge to the true solution; and/or **b)** Converge at the required region, but with significant number of search iterations. The novel PSO algorithm within the scope of this thesis is based on the global-based system. The method is implemented to converge to an acceptable solution with the integration of intelligent, iteration function based biological search operators that accelerate convergence to the required solution with minimal computational expense. This chapter provides a comprehensive overview of the developed methodology and a test evaluation process to verify algorithm feasibility.

3.3 Variants to the Particle Swarm Optimiser

The standard local and global based PSO methodology have been applied across disparate optimisation problem types and applications. The difference between GA and PSO is that the swarm process does not implement additional search operators such as mutation and crossovers, which require additional function evaluations, thus increasing computational time to convergence. Performance comparison between GA and PSO has shown that PSO is sensitive to premature convergence due to the presence of local sub-optimal solutions for complex multi-modal problems. The *lbest* variant of the PSO model, despite the theoretical merits of avoiding local solutions is sensitive to a stagnant search process and convergence at a sub-optimal region. Stagnant optimisation simulations are due to inefficient solution diversity in the search population. The issue is addressed by increasing the population size of the swarm, but does not guarantee global optima and is not preferred as additional function calls are required. The original *lbest* and/or *pbestg* PSO search algorithm must be modified to address the demerits of premature convergence to local solutions for multi-modal problems. An increase in search diversity by the swarm is a requirement while maintaining a low fitness function evaluation count for search efficiency. The theoretical computational time benefits of the swarm approach in comparison to GA must be maintained to justify the feasibility of the performance improvements of the variant PSO model in comparison to the original method. Current swarm algorithm research efforts focus on addressing this requirement.

A comprehensive overview of the related works that have focused on addressing the identified limitations of the base-PSO model is presented. Variants of the original PSO model have been developed and assessed through empirical simulations [8, 113–128] to address the identified demerits. A dissipative PSO was developed by Xie et al. [128] to avoid a stagnant evolution process, in the extreme case when all the particles in the swarm are in equilibrium with a common personal best and at the same position with zero velocity at a certain evolution stage. A non-equilibrium search was initiated with a negative entropy function that introduced chaos to the particles by updating the velocity and position, as a function of chaotic factors in the range [0,1]. These acted as multipliers to a uniformly generated random number to perturb the initial position and velocity from an equilibrium to a non-equilibrium state [128]. Due to the stochastic nature of population-based search agents, the convergence to global optima was sensitive to an exponential increase in the volume of the search space.

Bergh and Engelbrecht [129] proposed a cooperative search process by partitioning a D-dimensional solution vector into a smaller vector of s swarms with n particles. Thus, instead of applying the PSO to optimise the entire solution vector from one swarm, the dimensional vector was split. The partitioned dimensional vector was then optimised by separate swarms [129]. The proposed design architecture reduced the scope of the search topology from a multi to a uni-dimensional state and theoretically improved convergence to global optima for multi-modal problems.

Qin et al. [8], Zhen et al. [122] and Fan et al. [124] developed adaptive models to provide a balance between local and global search patterns by updating the constriction factor, thus inertia weight during the search process. Shi and Eberhart [121] designed fuzzy methods to nonlinearly modify the inertia weight. Ratnaweera et al. [113] introduced time-varying acceleration coefficients to modify c_1 and c_2, as a function of the current iteration k, including the maximum number of

allowable design evolutions and user-defined acceleration constants. The suitable range of acceleration constants were determined through benchmark simulations. These and are problem dependent and no guidelines governing the selection of an acceptable set of values were recommended in [113]. Cui et al. [123] examined adaptive velocity thresholds to provide an acceptable balance between speed to convergence and solution feasibility, by adapting the maximum speed of the particles based on the search experiences of the individual particles in the swarm. Fan and Shi [130] applied a linearly decreasing maximum velocity setting as a function of k, to localise the search process with time. Ratnaweera et al. [113] concluded that the initialisation velocity (Eqn. 3.1), must be defined to avoid particles stagnating to a local optimum at initialisation due to the lack of momentum. The search mechanisms of the algorithm at solution initialisation were modified to provide the required momentum for particles to converge about a global optima [113].

Hybridisation of the PSO has been examined by integrating evolutionary operators including selection, crossover and mutation to maintain only the 'best' search agents in the search process and eliminate sub-optimal points [131]. Diversity of the search population was addressed through breeding to mitigate premature convergence in [127]. Lovbjerg et al. [127] introduced diversity by randomly selecting two 'parent' particles from the swarm with probability. A set of offspring particles with new position and velocity vectors were generated with arithmetic crossover rules that were applied as a function of initial position and velocity of the selected 'parents'. Diversity was enhanced by dividing the swarm into a user-defined set of sub-populations. Parents for breeding were selected from the different population groups based on a probability function [127]. The proposed methodology will theoretically provide acceptable examination of the search space, since the offspring's are generated from the disparate positioning of the parents in the solution topology.

Diversity was also addressed with mutation by randomly relocating the position of select particles in the search space by Yao et al. [132]. The magnitude of relocation was governed by scalar distribution factors generated by a random uniform or probability distribution curve with user-defined means and standard deviations. The Gaussian and Cauchy distributions for mutation were examined. A Cauchy distribution is characterised by extended asymptotic tails, thus the probability of generating a distant mutated particle, in comparison to the position of the parent search agent is high. The method provided a coarse-grained search process with a high probability of mitigating search regions bounded by local plateau topologies. This is favorable if the sub-optimal solution region is large, relative to the velocity scalar magnitude applied to perturb the positioning of the particles.

The Gaussian distribution methodology has a rapid and sudden asymptote about the mean selected particle for mutation in comparison to Cauchy. Thus, a fine-grained search methodology was provided with the degree-of-mutation-magnitude restricted to search patterns centered about local neighborhoods [132]. Theoretically, the anticipated mutation with a local-based search process is necessary to establish the precise location of the global optima during the concluding stages of the search process, when the particles have completed the global search process and begin to conjugate to a common solution region-of-interest based on the shared personal best experiences of the particles in the swarm.

The two distribution methods differ by the degree-of-mutation-magnitude. Local search simulations were simulated with lower degree-of-mutation magnitude and global with higher degree-of-mutation rate. Chen et al. [114] exploited the merits of the two distribution curves with a hybrid

approach by integrating Gaussian and Cauchy methods at different stages of the evolutionary search process. The PSO was integrated to a Cauchy method for global search simulations at the early stages of the design optimisation process. The methodology adapts to a local search simulation as a function of the number of iteration by integrating a local-based External-Optimisation (EO) algorithm with mutation through a Gaussian method [114]. The defined process was numerically validated on benchmark test functions.

3.4 Adaptive-Mutation Particle Swarm Optimiser

The common theme observed across the disparate variants of the original PSO algorithms examined from the literature, is the attempt to introduce search diversity as a function of time. Position and velocity vectors are updated with a range of intelligent operators that are executed with user-defined strategies. Search diversity is introduced based on probability distribution methods as a function of evolution search stage. Concepts of partitioning the dimensional space by selecting parents to generate an offspring from different regions of the solution topology were identified to induce search diversity.

The operators developed in the literature are technically sound, but have only been validated on test models where the computation time for objective function evaluation is negligible. Irrespective of the operator type applied for search diversity, additional objective function simulations are needed to assess the feasibility of the solution, which increases the computational effort. The original PSO method was developed with the intent of minimising the number of search operators, thus reducing computational time in comparison to EA based simulations. The lack of solution diversity was identified as a demerit, thus disparate search operator types (Sec. 2.7), inspired from GA were developed to address this issue. If the search operators are exhaustively applied with additional fitness evaluations, then the theoretical advantages of a time-efficient and globally effective algorithm, which resulted in the development of the PSO method will diminish.

The feasibility of the search operators developed in the literature have been assessed on benchmark test functions [114, 116]. Minimal design attention was attributed to maintaining a low computational effort while concurrently establishing the global solution. The search operators have been developed and measured with an excessively high user-defined iteration count. The number of fitness evaluations needed to achieve a global solution was high. A numerical experiment to illustrate the affect of linearly-decreasing the number of user-defined iterations on the feasibility of the global optimal has not been addressed. The search operators have not been developed with the aim of minimising the number of objective function calls. Consequently performance assessment is limited to the feasibility of the final solution, without due consideration of the computational effort needed to achieve the desired result. The performance measures of any search operator must consider the feasibility of the solution coupled with the requirement of maintaining a low fitness function call for convergence.

When the objective function is computationally time-demanding with the integration of CFD solvers for aerodynamic shape optimisation simulations, the requirement of maintaining solution diversity with minimal fitness function calls for time-efficient design processes becomes a design challenge. The concepts developed in the literature do not address this criterion concurrently. A new

methodology is proposed which exploits the search experiences of the individual search agents in an adaptive sequence. The proposed strategy introduces diversity by an efficient mutation process, which is applied in an intelligent, evolution based adaptive manner to minimise additional functional calls as a result of introducing the diversity-based operator.

In population-based algorithms, the agents provide acceptable diversity during search commencement as the particles are randomly initialised in the dimensional search space. As the optimisation progresses, the particles converge to a common region of the search space. Theoretically, this is acceptable with the assumption that the agents are converging to a global optima. It has been shown that this assumption is not always valid as population-based models are susceptible to convergence at local regions. If the search process does not introduce diversity at the later stages of the search process, sub-optimal solutions will be generated.

Novel particle mutation operators are developed to address this issue. The probability of mutation is proportional to the relative positioning of the particles in the swarm. At solution initialisation, the lack of search diversity is not an issue due to a high sampling space of the particles, thus the probability of mutation is set low. As the search progresses and the particles converge to a common region, mutation is adapted proportionally to account for the reduced search diversity. Theoretically, if the swarm is converging to a local region, then mutation will offset this demerit. Alternately, if the swarm is converging to a global region, then mutation will have no influence on the search progress and the positioning of the particles will remain un-changed. In the developed method, mutation is initiated based on the relative positioning, hence search experiences of the particles to intelligently enhance diversity. Particle re-positioning by mutation is based on the search environment and experiences of the individual agents. The defined search adaptive-based principles have not been developed in the literature. The original variant of the PSO model is modified and an adaptive-mutation algorithm is proposed (AM-PSO).

The following modifications are incorporated into the developed algorithm relative to the original PSO:

3.4.1 Space Filling Design for Solution Initialisation

A space-filling methodology is needed to distribute a D-dimensional swarm in the solution topology. Method types include the following:

a) **Random Designs** - A sample of m designs are generated at random in the solution space;

b) **Grid Designs** - Each sample is examined at l equidistant levels and all factorial combinations are analysed, resulting in $m = l^n$ points; and

c) **Stratified Designs** - A sample of m designs are established by partitioning the search space into equal 'bins' to cover the search region.

Random designs do not guarantee that the design region of interest will be adequately explored. Grid designs require a large sample size for acceptable design space coverage. Stratified sampling

methods are designed to address the demerits of the random and grid space approach by providing an acceptable solution space coverage with minimal sample size.

The initial test-matrix in standard PSO is generated by a random normal distribution methodology. The random process establishes the length of the search sub-intervals on the basis of the probability density function, hence exhibit limited expected probabilistic coverage of the joint input space. Let $X1$ and $X2$ be two independent airfoil shape parameters. Applying order statistics, the expected probabilistic coverage of the input space for $X1$ and $X2$ with population n is calculated in Equation 3.4. Thus, with $n = 10$, 66.9% coverage of the input space is expected.

$$\left(\frac{n-1}{n+1}\right)^2 \tag{3.4}$$

The process of airfoil shape design is considered deterministic and a uniform probability distribution method is assigned to generate an even sub-division of each search variable dimensional interval. The expected distribution is improved with stratified sampling which theoretically provides greater design space coverage of the input variables in comparison to the random methodology. The Latin Hypercube Sampling (LHS) method developed by McKay et al. [133] is applied to initialise a swarm of X input variables in the search domain D. Theoretically the method ensures that all regions of D are explored such that each shape variable dimension is represented in the sampling, without conjugating the search about a mean value.

Consider generating m samples of five for variables $X1$ and $X2$, such that $X1, X2 \in [0, 1]$. Stratification is achieved by dividing the variables $i = 1, 2$ within the range bounded by $[X_{imin}, X_{imax}]$ into five equal intervals, thus resulting in a $5 \times 5 = 25$ cell matrix. A valid LHS is developed by starting with a sequence of m numbers $1, 2, \cdots, m$ and taking the permutations of this sequence. An LHS for a two-dimensional problem with five samples is presented in Table 3.1:

TABLE 3.1: Latin Hypercube Sample

(a) Unit Square with $m = 5$

0.90		2			
0.70					3
0.50			5		
0.30	1				
0.10				4	
$X1/X2$	0.10	0.30	0.50	0.70	0.90

(b) $LHS_{2,5}$ for $n = 2$ variables and sample size $m = 5$

Sample	$X1$	$X2$
1	0.10	0.30
2	0.30	0.90
3	0.90	0.70
4	0.70	0.10
5	0.50	0.50

Each column in Table 3.1(b), represents a stratified random permutation of the sequence of integers 1,2,3,4,5. Thus, a $LHS_{m,n}$, $m \times n$ test matrix is generated through random selection of n permutations from a sequence of integers $1, 2, \cdots, m$. Theoretically, stratified sampling is achieved by ensuring that each row and column of the test matrix for each variable, contains only one sample (Tab. 3.1(a)). Even with five samples for the intervals of $X1$ and $X2$, each step will be sampled. The computational process is set-up as follows for intervals $[i, j]$:

- Partition the distribution of each variable X_i within the search bounds $[X_{min}, X_{max}]$ into n non-overlapping intervals of equal length;
- The cumulative probability of X_1 and X_2 for the $[i, j]$ interval respectively is calculated in Equation 3.5:

$$Pr_{x1} = \left[\frac{(i - 1 + \zeta_{x1})}{n}\right] \quad Pr_{x2} = \left[\frac{(j - 1 + \zeta_{x2})}{n}\right]; \tag{3.5}$$

  Where:

$$\begin{aligned} n &= \text{Sample Size} \\ \zeta_{x1} \text{ and } \zeta_{x2} &= \text{Random numbers } [\zeta_{x1},\zeta_{x2} \in (0,1)] \end{aligned}$$

- Sample values X_1 and X_2 are calculated by transforming the inverse of the probability distribution function F^{-1} in Equation 3.6:

$$X_i = F^{-1}(Pr) \tag{3.6}$$

- The next step applies a random process to select a value from the m intervals for each variable. A random pair-wise (multi-variant randomness for $n > 2$ variables) process is applied to ensure the values in each column of matrix $m \times n$ in Table 3.1(a) are randomly ordered, thus generating a stratified sampling population.

The expected probabilistic coverage of the input space is calculated for LHS using order statistics. Since LHS requires that a single sample is selected from each of the extreme intervals $(0, 1/n)$ and $[(n - 1)/n, 1]$, this distribution is used to calculate the expected probabilistic coverage of the joint input space for variables X_1 and X_2, with sample n in Equation 3.7:

$$\left(\frac{n-1}{n}\right)^2 \tag{3.7}$$

At $n \geq 2$, Equation 3.7 will be greater than the expected input space coverage of the random distribution calculated in Equation 3.6. If ten shape variables are applied to represent an airfoil contour, the random distribution in Equation 3.6 provides an 66.9% coverage of the search space compared to 81% with LHS methodology. A visual comparison between the two methods, for a two-dimensional case is presented in Figures 3.2(a) - 3.2(b). In Figure 3.2(a) for LHS, the ten sample points generate a plan of experiment with only one sample site for each level such that no two points are at the same line. The random distribution process in Figure 3.2(b) does not provide the same level-of-uniformity and the data points are not efficiently distributed. Thus, for solution initialisation in PSO, the LHS process is applied to partition the particles in the search domain.

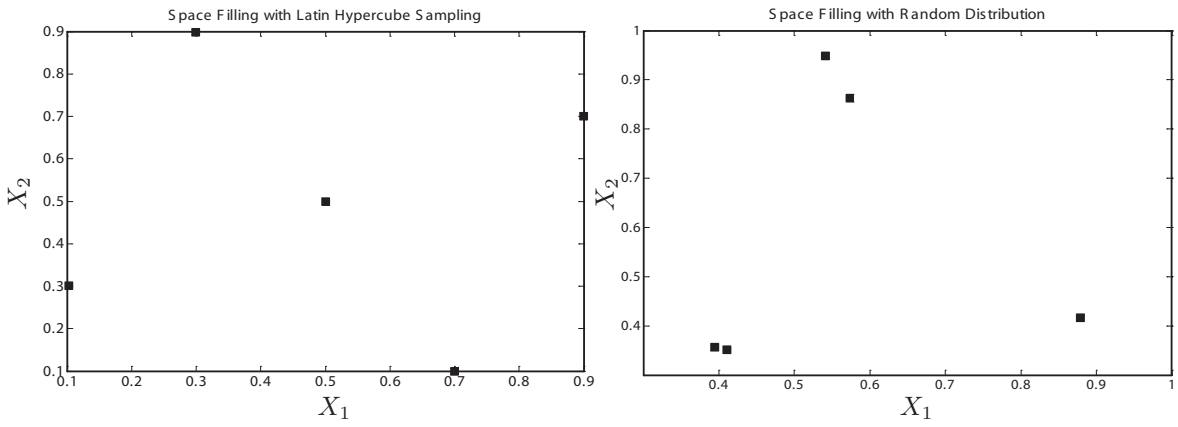

(a) A Two-Dimensional LHS Design

(b) A Two-Dimensional Random Distribution

FIGURE 3.2: Design of Experiments Space Filling

3.4.2 Adaptive Inertia Weight

During the search process each particle modifies personal position which is dependent on individual and global search experiences of the swarm. Since each search agent will be at a different region of the solution space, the particle will have different trade-offs between global and local search capabilities. In the original PSO model, pre-defined social and cognitive terms are applied for the search process. The adaptive approach introduces a dynamic balance between the two search phases, based on the search evolution of the swarm. An adaptive inertia weight (AIW) model is developed in the thesis to address this requirement (Eqn. 3.8). The formulation of the automatic, adaptive inertia weight factor formulates a personal search factor to attain an acceptable balance between global or local search exploration abilities by each particle in the respective dimension in Equation 3.8. The AIW is adjusted accordingly as follows:

$$AIW_{ij} = \frac{|x_{ij} - pbestg|}{\left|pbestg - pbest_i^D\right| + \epsilon_{AIW}} \tag{3.8}$$

Where:

$$\begin{aligned} x_{ij} &= \text{Position of the } i^{th} \text{ particle in the } j^{th} \text{ dimension} \\ \epsilon_{AIW} &= \text{A positive value close to zero} \end{aligned}$$

The computation of AIW requires information on personal and global best solutions of the swarm. In Equation 3.8, a small value of AIW represents a scenario where the personal best and current position of the particle are close, yet isolated from the global solution of the swarm. This indicates a local search process, which should be modified to balance the distance between personal and global best solutions. Alternately, a large value of AIW represents a particle with a global exploration tendency, since personal and global best solutions are close, yet distant to the current position. The dominating global search process is to be avoided with local search tendencies. A small value of AIW equates to a particle with a local search tendency and the inertia weight w, is increased in Equation 3.9, by a technique similar to the process developed by Qin et al. [8] to address this issue. A large value of AIW is representative of a global search process, which requires the minimisation of w (Eqn.

3.9), to provide an acceptable search balance.

$$w_{ij} = 1 + \alpha_{AIW} \left(\frac{1}{1 - e^{ISA_{ij}}} \right) \tag{3.9}$$

Where:

$$\alpha_{AIW} = \text{Inertia Weight Positive Constant in the range (0,1]}$$

The Equations 3.8 - 3.9, are adaptive to the evolution search process and are governed by the search experiences of the swarm. Theoretically, the adaptive process will converge to a global optima due to the balancing of the search parameters applied to control global and local search patterns. The proposed contribution to the computation of the inertia weight factor, will provide performance improvements in comparison to the standard PSO model (Alg. 2), where the search parameters are arbitrarily defined.

3.4.3 Wall Boundary Conditions

The search agents can violate the search domain at position update, such that $x_{ij}(k) \notin [x_{min,j}, x_{max,j}]$ in Equation 3.3. Regardless of adaptive inertia weights and limitations on the maximum allowable velocity, position updates can result in particles exceeding the physical dimensions of the problem. A scenario where the global optimum is located on the boundary of the solution space is sensitive to this performance. Wall boundary conditions are applied to constrain the movement of the particles in the form $x_{min,j} \leq x_j \leq x_{max,j}$, so that they are within the n_x - dimensional hypercube. Methods modeled include the following:

1. **Absorbing walls**, where the velocity of the violated particle is zeroed and the particle is pulled back to the boundary of the search space. The technique is representative of the original PSO variant, where the position of the violated particles outside of the solution space, are returned to the boundary of the search domain such that if $x_{ij}(k) < x_{min,j}$, let $x_{ij}(k) \equiv x_{min,j}$ and / or if $x_{ij}(k) > x_{max,j}$, let $x_{ij}(k) \equiv x_{max,j}$

2. **Reflecting walls**, where the sign of the velocity is reversed so that the particle is forced to reflect back into the search domain such that if $x_{ij}(k) \notin [x_{min,j}, x_{max,j}]$, let $x_{ij}(k) = x_{ij} + (v_{ij.-1})$.

3. **Invisible walls**, where no physical restrictions are imposed and if the particles exceed the search space, they are not evaluated for fitness. Since engineering design application use computationally expensive fitness solvers, the motivation behind this method is to reduce computation time by neglecting search agents which violate the search domain. Hence, computational resources are only used to evaluate particles that are within the defined search envelope.

4. **Random initialisation**, where the violated particles are randomly distributed back into the search domain such that if $x_{ij}(k) \notin [x_{min,j}, x_{max,j}]$, let $x_{ij}(k) = x_{min,j} + (x_{max,j} - x_{min,j}).rand.$

Numerical test experiments are simulated to evaluate and compare the performances of the absorbing, reflecting and random initialisation methods, on benchmark mathematical test functions (Sec. 3.6.2.2).

3.4.4 Adaptive Position Update Time-Variant Mutation

The rate-of-mutation during the search evolution stage as a function of the iterate k needs to be defined. Methods include the following:

1. **Constant mutations**, where the number of particles involved in the re-positioning process are fixed and constant during the design optimisation process;
2. **Linearly varying**, where mutation is proportionally increased during the evolution process; and
3. **Stagnant Mutation**, where diversity is applied to select particles only if the *pbestg* is stagnant over k successive iterations.

Constant mutation is computationally ineffective since mutation is simulated regardless of the search patterns of the swarm. The lack of solution diversity is not an issue during the early stages of the search process as the particles are initialised with stratified sampling methods. Thus, constant mutation will result in excessive computation time to convergence. Linearly varying mutations that adapt to the search environment can be applied to address this issue. A linearly decreasing method, as a function of search optimisation run was examined to allow greater search space exploration prior to the particles converging to a common region in [134]. The method is unsuitable, since mutation is unnecessarily applied at solution initialisation, when theoretically the agents are dispersed evenly across the search space. Also, the rate-of-mutation decreases linearly at the concluding stages of the search process when the particles are converging to a common region. This is based on the assumption that a solution region bounded by the global optima is located. As there is no guarantee that the mapped region of interest by the flock of particles is representative of a global minima point, a minimal mutation activity can correspond to swarm convergence at a sub-optimal point. Mutation at initialisation is only warranted if solution diversity is an issue. Greater particle repositioning by mutation is needed to mitigate sub-optimal regions when the swarm has reached a consensus on the location of the global point. Finally, mutation as a result of a stagnant global best solution over user-defined number of iterations has limitations. If the degree-of-mutation is limited, then the probability of escaping the local region is minimal. Thus, mutation should be applied prior to a search agent indicating a stagnant *pbestg* search pattern to mitigate this issue.

Mutation is integrated based on the collective search behavior of the swarm. Thus, instead of mutating each particle during the search evolution, the proposed particle re-positioning methodology follows a probabilistic process. Since stratified sampling with the LHS methodology is applied for search initialisation, limited diversity at commencement is not an issue. To mitigate the swarm conjugating at a local point during the later stages of the search process, a linearly increasing mutation method is proposed. The method permits a wide-range of search mechanisms during the initial stages of the search process and computational efficiency is addressed since the rate-of-mutation is minimal. The search efficiency is enhanced during the middle and later stages by gradually increasing the rate-of-mutation, while maintaining minimal particle re-positioning to minimise computational time for fitness evaluations.

The computational process of the proposed algorithm is set-up as follows:
Step 1: Define an estimated personal best fitness range of the swarm $p_f = (F_{pbesti,max}, F_{pbesti,min})$.

An estimate of the worst personal best of a particle in the swarm is denoted by a high fitness (for minimisation problems) and the global best by a lower objective magnitude. Since the nature of the problem is not *a-prior* knowledge, an arbitrarily high and low values for $F_{pbesti,max}$ and $F_{pbesti,min}$ respectively are set. At each iteration the objective distance metric d_s, of the swarm is calculated from the fitness of the worst performing particle subtracted from the fitness of the global best $|F_{pbesti,max} - F_{pbesti,min}|$. The calculated d_s is normalised $d_s \in [0, 1]$, to establish the probability of mutation in Equation 3.10:

$$pr_M = \left(\frac{d_s - F_{pbesti,max}}{F_{pbesti,min} - F_{pbesti,max}} \right) \tag{3.10}$$

In the proposed method, the probability of mutation is inversely proportional to d_s, such that $pr_M \propto \frac{1}{d_s}$. Thus, mutation is adaptive based on the search environment of the swarm. If the particles are dispersed, the personal best solutions will vary and the magnitude of $|F_{pbesti,max} - F_{pbesti,min}|$ will be high. Due to the large sampling area of the swarm, mutation is not necessary and pr_M will be low to minimise additional fitness function calls and reduce the computational time to convergence. As the swarm conjugates to a common region of the solution space, the particles will share a consensus on the personal best solution, thus $|F_{pbesti,max} - F_{pbesti,min}|$ will be low. To avoid convergence to local sub-optimal topologies, pr_M will be high to interact particles for mutation. Figure 3.3 presents pr_M as a function k, with $F_{pbesti,max} = 1$ and $F_{pbesti,min} = 0$. It is assumed that d_s decreases exponentially with k, hence an exponential increase in $pr_M(k)$. In multi-modal optimisation test problems, the magnitude of $|F_{pbesti,max} - F_{pbesti,min}|$ will vary throughout the search process as the particles navigate about local solution topologies. Variations in pr_M distribution curve, which adapts to the collective search behavior of the swarm, will reflect the search experiences of the particles with the presence of local solutions for multi-modal test problems.

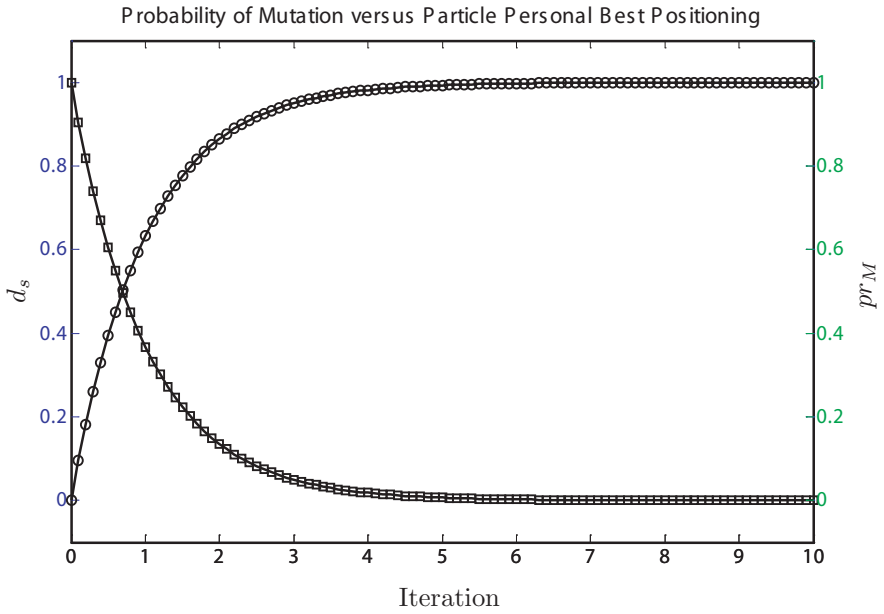

FIGURE 3.3: Adaptive-Based Swarm Probability of Mutation

Step 2: Generate a $(n \times 1)$ matrix of *random* numbers for each particle denoted by mr_i;
Step 3: Compare pr_M with mr_i of each particle;

Step 4: Particles where the condition $pr_M > mr_i$ is true, apply Gaussian mutation as;
Step 5: Randomly select one dimension j, for mutation and apply the following rule:

$$x_{ij,M}(k) = x_{ij}(k) + \sigma_{ij}^{D_j} \tag{3.11}$$

Where:

$$\begin{aligned} x_{ij,M}(k) &= \text{Position of particle } i \text{ with dimension } j \text{ mutated at iteration } k \\ x_{ij}(k) &= \text{Current position of particle } i \text{ with dimension } j \text{ at iteration } k \\ \sigma_{ij}^{Dj} &= \text{Number generated from Gaussian distribution for particle } i \text{ on randomly} \\ &\quad \text{selected dimension } D_j \text{ with mean zero and standard deviation } (std_M) \text{ of:} \end{aligned}$$

$$std_M = \omega_M \times (D_{j,max} - D_{j,min}) \tag{3.12}$$

Where:

$$\begin{aligned} \omega_M &= \text{User-defined mutation scalar factor} \\ x_{ij}(k) &= \text{Current position of particle } i \text{ with dimension } j \text{ at iteration } k \\ (D_{j,max} - D_{j,min}) &= \text{Length of selected search space for dimension } j \end{aligned}$$

Step 6: Apply wall-boundary conditions if $x_{ij,M}(k) \notin [x_{min,j}, x_{max,j}]$;
Step 7: Calculate $x_{ij,M}(k)$ fitness $F_{i,M}(k)$;
Step 8: Apply position update rule if the position of the mutated particle yields a lower fitness than the position of the particle without mutation $F_i(k)$. The particle is re-located to the mutated position such that:

$$\begin{cases} x_{ij}(k+1) = x_{ij,M} & \text{if } F_{i,M} < F_i(k) \\ x_{ij}(k+1) = x_{ij}(k) & \text{otherwise} \end{cases}$$

The position update rule operates by shifting the particle to a region of a solution space with lower fitness due to mutation. Else, the re-positioning is static if no improvements are observed. Thus, $x_{ij}(k+1)$, is the best current location of the particle. It is the personal best experienced by the agent if:
Step 9: Update personal best of particle i, if the mutated position yields a lower fitness than the previous personal best such that:

$$\begin{cases} pbest_i(k+1) = x_{ij,M} & \text{if } F_{i,M} < F_{pbest_i}(k) \\ pbest_i(k+1) = pbest_i(k) & \text{otherwise} \end{cases}$$

Thus, $x_{ij}(k+1)$ is the best current and best personal location found by the particle over the search process. It is not the best overall solution of the swarm, which is satisfied by the condition:
Step 10: Update global best of the swarm if the mutated position yields a lower fitness than the

previous best solution of the swarm such that:

$$\begin{cases} pbestg(k+1) = x_{ij,M} & \text{if } F_{i,M} < F_{pbestg}(k) \\ pbestg(k+1) = pbestg(k) & \text{otherwise} \end{cases}$$

Step 11: If the defined termination criteria is satisfied, then terminate the optimisation simulation. The termination rule applied is defined in the following sub-section.

3.4.5 Optimisation Termination

Various methods exist to determine if the solution has converged to a global point, hence terminating the search process. Methods include the following measures:

1. **Maximum iteration count**, when the maximum user-defined number of iterations are achieved, the solution is assumed to have converged;
2. **Measure of global best**, when *pbestg* is stagnant over user-defined number of iterations; and
3. **Hybrid methods**, defined by the measure of the maximum iteration count and the number of successive iterations for a stagnant *pbestg*.

The termination criteria must be well-defined to avoid premature convergence and to facilitate a valid output to the optimisation process.

As the scope of the solution space for AM-PSO validation over benchmark mathematical test functions (Tab. 3.2) is *a-priori* knowledge, the termination criteria applied is based on a stagnant collective personal best of the swarm and the overall global best solution over k iterations. If *pbestg* is stagnant over k iterations and $pbest_i$ of the best and worst performing particle in the swarm is within a user-defined tolerance factor ϵ_{end} (Eqn. 3.13), convergence to a valid region in the solution topology by the swarm is assumed and the optimisation process is terminated. The personal best fitness range of the worst and best performing particles in Equation 3.13, represents an agreed consensus between the particles on the feasibility of the solution topology. A small magnitude of the absolute difference between the personal best particles is representative of a swarm convergence to a specific region in the solution topology. The process of setting user-defined k iterations for a stagnant personal and global bests including the convergence tolerance factor is problem based and numerical experiments are required to determine a valid combination.

$$|max(pbest_i) - min(pbest_i)| < \epsilon_{end} \tag{3.13}$$

The Pseudocode of the novel, AM-PSO algorithm developed in the thesis is summarised in Algorithm 4:

Algorithm 4 AM-PSO Algorithm

1: **for all particles** i **do**
2: Initialise position $x_i^D(k)$
3: Initialise velocity $v_i^D(k) = 0$
4: Compute fitness f
5: Set personal best $pbest_i^D(k)$
6: Set global best $pbestg(k)$
7: **end for**
8: **while** termination criteria not satisfied **do**
9: k=0
10: **for all particles** i **do**
11: Update velocity of the particles by:
12: $v_i^D(k+1) = w \cdot v_i^D(k) + c_1 \cdot r_1 \cdot [pbest_i^D(k) - x_i^D(k)] + c_2 \cdot r_2 \cdot [pbestg(k) - x_i^D(k)]$
13: Update position of the particles by:
14: $x_i^D(k+1) = x_i^D(k) + v_i^D(k)$
15: Apply Random Initialisation Boundary Wall Condition for Dimensional Space Violated Agents:
16: $x_{ij}(k) = x_{min,j} + (x_{max,j} - x_{min,j}).rand$
17: Evaluate fitness of the new position
18: Update personal best position
19: **end for**
20: **INPUT:** Define Personal Best Fitness Range p_f (Sec. 3.4.4 - Step 1)
21: **OUTPUT:** Compute particle probability of mutation pr_m (Eqn. 3.10)
22: Generate a $(i \times 1)$ matrix of random numbers mr_i (Sec. 3.4.4 - Step 2)
23: **for all particles** i **do**
24: **if** $pr_m > mr_i$ (Sec. 3.4.4 - Step 3 & 4) **then**
25: Randomly mutate dimension j (Sec. 3.4.4 - Step 5; Eqn. 3.11)
26: Apply Random Initialisation Boundary Wall Condition for Dimensional Space Violated Agents - (Sec. 3.4.4 - Step 6):
27: $x_{ij}(k) = x_{min,j} + (x_{max,j} - x_{min,j}).rand$
28: Evaluate fitness of the new position by mutation $F_{i,m}$ - (Sec. 3.4.4 - Step 7)
29: Apply Position Update Rule - (Sec. 3.4.4 - Step 8)
30: **else**
31: No Mutation
32: **end if**
33: Update personal best position - (Sec. 3.4.4 - Step 9)
34: Update global best position - (Sec. 3.4.4 - Step 10)
35: **end for**
36: k=k+1
37: **end while**

In line 2, instead of randomly initializing the position vector about the search space as in the standard PSO method (Alg. 2), the LHS methodology is applied. The sampling facilitates symmetric distribution of the search agents about the search topology. A stratified sampling approach is preferred to avoid bias at initialisation by the random approach which can result in a concentration of particles restricted to a specific search space window. The LHS approach addresses this issue by evenly extending the initial search process which spans over the defined topology region.

The symmetric (LHS) and asymmetric, where the distribution of the initial population is restricted to a specific region of the search space was examined on four test functions by Angeline [135]. Performance differences between the two distribution methods was minimal, with symmetric and asymmetric methodologies indicating comparable mean fitness over a series of test simulations. The validation results indicated slight performance improvements with quicker convergence to the

theoretical minima with the asymmetric initialisation, but not significant to warrant the use of one method over the other [135]. The rapid convergence by the asymmetric approach for a specific test function was as a result of the user-defined asymmetric initialisation range that was within the global best region.

The location of the global minima is *a-priori* knowledge for the defined validation simulations in the thesis (Sec. 3.6). Hence, particle search initialisation at $k = 1$ is modeled with LHS in a search envelope that does not encompass the theoretical solution. By setting the initial swarm away from the theoretical minima with intent, the robustness and flexibility of the search algorithm is assessed accordingly.

3.5 Data Mining

A comprehensive DoE process is undertaken to verify the influence of the AM-PSO parameters (Sec. 3.1.1), on the search behavior of the algorithm. To extract the relationship and patterns between the optimisation search parameters and the performance of the algorithm, a data-mining technique is applied. The technique is proposed to facilitate a comprehensive DoE process. Sample case studies are presented to illustrate the principles of the method for feature extraction by visualisation.

3.5.1 Self-Organising Maps

The results to the DoE process for AM-PSO algorithm development are represented by SOM. If the data is two or three dimensions, then the relationship between input and output parameters is visually presented by 2D or 3D carpet charts respectively. Hence, a profile is generated and for a two-dimensional graph the dimensions are on the x-axis and the output on y-axis. In three-dimensions the relationship between the datasets is presented by reflecting the dimensions on the x and y-axis, with the output projected on the z-axis. If the dataset is in excess of three dimensions, then visual inspection is an issue. Extensive DoE simulations will result in large volume of datasets. A valid approach is required to transform the large-dimension results into easy-to-read charts. The application of SOM by Kohonen [136] is applied to address this limitation.

The principles of SOM are based on the analogy of a human brain for the purposes of systematically organising large volume of data into easy-to-inspect information that is processed in a logical manner. Mathematically, the methodology is based on the unsupervised neural network approach to model the nonlinear projection from a high-dimensional input space to a low-dimensional array of neurons. A SOM is primarily applied for data mining including pattern recognition and for data clustering. Clustering is applied to reduce the data dimensionality by partitioning results into similar groups based on a user-defined preference. An analogy of this principle is to define the relationship between variances in the maximum allowable velocity of the particles and the corresponding impact on fitness. The results are grouped with SOM by clustering the data that correspond to low-to-high fitness variances as a function of the change in velocity. The results are visually inspected with SOM to interpret the complex relationship between the defined parameters. The input parameter which govern low fitness performance are quickly and easily identified. The process is applied to facilitate

the definition of user-defined search parameters for problem specific applications by a comprehensive DoE analysis.

An example of a SOM structure is presented in Figure 3.4 and consists of input nodes and inner neurons within the map. The SOM is a $p \times q = 4 \times 4$, network where each neuron is directly connected to the input node, but not directly to each other. The neurons are represented in a 2-D chart for ease of data visualisation. The neurons are modeled with positioning coordinate (i, j), such that the Euclidean distance between the nodes and the input data can be computed.

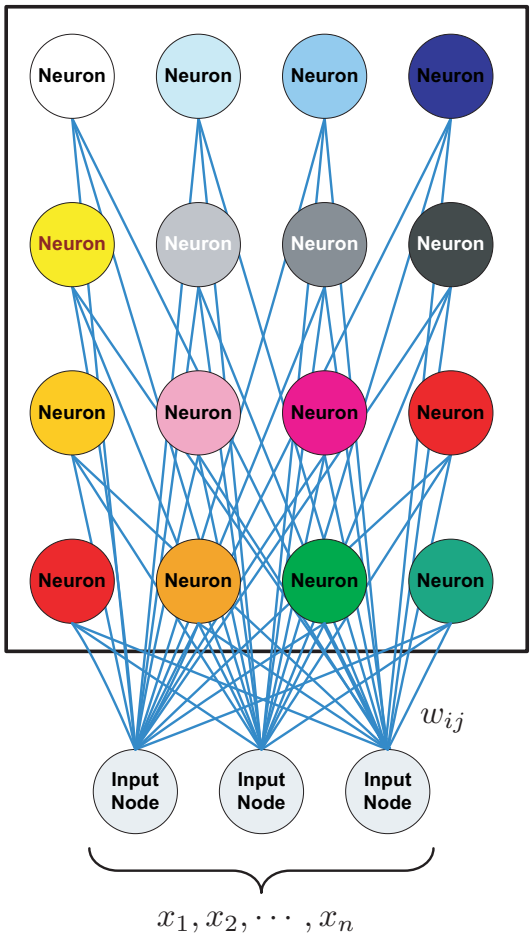

FIGURE 3.4: SOM Structure Representation

Mathematically, the definition of the SOM in Figure 3.4 is as follows:

$$SOM \subset \text{Input Node} \subset \text{Map Neurons} \subset \text{Weights} \tag{3.14}$$

In Equation 3.14, the SOM (Fig. 3.4) is defined by a set of input nodes at position (i, j), that are modeled with specific neurons, which are a subset of connecting weights between the input node and each neuron. The SOM principle is based on a competitive learning process within a neural network structure, where the neurons are sensitive to the changes in the input data and compete with the remaining neurons for activation. Hence, a division among the representing nodes emerges within the network, which has the effect of representing disparate pattern types to the input data.

The array M, with neurons n, in a two-dimensional SOM such that:

$$M = \{n_1, n_2, \cdots, n_{p\times q}\} \tag{3.15}$$

Where each neuron n_i, is related to a weight vector w, over a d-dimensional input space, with N number of neurons as:

$$w_i = [w_{i1}, w_{i2}, \cdots, w_{id}]; (i = 1, \cdots, N) \tag{3.16}$$

An iterative neural network training process is initiated with the neurons linked to neighboring neurons by a defined *neighborhood relation function*. The function influences the lattice of the network and is in the form of a rectangular or hexagonal type formation. The distances between the map units is defined and immediate neurons that are within a set threshold are related by a neighborhood function.

The computational training process for SOM development is defined as follows [136]:

1. Randomly initialise M nodes, with weights;
2. At iteration time step k, the vector x_k from the input set $\{x_i\}$ for $i = 1, 2, \cdots, N$ is randomly selected for teaching;
3. The Euclidean distance between x_k and the remaining node weight vectors w_d is computed;
4. Each node in the network is examined to establish node similarity with the input vector. A winning node, referred to as the Best Matching Unit (BMU) $w_{c(x_k)}$, is identified as a node vector that is closest to the input vector. A similarity measure is applied and includes an update process of the values of w_i in the neighborhood of the winner unit such that:

$$|w_{c(x_k)} - x_k| \leq |w_d - x_k|, \text{ for } m \in \{1, 2, \cdots, M\} \tag{3.17}$$

5. The radius of the neighboring nodes from the winning neuron $w_{c(x_k)}$ is established:

$$\sigma_{SOM}(k) = \sigma_0 e^{\left(-\frac{k}{\lambda}\right)} \tag{3.18}$$

   Where:

$$\begin{aligned} k &= \text{Current Iteration} \\ \lambda &= \text{Time Constant} = \frac{k}{\text{Map Radius}} \\ \sigma_0 &= \text{Radius of Map} \end{aligned}$$

   At initialisation, $\sigma_{SOM}(k)$ is arbitrarily defined to match the radius of the network. As the neurons take form, the radius of the network decreases exponentially at each time-step k;

6. The nodes (j, k) that are within the computed radius zone of the winning neuron (step 5), are adjusted to match the input vector by weight adjustment as:

$$w_d^{(k+1)} = w_m^{(k)} + \alpha_{SOM}(k)\, h_{jk}^{(k)} [x^{(k)} - w_m^{(k)}] \tag{3.19}$$

Where, $\alpha_{SOM}(k)$ is an exponential *learning rate* parameter as:

$$\alpha_{SOM}(k) = \alpha_{SOM_0} e^{\frac{-k}{\lambda}} \tag{3.20}$$

And, $h_{jk}^{(k)}$ is the *neighborhood relation function* and is in the form of a Gaussian-like function as:

$$h_{jk} = e\left(-\frac{d_{jk}^2}{r_k^2}\right) \tag{3.21}$$

Where:

$$\begin{aligned} r_k &= \text{Neighborhood radius} \\ d_{jk} &= \text{Distance between units } j \text{ and } k \text{ on map} \\ &= \|r_i - r_{cj}\| \end{aligned}$$

Where:

$$\begin{aligned} r_i \ \& \ r_{cj} &= \text{Coordinates of the } i\text{−th node and the winning unit } c \\ \|r_i - r_{cj}\| &= \text{Distance between winning node } c_j \text{ and node } i \text{ on grid} \end{aligned}$$

7. An iterative training process follows over a total of user-defined iterations.

At $k = 0$ (Eqn. 3.18), the neighborhood radius is maximum (Figs. 3.5 - 3.6(a)) and is the size of the initial lattice. As k increases, there is an exponential decay in radius (Figs. 3.6(b) - 3.6(d)) and will approach zero. The vector which has the closest Euclidean distance between the selected neuron to the sample in $\{x_i\}$, is identified as the BMU $w_{c(x_k)}$. As $k \to \infty$, the radius will approach zero and equate to the BMU neuron (Fig. 3.6(d)).

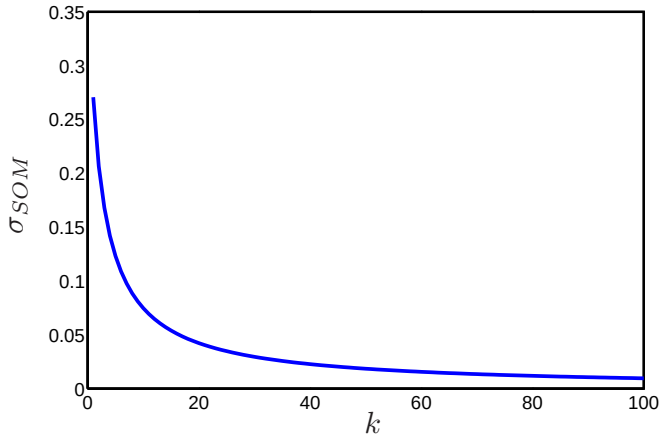

FIGURE 3.5: SOM Radius Neighborhood Function Representation

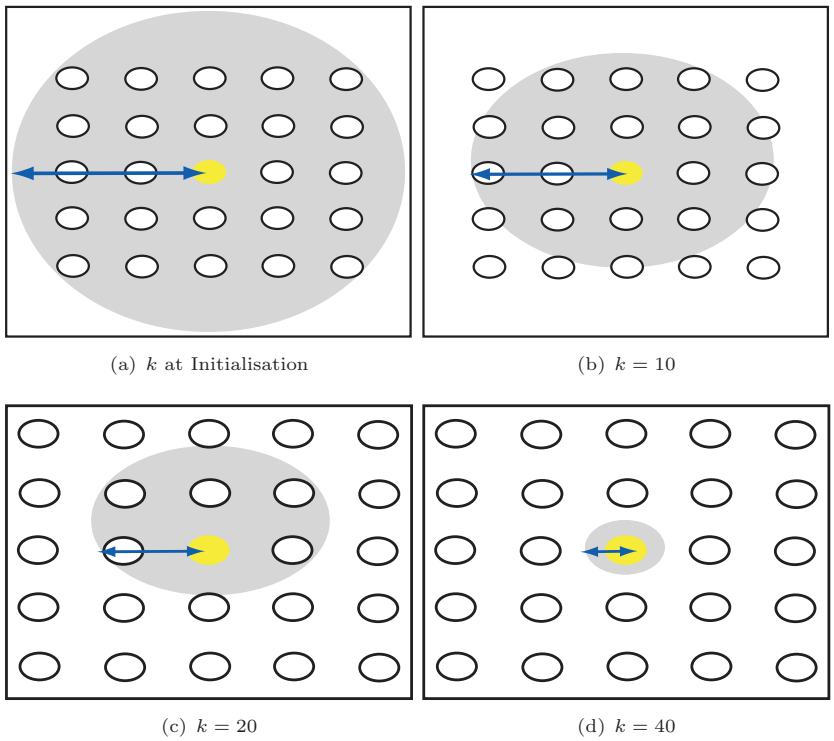

(a) k at Initialisation (b) $k = 10$

(c) $k = 20$ (d) $k = 40$

FIGURE 3.6: Exponential Decay in Radius of Neighborhood about the BMU as a function of k

The Pseudocode of the sequential-based SOM training algorithm is defined as follows:

Algorithm 5 Sequential SOM Training Algorithm

1: **Input:** Initialise array M with n neurons [Eqn. 3.15]
2: **Output:** Set of prototypes, $Y = \{y_1, \cdots, y_M\}$
3: Initialise weight vectors of the neurons [Eqn. 3.16]
4: **while** termination criteria not satisfied **do**
5: $k = 0$
6: **for epoch**=$1, \cdots, X$ **do**
7: **for input**=$1, \cdots, D$ **do**
8: **for** $n = 1, \cdots, N$ nodes **do**
9: Compute Euclidean distance between node weight and input vector
10: **end for**
11: Compute winning node [Eqn. 3.17]
12: **for** $n = 1, \cdots, N$ nodes **do**
13: Update / Adjust nodes by shifting closer to input vector [Eqn. 3.19]
14: **end for**
15: **end for**
16: Reduce learning rate [Eqn. 3.20]
17: **end for**
18: $k = k + 1$
19: **end while**

The training process involves sampling random points from $\{x_i\}$ and adapting the selected data to the SOM over M user-defined clusters. The SOM algorithm will output a prototype y_i, for each cluster M (line 2). In the defined algorithm, the number of neurons i, in each cluster M are defined (line 1) and the weights are normalised to range $(0, 1)$ (line 3). In the main loop (lines 6-18), an

element $x_k \in X$ is randomly selected. The distance between selected neuron, for input i, with all remaining neurons is computed (line 9). The neuron y^*, that is closest to x is identified by a similarity measure, BMU (line 11). In the inner-loop (lines 12-14), all the neurons y that are within the neighborhood $\sigma_{SOM}(y^*)$ of y^*, including y^*, are updated by Equation 3.19 (line 13). The process of updating the neurons, shifts y closer to input x. The learning parameter (Eqn. 3.20), directly influences the degree-of-movement of y toward x. It is applied during the update process and is exponentially represented (Eqn. 3.20). The weight contribution of the training vector to each node is based on the distance between the BMU of the specified training vector and the remaining nodes. The neighborhood function (Eqn. 3.19), is represented as a smoothing parameter where the nodes within the boundary of the winner and the BMU, update personal vectors that are closer to the training vector from the input data space (Eqn. 3.21). The closer a node is to the BMU, the greater the weights are adjusted. After each iteration within the while-loop process, the learning rate is reduced to facilitate convergence until the maximum user-defined iteration count is achieved. At convergence, the neurons y_i will transit into regions which are concentrated with x_j. Hence, each y_i will be represented by a cluster of data points that are characterised by neurons that are close to each other.

3.5.2 Kohonen's Batch SOM

An alternate to the sequential based SOM algorithm (Alg. 5), where a single data vector is presented to the SOM at each learning step and the weight vectors are updated accordingly, is a batch type method [136]. The batch model is computationally efficient and will generate similar results in comparison to the incremental learning based method (Alg. 5) [137]. The weight updates are not recursive, hence limiting the dependence of the order in which the input vectors are presented to the model [138]. By partitioning the dataset and integrating the inputs in parallel for training during a single-stage process, the demerit of the dominating influence of the presented input data vectors on training at the later stages by the sequential based SOM models is mitigated [138]. The learning parameter (Eqn. 3.20) in the batch training process is also not required and the potential for premature convergence to SOM training as a result of an ill-defined learning rate parameter is limited [138].

The computational process is defined as follows:

1. The input dataset and the weight vectors for SOM training are partitioned into $\{V_j\}_{j=1}^{D}$, regions by first and second principal components over a D-dimensional space, by the principal component analysis (PCA);
2. The input vector x_k is concurrently integrated to all the neurons in the PCA established regions;
3. The Euclidean distance between x_k and all the weight vectors w_d is computed. The input vector that is closest to the weight vector is identified as the winning neuron (Eqn. 3.17);
4. For n_j samples in each PCA region V_j, the mean of $\bar{x}_k$ is computed by:

$$\bar{x}_k = \frac{1}{n_j} \sum_{p=1}^{n_j} X_p \tag{3.22}$$

Where:

$$X_p \in V_j, 1 \leq p \leq n_j$$

5. The weight vectors are updated with the application of a linear weighted average model as:

$$w_d^{(k+1)} = \frac{\sum_{j=1}^{D} h_{jk}(k).n_j.\bar{x}_k}{\sum_{j=1}^{D} h_{jk}(k).n_j} \tag{3.23}$$

The Pseudocode of the batch learning SOM training algorithm is defined as follows:

Algorithm 6 Batch SOM Training Algorithm

```
1: Input: Initialise array M with n neurons [Eqn. 3.15]
2: Output: Set of prototypes, Y = {y_1, ··· , y_M}
3: Initialise weight vectors of the neurons [Eqn. 3.16]
4: while termination criteria not satisfied do
5:     k = 0
6:     for epoch=1, ··· , X do
7:         for input=1, ··· , D do
8:             for n = 1, ··· , N nodes do
9:                 Compute Euclidean distance between node weight and input vector
10:            end for
11:            Compute winning node [Eqn. 3.17]
12:            for n = 1, ··· , N nodes do
13:                Compute weight vector summation numerator and denominator [Eqn. 3.23]
14:            end for
15:        end for
16:        for n = 1, ··· , N nodes do
17:            Update weight vectors w_d, with the accumulated weight vector summation [Eqn.
               3.23]
18:        end for
19:    end for
20:    k = k + 1
21: end while
```

The notable difference between the sequential (Alg. 5) and the batch learning process (Alg. 6) is limited to the adjustment and the update of the weight vectors of the nodes at each iteration. The batch algorithm follows the logic presented for the sequential based methodology, with the noted difference limited to the summation of the numerator and denominator terms within the linear weighted average scheme, in Equation 3.23. This is presented in an inner-loop, as a function of the number of nodes N, in lines 12-14 in Algorithm 6. The summation form is then applied to update the weight of the node population within the batch training methodology in lines 16-18 (Alg. 6) accordingly.

The SOMs will be used with large datasets for optimisation pre and post-processing stages for the analysis presented in the thesis. The batch learning process will facilitate accelerated computational performance. The software package SOMine, by Viscovery Software GmbH [139] is based on the batch SOM algorithm and is suited for direct application for the purposes of this thesis. The computational process in SOMine applies a Gaussian function to define the topological connection

between two arbitrary nodes [139]. The radius of the Gaussian function is related to a user-defined tension parameter which governs the degree-of-smoothing of the map. A $k-$means method is applied to update the node vector by equating the parameter to the mean of the weighted data vector in Equation 3.23. Training efficiency is enhanced by starting the process with a small node population in the map and incrementally increasing the sampling size in increments to a user-defined number of nodes. Each training process is simulated over a set number of batch processes with a decrease in tension. As the node population increases, the growth in map topology is compensated with a decrease in tension, or the radius of the Gaussian function between two arbitrary nodes [139].

The SOM training process distributes the nodes in the map that gradually adapt to an intrinsic shape of the presented input data [140]. The distribution reflects the underlying features of the data which are directly converted into 2-dimensional charts to signify the relationship between the datasets within the emerging map on the grid. The SOMine software package facilitates intelligent, menu-driven commands to enable the visualisation of the dependencies between the presented data including the analysis of high-dimensional data into simplistic 2D models [139].

3.5.2.1 Visualisation by Data Cluster

In SOMine [139] data cluster for visualisation is based on the SOM-Ward clustering process. A hierarchical cluster algorithm based method is applied, where each node develops a cluster for a qualitative analysis. At each time step, two clusters in the map are interlinked and are governed with a minimal distance based on the SOM-Ward measure. The applied process factors the relative positioning of the clusters based on a defined measure constraint, where the clusters that are not adjacent are always at infinity. The clusters that merge are restricted to partitions which share topological similarities. A distance threshold measure between the nodes is applied to define the criterion for cluster generation. The distance between two neighboring nodes is computed. If the distance is greater than a defined cluster threshold, a line separator spanning the length of the map, from one edge to the other is applied and a data cluster is introduced for data visualisation.

In SOMine, the number of clusters can be user-defined to model the dependency between the design parameters and model output (i.e. objective function) including constraints. As an example, a SOM is applied to visualise the relationship between aircraft wing sizing shape variables on lift. The number of clusters in the map are defined to relate the shape variables to lift. Each shape coefficient is perturbed one factor at a time over i intervals. At each interval the lift is computed. If the lift is less than the user-defined minima, the shape is designated as a constraint violated design. A binary format is introduced to distinguish between a constraint satisfied and violated design with 1 and 0 integer representation respectively. The database is then applied to train a SOM with Algorithm 6 and is partitioned in accordance to the user-defined lift constraint binary separators.

The sample $\mathcal{S}$, with n wing shape variables is presented in array format $\mathcal{Q}_{\mathcal{S}n}$. Lift $\mathcal{L}_{\mathcal{S}}$ is computed for $\mathcal{S}$ and a binary integer applied to represent data cluster $\mathcal{C}_{\mathcal{S}}$, to signify a constraint satisfied or

violated design. The format of the input data set for SOM training is defined as:

$$\begin{bmatrix} \overbrace{\mathcal{S}_1}^{\text{Sample}} \\ \mathcal{S}_2 \\ \vdots \\ \mathcal{S} \end{bmatrix} \begin{bmatrix} \overbrace{\mathcal{Q}_{1,1} & \mathcal{Q}_{1,2} & \mathcal{Q}_{1,3} & \cdots & \mathcal{Q}_{1,n}}^{\text{Sample } n^{th} \text{ Degree Wing Shape Variables}} \\ \mathcal{Q}_{2,1} & \mathcal{Q}_{2,2} & \mathcal{Q}_{2,3} & \cdots & \mathcal{Q}_{2,n} \\ \vdots & \vdots & \vdots & \vdots & \vdots \\ \mathcal{Q}_{\mathcal{S},1} & \mathcal{Q}_{\mathcal{S},2} & \mathcal{Q}_{\mathcal{S},3} & \cdots & \mathcal{Q}_{\mathcal{S},n} \end{bmatrix} = \begin{bmatrix} \overbrace{\mathcal{L}_1}^{\text{Lift}} \\ \mathcal{L}_2 \\ \vdots \\ \mathcal{L}_{\mathcal{S}} \end{bmatrix} = \begin{bmatrix} \overbrace{\mathcal{C}_1}^{\text{Constraint; Cluster Definition}} \\ \mathcal{C}_2 \\ \vdots \\ \mathcal{C}_{\mathcal{S}} \end{bmatrix} \tag{3.24}$$

From the clusters, the data is visually inspected to evaluate the dependency of the design parameters on the objective function and constraint. The topology of the search space as a function of $\mathcal{Q}$, $\mathcal{L}$ and the user-defined constraints $\mathcal{C}$ will be established. The effect of each shape variable on the design problems is attained. Visual inspection by means of evaluating the relationship between a n^{th} degree dimensional data on the objective and constraint functions, by planar 2D and/or 3D charts is not possible for the defined test problem. The application of SOMs addresses the identified issue by transforming the high-dimensional data into simplistic 2D charts. Demonstration of the SOM principles are presented for 2D, 3D and 10D problems in the following sub-sections. The simplified case studies will confirm the merits of data visualisation by a qualitative means for direct application into the intent research field of study.

3.5.2.2 Case Study One: 2D Test Problem

The amplitude of a spring oscillation is defined by a decay function as:

$$x(t) = e^{-t}\cos(2\pi t) \tag{3.25}$$

The exponential decay of the amplitude x, at time t (Eqn. 3.25), is presented in Figure 3.7

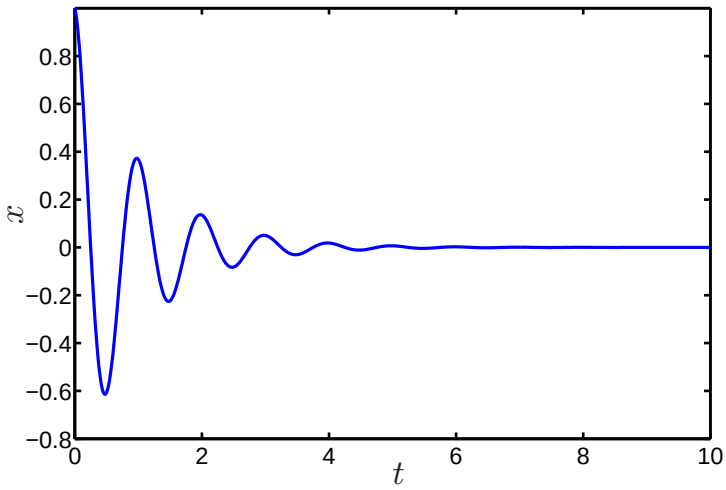

FIGURE 3.7: Spring Oscillation Decay with Time

The relationship between the dependent variables, amplitude and time is presented in Figure 3.7. The application of SOMs is not justifiable as the relationship between the design factors is evident since the dimensional size of the problem is less than three. The case study demonstrates the methodology to illustrate the potential of SOMs to transform n^{th} degree dimensional data into easy-to-read visualisation charts. The SOMs present a novel alternate to the 2D representation in Figure 3.7, to effectively model the dependency between t and x in Figure 3.8 as:

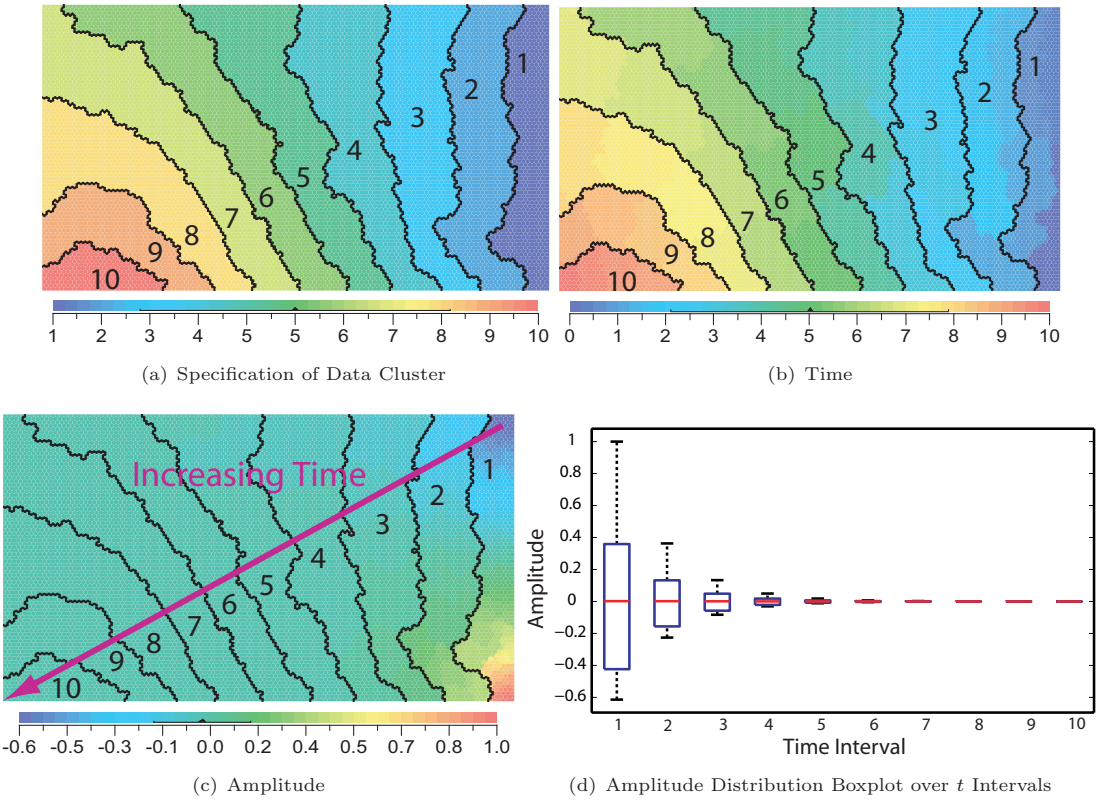

(a) Specification of Data Cluster

(b) Time

(c) Amplitude

(d) Amplitude Distribution Boxplot over t Intervals

FIGURE 3.8: SOM Representation of Spring Oscillation Decay with Time

The SOM is trained to model the relationship between t and x. The nodes in the map are partitioned with a user-defined cluster population size (Figs. 3.8(a) - 3.8(c)). Each partition, represents a one second duration in time and in total there are ten clusters to represent the span of the exponential decay of x over t (Fig. 3.8(a)). The sample of the input data applied for SOM training, with the specification of a user-defined cluster separator marker is:

$$\begin{bmatrix} \overbrace{0}^{t} \\ 0.01 \\ 0.02 \\ 0.03 \\ \vdots \\ 10 \end{bmatrix} = \begin{bmatrix} \overbrace{1}^{x} \\ 0.9881 \\ 0.9724 \\ 0.9532 \\ \vdots \\ 0 \end{bmatrix} = \begin{bmatrix} \overbrace{1}^{\text{Cluster Definition}} \\ 1 \\ 1 \\ 1 \\ \vdots \\ 10 \end{bmatrix} \tag{3.26}$$

The user-defined cluster markers (Eqn. 3.26), distribute the input SOM training data incrementally in one second intervals. As the SOM in Figure 3.8(a), is applied to partition the data, the nodes in each cluster are representative of the specified time interval and are of equal magnitude. In cluster one (Fig. 3.8(a)), the nodes equal to one as the data is representative of x over a time interval $t = 0 \rightarrow 1$ (Eqn. 3.26). In cluster two (Fig. 3.8(a)), the nodes equal two. The partitioning of the data is similarly presented as a function of time interval from $t = 1 \rightarrow 2$. The process is similarly defined for the test envelope over the ten seconds, hence resulting in ten clusters (Fig. 3.8(a)). As the magnitude of the nodes representing cluster separation definition are equal over the specified time interval, the contour color distribution in each partition is equally even (Fig. 3.8(a)).

The distribution of the interval $t = i \rightarrow i + 1$ (where $i = 0$ to 10 seconds for each cluster) is represented in the SOM in Figure 3.8(b). The bottom right corner of the map in cluster one, represents spring oscillation at initialisation ($t = 0$). The magnitude of time is represented by the contour markings with $t = 0$ denoted by a "cold" region with dark blue coloration (bottom right corner in Fig. 3.8(b)). The corresponding amplitude is $x = 1$ at $t = 0$ (Fig. 3.7). This is equally represented in the corresponding region of the SOM at the bottom right corner in Figure 3.8(c) with "hot", dark-red contour region. The SOM training has effectively modeled the expected system behavior. Within the time interval $t = i \rightarrow i+1$, the nodes in Figure 3.8(b), increase in magnitude in each cluster from bottom to top to represent the progression of time duration in the specified cluster. The top right region of the map in cluster one (Fig. 3.8(b)), represents nodes with $t \rightarrow 1$. The associated top right region in Figure 3.8(c), represents the magnitude of oscillation, which is low and is approaching $x \rightarrow -0.60$ as denoted by "cold" dark blue contour coloration.

The amplitude decay spans from right-to-left as a function of time (Fig. 3.8(c)), with cluster markers 1-10. The extremity in contour coloration range becomes smooth and consistent as the data spans from markers 1-10 (Fig. 3.8(c)). In cluster one, variances in contour color representation of x is evident. Red zones are present at the bottom right region and blue markers on the top right corner of the map, with a mix of the two patterns present between the two regions to represent the decrease in x as $t = 0 \rightarrow 1$. The variance of amplitude by the SOM is validated by a boxplot analysis in Figure 3.8(d). In cluster one the minimum and maximum magnitudes of the nodes are 1 and -0.60 respectively and are representative of the theoretical decay modeled in Equation 3.25 for $t = 0 \rightarrow 1$. In cluster two, variances in contour coloration (Fig. 3.8(c)) are also presented, but the extremity is not as obvious as noted in cluster one. The green markers at the bottom region in cluster two reflect the maximum amplitude magnitude in time interval $t = 1 \rightarrow 2$ of 0.363 and the cold dark nodes at the top region denote to the minima $x = -0.2259$. The intermediate nodes between the two extremities reflect the fluctuating decay process and the merging of the green and blue contours within the specified time zone. The variance of the data is validated in the boxplot analysis (Fig. 3.8(d)). Since the extremity of the amplitude decay in cluster two is less than cluster one, the inter-quartile range (IQR) is also lower than cluster one (Fig. 3.8(d)).

As the amplitude decay plateaus at zero over time (Fig. 3.7), the variances in SOM contour color markers for x (Fig. 3.8(c)), from right-to-left for clusters $i \rightarrow 10$ and the boxplot IQR (Fig. 3.8(d)), converge to zero. The observed pattern of x over t, equates to the theoretical behavior in Figure 3.7, hence validating the SOM training process. The SOM process presented yields a novel

data visualisation approach to effectively distinguish the dependency of the design variables on the objective function.

3.5.2.3 Case Study Two: 3D Test Problem

The demonstration of SOMs is extended to a 3D test problem. The test function applied is the De Jong's function. It is a continuous, convex and unimodal function (Fig. 3.9(a)) and is defined as:

$$f_1(x) = \sum_{i=1}^{n} x_i^2; \quad -1.00 \leq x_i \leq 1.00 \tag{3.27}$$

The solution landscape is presented in Figure 3.9(b). The top $(-1, 1)$ & $(1, 1)$ and bottom $(-1, -1)$ & $(1, -1)$, corners of the search space have extended peaks with a maximum $f(x)$ magnitude of two (Figs. 3.9(a) - 3.9(b)). The search space contour exhibits a rapid solution valley with lower $f(x)$ values as $x \rightarrow 0$. The theoretical global minimum $f(x) = 0$, is at $x_i = 0$ for $i = 1, \cdots, n$ and is modeled in Figure 3.9(b).

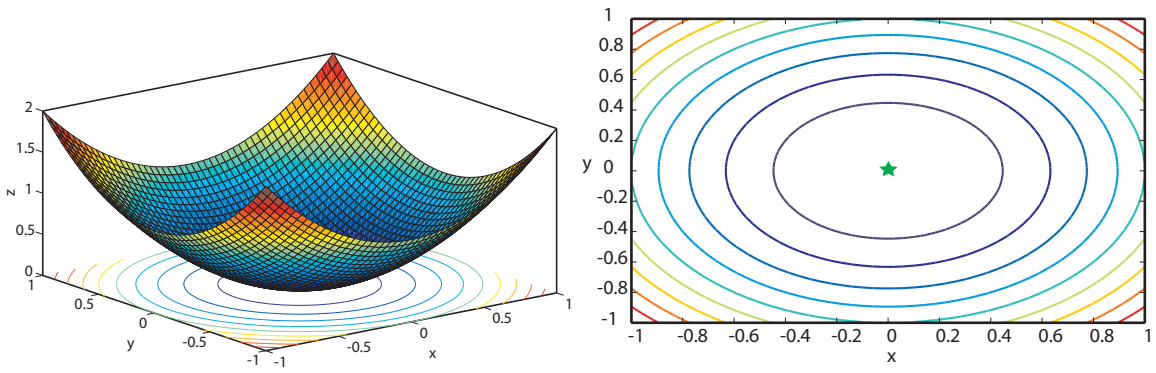

(a) 3D Function Representation

(b) Solution Topology

FIGURE 3.9: 3D De Jong's Function

To model the dependency between x and y on z, a SOM is trained to evaluate the relationship between the design variables on the objective function. The training comprises of the inputs x, y and output z (Eqn. 3.27) data points. A cluster separator is integrated to partition the input vector x and y into ten, user-defined even intervals in the search space $[-1, 1]$. The sample of the input data is:

$$\overbrace{\begin{bmatrix} -1 & -1 \\ -1 & -0.95918 \\ -1 & -0.91837 \\ -1 & -0.87755 \\ \vdots & \vdots \\ 1 & 1 \end{bmatrix}}^{\text{Inputs: } x \text{ \& } y} = \overbrace{\begin{bmatrix} 2 \\ 1.92 \\ 1.8434 \\ 1.7701 \\ \vdots \\ 2 \end{bmatrix}}^{\text{Output } z} = \begin{bmatrix} \overbrace{1}^{\text{Cluster Definition}} \\ 1 \\ 1 \\ 1 \\ \vdots \\ 10 \end{bmatrix} \tag{3.28}$$

The cluster definition marker (Eqn. 3.28), as applied to partition x, y and z in the defined search space is presented in Figure 3.10(a). The clusters are initiated at $x = -1$ and the intervals span the

search envelope such that:

$$\begin{aligned} x &= -1 \rightarrow -1 + \left\{ \frac{\text{Search Envelope}}{\text{No. of Intervals}} \right\} \\ &= -1 \rightarrow -1 + \left\{ \frac{2}{10} \right\} \end{aligned}$$

The nodes in the SOM for variable x (Fig. 3.10(a)) increase in magnitude for clusters spanning right-to-left for zones 1 to 10. The magnitude of the nodes and the contours represent the variances of x interval in the respective zones. In cluster 1, dark blue regions define nodes such that, $x = -1 \rightarrow -1 + \frac{2}{10}$. The contours become lighter with transition from right-to-left across the map and transform to dark red regions in clusters 9-10 (Fig. 3.10(a)), as the intervals approach the boundary of the search space, $x \rightarrow 1$.

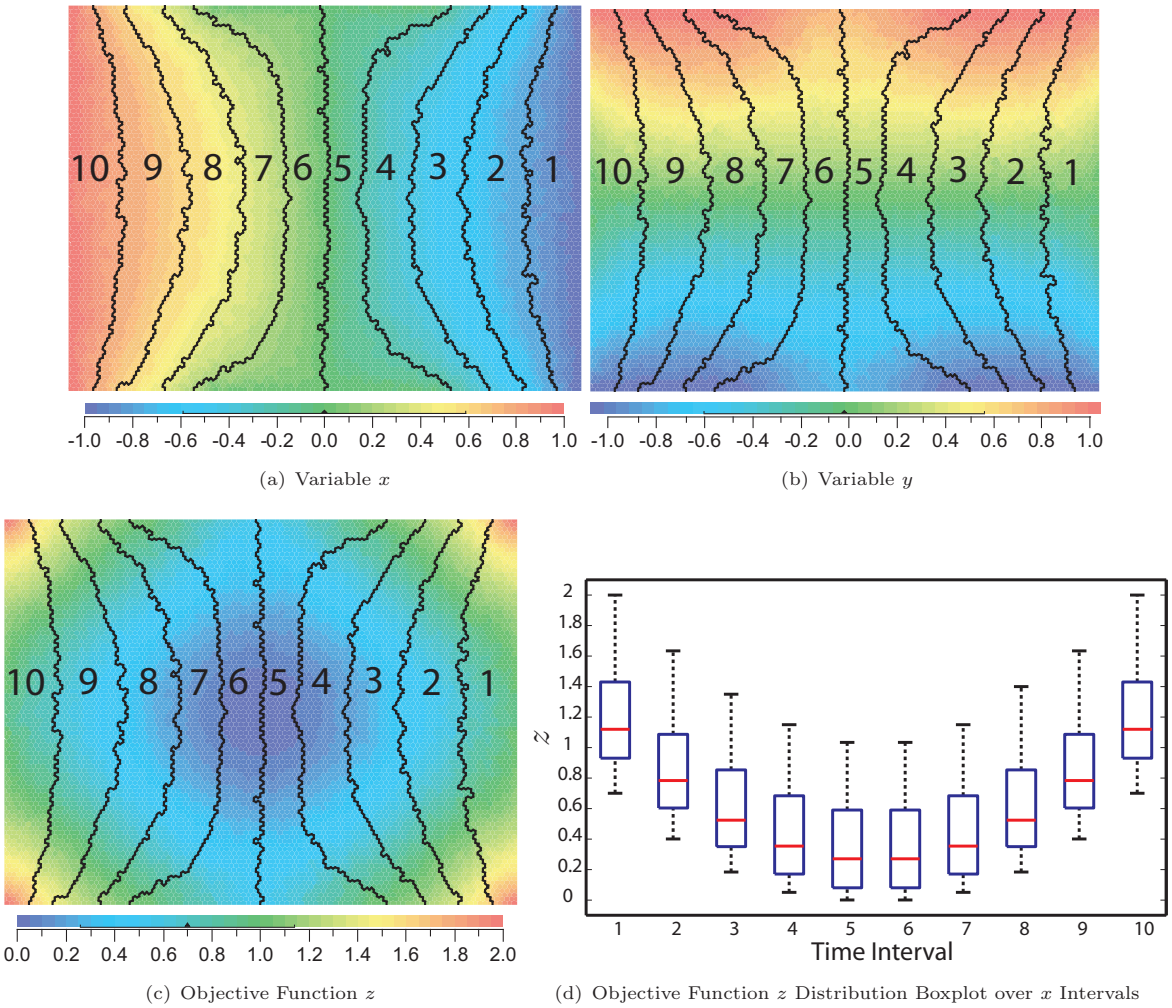

(a) Variable x

(b) Variable y

(c) Objective Function z

(d) Objective Function z Distribution Boxplot over x Intervals

FIGURE 3.10: 3D De Jong's Function

The corresponding magnitude of variable y for intervals x within the specified clusters are presented in Figure 3.10(b). The intervals of y are consistent for zones 1-10 and are partitioned evenly such

that:

$$\begin{aligned} y &= -1 \rightarrow -1 + \left\{ \frac{\text{Search Envelope}}{\text{User-defined } y \text{ Partitions}} \right\} \\ &= -1 \rightarrow -1 + \left\{ \frac{2}{50} \right\} \end{aligned}$$

The magnitude of the SOM nodes for variable y increase from bottom to top (Fig. 3.10(a)). Light blue contour regions are evident at the bottom and dark red zones at the top for each cluster within the SOM (Fig. 3.10(a)). The contour coloration is consistent across zones 1-10, thus illustrating the consistency of interval y, with variations in x for the equating cluster zone. The lower right corner of the SOM for variables x and y (Figs. 3.10(a) - 3.10(b)), equate to the search space at $x = y = -1$. Accordingly the contour colors represent "cold" dark blue regions to reflect the equating search space topology. The identified region is theoretically presented in the lower left corner of the solution topology in Figure 3.9(b). At this point, the objective function is maximum (Figs. 3.9(a) - 3.9(b)), with $z = 2$. The expected magnitude is verified by the objective function SOM in Figure 3.10(c), where the lower-right corner depicts an objective function with $z = 2$. The contour color is a "hot" zone with red color markers to define the maximum state of $f(x)$.

The upper and bottom most corners of the objective function SOM (Fig. 3.10(c)), indicate red markers, hence a maximum objective function state. The illustrated pattern is theoretically verified in Figures 3.9(a) and 3.9(b), where the peak of the objective function is isolated about the search space boundary. The extremity of the objective function nodes decreases as the clusters approach zones 5-6. The variances in the contour coloration becomes consistent as the cluster approach 5-6. The derived search space topology for the objective function z by the SOM training (Fig. 3.10(c)), is comparable to the theoretical characteristics of the test function search space in Figures 3.9(a) - 3.9(b). The outer regions of the search space boundary constitute to high fitness function values. As $x \rightarrow 0$ and $y \rightarrow 0$, the objective function z converges to the theoretical solution zero. The contour solution topology by the SOM representation in Figure 3.10(c) models the theoretical solution topology with acceptable accuracy.

The objective function output by SOM training, as a function of x for each cluster is presented by a boxplot analysis in Figure 3.10(d). As the test function solution landscape is symmetrical about the x and y axis, the variances of the minimum, maximum and mean values of the nodes in the defined clusters models this process. Cluster 1 presents the test landscape $x = -1 \rightarrow -1 + \frac{2}{10}$, with a maximum objective value of $z = 2$, which represents the boundary of the search space. As the x interval is isolated about the boundary of the search space, the mean of z is high. In cluster 2, the x test landscape is $x = -1 + \frac{2}{10} \rightarrow -1 + \frac{2}{10} + \frac{2}{10}$. As the input x interval is approaching zero, the maximum, minimum and mean of z are lower than cluster 1 (Fig. 3.10(d)). The minimum and maximum of the nodes including the variance of the mean continues to decrease and plateaus at clusters 5 and 6 (Fig. 3.10(d)). In cluster 6, a minima of $z = 0$ is presented at $x = y = 0$ (Fig. 3.10(d)). This is in agreement to the theoretical solution of the test function in Figure 3.9(b). The variances of the boxplots for clusters 1-4 match clusters 7-10 due to the symmetry of the test function. Clusters 1-4 equate to $x = -1 \rightarrow \frac{2}{10}$ and clusters 7-10 represent $x = \frac{2}{10} \rightarrow 1$. Cluster 5 and 6 represent the region about the theoretical region such that $x = -\frac{2}{10} \rightarrow \frac{2}{10}$, with the global minima at (0,0) in cluster 6.

The demonstration of the SOM methodology on a 3D test problem validates the effectiveness of the data mining approach to model the dependency of the design variables to the objective function. The results are in agreement with the theoretical solution. The global minima is computed at the theoretical point and the valleys in the solution landscape are modeled with acceptable accuracy by SOMs. Planar 2D (Fig. 3.7) and 3D (Fig. 3.9) charts effectively model the relationship between the design variables. The application of SOM for dimensional test problems with less than three variables is not a requirement. The validation studies with two and three dimensions are applied to define the fundamentals of the novel approach to represent the dependency between the design variables. To further exploit the merits of a SOM for design search space visualisation, the test problem is extended to ten dimensions in the following section.

3.5.2.4 Case Study Three: Wing Weight Estimation

The following problem models a ten-variable function applied to estimate the weight of a light aircraft wing for conceptual design [141]:

$$\mathcal{W}_{wing} = 0.036 S_w^{0.758} W_{fw}^{0.0035} \left(\frac{A}{\cos^2\Lambda}\right)^{0.60} q^{0.006} \lambda^{0.04} \left(\frac{100tc}{\cos\Lambda}\right)^{-0.30} (N_z W_{dg})^{0.49} + S_w W_p \qquad (3.29)$$

Where:

S_w = Wing Area; W_{fw} = Weight of Fuel in the Wing (lb);
A = Aspect Ratio; Λ = Quarter-chord sweep (deg);
q = Dynamic Pressure at cruise (lb/ft^2); λ = Taper Ratio;
tc = Airfoil thickness to chord ratio; N_z = Ultimate Load Factor;
W_{dg} = Flight design Gross Weight (lb); W_p = Paint Weight (lb/ft^2);

As the dimensional size is ten variables, the relationship between the design coefficients and weight cannot be represented by planar curves. The effect of each design parameter on the objective function needs to be established by a qualitative approach. The application of SOMs will address this requirement by mapping the interactions between the identified parameters from Equation 3.29. The methodology addresses the limitations of representing the interactions for problems with $D > 3$.

The training population for SOM generation is calculated from Equation 3.29. An estimate of the suitable range of values for each weight parameter is provided by Forrester [141]. From the identified intervals, the LHS approach is applied to obtain a stratified sampling $\mathcal{S}$, spanning 10,000 data points. The corresponding weight is computed accordingly (Eqn. 3.29). The data array of each sample (Eqn. 3.30), is then applied to train the SOM, to model the relationship between the problem parameters.

Sample $\mathcal{S}$	Wing Definition Inputs									
	S_w	W_{fw}	A	Λ	q	λ	tc	N_z	W_{dg}	W_p
1	177.95	258.86	8.0762	0.076288	24.429	0.98038	0.086335	2.8502	2199.8	0.032505
2	192.91	273.17	6.931	−0.057194	30.899	0.93678	0.10834	4.9589	2482	0.045958
3	151.65	274.39	9.0574	−0.10627	41.951	0.82408	0.10811	3.7479	2380.4	0.071159
4	179.59	293.48	7.8946	−0.034959	22.361	0.96293	0.11938	3.2425	2063.4	0.074063
⋮	⋮	⋮	⋮	⋮	⋮	⋮	⋮	⋮	⋮	⋮
10,000	167.28	285.46	6.6366	−0.040474	32.073	0.50303	0.092665	3.4392	1938.7	0.068458

$$= \begin{bmatrix} \overbrace{\quad}^{W_{wing}} \\ 259.14 \\ 327.88 \\ 277.65 \\ 248.35 \\ \vdots \\ 222.57 \\ \quad \end{bmatrix} \tag{3.30}$$

The results of the training process are presented in the following SOMs.

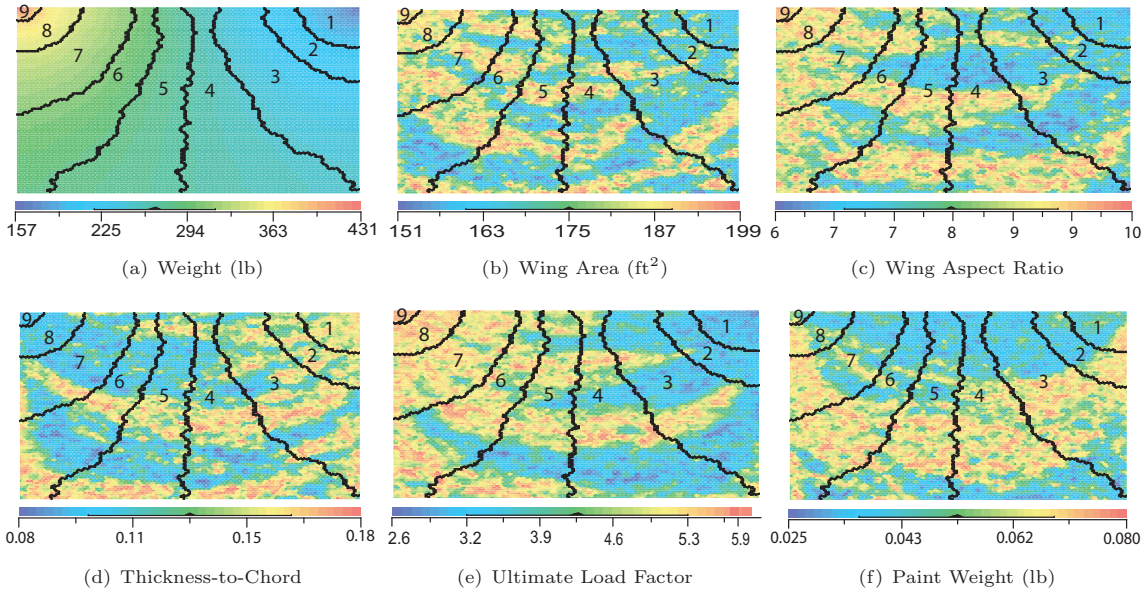

(a) Weight (lb) (b) Wing Area (ft^2) (c) Wing Aspect Ratio

(d) Thickness-to-Chord (e) Ultimate Load Factor (f) Paint Weight (lb)

FIGURE 3.11: SOM Representation of Aircraft Wing Weight Estimation with Ten-Variables

In the analysis, data clusters are applied based on the measure of radius of the neighboring nodes from the winning neuron. Nodes that are not within the boundary of the computed radius (Eqn. 3.18), are excluded from the particular group of nodes that are collectively adjusted to match the input vector by weight adjustment (Eqn. 3.19). Accordingly, there are nine clusters that partition the data (Fig. 3.11).

The interaction between the objective function weight and design coefficients including wing area, aspect and thickness-to-chord ratio, including ultimate load factor and weight of paint are collectively presented. Low weight performance is at top right-corner of the map in cluster 1 with dark blue zones in Figure 3.11(a). Aircraft wings with heaviest weight performance are isolated to cluster 9, at top left-corner with dark a red zone (Fig. 3.11(a)). The transition from cluster 1 to 9 (right-to-left) corresponds to an increased weight performance and the contour color transition from "cold" dark blue regions to "hot" red zones is evident in the intermediate clusters.

The impact of wing area (Fig. 3.11(a)) on weight (Fig. 3.11(b)) is examined. The wing area nodes in cluster 1, at top right-corner are modeled with dark blue contours and constitute to aircraft with low S_w, with a mean of 165.6 ft^2 (Fig. 3.11(b)). By cross-matching S_w to weight performance at equating cluster 1, the mean weight is 190.80 lb (Fig. 3.11(a)). At the extreme end of the spectrum,

cluster 9 for S_w (Fig. 3.11(b), top left-corner with dark red contours), models nodes with mean S_w of 188.5 ft^2. The equating mean wing weight at cluster 9 is 397.2 lb (Fig. 3.11(a)) and is higher than the mean weight in cluster 1. The results presented by the SOM analysis for direct comparison between weight and planform area conform to established aerospace design principles. Large wing area planforms are heavier than low wing area shapes.

The impact of the wing aspect ratio A, (Fig. 3.11(c)) matches the performance of S_w on weight (Fig. 3.11(a)). Low aspect ratio wings in cluster 1 (Fig. 3.11(c)), constitute to low weight performance at the equating cluster (Fig. 3.11(a)). High aspect ratio wings in cluster 9 (Fig. 3.11(c)), result in heavier wings in comparison. The intermediate clusters 2-8 model an increase in A which directly results to a gradual increase in weight at the corresponding clusters. The SOM validates the expected dependency of A on aircraft wing weight.

The impact of airfoil tc on weight is established in Figure 3.11(d). High tc airfoils are modeled in cluster 1 (Fig. 3.11(c)) and equate to low wing weight. Thicker airfoils do not require additional support mechanisms to maintain structural integrity, hence resulting in a lighter airframe. The transition from cluster 1 to 9 (right-to-left) within the tc SOM, results in clusters with lower magnitudes of tc nodes. Proportionally, the wing weight increases accordingly, as low thickness airfoils require extensive structural support systems for airframe integrity. The established relationship between planform thickness and wing weight by the SOM analysis is in accordance to the established design principles.

The impact of the ultimate load factor, which is directly related to the magnitude of the maximum aerodynamic load on the wing [141], is presented in Figure 3.11(e). It is evident that N_z has a significant impact on weight. The contours within the clusters for N_z distribution indicate a transition from low (dark blue) to high (dark red) load factors from right-to-left or from clusters 1 to 9 (Fig. 3.11(e)). By directly relating the observed N_z pattern to weight (Fig. 3.11(a)), it follows that a low N_z corresponds to low wing weight and high N_z will result in heavier wings in comparison. The interaction of N_z with A on weight is also established. Cluster 9 for N_z and A design coefficients refers to an aircraft wing with large g-forces and a high aspect ratio. A combination of high N_z and A equates to a heavy wing (cluster 9 in Fig. 3.11(a)), as a structurally viable planform is required to withstand the high aerodynamic loads. The analogy is related to highly maneuverable fighter jets which have high load factors and low aspect ratio wings to limit weight.

The impact of weight per unit surface area of the paint W_p, on total wing weight is established in Figure 3.11(f). Contour representation of low and high regions of W_p is consistent across the nine clusters. Unlike S_w, A, tc and N_z SOMs, where low and high contour regions are isolated to a specific zone within the map, the dispersion of W_p is evenly distributed across the nine clusters. Cluster 1 and 9, which constitute to the extremes in wing weight with low and high magnitudes respectively (Fig. 3.11(a)), are represented with consistent W_p contour markers (Fig. 3.11(e)) at the respective zones. The established pattern indicates that W_p has a minimal impact on weight relative to the rest wing parameters modeled in the analysis. This is further verified by Forrester [141] where the two-way interactions between W_p and the design coefficients in Equation 3.29, indicated a negligible impact of W_p on aircraft wing weight.

The application of SOMs for the case presented has validated the effectiveness of using a data mining technique to establish the design variable degree-of-impact on the objective function. By

concurrently presenting all the design variables that define the objective function, the interaction between the shape coefficients on the objective function is verified. Direct analysis of W_p with wing weight design coefficients indicates the negligible interactions of W_p with S_w, A, tc and N_z for weight estimation. The application of SOMs facilitates a valid approach to verify the interactions and dependency of the variables for objective functions with an extended dimensional search space ($D > 3$).

3.6 AM-PSO Design of Experiments

The data-mining process with SOMs is applied to fine-tune the input search parameters of the developed AM-PSO algorithm (Sec. 3.4). The AM-PSO specific search parameters are iteratively modified and the corresponding objective function is computed to measure the influence of the search parameter on solution feasibility. The output of the DoE process will result in large datasets. The results are interrogated by SOMs to evaluate the sensitivity of the user-defined optimisation parameter on search performance. The results will facilitate optimisation algorithm-based decisions to be implemented with confidence to ensure a valid airfoil shape design structure is defined.

3.6.1 Numerical Test Validation with Pre-Defined Termination Definition

The number of iterations to convergence is varied in increments of 500 from a minimum of 1,000 to a maximum of 2,000 for the purposes of validating the AM-PSO algorithm with published literature data. The AM-PSO demonstration process in this section does not focus on the convergence to the theoretical minima. Instead, the total number of design iterations to convergence is limited to verify the impact of the user-defined search parameters (Sec. 3.1.1), on the fitness evolution.

Benchmark test functions are applied in the DoE process. These include solution topologies that are uni and multi-modal. The complexity of the test problems is increased as a function of dimensional search space and the robustness of the model is verified accordingly. The Ackley, Michalewics, Rosenbrock and Schwefel functions (Table 3.2), are applied in the analysis.

Table 3.2: Benchmark Validation Test Functions

Function	Dimensional Search Space	Initialisation Range	Theoretical Global Minima
Ackley	-32.768 $\leq x_i \leq$ 32.768, i=1,2,...,n	-32.768 $\leq x_i \leq$ 16	X^*=(1,...,1) $f(x^*)$=0
Michalewics	$0 \leq x_i \leq \pi$, i=1,2,...,n	$0 \leq x_i \leq \pi$	X^*=$(2.20_1, ..., 1.57_{10})$ $f(x^*)$=-9.66
Rosenbrock	-2.048 $\leq x_i \leq$ 2.048, i=1,2,...,n	-2.048 $\leq x_i \leq$ 2.048	X^*=(1,...,1) $f(x^*)$=0
Schwefel	-500 $\leq x_i \leq$ 500, i=1,2,...,n	-500 $\leq x_i \leq$ 500	X^*=(1,...,1) $f(x^*)$=0

3.6.1.1 Rosenbrock Function

The Rosenbrock function in Figure 3.12 is unimodal (Eqn. 3.31), with the global optimum located on a long, flat, narrow parabolic shaped valley. Locating the valley in the search space is a non-trivial task. Optimisers with limited search capabilities have difficulties converging to the exact global minima point. The solution topology is characterised by a non-convex contour with the global minima x^* at $(x_1, x_2, ..., x_n = (1, ..., 1)$. At $n \geq 4$ the function has a local minima at $(x_1, x_2, ..., x_n = (-1, 1, ..., 1)$ Thus, with multiple minima in the solution topology, the search parameters required to define the AM-PSO algorithm to facilitate valid search simulations are defined accordingly.

$$f(x) = \sum_{i=1}^{n-1} [100(x_i^2 - x_{i+1})^2 + (x_i - 1^2)] \tag{3.31}$$

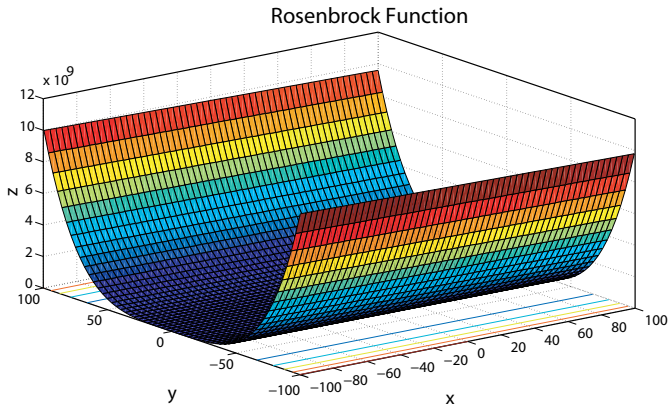

FIGURE 3.12: Rosenbrock Function

A. Effect of Maximum Velocity on Fitness

The effect of varying the maximum velocity of the particles is verified as a function of the limits of the dimension search space x_{max}. The performance of the standard Global-Based PSO (S-PSO) (Alg. 2), developed AM-PSO (Alg. 4) and AIWPSO [8] algorithm from the literature are compared in the validation process. The merits of the developed adaptive inertia weight function (Eqn. 3.8) is compared with the standard (Eqn. 3.2) and the function by Qin et al. [8] for the defined case study in this section. The principles of mutation in the AM-PSO method (Sec. 3.4.4), are not applied in the following simulations for the purposes of limiting the variances between the examined algorithms to the treatment of the adaptive inertia weight function only.

The magnitude of the maximum velocity on the search performance of the particles is problem based. A DoE simulation is defined to verify the influence of maximum velocity, which acts as a multiplier to x_{max}, on solution fitness in the range $0.1\% - 10\%$. To facilitate a comparative analysis with published data by the AIWPSO method [8], search termination is based on a pre-defined maximum iteration count. The set-up of the S-PSO, AIWPSO and AM-PSO algorithms is as follows:

TABLE 3.3: PSO Variant Types & Test Validation Set-Up

PSO Model	S-PSO	AIWPSO	AM-PSO (No Mutation)
Scaling Learning Factors	$c_1 = 2$ & $c_2 = 2$	$c_1 = 2$ & $c_2 = 2$	$c_1 = 2$ & $c_2 = 2$
Swarm Population	20,40 & 80	20,40 & 80	20,40 & 80
Dimensions	10,20 & 30	10,20 & 30	10,20 & 30
Maximum Iterations	1000,1500 & 2000	1000,1500 & 2000	1000,1500 & 2000
Inertia Weight	Equation 3.2	Qin et al. [8]	Equation 3.8
Maximum Velocity v_{max}	0.1-10% of x_{max}	100% of x_{max}	0.1-10% of x_{max}

To evaluate the performance of the S-PSO and AM-PSO model on fitness as a function of particle velocity, a SOM is applied to represent the performance variances between the two methods. The fitness convergence of the S-PSO (Fig. 3.13(b)) and AM-PSO (Fig. 3.13(c)) algorithms is examined. The termination criterion set at 2,000 iterations (Tab. 3.3). The effect of the scalar step length multiplier v_{max} (Sec. 3.1.1), as a percentage of search space x_{max} in Figure 3.13(a) is verified for the defined increments in Table 3.3. The clusters are partitioned with a user-defined binary integer format to distinguish the data as a function of the defined dimensional search space range.

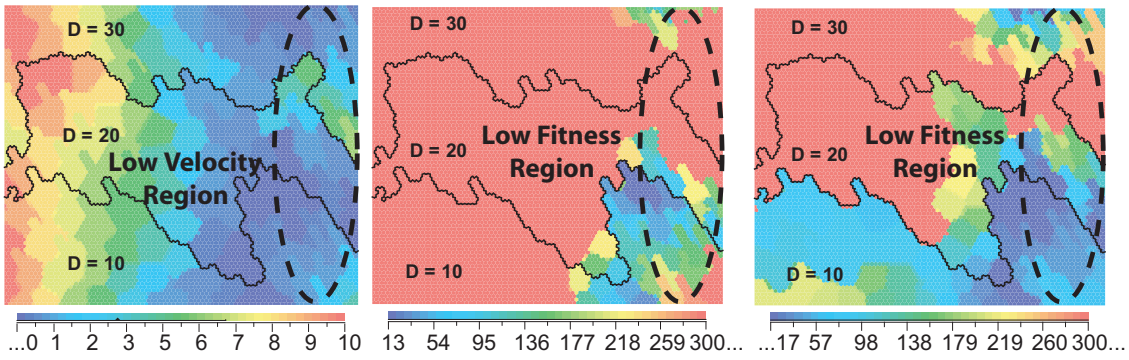

(a) Velocity % of x_{max} (b) S-PSO Fitness Distribution (c) AM-PSO Fitness Distribution

FIGURE 3.13: Rosenbrock Function SOM Representation of v_{max} as a function of Dimension Search Space for S-PSO & AM-PSO

The left region of the S-PSO (Fig. 3.13(b)) and AM-PSO (Fig. 3.13(c)) SOMs, indicate "hot" regions with red contour markers. This is directly related to v_{max} exceeding 5% of x_{max}. The observed pattern is evident across the defined test domain where an increase in D, corresponds to an increase in fitness. The results further verify that low velocity represents to low fitness for S-PSO and AM-PSO. The right side of the velocity SOM region (Fig. 3.13(a)) is modeled with blue contours, hence low velocity in comparison to the left side, which is characterised by high velocity with red contours. By directly relating the right side of the velocity SOM region to the fitness performance of the S-PSO and AM-PSO methods, low fitness performance is evident. To improve solution clarity for fitness convergence, the maximum contour limit is clamped at 300. Hence, high fitness regions are evident with dark red contours. Variations in low fitness regions with subtle changes in blue contour shades is evident to present the convergence toward an optima as a function of velocity for the respective optimisation algorithms.

Performance comparison between S-PSO and AM-PSO, indicates that the AM-PSO is superior over the evaluated test domain in comparison to the S-PSO model. The results indicate the S-PSO and AM-PSO have not converged to the theoretical minima. This is attributed to the implementation of the termination criteria, which ended the search prematurely. The S-PSO indicates greater areas of "hot" regions in red shade with higher fitness. Comparatively, the AM-PSO evolution at the same operating conditions, consists of larger "cold" regions in dark blue shade, thus indicating that the AM-PSO SOM consists of greater nodes with lower fitness in comparison to the S-PSO, across the testing domain envelope D. The analysis confirms that a linear decreasing inertia weight, where a global search process is enabled at the start of the search phase and local during the later stages exhibits acceptable solution convergence. A fixed inertia weight results in convergence instabilities as the search pattern (global versus local) does not adapt to the iterative search phase.

B. Effect of Swarm Population & Maximum Velocity on Fitness

The relationship between particle population ($m = 20, 40, 80$) and velocity for $D = 10$, as a function of fitness by the developed AM-PSO (without mutation) is represented in Figure 3.14. Higher particle population ($m = 80$), with the velocity restricted to $\approx 0.1\%$ of x_{max} equates to low fitness. At the same speed, with fewer particles ($m = 20$), the fitness increases by 4% in comparison. A large population of particles facilitates feasible convergence toward a low fitness region in the solution topology. At the extreme end of the test spectrum, the fitness computed is the highest when the velocity is set to $\approx 10\%$ of x_{max} with $m = 20$ particles. In comparison, with $m = 80$ at $\approx 10\%$ of x_{max}, the fitness computed is reduced by 64%. Hence, an increase in population size has a significant impact on fitness. The noted correlation between the design parameters is also valid for extended dimensional search spaces ($D = 20$ & 30). The corresponding data is presented in Appendix B - Figures B.1(a) - B.1(b).

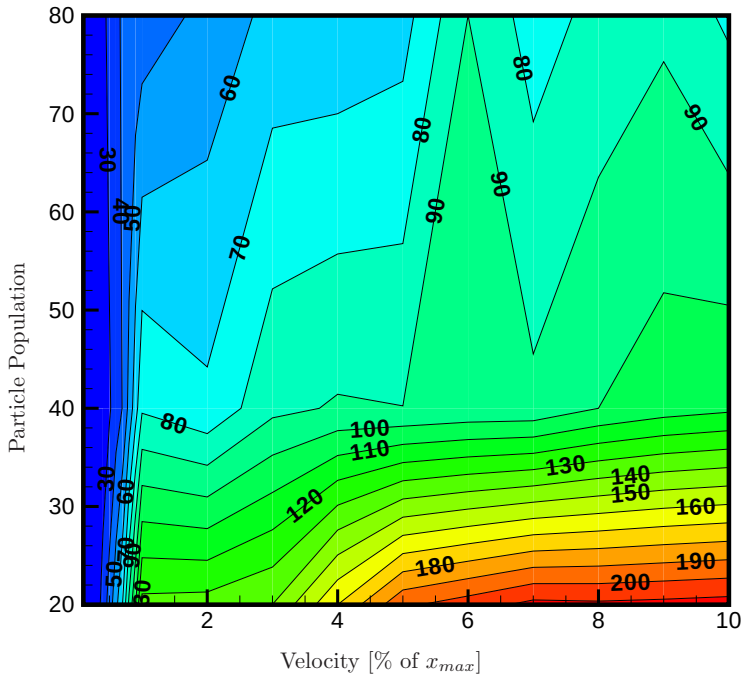

FIGURE 3.14: Effect of Particle Population and Velocity on Fitness by the AM-PSO Algorithm

Similarly, the fitness distribution as a function of swarm population and v_{max} for $D = 20$ & 30 is presented in Figure 3.15.

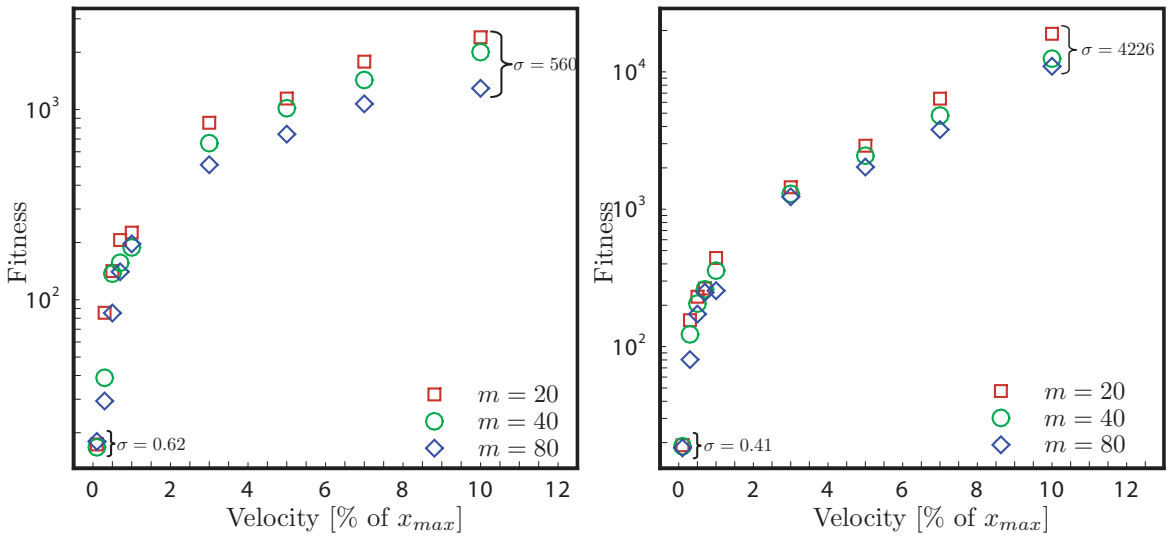

(a) $D = 20$ (b) $D = 30$

FIGURE 3.15: Effect of Particle Population, Maximum Velocity & Dimensional Search Space on Rosenbrock Function Fitness by the AM-PSO Algorithm

The velocity at $\approx 0.1\%$ of x_{max} equates to low fitness across the dimensional search domains in Figure 3.15. At $D = 20$ with $v_{max} \approx 0.1\%$ of x_{max}, the standard deviation of the fitness for $(m = 20, 40, 80)$ is 0.62 (Fig. 3.15(a)). When the velocity is increased to $v_{max} \approx 10\%$ of x_{max}, the fitness standard deviation increases to 560. Similarly for $D = 30$, the fitness standard deviation at the low spectrum of the velocity envelope for swarm population $(m = 20, 40, 80)$ is 0.41 (Fig. 3.15(b)). In comparison, with an increase in velocity to $v_{max} \approx 10\%$ of x_{max}, the standard deviation increases to 4226.

The results indicate the instability of solution convergence to a valid search space region as a function of particle maximum velocity. This is related to the unimodal solution topology of the Rosenbrock function. As there exists one global minima to the function, the particles overshoot the minima region at higher velocities. The sensitivity of a high scalar step length on fitness standard deviation with an increase in v_{max} is due to solution search space topology type. The search mechanisms of the optimisation algorithm guide the particles to the global minima. As the swarm size in increased, the probability of *pbestg* converging to a region about the optimal point with fewer design iterations in comparison to a low population of m becomes high. Hence, for a high swarm population at $m = 80$ for $D = 20$ & 30, the fitness is lower than a swarm defined with $m = 20$ & 40 across the tested v_{max} test envelope (Figs. 3.15(a) - 3.15(b)).

If the velocity for unimodal search topologies is high, the search merits of the optimisation algorithm are compromised due to an excessive step length. The particles transit rapidly across the boundaries of the search space and away from the global point. At low speeds, the scalar step length has minimal impact on particle transition per iteration. A search agent hovering about the search region bounded by the minima point, will oscillate at this position until convergence. The expected search behavior type is acceptable for unimodal search domains. If the search topology consists of

multiple local minima, then oscillation about a localised region will be a design issue and result in convergence to a sub-optimal point.

The fitness by the AM-PSO is evaluated against the published AIWPSO [8] for the Rosenbrock function. The disparity between the two algorithms (Tab. 3.3) is limited to: **a)** The setting of v_{max} which is fixed to the maximum distance of the dimension search space in AIWPSO [8]. In AM-PSO, v_{max}=0.10% of x_{max}; and **b)** A variant inertia weight function in the developed AM-PSO method in comparison to the methodology proposed in AIWPSO (Tab. 3.3). The results by the SPSO, AM-PSO and AIWPSO [8] algorithms is presented in Table 3.4.

TABLE 3.4: Rosenbrock Function: Fitness Evaluation Comparison by S-PSO, AIWPSO [8] & AM-PSO with Velocity at 0.10% of x_{max}

Swarm Population	D	Max. Iterations	S-PSO	AM-PSO (No Mutation)	AIWPSO [8]
20	10	1000	34.4393	**17.1394**	48.6378
	20	1500	92.4618	**17.3522**	115.1627
	30	2000	156.8884	**19.1374**	218.9012
40	10	1000	18.0475	**17.2192**	24.5149
	20	1500	85.2453	**16.7663**	60.0686
	30	2000	129.5636	**18.8235**	128.7677
80	10	1000	**13.2744**	17.8872	19.2232
	20	1500	79.2820	**17.9988**	52.8523
	30	2000	100.9905	**18.3088**	149.4491

† **Bold face indicates the best result for the respective PSO variant model**

The results by the S-PSO and AM-PSO methods in Table 3.4, correspond to a velocity threshold fixed at 0.1% of x_{max}, as the viability of a low speed setting was verified in Figures 3.13 - 3.15. Performance comparison between the S-PSO and AIWPSO model, indicates a lower fitness with S-PSO at select test conditions. The theoretical merits of a linearly decreasing inertia weight function in the AIWPSO model does not correlate to a lower fitness, due to a particle velocity set to 100% of x_{max}. The S-PSO model with a fixed inertia weight is defined at a lower velocity of 0.10% of x_{max} and outperforms the adaptive inertia weight function with higher velocity in comparison. The importance of correctly setting the maximum speed of the particles must be defined for problem-specific applications.

Performance comparison between the AM-PSO and AIWPSO processes indicates the viability of the AM-PSO over the examined test domain D, with lower fitness due to particle simulation at a low speeds in Table 3.4. To further evaluate the merits of the developed adaptive inertia weight function (Eqn. 3.8) with AIWPSO [8], the v_{max} is set to 100% of x_{max} in the AM-PSO definition to match the settings defined in AIWPSO in Table 3.5. Hence, a meaningful comparison is attained between the performance measure of the two methods.

TABLE 3.5: Rosenbrock Function: Fitness Evaluation Comparison by S-PSO, AM-PSO & AIWPSO [8] Algorithms with Velocity at 100% of x_{max}

Swarm Population	D	Max. Iterations	AM-PSO (No Mutation)	AIWPSO [8]
20	10	1000	**46.1222**	48.6378
	20	1500	**113.2213**	115.1627
	30	2000	222.1233	**218.9012**
40	10	1000	**24.2322**	24.5149
	20	1500	61.0032	**60.0686**
	30	2000	**126.3234**	128.7677
80	10	1000	19.78676	**19.2232**
	20	1500	**50.2134**	52.8523
	30	2000	151.1234	**149.4491**

† **Bold face indicates the best result for the respective PSO variant model**

The analysis verifies the viability of the adaptive inertia weight function to facilitate valid search simulations in comparison to the methodology proposed in literature [8] in Table 3.5. The fitness differences between the two methods is minimal for the test envelope examined. The highest percentage difference is $\approx 5\%$. The results in Table 3.5 are modeled with a velocity of 100% of x_{max} and significant performance differences between the AM-PSO and AIWPSO was established. The results validate the importance of the scalar step length for a valid search performance. By coupling the novel adaptive inertia weight function (Eqn. 3.8), with a velocity of the particles restricted to $\approx 0.10\%$ of x_{max} (Tab. 3.4), favorable results are attained for the examined test functions with a user-specified maximum number of 2,000 iterations.

3.6.1.2 Additional Test Evaluation

To further verify the impact of v_{max} as a function of x_{max} on fitness performance by the S-PSO and AM-PSO algorithms, a comprehensive validation analysis is undertaken. The effect of swarm population and v_{max} on fitness for a user-defined termination criteria, instead of a maximum iteration limit, is established. The test functions applied in the validation analysis are as follows:

A. Ackley Function

The Ackley function is multi-modal with widespread local minima that are dispersed evenly across the solution topology. The function is modulated by an exponential factor which acts as a multiplier to a cosine wave in Equation 3.32. This induces moderate oscillations in the solution space. The search topology further consists of a plateau outer region with a distinct central hole in Figure 3.16. The surface and the boundaries within the hole are also modeled with cosine waves. The surface irregularities consist of local peaks and troughs where the troughs signify local minima points. The function is ideal to verify the flexibility of the developed optimisation algorithm.

$$f(x) = 20 + e - 20e^{-\frac{1}{5}\sqrt{\frac{1}{n}\sum_{i=1}^{n} x_i^2}} - e^{-\frac{1}{n}\sum_{i=1}^{n} cos(2\pi x_i)} \tag{3.32}$$

Where:

$$x_i \quad = \quad \text{Search Domain}$$

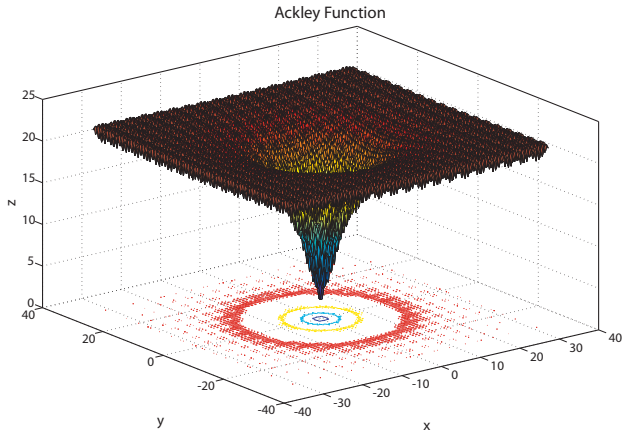

FIGURE 3.16: Ackley Function

B. Michalewics Function

The Michalewics is a multi-modal function with $n!$ local optima in Equation 3.33. The parameter m_{mich} defines the steepness of the valleys of the search space. A large m_{mich}, results in a complex solution map as the steepness of the valley increases proportionally and the optimiser has a very narrow peak to propagate through to the global minima in Figure 3.17. A large value of m_{mich} further exhibits little information on the location of the global minimum. The complexity of the search topology is user-controlled. A value of $m_{mich} = 10$ was applied in literature [114] and is further integrated in the presented numerical experiments for comparative analysis purposes between the two methods. An optimiser with limited search capabilities will have issues locating the global minima, thus Michalewics is an acceptable candidate for the validation of the AM-PSO algorithm.

$$f(x) = -\sum_{i=1}^{n} sin(x_i) \left[sin\left(\frac{ix_i^2}{\pi}\right)\right]^{2m} \tag{3.33}$$

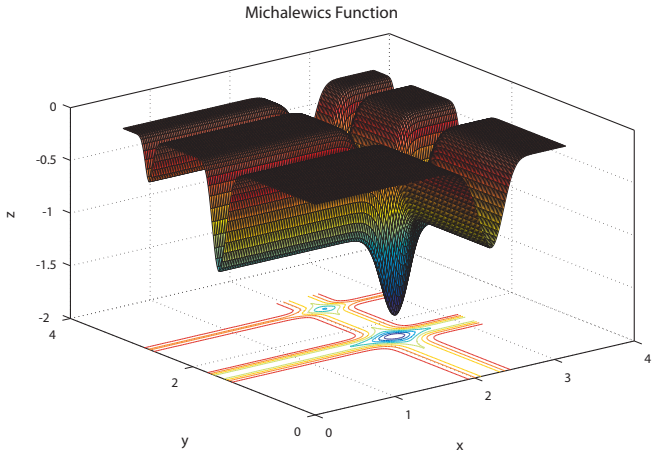

FIGURE 3.17: Michalewics Function

C. Schwefel Function

The search topology of the Schwefel function (Eqn. 3.34), is characterised by a several peaks and valleys in Figure 3.18. The function has a second best minima far from the global point and many search algorithms become trapped at this point. The global minima is also located on the bounds of the search domain and optimisers are sensitive to convergence in the opposite direction. The test function is an acceptable candidate to evaluate the effectiveness of the AM-PSO and for the validation of the identified wall boundary condition types.

$$f(x) = 418.9829n - \sum_{i=1}^{n}(x_i sin\sqrt{|x_i|}) \tag{3.34}$$

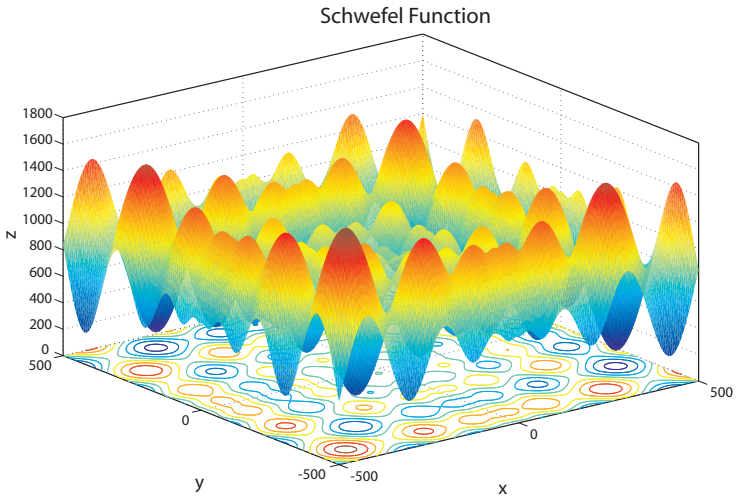

FIGURE 3.18: Schwefel Function

A. Effect of Maximum Velocity on Fitness

The impact of v_{max} as a function of x_{max} (Fig. 3.19(a)), over a dimensional search space $D = 10, 20$ & 30 and population size $m = 20, 40$ & 80, by the S-PSO (Fig. 3.19(b)) and AM-PSO (Fig. 3.19(c)) algorithms is evaluated for the Ackley function in Figure 3.19.

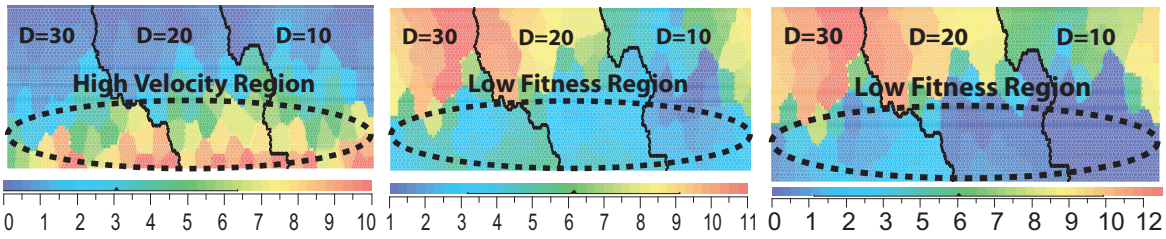

(a) Velocity % of x_{max} (b) S-PSO (c) AM-PSO

FIGURE 3.19: Ackley Function: SOM Representation of v_{max} as a function of Dimension Search Space for S-PSO & AM-PSO

The clusters are partitioned as a function of dimensional search space (Fig. 3.19). Each cluster is characterised by nodes that are representative of the fitness evolution over the evaluated v_{max} range $[0.10, \cdots, 10.00\%]$ of x_{max} with swarm population $m = 20, 40$ & 80. The SOM representing x_{max} to

v_{max} (Fig. 3.19(a)), indicates that velocity in excess of $\approx 10\%$ of x_{max} equates to low fitness with the S-PSO (Fig. 3.19(b)) and AM-PSO (Fig. 3.19(c)) methods. High velocity regions are equated with dark red regions on the lower side of the SOM, in comparison to regions with low velocity marked with dark blue contours on the upper side of the map (Fig. 3.19(a)). The noted pattern is consistent over the evaluated search space spanning $D = 10, 20$ & 30. The identified fitness distribution as a function of m and v_{max} for the defined search spaces is presented in Appendix B.2 for the modeled test function.

Direct comparison of the S-PSO and AM-PSO method validates the performance merits of the proposed optimisation method. The contours bounded about the low fitness region in the AM-PSO method (Fig. 3.19(c)) are represented by dark blue markers, hence signifying nodes with low fitness. In comparison, the S-PSO method at the equating low fitness region, the contours are of a lighter blue shade (Fig. 3.19(b)), hence indicating nodes with higher fitness than the AM-PSO across the tested dimensional search space spectrum. To further verify the fitness distribution of the nodes in each cluster for the S-PSO and AM-PSO algorithms, the fitness mean $\overline{z}$ and standard deviation σ_z, in the respective clusters is examined in Figure 3.20.

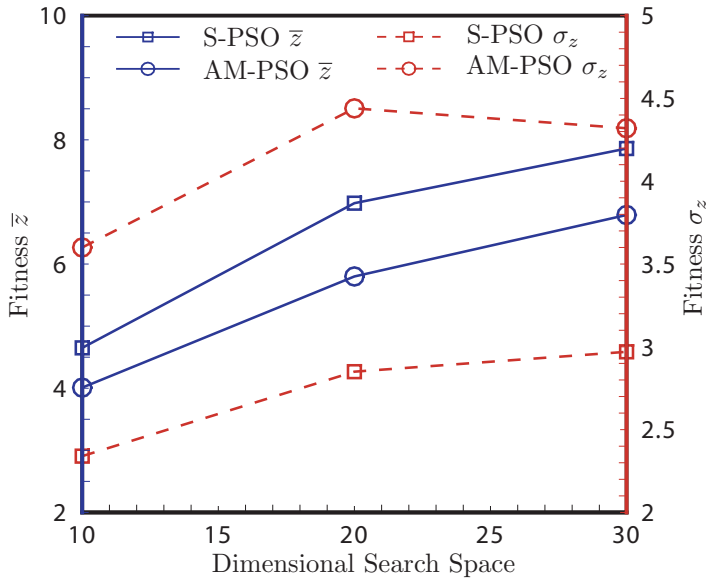

FIGURE 3.20: SOM Cluster Dimensional Space Fitness Mean & Standard Deviation Distribution; $m = 20, 40, 80$ & $v_{max} = [0.10, \cdots, 10.00]$ of x_{max}

The results confirm the viability of the AM-PSO method over the S-PSO for the Ackley function (Fig. 3.20). The $\overline{z}$ of the AM-PSO method is lower than the S-PSO algorithm across the evaluated test domain. As D increases, the complexity of the search space increases (Fig. 3.20). Accordingly the mean fitness increases proportionally to represent the non-convergence of the search agents with respect to the global optimal point. There exists a uniformity in fitness magnitude convergence by the two optimisation algorithms over the evaluated test domain.

The effect of v_{max} on fitness for the Ackley function (Appendix B.2), has an opposite effect to the observed pattern presented by the SOM analysis for the Rosenbrock function in Figure 3.13 and Appendix B.1. The results confirm the application of scalar step length is problem-based.

The effect of v_{max} on fitness is further evaluated on the Michalewics function in Figure 3.21.

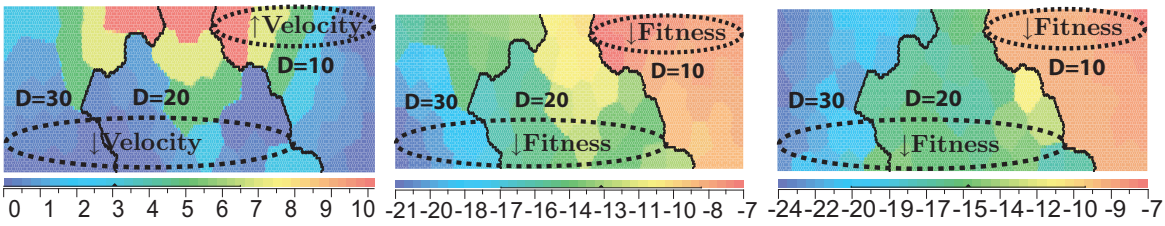

(a) Velocity % of x_{max} (b) S-PSO (c) AM-PSO

FIGURE 3.21: Michalewics Function: SOM Representation of v_{max} as a function of Dimension Search Space for S-PSO & AM-PSO

The SOM for the Michalewics function is partitioned by user-defined integer format to visually represent the search patterns of the dimensional search space ($D = 10, 20$ & 30). The impact of v_{max} on fitness is related to the size of D. At $D = 10$ a high velocity setting as denoted in the top right corner of the velocity SOM (Fig. 3.21(a)) with red contours. A high speed equates to a low fitness at the same map region for the S-PSO (Fig. 3.21(b)) and AM-PSO algorithms (Fig. 3.21(c) & Appendix B.3). When $D = 20$ & 30, a low v_{max} setting represented by the lower side of the velocity map region (Fig. 3.21(a)) with dark blue node markers, directly equates to low fitness at the designated map area for the S-PSO (Fig. 3.21(b)) and AM-PSO (Fig. 3.21(c)) methods.

At $D = 2$, there are two distinct minima solution valleys in the search topology where the global minima is isolated within a deep well/valley region and extends to $z = -1.8013$ (Fig. 3.17). As D increases, the complexity of the solution topology increases with the well comprising the global minima becoming deeper. The number of solution valleys also increases proportionally. At $D = 10$, the extent of the solution well protrudes to the global point $z = -9.66$ (Tab. 3.2). With limited complexity, a high velocity setting will facilitate rapid convergence to the minima region and mitigate a stagnant search process due to particle oscillation about a localised region at limited speeds.

With further increases in D, the velocity of the particles must be lowered for acceptable convergence. If v_{max} is high, the particles isolated within the well of the global region will escape the area of interest with ease due to the extended scalar step length. Accordingly, the v_{max} must be low to facilitate a valid and efficient scan of global solution well region without resulting in an overshoot of the particles from the area of interest. If v_{max} is high then the particles will protrude away from the global valley region and oscillate about the search boundaries.

Direct comparison of the S-PSO and AM-PSO validates the merits of the developed algorithm. The SOM contours of the AM-PSO method represents an extended area with "colder" node markers (Fig. 3.21(c)), hence low fitness in comparison to the S-PSO algorithm which is modeled with darker, higher contours for the equating area (Fig. 3.21(b)). To verify the feasibility of the AM-PSO method, the fitness $\overline{z}$ and σ_z for the S-PSO is compared to the AM-PSO algorithm for each cluster in Figure 3.22.

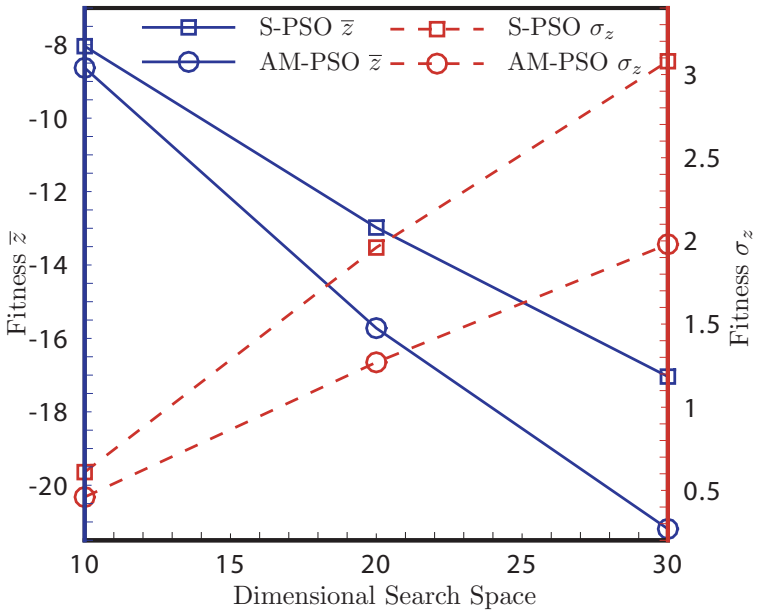

FIGURE 3.22: Michalewics Function: SOM Cluster Fitness Mean & Standard Deviation Distribution; $m = 20, 40, 80$ & $v_{max} = [0.10, \cdots, 10.00]$ of x_{max}

The distribution of $\overline{z}$ and σ_z of the nodes in each cluster validate the effectiveness of the developed AM-PSO method in comparison to the standard PSO algorithm (Fig. 3.22). The $\overline{z}$ and σ_z of the AM-PSO algorithm is lower for all clusters in comparison to the S-PSO (Fig. 3.22), hence validating the convergence of the AM-PSO method to a valid search domain.

The performance of the S-PSO and AM-PSO method is further analysed by the SOM distribution of fitness, as a function of v_{max} for the Schwefel test function in Figure 3.23.

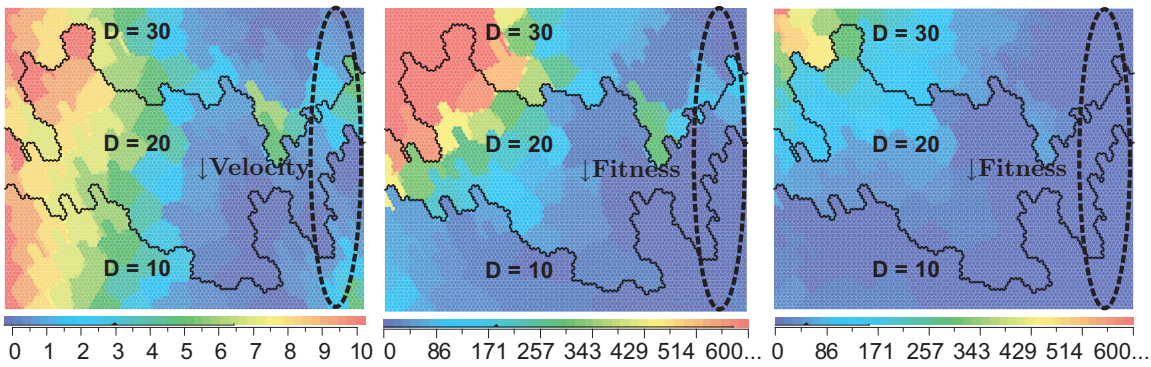

(a) Velocity % of x_{max} (b) S-PSO (c) AM-PSO

FIGURE 3.23: Schwefel Function: SOM Representation of v_{max} as a function of Dimension Search Space for S-PSO & AM-PSO

The data for the Schwefel function is partitioned by a user-defined cluster which distributes the nodes as a function of the dimensional search space in Figure 3.23. The visual representation of the relationship between the maximum velocity of the particles and fitness indicates that a low v_{max} at 0.10% of x_{max} equates to low fitness distribution for the S-PSO (Fig. 3.23(b)) and AM-PSO (Fig. 3.23(c)) methods (Appendix B.4). A low v_{max} performance is restricted to the right side of the

velocity SOM (Fig. 3.23(a)), with "cold" dark blue markers. Corresponding this region directly to the SOM for S-PSO and AM-PSO, "cold" blue contours are evident for fitness distribution at the specified velocity setting. An increase in v_{max} that is in excess of 1.0% of x_{max} equates to high fitness distribution (Appendix B.4). The left region of the v_{max} SOM (Fig. 3.23(a)) is marked with dark red contours to represent an increased v_{max}. The specified region is directly related to high fitness distribution (Appendix B.4). The left region of the S-PSO and AM-PSO maps is marked with "hotter", darker nodes than the right side, hence establishing the demerit of a high v_{max} on fitness for the Schwefel function.

The effect of increasing v_{max} is sensitive at higher dimensional search spaces. At $D = 10$ on the bottom side of the S-PSO and AM-PSO SOMs, the change in fitness distribution is minimal as a function of v_{max} for the domain spanning right-to-left in the map. The differential in contour color markers at $D = 10$ for the specified test envelope is minimal. The v_{max} envelope pertaining to low fitness distribution at $D = 10$ is limited to $v_{max} = [0.10, 1.00\%]$ of x_{max} (Appendix B.4(a)). At $D = 20$ & 30, the variance in fitness distribution from right-to-left of the S-PSO and AM-PSO SOM, with changes in v_{max} becomes active. Darker "cold", blue contours are established on the right side, which transform to "hotter" regions on the left side of the map, hence establishing the demerit of a high v_{max} on fitness for the Schwefel function.

Comparison of fitness performance variance between the S-PSO (Fig. 3.23(b)) and AM-PSO (Fig. 3.23(c)) algorithms validates the merits of the developed optimisation method. The AM-PSO region is marked with extended regions of "cold", dark blue markers, hence low fitness across the tested dimensional search space. Comparatively the S-PSO SOM is characterised by extended regions of high fitness, "hot" markers which are isolated to the right side of the map for $D = 20$ & 30. The drawback of a high v_{max} that is in excess of 10% of x_{max} has a significant performance impact on the search performance in the S-PSO method than the AM-PSO algorithm. The integration of the developed, novel adaptive inertia weight model (Eqn. 3.8) results in performance improvements in the AM-PSO method. To further model the performance variances between the two optimisation methods and the influence of v_{max} on fitness, the mean and standard deviation of the fitness in each data cluster is presented in Figure 3.24.

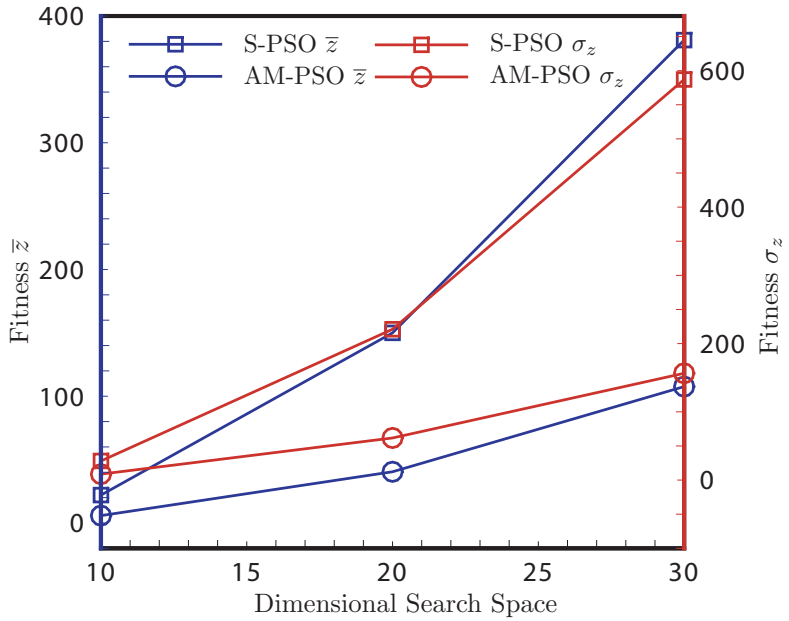

FIGURE 3.24: Schwefel Function: SOM Cluster Fitness Mean & Standard Deviation Distribution; $m = 20, 40, 80$ & $v_{max} = [0.10, \cdots, 10.00]$ of x_{max}

The results confirm the viability of the AM-PSO method over the S-PSO for the Schwefel function in Figure 3.24. The σ_z and $\overline{z}$ of the AM-PSO method is lower than the S-PSO algorithm across the evaluated test domain. As D increases, the complexity of the search space increases. Accordingly $\overline{z}$ increases proportionally to represent the non-convergence of the search agents with respect to the global optima point. The distribution of σ_z also increases across D to represent the disparity of fitness convergence state relative to the theoretical minima. The magnitude of σ_z variance between the S-PSO and AM-PSO method is significant. The S-PSO is sensitive to convergence to a local minima in the search topology in comparison to the developed AM-PSO method, hence resulting in the noted fitness variances in the respective data dimensional cluster in Figure 3.23.

3.6.2 Numerical Test Validation with Extended Termination Definition

The validation process in this section evaluates the performance of the AM-PSO algorithm for convergence to the theoretical minima for the identified test functions relative to published data [114, 116]. The maximum iteration limit to convergence is extended to 20,000 fitness calls in comparison to the data presented in Table 3.3. The termination definition as a function of solver iteration count is extended with intent to match the test conditions of the disparate algorithm types evaluated in the literature [114, 116] on the proposed test functions. It was shown that 20,000 fitness function iterations are adequate to facilitate convergence to the region bounded about the theoretical minima. Accordingly, the feasibility of the developed AM-PSO for convergence to the global minima can be established.

By extending the iterations to 20,000 function evaluations, the user-defined simulation time-span facilitates adequate iteration-based resources to the swarm for convergence to the theoretical solution. The methodology aids the development of novel convergence measure/s based on the collective search

behavior of the swarm. In airfoil design where the theoretical optimal is not *a-priori* knowledge, the optimisation termination measures developed in this section will be valid for the specified case studies. The application avoids the definition of an arbitrarily user-defined maximum iteration count to convergence, which can result in premature termination, hence a sub-optimal solution or convergence to the optimal point but with an extended search process which is computationally not viable.

3.6.2.1 AM-PSO Search Parameter Settings

As the developed AM-PSO methodology will be applied for airfoil shape design, the algorithm is set-up with reference to mathematical test functions where the dimensional search scope is representative of the design intent application. The airfoil shape parameterisation model types have a dimensional size of $D = 10 - 13$ and the flexibility of the AM-PSO model is validated within the identified dimensional limit. The dimension size of the test problems for algorithm validation is set to ten as published data is readily available with $D = 10$.

The cognitive and social scaling factors are set at two and this combination has been recognised as an acceptable choice for disparate problem types [114, 125, 142]. A comprehensive DoE analysis indicated that v_{max} and v_{min} must equal the search bounds of each variable or $v_{max} = x_{max}$ and $v_{min} = x_{min}$ respectively. Accordingly, the velocity thresholds are set to 100% of the dynamic range of each variable. The particle population size m is proportional to the computation time required for convergence. If too few particles are used, then an extended optimisation simulation becomes a requirement, to provide the agents sufficient time to locate the global minima with minimal resources. If m is excessive, then a time-intensive simulation will be the result and the demerit of an extended simulation time will outweigh the expected search merits of a large swarm size. Parametric studies for engineering design applications have shown that a population of 20-30 provides an acceptable balance between computational efficiency and solution feasibility. A swarm of 20 agents was successfully applied in electromagnetic design application [125]. Validation studies over the proposed test functions applied ten search agents [114, 116]. Hence, for the purposes of a comparative analysis between the literature based methods [114, 116] and proposed algorithm, the swarm size is set at 10. Consequently the setup of the test problem for validation is related to the intent airfoil shape design problem. The capability of the AM-PSO to converge to a feasible global point, with minimal computational resources due to a reduced search swarm size, across a multi-dimensional search domain is established.

The value of the inertia weight positive constant α_{AIW} in Equation 3.9 was defined by a DoE process on several test function types. As $\alpha_{ISA} \rightarrow 1$, the rate-of-change of w_{ij} (Eqn. 3.9) decreases proportionally as a function of search evolution time. At the presented analysis with $D = 10$, the results indicated that $\alpha_{ISA} = 0.90$ facilitates valid search design simulations.

The personal best fitness range of the particles p_f (Step 1: Sec. 3.4.4), applied to calculate the probability of mutation in Equation 3.10, was defined based on *a-priori* knowledge of the solution search space type for the test problems. The maximum fitness that a particle can take in $F_{pbesti,max}$ was defined by establishing the maximum point of the test function, hence worst solution available in the search space. The global best is *a-priori* knowledge and this data point was assigned to $F_{pbesti,min}$, thus $p_f = (F_{pbesti,max}, F_{pbesti,min})$, and is defined from the topology of the test function.

The mutation scalar factor ω_M (Step 5: Sec. 3.4.4), was set to 10% of dimension search space by Sriyanyong [143]. Through experimentation it was observed that a static ω_M is not suitable since the magnitude-of-mutation remains constant and is not adaptive to the search environment. A low value at initialisation is suitable to promote a local search process. Thus, particle repositioning due to mutation must be minimal such that $x_{ij,M}(t) = x_{ij}(t) + (\sigma_{ij}^{D_j})_{min}$, as the swarm is evenly partitioned in dimension space due to LHS and excessive repositioning is not warranted. As the particles conjugate to a common region during the progression of the search process, global search is proposed and is achieved by increasing the scope of particle repositioning such that $x_{ij,M}(t) = x_{ij}(t) + (\sigma_{ij}^{D_j})_{max}$, with a high value of ω_M. This will mitigate convergence of a particle to a local point. The proposed methodology of varying the magnitude of particle repositioning due to mutation, with varying scalar factor, is similar to the process applied by Yao et al. [132] where Gaussian and Cauchy distributions were implemented for the outlined reasons. Numeric experimentation indicated a value of $\omega_M = 0.05$ and 0.75 during the first and second halves of the search process to provide acceptable local-global search variances respectively.

Optimisation termination occurs when *a-priori* defined global solution is achieved or when the maximum iteration count of 20,000 fitness calls is reached. The personal best tolerance factor (Eqn. 3.13), of the two extremum particles at convergence is computed to establish the search behavior of the swarm in relation to the global best. The swarm fitness standard deviation at the maximum, user-defined iteration count k_{max}, will define the collective search patterns of the particles as a function of solution topology. Theoretically at convergence there must be a consensus between the search agents in regards to the optimality of the end point. The particles must be at one common region of the search space with matching position vectors. In application, due do the randomness in the search mechanisms, the positioning of the particles will be separated. The minimum magnitude-of-separation, measured by the standard deviation of the swarm, that conforms to a converged search process, hence an optimal solution must be defined and is problem based. The validation analysis in this section will address this requirement.

As the AM-PSO is a probabilistic search method type, simulations are repeated over user-defined number of trials. The success, hence robustness of the algorithm is measured as a percentage of simulations which converge to a global solution. Each function is simulated over 30 independent trials and comparisons between the proposed AM-PSO and the variants developed in the literature [114, 116] are made. The standard deviations of the global fitness and iteration to convergence represent the robustness of the algorithm.

The following data is extracted from the simulations to evaluate the effectiveness of the AM-PSO model:

1. **Worst Fitness:** The simulation with the worst (maximum) global best fitness;
2. **Best Fitness:** The simulation with the best (minimum) global best fitness;
3. **Success Rate:** Measured as a percentage of simulations that converge to a global solution;
4. **Average Fitness:** The mean global best fitness from the 30 trails;
5. **Fitness Standard Deviation:** The variance of global best solution from the 30 trials;

6. **Min. & Max. Iteration:** The lowest and highest iteration count respectively for convergence to *pbestg* from the 30 trials;
7. **Average Iteration:** The mean iteration count from the 30 trials; and
8. **Iteration Standard Deviation:** The spread of iteration count from the 30 trials

3.6.2.2 Simulation Results and Discussion

Simulations to evaluate the success of convergence with disparate wall boundary function types (Sec. 3.4.3), is examined. The average of the global best fitness over the 30 trials versus iteration is modeled for each boundary condition in Figure 3.25. The optimiser setup is consistent across all experiments.

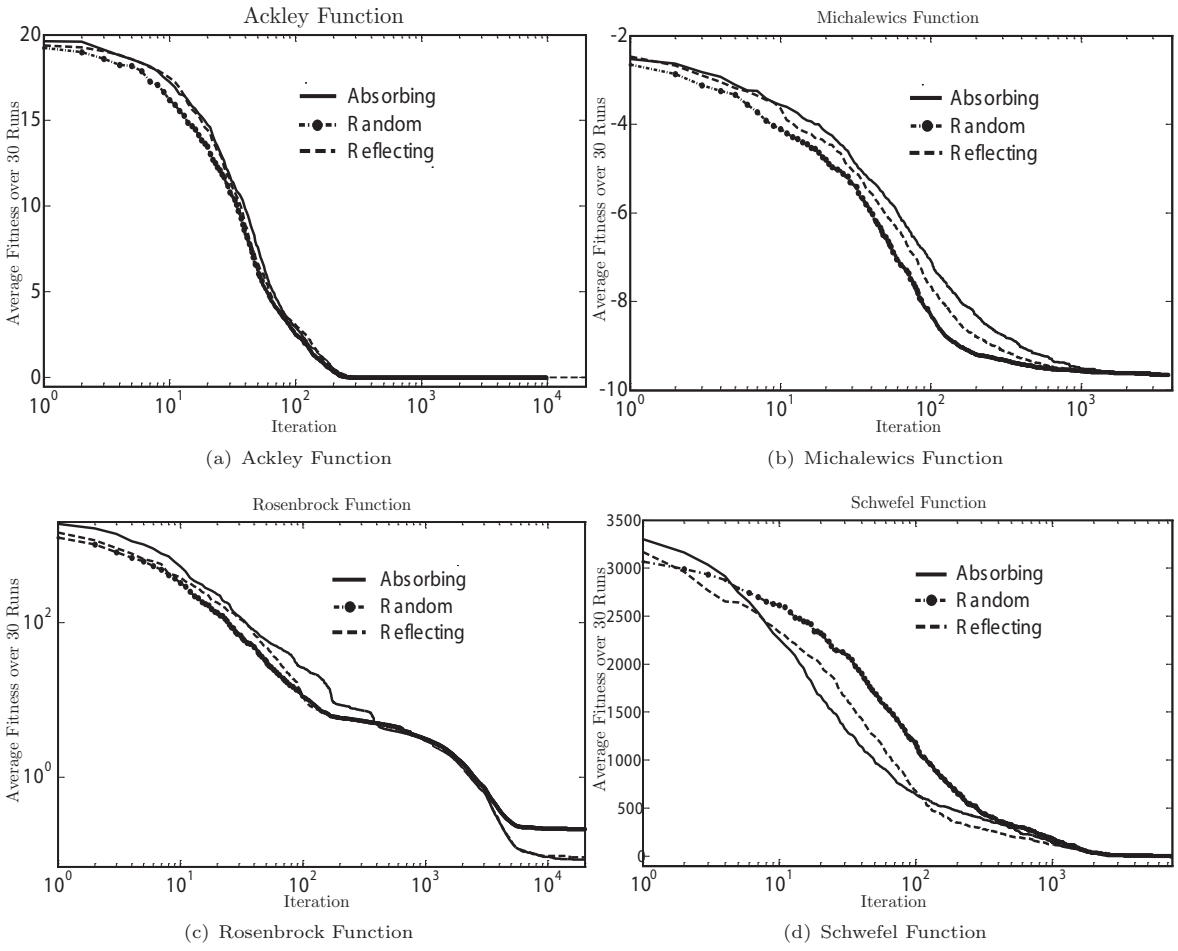

(a) Ackley Function (b) Michalewics Function

(c) Rosenbrock Function (d) Schwefel Function

FIGURE 3.25: Effect of Wall Boundary Conditions on Solution Convergence

The convergence history evolution represents consistency in results for the three boundary conditions on the Ackley, Michalewics, Rosenbrock and Schwefel functions in Figure 3.25. The absorbing condition has a higher personal best fitness at the early stages of the optimisation process. Since the method clamps the position of the violated particle to the boundary of the search domain, a global search is diminished as the repositioning is localised to the search bounds. The optimal solution of the Ackley (Fig. 3.25(a)), Michalewics (Fig. 3.25(b)) and Rosenbrock (Fig. 3.25(c)) functions are not

restricted to the search boundary (Table 3.2) and the absorbing method has a higher average global best fitness throughout the optimisation cycle. The Schwefel function (Fig. 3.25(d)), with a global solution near the search boundary (Table 3.2), benefits from the absorbing technique as re-positioning is initiated about the global solution. The average global best achieved by the absorbing condition on the Schwefel function is lower during the optimisation cycle and levels off to the performances of the random and reflecting conditions. The absorbing condition is suitable when the global minimum is at the bounds of the search domain, since a localised search is facilitated about this point.

The benefits of introducing search diversity with random wall boundary conditions is observed with lower global best fitness at the early stages of the optimisation cycle over the four functions tested. At optimisation commencement, the search experience of the particles is limited. The random re-positioning methodology maximises the exposure of the particles to the solution domain and increases the probability of the agents converging into a region with lower fitness. In the multi-modal Ackley (Fig. 3.25(a)) and Michalewics (Fig. 3.25(b)) functions, it is observed that a degree-of-randomness is required to facilitate a global search through random dispersion of the particles with violated positioning. A unimodal solution topology of the Rosenbrock (Fig. 3.25(c)) function, also benefits with random distribution which accelerates convergence to a global point in comparison to the absorbing and reflecting techniques. In the Schwefel function (Fig. 3.25(d)) where the global point is at the search boundary, the random distribution has the worst performance. The search mechanisms of the AM-PSO will encourage particles to conjugate at the search boundary, hence global point. A search agent violating this region is randomly dispersed away from this region, thus slowing the convergence to the optima.

The reflecting boundary wall condition has a low fitness convergence for the Schwefel function at the concluding stages of the search process, in comparison to the absorbing and random techniques (Fig. 3.25(d)). This is indicative of the search mechanisms of the AM-PSO method. As the search progresses, the positioning of the particles will be at the global point, hence at the boundary of the search domain. Violated particles are re-initialised in the search domain by the opposite sign of the velocity magnitude (Sec. 3.4.3), but the search direction of the position vector remains static. Thus, velocity magnitude will influence the positioning of the particles relative to the global solution. In the Schwefel function, the velocity magnitude will have to be minimal to mitigate particles 'flying' over the global point. The performance of the reflecting and absorbing conditions are similar, thus indicating the merits of employing localised methods when the global solution is restricted to the search bounds.

In multi-modal solution topologies associated with the Ackley (Fig. 3.25(a)), Michalewics (Fig. 3.25(b)) and Rosenbrock (Fig. 3.25(c)) functions, the reflecting condition has similar performance traits to the random methodology with slightly higher global best fitness. It is concluded that diversity through stratified sampling with random wall boundary condition is required for multi-modal problems, thus resulting in low fitness magnitudes. The reflecting condition partially addresses this requirement by maintaining the initial position of the particle, which incorporates diversity since it is generated by the search mechanisms of the AM-PSO algorithm. Particle re-positioning is localised since the direction of the velocity magnitude is reversed by the original scalar.

A. Demonstration of Swarm Search Process

The search process of the particles during the optimisation simulation for the Schwefel function is

demonstrated in Figure 3.26. The contour map represents the scope of the solution topology with equating fitness peaks and troughs. The search is represented as a function of particle position of each member in the swarm, relative to the theoretical solution at iteration t.

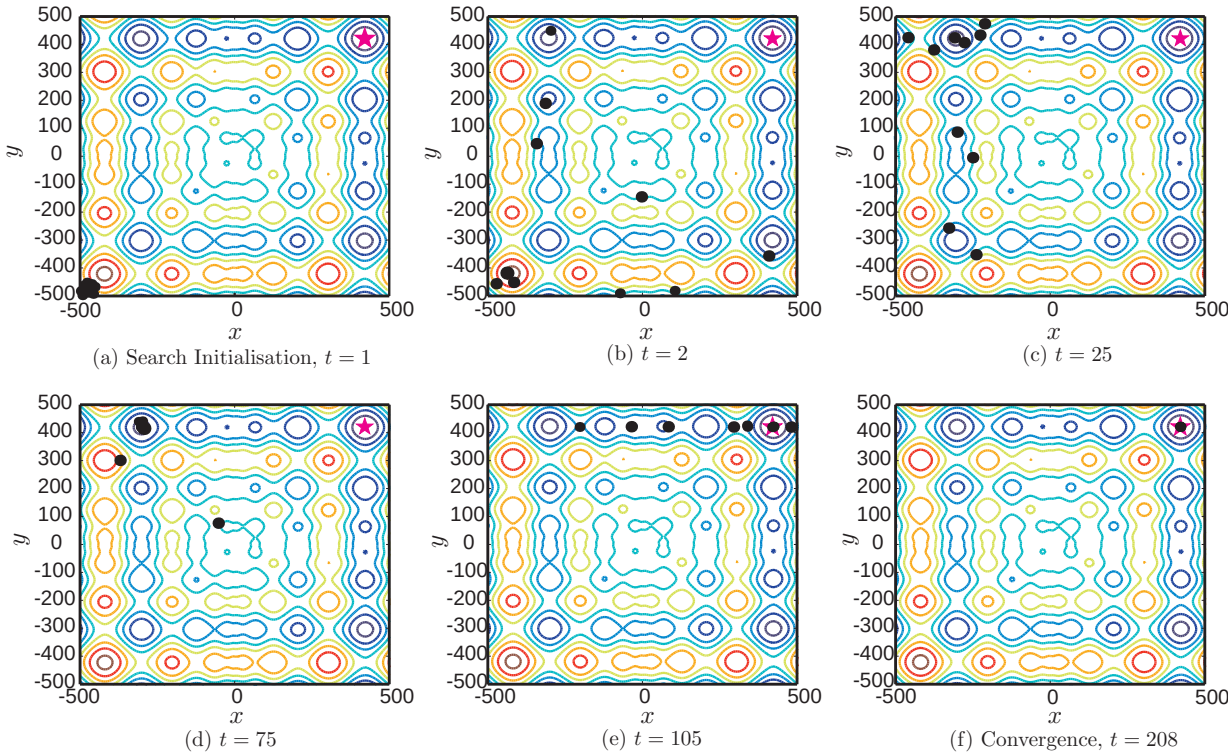

(a) Search Initialisation, $t = 1$ (b) $t = 2$ (c) $t = 25$

(d) $t = 75$ (e) $t = 105$ (f) Convergence, $t = 208$

FIGURE 3.26: Schwefel Function: Demonstration of Swarm Search Progress to Global Point

The particles are initialised well-away from the theoretical solution with intent to validate the flexibility of the swarm algorithm. The search initialisation phase of the swarm in represented in Fig. 3.26a. A swarm with ten particles is isolated at the bottom left corner and represents the boundary of the search envelope. The solution landscape at this region consists of high fitness magnitudes and is characterised by high (red) contour readings. The fitness of the particles is proportionally high. The theoretical solution denoted by the star symbol is on the opposite side of the search space.

The theoretical search mechanisms of the swarm algorithm govern the positioning of the particles in Figures 3.26b-f. At $t = 2$, the first design iteration following user-defined search initialisation, the relative positioning of the search agents is open and wide. A select few particles are drawn to local solution topologies at bottom right and upper left regions (Fig. 3.26b). The search process for a select few particles is isolated about the initialisation point from $t = 1$, with particles conjugated at the lower left corner of the solution topology (Fig. 3.26b). At $t = 25$ the particles have converged at unique local solution regions in the defined search topology. A large search population has converged at a local point in the upper left region and a band of local solutions with trapped particles exist directly below this region. At $t = 75$, the swarm has converged at a local point in the upper left corner (Fig. 3.26d). At $t = 105$, the particles restrict the search to a region isolated by local solutions with $X_2 \approx 420$ and deviations to X_1 which varies over a span of local solutions $-203 < X_1 < 480$ in Figure 3.26e. One particle has converged to the global optima $(420.9687, 420.9687)$, with several

remaining agents isolating the search to a region bounded by the global point on the upper right corner of the search space.

The process of mutation is initiated at $t = 105$ (Fig. 3.26e), for search diversity as the relative positioning of the particles with respect to each another is below a user-defined threshold. This indicates an issue with diversity and the developed adaptive-based mutation process, in accordance with the positioning of the particles in the swarm is initiated. The effect of mutation spanning over $t = 105$ to $t = 208$ (Fig. 3.26f), results to an increase in search diversity based on the positioning of the personal best solutions of each particle in the swarm. At $t = 208$, the swarm has converged to the global point on the upper right corner of the search space (Fig. 3.26f). The user-defined search termination criterion is achieved, hence convergence is assumed.

The defined termination criteria is in accordance with two defined measures. The first criterion is in reference to the absolute difference between the highest and lowest personal best fitness magnitude of the two extremum particles in the swarm. The fitness difference between the extremum points must be below a user-defined threshold of 10^{-4}. The fitness standard deviation of the swarm must also be below a user-defined threshold. The two measures are consistently satisfied over a number of user-defined search iterations to confirm convergence. During this time, further mutation processes do not result in solution improvement. Hence, convergence to the global point is assumed and the search topology with equating particles (Fig. 3.26), confirms the validity of this assumption. The feasibility of the swarm algorithm for function optimisation with multi-modal search regions is validated. The search phase of the Ackley (Fig. C.1), Michalewics (Fig. C.2) and Rosenbrock function (Fig. C.3), is presented in Appendix C.

B. Summary of Validation Results

The results of the simulation trials for the four test functions is presented in Table 3.6. In the Ackley, Michalewics and Rosenbrock functions, the data is in accordance to the random initialisation wall boundary condition. The absorbing technique is applied for the wall bounded global solution of the Schwefel function. The best reported solution form the literature is presented to validate the feasibility of the developed AM-PSO structure. In the Ackley, Rosenbrock and Schwefel functions, data is taken from the publication by Liang et al. [116] where the performances of nine disparate PSO types were examined over the identified test functions. Included are *lbest* PSO types (Sec. 3.2.1), with an integration of an inertia weight factor function and a variant *lbest* model with a constriction factor (Eqn. 3.2) term only [116]. In the Michalewics model the best reported result from Chen et al. [114] is used where three variants of the PSO method type including a GA were used to optimise the function.

TABLE 3.6: Test Function Simulation Results

Function	Ackley	Michalewics	Rosenbrock	Schwefel
Wall Boundary Condition	Random	Random	Random	Absorbing
Worst Fitness	4.44e-015	-9.66	3.98	1.97e-004
Best Fitness	4.44e-015	-9.66	4.30e-002	1.27e-004
Success Rate (%)	100	100	97	100
Average Fitness				
• Best in Literature	3.75e-015[116]	-9.66e+000[114]	6.98e-001[116]	0[116]
• AM-PSO	4.44e-015	-9.66e+000	2.15e-001	1.55e-004
Fitness Standard Deviation				
• Best in Literature	2.13e-014[116]	1.58e-003[114]	1.46e+000[116]	0[116]
• AM-PSO	0	4.88e-005	7.13e-001	2.41e-005
Maximum Iteration				
• Literature	30,000[116]	20,000[114]	30,000[116]	30,000[116]
• AM-PSO(Standard + Mutation)	18,459	6,257	28,623	6,164
Standard PSO Operation	9,809	3,792	20,000	3,184
Mutation	8,650	2,465	8,623	2,980
Minimum Iteration	1,840	814	1,171	538
Standard PSO Operation	975	472	659	306
Mutation	865	342	512	232
Average Iteration	2,067	1,844	5,763	1,487
Iteration Standard Deviation	2,280	911	3,856	769

A comparative analysis between the performances of the AM-PSO and the reported algorithms in the literature [114, 116], validate the merits of the developed AM-PSO algorithm in Table 3.6. The success rate from the 30 independent runs is 100% for the multi-modal Ackley, Michalewics and the Schwefel model. The standard deviation of the best solution form the 30 simulations is ≈0, thus signifying the consistency at which AM-PSO converges to the global point. The requirement of converging to the global optima, integrated with an accelerated search process is noted. The total iteration required for convergence is the summation of the function calls at each iteration as a result of AM-PSO search mechanisms plus the fitness calls due to mutation. The maximum iteration count by the AM-PSO method is superior to the solutions presented in the literature. The AM-PSO requires 38%, 69% and 80% fewer iterations for the Ackley, Michalewics and Schwefel functions respectively than the best reported solution in [116].

The computational time savings are significant if the minimal time required to convergence from the 30 trials by the AM-PSO method is compared to the findings in the literature. Savings in excess of 94%, 96% and 98% for the Ackley, Michalewics and Schwefel functions respectively are computed in Table 3.6. On average, the total number of iterations required for convergence is ≈80% less than the reported solution in the literature. A low iteration standard deviation confirms the consistency at which AM-PSO accelerates to the optimal solution. The test simulations verify that the AM-PSO is suited for multi-modal problems and exhibits acceptable convergence characteristics than the algorithms reported in the open literature.

The analysis over the unimodal Rosenbrock function also yields favorable results in Table 3.6. From the 30 independent trails, one simulation fails to converge at the global point in the allocated 20,000 maximum iteration count. Accordingly, the worst reported solution is 3.98. The remaining 29 simulations converge to the global point with a success rate of 97%. Despite one failed simulation, the average global best from the 30 runs is lower than the results reported by Chen [114]. A low fitness standard deviation illustrates that the final solutions have minimal spread about the global best compared to a higher magnitude computed by Chen [114].

The maximum iteration count to convergence matches the value reported in the literature due to the failed run. Alternately, the fastest recorded simulation converged to the global point with only 1171 iterations, thus requiring 96% fewer function calls than the data in [114]. The average iteration count to convergence over the 30 simulations requires 81% fewer solver calls than the method reported in [114]. The presence of an outlier from the failed simulation results in a large converged fitness standard deviation and also increases the mean time to convergence. Despite the failed simulation, the results established with the AM-PSO are superior than the reported method outlined in [114].

From the comparative analysis of the algorithm test verification process, the stability and robustness of the developed AM-PSO algorithm is demonstrated and validated. The novel optimisation algorithm achieves a high success rate by consistently converging to the theoretical global point. The developed adaptive mutation process significantly enhances the computational efficiency and is in excess of 96% for select cases in comparison to the data reported in the literature. The results validate that the developed AM-PSO method has superior search performance merits than the local-based *lbest* method (Sec. 3.2.1). The requirement of maintaining a low fitness function solver call to minimise the computational resources has been addressed. The algorithm indicated acceptable performances on both uni and multi-modal test functions. The developed approach is well suited for complex high dimensional aerodynamic shape optimisation problems.

3.7 Summary

A novel variant to the PSO model by Kennedy [94] is developed and validated. An AM-PSO algorithm is proposed to address the limitations of the original PSO and Genetic algorithm based methods. The fundamentals of the novel AM-PSO model are: **a)** A Gaussian-based mutation operator; **b)** Probability-of-mutation term; and **c)** Particle position update rule.

The three modules address the limitation of the original PSO method by introducing search diversity, hence convergence to the true optima. An intelligent, Gaussian-based mutation operator is applied to avoid premature convergence at a local solution for multi-modal test problems. The second and third modules are developed with the motivation of matching the success and search flexibility of the Genetic Algorithm without resorting to a computationally intensive simulation process. The search mechanisms of the AM-PSO method control the extent of mutation per iteration and the overall computational expense. A novel probability-of-mutation operator was integrated into the design algorithm to control the swarm mutation population size. To ensure a valid search process, a position update rule is applied (Alg. 4). The position of the particles is modified if fitness improvements are computed due to mutation. The improvements result in an update of particle personal and swarm

global best positions. The methodology is developed with the motivation of shifting the collective search pattern of the swarm toward the global best solution region.

The comprehensive design development and validation process of the AM-PSO algorithm in this chapter confirmed the viability of integrating the search methodology for multi-modal solution topologies. The novel design approach will be applied for airfoil aerodynamic optimisation simulations by the direct and surrogate-assisted design methods.

Chapter 4

Aerodynamic Design Optimisation Architecture Development & Validation

4.1 Overview

The AM-PSO algorithm is a critical design module within the DNO architecture. The novel optimisation algorithm was developed and validated in Chapter 3. The second component of the DNO architecture within the airfoil design process is the geometrical parameterisation model. Several function types exist and the merits of each method need to be assessed for the defined test problem. The sub-components of the geometrical parameterisation model are developed. The impact of airfoil design variables on the objective function are established. If the design variables are ill-defined then a sub-optimal solution will ensue. The search intervals of the airfoil variables are verified to facilitate an efficient design process.

The sub-systems addressed in the geometrical parameterisation module include:

1. **Assessment of Airfoil Function Type:** Design development of a novel test methodology to assess and evaluate the flexibility and accuracy of several shape function types (Sec. 2.5), for airfoil design at the defined flight conditions;
2. **Design Variable Pre-Screening:** Design development of a novel test methodology to compute the importance of each airfoil variable on profile aerodynamics, hence the objective function; and
3. **Solution Search Space Mapping:** Design development of a novel test methodology to map the search intervals of the design variables, hence the solution search space for airfoil design at HALE and transonic Mach numbers.

This chapter will address the design requirements of the geometrical parameterisation module within the DNO structure. The design development and validation of the AM-PSO algorithm (Chapter 3), coupled with a valid shape function type will facilitate a valid airfoil design optimisation architecture.

4.2 Geometrical Parameterisation Model

The mathematical function for airfoil parameterisation governs the solution space, hence the optimality of the solution. The two design principles that need to be addressed when implementing a candidate shape function are: **a)** Flexibility; and **b)** Accuracy. Flexibility is defined by the objective function that minimises the geometrical difference between target and approximated airfoil by the mathematical function. Hence, flexibility refers to the ability of the shape function to represent disparate airfoil types by modeling critical shape features including leading edge radius, trailing edge wedge angles, chordwise location of the maximum thickness point for structural integrity and airfoil camber.

Airfoil performance is sensitive to surface perturbations and has a dominant impact on the pressure distribution, hence lift, drag, moment and flow transition points. The measure of accuracy refers to the 'goodness' of the geometrical fit by evaluating the aerodynamic convergence of the target profile with the approximated solution. Shape convergence studies are an acceptable measure of 'goodness' of the proposed parameterisation model. A novel geometrical and aerodynamic convergence test methodology is developed by a least-squares optimisation analysis to evaluate the flexibility and accuracy of the parameterisation model against several airfoil class types.

The following requirements need to be achieved by the identified shape parameterisation models from Section 2.5:

- Generate smooth and realistic shapes;
- Mathematically efficient so that shapes are generated with negligible computational effort;
- Minimal design variable population while satisfying an acceptable design solution space;
- Provide direct control over airfoil thickness-to-chord, camber, leading edge radius, trailing-edge wedge angles and trailing edge direction;
- Implement geometrical constraints including minimum thickness requirements at specific airfoil chord-station for structural requirements due to the location of spars;
- Provide ease of control for airfoil curve editing / modifications for a given optimal shape; and
- The design variables must be intuitive to geometric interpretation so that optimisation process is guided by the shape variables to a feasible solution.

4.2.1 Inverse Shape Fitting

To assess the feasibility of the disparate airfoil parameterisation function types, an inverse shape fitting test methodology is developed. The AM-PSO method is applied to assess the flexibility and accuracy of the function type. The process is defined as follows and is further modeled in Figure 4.1:

1. **Define Problem Space:** The process involves defining the shape function type under investigation (Sec. 2.5) and the search limits of n_{vars} design variables $X_i, \cdots, X_{n_{vars}}$;

2. **Generate Test Matrix:** A matrix of test airfoils of size $n_{swarm} \times n_{vars}$ is generated for a user-defined swarm population size in the AM-PSO architecture;

3. **Inverse Shape Fitting:** The AM-PSO simulates the inverse shape fitting process by approximating the user-defined target airfoil by the shape function. The objective function $\mathcal{J}$, is defined to minimise the absolute error and is calculated from the permutation of shape variables that $\mathcal{J}_{minimise}$, the geometrical difference between target $(y/c)_{target}$ and approximate $(y/c)_{approx}$ shape at each airfoil chord station M_i in Equation 4.1:

$$\mathcal{J}_{min} = \sum_{i=1}^{M} \left| (y/c)_{i_{approx}} - (y/c)_{i_{target}} \right| \tag{4.1}$$

4. **AM-PSO Convergence:** The AM-PSO algorithm proceeds until convergence based on a user-defined objective function (Eqn. 4.1) is achieved. The termination criteria is based on the measure of accuracy of the approximating airfoil against the target shape. Convergence occurs when:

   (a) **Criteria 1:** The absolute difference between target λ_{T_i} and approximated λ_{A_i} airfoil, over i chord stations is less than a user-defined threshold ϵ, such that (Fig: 4.1):

   $$|\lambda_{T_i} - \lambda_{A_i}| < \epsilon \tag{4.2}$$

   (b) **Criteria 2:** *Criteria 1*, is consistently achieved over n_{end} consecutive iterations

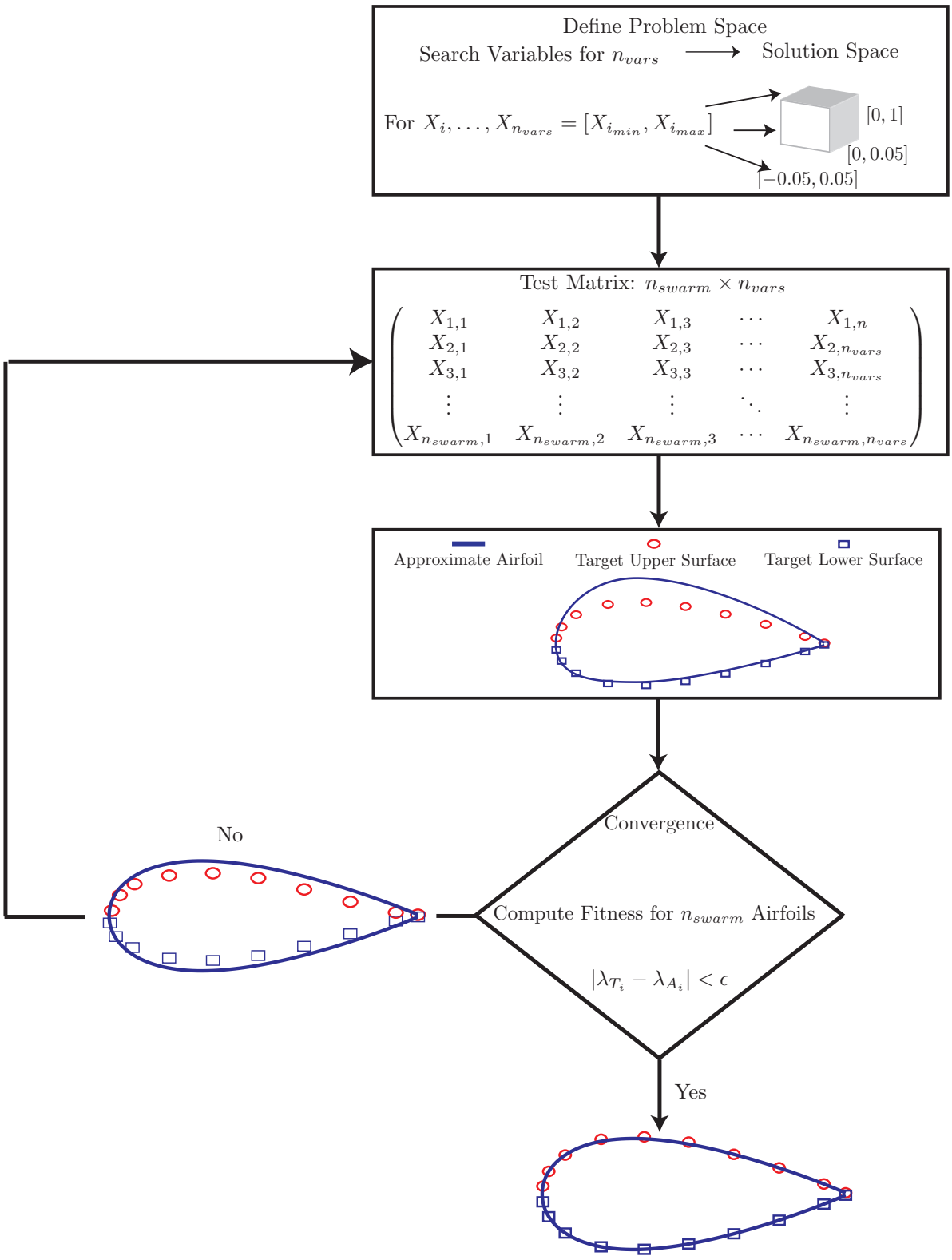

FIGURE 4.1: Inverse Airfoil Shape Fitting

4.2.1.1 Inverse Shape Fitting Analysis by the Analytical Approach

A. Test Methodology

The feasibility of the analytical-based approach for airfoil representation is examined by the developed inverse shape fitting process from Figure 4.1. Methods evaluated include the Hicks-Henne [35], Wagner [52], Legendre, Bernstein, and NACA normal modes [29, 53]. The mathematical representation of the analytical approach was defined in Section 2.5.3.

A symmetrical NACA 0015 profile is applied as the base airfoil. Sixteen target sections are integrated into the inverse shape fitting process. Airfoil types include low speed and long endurance shapes, high-subsonic and transonic Mach number based airfoils, thick airfoils, symmetrical, highly-cambered, low Reynolds number including low-speed and high-speed natural laminar flow profiles. The user-defined target shapes have disparate contour variations on upper and lower surfaces, hence the validation analysis provides the avenue to test the flexibility and accuracy of the modeled shape functions. A hybrid optimisation methodology comprising of a population-based AM-PSO and gradient-based method are used in the inverse shape fitting analysis. The design algorithms iterates the design variables to modify the base airfoil until convergence is achieved in accordance to the defined termination criterion from Section 4.2.1.

The parameters of the shape functions modeled in the inverse shape fitting optimisation analysis are presented in Table 4.1. Each method requires the definition of a user defined design variable population size n_{vars} and the corresponding variable magnitude $|X_i, \cdots, X_{n_{vars}}|$, that minimises the objective function, hence the disparity between approximated and target airfoil (Eqn. 4.1).

TABLE 4.1: Inverse Shape Fitting by the Analytical Approach Function Definition

Polynomial	Optimisation Parameters	Symbol
Hicks-Henne	Function Degree-of-Freedom	n_{vars}
	Peak Contour Abscissa	$(\alpha_1, \cdots, \alpha_{n_{vars}})$
	Peak Contour Magnitude	$(\pi_1, \cdots, \pi_{n_{vars}})$
	Magnitude of Design Variable/s	$\lvert X_i, \cdots, X_{n_{vars}}\rvert$
Wagner	Function Degree-of-Freedom	n_{vars}
	Magnitude of Design Variable/s	$\lvert X_i, \cdots, X_{n_{vars}}\rvert$
Legendre	Function Degree-of-Freedom	n_{vars}
	Magnitude of Design Variable/s	$\lvert X_i, \cdots, X_{n_{vars}}\rvert$
Bernstein	Function Degree-of-Freedom	n_{vars}
	Magnitude of Design Variable/s	$\lvert X_i, \cdots, X_{n_{vars}}\rvert$
NACA	Function Degree-of-Freedom	n_{vars}
	Magnitude of Design Variable/s	$\lvert X_i, \cdots, X_{n_{vars}}\rvert$

B. Inverse Shape Fitting by AM-PSO: Results and Discussion

As the AM-PSO is a probabilistic-based algorithm due to the random initialisation of the search agents, five independent simulations are executed for each inverse shape fitting case study from Table 4.1. The impact of wall boundary condition type for dimensional space violated particles on solution

convergence is examined. The random and reflected wall methods are evaluated. The Hicks-Henne shape function with a dimensional space of $n = 4$ and $n = 20$ is applied for wall boundary condition performance evaluation. Three target airfoils are applied in the analysis with geometry initialisation at the symmetrical NACA 0015 airfoil in Figure 4.2.

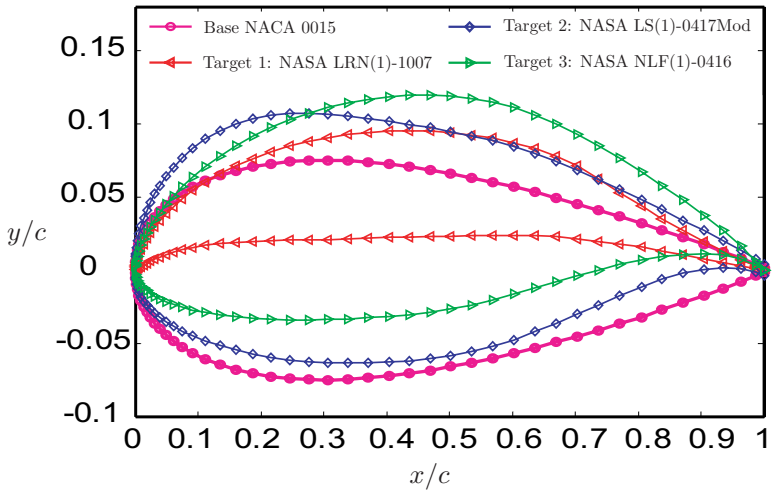

FIGURE 4.2: Representation of Base & Target Airfoils for Evaluation of Wall Boundary Condition type by the Inverse Shape Fitting Approach with Hicks-Henne Shape Functions

The shape convergence over pressure and suction surfaces for the target NASA LRN(1)-1007 airfoil is presented in Figure 4.3. The figure inset represents the evolution of airfoil convergence of the approximated profile toward the target shape.

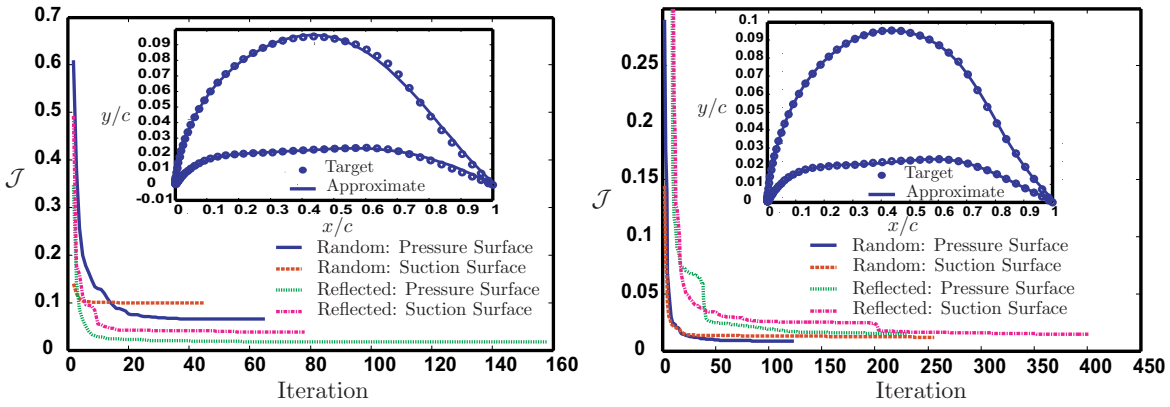

(a) $D = 4$ (b) $D = 20$

FIGURE 4.3: NASA LRN(1)-1007 Inverse Shape Fitting: Effect of Wall Boundary Condition Type on Objective Function

At $D = 4$ in Figure 4.3(a), the reflected condition yields a lower fitness (Eqn. 4.1) for both the upper and lower airfoil surfaces in comparison to the random initialisation approach. The figure inset validates a minor miss-match in shape convergence between the target points and approximated profile on upper surface by the reflected boundary condition method. The identified differences are evident for chord location exceeding $x/c \approx 0.60$, with transition toward the trailing edge region. The

lower surface is also characterised by a miss-match between the identified datasets for chord stations exceeding $x/c \approx 0.80$ including and up to the trailing edge zone.

The demerit of the reflected approach is an extended computational simulation process relative to the random method. As the solution is restricted at the boundary of the defined variable search limits, the probability of locating the global minima is improved through the oscillation of particles between the outermost boundary region and the inner space of the solution space without altering the trajectory of the position vector relative to the original search direction. Due to the overshoot response of the particles, the reflected boundary condition reflects the particles back into the solution domain and consequent iterations oscillate about this point for convergence. This results in a higher computational expense.

The solution at $D = 20$ is not at the boundary of the search space in Figure 4.3(b). The random initialisation approach yields superior convergence than the reflected method. The figure inset further confirms an acceptable shape convergence fit by the random approach as the difference between the target and approximated data sets is negligible on profile upper and lower surfaces. The diversity of the search process is enhanced by the random distribution relative to the reflective method. The reflected boundary condition is characterised by an extended iterative process due to the oscillation of the search agents about the search boundary. The random dispersion of the particles enhances the search diversity, hence probability of convergence to a valid solution region is increased instead of restricting the search to a specific solution zone only as is representative by the reflective approach.

The fitness convergence of the three target airfoils from Figure 4.2, as approximated by the Hicks-Henne shape functions with the identified wall boundary condition types at $D = 4$ and $D = 20$ is presented in Table 4.2.

TABLE 4.2: Effect of Wall Boundary Condition Type on Inverse Shape Fitting by the Hicks-Henne Functions

Design Variables Population Size; $D = 4$								
	Fitness Function				**Iterations**			
Airfoil	*Random Suction*	*Reflected Suction*	*Random Pressure*	*Reflected Pressure*	*Random Suction*	*Reflected Suction*	*Random Pressure*	*Reflected Pressure*
Target 1	0.0996	**0.0389**	0.0655	**0.0170**	**45**	78	**65**	158
Target 2	0.0330	**0.0272**	0.0219	**0.0409**	**83**	344	**51**	59
Target 3	0.0613	**0.0186**	**0.0451**	0.0619	**70**	77	**83**	88
Design Variables Population Size; $D = 20$								
Target 1	**0.0122**	0.0146	**0.0084**	0.0154	**256**	401	**124**	231
Target 2	**0.0242**	0.0276	**0.0161**	0.0278	**203**	204	**79**	401
Target 3	**0.0111**	0.0129	**0.0116**	0.0125	**401**	**401**	**175**	384

At $D = 4$ in Table 4.2, the reflected boundary condition is superior for all three target airfoils over the suction surface and exhibits a lower fitness distribution on shape pressure contour for two out of the three airfoils. The reflected boundary condition indicates superior convergence over the random approach for the identified test cases. The demerit is the computational inefficiency of the method. The reflected approach yields a higher computational expense than the random method as

a function of the total number of iterations required to achieve convergence due to the oscillation of the particles between the inner and outer limits of the search boundary.

The random methodology exhibits superior performance in all cases modeled than the reflected approach for a large search domain ($D = 20$). A global search process is required for multi-dimensional solution domains and the random initialisation of the particles promotes the required search pattern. A linear/local search process by the reflecting condition is ineffective for an extended size of D. The results by the inverse shape fitting analysis correspond to the findings for boundary condition performance evaluation on mathematical test validation functions in Section 3.6.2.2.

Based on the findings in Figure 4.3 and Table 4.2, the inverse shape fitting analysis for the remaining target airfoils with variations in shape function type (Tab. 4.1) will be based on the random initialisation approach. The presented results validate the merits of the random wall boundary condition type to yield acceptable shape generation flexibility.

The aggregate of the shape fitness (Eqn. 4.1) at $D = 4, 6, 8, ..., 20$ of the target airfoils with the Bernstein, Hicks-Henne, NACA and Wagner shape functions is presented in Figure 4.4.

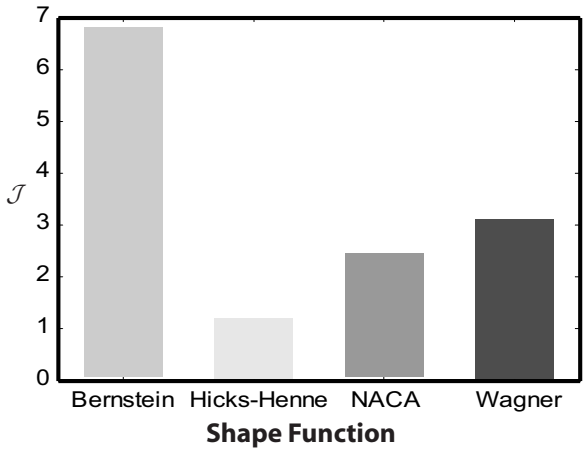

FIGURE 4.4: Inverse Shape Fitting Fitness Distribution by the AM-PSO with Random Initialisation Wall Boundary Condition

The Hicks-Henne exhibits the lowest fitness for the sixteen target airfoils over the balance parameterisation methods. The Legendre was omitted from the analysis due to the computational expense attributed to the derivation of a factorial and derivative term at each iteration. Even for a limited dimensional space at $D = 2$, convergence time was 8 and 14 minutes for the NASA LRN(1)-1007 and NASA LS(1)-0417 Mod airfoils respectively, on a CPU running at 2.20GHz with 1.0 GB of RAM. Comparatively at the same test condition, the remaining shape functions recorded an average convergence time of <1 minute.

B. Inverse Shape Fitting by Hybrid Line Search & AM-PSO Methods: Results and Discussion

The merits of the inverse shape fitting test methodology by the developed AM-PSO algorithm relative to a gradient optimisation method is verified. The corresponding fitness of the identified shape function types is presented in Figure 4.5. Each bar is representative of the cumulative fitness of the sixteen target airfoils that are applied in the inverse shape fitting process.

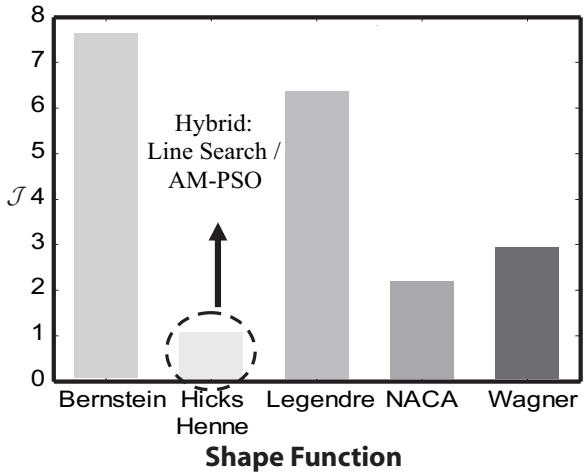

FIGURE 4.5: Inverse Shape Fitting Cumulative Fitness Distribution by the Line Search Method with Random Initialisation Wall Boundary Condition over Sixteen Target Airfoils

The results in Figure 4.5 indicate a similar fitness convergence pattern by the gradient optimisation approach relative to the AM-PSO method for the Bernstein, Legendre, NACA and Wagner polynomials. There is no justification for the use of the AM-PSO method for shape mapping with the identified functions as the gradient-method yields similar fitness convergence. The hybrid optimisation approach was also modeled by the integration of the AM-PSO solution as the starting point for a gradient simulations. There were negligible improvements in fitness convergence relative to the stand-alone AM-PSO and gradient method for the Bernstein, Legendre, NACA and Wagner functions. The hybrid optimisation approach encompassing the AM-PSO and gradient methodology exhibits performance improvements in comparison to the stand-alone AM-PSO and gradient optimisation method for the Hicks-Henne model.

The improved performance of the hybrid optimisation approach with the Hicks-Henne function is attributed to the adjustment of constants α_{HH} and π_{HH} with AM-PSO (Tab. 4.1). Due to the adjustment of multiple variable types in the Hicks-Henne functions, the solution space is complex for gradient search optimisers. The robustness of the search path for non-linear solutions is influenced by the location of the initial guess. Due to a multi-modal solution topology, several local minima are present. The definition of a well-defined solution starting point is a design challenge. To address this issue, the AM-PSO algorithm with random initialisation wall boundary condition is integrated into the search process and an initial estimate of α_{HH} and π_{HH} is established. The parameters are used as inputs into a gradient-based line search method to reduce the scope of the design problem from multi-to-single variable problem. The AM-PSO provides a valid staring point for the line search method and iterates by reducing the fitness even further due to a well defined starting point.

The analysis validates the demerit of the Bernstein, Legendre, NACA and Wagner functions for shape convergence (Figs. 4.4 - 4.5). The Legendre polynomials are computationally inefficient for a line search simulation, hence were not considered in the exhaustive search process by the AM-PSO algorithm. The Hicks-Henne model was computed with the lowest fitness of all the shape polynomials examined. Performance comparison between a uni-based AM-PSO model and a hybrid search algorithm validates the performance merits of the hybrid technique, with lower fitness distribution by the Hicks-Henne method in Figure 4.6.

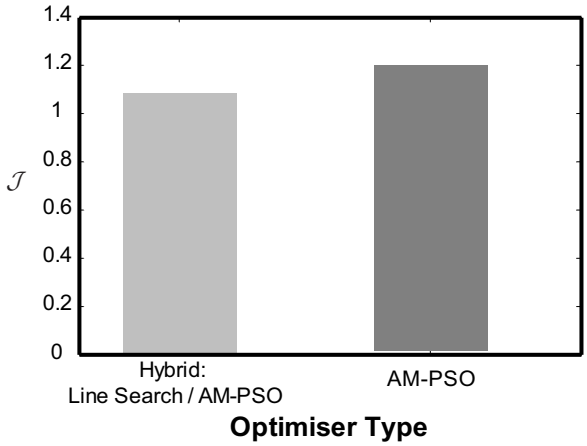

FIGURE 4.6: Inverse Shape Fitting Fitness by Hicks-Henne Shape Function: Comparison of Uni & Hybrid Based Optimisation Process

C. Inverse Shape Fitting by the Analytical Approach: Summary of Results

The inverse shape fitting results by the analytical airfoil parameterisation approach is summarised as follows:

1. The AM-PSO algorithm with random initialisation wall boundary condition has design merits resulting to accurate and rapid shape convergence in comparison to the reflecting wall method for the sample airfoils examined (Fig. 4.3);

2. Shape functions requiring the adjustment of a single coefficient (Tab. 4.1: Wagner, Legendre, Bernstein, and NACA normal modes), gradient and global search algorithms exhibit similar inverse shape fitting convergence (Figs. 4.4 - 4.5). Gradient-based line search method is computationally efficient in comparison to the AM-PSO with fewer design iterations required to convergence;

3. The Hicks-Henne method converged with the lowest fitness of all the shape functions examined regardless of the optimisation algorithm type applied (Figs. 4.4 - 4.5); and

4. A hybrid optimisation-based technique with AM-PSO method was applied to obtain an initial estimate of the Hicks-Henne function coefficients α_{HH} and π_{HH} (Tab. 4.1). The parameters are integrated into a gradient-based line search method. The hybrid search process results to a low fitness convergence in comparison to the standard AM-PSO algorithm for the sixteen target airfoils in Figure 4.6

Despite the merits of an enhanced design flexibility by the Hicks-Henne model in the analytical shape parameterisation approach, the method has design limitations. The Hicks-Henne variables for airfoil representation $|X_i, \cdots, X_{n_{vars}}|$, are not directly correlated to profile geometry parameters. The application of shape constraints will be an issue. Hence, alternate airfoil parameterisation approach types need to be evaluated to address this requirement.

4.2.1.2 Inverse Shape Fitting Analysis by Polynomial-Based Functions

Three polynomial based, airfoil parameterisation methods are examined and include: **a)** Kulfan's [60] CST method; **b)** PARSEC method by Sobieczky [28]; and **c)** A novel PARSEC-Modified method. The merits of each method for airfoil parameterisation in the DNO methodology are evaluated. Novel design processes are developed to assess the flexibility and accuracy of each method. The issues and challenges are identified and novel airfoil parameterisation principles are developed to address the identified demerits.

A. CST Approach

The flexibility and accuracy of the CST method (Sec. 2.5.4), over the defined 16 target airfoils is established by the inverse shape fitting process. The AM-PSO algorithm is used to establish the magnitude of the CST design coefficients that minimise $\mathcal{J}$ (Eqn. 4.1), for airfoil upper and lower surfaces. The geometrical convergence on a sample NLF(1)-0416 airfoil with variations in the order of the BP function is presented in Figure 4.7.

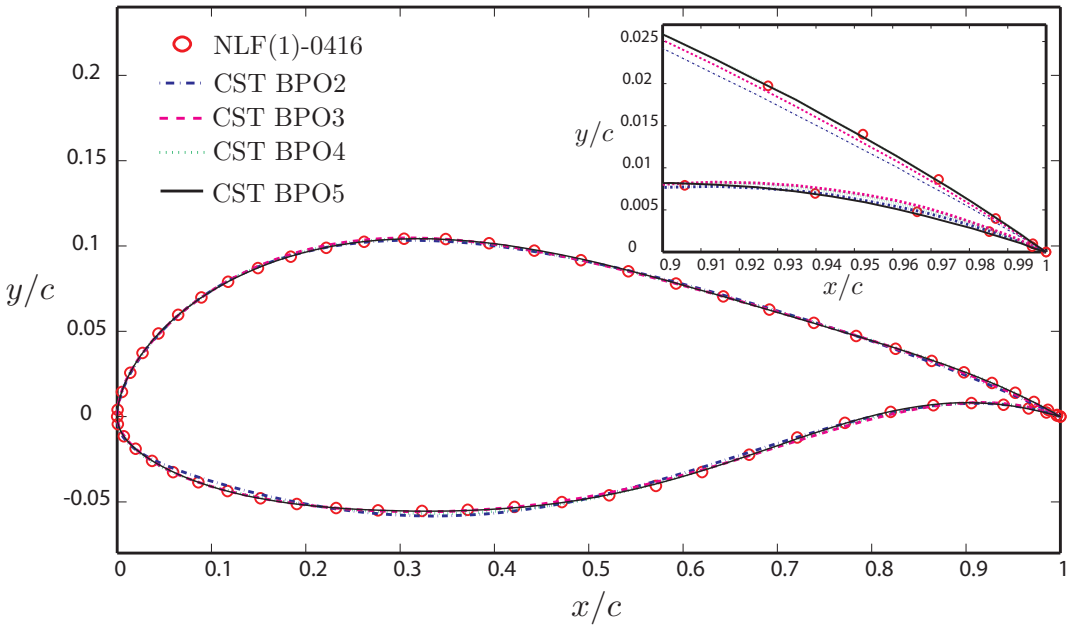

FIGURE 4.7: NLF(1)-0416 Airfoil Convergence by the CST Method

The CST methodology represents acceptable shape convergence to the NLF(1)-0416 target airfoil in Figure 4.7. The leading edge of the benchmark airfoil is modeled with moderate camber. The trailing edge is characterised by a divergent zone ($x/c = 0.90 - 1.00$). Geometrical agreement is enhanced with an increase in the order of the BP function. An increase in BP order has the merits of enhancing the shape closure to the target profile about the leading edge. The effect of BP order at the trailing edge region is further represented (inset of Fig. 4.7). An increase in BP order has the effect of minimising $\mathcal{J}$ (Eqn. 4.1), about the identified trailing edge chord zone ($x/c = 0.90 - 1.00$).

The distribution of shape convergence error is modeled in Figure 4.8. The geometry miss-match between target λ_{T_i} and approximated λ_{A_i} profile at chord station i spanning $0 \rightarrow 1$, as a function of the order of the BP function is presented.

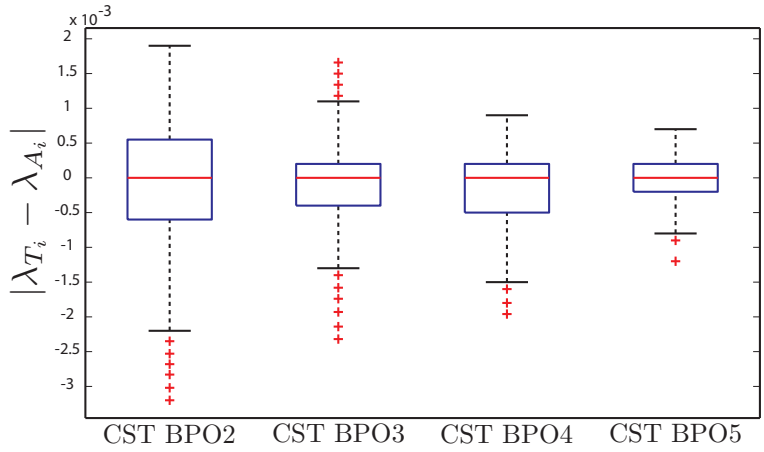

FIGURE 4.8: NLF(1)-0416 Boxplot of Shape Convergence Error Distribution by the CST Method

In each boxplot in Figure 4.8, the mean shape match error distribution at chord station i between benchmark and CST modeled profile is ≈ 0. The scatter of error intervals reduces with an increase in the order of the BP function. The marked outliers are representative of the excessive shape convergence error at the leading and trailing edge region. The miss-match in shape convergence at the identified zones is reduced with an increase in BP order and is minimal at BPO5.

The merits of the developed AM-PSO algorithm is validated by the inverse shape mapping process of the NLF(1)-0416 airfoil. The magnitude of the CST coefficients by the AM-PSO algorithm, hence $\mathcal{J}$ (Eqn. 4.1) is compared with the gradient-based method by Kulfan[1] for the sample NLF airfoil. The results are represented by the absolute shape difference error from $\mathcal{J}$ at chord station i, between target λ_{T_i} and approximated λ_{A_i} profile, as a function of the BP order by the two optimisation methods in Figure 4.9.

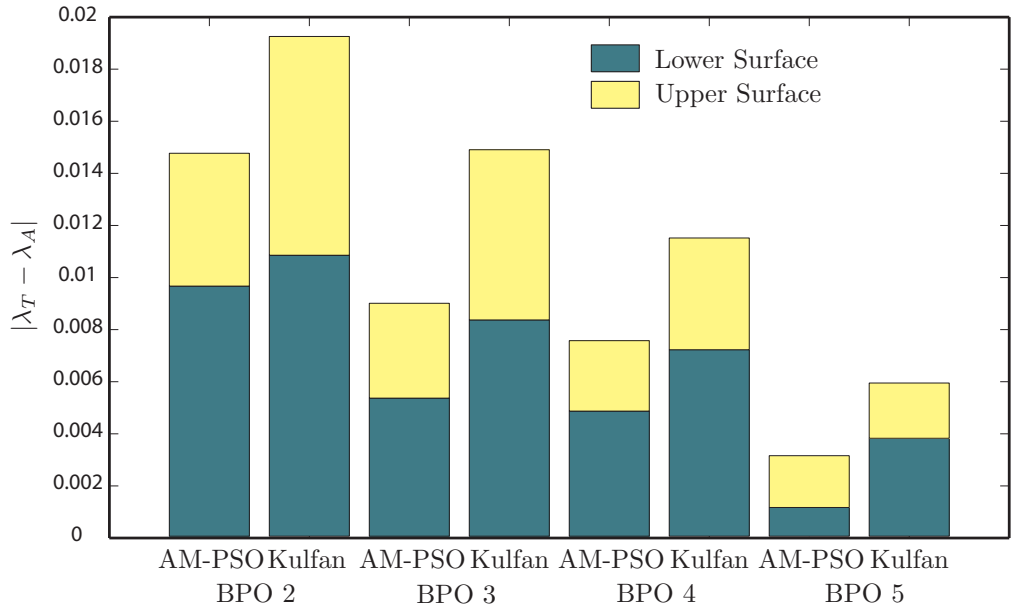

FIGURE 4.9: NLF(1)-0416 Inverse Airfoil Fitting with CST by AM-PSO & Kulfan Numerical Method

[1]Magnitude of CST coefficients as a function of BP order for NLF(1)-0416 airfoil are obtained directly from Brenda Kulfan [60], by email correspondence

The distribution of the absolute shape miss-match between target and approximated profile decreases with an increase in the order of the BP function in Figure 4.9. The results conform to the boxplot error distribution data in Figure 4.8. At each BP order the magnitude of $\mathcal{J}$, on airfoil upper and lower surfaces by the developed AM-PSO algorithm is lower than the gradient-based method applied by Kulfan[1]. The AM-PSO exhibits an accurate measure of the CST shape function flexibility, hence fitness than the gradient method. The feasibility of the CST method is assessed accordingly with the availability of valid performance data by the computational process.

In the shape fitting analysis for the analytical-based parameterisation methods, the AM-PSO algorithm did not yield performance advantages relative to the gradient method. The results for the CST method in Figure 4.9 confirm the AM-PSO method corresponds to performance merits with accurate computation of $\mathcal{J}$ over the modeled test envelope size than the gradient algorithm. This is attributed to the multi-modal solution search space associated with the CST shape function. The performance of the AM-PSO algorithm was validated in Chapter 3 to yield acceptable design processes on complex solution topologies relative to the gradient method. The validated findings confirmed on the identified test functions are transferable to inverse shape fitting processes. The limitation of the gradient-simulation for the CST analysis is also attributed to the definition of an ill-defined starting point. The combination of a complex solution topology and a false search initialisation point will result to the modeled performance variances between the global and local optimisation methods in Figure 4.9.

The data validates the importance of integrating a feasible optimisation algorithm for inverse shape fitting applications. An optimisation algorithm with limitations will generate a sub-optimal solution for the defined test problem (Eqn. 4.1). The results will not be indicative of the shape function flexibility and accuracy due to the fundamental limitations within the applied search method. The comparative analysis of the fitness distribution by the AM-PSO and gradient-based method is an example of the defined point in Figure 4.9. As the computational effort required to compute the fitness in Equation 4.1 is negligible, the AM-PSO algorithm needs to be used to assess the performance of the respective shape function type to yield accurate data relative to the gradient method.

The modeled flexibility of the CST function is assessed against the accuracy by an aerodynamic convergence analysis in Figure 4.10

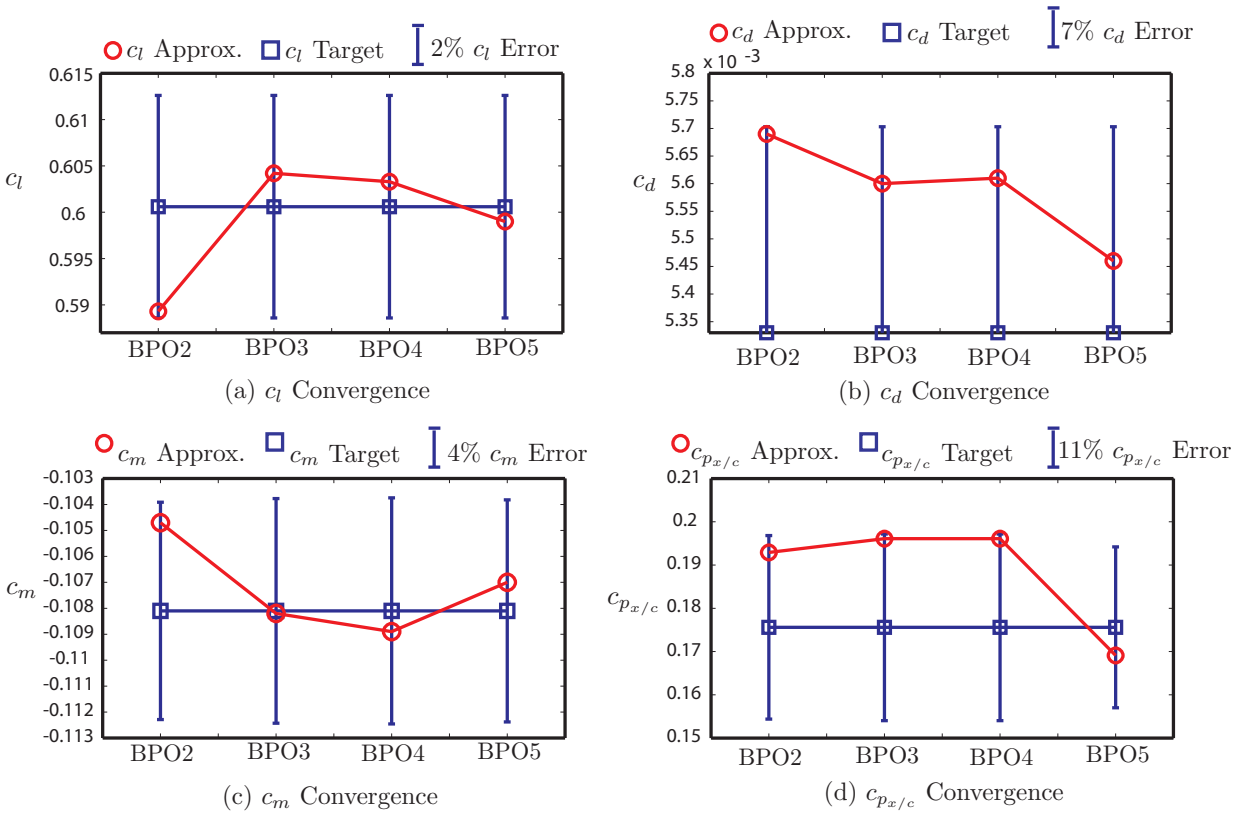

(a) c_l Convergence (b) c_d Convergence

(c) c_m Convergence (d) $c_{p_{x/c}}$ Convergence

FIGURE 4.10: NLF(1)-0416 Airfoil Aerodynamic Convergence by the CST Method

The effect of shape flexibility on accuracy as a function of the order of the BP function on c_l, c_d, c_m and chord location of the minimum coefficient of pressure point $c_{p_{x/c}}$ is modeled in Figure 4.10. The respective aerodynamic quantity of the base NLF(1)-0416 airfoil is modeled in each sub-figure. An error bar about the target aerodynamic parameter is modeled to represent the degree-of-shape convergence, hence the measure of accuracy by the CST model relative to the defined target airfoil.

The convergence of c_l represents improvements in accuracy with an increase in BP order in Figure 4.10(a). At BPO2, the error between target and approximated profile is $\approx 2\%$. With an increase in order of the BP, the error is reduced to $\approx 0.30\%$ at BPO5. The effect on c_d with an increase in BP order has a similar effect in Figure 4.10(b). At BPO2, the error between benchmark and approximated shape is $\approx 7\%$. At BP order three and four, the error is stagnant at $\approx 5\%$. The miss-match is reduced to $\approx 3\%$ at BPO5. The error between target and approximated data is negligible for c_m at BPO3 in Figure 4.10(c). An increase in BP order has the demerit of increasing the miss-match between the two shapes. The percentage difference increases to $\approx 1\%$ at BPO5. The error is stagnant across BPO2 to BPO4 at $\approx 10\%$ for $c_{p_{x/c}}$ and is reduced to the established minima of $\approx 4\%$ at BPO5 in Figure 4.10(d).

An increase in the order of the Bernstein polynomials enhances the accuracy of the CST model for NLF airfoil profile approximation. The results to the aerodynamic convergence analysis in Figure 4.10, validates the merits of an increase in BP order for function flexibility and accuracy. The percentage error distribution of the aerodynamic parameters indicates the non-convergence of the approximated profile to the theoretical solution. With a further increase in BP order, it is hypothesised that the

miss-match in aerodynamics between target and approximated profile will stagnate to a minimum threshold. The flexibility and accuracy of the CST function can be enhanced further at the expense of an increase in BP order with greater design variable population size for shape parameterisation. The error boxplot distribution in Figure 4.8, confirms the convergence to a minima threshold of ≈ 0. With further increases in the BP order, it is expected that the error intervals will reduce further.

Analysis into the CST methodology has confirmed the absence of direct relationship between CST variables and airfoil geometry. The application of shape constraints for airfoil design simulation will be an issue. The analysis also confirmed that the CST variables are sensitive to the generation of un-smooth and un-realistic airfoils. Minor variable perturbations can result in shape transition from smooth and realistic shapes to aerodynamically infeasible and undulating profiles. Flow solver analysis on infeasible shapes by a high-fidelity method will result in a false computational process and an inefficient design optimisation process will follow. In-lieu of a direct relationship between CST shape coefficients and airfoil geometry features and to further mitigate the generation of un-realistic shapes, the definition of a valid CST design variable search intervals range for airfoil design simulations will be a design challenge. Hence, alternate airfoil parameterisation techniques are examined to address the identified issues and challenges.

B. PARSEC Function - Test of Variable Impact on Airfoil Geometry & Aerodynamics
The theoretical merits of the PARSEC function relate to the direct relationship between the shape variables and airfoil geometry (Fig. 2.4(a)). The eleven design coefficients used to represent disparate airfoil class types include:

Table 4.3: PARSEC Airfoil Design Parameters

Description	**Symbol**	**Description**	**Symbol**
Leading Edge Radius	r_{le}	Lower Crest Curvature	z_{xxl}
Upper Crest Abscissa	x_{up}	Trailing Edge Ordinate	z_{te}
Upper Crest Ordinate	z_{up}	Trailing Edge Thickness	Δz_{te}
Upper Crest Curvature	z_{xxu}	Trailing Edge Direction	α_{te}
Lower Crest Abscissa	x_l	Trailing Edge Wedge Angle	β_{te}
Lower Crest Ordinate	z_l		

The relationship between PARSEC parameters and airfoil geometry and aerodynamics is evaluated. The process applied is as follows:

1. Generate a base PARSEC airfoil with arbitrarily defined variables;
2. Select one PARSEC variable for sensitivity analysis with remaining ten variables constant (Tab. 4.3);
3. Arbitrarily establish variable test search interval range;
4. Establish variable test increment perturbation magnitude;
5. Generate PARSEC airfoils within the identified test domain (Step 3), over n user-defined incremental (Step 4) variable changes;

6. Measure airfoil geometry (Leading Edge Radius, Maximum Thickness, Maximum Thickness Location, Camber, Camber Location and Trailing Edge Wedge Angle);
7. Compute airfoil aerodynamic coefficients of lift, drag and moment of each PARSEC airfoil;
8. Repeat test (Steps 2-7) for all variables; and
9. Repeat test with variations over four independent base airfoils

The results to the defined DoE test to assess the impact of the PARSEC shape variables on airfoil geometry and aerodynamics is represented by SOMs for ease-of-data interpretation. The four base PARSEC airfoils integrated into the defined test process (Steps 1 & 9 above) and evaluated over the user-defined test domain (Step 3), are summarised in Table 4.4. The corresponding airfoils are modeled in Figure 4.11. The airfoils with disparate geometrical feature types are integrated into the defined test process with intent to evaluate the impact and consistency of the relationship between the PARSEC shape coefficients on airfoil geometry and aerodynamics. To facilitate valid airfoil computations by the select flow solver type, the variable t_{te} is not used in the analysis.

TABLE 4.4: PARSEC Airfoil Design Variable Definition Test Case Study

PARSEC Variable	**Test Domain**	**Case 1**	**Case 2**	**Case 3**	**Case 4**
r_{le}	[0.01,0.04]	0.01	0.01	0.01	0.01
y_{te}	[-0.02,0.02]	0	0	0	-0.004
t_{eg}	$[-2^\circ, -25^\circ]$	0°	-6.8°	-10°	-10.5°
t_{ew}	$[3^\circ, 40^\circ]$	17°	8.07°	5.6°	4.4°
x_u	[0.30,0.60]	0.30	0.4324	0.42	0.418
y_u	[0.07,0.12]	0.06	0.063	0.058	0.055
y_{xxu}	[-1.0,0.20]	-0.45	-0.4363	-0.35	-0.22
x_l	[0.20,0.60]	0.30	0.3438	0.36	0.4182
y_l	[-0.02,-0.08]	-0.06	-0.059	-0.057	-0.082
y_{xxl}	[0.20,1.20]	0.45	0.70	0.03	-0.35

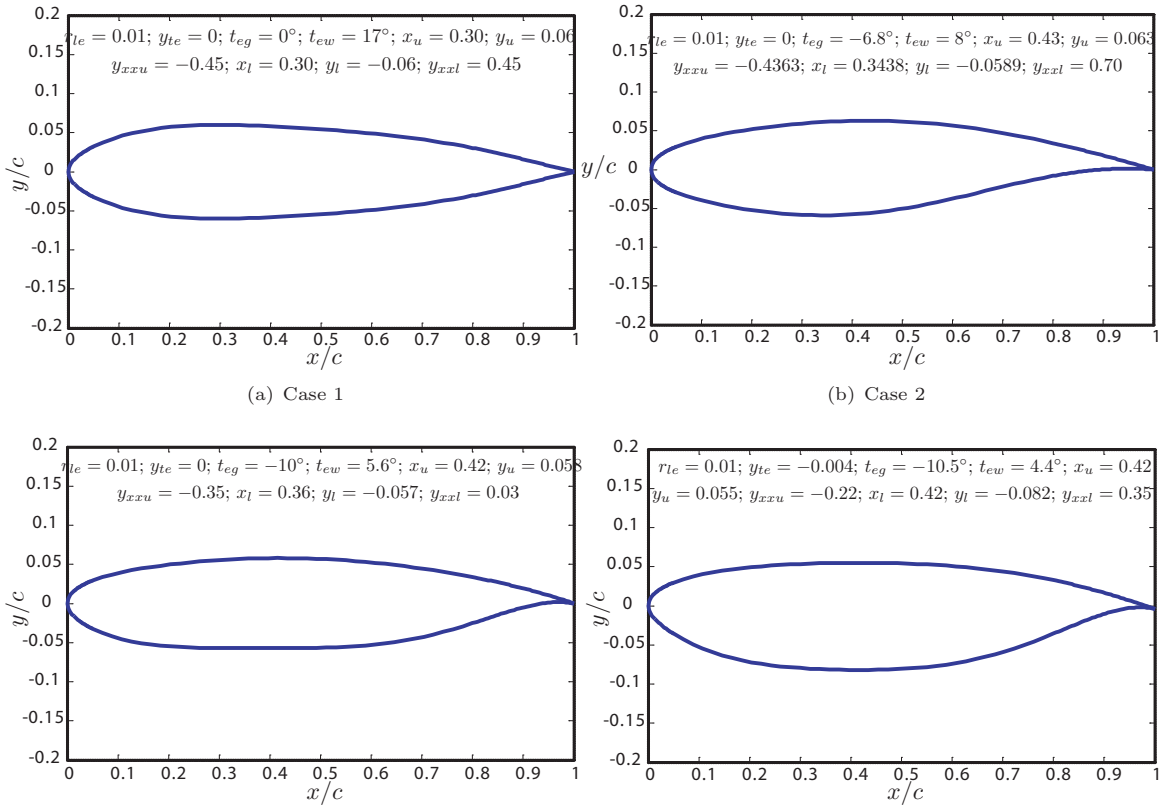

(a) Case 1 (b) Case 2

(c) Case 3 (d) Case 4

FIGURE 4.11: Base Airfoils for PARSEC Airfoil Definition

Variations in Leading Edge Radius

The effect of varying r_{le} one factor-at-a-time, over $n = 40$ equal increments on the identified case airfoils from Figure 4.11 and in the defined test range [0.01, 0.04] (Tab. 4.4), on airfoil geometry is modeled. The remaining nine variables are constant to the baseline value. Each SOM cluster is representative of the case airfoil in Figure 4.12.

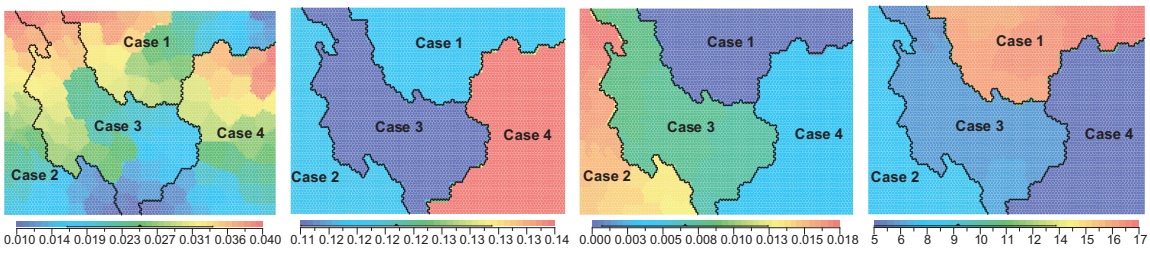

(a) r_{le} (b) t/c (c) Camber (d) t_{ew}

FIGURE 4.12: Effect of r_{le} on Airfoil Geometry

The minimum and maximum values of r_{le} are represented by "cold" and "hot" regions respectively for each case in Figure 4.12(a). An increase in r_{le}, has a negligible effect on thickness-to-chord (Fig. 4.12(b)) and trailing edge wedge angle (Fig. 4.12(d)), with slight variations in camber (Fig. 4.12(c)), for airfoil case two. A one-to-one control over thickness-to-chord, camber, and trailing edge wedge angle is evident with variations in leading edge radius for PARSEC airfoils. The analysis confirms that

radius perturbations will not affect shape thickness which is a critical design constraint for structural strength and payload volume design requirements.

The corresponding impact of r_{le} on airfoil aerodynamic is presented in Figure 4.13.

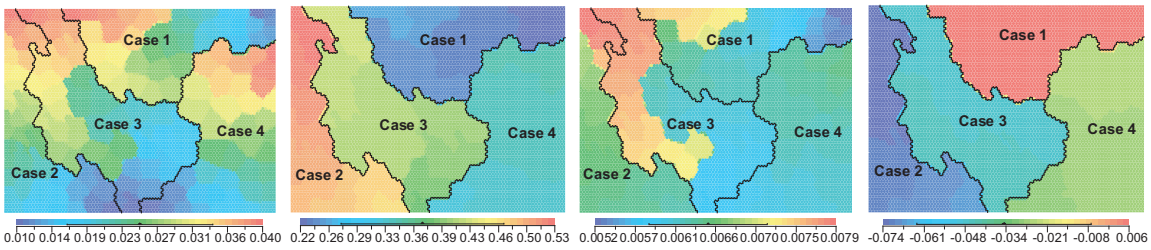

(a) r_{le} (b) c_l (c) c_d (d) c_m

FIGURE 4.13: Effect of r_{le} on Airfoil Aerodynamics

The low-fidelity solver XFOIL is used to compute the aerodynamics at an operating Reynolds Number of 6.0×10^6 at Mach 0.40. The results validate that r_{le} has a dominating influence on c_l in Figure 4.13(b) and c_d in Figure 4.13(c), but a minor impact on c_m in Figure 4.13(d). Optimisation of the leading edge radius is critical for improved drag performance. An increase in r_{le} results in an increase in lift and drag performance. The visualised relationship between r_{le} and airfoil aerodynamics (Fig. 4.13), is in accordance with established performance principles. The results are also confirmed by Jeong [58] at a transonic flight envelope. The data validates that airfoil geometry including t/c, camber, trailing edge wedge angles and direction are not interlinked to r_{le} perturbations (Fig. 4.12). The r_{le} search intervals can be constrained to facilitate airfoil design with low drag performance, while conforming to structural thickness requirement.

Variations in Upper Crest Ordinate

The affect of varying y_u is presented in Figure 4.14.

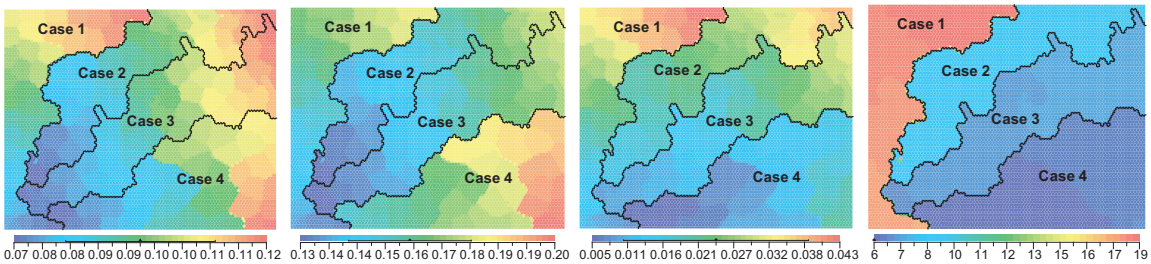

(a) y_u (b) t/c (c) Camber (d) t_{ew}

FIGURE 4.14: Effect of y_u on Airfoil Geometry

The analysis validates that thickness-to-chord in Figure 4.14(b) and camber (Fig. 4.14(c)) increase proportionally as y_u increases. The trailing edge wedge angle (Fig. 4.14(d)), is not sensitive to y_u perturbations only. Analysis of PARSEC variable y_l for control over airfoil thickness contour on pressure side, represents a similar pattern in Appendix D.7. The results demonstrate variations in y_u and y_l exhibit one-to-one thickness control which is a key requirement for airfoil design. By integrating

the two control parameters, shape thickness constrains can be imposed by variable manipulation. The optimal shape will conform to user-defined thickness requirements.

Aerodynamic performance with y_u variations is presented in Figure 4.15.

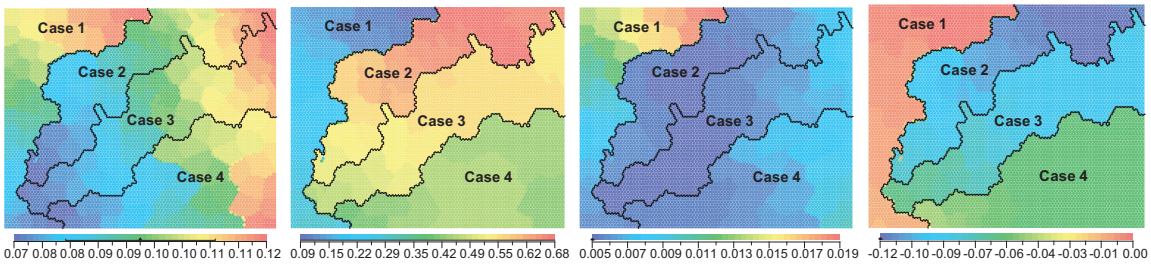

(a) y_u (b) c_l (c) c_d (d) c_m

FIGURE 4.15: Effect of y_u on Airfoil Aerodynamics

The distribution of aerodynamic coefficients by perturbing y_u only (Fig. 4.15), conforms with established airfoil aerodynamic performance principles of thick sections. The c_l (Fig. 4.15(b)) and c_d (Fig. 4.15(c)) increase as airfoil thickness is increased. Airfoil aerodynamic analysis indicates a delay in the onset of stall with a rise in $c_{l_{max}}$ as airfoil thickness is increased. Smaller values of y_u are related to acceptable lift-to-drag performance.

The impacts of PARSEC variables y_{te}, t_{eg}, t_{ew}, x_u, y_{xxu}, x_l, y_l and y_{xxl}, on airfoil geometry and aerodynamics is computed by the defined test process. The results are represented by SOMs in Appendix D.

PARSEC Design Variable Analysis: Summary of SOM Analysis

The goal of applying SOMs to PARSEC airfoil definition is not to locate an optimal shape, but to establish the relationship between the airfoil parameterisation coefficients and corresponding geometry and aerodynamics. The methodology yields critical data in regards to the sensitivity of the shape variables. The SOM analysis was simulated over ten PARSEC design coefficients and the relationship between variable, airfoil geometry and aerodynamics mapped. The analysis validates the search window that exhibits the required one-to-one geometrical control for each variable.

Parameters x_u and x_l which control the chord-wise location of the maximum thickness point on upper and lower surfaces are sensitive to the generation of smooth and aerodynamically realistic shapes. Accordingly, the search limits of the design parameters must be well defined to mitigate the generation of un-realistic shapes. Search limits within a threshold $0.20 \leq x_u \leq 0.60$ for upper and $0.20 \leq x_l \leq 0.70$ for lower contours will result in realistic shapes. The function loses the generalised one-to-one shape control if the search limits exceed the identified range. Undulating airfoils are generated for an ill-defined search window. The findings are applied in the development of a well-defined search limit for each variable. The shapes generated during the design optimisation process will conform to user-defined geometry constraint requirements, hence the optimiser will not waste computational resources examining airfoils that are aerodynamically and geometrically ill-defined.

The aerodynamic performance data identified the impact of shape coefficients on airfoil aerodynamics. Geometry parameters with acceptable drag performance may not satisfy minimum, user-defined

lift requirement. The merits of the developed AM-PSO method will intelligently perturb the shape coefficients to finalise the permutation of design variables that corresponds to low drag performance, while conforming to user-defined aerodynamic and shape constraints of lift and thickness distribution for wing spar location respectively.

PARSEC Function - Inverse Shape Fitting

The flexibility and accuracy of the PARSEC shape function [28] (Sec. 2.5.4) is evaluated by the developed inverse shape fitting process from Figure 4.1. The approach has design merits as the definition of an arbitrary, user-defined base airfoil is not required unlike the analytical approach. To facilitate a valid comparative analysis between the analytical and polynomial base method, the 16 target airfoils used in the analytical function analysis are applied in the evaluation of the PARSEC method. The stand-alone AM-PSO algorithm is applied to establish the magnitude of the PARSEC shape coefficients for the respective target airfoil. The results are presented in Figure 4.16.

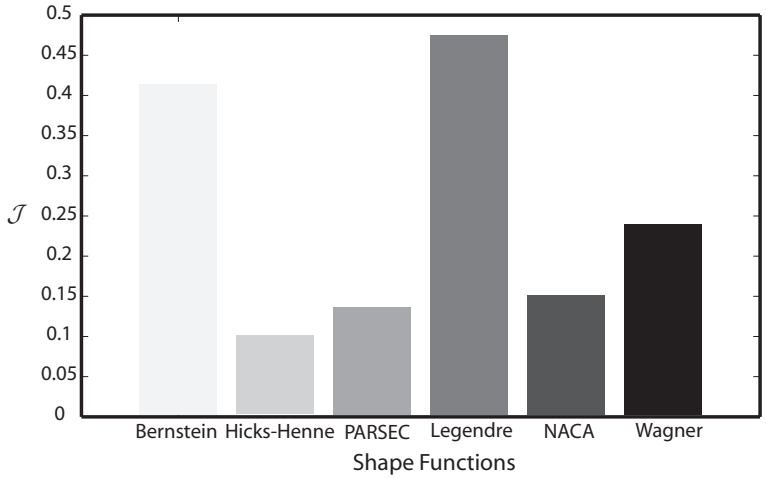

FIGURE 4.16: Inverse Shape Fitting Fitness Distribution Comparison between Analytical & Polynomial Based Approach

The fitness distribution of the PARSEC model in Figure 4.16 indicates a geometrical miss-match that is slightly greater than the Hicks-Henne function and is lower than the remaining test functions evaluated. From the established measure of shape flexibility by the PARSEC method, the following is summarised.

1. The shape variables in the PARSEC method are directly related to airfoil geometry features; and
2. The PARSEC approach has limited design flexibility in comparison to the Hicks-Henne method.

The PARSEC approach uses ten design variables to represent an arbitrary airfoil type. The analytical-based Hicks-Henne approach is characterised by ten design variables to represent airfoil upper and lower surface, hence 20 design variables to parameterise the airfoil contour. The benefits of incorporating ten additional design variables with the Hicks-Henne approach was confirmed from the inverse shape fitting process. The analytical-based approach yielded lower fitness (Eqn. 4.1), for the sample airfoils examined, hence superior design flexibility in comparison to the PARSEC method.

The shape variables in the Hicks-Henne approach are not directly related to airfoil geometry and the definition of shape constraints is a design issue.

The application of fewer design variables for airfoil parameterisation has merits. Theoretically, the PARSEC approach will exhibit an accelerated and efficient search computation process to convergence due to the application of ten fewer design variables in comparison to the Hicks-Henne approach. Comparatively, the Hicks-Henne method will be computationally inefficient due to the integration of a larger design variable population size. The developed AM-PSO algorithm (Chapter 3), will also have search issues handling an airfoil design optimisation simulation with excessive design variable population size ($D \geq 20$). The integration of the PARSEC method will suffice for the purposes of enhancing the computational efficiency of the design process and to further address the limitations of the AM-PSO method. The demerit will be the generation of a sub-optimal airfoil due to the limited design flexibility.

A novel airfoil parameterisation approach is required to exploit the merits of the PARSEC function while concurrently addressing the identified limitations. The proposed method must maintain a direct relationship between the design coefficients and airfoil geometry for the ease-of-application of shape constraints, as in the case of the PARSEC method. The identified approach needs to extend the design flexibility of the shape function in comparison to the original PARSEC model without a significant increase in the dimensional size as this will correspond to an inefficient and computationally time-intensive design process. A PARSEC-Modified approach is proposed to address the identified requirements.

4.2.1.3 Inverse Shape Fitting Analysis by the Polynomial-Based PARSEC-Modified Approach

In the PARSEC-Modified approach, the generation of airfoil upper and lower surfaces is decoupled to address the design requirements of increased flexibility. The methodology is ideal for highly cambered nose airfoils and divergent trailing edge (DTE) profiles [144]. At low subsonic Mach numbers, premature separation about the nose leading edge is a performance issue. Highly cambered nose sections are applied to offset the excessive negative peak pressure coefficient at the leading edge to address the identified performance issue.

At transonic Mach numbers, shock-induced drag is a flight performance issue. A DTE airfoil class type was developed by Henne et al. [144] to address this demerit. Theoretically, a DTE airfoil exhibits equal lift at a lower angle-of-incidence and drag, hence resulting in a significant increase of the lift-to-drag ratio at transonic cruise conditions. Geometrically, a DTE airfoil is a combination of a blunt base airfoil with a local region of high surface curvature on profile pressure surface, including airfoil upper and lower surface trailing edge slopes that diverge from each other. The modifications result in a decrease of drag creep due to the reduction in wave drag. The contour modifications at the trailing edge facilitates an extended wake flow recirculation which has an effect of relocating and weakening the shock intensity [144].

The PARSEC-Modified method introduces three new variables in addition to the eleven coefficients from the original PARSEC model (Tab. 4.5) in Equation 4.3. The additional shape coefficients

modify profile trailing edge geometry including the partitioning of the leading edge radius that is representative of airfoil upper and lower contour curves. The leading edge radius is not measured from the mean camber line in the modified method. Instead the radius center is evaluated from the $x-axis$, hence an independent measure of surface upper and lower radius of curvature is established.

$$
\begin{aligned}
Z_{\text{PARSEC-Modified}} = & \underbrace{\sum_{n=1}^{6} a_n(p).X^{n-\frac{1}{2}}}_{\text{PARSEC Original: Airfoil Thickness \& Crest Definition}} \\
+ & \underbrace{\sum_{n=1}^{5} b_n(p).X^{n-\frac{1}{2}}}_{\text{PARSEC Original: Airfoil Angles \& LE Definition}} \\
+ & \underbrace{\sum_{n=1}^{3} c_n(p).X^{n}}_{\text{PARSEC Additional TE Angle Terms}}
\end{aligned}
\tag{4.3}
$$

The corresponding design variables of the PARSEC-Modified function from Equation 4.3 are presented in Table 4.5.

TABLE 4.5: PARSEC-Modified Airfoil Design Parameters

Description	**Symbol**	**Description**	**Symbol**
Upper Leading Edge Radius	$r_{le_{up}}$	Lower Leading Edge Radius	$r_{le_{low}}$
Upper Crest Abscissa	x_{up}	Lower Crest Abscissa	x_l
Trailing Edge Ordinate	z_{te}	Trailing Edge Thickness	Δz_{te}
Upper Crest Ordinate	z_{up}	Lower Crest Ordinate	z_l
Upper Crest Curvature	z_{xxu}	Lower Crest Curvature	z_{xxl}
Upper Trailing Edge Direction	$t_{eg_{up}}$	Lower Trailing Edge Direction	$t_{eg_{low}}$
Upper Trailing Edge Wedge Angle	$t_{ew_{up}}$	Lower Trailing Edge Wedge Angle	$t_{ew_{low}}$

The thickness at the trailing edge Δz_{te} is not used for airfoil design to ease the computational mesh generation process. The total number of design variables is reduced to 13 from 14 accordingly. The graphical representation of the proposed shape parameterisation method is presented in Figure 4.17.

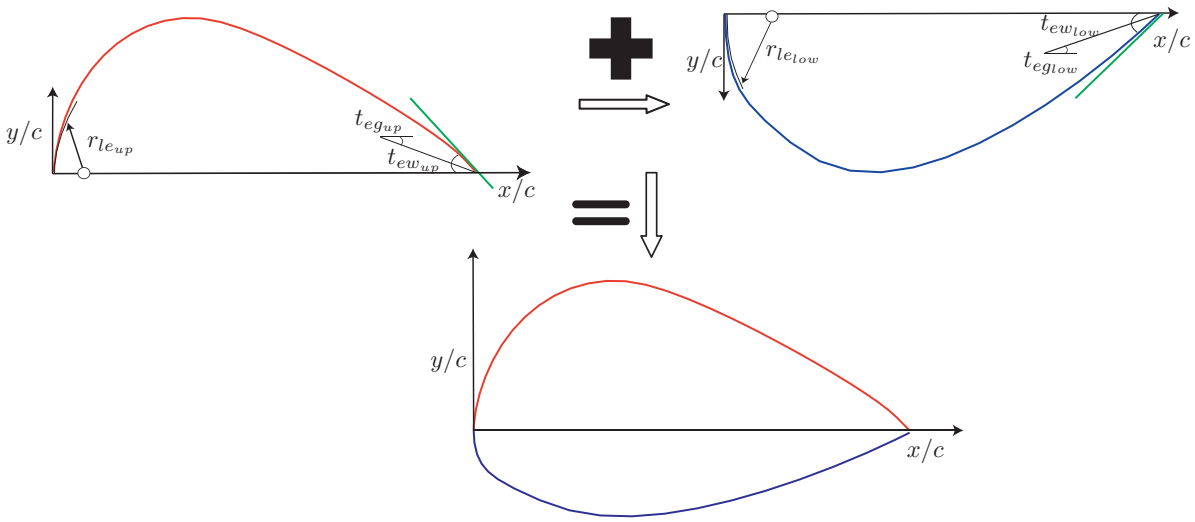

FIGURE 4.17: PARSEC-Modified Representation

The de-coupling of airfoil surfaces has issues and challenges that need to be addressed and considered. There remains the issue of generating fish-tail airfoils due to the trailing edge closure term and by the definition of independent angles that model airfoil upper and lower trailing edge regions. The defined methodology is not ideal for all cambered airfoil family types due to the generation of cross-over airfoils. The identified demerit is addressed by mapping the search intervals of the design variables, such that the solution topology that is representative of fish-tail airfoils is minimised without compromising shape generation flexibility. Theoretically, if the identified issue is adequately addressed, the modified shape parameterisation function will facilitate an airfoil design simulation that aids convergence to the global optimal due to the enhanced shape generation flexibility relative to the original PARSEC model.

The performance of the AM-PSO is valid for optimisation simulations by the PARSEC function as the flexibility of the design algorithm was confirmed for a dimensional search volume that characterises the PARSEC methodology in Section 3.6. The search capabilities of the AM-PSO was validated with published data across disparate problem types at $D = 10$. The PARSEC-Modified function is characterised by $D = 13$ (Eqn. 4.3). It is assumed that the performance of the AM-PSO method is valid at $D = 13$ based on the presented simulation results (Sec. 3.6), despite the minor miss-match between domain size validation specific simulations and airfoil design problem type by the PARSEC-Modified function. Theoretically, airfoil design simulations will benefit due to an efficient computational process by the integration of the novel AM-PSO algorithm coupled with the developed PARSEC-Modified method.

Airfoil inverse shape mapping by the PARSEC and PARSEC-Modified function for a select NLF airfoil is presented to validate the flexibility of the proposed shape parameterisation method in Figure 4.18. The magnitude of the design variables for inverse shape fitting (Eqn. 4.1), are established by the AM-PSO algorithm.

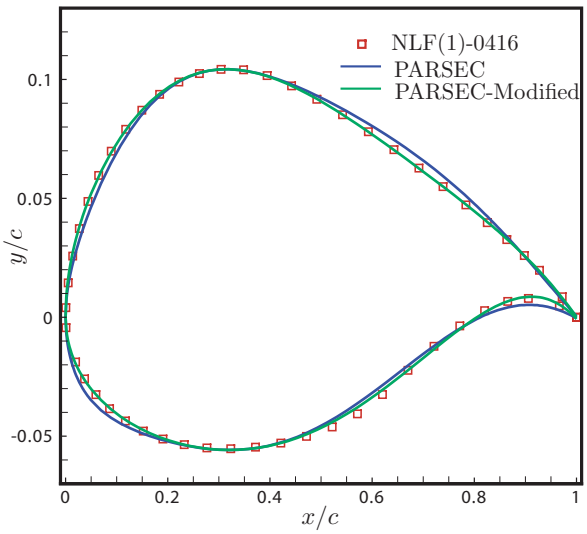

FIGURE 4.18: NLF Airfoil Representation by PARSEC & PARSEC-Modified Method

The PARSEC-Modified method exhibits acceptable shape convergence in comparison the original method in Figure 4.18. The merits of decoupling airfoil upper and lower surfaces for shape modeling in the variant PARSEC-Modified method is confirmed. The PARSEC-Modified function exhibits an exact shape match spanning a chord length interval $[0, 0.20]$, in comparison to the PARSEC method. The theoretical design principles of incorporating a highly cambered nose leading edge airfoil for low subsonic flight operations is modeled with acceptable accuracy by the PARSEC-Modified method. The variant airfoil generation method also achieves superior shape convergence at the trailing edge region in comparison to the original PARSEC model. The application of independent airfoil trailing edge wedge angle and direction contour coefficients for profile upper and lower surfaces corresponds to superior shape flexibility. The PARSEC-Modified converges to the theoretical benchmark for airfoil chord length spanning $[0.50, 1.00]$. The original PARSEC exhibits poor shape convergence over the identified interval range in comparison.

The cumulative sum of the inverse shape fitness from Equation 4.1, spanning 16 target airfoils is presented in Figure 4.19. The data is modeled to further verify the viability of the PARSEC-Modified function for airfoil parameterisation. The results are directly compared to the performance by the analytical (Sec. 4.2.1.1 - Fig. 4.5) and polynomial based (Fig. 4.16) functions.

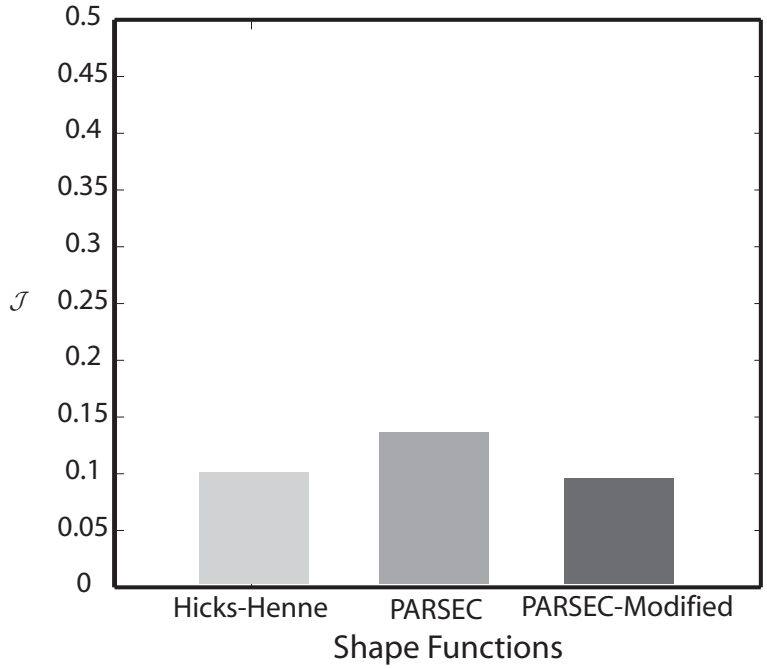

FIGURE 4.19: Inverse Shape Fitting Fitness Distribution Comparison between Hicks-Henne, PARSEC & PARSEC-Modified Approach

The fitness distribution by the PARSEC-Modified inverse shape fitting process spanning 16 target airfoils is the lowest of all the shape functions examined in Figure 4.19. The advantage of enhanced design flexibility with the integration of additional trailing edge shape coefficient terms is verified. The accuracy of the shape function is further assessed by an aerodynamic convergence analysis on select target airfoils in Figure 4.20.

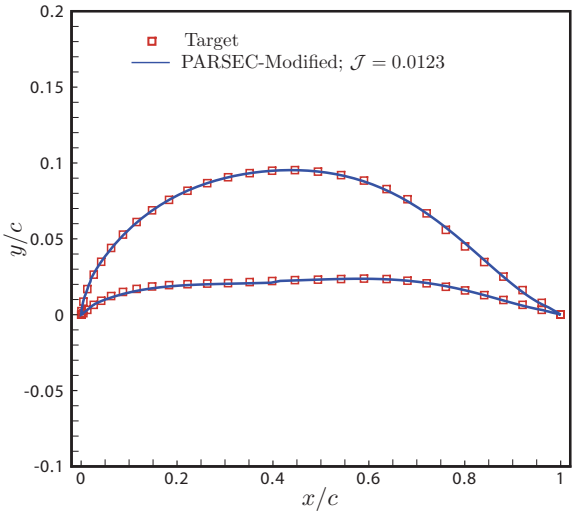

(a) NASA LRN(1)-1007 Shape Convergence

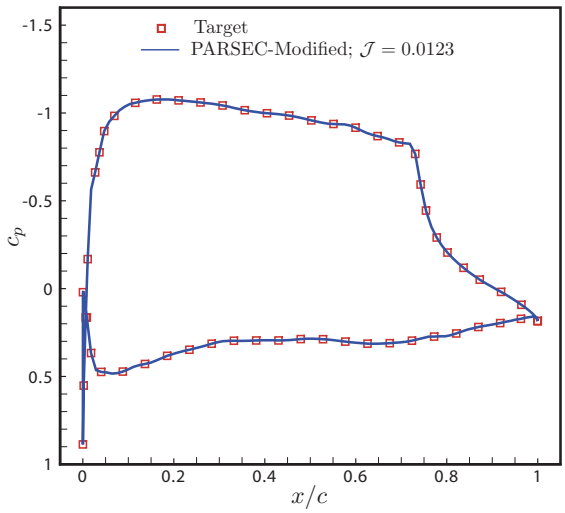

(b) NASA LRN(1)-1007 c_p Convergence

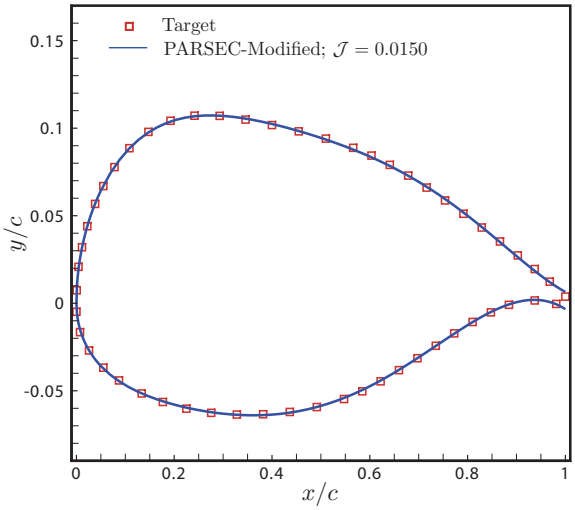

(c) NASA LS(1)-0417 Mod Shape Convergence

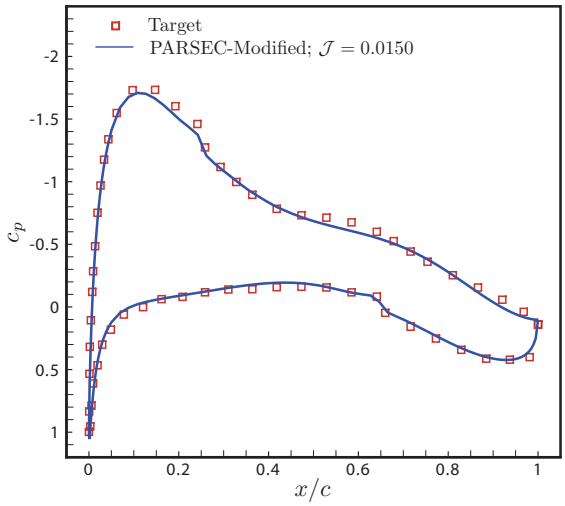

(d) NASA LS(1)-0417 Mod c_p Convergence

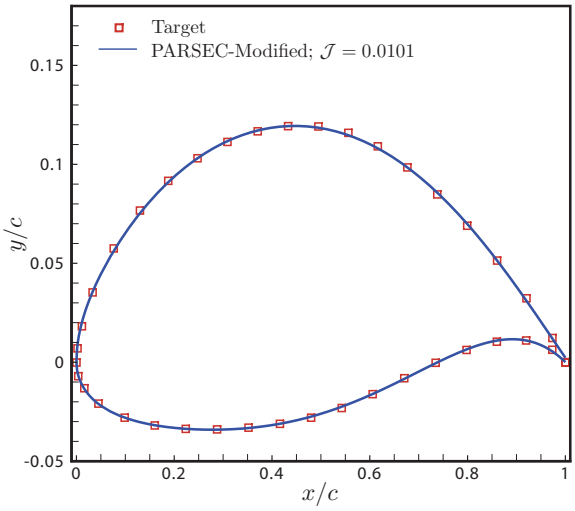

(e) NASA NLF(1)-1015 Shape Convergence

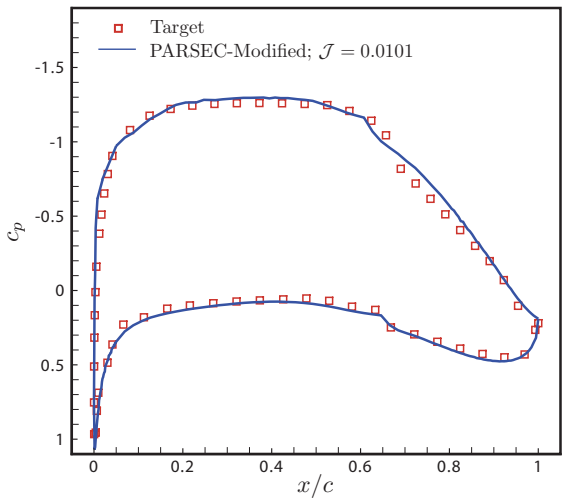

(f) NASA NLF(1)-1015 c_p Convergence

FIGURE 4.20: Inverse Shape Fitting by the PARSE-Modified Approach

The corresponding aerodynamic coefficients of the approximated airfoils relative to the defined target by the PARSEC-Modified parameterisation approach is presented in Table 4.6.

TABLE 4.6: Inverse Shape Fitting Measure of Accuracy of the PARSEC-Modified Approach by an Aerodynamic Convergence Analysis; $\alpha = 2^{\circ}$, $R_n = 3.0 \times 10^6$ & Mach=0.50

Aerodynamic Coefficient	**Target**	**Approximated**
NASA LRN(1)-1007		
c_l	1.03	1.02 ($\approx 0.50\%$)
c_d	0.0083	0.0081 ($\approx 3\%$)
NASA LS(1)-0417Mod		
c_l	0.844	0.8241 ($\approx 2\%$)
c_d	0.0082	0.0083 ($\approx 1\%$)
NASA NLF(1)-1015		
c_l	1.113	1.130 ($\approx 2\%$)
c_d	0.0055	0.0056 ($\approx 2\%$)

The shape convergence of the LRN airfoil indicates acceptable geometry closure between theoretical and approximated profile in Figure 4.20(a). The measure of geometry fit between the two shapes is validated in the c_p analysis in Figure 4.20(b). Excellent aerodynamic convergence is attained by the PARSEC-Modified airfoil in comparison to the target. The measure of accuracy is further validated by the convergence of c_l and c_d parameters in Table 4.6. The percentage difference between benchmark and PARSEC-Modified data is $\approx 0.50\%$ and $\approx 3\%$ respectively. In comparison, the Hicks-Henne converged with a percentage difference of $\approx 7\%$ and $\approx 4\%$, for c_l and c_d respectively with a geometry match fitness of 0.0179. The magnitude of shape match fitness (Eqn. 4.1), is directly related to the measure of function accuracy. A fitness of 0.0123 by the PARSEC-Modified method (Figs. 4.20(a) - 4.20(b)), corresponds to a close aerodynamic match relative to the defined theoretical benchmark. In comparison, the Hicks-Henne method modeled the LRN profile with a fitness that is $\approx 31\%$ greater than the PARSEC-Modified method. The effect of a high miss-match in fitness distribution has an unfavorable impact on the convergence of the aerodynamic data, hence measure of accuracy between target and approximated airfoil at LRN flight conditions.

The shape and aerodynamic convergence of the NASA LS(1)-0417 Mod airfoil to the defined target by the PARSEC-Modified function is modeled in Figures 4.20(c) and 4.20(d) respectively. The converged fitness is $\approx 37\%$ lower than the Hicks-Henne function for the respective airfoil type. The impact of a lower fitness, hence a closer geometry fit between target and approximated airfoil is assessed by an aerodynamic convergence analysis. The c_p distribution validates a close match between target and approximated airfoil. The approximated shape is modeled in agreement to the theoretical profile, with boundary layer transition points computed with acceptable accuracy and correspond to $x_{tr_{up}} \approx 0.25$ and $x_{tr_{low}} \approx 0.65$, on surface upper and lower surfaces respectively.

The converged c_l and c_d of the NASA LS(1)-0417 Mod airfoil by the PARSEC-Modified method, drives the shape fitness $\mathcal{J}$ (Eqn. 4.1), toward the defined target in Table 4.6. A c_l percentage difference of $\approx 2\%$ is computed relative to the defined target and is marginally greater than 1% for the approximated airfoil by the Hicks-Henne model. The miss-match in c_d between target and approximated airfoil is limited to $\approx 1\%$ and matches the performance of the Hicks-Henne functions. Despite,

a miss-match in shape fitness of $\approx 37\%$ between polynomial based, PARSEC-Modified method and the Hicks-Henne approach, the difference in aerodynamic coefficients of the approximated airfoil by the two functions is negligible. Unlike the LRN airfoil, where the aerodynamic coefficients of the approximated airfoil were sensitive to the measure of shape convergence fitness, the difference in function flexibility, hence accuracy of the Hicks-Henne and PARSEC-Modified method for a LS airfoil type is negligible.

The convergence of the NLF airfoil by the PARSEC-Modified method toward target profile exhibits a close fit between the two shapes in Figure 4.20(e). The converged fitness is $\approx 41\%$ lower than the PARSEC model. The merits of shape convergence on function accuracy is assessed by an aerodynamic convergence analysis of the approximated profile to the theoretical target. The c_p distribution identifies an acceptable match between the two data sets in Figure 4.20(f). The PARSEC-Modified base profile accurately models the onset of flow transition on upper and lower surfaces at $x/c_{up} \approx 0.60$ and $x/c_{low} \approx 0.65$ respectively. A miss-match between approximated and target c_p distribution is evident for ensuing flow following transition on surface suction side toward the trailing edge.

The disparity in c_p distribution has a minor impact on c_l convergence with a percentage difference between approximated and target data limited to $\approx 2\%$ in Table 4.6. The percentage variance between the two datasets is lower than the computed differences by the original PARSEC model. The convergence of c_d is close to the defined benchmark by the PARSEC-Modified method in comparison to the original PARSEC function. A percentage difference of $\approx 2\%$ is computed by the PARSEC-Modified method in comparison to $\approx 7\%$ by the PARSEC model with ten design variables. Hence, a lowering of shape convergence fitness by $\approx 41\%$ by the PARSEC-Modified model in comparison to the original PARSEC function, corresponds to an increase in function accuracy for a NLF airfoil. A low $\mathcal{J}$ from Equation 4.1, results in shape and aerodynamic approximation that closely matches the theoretical target by the PARSEC-Modified method. The data validates the merits of the developed PARSEC-Modified approach for airfoil parameterisation.

4.2.2 Design Variables Pre-Screening

Fuhrmann [54] acknowledged that the PARSEC function has the flexibility to generate disparate airfoil class types. Generation of shapes which are aerodynamically not feasible, including 'fish-tail' profiles where the upper and lower surfaces intersect and airfoils with surface irregularities and/or rippling, are possible. It was concluded that the shape parameters must be carefully defined to address this issue. A recommended option was to vary the shape parameters in a consistent and logical manner. Options include shape variations which are isolated to limited changes from a smooth base airfoil and/or blending between realistic shapes to avoid severe and drastic shape alterations [54].

By selecting a smooth base airfoil for surface perturbations to avoid unrealistic shape generation, the proposed methodology will be adaptable to optimisation by gradient-based methods. A smooth and realistic base airfoil applied for search initialisation will localise shape changes about the starting point, hence ensuring realistic shapes are parameterised. The proposal by Fuhrmann [54] limits the PARSEC method to gradient-based optimisation algorithms. The process of randomly manipulating the shape coefficients in a defined search space, a trait in population based search algorithms is not recommended [54], as this lends to the generation of unrealistic profiles.

The issues acknowledged by Fuhrmann [54] are addressed. Airfoil shape changes must not be influenced by a user-defined base profile. Shape functions must be adaptable to global optimisers to facilitate convergence at a valid optimal due to the multi-modal solution topology. Mutation of candidate solutions is an integral component in evolutionary algorithms and involves randomness which is controlled intelligently for search diversity. The flexibility of the global method in comparison to gradient based algorithms must not be compromised due to a limited shape parameterisation model. The shape variables must be adaptable to random variations without exerting to unrealistic shapes. To address this issue, the shape parameters need to be mapped to facilitate smooth and realistic shape generation without compromising design space flexibility.

In the literature, the definition of the design variable solution search space envelope is based on designer experience that is justified by simplified DoE simulations that model the affect of shape variable manipulation on airfoil geometry. Alternately, the bounds of the geometry search intervals are arbitrarily defined and constraints are imposed to avoid unrealistic shapes including fish-tail profiles. The application of the CST method for 2D and 3D transonic shape design in [62] was limited as the scope of the search intervals were not justified. Jeong et al. [57] arbitrarily defines the search limits of the PARSEC function with no valid justification supporting the design decision. Vavalle and Qin [56] define the percentage of search variable perturbations from a base airfoil with the PARSEC methodology. No justifications were provided to reason the magnitude of shape changes implemented. The methodology has issues as the search flexibility is limited to a search process about a user-defined base profile. The affect of varying the benchmark shape on the search limits, hence optimisation results was not presented. Novel design strategies are needed to map the search intervals of the shape variables. Hence, a global optimal shape can be established based on the set design goals.

Solution space mapping must not be influenced by a user-defined base airfoil. The search limits must be restricted to a region that contain aerodynamically acceptable profiles such that computational resources are not exhausted on shapes which are aerodynamically infeasible. To address the identified requirements, the search space must be defined as a function of airfoil operating conditions. This is based on the assumption of similarity, where airfoil class types are directly related to design lift, drag, moment and Reynolds number conditions. The shapes in the particular class type will be related to the defined operating aerodynamic performance. The flight conditions of the candidate shapes examined during optimisation will closely match the design intent. Sobester [145] proved the assumption of similarity for the CST shape function parameters over twelve supercritical airfoils. The similarity assumption was based on airfoil parameters c_l and shape t/c. The results indicated a recognisable scatter of design coefficient pattern and the validity of the similarity assumption was confirmed.

The contribution of this thesis in the context of variable mapping is defined as follows:

- Development and application of a novel inverse shape fitting test methodology (Sec. 4.2.1), to facilitate airfoil design variable search mapping;
- Several off-the-shelf base airfoils for HALE and transonic flight conditions are identified;
- Setting A to represent the approximation of a target airfoil, the shape parameters are computed by the AM-PSO that minimise the mean-squared-error between A and target profile (Eqn. 4.1);

- The shape parameters of each airfoil A, are independently grouped as a function of similarity operating condition parameters at low and high Mach numbers, to identify the scope of the design space; and
- The search limits are defined from the grouping of the shape parameters. The methodology ensures the variable search limits are restricted to regions that contain physically sensible shapes that are close to the design intent.

Despite the identified limitations of the PARSEC and CST methods for airfoil parameterisation (Sec. 4.2.1.2), the transformation of the identified issues and challenges on airfoil design simulations at HALE and transonic flight conditions is validated in Chapter 6. Prior to the integration of the shape function type in the DNO architecture, a novel design variable pre-screening analysis is defined to evaluate the search limits and the importance of each shape coefficient on the objective function.

The design variable pre-screening analysis is defined to: **a)** Establish the search space of each variable with an inverse shape optimisation analysis (Sec: 4.2.1); and **b)** Establish the importance of each variable to airfoil aerodynamics, hence the objective function by a quantitative measure. Theoretically the design variable pre-screening analysis will facilitate an efficient shape optimisation process by mapping the search domain to solution topologies that is restricted to the defined design goals.

4.2.2.1 Solution Search Space

The search intervals of the design variables applied for AM-PSO validation on the benchmark test functions was *a-priori* knowledge in Table 3.2. The search window of the design variables in the select shape parameterisation model type for HALE and transonic airfoil optimisation needs to be defined. The developed inverse shape fitting optimisation process (Sec. 4.2.1) is used to compute the magnitude of the shape coefficients of the target airfoil. Each independent variable is then mapped as a function of the intent operating condition. The distribution of the estimated shape coefficient of the respective airfoil, relative to the other profiles in the analysis is identified and the intervals are defined accordingly.

To represent the data scatter of the geometry variables based on the intent design goals of the target airfoil, different profile types are applied in the inverse shape fitting optimisation analysis. Airfoil types examined are classified into five categories and include the following:

1. HALE: High Reynolds Number (HRN);
2. HALE: Medium Reynolds Number (MRN);
3. NACA 5-6 series type including symmetrical and non-symmetrical profiles;
4. Low Reynolds Number (LRN) sections used in Micro UAVs; and
5. HRN at high transonic speeds.

The aerodynamic performance range and the t/c of the base airfoils for each identified category is summarised in Table 4.7.

TABLE 4.7: Airfoil Category types for Solution Space Mapping

Airfoil Type	$[\text{Mach}_{min}, \text{Mach}_{max}]$	$[R_{n_{min}}, R_{n_{max}}] \times 10^6$	$[t/c_{min}, t/c_{max}]$	$[c_{l_{min}}, c_{l_{max}}]$
a) HALE: HRN	0.10 - 0.50	9.0 - 10.0	0.14 - 0.15	0.10 - 0.46
b) HALE: MRN	0.10 - 0.60	3.80 - 4.0	0.15 - 0.17	0.40 - 0.56
c) NACA	0.70 - 0.75	9.0 - 10.0	0.12 - 0.15	0.30 - 0.70
d) LRN	0.10 - 0.55	0.15 - 0.50	0.073 - 0.15	1.00 - 1.10
e) HRN: High-Speed	0.70 - 0.73	7.0 - 11.0	0.12 - 0.13	0.25 - 0.79

Shape geometry is correlated with operating conditions ϕ_{op}, which is the summation of airfoil characteristics from Table 4.7 as:

$$\phi_{op} = \left| Mach + R_n + t/c + c_{l_{design}} \right| \tag{4.4}$$

The term ϕ_{op} is calculated for each airfoil from Equation 4.4 as a function of the four identified airfoil measuring units (Tab. 4.7). Due to the large scalar deviation in the magnitudes of the four operating units with R_n measured in 10^6 and M_∞, t/c and $c_{l_{design}}$ of order one, the results are normalised to range [0,1] for ease-of-inspection.

The airfoil characteristics from ϕ_{op} are related to the shape parameterisation variable. High-speed airfoils are modeled with sharp nose regions and a low r_{le} is expected to avoid premature flow transition about the leading edge due to peak negative pressure coefficients followed by rapid adverse pressure gradients. Thus, airfoils operating under disparate operating conditions are introduced with the intention of identifying data dispersion in the mapping analysis as a function of ϕ_{op}.

As the mission profile of the MM-UAV will operate at different Reynolds number flight conditions with variations in cruise Mach number and altitude, the search bounds of the shape variables are established by mapping regions which correspond to airfoils designed for low speed for HALE shape design and high-speed for transonic design analysis. The inverse shape fitting will group the design variables of the parameterisation model based on the design intent as:

- **HALE Airfoil Design:** Variables grouped in accordance to ϕ_{op} at HALE-MRN to HRN environments; and
- **Transonic Airfoil Design:** Variables grouped in accordance to ϕ_{op} at HRN: High-Speed conditions.

An alternate approach for solution search space mapping is to introduce additional design parameters in Equation 4.4, as a function of airfoil geometry features and performance aerodynamics. The metric applied to correlate airfoil characteristics to shape parameterisation variables will be improved accordingly. Airfoil features including leading edge radii, camber, trailing edge wedge angles and aerodynamic performance measures including the chord location of boundary layer trip points and shock location at low-and-high Mach numbers respectively, are candidate parameters that are

applicable for the intent requirement. The partition of airfoil geometry and aerodynamic parameters is also viable such that two independent equations, based on the implementation from Equation 4.4 are established. An independent magnitude of ϕ_{op} as a function of shape contour features and aerodynamics will yield a detail analysis of the correlation between geometry parameterisation coefficients and the intent airfoil application goal for solution search space mapping.

A. PARSEC-Modified Search Variables Interval Definition for HALE Shape Design

The search variable interval mapping process is presented for the PARSEC-Modified method. Airfoil variables for HALE performances are grouped in accordance to off-the-shelf shapes designed for low-speed operations at medium to high Reynolds numbers. At transonic flight envelopes, the variables are defined by mapping about identified base airfoils designed for high-speed performances at high R_n. Accordingly the mapped solution search space for airfoil design by the PARSEC-Modified methodology at HALE conditions is presented in Figure 4.21 and Table 4.8.

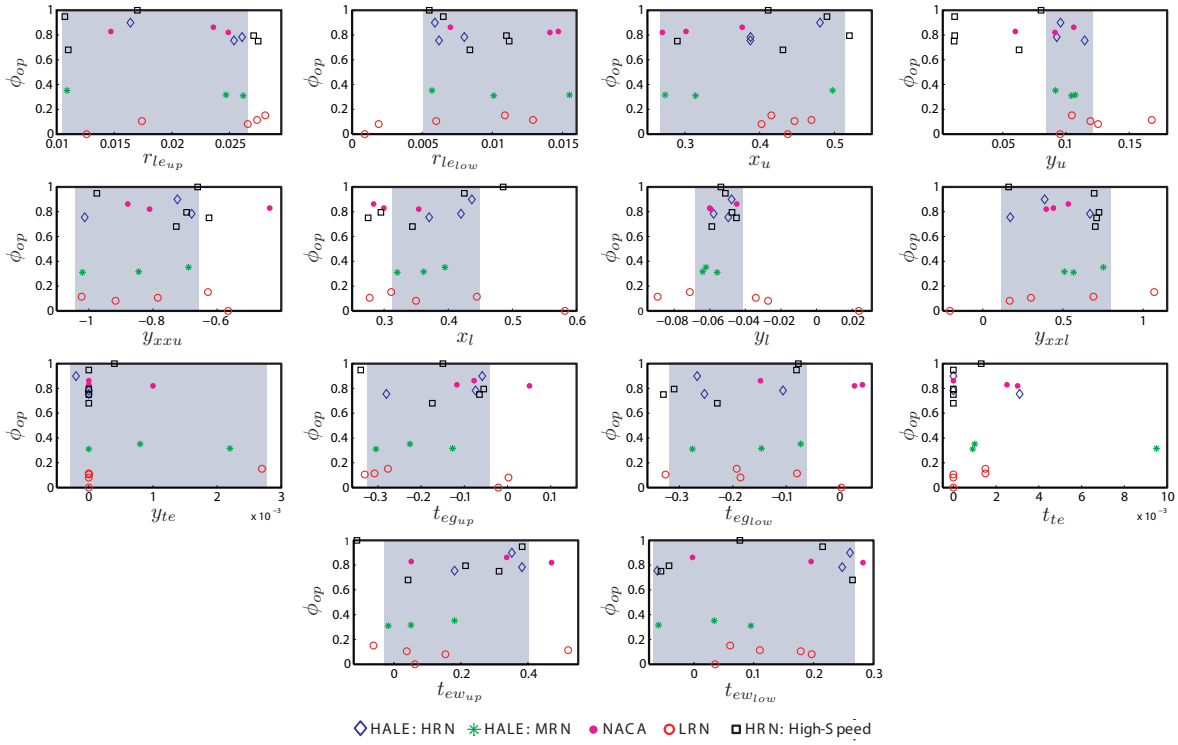

FIGURE 4.21: PARSEC-Modified Variables Solution Space Mapping for Airfoil Design at HALE Mach Numbers

Despite the applied mapping process, the generation of fish-tail airfoils is a design challenge. The PARSEC-Modified variant is sensitive to this issue in comparison to the original method, since the upper and lower surfaces are independently modeled. The trailing edge direction and wedge angles for upper and lower contours contribute to this undesirable effect. If the search limits of the variables $t_{eg_{up}}$, $t_{eg_{low}}$, $t_{ew_{up}}$ and $t_{ew_{low}}$ are mapped in accordance to the identified threshold limits of the current base airfoils, then crossover airfoils will be modeled in the defined search space. The search envelope for the identified variables is compromised from the original HALE: MRN to HRN mapping measure by reducing the domain size accordingly to control this issue. The search domain of the PARSEC-Modified method is presented in Table 4.8.

TABLE 4.8: PARSEC-Modified Solution Search Space for Airfoil Design at HALE Mach Numbers

	Shape Parameter	Minimum	Maximum
$r_{le_{up}}$	: Leading edge radius - Upper Surface	0.0105	0.0285
$r_{le_{low}}$	: Leading edge radius - Lower Surface	0.0050	0.0150
x_u	: Crest of upper surface's x abscissa	0.2873	0.5343
y_u	: Crest of upper surface's y ordinate	0.088	0.125
y_{xxu}	: Curvature at the crest of upper surface	-1.05	-0.620
x_l	: Crest of lower surface's x abscissa	0.310	0.450
y_l	: Crest of lower surface's y ordinate	-0.073	-0.0430
y_{xxl}	: Curvature at the crest of lower surface	0.170	0.750
y_{te}	: Trailing-edge ordinate	-0.020	0.020
$t_{eg_{up}}$	: Trailing-edge direction - Upper Surface (degrees)	-20.05°	-2.86°
$t_{eg_{low}}$	: Trailing-edge direction - Lower Surface (degrees)	-20.05°	-4.01°
t_{te}	: Thickness at trailing-edge	0	0.0030
$t_{ew_{up}}$	: Trailing-edge wedge angle - Upper Surface (degrees)	-3.72°	22.92°
$t_{ew_{low}}$	: Trailing-edge wedge angle - Lower Surface (degrees)	-3.72°	15.47°

The minimum value for $t_{ew_{low}}$ from the variable mapping process in Figure 4.21 is not used in Table 4.8. Instead a DoE analysis confirmed that if the minimum is increased from the initially specified measure of $\approx -57°$ in Figure 4.21 to -3.72°, then the scope of the solution search space that is representative of cross-over airfoils will be minimised. An airfoil generated with shape parameters $t_{ew_{up}}$ and $t_{ew_{low}}$ set at $< -3.72°$ can occur during the iterative airfoil optimisation cycle and may result in the generation of a fish-tail profile. This will only be evident if the remaining shape variables are permutated to values that are restricted to the limited search region that is representative of cross-over airfoils. The application of shape constraints becomes a design requirement to avoid unnecessary CFD computations on unrealistic shapes.

Based on the defined search limits, the generation of zero included wedge angle profiles is also likely during the airfoil optimisation phase. The candidate shape will be characterised by undesirable aerodynamic performances. The theoretical and intelligent mechanisms of the developed optimisation algorithm will be adaptive to this issue and will concurrently avoid solution topologies that are representative of such airfoils.

B. PARSEC-Modified Search Variables Interval Definition for Transonic Shape Design
The PARSEC-Modified shape parameterisation function variable interval mapping at transonic flight envelopes is modeled. The mapping of each variable is about current off-the-shelf, high R_n based airfoils designed for operations at transonic Mach numbers in Figure 4.22.

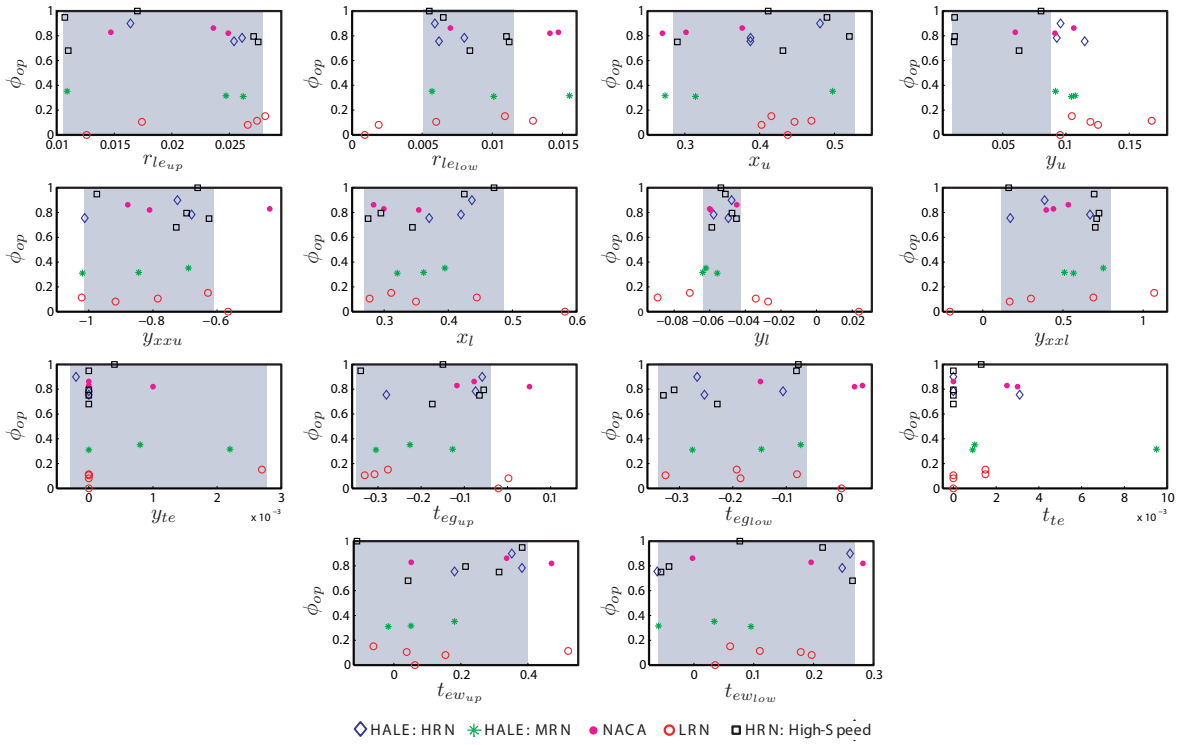

FIGURE 4.22: PARSEC-Modified Variables Solution Space Mapping for Airfoil Design at Transonic Mach Numbers

The relating intervals from the mapping process in Figure 4.22 are presented in Table 4.9.

TABLE 4.9: PARSEC-Modified Solution Search Space for Airfoil Design at Transonic Mach Numbers

	Shape Parameter	Minimum	Maximum
$r_{le_{up}}$	: Leading edge radius - Upper Surface	0.0075	0.0285
$r_{le_{low}}$	: Leading edge radius - Lower Surface	0.0050	0.0115
x_u	: Crest of upper surface's x abscissa	0.2873	0.5343
y_u	: Crest of upper surface's y ordinate	0.0470	0.095
y_{xxu}	: Curvature at the crest of upper surface	-1.05	-0.620
x_l	: Crest of lower surface's x abscissa	0.260	0.480
y_l	: Crest of lower surface's y ordinate	-0.073	-0.0430
y_{xxl}	: Curvature at the crest of lower surface	0.170	0.750
y_{te}	: Trailing-edge ordinate	-0.020	0.020
$t_{eg_{up}}$	: Trailing-edge direction - Upper Surface (degrees)	-22.05°	-2.86°
$t_{eg_{low}}$	: Trailing-edge direction - Lower Surface (degrees)	-21.05°	-4.01°
t_{te}	: Thickness at trailing-edge	0	0.0030
$t_{ew_{up}}$	: Trailing-edge wedge angle - Upper Surface (degrees)	-9.45°	22.92°
$t_{ew_{low}}$	: Trailing-edge wedge angle - Lower Surface (degrees)	-3.72°	15.47°

Notable differences between variable mapping limits at HALE and transonic flight envelopes by the PARSEC-Modified method is isolated to the modeling of the pressure side leading edge radius. In high-speed operations the search space for $r_{le_{low}}$ is restricted to smaller nose radii (Max. $r_{le_{low}}$ = 0.0115) in Table 4.9 in comparison to operations at HALE conditions (Max. $r_{le_{low}}$ = 0.0150) in Table 4.8. The extended nose radii at low speeds is a requirement to mitigate the offset of laminar separation bubbles which can translate to premature flow transition and separation, hence an increase in drag. At high transonic Mach numbers, sharper nose radii are required to delay the generation of shock waves which result in an increase in wave drag. The modeled mapping envelope for airfoil nose radius at HALE and transonic flight conditions, conform to the established airfoil aerodynamic flow principles.

C. Kulfan's [60] CST & PARSEC Method Search Variables Interval Definition

The developed design variable space mapping process is further applied to define the search intervals of the PARSEC and the CST method as a function of the order of the BP in Appendix E, at HALE and transonic flight envelopes. The mapped variable search limits of the CST, PARSEC and PARSEC-Modified methods will be integrated into the DNO approach for airfoil optimisation in Chapter 6.

The impact of a limited shape generation flexibility by the PARSEC method including constraint definition challenge by variable manipulation with the CST approach, on airfoil design simulations will be confirmed in Chapter 6. The defined design variable interval mapping process will facilitate a valid optimisation simulation for the respective shape function type as the search limits are restricted to airfoils that match the design intent. The impact of the identified issues and challenges with the PARSEC and CST methods on airfoil design is assessed accordingly.

4.2.2.2 Design Variables Measure of Importance

With the search limits of the design coefficients established, the importance of each variable on the objective function for HALE and transonic airfoil design is established. The search performance of the optimiser is directly related to the size of the input factor. Consider a one-variable design space measured in n locations by the optimiser. A k-dimensional input factor will require n^k calculations to maintain the same degree-of-measurement. Evaluating the objective function of drag for airfoil design with a high-fidelity CFD solver for every permutation of the design variable combination for a full factorial experiment, will result in a computationally time-intensive simulation. The scenario is referred to as the 'curse-of-dimensionality', where an exponential growth of a hyper-volume as a function of problem space dimensionality occurs in direct optimisation and surrogate modeling processes.

Introduction of multiple-dimensions impacts the location of the global solution. A multiple-dimensional search domain with shape and flow constraints can shift the location of the optimal solution to the intersection of the hyper-surfaces of the different dimensions. A limited search algorithm will have issues establishing the global optimal. Evolutionary search models are preferred over local gradient methods to mitigate the identified demerits (Sec. 2.7.3). Implementing global search models for multi-dimensional problems can result in a sub-optimal solution and computationally time consuming simulations if the search space is ill-defined.

A design variable screening technique is applied to compute the complexity of the search model. The contribution of each shape variable to airfoil aerodynamics, hence objective function is established. The importance of the design factors is ranked and geometry variables with minimal influence identified and eliminated from the search process to reduce the complexity of the design problem. The screening technique developed by Morris [146] is applied, with the assumption that the objective function is deterministic. The algorithm calculates the affect of each variable and establishes the correlation type between input-output as: **a)** Negligible; **b)** Linear and additive; or **c)** Non-linear or involved in interactions with other factors [147].

The algorithm measures the sensitivity of the i^{th} variable to airfoil aerodynamic coefficient as output. Each geometry variable is perturbed one-factor-at-a-time for a discrete number levels p, along each dimension in the defined interval range. Consider a k-dimensional input vector x_i, over a p-level factorial grid, normalised into a unit cube of $[0,1]^k$. The components of x_i, are a set of values such that $x_i \notin \{0, 1/(p-1), 2/(p-1), ..., 1\}$, for $i = 1, ..., k$. The output of the objective function y, is established for the baseline value $x \in D$ and the elementary effect $d_i(x)$ of the i^{th} input factor is calculated in Equation 4.5 [141]:

$$d_i(x) = \frac{y(x_1, x_2, ..., x_{i-1} + \Delta, x_{i+1}, ..., x_k) - y(x)}{\Delta} \tag{4.5}$$

Where:

$$\begin{aligned} y &= \text{Function Output / Aerodynamic Coefficient from Flow Solver} \\ k &= \text{Number of Design Variables} \\ \Delta &= \xi/(p-1); \xi \in IN^*, \text{Elementary Effect step length factor;} \\ & \quad p = \text{No. of Discrete Levels along dimension } x \in D \text{ such that } x_i \leq 1 - \Delta \end{aligned}$$

The distribution of $d_i(x)$ for each x_i is measured at different parts of the design space to establish the relative importance of the shape variable in the select parameterisation model type on airfoil aerodynamics. The mean μ and standard deviation σ of $d_i(x)$ are used as distribution parameters. A large μ indicates the shape variable has an important influence on a corresponding output aerodynamic coefficient. A large spread suggests simultaneous interactions between two variables have a strong influence on airfoil aerodynamics. The computational setup of the algorithm is as follows [141]:

1. Denote sampling matrix B of 0s and 1s with dimensions $k+1 \times k$, such that each column index $i = 1, 2, ..., k$ contains two rows of B that differ only in the i^{th} entry. Consider a lower triangle matrix of 1s as:
$$\begin{bmatrix} 0 & 0 & 0 & \dots & 0 \\ 1 & 0 & 0 & \dots & 0 \\ 1 & 1 & 0 & \dots & 0 \\ 1 & 1 & 1 & \dots & 1 \end{bmatrix}$$
2. A random orientation of matrix B, denoted by B* is established in Equation 4.6.

$$B^* = (1_{k+1,1}x^* + (\Delta/2)[(2B - 1_{k+1,k})D^* + 1_{k+1,k}])P^* \tag{4.6}$$

Where:

D^* = $k - D$ diagonal matrix with each diagonal element either +1 or -1 with probability

1 = Matrix of 1s of size $k + 1, k$

x^* = Randomly selected 'base value' of x from the discretised, $p-$ level design space $\{0, 1/(p-1), 2/(p-1), \ldots, 1 - \Delta\}$

P^* = A $k \times k$ random permutation matrix in which each column contains one element of 1 and remaining zero. No two columns have 1s in the same position

Matrix B^* provides one elementary effect per input variable. The data is stored as $X = B^*$, to represent the screening plan of the experiment. The sampling plan provides r elementary effects for each variable. If r is low, then not all permutation levels of the design variable within the search bounds, related by factor p are examined. A high value of p will increase the number of discrete levels to be explored in each dimension. By increasing r, thus re-generating B^* r times, the probability of covering all levels of the design variable at least once is increased. The accuracy of the sampling plan will establish a valid representation of the sensitivity of the shape variable. In r independent orientations of B^*, to represent multiple elementary effects due to a high value of p, the screening plan X for r orientations becomes:

$$\begin{bmatrix} B_1^* \\ B_2^* \\ \vdots \\ B_r^* \end{bmatrix}$$

3. The objective function for each row of X, which corresponds to the k^{th} design variable is calculated and stored in t as $r(k+1) \times 1$ column vector. The adjacent rows of the sampling plan and the corresponding objective function from t, are used to establish $d_i(x)$ from Equation 4.5 for k elementary effects.

4. The mean and standard deviation of the r elementary effects for each variable is computed and represented to determine the variable activity.

A. Problem Formulation

The pre-screening computational methodology is applied to establish the sensitivity of geometry variables on airfoil aerodynamics. Since, the variables are expressed in varying degree-of-orders of magnitude, the shape coefficients are uniformly distributed in interval [0,1] for the sensitivity analysis. These are then scaled from a unit hypercube to the original distribution without the loss of generality. The aerodynamic goal of airfoil design for HALE and transonic-based platforms requires minimising drag, with constraints on minimum cruise lift. The sensitivity of the airfoil parameterisation model is independently verified to determine the degree-of-activity of the shape variable on lift, drag and moment coefficients. Flow transition point influences drag and can result in premature stall if located about the LE on airfoil upper surface due to surface contamination. The effect of airfoil parameterisation variables on boundary layer transition points on suction and pressure airfoil surfaces is also established.

Coupling the aerodynamic coefficients to measure lift-to-drag is not a viable option. Consider the k^{th} shape variable which may have minor influence on lift but significant on drag. Representing the sensitivity of the variable with lift-to-drag will indicate significant activity due to the drag sensitivity. The specific aerodynamic coefficient contributing directly to the overall sensitivity will not be established due to the coupling affects of the two coefficients. The terms of the objective function and the constraints must be separately analysed so that the sensitivity of the variable on the aerodynamic coefficient is directly established.

The sensitivity of the airfoil parameterisation type is examined. The validity of the pre-screening process is enhanced by addressing the following:

1. The search limits of the design variables is extended to maximise the availability of all airfoil class-types to facilitate an extensive sensitivity analysis. The number of random orientations or the elementary effect of each variable r is set accordingly. Data collated from a reduced design envelope will not provide a valid representative of the level-of-activity of the shape variable; and

2. Failures in solver simulations used to establish the aerodynamic coefficients due to shape irregularities to flow residual convergence issues, will generate false aerodynamic data and/or no results for failed simulations. To address this issue, the sampling plan can be re-generated to ensure the data is noise free such that the pre-screening analysis is representative of converged solutions only. Experiments using XFOIL sampled over 100 airfoils indicated on average three failed simulations and the occurrence of ill-defined solutions is minimal. To represent non-converged data in the pre-screening analysis, aerodynamic coefficients are user-defined with a high magnitude so that they are present as outliers in the screening study.

The interaction between airfoil variables and aerodynamic coefficient as output are qualitatively represented by two-way interaction-based contour plots. In the visualisation approach, the aerodynamic output is decomposed for each variable and the corresponding two-way interactions between the problem design coefficients is modeled. The results are presented in Appendix F. A detailed and valid measure of variable sensitivity to the defined objective is by a statistical measure. The quantitative approach by Morris's [146] algorithm is applied. The methodology facilitates the ranking of the design variables based on the computed level-of-impact to the defined objective function.

The sensitivity of the design variables in the airfoil parameterisation function type is computed at HALE and transonic flight conditions for the MM-UAV design application platform. The XFOIL [78] solver is used for low-subsonic flow computations at HALE conditions at $\alpha = 2°$, Reynolds and Mach number of 4.0 million and 0.10 respectively. The low-fidelity solver TSFOIL [148] is used for transonic flow analysis. The flow settings are simulated to achieve $c_{L^T} = 0.733$, at Reynolds and Mach number of 2.76×10^6 and 0.74 respectively.

The impact of the original PARSEC shape function on airfoil aerodynamics at HALE flight conditions is modeled in Appendix G - Section G.1. The corresponding variable influence by the PARSEC-Modified function is presented in the following sub-section.

PARSEC-Modified Shape Function - Quantitative Measure of Sensitivity at HALE Flight Envelope

Shape variable impact for HALE airfoil design by the PARSEC-Modified method is presented. The design variables are ranked with corresponding impact on the objective function c_d and constraint c_{lmax} in Table 4.10.

TABLE 4.10: PARSEC-Modified Variables Contribution to c_d at HALE Flight Conditions; Mach=0.10, $R_n = 4.00 \times 10^6$, $\alpha = 2^\circ$ & $c_{l_{max}}$ at Mach=0.10, $R_n = 3.00 \times 10^6$ & $\alpha = \alpha_{c_{l_{max}}}$

c_d					c_{lmax}				
PARSEC Modified	μ_M	μ^*	σ_M	Ranked μ^*	PARSEC Modified	μ_M	μ^*	σ_M	Ranked μ^*
x_u	0.0018	0.0074	0.0149	1	x_l	-0.0126	1.4879	4.0614	1
x_l	0.0005	0.0037	0.0131	2	$t_{ew_{low}}$	-0.0117	1.4672	3.9426	2
$t_{eg_{up}}$	-0.0001	0.0035	0.0137	3	y_u	0.2862	1.4652	4.0609	3
y_u	-0.0006	0.0033	0.008	4	$t_{eg_{low}}$	-0.1774	1.435	4.3183	4
y_{xxl}	-0.0001	0.0027	0.0105	5	x_u	0.0922	1.3927	3.8688	5
y_{xxu}	0.0006	0.0026	0.0086	6	y_l	0.2029	1.3517	3.2613	6
$r_{le_{up}}$	-0.0005	0.0025	0.0085	7	y_{xxl}	-0.0495	1.3278	4.0677	7
y_{te}	0.0003	0.0024	0.0089	8	$t_{eg_{up}}$	0.0834	1.2861	4.2082	8
y_l	0	0.0021	0.0097	9	$r_{le_{low}}$	0.1377	1.2074	3.7955	9
$r_{le_{low}}$	-0.0001	0.0019	0.0101	10	y_{te}	0.0891	1.2009	3.0389	10
$t_{ew_{low}}$	-0.0012	0.0019	0.0089	11	$r_{le_{up}}$	-0.118	1.172	3.5293	11
$t_{ew_{up}}$	0.0001	0.0018	0.0112	12	$t_{ew_{up}}$	-0.0024	1.0779	3.8348	12
$t_{eg_{low}}$	-0.0004	0.0016	0.0087	13	y_{xxu}	0.0226	0.8672	3.1503	13

Priority to drag minimisation resulted in the identification of $t_{eg_{low}}$ with a minimal contribution to c_d relative to the rest shape functions modeled in Table 4.10. The variance B^* (Eqn. 4.6), for the ranked PARSEC-Modified variables in Table 4.10, on c_d and c_{lmax} is presented in Figure 4.23.

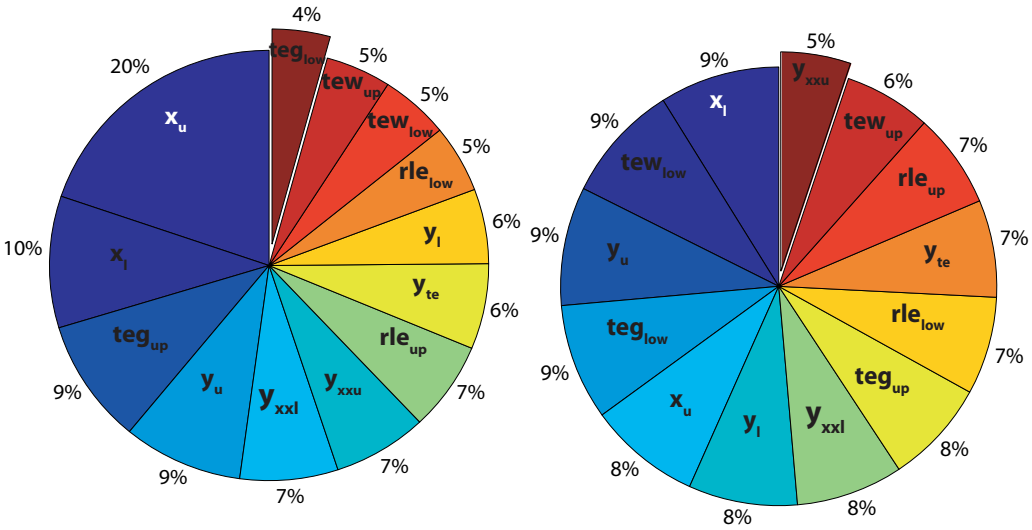

(a) c_d; Mach=0.10, $R_n = 4.00 \times 10^6$, $\alpha = 2^\circ$

(b) $c_{l_{max}}$; Mach=0.10, $R_n = 3.00 \times 10^6$ & $\alpha = \alpha_{c_{l_{max}}}$

FIGURE 4.23: PARSEC-Modified Variables Contribution to c_d & $c_{l_{max}}$ at HALE Flight Envelope

The variable $t_{eg_{low}}$ is modeled with the lowest variance of 4% to c_d in Figure 4.23(a). The graphical representation of variable impact on $c_{l_{max}}$ represents an even distribution of variance with $t_{eg_{low}}$

modeled with 9% level-of-influence in Figure 4.23(b). As the $c_{l_{max}}$ constraint is a secondary design requirement in-lieu of the design objective of minimising c_d, the lowest ranked c_d variable $t_{eg_{low}}$, is identified and eliminated as a permutation design coefficient by the AM-PSO algorithm for HALE airfoil design simulations in Chapter 6. Instead, $t_{eglow} = -15.80°$ and is representative of the design coefficient of the baseline, off-the-shelf NLF(1)-0416 airfoil as computed by the developed inverse shape fitting optimisation process from Section 4.2.1.

The impact of the shape variables on c_l, c_m, c_l/c_d, $x_{tr_{up}}$ and $x_{tr_{low}}$ is presented in Appendix G - Section G.3.

PARSEC-Modified Shape Function - Quantitative Measure of Sensitivity at Transonic Flight Envelope

The impact of the PARSEC-Modified shape variables on transonic airfoil aerodynamics is quantitatively evaluated. Wave drag minimisation is the primary design goal in transonic shape optimisation. The shape variables are ranked as a function of the objective function in accordance to the defined criterion developed by Morris [146] and Campolongo et al. [149] in Table 4.11.

TABLE 4.11: PARSEC-Modified Variables Contribution to $c_{d_{wave}}$ at Transonic Flight Envelope; Mach=0.74, $R_n = 2.70 \times 10^6$ & $c_l = 0.733$

	$c_{d_{wave}}$			
PARSEC Modified	μ_M	μ^*	σ_M	Ranked μ^*
y_u	-0.0012	0.0382	0.0625	1
x_u	0.0077	0.0370	0.0968	2
y_{xxu}	0.0019	0.0303	0.0459	3
y_{te}	0.0027	0.0184	0.0375	4
$t_{eg_{up}}$	-0.0012	0.0121	0.0299	5
$r_{le_{up}}$	-0.0024	0.0117	0.0340	6
$t_{ew_{up}}$	0.0006	0.0116	0.0287	7
y_l	-0.0004	0.0057	0.0139	8
x_l	-0.0024	0.0054	0.0270	9
y_{xxl}	-0.0005	0.0025	0.0140	10
$r_{le_{low}}$	-0.0014	0.0022	0.0192	11
$t_{ew_{low}}$	0.0012	0.0019	0.0154	12
$t_{eg_{low}}$	-0.0004	0.0012	0.0074	13

The distribution of $c_{d_{wave}}$ ranking (Tab. 4.11), is quantitatively presented in Figure 4.24.

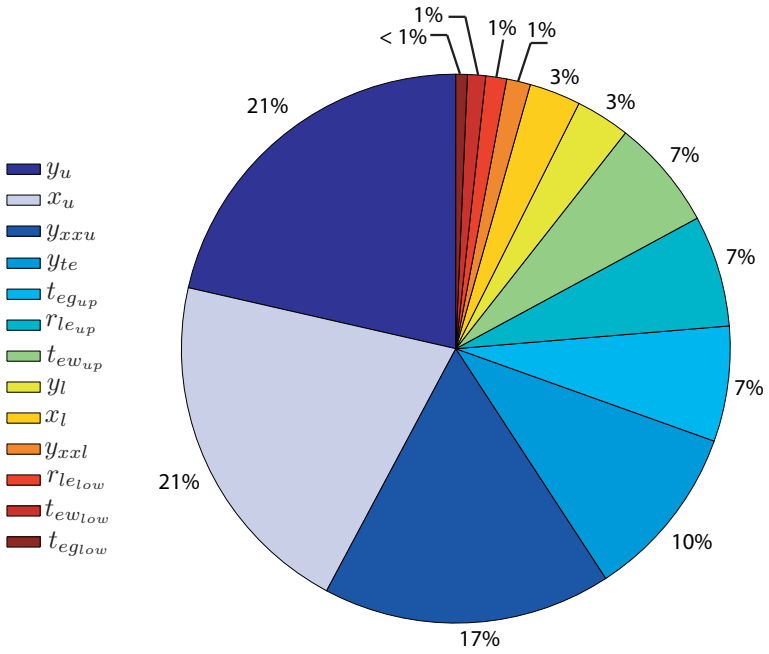

FIGURE 4.24: PARSEC-Modified Variables Contribution to Airfoil Aerodynamics at Transonic Flight Envelope; Mach=0.74, $R_n = 2.70 \times 10^6$ & $c_l = 0.733$

At transonic Mach numbers, airfoil wave drag is directly related to the generation of surface shock waves/s. To further analyse the distribution of $c_{d_{wave}}$ as a function of the PARSEC-Modified design variables from Figure 4.24, the results are quantitatively related to the chord location of airfoil surface shock in Figure 4.25.

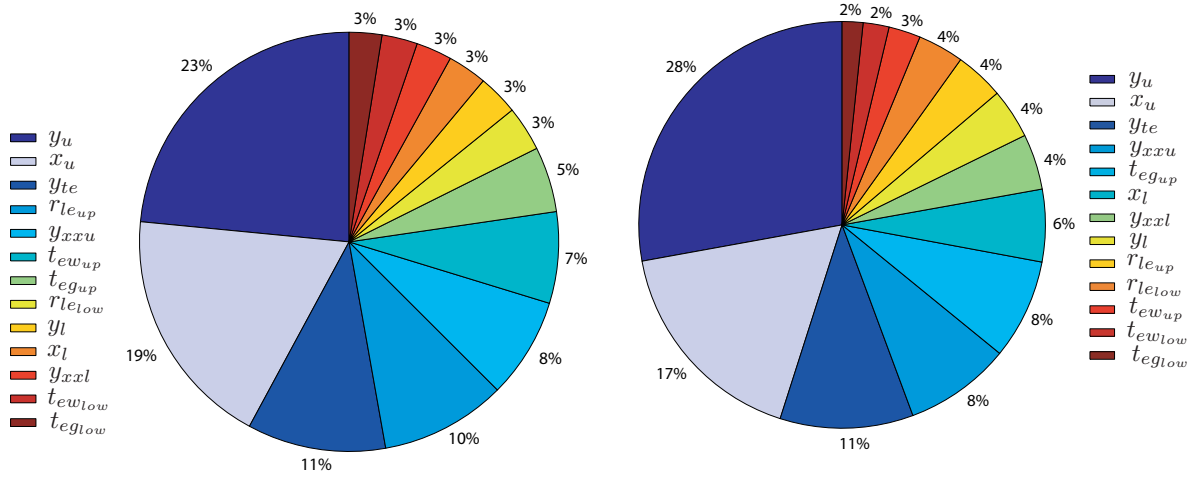

(a) $x/c_{shock\ 1}$ (b) $x/c_{shock\ 2}$

FIGURE 4.25: PARSEC-Modified Variables Contribution to $x/c_{shock\ 1}$ & $x/c_{shock\ 2}$ at Transonic Flight Envelope

The variable y_u has a dominating impact an airfoil wave drag in Table 4.11 and Figure 4.24. Shape coefficient y_u directly controls the maximum upper crest limit of the profile. The results validate the sensitivity of airfoil surface shock to thickness distribution definition. The coefficient for the measure of design variable interaction σ_M for y_u is high (Tab. 4.11), hence representing an active two-way

interaction of y_u on wave drag with all PARSEC-Modified shape variables. A visual representation of shape variable interactions with y_u in Figure F.3, validates an active level-of-activity toward $c_{d_{wave}}$. The quantitative measure-of-activity with $\sigma_M = 0.0625$ for y_u (Tab. 4.11), validates the findings by the qualitative approach.

The effect of wave drag by y_u is directly related to surface shock waves in Figures 4.25(a) and 4.25(b), for shock one and two respectively. The results confirm the dominance of y_u with a percentage impact of 23% and 28% for shock one and two respectively. Variable y_u has the greatest impact on airfoil surface shocks in comparison to the rest PARSEC-Modified shape variables and is modeled with a dominating impact on wave drag in Figure 4.24. Direct comparison of the findings by the quantitative approach (Tab. 4.11 & Figs. 4.24 - 4.25), to the two-way interaction contour plots in Figures F.4 and F.5, for airfoil surface shock one and two respectively, validate the impact of y_u on shock wave generation, hence wave drag. The variable y_u is modeled with an active two-way, level-of-interaction with rest shape variables as a function of surface shock waves. The quantitative measure of the two-way interaction activity by σ_M for wave drag computation, validates the influence of y_u to induce surface shocks, hence a dominating impact on wave drag. The results by the quantitative and qualitative approach support these findings.

The variable $t_{eg_{low}}$ is modeled with the lowest impact on wave drag ($\mu^* = 0.0012$), in comparison to the evaluated shape variables (Tab. 4.11 & Fig. 4.24). The coefficient $t_{eg_{low}}$ is also modeled with a minimal two-way interaction measure with $\sigma_M = 0.0074$, hence represents a minimal relationship between the rest PARSEC-Modified shape variables on $c_{d_{wave}}$. The quantitative results validate the findings of the two-way qualitative $c_{d_{wave}}$ contour chart in Figure F.3, where a visual inspection of the variance of $t_{eg_{low}}$ on drag, validates a minimal level-of-activity and interaction with the defined shape variables.

The quantitative measure-of-impact of $t_{eg_{low}}$ confirms the negligible influence on wave drag with a minimal percentage impact of 3% and 2% on shock one and two in Figures 4.25(a) and 4.25(b) respectively. The identified minimal influence of $t_{eg_{low}}$ on shock wave generation is directly attributed to the low impact of the identified shape coefficient on $c_{d_{wave}}$ in Figure 4.24. The inspection of airfoil shock wave contour plots due to design variable interactions in Figures F.4 and F.5 for shock one and two respectively, confirm the negligible impact of $t_{eg_{low}}$ on surface induced shock/s. The contour tiles for $t_{eg_{low}}$ versus the rest PARSEC-Modified shape variables for shock one and two represents an even contour color marker distribution, hence corresponding to a minimal impact on surface generated shocks. The visual findings of design variable perturbation induced shocks by the qualitative method validates the data by the quantitative approach. The corresponding degree-of-impact of the PARSEC-Modified design variables on c_m and the minimum chord location of c_p is modeled in Appendix G - Section G.4

The results to the design variable measure of importance/impact on the objective function will be applied for airfoil design simulations at HALE and transonic flight envelopes in Chapter 6. Shape coefficients identified with minimal impact on the design goal will be eliminated as a variable to the design problem. Theoretically, the search performance and the efficiency of the developed AM-PSO algorithm will be enhanced by the developed, design variable pre-screening analysis. The airfoil design simulations will confirm the design merits of the: **a)** Developed inverse shape fitting optimisation architecture to evaluate the accuracy and flexibility of several shape parameterisation model types;

b) The validity of the design variable search limits; **c)** The impact of eliminating shape variables with negligible impact on the objective function; and **d)** Measure of feasibility of the developed DNO structure by validating the optimal shape with published off-the-shelf HALE and high-speed profiles.

4.3 Summary

A state-of-the-art airfoil design structure was developed. The fundamental sub-components that govern a valid optimisation architecture are defined and include (Sec. 4.1):

1. A PARSEC-Modified airfoil generator to theoretically maximise function flexibility and accuracy relative to current off-the-shelf parameterisation models.
2. A novel inverse shape fitting optimisation structure to:
   (a) Evaluate the flexibility and accuracy of several airfoil parameterisation models types; and
   (b) Map a valid solution search space for airfoil design simulations at HALE and transonic flight envelopes
3. Design variable pre-screening to assess the impact of airfoil parameterisation variables on the objective function with the aim of enhancing the computational efficiency of the profile design simulation process;

The theoretical merits of the developed design structure will be verified by airfoil optimisation simulations in Chapter 6.

Chapter 5

Flow Solver Validation for Airfoil Design Fitness Function Evaluation

5.1 Overview

The final component in the DNO process is by the integration of low and high-fidelity solvers in the design cycle. To facilitate accurate airfoil design simulations, the computational flow solver for fitness function evaluations needs to be validated. The development of a DNO architecture is governed by extensive DoE simulations to define the setup of the design structure. A low-fidelity solver is preferred for optimisation model definition as it facilitates rapid computational turn-over time to support a comprehensive optimisation model design development process.

A high-fidelity solver is applied for detail airfoil design to enhance the accuracy of the aerodynamic coefficients. The improvement in solver accuracy relative to low-fidelity methods facilitates the definition of critical design-based decisions to be addressed. The validation of a computational domain type for flow analysis at low-subsonic and transonic flight envelopes is addressed in this chapter. The design requirements presented are structured as follows:

1. **Low-Fidelity Solver Validation:** The convergence of solver output as a function of panel node distribution size is established. The defined process aims to minimise the demerits of solver instabilities due to an ill-defined model setup on the DNO structure development process. Computationally cheap fitness function evaluators are needed for:

   (a) *Inverse Shape Fitting*: Required to define airfoil design solution search space by computing airfoil aerodynamics for variable pre-screening from Section 4.2.2.

   (b) *DNO Structure Validation*: To confirm the validity of the developed design optimisation architecture by airfoil design simulations in Chapter 6. The convergence of the solution search space needs to be established by a comprehensive DoE analysis. Computationally time efficient low-fidelity solvers facilitate this requirement.

2. **High-Fidelity Solver Validation:** Procedures are needed to develop a computational test domain with acceptable mesh structure and compatible turbulence model type for accurate aerodynamic performance computation. The validity of the computational process needs to be confirmed with published experimental data to address the following:

   (a) *Expected flow features at HALE flight envelopes*: A boundary layer transition prediction methodology is required for accurate viscous drag prediction at low Mach numbers.

   (b) *Expected flow features at transonic Mach numbers*: Accurate surface shock wave location prediction methodology is needed to estimate wave drag and the corresponding impact on profile aerodynamics including lift and moment.

3. **Angle-of-Attack for Trimming**: Methodology required to estimate AoA for a corresponding user-defined target lift coefficient.

   (a) An aerodynamic constrain to airfoil design is a minimum cruise-specific target lift coefficient c_L^T. The angle-of-attack can be used as a design variable to achieve the user-defined c_L^T. Instead of applying α as a design variable to the problem, a trimming process is used to estimate α for specific c_L^T. Theoretically an efficient design optimisation process will follow as the complexity of the dimensional search space is reduced by neglecting the AoA as a problem variable. The methodology was successfully applied by Namgoong [41] for transonic airfoil design.

   An accurate high-fidelity flow solver is needed to address the defined requirements. The viability of the developed trimming process is confirmed by comparing an estimated lift curve slope of a benchmark shape with published experimental data. An acceptable comparative analysis performance between the two datasets is related to the feasibility of the developed principles in the trimming approach and the computational accuracy of the high-fidelity solver setup.

The listed modules will be addressed in this chapter by a comprehensive design development and validation process. The sub-systems developed will be applied in Chapter 6 for airfoil design by the direct optimisation approach at HALE and transonic flight envelopes.

5.2 Flow Solver Definition

Numerical computation of flow past airfoils needs to be resolved to assess the feasibility of the candidate profile relative to the defined goals. At HALE and transonic Mach Numbers, flow physics is complex due to high viscous effects and the onset of shock wave development respectively. The solver type applied for aerodynamic computation needs to be validated with published experimental data. Accordingly the aerodynamic performance of the established optimal shape will be within an identified solver tolerance limit.

The source of errors by numerical computations must be identified and controlled in the design optimisation process. If the error magnitude is significant, then the optimisation process will generate an aerodynamically infeasible shape and result in a sub-optimal solution. At conceptual design stage,

low-fidelity panel method solvers are applied due to the rapid computation turn-over time. The source and error magnitude of the solver needs to be identified and controlled accordingly. The relationship between node population and the aerodynamic coefficients must be established. A node-independent solver setup is needed to attain a converged aerodynamic coefficient solver analysis.

Low and high-fidelity solvers are applied in the design optimisation process. The accuracy of the solvers varies and the corresponding error thresholds of the respective computational method needs to be verified. In low-fidelity methods, the population size of surface node points influences the accuracy of the algorithm. If the panel node population size is ill-defined then the aerodynamic data will be filtered with noise due to the non-convergence of the flow equations. Accordingly, the design definition of the DNO model will be affected due to the identified limitations within the integrated solver. The setup of the low-fidelity computational algorithm needs to be defined to govern a valid optimisation structure development process.

Despite the disparity of data accuracy by the different variable-fidelity flow solvers, it is assumed that the integrated solver will model the topology of the objective function. A change in solver type will not influence the search process of the optimisation algorithm. The assumption was validated by Hacioglu [150] for transonic airfoil design by the inverse and direct design methods using Neural Networks. The solvers applied in the thesis are as follows:

1. **Low-Fidelity Solvers**

   (a) HALE Mach Numbers - XFOIL [78]: A high-order panel method solver developed by Drela and Youngren [78] with fully-coupled viscous/inviscid interactions is used for low-speed aerodynamic analysis. The inviscid method consists of a linear-vorticity stream function panel method, with finite trailing edge thickness to model a source panel. The Kutta condition is applied to close the flow equation. A Karman-Tsien compressibility correction method is integrated and is valid for flows at low-to-high subsonic Mach numbers.

   (b) Transonic Mach Numbers - TSFOIL [148]: The program solves the transonic small-disturbance theory equations for two-dimensional flow over airfoils. Flow circulation is resolved by either the Kutta condition such that the corresponding c_l is computed as one of the outputs to the solver. Alternately, the lift can be applied as solver input, thus eliminating the Kutta condition requirement. Alternately, the lift and Kutta condition can be set as inputs and the corresponding AoA is established as an output. Boundary conditions are applied to represent wind-tunnel wall effects at subsonic and supersonic free-stream flow conditions [148]. The performance of the solver has been evaluated by Mason [151] at Mach 0.75 and low freestream AoA. The solver outputs a solution with negligible computational effort and is applied in the thesis for the design development of the DNO model for transonic airfoil design simulations.

2. **High-Fidelity Solver**

   (a) HALE and Transonic Mach Numbers - FLUENT [152]: A commercial CFD software which solves the fluid-flow equations by the control-volume approach is used in the thesis. The software facilitates near-wall treatment to resolve viscous and shear strain stresses at airfoil wall region. The transport quantities in the fluid-flow equations are resolved with

turbulence modeling. The software provides choice of several turbulence model types for disparate flow conditions. The accuracy of the RANS flow solver is related to the performance of the turbulence model and the computational mesh domain. No single turbulence model is universally accepted for all class of problems. A validation analysis is needed to define a test model at the defined flight conditions. The solver provides flow transition prediction models to estimate boundary layer trip points which is critical at low-speeds for HALE operations [152]. Theoretically, the tools available in the software will facilitate an accurate analysis of the viscous and wave drag at low and high-speed flight envelopes respectively.

The identified solver-based requirements are addressed in this chapter. The validity of the low-fidelity model is confirmed by empirical experiments. The accuracy of the high-fidelity solver FLUENT [152], including the merits of the developed computational domain topology type and select flow turbulence model is established relative to published experimental data. The results will confirm the magnitude of error threshold in the fitness function evaluator.

5.3 Low-Fidelity Solver Validation

Low-fidelity solvers are applied to develop the DNO architecture. Rapid computation turn-over time is required and low-fidelity solvers facilitate this requirement. The performance of the solvers is sensitive to the setup of the computational algorithm. The accuracy of the solver relative to published experimental data is not a requirement. Instead the aerodynamic output must be converged as a function of the node population size. Empirical test simulations are presented to address this requirement.

The accuracy of XFOIL [78] as a function of node distribution size is validated. Drela and Youngren [78] recommend 160 data points for airfoil surface modeling. A test methodology is applied to verify this recommendation. The convergence of c_l, c_d, c_m and the chord location at minimum c_p are applied in the validation analysis. Test airfoils applied include the NLF(1)-0416, NACA 0012, NACA 63_2615 and LS(1)0417-Mod. The convergence of the aerodynamic parameters as a function of the node distribution size is presented in Figure 5.1.

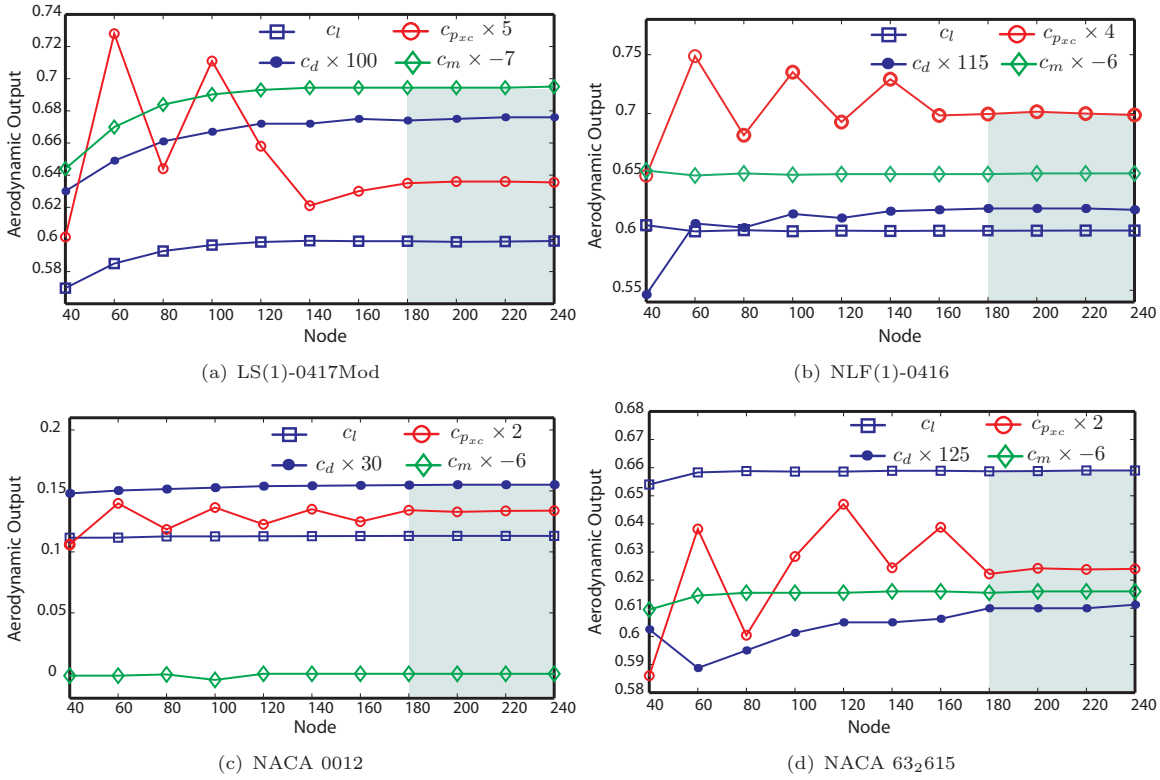

(a) LS(1)-0417Mod

(b) NLF(1)-0416

(c) NACA 0012

(d) NACA 63_2615

FIGURE 5.1: Effect of XFOIL Node Distribution on Aerodynamic Convergence at HALE Conditions; Mach=0.10, $R_n = 4.00 \times 10^6$ & $\alpha = 2^\circ$

Aerodynamic convergence of the modeled parameters is attained at 180 points on each sample airfoil tested in Figure 5.1. Further increases in node population exceeding 180 points does not result in significant changes to the solver output. The shaded region beyond 180 points up to the maximum 240 sample size, confirms the negligible variances in computational data for the respective airfoil. The empirical analysis confirms aerodynamic convergence by XFOIL for the defined flight test conditions is achieved at 180 node points.

The presented test validation process is repeated on the TSFOIL solver to confirm the relationship between node distribution size and airfoil aerodynamics convergence. The empirical experiment on select airfoils confirmed the definition of 160 node panels to facilitate valid and stable aerodynamic analysis by the transonic-based, low-fidelity solver. The evolution of the aerodynamic parameter convergence as a function of node distribution population size, for the modeled airfoils is presented in Appendix H.

5.4 Flow Analysis by a High-Fidelity Solver

Shape optimisation simulations with the integration of high-fidelity flow solvers require a valid computational domain topology to accurately resolve the complex flow features. Airfoil flows are modeled by solving the RANS equations using viscosity models. The pre-processing to the computational analysis requires the definition of a valid mesh topology structure. The turbulence model and wall-functions need to be defined in accordance with the proposed mesh topology to facilitate an accurate

computational analysis. A balance between solver accuracy and computation time to flow residual convergence needs to be defined to attain an efficient and solution accurate aerodynamic airfoil optimisation process.

Flow turbulence has a dominant effect in the transport of mean momentum at transonic Mach Numbers due to the development of shock waves. At the defined flight envelope, there is a strong interaction between the mean flow and turbulence quantities. Airfoil surface will be modeled by large regions of turbulent flow as flow transition can occur rapidly about the leading edge nose radius [9]. Turbulent flows are also effected by the shape contour at the wall surface. The no-slip boundary condition has to be satisfied which affects the mean velocity field. Viscous damping near the wall reduces the tangential velocity fluctuations and the kinematic blocking also minimises the normal fluctuations in the flow. Normal to the wall surface toward the outer portions of the region, turbulence is augmented by the generation of turbulence kinetic energy as a result of the large mean velocity gradients. The expected flow features must be adequately modeled by the defined computational domain structure. The numerical analysis will be sensitive to the mesh topology. A mesh dependency simulation is required such that the turbulence quantities are resolved with acceptable accuracy relative to published experimental data. The mesh generation process must factor the identified flow features into consideration to facilitate an accurate drag prediction methodology.

A fine mesh is required at regions where the mean flow experiences sudden changes and the shear layers are characterised by large strain rates. A fine mesh at the wall-surface affects the fidelity of the numerical computational analysis. Flow reversal by shock development and/or separation must be accurately resolved for accurate drag prediction. The flow residuals at the wall are characterised by large gradients where the momentum and scalar transports are active. A fine mesh will resolve the identified wall-bounded turbulent flows. The level-of-accuracy needs to be identified relative to published experimental data.

5.4.1 Review of One-Equation Turbulence Model Application

An accurate boundary layer transition prediction methodology is needed to resolve wall viscous drag at low R_n for HALE flight conditions. The standard Spalart-Allmaras (SA) model in FLUENT [153] does not facilitate a transition prediction methodology. Instead user-defined functions are integrated to address this requirement. Alternately if the location of the flow transition point is *a-priori* knowledge, then a two-zonal grid system can be applied to simulate regions of laminar and turbulent fluid zones. Extended regions of laminar flow on airfoil upper surface is required to minimise viscous drag for airfoil optimisation at HALE conditions. This is achieved by delaying the onset of flow transition from laminar-to-turbulence further downstream of the leading edge. The requirement is directly stipulated in the design objective function. Manually integrating a flow trip point for HALE airfoil optimisation is not a viable option and a valid transition prediction methodology is needed.

The SA model has been modified in the literature to account for flow transition. Driver and Zingg [154] modified the production and destructive terms in the transport equation by introducing a transition trip term. This acted as a source for the evolution of the turbulent growth in the boundary layer. The method was limited since the accuracy of the flow transition point was dependent on the solution of the MSES [155] solver.

An alternate approach was to exploit the accuracy of the SA model for transition point estimation. Basha and Ghaly [156] introduced flow transition by integrating user-defined functions to modify the SA model in FLUENT [153]. Transition was quantified by an intermittency function to modify the effective viscosity which acted as a multiplier to the turbulent viscosity. Correlation factors were applied based on Thwaites method to approximate the boundary layer parameters for attached flows with R_n greater than 2 million. The inviscid flow velocity along the airfoil was computed by solving the Euler equations in FLUENT. The velocity at the boundary layer edge was calculated to establish the momentum thickness. The onset of flow transition using Michel's theorem was computed and the intermittency function developed by Cebeci [156] was evaluated. Valid computational agreement relative to published experimental data was attained with a boundary layer mesh spacing of $y^+ \approx 1$. The analysis demonstrated the effectiveness of integrating a transition prediction methodology in the RANS solver coupled with a valid turbulence model.

5.4.2 Review of Computational Model Requirements

To facilitate an accurate aerodynamic computational analysis, the mesh domain structure must be well-defined for the intent design application. The mesh wall spacing must be compatible with the theoretical principles of the applied turbulence model such that the accuracy of the computational algorithm is exploited to attain accurate drag prediction. If y^+ is ill-defined (greater than 1), then the estimated transition points can shift upstream of the airfoil surface and result in false drag readings. A $y^+ \approx 1$ is the recommended mesh distance size from the wall surface to the first grid point [157].

Accurate estimation of flow transition points is a critical design goal at HALE flight envelopes. A novel flow transition prediction turbulence model developed by Langtry et al. [158] is applied in the analysis. The transition SST model is based on the coupling of the SST $k-\omega$ transport equations with two additional transport equations that include [157]: **a)** Intermittency; and **b)** Transition onset criteria in the form of the momentum-thickness Reynolds number. To confirm the merits of the 4 equation SST transition prediction model, the performance of the computational algorithm is evaluated against the 3 equation $k-kl-\omega$ model [157] on a test validation case.

5.4.3 High-Fidelity Flow Solver Validation at HALE Flight Envelope

The high-fidelity flow solver is validated for airfoil optimisation at HALE flight envelopes on four grid types with varying degree-of-resolution. Computational domain size is defined by the node population on airfoil upper and lower surface times the node resolution in the $y-$axis. The test domain stretches 20 chord lengths from airfoil body upper, lower and aft of the trailing edge region to the farfield boundary. The distance from airfoil nose to velocity inlet boundary condition is set at 10 chord lengths. The representation of a coarse and fine grid type applied in the validation analysis is presented in Figure 5.2

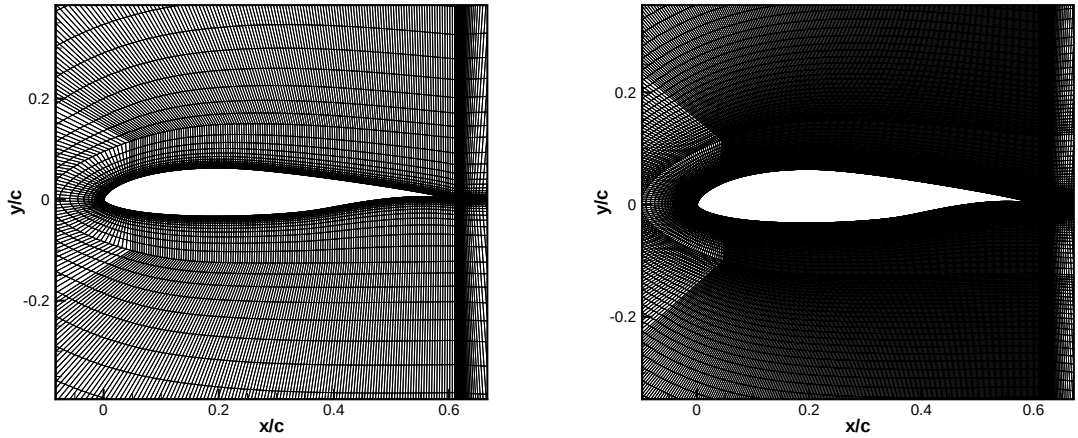

(a) Grid 3 - 144 by 60

(b) Grid 4 - 268 by 60

FIGURE 5.2: NLF(1)-0416 C-Type Computation Grid Domains

The grid wall spacing of the first node point from airfoil surface is set at $y^+ \approx 1$ for all mesh types modeled. The effect of varying the node resolution in the $x-$axis with fixed wall spacing has the effect of modifying cell aspect ratio dx/dy. Airfoil surface bounded cells are characterised with a maximum limit of dx/dy at ≈ 750 in the coarse grid in Figure 5.2(a). This is reduced to ≈ 150 for a fine mesh in Figure 5.2(b). The validity of the high-fidelity solver with varying mesh degree resolution is evaluated. The average percentage error difference $\%\Delta$ of FLUENT [153] and XFOIL [78] relative to published experimental data for a low-speed NLF(1)-0416 airfoil [6] is presented in Table 5.1.

TABLE 5.1: NLF(1)-0416 Airfoil Validation with Experiment [6] by the 3 Equation $k-kl-\omega$ Transition Turbulence Model; $M_\infty = 0.10$, $\alpha = [-3^\circ, \cdots, +10^\circ]$ & $R_n = 4.0 \times 10^6$

Data Type	$\%\Delta c_{l_{\alpha_{[-3,10]}}}$	$\%\Delta c_{d_{\alpha_{[-3,10]}}}$	$\%\Delta c_{m_{\alpha_{[-3,10]}}}$
XFOIL	8.71	9.45	2.95
Mesh 1: 220 by 60	13.60	9.95	3.60
Mesh 2: 210 by 60	14.80	9.19	3.40
Mesh 3: 144 by 60	13.56	9.98	3.57
Mesh 4: 268 by 60	12.78	9.25	3.53

† Shaded row indicates grid with acceptable balance between accuracy & computational efficiency

The computational data from FLUENT is represented by a 3 equation $k-kl-\omega$ turbulence model [157] with integrated transition prediction methodology in Table 5.1. The $\%\Delta$ measure is assessed over a linear AoA range of $[-3^\circ, \cdots, +10^\circ]$ for c_l, c_d and c_m. The shaded results by the low-fidelity solver XFOIL [78] represents a low $\%\Delta$ aerodynamic convergence distribution in comparison to the four disparate mesh types modeled and computed by in FLUENT. The convergence of $\Delta c_{d_{\alpha_{[-3,10]}}}$ by XFOIL is comparable to the computational data by FLUENT with mesh types 1-4. The parameters c_l and c_m by XFOIL yield a lower magnitude of $\%\Delta$ for the identified AoA test range than FLUENT.

Direct comparison of the data by FLUENT with variances in mesh resolution validates the merits of a fine mesh for valid agreement with published experimental data [6]. The low cell aspect ratio distribution ($dx/dy \approx 150$) about airfoil surface with mesh 4, has the effect of resolving the viscous drag with a lower $\Delta c_{d_{\alpha_{[-3,10]}}}$ measure than the data attained by the coarser mesh type 3 (9.25 versus 9.98 in Tab. 5.1). The corresponding $\Delta c_{l_{\alpha_{[-3,10]}}}$ distribution by the finer mesh type 4, further yields a lower magnitude than the coarse mesh type 3 (12.78 versus 13.56) which is characterised by high a $dx/dy \approx 750$ airfoil surface-based cell distribution. The merits of defining a valid cell aspect ratio cell distribution for accurate aerodynamic data predictions is validated.

The 3 equation turbulence model with the $k-kl-\omega$ scheme did not yield acceptable results in comparison to XFOIL. At the defined flow conditions a low-fidelity solver for airfoil optimisation simulations would suffice due to the acceptable accuracy of the model relative to the high-fidelity algorithm. To further evaluate the merits of the high-fidelity solver with experiment and XFOIL, the performance of the 4 equation $k-\omega$ SST transition turbulence model [158] is assessed in Table 5.2.

TABLE 5.2: NLF(1)-0416 Airfoil Validation with Experiment [6] by the 4 Equation $k-\omega$ SST Transition Turbulence Model; $M_\infty = 0.10$, $\alpha = [-3^\circ - 10^\circ]$ & $R_n = 4.0 \times 10^6$

Data Type	$\%\Delta c_{l_{\alpha_{[-3,10]}}}$	$\%\Delta c_{d_{\alpha_{[-3,10]}}}$	$\%\Delta c_{m_{\alpha_{[-3,10]}}}$
XFOIL	8.71	9.45	2.95
Mesh 1: 220 by 60	8.03	5.04	2.97
Mesh 2: 210 by 60	9.04	5.06	2.49
Mesh 3: 144 by 60	8.75	5.07	2.69
Mesh 4: 268 by 60	8.77	5.19	1.05

† **Shaded row indicates grid with acceptable balance between accuracy & computational efficiency**

The distribution of $\Delta c_{l_{\alpha_{[-3,10]}}}$ by FLUENT with variances in grid resolution yields comparable results relative to XFOIL in Table 5.2. The viability of the 4 equation turbulence model is confirmed by solver accuracy with lower $\%\Delta$ error for drag and moment prediction by the four mesh types modeled in comparison to the 3 equation $k-kl-\omega$ data from Table 5.1. The degree-of-accuracy by the 4 equation $k-\omega$ SST model is superior in comparison to XFOIL.

The solver validation results confirm the magnitude of errors for c_l prediction by computational means with the 3 (Tab. 5.1 and 4 (Tab. 5.2 equation turbulence models is significant. The 4 equation model does improve drag and moment prediction relative to experiment in comparison to the 3 equation model. The large and consistent error magnitudes for c_l estimation by the 3 and 4 equation models can be attributed to possible experimental issues in the wind tunnel that may have had an unfavorable impact on the c_l recording. The issue of experimental disturbances subject to uncertainties of wind tunnel corrections and wall effects can degrade the c_l performance of the candidate airfoil. In light of the presented results, the possibility of experimental errors needs to be considered in the validation analysis, hence resulting in excessive ($\approx 9\%$) c_l prediction errors relative to wind tunnel data.

The effect of grid resolution on airfoil aerodynamics by the 4 equation $k-\omega$ SST transition turbulence model is presented in Figure 5.3.

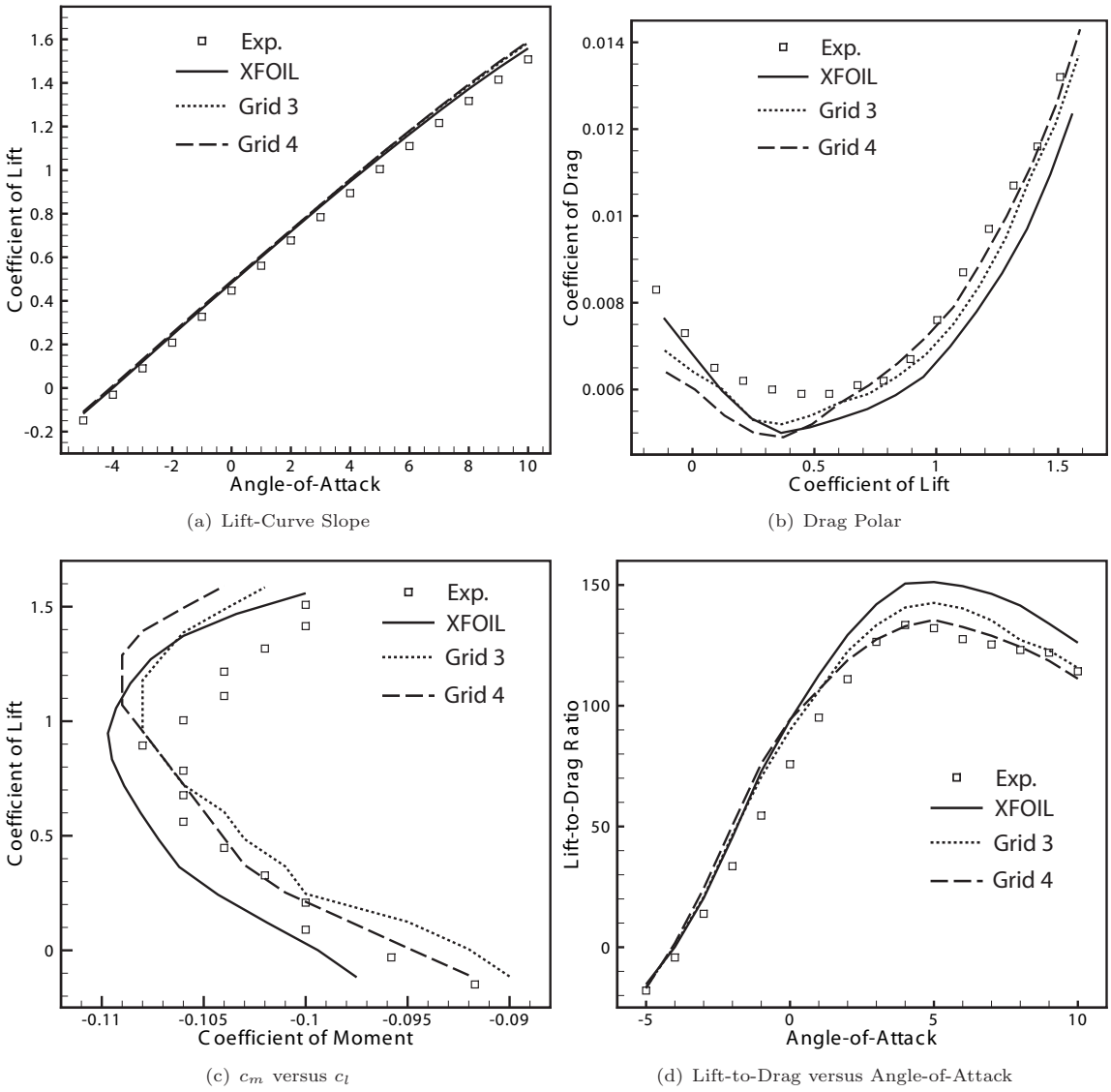

(a) Lift-Curve Slope

(b) Drag Polar

(c) c_m versus c_l

(d) Lift-to-Drag versus Angle-of-Attack

FIGURE 5.3: NLF(1)-0416 CFD Computation Validation with Experiment [6] by the 4 Equation $k-\omega$ SST Transition Turbulence Model; $R_n = 4.0 \times 10^6$; $M_\infty = 0.10$

The convergence of the lift curve slope by the modeled mesh types indicates a negligible impact of grid resolution on solver accuracy in Figure 5.3(a). The low-fidelity solver XFOIL, exhibits a marginally superior solver agreement to experiment at higher AoA in comparison to the data derived by the high-fidelity algorithms. The performance variation between the low and high-fidelity methods on the lift curve slope is minimal.

The impact of grid resolution and solver fidelity on drag is modeled in Figure 5.3(b). The convergence of drag to experiment by XFOIL is acceptable at a low c_l envelope such that $c_l <\approx 0.40$. At $c_l >\approx 0.40$ the accuracy of XFOIL diminishes in comparison to the output from FLUENT. The convergence of drag by the coarse and fine mesh types vary for the defined validation test envelope. The coarser mesh exhibits superior convergence to experiment for a c_l flight envelope restricted to $c_l <\approx 0.60$. The fine mesh type 4 outputs acceptable solver accuracy in comparison to the coarse computational domain for a flight profile defined by $c_l >\approx 0.60$. Airfoil optimisation for HALE flight

profiles will be defined by a constraint on cruise c_l such that $c_L^T = 0.40$ (Chapter 6). The c_d validation analysis confirms the viability of the coarse mesh type 3 to yield acceptable solver accuracy for a c_l flight domain that is within the user-defined c_L^T design intent requirement. The application of mesh 3 for accurate drag computation for airfoil design at the defined flight profile is justified.

The effect of solver fidelity on c_m is validated in Figure 5.3(c). The merits of the high-fidelity solver is confirmed in comparison to XFOIL for c_m convergence to published experimental data [6]. At $c_l >\approx 1.35$, XFOIL exhibits accurate convergence to experiment in comparison to FLUENT. The aerodynamic convergence to experiment by the coarse and fine mesh types is similar. At c_l flight envelope such that $c_l <\approx 0.90$, the finer mesh type 4 exhibits accurate c_m convergence to experiment in comparison to the coarse grid type 3. At c_l flight performance exceeding the defined favorable flight zone for mesh type 4, the coarse grid resolution (mesh 3) yields acceptable c_m agreement to experiment. The disparity in solver accuracy between the coarse and fine mesh types is minimal at the user-defined $c_L^T = 0.40$ design requirement. Despite the finer mesh yielding favorable convergence to published experimental data for the defined shape design flight profile, the integration of a coarser grid type in the DNO process is acceptable due to the minimal performance disparity between mesh types 3 and 4.

The impact of solver fidelity and mesh resolution on aerodynamic efficiency (L/D) as a function of the AoA is modeled in Figure 5.3(d). The performance between the high-fidelity solvers as a function of grid resolution is consistent with negligible performance variances for a lower AoA flight envelope such that $[\alpha = -5°, ..., \alpha = 0°]$. Comparatively the data by XFOIL is modeled with performance variances at the defined flight envelope. At higher AoA flight profiles such that $\alpha > 0°$, the effect of computational model setup on solver accuracy is evident. The output by XFOIL deviates from published experimental data with solver accuracy compromised. Comparatively mesh 4 outputs acceptable convergence to published data than mesh 3 at the defined AoA flight profile ($\alpha > 0°$).

In HALE airfoil design, the maximisation of flight L/D with constraint on c_L^T is a design requirement. At cruise AoA the accuracy of the computed L/D by the high-fidelity solver exhibits acceptable convergence to theory [6] in Figure 5.3(d). The integration of a grid type to the DNO process characterised by rapid computational turn-over without compromising solver accuracy is a design intent. Mesh type 3 adheres to the stipulated design goals.

The effect of solver setup on c_p is modeled in Figure 5.4

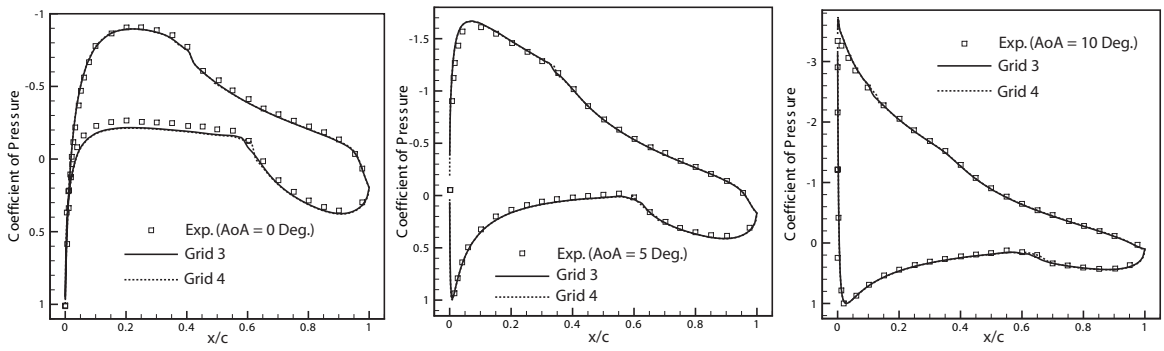

(a) $\alpha = 0°$ (b) $\alpha = 5°$ (c) $\alpha = 10°$

FIGURE 5.4: NLF(1)-0416 c_p CFD Computation Validation with Experiment [6] by the 4 Equation $k - \omega$ SST Transition Turbulence Model; $R_n = 4.0 \times 10^6$; $M_\infty = 0.10$

At $\alpha = 0°$ the upper suction surface is modeled with acceptable accuracy relative to experiment by mesh 3 and 4 in Figure 5.4(a). The theoretical boundary layer transition point from experiment at $x/tr_{up} \approx 0.32$ is resolved by the computational methods. The convergence of c_p to experiment on airfoil pressure surface is overestimated by the two mesh types modeled. The flow transition point $x/tr_{low} \approx 0.50$ is resolved by the coarser mesh type 3 and is overestimated by the finer mesh type 4. The overall impact of the identified discrepancy between the c_p profile and the miss-match in flow transition point on airfoil lower surface has a negligible impact on c_l. The lift curve slope at $\alpha = 0°$ in Figure 5.3(a) confirms this point.

The c_p profile by the two mesh types at $\alpha = 5°$ is validated with experimental data in Figure 5.4(b). Acceptable agreement between the coarse and fine mesh types is attained on airfoil upper and lower surfaces. The boundary layer flow transition points are modeled with acceptable accuracy. The impact of acceptable c_p convergence to experiment on c_l at $\alpha = 5°$ is validated in the lift curve slope in Figure 5.3(a). The variance in lift between experiment and computational data by the respective mesh domains is minimal (Fig. 5.3(a)). The impact of accurately modeling airfoil surface boundary layer transition points on drag is modeled in Figure 5.3(b). At $\alpha = 5°$, $c_l \approx 1.0$ (Fig. 5.3(a)) and $c_d \approx 0.0075$ (Fig. 5.3(b)). The finer mesh type 4 converges directly to the theoretical drag. The coarser mesh type 3 is modeled with $\approx 1\%$ variance in comparison to the published theoretical data. The identified miss-match by the coarser grid is minimal and the integration of mesh 3 for airfoil design simulations is justified with due consideration to the balance between computational accuracy and efficiency.

The c_p convergence to experiment at $\alpha = 10°$ by a coarse and fine grid type is modeled in Figure 5.4(c). The computational distribution by the two mesh types converge to the theoretical data with acceptable accuracy. The peak negative pressure curve about airfoil leading edge is accurately modeled. The boundary layer transition point on airfoil upper surface is resolved by the coarse and fine mesh. On airfoil lower surface, mesh type 4 overestimates flow transition point. Elsewhere, the agreement between computational and experimental c_p data is sound. The impact of c_p convergence to experiment and the merits of accurately predicting flow transition points with acceptable accuracy on L/D was modeled in Figure 5.3(d). At $\alpha = 10°$ airfoil L/D was accurately resolved by the high-fidelity solver relative to published experimental data. The coarser grid type with mesh 3 converges directly to theory while mesh 4 represents a slight deviation from the established data point. The

overall miss-match between a coarse and fine mesh domain type relative to experimental data at $\alpha = 10°$ is negligible at $\approx 1\%$. The validation analysis confirms that at a higher AoA, a coarser grid exhibits an acceptable balance between solver accuracy and computational efficiency.

The shaded mesh 3 in Table 5.2 is selected for low-speed airfoil design simulations by the developed AM-PSO algorithm. The mesh represents an acceptable balance between computational accuracy and efficiency. Mesh 3 is characterised by a low cell count of 8,640 in comparison to 16,080 for the finer grid type mesh 4. The coarser grid demands less computational memory resources and an efficient solver simulation process ensues. The validation results in comparison to published experimental data [6] for the defined test envelope by mesh type 3 validates the merits of the grid type for airfoil design. In comparison the finer mesh type 4 requires greater computing resources with negligible improvements in solver accuracy.

To further confirm the accuracy of the 3 transport equation $k - kl - \omega$ and 4 equation $k - \omega$ turbulence models with experiment [6], the aerodynamic performance charts from the respective models is presented in Figure 5.5

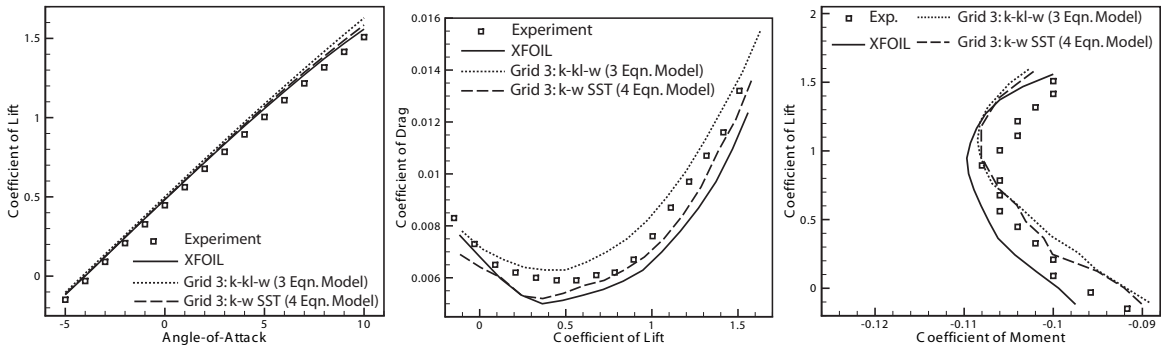

(a) Effect of Transition Model on NLF(1)-0416 Lift-Curve Slope

(b) Effect of Transition Model on NLF(1)-0416 Drag-Polar

(c) Effect of Transition Model on NLF(1)-0416 c_l versus c_m

FIGURE 5.5: NLF(1)-0416 Aerodynamic Computation Comparison by $k - kl - \omega$ & $k - \omega$ SST Transition Models with Experiment [6]; $R_n = 4.0 \times 10^6$; $M_\infty = 0.10$

The distribution of the lift curve slope is modeled in Figure 5.5(a). The cumulative $\Delta\%$ is less than 10% for the modeled AoA test envelope $(-3°, ..., +10°)$ by the low and high-fidelity solvers. The disparity between the computational and experimental datasets increases as the AoA increases. At the lower end of the AoA spectrum ($\alpha = -3°$), the maximum percentage difference by mesh 3 with the $k - kl - \omega$ model is $\approx 38\%$. Comparably XFOIL is modeled with a maximum miss-match of $\approx 25\%$ and $k - \omega$ by $\approx 27\%$ with the same mesh type at the respective AoA. At the extreme AoA test validation spectrum ($\alpha = 10°$), the maximum $\Delta\%$ is reduced. The $\Delta\%$ for mesh 3 with the $k - kl - \omega$ and $k - \omega$ model is $\approx 7\%$ and $\approx 3\%$ respectively. Computation by the low-fidelity solver is modeled with $\approx 3\%$ disparity. The lift-curve representation by XFOIL exhibits the lowest $\Delta\%$ variance between experimental and computational data than the high-fidelity model in Figure 5.5(a). The disparity between $k - \omega$ and XFOIL solver outputs is negligible for the represented AoA test envelope (Tab. 5.2 & Fig. 5.5(a)).

The effect of examined turbulence models on airfoil drag is presented in Figure 5.5(b). The drag is overestimated by the 3 equation $k - kl - \omega$ turbulence model with a percentage variance of $\Delta \approx 10\%$

in comparison to experimental data for the defined test envelope (Tab. 5.2). The data by XFOIL and the 4 equation $k-\omega$ turbulence model is underestimated in comparison to experiment. The low-fidelity solver convergence is underestimated by $\Delta \approx 10\%$ (Tab. 5.2), with variances in excess of $> 5\%$ limited to the lower end of the c_l flight spectrum. The convergence by mesh 3 with the $k-\omega$ turbulence model is acceptable with a tolerance of $\approx 5\%$ (shaded row in Tab. 5.2) in comparison to published wind-tunnel data for the defined test spectrum. Similar to XFOIL, the $k-\omega$ exhibits a variance in excess of $> 5\%$ in comparison to experiment at the lower c_l flight spectrum ($c_l <\approx 0.40$). At $c_l >\approx 0.40$ the computed c_d approaches experiment and is within an acceptable tolerance of $< 5\%$ and remains within the identified accuracy limits up to the upper limits of the defined test envelope.

The convergence of the flow solvers to experiment for c_m as a function of computational fidelity is presented in Figure 5.5(c). The disparity between the datasets is similar by the modeled solvers. The percentage difference between the datasets is $\approx 3\%$ by XFOIL (Tab. 5.2) with c_m underestimated for the defined test envelope in comparison to the theoretical data. The analysis of c_m by the high-fidelity solvers with $k-kl-\omega$ and $k-\omega$ turbulence model is overestimated in comparison to published data. The convergence of c_m by the 3 equation $k-kl-\omega$ model with mesh 3 is represented with a $\Delta\%$ variance of $\approx 4\%$ (mesh 3 in Tab. 5.1) and is marginally greater than XFOIL (Tab. 5.1 $\approx 3\%$ for XFOIL versus $\approx 4\%$ with mesh 3). The computation of c_m by the 4 equation $k-\omega$ turbulence model is also overestimated, yet it exhibits acceptable convergence to experiment. A $\Delta\%$ variance of $\approx 3\%$ is computed for the defined solver setup (shaded mesh 3 in Tab. 5.2). The variance of c_m as a function of c_l is within an acceptable error threshold of $\approx\leq 3\%$ in comparison to the published data. The disparity of the miss-match exceeds $\approx 6\%$ for $c_l > 1.00$. At lift conditions lower than the identified high error threshold, the miss-match between experiment and computational data is $\approx\leq 2\%$.

The boundary layer flow transition points must be accurately resolved to attain a valid estimate of drag. The experiment [6] is executed with surface based microphones attached to the test model (airfoil). The methodology is defined to measure the development of the boundary layer at the nose leading edge, which progresses downstream toward the trailing edge region. The development of a turbulent boundary layer is defined by an increase in noise levels. Comparatively, the laminar boundary layer is silent. Microphones are strategically attached to the airfoil surface to incrementally measure the noise levels over the airfoil, hence the extent of flow transition from laminar to turbulent [6].

The variation in flow transition points by the 4 equation $k-\omega$ SST transition turbulence model on airfoil upper and lower surfaces is presented. Orifice locations representing laminar (Fig. 5.6) and turbulent flow (Fig. 5.7) are modeled.

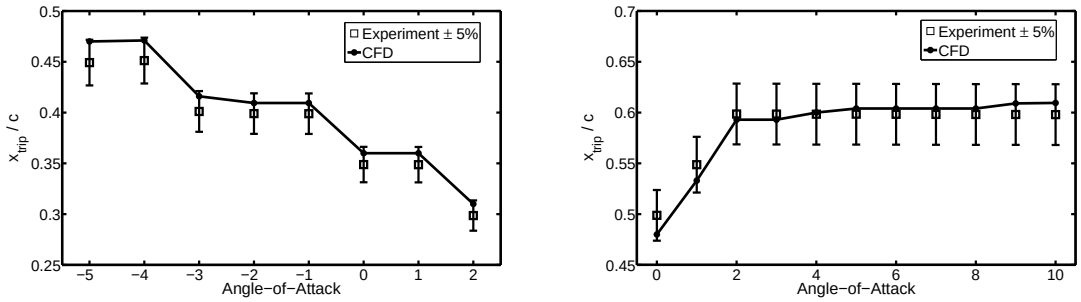

(a) NLF(1)-0416 Upper Surface (b) NLF(1)-0416 Lower Surface

FIGURE 5.6: Comparison of NLF(1)-0416 Boundary Layer Transition (Laminar Flow) Location by Experiment [6] & $k-\omega$ SST Transition Turbulence Model (Mesh 3); $R_n = 4.0 \times 10^6$ & $M_\infty = 0.10$

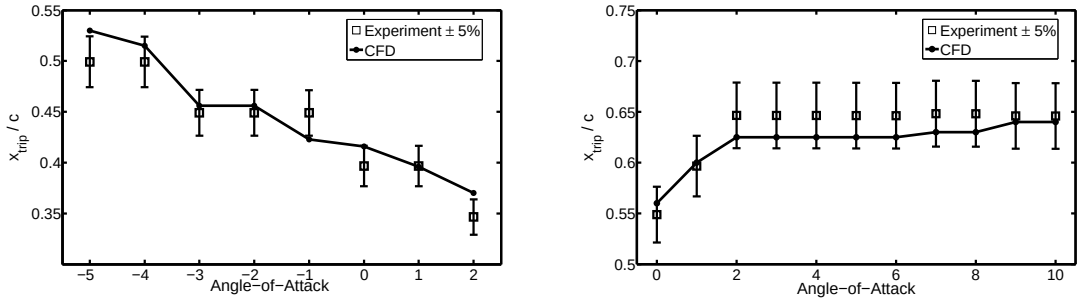

(a) NLF(1)-0416 Upper Surface (b) NLF(1)-0416 Lower Surface

FIGURE 5.7: Comparison of NLF(1)-0416 Boundary Layer Transition (Turbulent Flow) Location by Experiment [6] & $k-\omega$ SST Transition Turbulence Model (Mesh 3); $R_n = 4.0 \times 10^6$ & $M_\infty = 0.10$

The experimental data is represented with ±5% error variances to assess the merits of the applied computational model. The orifice locations at which the flow is laminar in Figure 5.6 is aft of the chord location at which the flow is turbulent in Figure 5.7 for the respective airfoil surface and AoA. The intermediate chord region between laminar and turbulent chord stations represents the flow transitional zone.

On airfoil upper surface the error tolerance for laminar flow estimation between computational and experimental data is characterised by a variance of 5% for an AoA envelope range of $[\alpha = -5°, ..., \alpha = -3°]$ in Figure 5.6(a). The disparity between the dataset decreases as the AoA increases to a testing envelope of $\alpha \geq -2°$. The onset of laminar flow estimation on airfoil lower surface in Figure 5.6(b) is modeled with a lower and consistent variance between the defined datasets for the modeled AoA test envelope. The error variance is at a maximum limit of $\approx 5\%$ at $\alpha = 0°$. The disparity reduces as α increases. The miss-match between the datasets is consistent at $\approx 1\%$ for the modeled AoA test validation range of $[\alpha = 2°, ..., \alpha = 9°]$, hence confirming the merits of the $k-\omega$ SST transition based turbulence model.

The onset of flow transition to turbulence is modeled in Figure 5.7. On airfoil upper surface as the AoA increases, flow transition to turbulence from laminar transits toward the leading edge region in Figure 5.7(a). The variance between computational and experimental data is in excess of 5% at $\alpha = -5°$. There is no distinct pattern between turbulent chord station data variances by experimental

and computational data as a function of the modeled AoA test range. At $\alpha = 1°$, the orifice location at which the flow is turbulent is modeled exactly by the flow solver. At $\alpha = 2°$, the data disparity is in excess of 5%, hence validating the sensitivity of flow transition to turbulence as a function of the AoA.

On airfoil lower surface in Figure 5.7(b), the chord station for turbulent flow shifts aft of the leading edge toward the trailing edge zone as the AoA increases. The chord station transition point as a function of the AoA stabilises over a defined range $[\alpha = 2°, ..., \alpha = 10°]$. The miss-match between the computational and experimental data is modeled with a lower percentage error difference than the data represented for airfoil upper surface (Fig. 5.7(a)). As the AoA increases from $\alpha = 0°$ to $\alpha = 2°$, the error between the datasets reduces significantly. The AoA test range with theoretically stable flow transition point movement from experiment is represented by a consistent turbulent point prediction pattern by the flow solver. The error threshold between the two datasets is constant for the defined AoA range. As the AoA increases and is within the range $[\alpha = 8°, ..., \alpha = 10°]$, the accuracy of the flow solver is further enhanced with a percentage error threshold of $<\approx 1\%$.

The presented data has confirmed the merits of the 4 equation SST $k - \omega$ transition turbulence model [158] for shape optimisation applications at HALE flight conditions. Relatively the 3 equation $k - kl - \omega$ turbulence model did not exhibit performance gains in comparison to XFOIL over the modeled flight test envelope. The error distribution by the 3 equation and the low fidelity method were higher than the 4 equation model. The validity of the SST $k - \omega$ transition turbulence model is confirmed relative to experimental data. The error computed tolerances are within an acceptable threshold. The definition of a coarse grid facilitates an efficient computational analysis while maintaining an acceptable level-of-accuracy.

5.4.4 Angle-of-Attack Trimming Validation for HALE Airfoil Optimisation

The last component that requires design definition in the context of the topics to be presented in this chapter (Sec. 5.2) is an angle-of-attack trimming methodology. The design approach will estimate α for a user-defined cruise c_L^T, instead of directly integrating the parameter as a design variable to the problem. The airfoil lift curve slope is estimated by computing the c_l at a user-defined lower and upper AoA design points. A linear lift curve slope is assumed between the defined data points and curve interpolation/extrapolation is applied to estimate α for a user-defined c_L^T. The estimated α is then used as an input to the flow solver to compute the aerodynamic parameters at the defined target lift coefficient and the objective function is established accordingly.

Theoretically by avoiding the integration of α as a design variable to the problem, efficient optimisation simulations will follow. The complexity of the search topology is enhanced as the measuring location of the objective function by the AM-PSO algorithm is reduced. The validity of the developed AM-PSO algorithm was confirmed for a dimensional search space at $D = 10$ (Sec. 3.6). The trimming approach will reduce the complexity of the search space as one less design variable is applied to define the problem scope.

The estimation of α for a user-defined c_L^T requires two additional flow solver simulations instead of one only if the AoA was to be used as a variable to the problem. The feasibility of the candidate airfoil is governed by three CFD simulations. Flow solver computations are required at the user-defined α lower and upper data points to estimate the lift curve slope. A third solver simulation is then required to compute airfoil aerodynamics at the estimated α from the established lift curve slope by data interpolation/extrapolation.

The lift curve slope of a low-speed NLF(1)-0416 airfoil is estimated by the defined trimming methodology in Figure 5.8

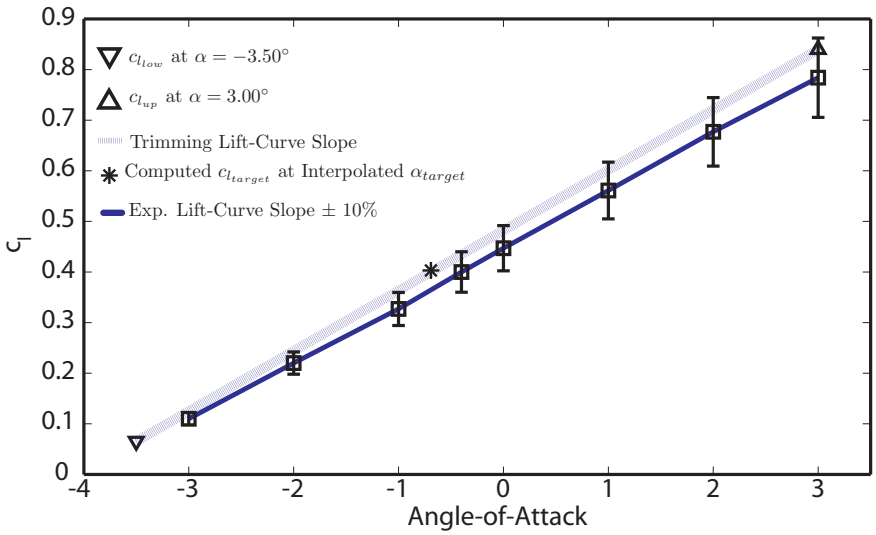

FIGURE 5.8: NLF(1)-0416 Lift-Curve Slope Validation by α_{trim} Approach with Computational Domain Mesh Type 3

The c_l of the NLF(1)-0416 airfoil at a lower limit of $\alpha = -3.50°$ and upper at $\alpha = 3.00°$ is computed from the flow solver. The trimming lift curve slope is estimated by the linear interpolation of the user-defined α data points. The AoA for a cruise c_l of 0.40 is established from the estimated lift curve slope by interpolation at $-0.675°$ in Figure 5.8.

To confirm the validity of the presented trimming approach for lift curve slope estimation, the computational data is compared with experiment [6]. Error whiskers with boundary limits of ±10% are presented about the theoretical lift curve slope for comparative analysis purposes in Figure 5.8. The variance of the experimental versus estimated lift curve slope is within the defined error threshold for the modeled test envelope. Direct comparison between the two datasets confirms the trimming slope is overestimated in comparison to the experimental profile for the defined AoA test spectrum. As the AoA increases, the estimated lift curve slope deviates away from the theoretical profile. At the lower end of the AoA spectrum ($\alpha < -2°$), the variance between estimated and experimental lift curve slope is minimal. At an AoA range exceeding 0°, the miss-match between estimated and experimental slope profile reaches a maximum error limit of $\approx 10\%$. The modeled variances between the datasets has the effect of resulting to a miss-match of cruise based α for $c_L^T = 0.40$. The trimming based cruise α is underestimated in comparison to the experimental magnitude.

The comparative analysis between trimming and experimental based lift curve slope in Figure 5.8 confirmed a miss-match in cruise based AoA between the two datasets. As the estimated AoA is filtered with source errors, the integration of a false AoA to airfoil design process will result in a false measure of shape performance. The extent of the expected errors is modeled in Figure 5.9.

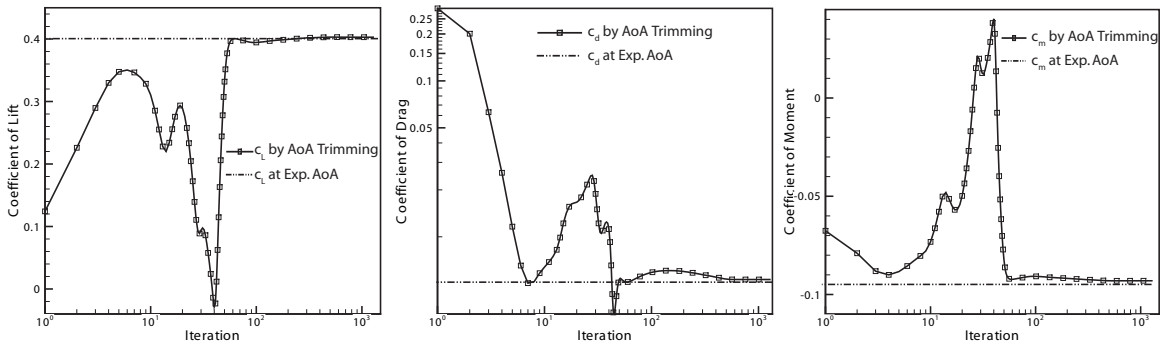

(a) NLF(1)-0416 Convergence to $c_{l_{target}} = 0.40$ by α_{trim}

(b) NLF(1)-0416 Convergence to $c_{d_{target}} = 0.0057$ by α_{trim}

(c) NLF(1)-0416 Convergence to $c_{m_{target}} = -0.098$ by α_{trim}

FIGURE 5.9: NLF(1)-0416 Aerodynamic Coefficients at Target α_{trim} with Computational Domain Mesh Type 3

Airfoil aerodynamics at the trimming-based AoA is compared with shape performance at the theoretical α from experiment in Figure 5.9. The c_l at the trimming-based AoA converges to the user-defined $c_L^T = 0.40$ in Figure 5.9(a). This is expected as the estimated AoA is established from the trimming-based lift curve slope for a c_l at 0.40 in Figure 5.8.

The effect of a trimming-based AoA on airfoil drag is modeled in Figure 5.9(b). A miss-match in drag performance between theoretical and estimated α is expected due to the source-errors within the trimming-based AoA. The trimming approach overestimates c_d by $\approx 0.50\%$. A higher drag magnitude by the trimming-based α approach is justifiable in comparison to the theoretical based α, as the trimming AoA is greater than actual magnitude for the user-defined $c_L^T = 0.40$ in Figure 5.8. The computed variance between the two drag measures is minimal. The effect of an AoA miss-match between the theoretical and trimming-based approach on c_m is modeled in Figure 5.9(c). The variance between the two magnitudes is minimal at $<\approx 1\%$.

The fundamentals of the trimming approach for AoA estimation is demonstrated. The limitations of the proposed methodology is presented. It is shown that the estimated AoA can result to a false interpretation of airfoil aerodynamics due to the errors in the estimated lift curve slope. If the estimated AoA results to a c_l that is less than the user-defined target, a lift-constraint penalty function will be a design requirement. Airfoil drag will also be not representative of shape performance at the intent cruise-specific c_L^T due to an ill-defined AoA. The AoA estimation errors can further result to a false optimal as a potential solution may be unnecessarily penalised for violating the user-defined constraints, which is attributed to the definition of an incorrect AoA by the trimming approach.

The demonstration and validation of the applied trimming principles confirmed the errors in AoA estimation have a minimal affect on airfoil aerodynamics. The lift is estimated with precision and conforms to the user-defined minimum cruise flight-based target requirement. The affect of data disparity between the experimental and trimming-based AoA on drag and moment is restricted to

$<\approx 1\%$ (Figs. 5.9(b) - 5.9(c) respectively). The computed differences are minimal in the context of airfoil design simulations.

5.4.5 High-Fidelity Flow Solver Validation at Transonic Flight Envelope

A computational domain is defined for flow analysis at transonic Mach numbers. The validated model will be applied for high-speed airfoil design by the AM-PSO algorithm in Chapter 6. A C-H grid configuration is modeled and stretches 20 chord lengths from airfoil upper, lower and aft of trailing edge region to the farfield boundary. The distance from velocity inlet to airfoil nose is ten airfoil chord lengths. The domain and configuration sizing is verified by a comprehensive validation process. The distribution of cell aspect ratio about the airfoil nose and wake region is presented in Figure 5.10.

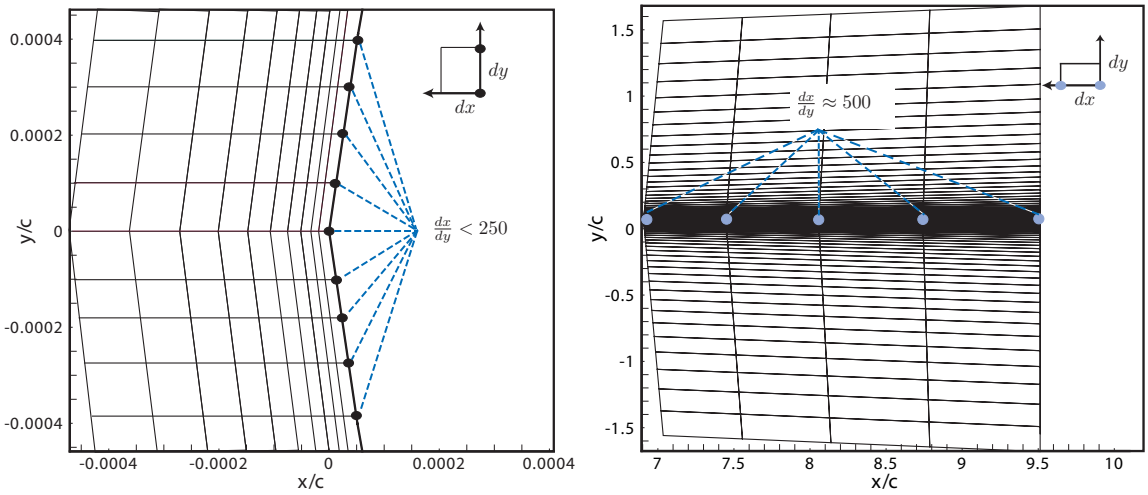

(a) Cell Aspect Ratio at Airfoil Nose Region

(b) Cell Aspect Ratio at Airfoil Wake Region

FIGURE 5.10: Cell Aspect Ratio Representation around Computational Domain

At airfoil wall surface a structured boundary layer is attached to control cell aspect ratio in Figure 5.10(a). It is recommended that the maximum wall cell aspect ratio with flow residuals must not exceed 250 for 2D RANS simulations [153]. At farfield wake regions and domain boundaries where flow residuals are constant, the dx/dy threshold can be increased to a maximum 500. At airfoil wall region a boundary layer is attached to conform with the defined cell size requirements. At the nose region, the maximum dx/dy is ≈ 205. Aft of airfoil leading edge up to the trailing edge zone, the maximum limit of dx/dy increases to ≈ 245.

At the wake region the flow residuals are constant and cell aspect ratio is increased to ≈ 500 in Figure 5.10(b). The minimum distance in the $y-$axis is fixed to attain the required y^+ tolerance. The node population in the $x-$axis is reduced, which increases the cell aspect ratio. By increasing the limits of dx/dy, the mesh node population is controlled and the computational mesh size is minimised. Theoretically a computational domain with nodes clustered in flow residuals regions and fewer cells at farfield boundaries will correspond to an efficient computational analysis without compromising solver accuracy.

Flow solver validation is performed on a current off-the-shelf transonic based RAE 2822 airfoil [9]. Comparison of solver aerodynamics with published wind-tunnel experimental data is performed to verify the accuracy of the high-fidelity solver. Four computational grids with varying degrees-of-resolution are examined. The coarsest of the four grids is presented in Figure 5.11.

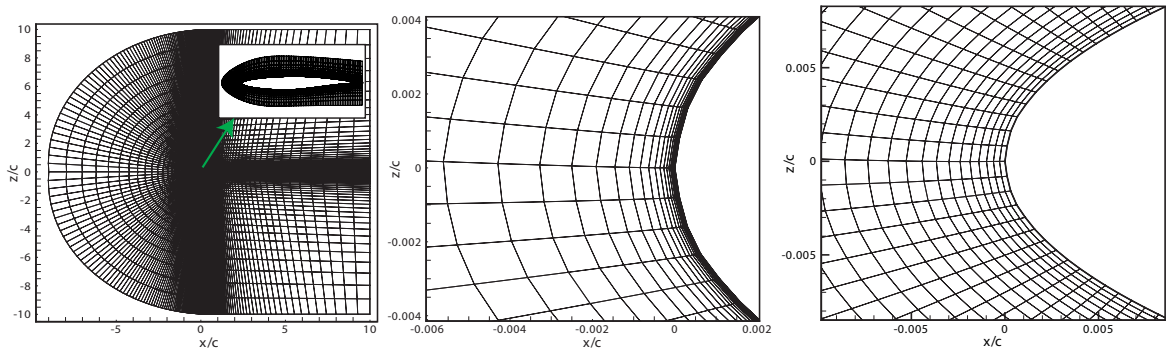

(a) Test Grid (b) $y^+ \approx 1$ (c) $y^+ > 30$

FIGURE 5.11: RAE 2822 Airfoil 29 by 29 Computational Domain

The layout of the C-H type grid is modeled in Figure 5.11(a) with figure inset representing the attached, structured mesh boundary layer on airfoil surface. The distribution of the cells about the surface correspond to a wall spacing of $y^+ \approx 1$ in Figure 5.11(b). The effect of increasing the wall-spacing threshold to $y^+ \approx 30$ on solver accuracy by the select turbulence model relative to published experimental data is verified. The distribution of the cells about airfoil nose region with spacing $y^+ \approx 30$ is presented in Figure 5.11(c).

The finer of the four grid types modeled is presented in Figure 5.12

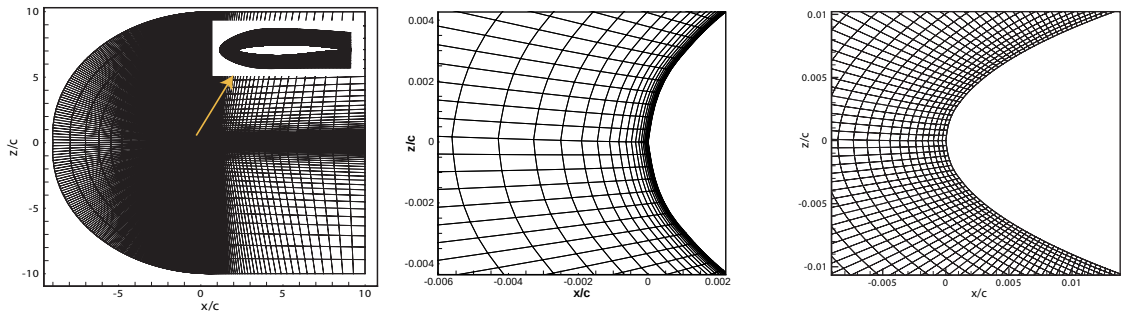

(a) Mesh 4 Test Grid (b) $y^+ \approx 1$ (c) $y^+ > 30$

FIGURE 5.12: RAE 2822 Airfoil 129 by 129 Computational Domain

The dense population of surface nodes represents a larger computational domain cell size distribution in Figure 5.12(a) relative to the coarser grid in Figure 5.11(a). Due to the increase in grid wall surface node population, the maximum surface attached cell aspect ratio is reduced from ≈ 250 for the coarse grid, to ≈ 55 for the finer mesh representation. At the wake region, cell dx/dy is reduced from ≈ 500 to ≈ 250, from the coarse to fine mesh respectively.

The modeled cell distribution comparison between coarse and fine grids is also established at $y^+ \approx 30$. The cell aspect ratio is lower about the airfoil wall surface in Figure 5.12(c) in comparison to the coarse grid in Figure 5.11(c), due to an increase in node distribution size about the x and $y-$axis. The cell stretch ratio is further reduced and an extended number of cells with low dx/dy distribution are within the airfoil wall surface. The reduction in dx/dy is extended across the mapped computational domain due to the increase in node population definition by the fine mesh representation.

The published experimental data for the RAE 2822 airfoil [9] is used to assess the accuracy of FLUENT as a fitness function evaluator for airfoil design at transonic flight envelopes. The experiment was setup with surface roughness to induce boundary layer tripping at a specific chord location. The defined test conditions are transferred into the computational domain to facilitate a valid comparative analysis between experiment and computational data. The computational domain is defined with distinct fluid zones in Figure 5.13.

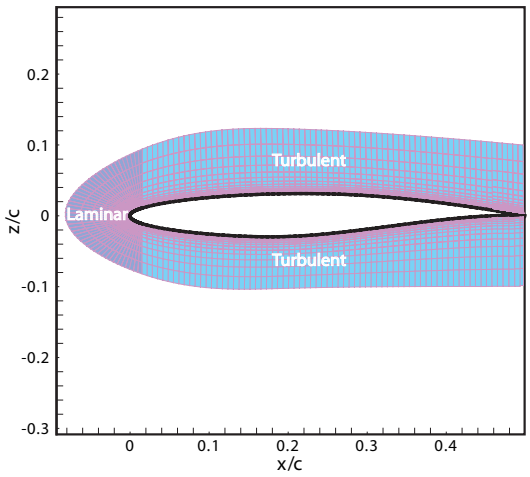

FIGURE 5.13: Boundary Layer Fluid Sub-domain Zones for Transition Modeling around RAE 2822 Airfoil

Boundary conditions are imposed in the defined laminar and turbulent fluid zones in FLUENT [153] to duplicate boundary layer tripping settings from the experiment. The turbulent kinematic viscosity in the laminar zone is set at zero and is activated in the turbulent region. The defined setup does not model the fluid transition region from laminar to turbulent. Instead, the flow is activated from laminar to turbulent due to fluid transition between the adjoining zones in Figure 5.13.

The solver output simulating the aerodynamics of the RAE 2822 airfoil at experiment conditions of M_∞=0.740, $\alpha = 3.19°$ and $R_n = 2.7 \times 10^6$ is established and compared with wind-tunnel data [9]. The effect of grid density and wall-spacing on airfoil aerodynamics is modeled with the aim of achieving a grid-independent solution. The validity of the $k-\omega$ SST transition turbulence model [158] with the following flow initialisation schemes are examined: **a)** The Full Multigrid (FMG) method [159]; and **b)** Mean inlet velocity set within the defined computational domain envelope. The results are presented in Table 5.3.

TABLE 5.3: RAE 2822 Computational Data Comparison with Experiment [9] by the $k-\omega$ SST Transition Turbulence Model with Mean Velocity for Flow Initialisation; M_∞=0.740, $\alpha = 3.19°$ & $R_n = 2.7 \times 10^6$

(a) $y^+ \approx 1$ Wall Spacing

Data Type	c_l	c_d	c_m
Experiment [9]	0.733	0.0188	-0.0860
Mesh 1: 220 by 60	0.741	0.0197	-0.0840
Mesh 2: 210 by 60	0.737	0.0198	-0.0833
Mesh 3: 144 by 60	0.732	0.0198	-0.0838
Mesh 4: 268 by 60	0.731	0.0198	-0.0833

(b) $y^+ > 30$ Wall Spacing

Data Type	c_l	c_d	c_m
Experiment [9]	0.733	0.0188	-0.0860
Mesh 1: 220 by 60	0.739	0.0215	-0.0844
Mesh 2: 210 by 60	0.737	0.0214	-0.0842
Mesh 3: 144 by 60	0.735	0.0215	-0.0840
Mesh 4: 268 by 60	0.740	0.0217	-0.0847

† **Shaded row indicates grid with acceptable balance between accuracy & computational efficiency**

The effect of applying the mean velocity for flow initialisation to the computational domain on solver aerodynamics is evaluated in Table 5.3. The shaded grid arrangement exhibits an acceptable compromise between solver accuracy and efficiency. The coarse mesh 3 converged in six minutes compared to 13 minutes with the higher-resolution mesh 4. The effect of minimum grid spacing distance from airfoil wall to the first cell point y^+, on solver accuracy is evaluated. The merits of setting y^+ to ≈ 1 in Table 5.3(a) on solver accuracy is validated in comparison to $y^+ \approx 30$ in Table 5.3(b). The percentage difference between converged c_l with mesh 3 to published experimental data at $y^+ \approx 1$ is negligible. The c_p as a function of wall grid spacing is presented in Figure 5.14.

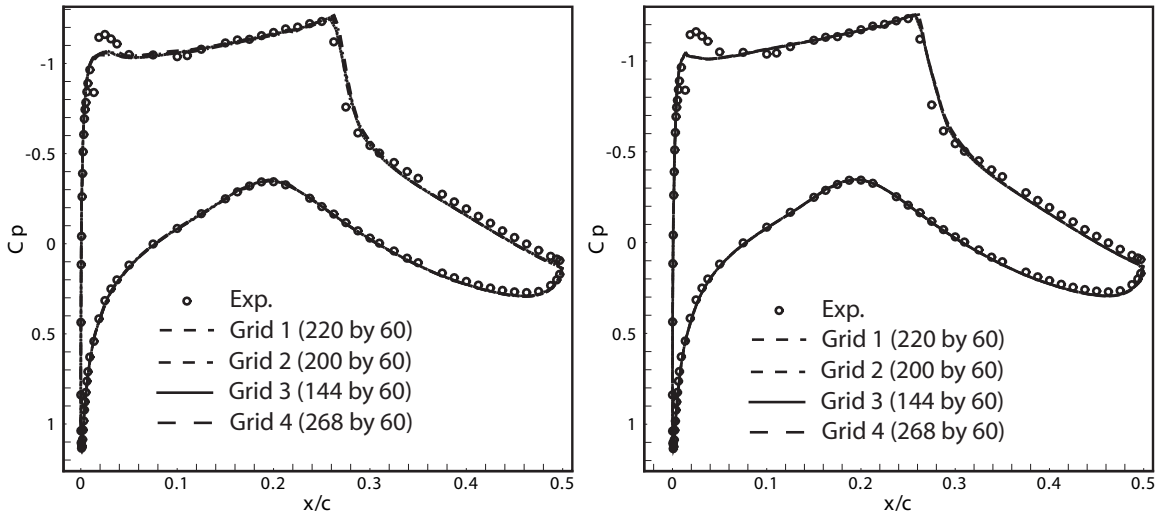

(a) $y^+ \approx 1$ (b) $y^+ > 30$

FIGURE 5.14: c_p Computational Data Comparison with Experiment by $k-\omega$ SST Transition Turbulence Model with Mean Velocity for Flow Initialisation; M_∞=0.740, $\alpha = 3.19°$ & $R_n = 2.7 \times 10^6$

The c_l variance between mesh types modeled with wall-spacing $y^+ \approx 1$ and $y^+ \approx 30$ is limited to the suction peak c_p miss-match between theoretical and computational data in Figure 5.14. The mesh with wall-spacing $y^+ \approx 1$ exhibits an acceptable c_p agreement between computational and

experimental data over the airfoil surface in Figure 5.14(a). The aerodynamic performance difference is restricted about the leading edge region and a miss-match between the two datasets is established. An increase in mesh resolution from coarse to fine grids does not improve c_p modeling about the identified region. Elsewhere the match between experimental and computational data is acceptable with the solver accurately resolving surface shock location.

The effect of increasing y^+ to $\approx$ 30 degrades the c_p convergence by the solver relative to the experimental data about the leading edge zone in Figure 5.14(b). The miss-match between the two datasets at the identified region is greater than the case modeled with $y^+ \approx 1$ (Fig. 5.14(a)). Elsewhere there is an acceptable agreement between the two datasets as a function of mesh size resolution with each grid accurately modeling surface shock location. Despite the issues of resolving the peak c_p distribution by the solver, the overall affect on c_l is negligible for the two wall-spacing experiments tested in Table 5.3. The c_m performance is also not affected as airfoil aft loading by the solver is modeled with accuracy for all grid spacing and mesh resolution types examined in Figure 5.14.

The percentage difference variation in c_d and c_m from experiment is $\approx 5\%$ and $\approx 3\%$ respectively with $y^+ \approx 1$ in Table 5.3(a). An increase of y^+ to ≈ 30 does not affect the convergence of computed c_l and c_m parameters (Tab. 5.3(b)). The percentage difference of c_l between computed and experiment remains negligible. The miss-match in c_m is reduced to $\approx 2\%$ in Table 5.3(b) in comparison to the finer mesh at $y^+ \approx 1$ (Tab. 5.3(a)). The c_d is sensitive to grid wall-spacing. At $y^+ \approx 30$ the percentage difference between experiment and computed data increases to $\approx 30\%$ in comparison to $\approx 5\%$ with $y^+ \approx 1$.

The effect of flow initialisation by the FMG scheme on computational accuracy is modeled in Table 5.4.

TABLE 5.4: RAE 2822 Computational Data Comparison with Experiment [9] by $k-w$ SST Transition Turbulence Model with the FMG Initialisation Approach; M_∞=0.740, $\alpha = 3.19^\circ$ & $R_n = 2.7 \times 10^6$

(a) $y^+ \approx 1$ Wall Spacing

Data Type	c_l	c_d	c_m
Experiment [9]	0.733	0.0188	-0.0860
Mesh 1: 220 by 60	0.737	0.0197	-0.0833
Mesh 2: 210 by 60	0.776	0.0198	-0.0873
Mesh 3: 144 by 60	0.733	0.0196	-0.0831
Mesh 4: 268 by 60	0.742	0.0200	-0.0838

(b) $y^+ > 30$ Wall Spacing

Data Type	c_l	c_d	c_m
Experiment [9]	0.733	0.0188	-0.0860
Mesh 1: 220 by 60	0.735	0.0212	-0.0840
Mesh 2: 210 by 60	0.734	0.0212	-0.0838
Mesh 3: 144 by 60	0.737	0.0216	-0.0843
Mesh 4: 268 by 60	0.740	0.0216	-0.0845

† Shaded row indicates grid with acceptable balance between accuracy & computational efficiency

The FMG initialisation approach yields an improvement in solver accuracy for the two grid wall-spacing configurations examined in Table 5.4, in comparison to the mean velocity inlet initialisation method in Table 5.3. At $y^+ \approx 1$, mesh 3 represents an accurate aerodynamic convergence to the theoretical data in comparison to the other mesh configurations modeled in Table 5.4(a). The c_l converges directly to the experimental data and the miss-match in c_d is reduced from $\approx 5\%$ with

mean velocity initialisation scheme to ≈ 4% with FMG at $y^+ \approx 1$ wall spacing. There is a subtle increase in the miss-match of c_m by the FMG initialisation approach at ≈ 3.40% in comparison to ≈ 3% with mean velocity initialisation method. Relatively an increase in wall spacing distance to $y^+ \approx 30$ has limited accuracy for the respective mesh types in Table 5.4(b). To further model the affect of the FMG initialisation approach on airfoil aerodynamics with $y^+ \approx 1$ and $y^+ \approx 30$, the c_p distribution is examined in Figure 5.15.

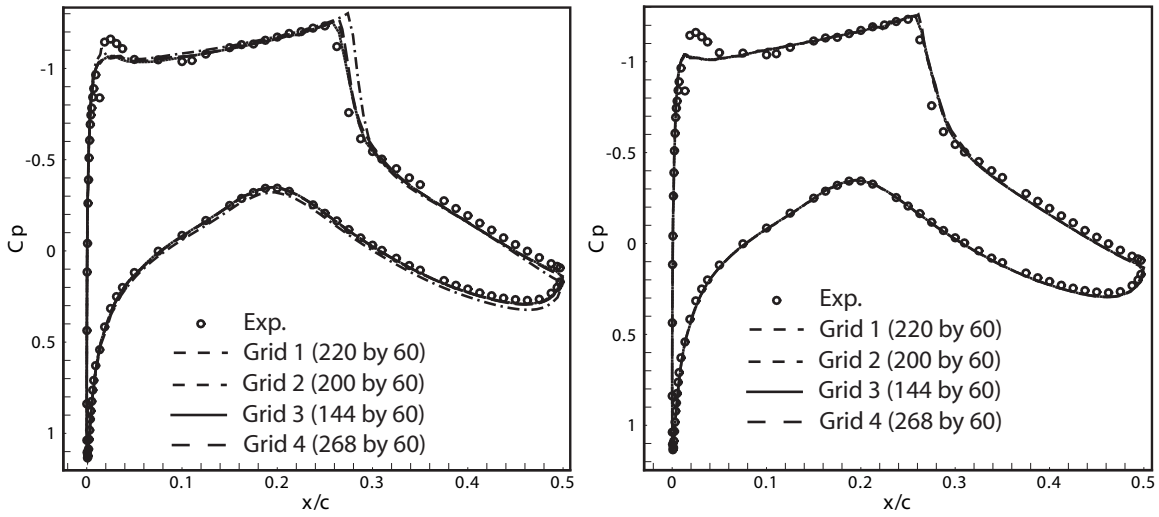

(a) $y^+ \approx 1$ (b) $y^+ > 30$

FIGURE 5.15: c_p Computational Data Comparison with Experiment by $k - \omega$ SST Transition Turbulence Model with FMG Flow Initialisation; M_∞=0.740, $\alpha = 3.19°$ & $R_n = 2.7 \times 10^6$

The effect of the FMG initialisation scheme has a limited impact on c_p in comparison to the flow initialisation approach by the mean inlet velocity method. A miss-match between experimental and computational suction peak c_p performance about airfoil nose region is evident for $y^+ \approx 1$ and $y^+ \approx 30$ in Figure 5.15. The miss-match pattern was also modeled in Figure 5.14 for flow initialisation by the mean inlet velocity approach. Regardless of grid resolution and wall spacing distance, the variance between the two datasets at the nose region remains with negligible convergence improvements as a result of implementing the FMG model.

The effect of increasing y^+ to ≈ 30 corresponds to a c_p convergence in Figure 5.15(b) that is similar to the data modeled by the mean inlet flow initialisation approach in Figure 5.14(b) at the respective wall-spacing distance. A peak negative suction c_p miss-match about the leading edge region for all grid types examined is evident. Elsewhere the computational data converges to the experimental c_p distribution with acceptable agreement. The shock location and airfoil aft loading are accurately represented.

The demerit of increasing the distance between airfoil wall and the first grid point with $y^+ \approx 30$ on solver accuracy was established in Table 5.4(b). A y^+ which exceeds the viscous sub-layer has the affect of reducing the accuracy of c_d. The shaded mesh two resulted in a closer agreement with experiment data in comparison to the rest mesh types modeled. The accuracy of c_l convergence is acceptable. The miss-match in c_m is ≈ 3% and corresponds to the best result established in the validation analysis ($y^+ \approx 1$ grid - mesh 3 in Tab. 5.3(a)). The miss-match in c_d is high in comparison

to the data at $y^+ \approx 1$ (Tab. 5.4(a)) at $\approx 11\%$. The miss-match is lower than the $\approx 30\%$ variance computed with the mean velocity initialisation approach at the same grid type (Tab. 5.3(b)).

The inspection of airfoil surface induced shock at $y^+ \approx 1$ by the computational method with shaded mesh type 3 from Table 5.4(a) is presented in Figure 5.16.

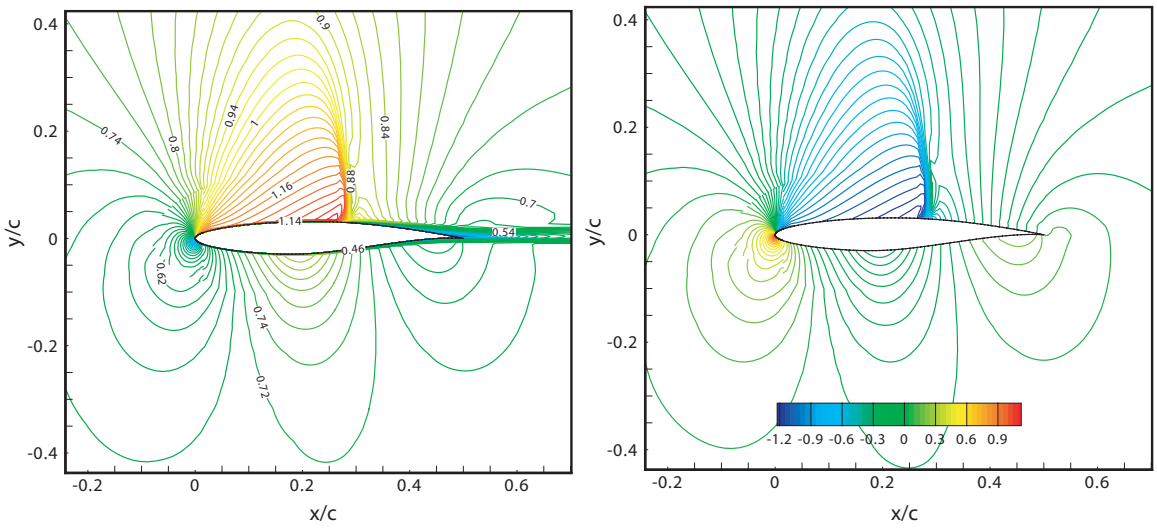

(a) M_∞ (b) c_p

FIGURE 5.16: RAE 2822 Aerodynamic Performance Contours; $M_\infty = 0.740$, $\alpha = 2.87°$, $R_e = 2.7 \times 10^6$ & $c_l = 0.733$

The Mach (Fig. 5.16(a)) and pressure (Fig. 5.16(b)) contours confirm airfoil surface shock at chord station $x/c \approx 0.27$. Peak negative pressure about airfoil surface nose region corresponds to supersonic Mach numbers at the surface. As the flow approaches freestream about the airfoil nose, the peak negative pressure subsides and the Mach number decreases. The pressure at airfoil wall region is low and the corresponding Mach number is supersonic. Upstream of airfoil wall surface toward freestream conditions, the pressure increases and the Mach number decreases proportionally. Downstream of chord shock location at $x/c \approx 0.27$ toward the trailing edge region, airfoil wall Mach numbers are at low subsonic speeds in Figure 5.16(a) and the pressure distribution matches freestream conditions accordingly in Figure 5.16(b).

To verify the computational merits of the FMG approach, the convergence of the aerodynamic performance parameters as a function of solver iterations is examined in Figure 5.17.

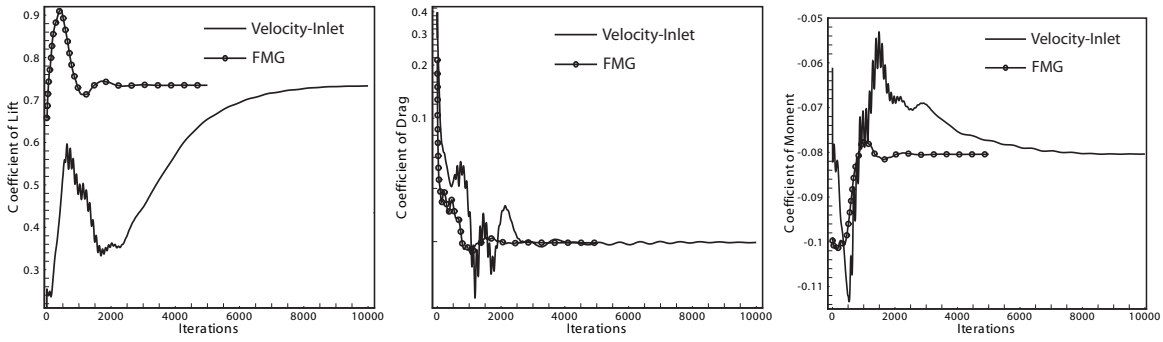

(a) c_l (b) c_d (c) c_m

FIGURE 5.17: Aerodynamic Coefficient Convergence History by the Mean Velocity & FMG Flow Initialisation Approach

The efficiency of the FMG approach is validated in Figure 5.17. The aerodynamic parameters c_l, c_d and c_m converge with fewer solver iterations in comparison to the mean velocity initialisation method. Convergence occurs when the flow residuals between the subsequent iterations are less than 10^{-6}. The theoretical merits of the FMG approach to facilitate a valid estimate of the flow initialisation test conditions in comparison to arbitrarily defining the test envelope at the mean inlet velocity conditions is validated. The convergence of the aerodynamic parameters by the FMG method do not exhibit severe instabilities during the computational cycle which is attributed to the validity of the initial flow starting phase. Comparatively the aerodynamic convergence by the mean inlet velocity approach is modeled with instabilities due to the ill-defined flow starting phase.

The application of the FMG approach has the merits of enhancing the accuracy of the solver in comparison to the mean inlet velocity initialisation method. The approach also accelerates convergence with fewer solver iterations required due to a well-defined estimate of the initial test flow conditions. The FMG method is valid for integration into the high-fidelity solver design module within the DNO architecture for airfoil design simulations at transonic flight envelopes.

5.4.6 Angle-of-Attack Trimming Validation for Transonic Airfoil Optimisation

The accuracy of the developed AoA trimming methodology at transonic flight conditions is verified. The sequence of steps applied for the validation of the AoA estimate at HALE flight conditions in Figures 5.8 and 5.9 are presented to demonstrate the viability of the developed approach at transonic flight envelopes. The lift curve slope of the benchmark RAE 2822 airfoil is estimated and the corresponding AoA at the defined target lift coefficient is established. The estimated $\alpha_{est.}$ is compared to the theoretical magnitude $\alpha_{exp.}$ in Appendix I - Figure I.1. The variance between the two parameters at the defined $c_L^T = 0.733$ is $\approx 10\%$.

The aerodynamics of the RAE 2822 airfoil at $\alpha_{est.}$ is compared to the shape performance at the experimental based AoA at the user-defined $c_L^T = 0.733$ in Appendix I - Figure I.2. The miss-match in AoA between experimental and estimated magnitudes corresponds to a c_l variance of $\approx 5\%$ between

the two measures. The variance between experimental-based and estimated AoA on c_d is $\approx 13\%$ and $\approx 4\%$ for c_m.

The c_p from the following methods is analysed and the performances are compared accordingly: **a)** Directly from experiment [9] at the user-defined c_L^T; **b)** Computational analysis at the experiment-based AoA for the user-defined c_L^T; and **c)** Computational analysis at trimming-based AoA for the user-defined c_L^T. The corresponding results by the defined methods are presented in Figure 5.18.

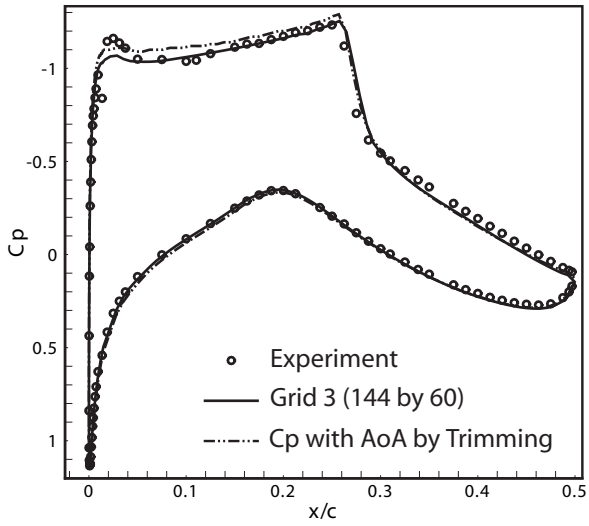

FIGURE 5.18: RAE 2822 c_p Convergence by α_{trim} Approach to Theoretical and Experimental Distribution; ($M_\infty = 0.740$, $R_e = 2.7 \times 10^6$)

Acceptable agreement between experiment and computational simulation at the experiment-based AoA is modeled in Figure 5.18. There are convergence issues between the two datasets about the leading edge nose, for c_p peak suction performance modeling. Elsewhere the agreement is acceptable with the flow solver accurately modeling airfoil shock location, including aft loading. Comparison of the aerodynamic performance by the estimated trimming-based AoA with experiment represents subtle performance variances between the datasets. As the estimated AoA by trimming is higher than the theoretical magnitude (Fig. I.1), the converged c_l was greater than experiment measure in Figure I.2(a). This is represented in the c_p distribution analysis where the pressure profile by the trimming-based AoA is less than the experiment profile on airfoil suction surface up to the shock chord station. This corresponds to an increased lift performance in comparison to experiment in Figure I.2(a). On airfoil pressure surface, the agreement between trimming-based AoA with experiment yields acceptable agreement. The shock location is accurately resolved, hence a valid estimate of wave drag is established in Figure I.2(b). There is a minor performance miss-match in airfoil aft loading convergence, hence c_m performance variance is attained in Figure I.2(c).

5.5 Summary

The computational domain was defined to facilitate accurate flow solver simulations at HALE and transonic flight envelopes. The developed model will be used by the AM-PSO algorithm in Chapter 6 for airfoil design fitness function evaluations. The summary of findings are as follows:

1. **Low-Fidelity Solver Validation**

   (a) Low fidelity solvers are applied for DNO architecture design development due to rapid computational turn over time. A node convergence analysis on shape aerodynamics confirmed 180 points are needed with XFOIL in Figure 5.1. At transonic flight conditions with TSFOIL, the DoE analysis resulted in aerodynamic convergence at 160 data points in Figure H.1.

2. **High-Fidelity Solver Definition**

   (a) The 4 equation $k-\omega$ SST transition turbulence model by Langtry et al. [158] will be used for airfoil design flow analysis. Validation analysis verified the accuracy of the computational algorithm relative to published experimental data. The 3 equation $k-kl-\omega$ scheme and XFOIL generated unfavorable performance agreement relative to the 4 equation model.

   (b) At transonic flight conditions, the FMG flow initialisation model presented errors that were within an acceptable tolerance relative to published wind-tunnel data. The methodology represented rapid computational turn over time than the mean inlet velocity flow initialisation scheme.

3. **Angle-of-Attack for Trimming**

   (a) An AoA trimming process was defined and validated. The methodology eliminates the integration of α as a design variable to the problem. Validation analysis demonstrated the principles of the developed approach. The error magnitudes between experimental and computational data were within an acceptable tolerance.

Chapter 6

Aerodynamic Shape Optimisation by Direct Approach

6.1 Overview

The developed DNO process is applied for airfoil design for the MM-UAV platform. Airfoil development focuses on attaining an optimal profile for flight operations at: **a)** Low-speed, HALE performance with extended endurance for ISR sorties (Fig. 6.1); and **b)** Rapid dash segments at high-speed operations for SEAD missions at transonic flight envelopes (Fig. 6.1). The MM-UAV from Figure 1.3(b) needs to attain optimal flight performance at the defined mission segments. The design development of mission-segment based airfoils is a design goal.

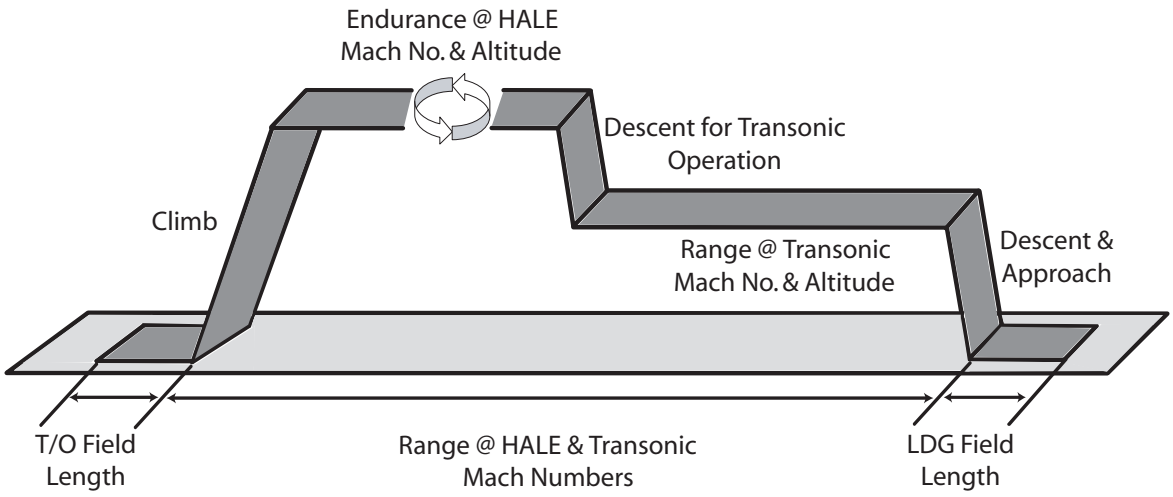

FIGURE 6.1: MM-UAV Mission Profile

The data to the conceptual sizing process of a MM-UAV platform [3–5, 7, 27] for Australian industry requirements [23] resulted in the following aerodynamic design conditions for HALE and transonic based operations.

Table 6.1: MM-UAV Mission Profile Aerodynamic Design Conditions

	HALE Low-Speed	**Rapid Dash High-Speed**
Target Coefficient of Lift c_l^T	0.40	0.733
Mach Number	0.10	0.740
Reynolds Number	4.0×10^6	2.7×10^6

Airfoil design simulations are presented with the developed DNO architecture. Low and high-fidelity solvers are applied in the design process. The merits of the novel AM-PSO algorithm are verified by comparing the search performance of the population based process with current off-the-shelf gradient-based methods. The results to the optimisation design process are further verified with published data. The aerodynamic performance of the optima is directly evaluated against airfoils in the literature designed at the intent, user-defined conditions. The viability of the developed optimisation structure is confirmed.

6.2 Limitations of the Stand-Alone Local Gradient-Based Method for HALE Airfoil Optimisation

Gradient-based optimisation methods (GM) yield rapid convergence but limit the search to local solution regions. Initialising the starting phase with disparate airfoil types that are similar to the intent design goal can address the identified issue. Test simulations are presented to verify the theoretical principles of the GM algorithm and the impact of variances in search starting point on the converged optimal. The Sequential Quadratic Programming (SQP) algorithm implemented in MATLAB [53] is used for the intent design problem.

In the analysis by Namgoong [41] the role of a gradient-based optimiser on transonic airfoil design was investigated. It was concluded that the search region is highly multi-modal and the gradient method converges to the local solution about the user-defined starting point. The application of a GM process is not viable for transonic airfoil design. The simulations presented in the thesis investigate the role and the merits of the local-based method on HALE airfoil design. The flexibility of the GM algorithm is investigated by initialising the search process from disparate starting points. The variance of results with different initialisation points will map the scope of the solution topology and the extent of local minima regions for the modeled test problem. The data will provide an avenue to assess the feasibility of the current off-the-shelf design algorithms for MM-UAV airfoil design test problem. The results will further map the potential of the AM-PSO algorithm to exploit the solution region for convergence to a true global optima in comparison to current design systems in the literature.

To demonstrate the role of a gradient-based method for HALE airfoil design, a single-point objective function is defined. The PARSEC-Modified shape function is applied coupled with the low-fidelity

solver XFOIL for flow simulations. The objective aims to minimise $\mathcal{J}$, hence drag at cruise with respect to a set of user-defined flight parameters that must be achieved in Equation 6.1.

$$\mathcal{J}_{min} = \left[\left(c_l - c_l^T \right)^2 + c_d \right] \tag{6.1}$$

Where: $\alpha = 2°$; $R_n = 4.0 \times 10^6$; Mach $= 0.10$; & $c_l^T = 0.40$

The base airfoils integrated in the test are: **a)** Symmetrical subsonic NACA 0012 profile; **b)** Natural Laminar Flow (NLF) shape designed for low-speed operations, NLF(1)0115; and **c)** High-speed, RAE 2822 cambered airfoil designed for wave drag minimisation at transonic Mach numbers. The convergence of the optimal airfoil with disparate user-defined base profile types for a GM optimisation cycle and its associated fitness magnitude is presented in Figures 6.2 - 6.4. The corresponding c_l and c_d of the converged shape as a function of the modeled base airfoil is summarised in Table 6.2. The evolution of the airfoil contour during the iterative optimisation cycle is superimposed to represent the profile modifications during the design phase.

Airfoil optimisation with the symmetrical NACA 0012 base airfoil as the search starting point is presented in Figure 6.2. Airfoil variances are evident between the initial and final geometries in Figure 6.2(a). Significant fitness magnitude reduction is computed during iterations 1 to 4 in Figure 6.2(b). This is attributed to the optimiser establishing the lift coefficient of the candidate airfoil toward the specified target. Drag performance improvements correspond to further fitness reduction following the fourth design iteration.

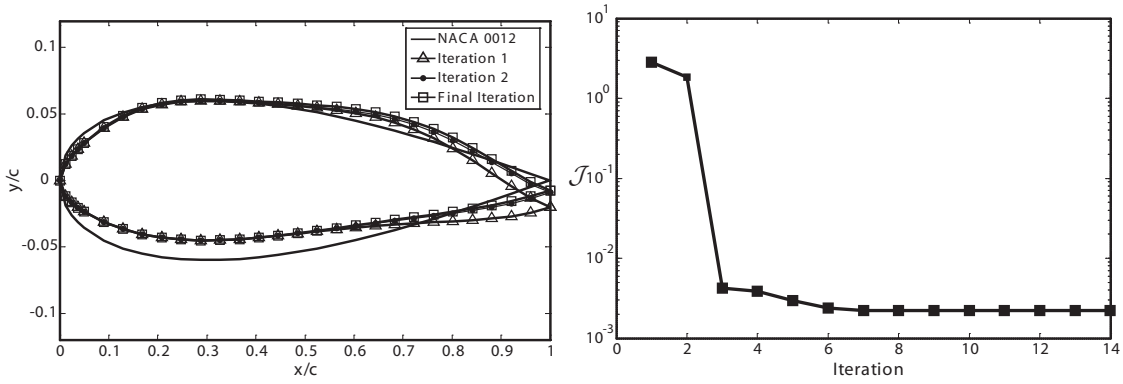

(a) Airfoil Convergence (b) Fitness History

FIGURE 6.2: Airfoil Design by Gradient Method with NACA 0012 Base Airfoil

The integration of the NLF(1)-0115 airfoil as the base profile for GM search initialisation results in negligible shape changes during the design iteration process in Figure 6.3(a) in comparison to the NACA 0012 (Fig. 6.2(a)). The converged and initial starting profiles share similar geometry traits, hence indicating the convergence toward a local solution about the defined starting point. The fitness convergence with the NLF(1)-0115 initialisation profile represents minimal design improvements in Figure 6.3(b) in comparison to the symmetrical profile (Fig. 6.2(b)). The NLF airfoils by NASA are designed for low-speed operations. Theoretically the NLF airfoil is a solution to the design problem (Eqn. 6.1) and the results by the GM analysis in Figure 6.3 confirms these findings.

The NACA 0012 is designed for off-design flight conditions relative to the design intent in Equation 6.1. The solution region comprising the NACA 0012 is at a local topology and the optimiser ensues an active search process to avoid this region in Figure 6.2(b). Comparatively the NLF airfoil is within the global optimal region and the level-of-search activity is minimal in Figure 6.3(b). The NLF(1)-0115 base shape exhibits an acceptable converged solution to the optimisation cycle in comparison to the NACA 0012 airfoil by conforming to the target lift coefficient coupled with lower drag performance (shaded row in Table 6.2).

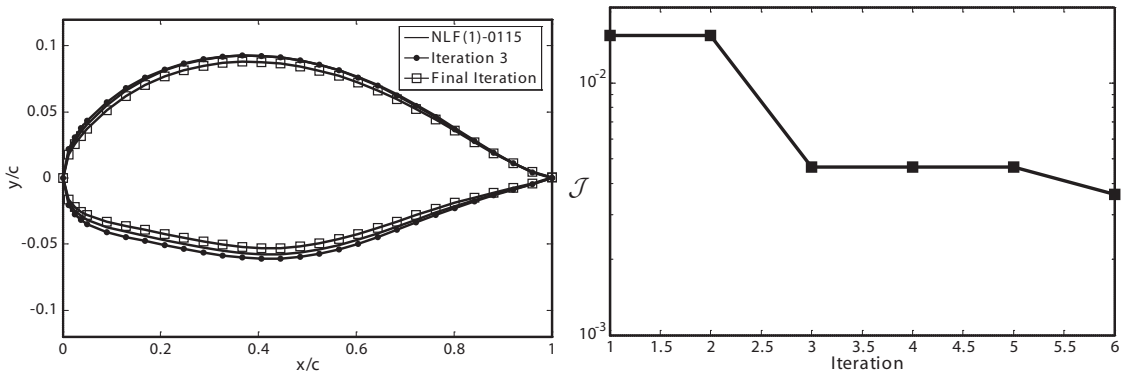

(a) Airfoil Convergence (b) Fitness History

FIGURE 6.3: Airfoil Design by Gradient Method with NLF(1)-0115 Base Airfoil

Design optimisation with the application of the RAE 2822 airfoil as the base profile to a GM analysis is modeled in Figure 6.4. The converged airfoil is thicker with remaining shape features matching the initial profile in Figure 6.4(a). The magnitude of the fitness reduction at search commencement is attributed to the shape change forced by the optimiser to conform to the user-defined objective (Eqn. 6.1) in Figure 6.4(b). The overall shape change between initial and final airfoil is significant relative to the symmetrical (Fig. 6.2(a)) and low-speed base NLF profile (Fig. 6.3(a)). The RAE 2822 airfoil is designed for high-speed operations and the defined objective conflicts with the design intent of the select base airfoil. The GM simulates the shape variances between the initial and converged airfoils to transpose a high-speed profile to a low-subsonic design with low drag performance, while concurrently conforming to the user-defined minimum target lift coefficient constraint in Table 6.2.

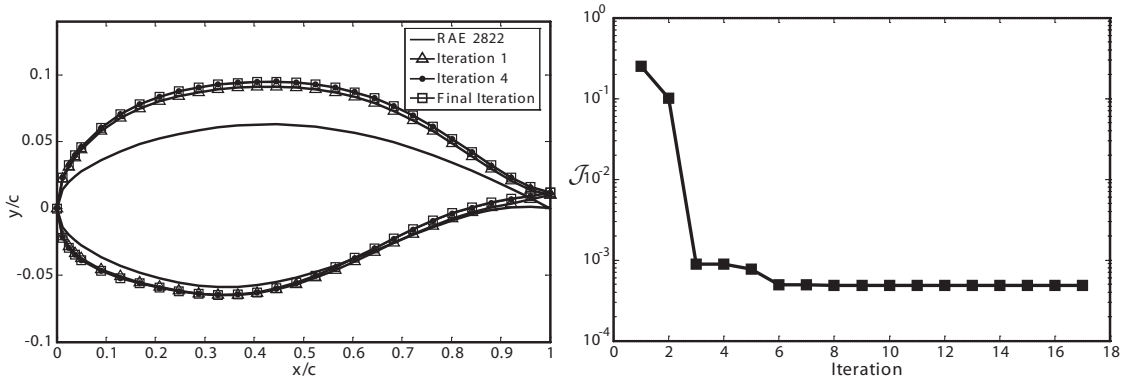

(a) Airfoil Convergence (b) Fitness History

FIGURE 6.4: Airfoil Design by Gradient Method with RAE 2822 Base Airfoil

To confirm the impact of a gradient optimisation process for HALE airfoil design based on the defined objective from Equation 6.1, the aerodynamics of the converged optimal shape with solution initialisation by different base airfoil types is compared in Table 6.2.

TABLE 6.2: Aerodynamics of Converged Shapes with Disparate Initial Starting points for HALE Airfoil Optimisation with Gradient Method

Base Airfoil	**Converged Optimal Airfoil**		**Iterations**
	c_l	c_d	
NACA 0012	0.3957	0.0054	334
NACA 23015	0.3898	0.0064	190
NACA 63_2615	0.3900	0.0068	275
NLF(1)0115	0.4159	0.0048	55
NLF(1)0416	0.4022	0.0060	116
RAE 2822	0.4000	0.0069	385

The results in Table 6.2 represent the sensitivity of the gradient optimisation method for HALE airfoil design. The validity of the defined objective function in Equation 6.1 for target lift constraint definition is confirmed. Three of the six base airfoils integrated into the design problem converge about the user-defined $c_l^T = 0.40$. A higher weight, applied as a multiplier to term $(c_l - c_l^T)^2$ can be imposed to facilitate $c_l = c_l^T = 0.40$ (Eqn. 6.1), such that the c_l^T constraint is consistently achieved irrespective of the base starting airfoil in the GM analysis for the defined objective function.

The effect of gradient initialisation point on the search process is evident from c_d and the number of iterations needed to achieve convergence in Table 6.2. The two airfoils that are offset to the specified design goal are the symmetrical NACA 0012 and the high-speed RAE 2822 profile. The identified shapes exhibit an extended design simulation process in comparison to the other airfoils modeled due to the extended degree-of-disparity between defined design goals and the original objectives of the identified base airfoil. The optimal drag is different for each base airfoil, hence validating convergence about the initial starting point. As the NLF(1)0115 airfoil closely matches the design goal, the converged shape exhibits the lowest drag in comparison to the other presented cases. The RAE 2822 airfoil is modeled with the largest drag due to the disparity between the original design intent and the stipulated objective goal by the defined optimisation process.

The variances in drag performance as a function of the search starting point by the gradient-method confirms the non-convergence of the airfoils to a global solution region. The optimisation strategy needs to be modified to attain a true optimal for the defined test problem. Accordingly the feasibility of the gradient optimisation solution with the NLF(1)0115 airfoil as the starting point (shaded in Table 6.2) can be verified. The following optimisation strategies are used: **a)** Developed AM-PSO algorithm; and **b)** Hybrid approach with the integration of the AM-PSO solution from **a)** as the starting point to the gradient method.

The AM-PSO algorithm does not require the definition of a user-defined starting point as the initial swarm is generated by Latin hypercube sampling. To demonstrate the negligible impact of the initialisation phase on AM-PSO search convergence, the initial swarm is generated about the starting shapes applied in gradient optimisation simulations with subtle disturbances $\Delta_{dist.}$. The aim of the

defined problem analysis is to confirm that the converged solution by the developed swarm algorithm is not sensitive to a user-defined starting point as in gradient optimisation methods. An example of a swarm with 20 particles generated about the NACA 0012 airfoil is presented in Figure 6.5 and the disturbances are modeled in figure inset.

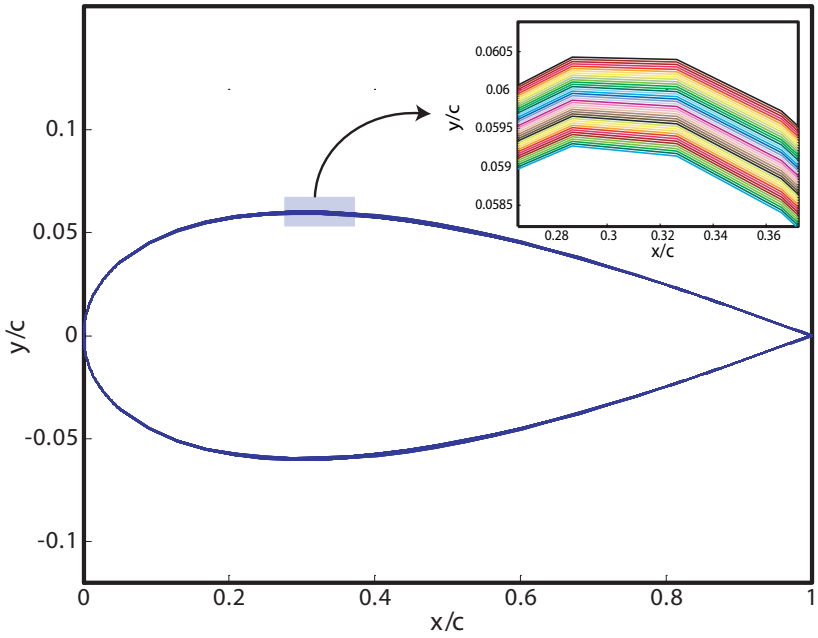

FIGURE 6.5: AM-PSO Swarm Initialisation about NACA 0012 Airfoil

The disturbances to the swarm population are sequentially induced by perturbing the y/c ordinates of each airfoil. Particle 1 is representative of the theoretical NACA 0012 base airfoil. Particle 2 is generated about the NACA 0012 profile with disturbances to the y/c ordinates of magnitude 10^{-6}. Particle 3 is generated about particle 2 with y/c perturbations of 10^{-6}. The process follows through over the defined swarm population size.

The results to the defined test problem (Eqn. 6.1) for the identified design optimisation strategies is presented in Table 6.3

TABLE 6.3: Aerodynamics of Converged Shapes with Disparate Initial Starting points for HALE Airfoil Optimisation with Gradient Method, AM-PSO & Hybrid Optimisation Strategy

Base Airfoil/s	**Optimisation Strategy**	c_l	c_d	**Iterations**
NACA 0012	GM	0.3957	0.0054	334
NACA 0012 + $10^{-6}(\Delta_{dist.})$	AM-PSO	0.4002	0.0045	2000
Solution of AM-PSO to GM	AM-PSO / GM	0.4000	0.0044	2000+22
NACA 23015	GM	0.3898	0.0064	190
NACA 23015 + $10^{-6}(\Delta_{dist.})$	AM-PSO	0.3994	0.0044	2960
Solution of AM-PSO to GM	AM-PSO / GM	0.4000	0.0043	2960+125
NACA 63_2615	GM	0.3900	0.0068	275
NACA 63_2615 + $10^{-6}(\Delta_{dist.})$	AM-PSO	0.4100	0.0046	2350
Solution of AM-PSO to GM	AM-PSO / GM	0.4000	0.0045	2350+173
NLF(1)-0115	GM	0.4159	0.0048	55
NLF(1)-0115 + $10^{-6}(\Delta_{dist.})$	AM-PSO	0.4000	0.0045	1950
Solution of AM-PSO to GM	AM-PSO / GM	0.4000	0.0045	1950+22
NLF(1)-0416	GM	0.4022	0.0060	116
NLF(1)-0416 + $10^{-6}(\Delta_{dist.})$	AM-PSO	0.4070	0.0044	2100
Solution of AM-PSO to GM	AM-PSO / GM	0.4000	0.0043	2100+318
RAE 2822	GM	0.4000	0.0069	385
RAE 2822 + $10^{-6}(\Delta_{dist.})$	AM-PSO	0.4002	0.0045	2160
Solution of AM-PSO to GM	AM-PSO / GM	0.4000	0.0044	2160+47

The c_d by the AM-PSO algorithm is consistently lower than the drag magnitude by the stand-alone gradient method irrespective of the initial base airfoil in Table 6.3. The mean c_d by AM-PSO across the sample base airfoils is 0.0045 with a standard deviation of 7.5×10^{-5}. Comparably the mean c_d by the gradient analysis is higher at 0.0061 with a standard deviation of 8.2×10^{-4}. The analysis confirms that the gradient search process did not converge to a global solution. Even for the NLF(1)-0115 airfoil which is similar to the design objective, the drag performance of the GM converged shape is not optimal. The results to the AM-PSO method are feasible in comparison and converge to a common region in the solution topology with lower drag performance. The search process is not influenced by the state of the initial swarm as defined by the disparate base airfoil types with induced disturbances over the sample swarm population size. The converged airfoil contours by the AM-PSO method with disparate base airfoil types for search initialisation is presented in Figure 6.6.

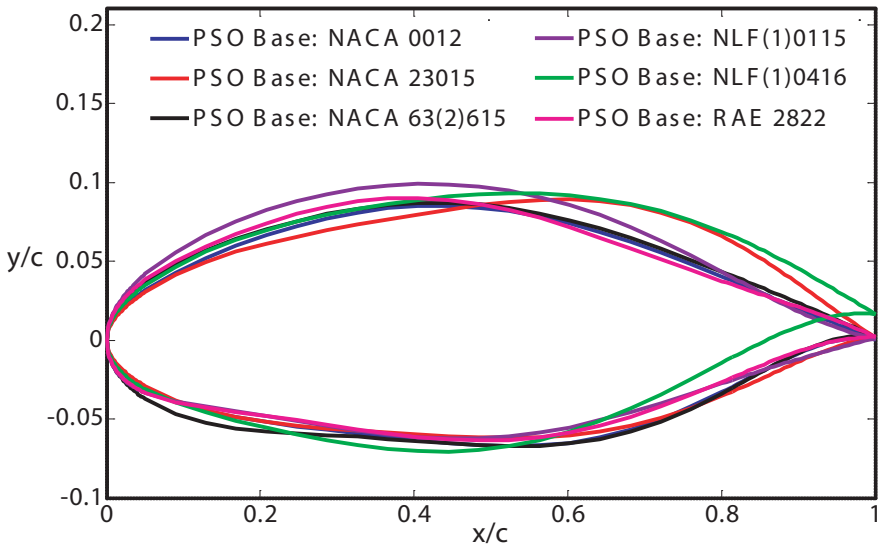

FIGURE 6.6: AM-PSO Airfoil at Convergence (Eqn. 6.1) with Disparate Swarm Initialisation Base Shapes

The variation in converged airfoil contours confirms the multi-modal scope of the solution topology. There exists several airfoils with same drag performance for the defined test problem from Equation 6.1. To isolate the solution to one final shape, additional objectives and/or constraints need to be imposed to the design problem.

The theoretical advantages of the gradient method with local search mechanisms is exploited by integrating the search algorithm into the AM-PSO method. The converged shape by the AM-PSO is used as a starting airfoil to a gradient search simulation. The fundamental theory supporting the defined methodology is based on the hypothesis that the solution to the AM-PSO method is within a solution topology bounded by the true optima, yet it is not the global minima to the design problem. The integration of a local search process will facilitate the transition of the AM-PSO solution to the true optimal as the starting airfoil is within a well-defined solution region.

The results by the defined hybrid search process comprising of the AM-PSO and gradient method validate the supported hypothesis in Table 6.3. The mean c_d by the hybrid approach is 0.0044 with a standard deviation of 8.94×10^{-5}. The performance measuring units are lower than the computed magnitudes for the stand alone AM-PSO method. The consistency of the converged c_d validates the negligible impact of the variance in base airfoils on solution convergence with the application of the AM-PSO method.

The results confirm the merits of the AM-PSO method for HALE airfoil design. The gradient optimisation method does not converge to the true optimal shape as it requires the definition of a well-defined search initialisation point. Despite the integration of an off-the-shelf airfoil with similar operating performance to the design goal, the gradient search simulation does not converge to the true solution. The feasibility of the search starting point is enhanced if the initialisation point is estimated by the AM-PSO algorithm. The population-based search method converges to a global solution region and facilitates the integration of the gradient method which exploits the area with local search principles. This leads to further fitness function minimisation and convergence to the global optima is achieved.

6.3 MM-UAV HALE Airfoil Design Definition

The aerodynamic performance requirements for HALE operations for the MM-UAV (Fig. 6.1 & Tab. 6.1), match the design specifications of the current NLF(1)-0416 airfoil developed by NASA for general aviation applications [6]. The conceptual design efforts into the MM-UAV platform integrate the NLF(1)-0416 shape due to the extended regions of surface laminar flow which translates to low drag performance at cruise c_l^T. The developed DNO process will aim to improve on the current performance of the NLF(1)-0416 airfoil for application into the MM-UAV platform. The NLF(1)-0416 design specification published data [6] will provide an avenue to compare and validate the efficacy of the optimal shape derived by the proposed DNO process.

The design goals of the MM-UAV platform for HALE operations are in accordance to the design objectives of the NLF(1)-0416 airfoil as:

1. The c_{lmax} at $R_n = 3.0 \times 10^6$ must be greater than 1.76. The maximum lift coefficient should not decrease with transition fixed at the leading edge due to surface contamination by insect remains; and
2. Obtain low profile drag-coefficients at $R_n = 4.0 \times 10^6$ for cruise target lift coefficient of 0.40 and climb lift coefficients of $c_l^T = 0.50 - 1.00$.

The following constraints apply:

1. Extent of the favorable pressure gradient $\frac{d_{cp}}{d_x} < 0$ on airfoil upper surface at cruise c_l must not exceed 30-percent chord;
2. Airfoil t/c must be greater than 12 percent; and
3. Pitching-moment coefficient at zero lift c_{m0} must be $c_{m0} \geq -0.10$

A favorable pressure gradient on the upper surface is required up to the maximum extent allowed by the constraint $(x/c)_u \leq 0.30$. Aft of 0.30c on the upper surface, a short region of slightly adverse pressure gradient is needed to promote efficient transition from laminar to turbulent flow. This ensures that the initial slope of the pressure recovery is relatively shallow. This short region is then followed by a steeper, concave pressure recovery which produces lower drag and has less tendency to separate than the corresponding linear or convex pressure recovery pattern.

The extent of airfoil camber is limited by the pitching-moment constraint ($c_{m0} \geq -0.10$), which is defined to maximise c_{lmax}.

6.3.1 Parallel Computing Set-Up

An automated optimisation architecture with the integration of the DNO components is developed. The optimisation script including structure sub-routines for airfoil development and aerodynamic solver computation are setup in MATLAB. The partial derivatives needed to determine the local gradient are computed in parallel for GM simulations. Heuristic search methods are adaptable to

parallelism and an efficient computation model is developed to accelerate AM-PSO simulation with MATLAB's distributed computing toolbox [160]. Shell scripts are prepared in MATLAB to distribute each particle to a processing unit on a super-computing facility at the Victorian Partnership for Advanced Computing (VPAC) center. The optimisation structure is prepared on a host client and submitted for parallel computing to the VPAC server.

The shape parameterisation model generates the airfoil ordinates which are saved as a text file and used as inputs for aerodynamic coefficient computation. Grid generation is not required for low-fidelity simulations by XFOIL. Instead XFOIL interpolates the discrete points to generate the airfoil contour for flow analysis. A UNIX shell script is generated as a sub-routine from MATLAB to handle the inputs into XFOIL. The script manipulates XFOIL's menus to load airfoil geometry, establish surface panel population, toggle viscous solver and input flow parameters including Mach and Reynolds Number. The flow simulations are initiated with c_l^T used as a solver input and the corresponding drag, moment, pressure, moment at zero lift and c_{lmax} parameters recorded as outputs. The results are transferred from VPAC's server client to host PC for the purposes of optimisation and post-processing.

Contingencies are defined to ensure the optimisation cycle is not prematurely terminated. Flow simulations where local surface Mach number exceeds the transonic range for ill-conditioned shapes will result in solver termination and/or a non-convergence state. The result field generated by the solver is an empty array of aerodynamic coefficients. The optimisation simulation in MATLAB inadvertently terminates since the feedback loop from the solver has crashed. A script is developed to handle these conditions by setting the aerodynamic coefficients to pre-defined parameters for optimisation continuation. The post-processing module as a result of the optimisation process uses the text file of the optimal shape to examine airfoil flow features. The distribution of coefficient of pressure, generation of a LSB, including flow transition and separation are flow features of interest in the development of HALE airfoils.

6.3.2 HALE Airfoil Design Objective Function / Constraints Set-Up

The HALE airfoil design for the MM-UAV is regarded as a single objective problem with drag minimisation at cruise c_l^T a primary goal. Despite the performance requirements stipulating the maximisation of c_{lmax} as a design objective, the condition is defined as a constraint to the optimisation problem. The design objectives and constraints of the MM-UAV as a function of the design goals of the NLF(1)-0416 airfoil from Section 6.3 are transformed into the AM-PSO search algorithm as

follows:

$$\begin{aligned}
&\text{At } R_n = 4.0 \times 10^6 \\
&\text{minimise } c_d \\
&\text{Subject to:} \\
&\Rightarrow \frac{d_{cp}}{d_x}(x, \alpha, M_\infty) \leq 0.30c \\
&\Rightarrow c_{m0}(x, \alpha, M_\infty) \geq -0.10 \\
&\Rightarrow t/c_{max}(x) \geq 0.12 \\
&\text{At } R_n = 3.0 \times 10^6 \\
&\Rightarrow c_{lmax}(x, \alpha_{max}, M_\infty \geq) 1.76
\end{aligned} \tag{6.2}$$

Where: x is the vector of airfoil shape function design variables.

Constraints are applied by penalty functions to the objective function to ensure minimum drag performance is not compensated by a constraint violated design. A static penalty function is introduced and is normalised to (0, 1) if the aerodynamic and/or geometric constraints (Sec. 6.3) are violated such that:

$$f_p(x) = \mathcal{J}(x) + \sum_{j=1}^{\eta_{con}} c_j \tag{6.3}$$

Where:

f_p = Fitness as a result of penalty

cj = Expected maximum cost to repair constraint j (i.e alter x so that it is feasible); normalised to (0,1)

η_{con} = Number of Constraints

The term c_j represents the magnitude of the penalty and is constraint specific. An estimate of the worst solution for the defined constraint j is required. The metric $c_{t/c}$ is related to the t/c distribution and is established from the mapped search intervals y_u and y_l for the PARSEC-Modified shape function variables in Table 4.8. Equating the upper and lower limits of y_u and y_l to thickness, profiles with surface thickness-to-chord ratio of [0.1187,0.198] are attainable during the optimisation cycle. The design constraint stipulates airfoil t/c to be ≥ 0.12 and the maximum cost repair metric is $c_{t/c} = 0.12 - 0.1187 = 0.0013$ which is normalised accordingly to (1,0) for values of t/c in the range (0.1187, 0.12) respectively. When $t/c \geq 0.12$, $c_{t/c}$ is zero as the shape constraint is satisfied. The metric c_j for the remaining problem constraints are estimated from numeric experimentation. Constraint normalisation with estimates of c_j for c_{lmax}, $\frac{d_{cp}}{d_x}$, c_l^T, t/c and c_{m0} are presented in Equations 6.4 - 6.8:

- Constraint: c_{lmax}

$$\begin{aligned}
&\text{if } c_{lmax} < 1.76 \\
&c_{c_{lmax}} = 0.76 \\
&c_{lmax_{pen}} = \frac{|c_{lmax} - 1.76|}{c_{c_{lmax}}}
\end{aligned} \tag{6.4}$$

- Constraint: $\frac{d_{cp}}{d_x}$

$$\begin{aligned} &\text{if } \frac{d_{cp}}{d_x} > 0.30 \\ &c_{\frac{d_{cp}}{d_x}} = 0.60 \\ &c_{\frac{d_{cp}}{d_x}pen} = \frac{|\frac{d_{cp}}{d_x} - 0.30|}{c_{\frac{d_{cp}}{d_x}}} \end{aligned} \tag{6.5}$$

- Constraint: c_l^T

$$\begin{aligned} &\text{if } c_l^T < 0.40 \\ &c_{c_l^T} = 0.10 \\ &c_{c_l^T{}_{pen}} = \frac{|c_l^T - 0.40|}{c_{c_l^T}} \end{aligned} \tag{6.6}$$

- Constraint: t/c

$$\begin{aligned} &\text{if } t/c < 0.12 \\ &c_{t/c} = 0.0013 \\ &c_{t/c_{pen}} = \frac{|t/c - 0.12|}{c_{t/c}} \end{aligned} \tag{6.7}$$

- Constraint: c_{m0}

$$\begin{aligned} &\text{if } c_{m0} < -0.10 \\ &c_{c_{m0}} = 0.15 \\ &c_{c_{m0}pen} = \frac{|-c_{m0} - 0.10|}{c_{c_{m0}}} \end{aligned} \tag{6.8}$$

At each search evolution the aerodynamic and geometric quantities of the candidate solution are computed. The summation of c_j for each constraint is added to the fitness to penalise the particle for violating the respective constraint.

6.4 MM-UAV HALE Airfoil Optimisation by the AM-PSO Algorithm with a Low-Fidelity Solver

HALE airfoil optimisation with single and multi-point designs is modeled. Single-point performances minimise drag at cruise $c_l^T = 0.40$. As fitness for constraint violation is normalised to range (0,1), the magnitude of c_d is manipulated to transpose an even contribution to the objective term relative to the penalty magnitude. A multiple of 100 to c_d is applied to ensure the contribution of drag is not diminished by the normalised magnitude of the penalty function. The objective is substituted into

the search algorithm in Equation 6.9:

$$\text{minimise} : 100 \times c_d \tag{6.9}$$

In multi-point designs, drag minimisation at the lift coefficient envelope for climb and cruise are applied into the objective function. The flight points are cruise $c_l^T = 0.40$ and climb $c_l^T = 1.00$. The corresponding objective function is defined as:

$$\text{minimise} : 100 \times c_{d_{cruise}} + 100 \times c_{d_{climb}} \tag{6.10}$$

Airfoil single and multi-point design optimisation problem (Eqn. 6.9 and 6.10 respectively) are integrated into the developed AM-PSO model. The search algorithm is set up as follows:

- Swarm population: 30;
- Optimisation with full set of design variables: 10 PARSEC & 13 PARSEC-Modified (Δz_{te} not used in both models);
- Optimisation with the identified least important design variable to the objective function is eliminated from the search process (Sec. 4.2.2.2) - 9 PARSEC with t_{ew} omitted (Fig. G.2) & 12 PARSEC-Modified with teg_{low} omitted (Tab. 4.10 & Fig. 4.23);
- LHS is applied for initial swarm search initialisation to address diversity;
- The minimum and maximum velocity of the particles in the swarm equals the dimensional search space of the respective design variable such that, $[v_{min}, v_{max}] = [x_{j,min}, x_{j,max}]$;
- Wall Boundary Condition: Random initialisation approach is used since the solution topology is multi-modal with local minima in the search domain. Test validations on mathematical test functions (Sec. 3.6.2.2) validated the merits of the random initialisation methodology on multi-modal solution topologies, hence the approach is used for airfoil design simulations;
- Personal best fitness range $p_f = (F_{pbesti,max}, F_{pbesti,min}) =$ (5, -0.01) (Sec. 3.4.4 - Step 1) - Based on the assumption that the worst solution is a particle with all five constraints (Eqns. 6.4 - 6.8) violated to the maximum limit of one. An excessively high drag performance of 0.01 is also assumed, thus $F_{pbesti,max}$ is established in Equation 6.12 as:

$$\begin{aligned} F_{besti,max} &= \left(c_{lmax_{pen}} + c_{\frac{d_{cp}}{d_x} pen} + c_{t/c_{pen}} + c_{c_{m0} pen} + c_{d_{max}} \right) \\ &= [1 + 1 + 1 + 1 + (0.01 \times 100)] \end{aligned} \tag{6.11}$$

  The magnitude of $F_{pbesti,min}$ is a value less than zero. This is defined to ensure if the particles converge to 1×10^{-4} of each other, the probability of mutation p_r is not one. If $F_{pbesti,min} = 0$ then $p_r = 1$ and each particle in the swarm will be mutated. This will correspond to a computationally time-intensive simulation. By minimising $F_{pbesti,min}$ to a value less than zero, a degree-of-certainty will ensure the probability of mutation is less than the randomly generated number for particle i, such that mutation is avoided for the respective search agent. A select few particles will not be mutated and computational time savings will follow. The magnitude of $F_{pbesti,min}$ is set to -0.01;

- Mutation scalar factor $\omega_M = 0.05$ for $t = (1, 400)$ & $\omega_M = 0.10$ for $t = (401, 800)$ (Sec. 3.4.4 - Step 5, Eqn. 3.12). Local search is initiated during the first half of the simulation process as the particles are theoretically dispersed at different regions of the solution search space and reduced solution diversity is not an issue. Global search simulations are defined for the second half of the simulation process to address particle stagnation at a common solution region; and

- Maximum iteration to termination is 800 - As the particles conjugate to a specific region in the defined solution topology, the fitness difference between the worst and global best particle in the swarm will vary. The percentage difference between the worst and best performing particle at $t = 800$ relative to the measure at search initialisation ($t = 1$) is computed. The relative percentage difference between the two measures at $t = 1$ and $t = 800$ is representative of the fitness improvement in the swarm due to the iterative design cycle.

  The knowledge gained from the low-fidelity simulation is used in high-fidelity design processes to define the termination criteria. Instead of using a maximum iteration limit for search termination, convergence will be initiated if the fitness percentage improvement between the current swarm state (difference between worst and global best solution) relative to the initialisation stage at $t = 1$, is within the threshold established from low-fidelity simulations. The requirement maybe satisfied before the 800^{th} iteration, thus resulting in computation time savings. Since a low-fidelity solver is initially implemented in the design effort, the number of generations to convergence is set high with intent. Sufficient data will be gathered to establish an appropriate magnitude of the percentage difference between the worst and global best particle in the swarm at initialisation and at the maximum iteration limit of 800. The established measure will then be applied to define search termination for time-intensive, high-fidelity solver based simulations.

6.4.1 MM-UAV HALE Single-Point Airfoil Optimisation

The single-point optimisation from Equation 6.9 is modeled with AM-PSO. The merits of the design variable pre-screening study (Sec. 4.2.2) are verified in the analysis. Results of the PARSEC and PARSEC-Modified airfoil shape functions with a full and reduced set of design variables are compared. Airfoil geometry and aerodynamic performance comparisons between the benchmark NLF(1)-0416 and AM-PSO derived solution is presented in Figure 6.7.

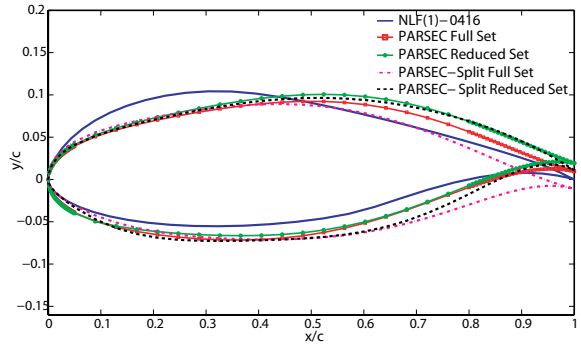

(a) NLF(1)-0416 Airfoil & Single-Point Optimised Shapes

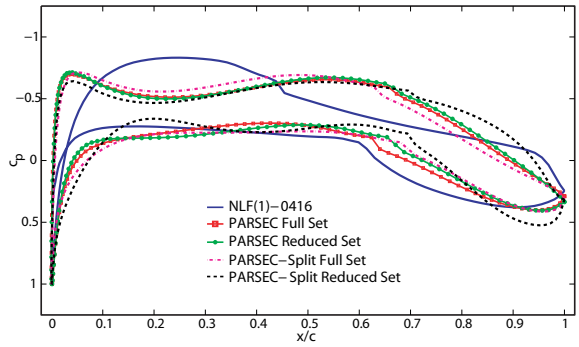

(b) c_p of NLF(1)-0416 Airfoil & Single-Point Optimisation Results at cruise $c_l^T = 0.40$ 0.40

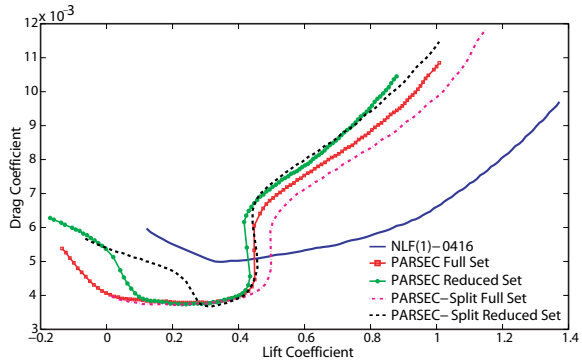

(c) Drag Polar of NLF(1)-0416 & Single-Point Optimisation Results at $R_n = 4.0 \times 10^6$

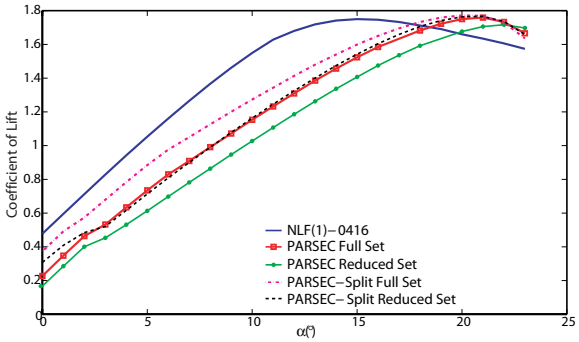

(d) c_{lmax} of NLF(1)-0416 & Single-Point Optimisation Results at $R_n = 3.0 \times 10^6$

FIGURE 6.7: HALE Single-Point Airfoil Optimisation Results by the AM-PSO Method with XFOIL

A comparison between validation and AM-PSO airfoil shapes shows that simulation results are characterised with extended x_u and y_l coefficients in Figure 6.7(a). The trailing edge ordinate is also unique for each shape. Increasing x_u minimises drag for HALE performances due to extended regions of adverse pressure gradients. The results of the AM-PSO simulations are representative of the theoretical principles of HALE airfoil design with the maximum thickness point in excess of 0.50c. Hence, extended regions of adverse pressure gradients are observed in Figure 6.7(b). Transition is delayed and is in excess of 0.60c on both upper and lower surfaces compared to 0.43c and 0.57c on suction and pressure surfaces respectively for the NLF(1)-0416 profile. Delayed transition with extended x_u minimises skin-friction drag. The corresponding drag performances are compared in Fig. 6.7(c). A 'drag bucket' bounded about the user-specified $c_l^T = 0.40$ is observed. Drag at the specified flight condition is the 'global' solution to the single-point problem and is minimal compared to the validation case. Elsewhere drag is significantly higher with a rapid performance degradation at off-design conditions. The performance is related to the localised effects of the optimiser, hence verifying the demerits of a single-point design approach.

The variance of y_{te} in airfoil shapes is related to the performance of the maximum lift coefficient. Relatively it was shown that y_{te} has a minimal affect on drag but significant on c_{lmax} in Figure G.2. The pre-screening analysis from Section 4.2.2 established that y_{te} has a variance of 8% to drag and the contribution is minimal relative to x_u with a variance of 30% (Fig. G.2(a)). Comparatively y_{te} indicated an even variance to c_{lmax} relative to the remaining PARSEC coefficients with a contribution of 8% (Fig. G.2(b)). A qualitative two-way interaction analysis indicated that with an incremental

decrease in y_{te} relative to the rest PARSEC coefficients, the c_{lmax} of the airfoil increases proportionally. The lift-curve slope models the affect of y_{te} on c_{lmax} in Figure 6.7(d). The PARSEC simulation with the t_{ew} eliminated as a design variable has an extended y_{te} and the corresponding c_{lmax} is low. Comparatively the PARSEC-Modified simulation with a full set of 13 design variables has a lower y_{te} and c_{lmax} is proportionally greater in comparison. The aerodynamic measure of merit by the defined objective function (Eqn. 6.9) and constraint distribution of the base and optimised airfoils is summarised in Tables 6.4 and 6.5 respectively.

TABLE 6.4: HALE Single-Point Airfoil Optimisation Objective Measure by the AM-PSO Method with XFOIL

Airfoil	t/c	Max Camber	c_l	AoA(°)	c_d	% c_d Gain*
NLF(1)-0416	0.16	0.025	0.40	-0.695	0.00502	—
PARSEC (Full Set)	0.16	0.016	0.40	1.432	0.00398	-↓20.72
PARSEC (Reduced Set - t_{ew})	0.163	0.016	0.40	1.989	0.00399	-↓20.52
PARSEC - Modified (Full Set)	0.160	0.014	0.40	0.203	0.00390	-↓22.31
PARSEC - Modified (Reduced Set - teg_{low})	0.165	0.019	0.40	0.910	0.00392	-↓21.91

* **Relative to the benchmark NLF(1)-0416 Airfoil**

TABLE 6.5: HALE Single-Point Airfoil Optimisation Constraints Measure by the AM-PSO Method with XFOIL

Airfoil	c_{lmax} $R_n = 3 \times 10^6$	$\%c_{lmax}$ Gain*	$\frac{d_{cp}}{d_x}$	c_{m0}
NLF(1)-0416	1.7500	—	0.2493	-0.0994
PARSEC (Full Set)	1.7589	+↑0.51	0.0388	-0.0822
PARSEC (Reduced Set - t_{ew})	1.7165	-↓1.91	0.0408	-0.0839
PARSEC - Modified (Full Set)	1.7717	+↑1.22	0.0542	-0.0639
PARSEC - Modified (Reduced Set - teg_{low})	1.7661	+↑0.91	0.0432	-0.0969

* **Relative to the benchmark NLF(1)-0416 Airfoil**

The results indicate the geometrical constraint of $t/c > 0.12$ is satisfied by all designs in Table 6.4. The optimisation simulations converge to the t/c of the benchmark airfoil. The maximum camber of the simulation shapes is lower than the validation profile and a higher AoA is required to compensate for the low camber to achieve cruise c_l^T. A reduction of drag in excess of 20% is observed across the simulation data. It is observed that with an increase of polynomial order for airfoil representation, drag decreases proportionally. A full set of 10 PARSEC variables has lower drag ($c_d = 0.00398$) compared to the analysis with t_{ew} eliminated ($c_d = 0.00399$). A percentage difference of $\approx 0.25\%$ is minimal. The effect of eliminating t_{ew} by the pre-screening analysis due to a low drag contribution is validated. A minimal variance of 3% to drag was established from the sensitivity study (Fig. G.2).

The original PARSEC method indicates a drag reduction in excess of ≈ 20% compared to the base NLF(1)-0416 airfoil.

The PARSEC-Modified method with a full set of thirteen variables exhibits the lowest drag (c_d = 0.00390) corresponding to a reduction of ≈ 22% in comparison to the benchmark airfoil. Drag increases slightly (c_d = 0.00392) with the elimination of teg_{low} (Tab. 6.4), thus corresponding to a percentage difference of ≈ 0.50% between the full and reduced variable population sets. The effect of eliminating un-important variables by a sensitivity analysis on drag is validated. The pre-screening analysis of the PARSEC-Modified function identified $t_{eg_{low}}$ with the lowest contribution to drag (Fig. 4.23(a)). The effect of setting $t_{eg_{low}}$ to the baseline value representative of the NLF(1)-0416 airfoil has a minor affect on drag of the optimal shape between full and reduced data sets. The validity of the design variable pre-screening methodology is confirmed. Comparatively a drag reduction of ≈ 22% relative to the baseline shape is computed even with the reduction of a design variable from the analysis.

The effect of varying the polynomial order of the airfoil shape function on c_{lmax} is identified in Table 6.5. An increase in design variable population size has the merits of increasing the c_{lmax} of the optimised airfoils. The original PARSEC model with a full set of 10 design variables matches the c_{lmax} of the base airfoil with a minimal increase of ≈ 0.50%. The number of design variables applied for shape optimisation are minimised by eliminating t_{ew} from the PARSEC function. Coefficient t_{ew} has a variance of 6% to c_{lmax} compared to the least important factor y_{xxl} which exhibits a 5% contribution in Figure G.2(b). The shape coefficient t_{ew} was eliminated based on the minimal contribution to drag only (Fig. G.2(a)). The influence of t_{ew} on c_{lmax} was not considered. The c_{lmax} of the PARSEC reduced-set with 9 variables decreases to 1.72 in comparison to 1.76 with ten design variables (Tab. 6.5). This corresponds to a percentage difference of ≈ 2% between the two sets. The c_{lmax} of the reduced method with 9 variables is also the lowest of all shapes and the constraint $c_{lmax} > 1.76$ (Sec. 6.3.2) is violated. The results by reduced variable modeling represent a compromised design performance of reduced drag and c_{lmax} relative to the benchmark profile.

The PARSEC-Modified function with a full set of 13 design variables exhibits the highest c_{lmax} with an increase of ≈ 2% in comparison to the benchmark profile (shaded row in Tab. 6.5). The c_{lmax} with the reduced set at 12 variables is ≈ 1% greater than the base NLF(1)-0416 airfoil. A minimal c_{lmax} percentage difference of ≈ 0.30% is computed between the full and reduced PARSEC-Modified function sets. Since $t_{eg_{low}}$ simultaneously exhibits the lowest variance to c_d and c_{lmax}, the percentage differences of the aerodynamic performances of the final shape between the full and reduced sets is minimal. The computed pattern differs to the original PARSEC method where a conflicting contribution of t_{ew} on c_d and c_{lmax} was observed.

The analysis confirms that if a design variable has a low and consistent contribution over disparate aerodynamic coefficient types, the performances of the optimal shapes are similar. This expected behavior is validated in the analysis of the PARSEC-Modified function. A conflicting contribution will result in a design compromise as observed in the analysis by the original PARSEC model.

The constraint relating to the extent of the favorable pressure gradient is satisfied in all designs in Table 6.5. The peak of the negative pressure coefficient is located about the leading edge in comparison to the NLF(1)-0416 which is further downstream (Fig. 6.7(b)). The chordwise location

of the maximum thickness point is in excess of 0.50c (Fig. 6.7(a)) to delay flow transition. The peak of d_{cp}/d_x is shifted downstream to facilitate a gradual pressure gradient downstream of the leading edge to maintain extended regions of laminar flow.

The c_{m0} is also satisfied in all design simulations in Table 6.5. The magnitude of c_{m0} is directly related to airfoil aft loading. The PARSEC-Modified method with $t_{eg_{low}}$ eliminated is aft loaded (Fig. 6.7(a)) and is characterised by a high c_{m0} that is within the defined design constraint limit. The PARSEC-Modified method with 13 design variables has moderate aft loading in the range x/c $\approx$ 0.65-1.00 (Fig. 6.7(a) - 6.7(b)) and c_{m0} is low accordingly.

Solution termination is measured as a function of the global best particle including the personal best fitness range p_f. Since p_f is a measure of performance on two particles only; the absolute difference in fitness of the worst and best performing particle, a third measure based on the fitness spread of the entire swarm is proposed, by σ_t. The proposed termination measures are defined to establish the relationship between the evolution of the global best particle and the search patterns of the swarm with p_f and σ_t. Depending on the degree-of-solution improvement relative to the global best solution, p_f will deviate proportionally. The measure of spread will represent the search pattern of the swarm and is not restricted to the performance of a select few particles. Even with a stagnant global best solution, the search experience of the swarm is observed and applied to influence termination. The defined measures must share a common consensus before convergence is assumed. In this case, convergence is assumed only when the three quantities are stagnant for a set number of iterations. The fitness convergence history of the defined search termination measures is presented in Figure 6.8 for the PARSEC and PARSEC-Modified methods with the full and reduced set of design variables.

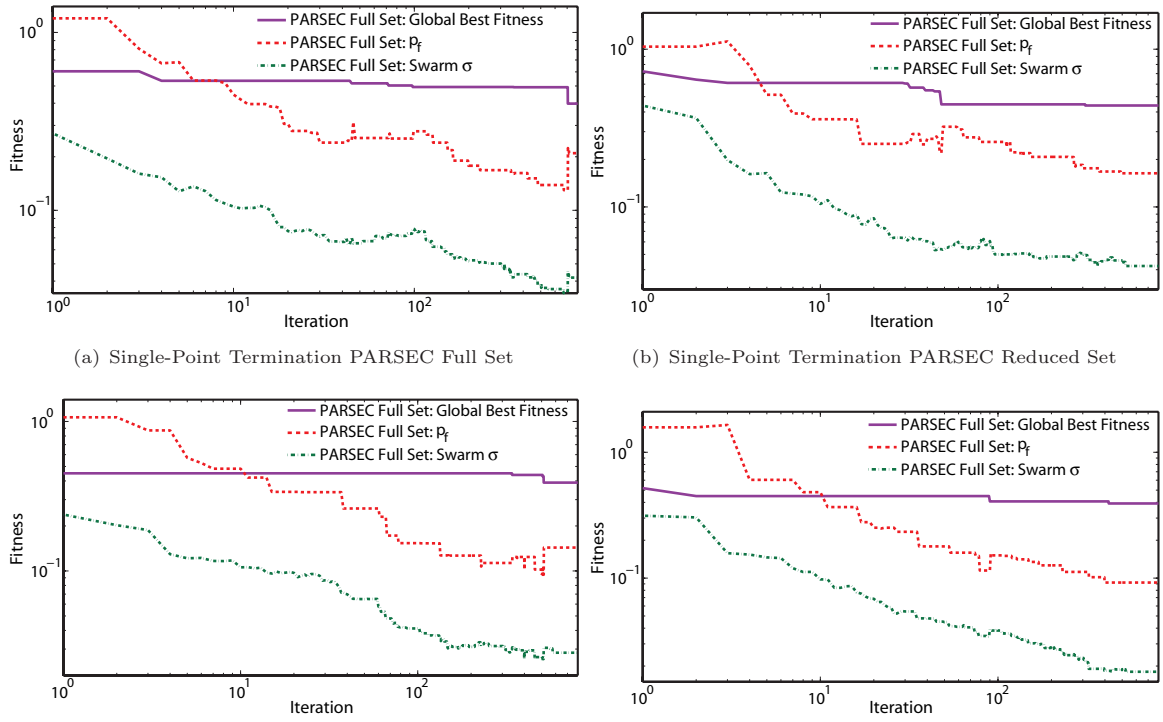

(a) Single-Point Termination PARSEC Full Set

(b) Single-Point Termination PARSEC Reduced Set

(c) Single-Point Termination PARSEC-Modified Full Set

(d) Single-Point Termination PARSEC-Modified Reduced Set

FIGURE 6.8: HALE Single-Point Airfoil Optimisation - Analysis of Solution Convergence by AM-PSO and XFOIL with PARSEC & PARSEC-Modified Variants

An extended region of a stagnant global best solution as a function of iteration time is observed for the respective shape function types in Figure 6.8. Concurrently p_f and σ_t deviate simultaneously and represent an active search history in the swarm. In the PARSEC original method with a full set of 10 design variables (Fig. 6.8(a)), the three termination quantities *pbestg*, p_f and σ_t indicate a stagnant search process from the 705^{th} iteration. The repeat of the simulation with t_{ew} eliminated indicates stagnation from the 522^{nd} generation (Fig. 6.8(b)). Convergence is achieved with ≈26% fewer iterations between the full and reduced sets. The merits of applying fewer search iterations results in significant computational time savings to convergence. The true benefits are derived if high-fidelity solvers are applied instead. The benefits of accelerated convergence to search termination does not compromise the aerodynamics of the optimal airfoil.

Solution convergence with the PARSEC-Modified method is presented in Figures 6.8(c) and 6.8(d). A simulation with the full set of 13 design variables (Fig. 6.8(c)), indicates a stagnant search process from the 578^{th} iterate with σ_t representing convergence to a specific value. The quantities *pbestg* and p_f converged at the 514^{th} iterate. The benefits of implementing the defined termination measures are evident in this analysis. An extended flat plateau of the global best solution from search initialisation to the 340^{th} search generation is observed (Fig. 6.8(c)). If termination was defined based on an extended global best solution only, then a sub-optimal solution would be the result. Simultaneous examination of p_f and σ_t indicates consistent search deviations despite a stagnant global best. Due to an active search history in the swarm, the optimisation process continued. Global best solution improvements are observed during the later stages of the search process. Termination is initiated when the three quantities represent an in-active search evolution phase.

By eliminating $t_{eg_{low}}$ in the PARSEC-Modified method, the global best stagnates at the 420^{th} iterate, p_f at the 398^{th} and σ_t at the 523^{rd} generation (Fig. 6.8(d)). If the AM-PSO search process was terminated at the 523^{rd} search evolution due to the three termination quantities indicating a stagnant search performance, significant computational time savings would follow. The aerodynamics of the optimal airfoil is compromised by ≈0.50% (Tab. 6.4) by the omission of $t_{eg_{low}}$, in comparison to the full set of shape variables. The potential computational time savings are significant. The true benefits of the developed, design variable pre-screening analysis will ensue with the integration of high-fidelity solvers in the DNO design loop. The results validate the effectiveness of eliminating un-important design variables by a design variable pre-screening study on computational efficiency.

6.4.2 MM-UAV HALE Multi-Point Airfoil Optimisation

To address the off-design performance demerits of the single-point design approach, a multi-point methodology is applied to minimise drag over an extended lift coefficient flight envelope at climb and cruise conditions. The problem is formulated by taking the summation of the drag performances at the defined flight conditions in Equation 6.10. Theoretically the multi-point design formulation will result in consistent drag performance over the user-defined lift envelope. The constraints applied in the single-design approach (Eqns. 6.4 - 6.8), are integrated into the multi-point definition to ensure the optimal profile does not violate user-defined geometrical and aerodynamic conditions. Drela [161] proposed the application of weights to represent the importance of each flight condition in the mission profile to the design optimisation algorithm.

Huyse et al. [68, 162] proposed the application of a normal distribution method to establish the weights at off-flight conditions relative to the primary flight phase. The number of flight conditions selected for design optimisations needs to be high. A rule-of-thumb estimation is provided such that the number of flight points used to define the multi-point design must match the design variable population size to minimise the drag 'bumps' at off-design conditions. This will result in a computationally heavy simulation as the flow solver is applied at several flight conditions. The analysis was based on the design optimisation of transonic airfoils where drag 'bumps' were evident due to the sensitivity of the flight Mach number to surface generated shock waves. Hence, sampling the design condition at several conditions was justified.

As wave drag is not a performance issue at HALE conditions, the number of flight points used in the multi-point optimisation approach is minimised to address the computational cost demerit. The effectiveness of the multi-point design over the single-point approach at two flight conditions is examined. Drag minimisation at climb and cruise is specified which relates to a c_l^T of 1.00 and 0.40 respectively. Drag at each c_l^T is weighted equally ($w_i = 1$) to represent an even importance between the two flight parameters for design analysis (Eqn. 6.10). Similar to the single-point analysis, the effect of applying the PARSEC and PARSEC-Modified functions with a full and reduced set of design variables is examined. The airfoil geometry and corresponding aerodynamic performance comparisons between benchmark NLF(1)-0416 and multi-point AM-PSO based optimisation profile are presented in Figure 6.9.

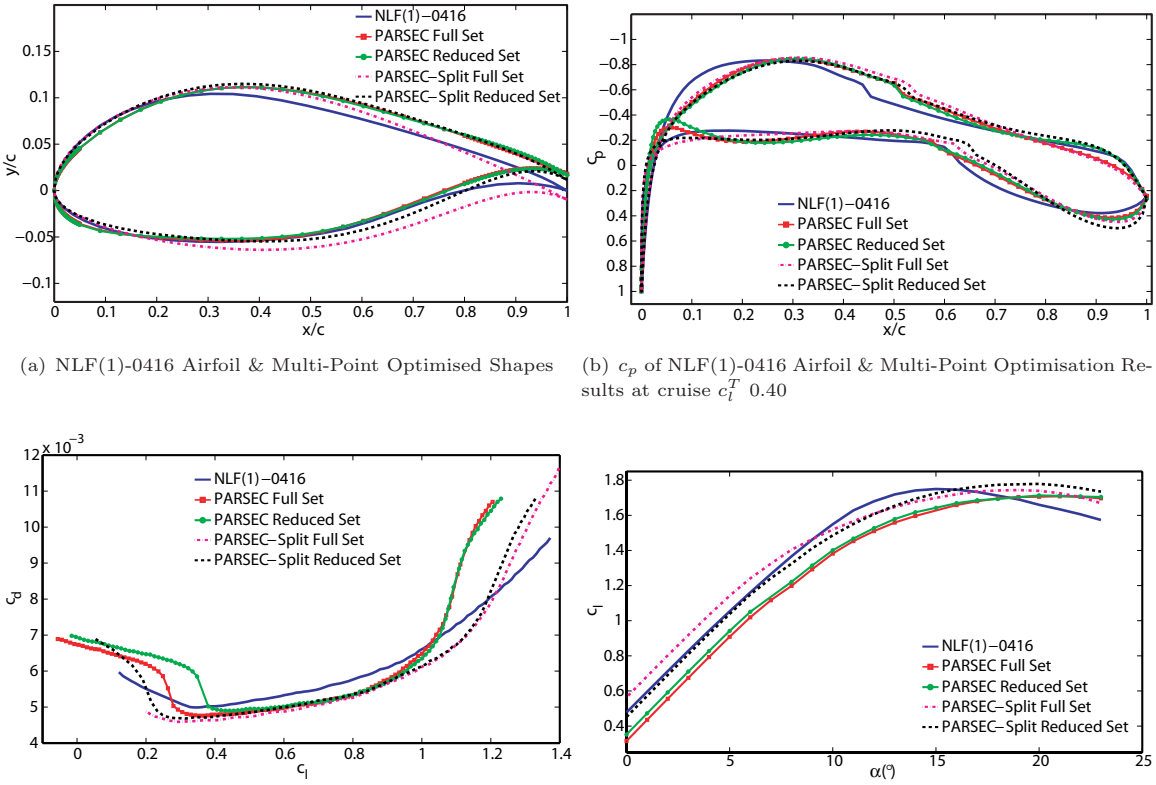

(a) NLF(1)-0416 Airfoil & Multi-Point Optimised Shapes

(b) c_p of NLF(1)-0416 Airfoil & Multi-Point Optimisation Results at cruise c_l^T 0.40

(c) Drag Polar of NLF(1)-0416 & Multi-Point Optimisation Results at $R_n = 4.0 \times 10^6$

(d) c_{lmax} of NLF(1)-0416 & Multi-Point Optimisation Results at $R_n = 3.0 \times 10^6$

FIGURE 6.9: HALE Multi-Point Airfoil Optimisation Results by the AM-PSO Method with XFOIL

The geometry features of the optimal airfoils by the multi-point design method match the benchmark profile in Figure 6.9(a). The multi-point designs are adapting to the flight conditions of the baseline shape with drag minimisation over an extended lift coefficient envelope. The multi-point shapes are also modeled with extended x_u and y_l coefficients, but limited in comparison to single-point designs (Fig. 6.7(a)). Variations in y_{te} are evident relative to the baseline shape. The magnitude x_u of the optimised shapes is $\approx 0.35 - 0.40$ and is lower than the magnitude attained in single-point designs. This affects flow transition which shifts aft of the trailing edge to ≈ 0.47 and ≈ 0.60 for upper and lower surfaces respectively in Figure 6.9(b). In comparison to the baseline shape, multi-point designs exhibit delayed flow transition.

A point-of-issue with the contour of the converged optimal shapes in Figure 6.9(a) is the layout of the internal wedge geometry at the trailing edge. This is limited to small angles that is approaching zero degrees. A small internal wedge will result in manufacturing challenges. To address this issue, structural constraints need to be imposed including the re-definition of the solution search space variables that control the internal wedge angles at the trailing edge. The recommended changes to the problem definition will facilitate the definition of an allowable minimum internal wedge angle tolerance such that realistic shapes from a manufacturing perspective can be achieved, while concurrently conforming to the aerodynamic performance requirements by the shape optimisation process. The implementation of structural constraints is not considered in this thesis.

In single-point designs, the cruise $c_l^T = 0.40$ was integrated into the design process only. The AoA required at cruise was low (Tab. 6.4) and skin-friction drag was minimised by maintaining extended regions of laminar flow on airfoil pressure and suction surfaces. A low AoA delayed transition in excess of 0.60c for acceptable drag performance. In multi-point designs, variations in flight AoA are required to satisfy minimum lift at climb and cruise segments. A minimum drag compromise at the two flight conditions is a result. The AM-PSO delays transition to minimise drag at $c_l^T = 0.40$ by inducing extended regions of laminar flow. Concurrently to achieve the $c_l^T = 1.00$ for climb, the AoA is increased and this has an affect of shifting transition toward the leading edge. The two flight conditions have a conflicting affect on the location of the tripping point. A design compromise between the two flight conditions has the affect of shifting transition aft of the trailing edge (Fig. 6.9(b)), in comparison to single-point designs (Fig. 6.7(b)).

The effect of a multi-point design process on drag is modeled in Figure 6.9(c). An extended 'drag bucket' is evident in comparison to single-point design, which was localised about the cruise $c_l^T = 0.40$ (Fig. 6.7(c)). In multi-point simulations, favorable drag performance is observed over an extended input c_l^T range for climb and cruise. The drag performances of all airfoils achieved by the AM-PSO simulations are lower than the baseline shape for the defined flight lift envelope. The merit of a multi-point design approach on drag minimisation is validated. At off-conditions for $c_l < 0.40$ and $c_l > 1.00$ (Fig. 6.9(c)), the drag performance degrades significantly.

The variation of y_{te} for the shapes generated by the original PARSEC method are attributed to the c_{lmax} performance, similar to single-point designs. Since y_{te} has a minimal impact on c_d (Fig. G.2(a)) relative to c_l (Fig. G.4(b)), the variance of y_{te} on airfoils by the PARSEC method (Fig. 6.9(a)) is related to the c_{lmax} constraint. The PARSEC method with t_{ew} eliminated has a lower y_{te}, hence a higher c_{lmax} in Figure 6.9(d). Comparatively the PARSEC method with a full set of 10 design coefficients is characterised by a higher y_{te} and a lower c_{lmax}. The observed relationship

of y_{te} on c_l was validated in the two-way interaction contour plots in Figure F.1(a). Relatively the two-way interaction plots of y_{te} on c_d, with the rest PARSEC coefficients indicated a minimal activity in comparison (Fig. F.1(b)).

The PARSEC-Modified variant achieves a higher c_{lmax} than the PARSEC original method in Figure 6.9(d). The simulation with $t_{eg_{low}}$ eliminated generates the highest c_{lmax}. The disparity in the optimal shapes by the PARSEC-Modified method is not isolated to variances in y_{te} only as in the original PARSEC function. It is also related to the contribution of the trailing edge angles and the direction of upper and lower surfaces. Shape differences are isolated to an airfoil chord bounded by $x/c \approx 0.60 - 1.00$. The contribution of additional shape variables are enhancing the c_{lmax} performance and not y_{te} only as in the original PARSEC method. The aerodynamics of the benchmark and optimised airfoils at cruise $c_l^T = 0.40$ is summarised in Table 6.6.

TABLE 6.6: HALE Multi-Point Airfoil Optimisation Objective Measure at Cruise $c_l^T = 0.40$ by the AM-PSO Method with XFOIL

Airfoil	t/c	Max Camber	c_l	AoA(°)	c_d	% c_d Gain*
NLF(1)-0416	0.16	0.025	0.40	-0.695	0.00502	—
PARSEC (Full Set)	0.165	0.022	0.40	0.675	0.00479	-↓4.58
PARSEC (Reduced Set - t_{ew})	0.163	0.024	0.40	0.355	0.00495	-↓1.40
PARSEC - Modified (Full Set)	0.175	0.027	0.40	-1.396	0.00464	-↓7.57
PARSEC - Modified (Reduced Set - teg_{low})	0.170	0.026	0.40	-0.484	0.00473	-↓5.78

* **Relative to the benchmark NLF(1)-0416 Airfoil**

The results conform to minimum t/c constraint with multi-point airfoils thicker than single-point designs. The maximum camber is also higher than single-point designs and the results are converging to the baseline value of the benchmark airfoil. The AoA required to achieve cruise $c_l^T = 0.40$ is lower in comparison to single-point designs where the camber was significantly lower and a higher AOA was required to compensate for minimum lift. A drag reduction of $\approx 1\% - \approx 7\%$ is computed across the optimal shapes generated at cruise c_l^T in comparison to the validation airfoil. The drag reduction magnitude does not match single-point designs where drag minimisation was in excess of $\approx 20\%$ relative to the NLF(1)-0416 profile. The results established signify a design compromise between the two flight conditions. The single-point design minimises drag at one condition and a global solution is achieved. In multi-point designs a compromise between disparate flight conditions is established and a localised solution about the specified flight point is generated resulting in sub-optimal drag reduction in comparison to the single-point designs. The best drag at cruise c_l^T with the multi-point design by the PARSEC-Modified variant ($c_d = 0.00464$) is $\approx 16\%$ greater than the minimum drag performance by the single-point design ($c_d = 0.00390$) with the respective shape function. The localised affects of drag in multi-point designs is evident in comparison to single-point solutions.

Similar to single-point designs, an increase in the polynomial order applied for airfoil shape generation in multi-point formulations, increases the magnitude of drag reduction in Table 6.6. The PARSEC method with a full set of 10 design coefficients minimises drag by $\approx 4.5\%$ compared to $\approx 1\%$ with

the elimination of t_{ew} from the population set. The highest drag reduction is observed with the PARSEC-Modified method utilising the full thirteen variables with a drag reduction of $\approx 7.5\%$. This is reduced to 6% with the elimination of $t_{eg_{low}}$ from the shape function. The percentage difference in drag between the full and reduced set of design variables with PARSEC and PARSEC-Modified methods are pronounced in multi-point designs than single-point formulations. A percentage difference of $\approx 3\%$ between the PARSEC full set ($c_d = 0.00479$) and PARSEC reduced method with t_{ew} eliminated ($c_d = 0.00495$) is computed compared to $\approx 0.25\%$ in single-point designs. Similarly for the PARSEC-Modified method, the percentage difference between the full set ($c_d = 0.00464$) and reduced set with $t_{eg_{low}}$ eliminated ($c_d = 0.00473$) is $\approx 2\%$ compared to $\approx 0.50\%$ in single-point designs.

The converged aerodynamics of the benchmark and optimal airfoils at the second, user-defined flight condition for climb at $c_l^T = 1.00$ is presented in Table 6.7.

TABLE 6.7: HALE Multi-Point Airfoil Optimisation Objective Measure at Climb $c_l^T = 1.00$ by the AM-PSO Method with XFOIL

Airfoil	Max Camber	c_l	AoA(°)	c_d	% c_d Gain*
NLF(1)-0416	0.025	1.00	4.479	0.00661	—
PARSEC (Full Set)	0.022	1.00	5.798	0.00648	-↓1.97
PARSEC (Reduced Set - t_{ew})	0.024	1.00	5.496	0.00635	-↓3.93
PARSEC - Modified (Full Set)	0.027	1.00	3.677	0.00612	-↓7.41
PARSEC - Modified (Reduced Set - teg_{low})	0.026	1.00	4.60	0.00613	-↓7.26

* **Relative to the benchmark NLF(1)-0416 Airfoil**

The optimal shapes by the multi-point design optimisation process in Figure 6.9(a) represent lower drag at climb than the validation profile in Table 6.7. A maximum reduction of $\approx 7.50\%$ is established with the full set of design variables by the PARSEC-Modified function. Comparing the performances of the shape functions, it is observed that the drag at climb is lower with the PARSEC-Modified method in comparison to the original PARSEC model. An increase in design variable population size has the affect of decreasing drag accordingly.

The impact of design variable elimination with the PARSEC original and PARSEC-Modified variants, results in a design compromise between drag at climb (Tab. 6.7) and cruise (Tab. 6.6). The original PARSEC method with t_{ew} eliminated, indicates lower drag at climb ($c_d = 0.00635$) than the PARSEC method with a full set ($c_d = 0.00648$) by 2% (Tab. 6.7). A design compromise at cruise is observed with drag $\approx 3\%$ higher with t_{ew} set to the baseline value ($c_d = 0.00495$) compared to the PARSEC original method ($c_d = 0.00479$).

The effect of eliminating $t_{eg_{low}}$ from the PARSEC-Modified function increases drag at climb (Tab. 6.7) and cruise (Tab. 6.6), in comparison to the shape function with the full set of 13 design coefficients. At climb, a drag rise of $\approx 0.20\%$ is calculated by a simulation with twelve design coefficients ($c_d = 0.00613$) compared to an optimisation with thirteen variables ($c_d = 0.00612$). The percentage

difference is assumed to be negligible. At cruise, the percentage increase as a result of variable elimination is ≈ 2%. Even with design variable elimination by the PARSEC-Modified method, the drag performances of the optimal shape generated by the AM-PSO method are favorable in comparison to the benchmark NLF(1)-0416 profile.

In single-point design analysis, the effect of eliminating a design variable increased drag and reduced c_{lmax} in comparison to the full set of design coefficients for the respective shape function type (Tab. 6.5). The feasibility of the multi-point design for airfoil design with coefficient elimination by a pre-screening analysis is established. Design variable elimination increased drag at cruise c_l^T by ≈ 3% with t_{ew} set at a baseline value relative to the PARSEC shape function with the full set of 10 variables. The omission of $t_{eg_{low}}$ from the PARSEC-Modified analysis increased drag by ≈ 2% relative to the shape function with full 13 design variables. At climb, minimal drag variances between full and reduced sets are observed in Table 6.8. A reduction of 2% is calculated as a result of eliminating t_{ew} from the PARSEC set and a negligible gain of ≈ 0.20% by setting $t_{eg_{low}}$ in the PARSEC-Modified function to the baseline coefficient of the benchmark airfoil.

The constraints of the optimal airfoils at climb and cruise are presented in Table 6.8.

TABLE 6.8: HALE Multi-Point Airfoil Optimisation Constraints Measure by the AM-PSO Method with XFOIL

Airfoil	c_{lmax} $R_n = 3 \times 10^6$	$\%c_{lmax}$ Gain*	$\frac{d_{cp}}{d_x}$	c_{m0}
NLF(1)-0416	1.7500	—	0.2493	-0.0994
PARSEC (Full Set)	1.7084	-↓2.38	0.2909	-0.0951
PARSEC (Reduced Set - t_{ew})	1.7137	-↓2.07	0.3049	-0.1037
PARSEC - Modified (Full Set)	1.7440	-↓0.34	0.3056	-0.0901
PARSEC - Modified (Reduced Set - teg_{low})	1.780	+↑1.69	0.3017	-0.0978

* **Relative to the benchmark NLF(1)-0416 Airfoil**

As the c_{lmax} is a performance constraint and not a design objective, the performance deviations are comparable to single-point designs. The c_{lmax} percentage loss (-%), between shape optimisation results and benchmark validation profile with multi-point designs in Table 6.8, is greater than single-point performance from Table 6.5. The c_{lmax} of single-point designs converged about the validation airfoil. The performance of c_{lmax} is sensitive to drag minimisation at multiple flight conditions as opposed to single-point designs. The PARSEC original method with full and reduced set of design coefficients exhibits lower c_{lmax} than the PARSEC-Modified method. An increase in the order of the polynomial shape function increases the c_{lmax} of the optimal shapes accordingly.

The c_{lmax} of the optimal shapes with design variable elimination in multi-point designs is greater than the single-point results. In the reduced variable dimensional data set for single and multi point designs, c_{lmax} with the PARSEC methodology is 1.7165 (Tab. 6.5) and 1.7137 (Tab. 6.8) respectively. In multi-point design with teg_{low} eliminated in the PARSEC-Modified function, the c_{lmax} is 1.780 (Tab. 6.8) compared to 1.7661 (Table 6.5) in single-point analysis with a variance of ≈ 1% between

the two datasets. The effect of design variable elimination with multi-point designs has a greater influence on drag at climb (Tab. 6.7) and cruise (Tab. 6.6) than single-point optimisations (Tab. 6.4). The c_{lmax} variances are also further pronounced with multi-point formulations.

The constraint relating to the extent of the favorable pressure gradient is observed to converge about the baseline value of the NLF(1)-0416 airfoil for all cases examined in Table 6.8. The minimum chord location of $\frac{d_{cp}}{d_x} < 0.30$ constraint (Eqn. 6.5), is violated in three out of the four simulations with a minimal deviation from the user-specified design requirement. The $\frac{d_{cp}}{d_x}$ has shifted aft of the leading edge in comparison to single-point designs to compensate for delayed flow transition at two disparate flight conditions instead of a uni-based design phase. Multi-point designs are characterised by aft pressure loadings (Fig. 6.9(b)), relative to single-stage designs (Fig. 6.7(b)), for chord regions bounded by $x/c \approx 0.70 - 1.00$. Accordingly the magnitude of c_{m0} increases (Tab. 6.8) and one simulation violates the constraint with a magnitude of -0.1037 (Eqn. 6.8). The violation is minimal and assumed negligible in the design process.

The swarm convergence in the AM-PSO optimisation method as a function of the design iterations and the collective search behavior of the particles is analysed for multi-point designs. The impact of variable elimination from the design process is verified to establish if the theoretical merits of enhanced computing efficiency by the defined variable pre-screening analysis has been achieved. The three termination measures including the search history of the global best, the lower and upper most extreme fitness points p_f and the swarm fitness spread σ_{swarm} are applied in the convergence assessment. Multi-point designs require additional fitness function evaluations by the flow solver at each iteration than single-point processes due to the inclusion of additional flight points in the design analysis. The computational wall-time to convergence is increased in comparison to single-point design processes. The relative impact of variable elimination in comparison to a simulation with a full set of design coefficients is examined. The iteration history plots with the defined swarm search behavior measures as a function of the airfoil shape parameterisation model type is presented in Figure 6.10:

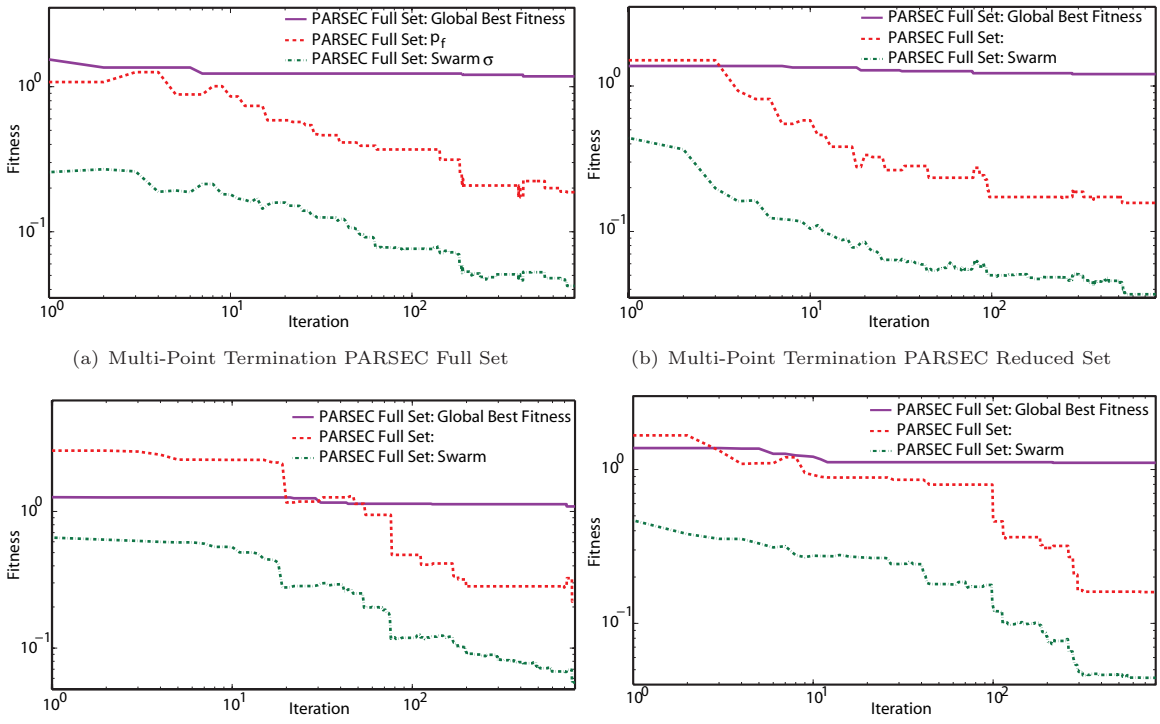

(a) Multi-Point Termination PARSEC Full Set

(b) Multi-Point Termination PARSEC Reduced Set

(c) Multi-Point Termination PARSEC-Modified Full Set

(d) Multi-Point Termination PARSEC-Modified Reduced Set

FIGURE 6.10: HALE Multi-Point Airfoil Optimisation - Analysis of Solution Convergence by AM-PSO and XFOIL with PARSEC & PARSEC-Modified Variants

The evolution of the global best particle indicates extended regions of search stagnation in comparison to the measures p_f and σ_{swarm} in Figure 6.10 for the respective shape function type. The PARSEC methodology with a full set of design variables (Fig. 6.10(a)), converged at the 716^{th} iterate. The global best and p_f converged at the 410^{th} and 659^{th} iterate respectively, followed by the convergence of σ_{swarm} at the 716^{th} iterate. A stagnant global best solution extending over 219 iterations from the $190^{th} - 409^{th}$ evolution is observed. If solution convergence was based on the performance of the *pbestg* only, then premature convergence would ensue and a sub-optimal solution would be the result.

The termination measures for the PARSEC methodology with t_{ew} eliminated converged at the 544^{th} iterate in Figure 6.10(b). In comparison to a simulation with a full set of design variables, 172 fewer (716-544) iterations are required. In multi-point design optimisation by high-fidelity solvers, this will result in significant computational time savings. The analysis confirms the merits of eliminating un-important design variables to the defined objective function on computational time savings. The process of integrating three disparate terminations measures to mitigate premature convergence is also validated as the search evolution of the global best point indicates extended regions of stagnation in comparison to p_f and σ_{swarm}. Delaying convergence based on a stagnant p_f and σ_{swarm} instead of *pbestg* only results in a decrease of the fitness function and convergence to the true optima is achieved.

The search process with the PARSEC-Modified method with thirteen design variables converges at the 774^{th} iterate in Figure 6.10(c). The defined termination parameters remain constant from the 774^{th} evolution up to the maximum iteration count of 800, hence representing a converged state. In comparison the simulation with twelve design coefficients converges at the 661^{st} search evolution

in Figure 6.10(d). A reduction of 113 design iterations between the two simulations (774 - 661) is significant and the potential for excessive computational time savings is evident. The process of design variable elimination for balance between solution feasibility and solver efficiency is validated. The applied process will benefit airfoil design simulations with high-fidelity solvers in the DNO structure (Secs. 6.6 & 6.8).

6.4.3 MM-UAV HALE Airfoil Optimisation by a Robust Design Approach

The results by the multi-point approach (Sec. 6.4.2) yielded acceptable drag performance in comparison to benchmark profile for the defined lift coefficient flight envelope. Despite the performance gains, there are issues and challenges to the multi-point approach that must be addressed and include: **a)** Selection of c_l^T flight points for integration into the AM-PSO algorithm; **b)** Number of flight points for design optimisation; and **c)** Definition of weight factors which act as multipliers to the objective function.

The consensus in the literature governs the selection of flight points based on the stipulated problem design goals. Airfoil optimisation for cruise performance requires the definition of a cruise-specific c_l^T which is used as a design point for optimisation analysis. Optimisation of climb profile is defined by the integration of climb profile c_l^T. The defined design process was successfully demonstrated in Section 6.4.2.

To address the identified challenge of selecting a valid number of c_l^T flight points, the following factors must be considered:

1. **Flexibility of the Applied Optimisation Algorithm:** The scope of the problem is a function of the defined dimensional search space size. It is also affected by the population of flight points applied in the design analysis. The size of the user-defined flight points must not exceed the established flexibility of the search method else a sub-optimal result will follow.
2. **Availability of Computing Resources:** The integration of a specific c_l^T flight point to the design analysis demands personal fitness function execution by the flow solver at each design iteration. If the size of the selected flight points is excessive, the computational efficiency will be degraded. Greater computing memory resources will be required to address this issue.

The definition of acceptable weight factors is directly related to the selection of flight c_l^T points. The definition of the weights is based on designer experience and/or with the support of an extensive DoE analysis. As the mission profile of the MM-UAV is dominated by a cruise phase at low-speeds for HALE operations and high-speed dash segments for SEAD sorties (Fig. 6.1), the weighting can be influenced for emphasis on cruise and high-speed dash segments, with less importance on the climb profile. The definition of an acceptable weighting methodology is based on designer preference and is in accordance to the interpreted importance of a specific flight segment relative to the overall mission profile.

The c_l^T points are selected to represent the flight envelope that needs to be optimised. An extensive DoE analysis can be established by incrementally varying the weight factors and/or integrating

different combinations of c_l^T points for specific flight segments. The corresponding impact on airfoil performance can be identified to verify the feasibility of the selected flight points and the weight factors relative to the design goals and objectives. A comprehensive DoE process is computationally time consuming and is avoided.

In-lieu of a multi-objective approach, a robust airfoil design algorithm is developed. The application of fixed, user-defined c_l^T points in the multi-point approach has demerits. The flight profile will not always be stable at the defined cruise and climb specific c_l^T due to the uncertainty in flight operations. Deviations about the defined c_l^T flight points will result in performance degradation. The climb profile is not restricted to just one c_l^T, but is modeled over an extended c_l envelope due to changes in maneuver altitude. The climb profile must be optimised over an extended lift coefficient envelope to attain an aerodynamically efficient profile performance. At cruise, mission operations can result in a change in operating altitude that is offset to the airfoil-specific cruise c_l^T condition. The transition to the new flight point will result in a c_l that is different to original c_l^T and the airfoil will no longer output efficient operating performance.

The multi-point design method does not explicitly factor the changes in flight c_l^T from the originally specified to a new point due to flight uncertainty. Performance degradation will follow at the new operating condition as the airfoil was not designed to factor the changes in flight profile. From an operational perspective, the identified issue is not acceptable and must be addressed.

The flight Mach number is sensitive to surface shock in transonic airfoil design. Robust optimisation methodologies have been developed in the literature to attain acceptable aerodynamic performance over an extended Mach number envelope [68, 162–167]. Deviations in flight operations with altitudes and/or speeds result in variation of flight Mach and Reynolds number. This can induce rapid and sudden shock wave development. A robust design method incorporates the uncertainty in flight performance into the design process. The objective function was defined as the integrated sum of c_d over a user-defined Mach number range. The design process was defined to minimise drag over the defined flight Mach number range, instead of a single Mach number point only. The design effort had the merits of minimising the impact of shock waves over an extended transonic flight envelope due to the changes in flight operations. The shape sustained optimal aerodynamic performance, with flexibility to alter flight profile within a defined operating threshold without degrading airfoil aerodynamics. The development of a robust design effort for HALE airfoil design has not been addressed.

The design effort presented focuses on developing a robust design method for HALE airfoil design. The flight uncertainty parameter under investigation is the c_l^T. Flight deviations from the originally specified c_l^T will increase profile drag. The identified performance issue was modeled by the rapid increases in drag outside of the established 'drag-bucket' in single (Fig. 6.7(c)) and multi-point (Fig. 6.9(c)) designs. The 'drag-bucket' is the result of integrating a user-defined c_l^T into the airfoil design process. The AM-PSO focuses on minimising drag at the user-specified c_l^T point/s only and does not factor changes in flight operations that are offset to the specified target. If flight operations exceed the defined c_l^T envelope, excessive increases in drag will follow. The aim of the robust design effort is to maintain an extended 'drag-bucket' in comparison to the multi-point approach.

To address the requirement of an extended 'drag-bucket' with low drag performance relative to the benchmark profile, c_l^T points are intelligently selected by incorporating flexibility in flight operations

due to uncertainty. Instead of arbitrarily integrating c_l^T design points for specific flight segments, an intelligent process is developed which does not require designer intervention for flight design selection efforts. The methodology defines the flight points for analysis through an iterative process. The optimisation simulation aims to develop an airfoil with performance gains in drag over an extended flight envelope in comparison to the benchmark and multi-point design.

A robust airfoil optimisation methodology is proposed based on the principles applied by Lee et al. [168] and Lurati [169]. The uncertainty in flight operations is implemented in the optimisation process by integrating a probabilistic approach based on the stratified random sampling of the flight target lift coefficient. The analysis defines the range of the target lift coefficients $\left[c_{l_{min}}^T, c_{l_{max}}^T\right]$, which reflect the uncertainty in flight operations in the design search space $\mathcal{S}$.

The robustness in the shape design process under uncertainty on c_l^T is defined by evaluating $\mathcal{S}$, that minimises the objective function defined as the mean of the drag coefficient $\mu(c_d)$ over the mapped sampling variances in the c_l^T envelope in Equation 6.12. The drag is minimised concurrently over an extended c_l^T flight envelope as a function of the changes in flight conditions due to uncertainty. The AoA is not defined in the problem for c_l^T as XFOIL has a built-in trimming function that calculates the angle required to achieve the user-defined lift coefficient. The subroutine applies a set of user-defined iterations with a tolerance of 1.0×10^{-6} [78] to iteratively calculate the angle for an input c_l^T. Mathematically the formulation is presented in Equation 6.12.

$$\mu =_{\mathcal{S}}^{min} \int_{c_{l_{min}}^T}^{c_{l_{max}}^T} c_d\left(\mathcal{S}, c_l^T\right) dc_l^T \tag{6.12}$$

The integration of drag over the defined c_l^T range in Equation 6.12, models the area under the drag profile, hence μ is considered as the mean drag coefficient. By a statistical view point, the integral representation of the objective function is modeled by the average of drag over $\mathcal{N}$ c_l^T sample points within $\mathcal{S}$, in Equation 6.13.

$$\mu =_{\mathcal{S}}^{min} \sum_{i=0}^{\mathcal{N}} c_d(\mathcal{S}, c_l^T)\omega_i \tag{6.13}$$

The uncertainty in flight operations in speed and/or altitudes are incorporated in the design process by the random sampling of the c_l^T points for integration into the objective function (Eqn. 6.13) such that, $\bar{c_l^T} = \left[c_{l_1}^T, \cdots, c_{l_n}^T\right] \subset \left[c_{l_L}^T, c_{l_U}^T\right]$. The selection of $\mathcal{N}$ design points within the user-defined lower and upper limits of c_l^T for analysis by the objective function must be well-defined. If the selected points are within a minimum threshold of each other, then bias selection will result in a ill-defined design analysis. If the c_l^T points selected are $[c_{l_1}^T = 0.40, c_{l_2}^T = 0.40 \pm 0.01]$, then μ of c_d at the defined points will not model the true diversity of the flight uncertainty. Alternately if the flight points are dispersed, the magnitude of μ is a valid indication of the flight profile uncertainty. To mitigate the possibility of a biased selection of $\mathcal{N}$ for valid μ computation, a stratified sampling method based on a partitioned flight envelope spacing method is applied. The proposed methodology is presented in Figure 6.11

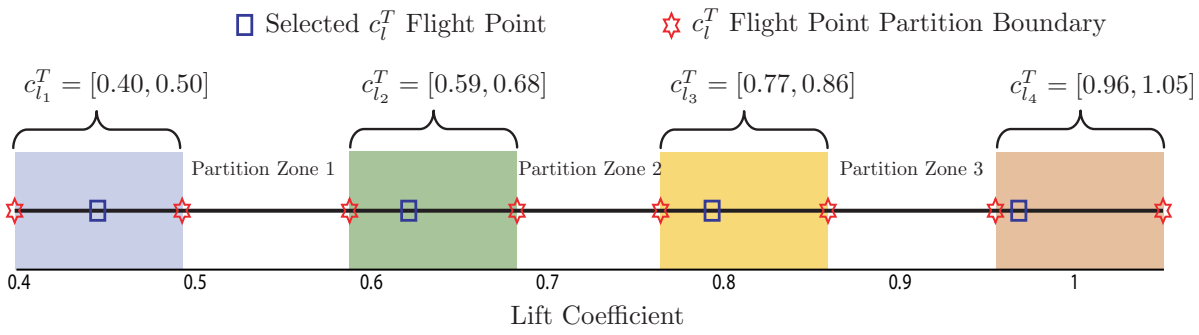

FIGURE 6.11: Definition of Target Lift Coefficient Design Flight Points $\mathcal{N}$ for Airfoil Optimisation by the Robust Approach

In the defined analysis $\mathcal{N} = 4$ and the drag is optimised concurrently at four disparate flight points. The scope of the lift coefficient envelope for shape design analysis is defined with the integration of c_l^T points for drag minimisation at climb and cruise flight segments. The objective function is modeled by the minimisation of the mean c_d over four c_l^T points that are partitioned within an interval of [0.40, 1.05], for cruise and climb segments. The merits of the robust approach in comparison to the multi-point philosophy is in the application of the flight points into the AM-PSO algorithm. Instead of fixing the c_l^T at specific pre-defined values within the mapped c_l^T interval range, the robust approach will randomly select flight points for design optimisation from the defined flight envelope.

The selection of flight points is based on a partitioning methodology to mitigate biased selection. The defined interval range [0.40, 1.05] is split into segments that define flight selection and exclusion zones in Figure 6.11. The first zone models the $c_{l_1}^T$ interval range of [0.40, 0.50] for design point selection. The robust approach randomly selects the first $c_{l_1}^T$ point from this region. Following is a exclusion zone, where no flight points are selected for design analysis. This is applied with intent to avoid the selection of flight points that are close to each other due to biased selection, which will result in a false interpretation of $\mu(c_d)$, hence objective function. By modeling a separation zone between adjoining flight point selection segments, design robustness due to flight uncertainty in operating conditions is maintained. Following the first exclusion zone, the second flight $c_{l_2}^T$ point selection area is defined over an interval [0.59, 0.68]. The developed robust approach within the AM-PSO method will randomly select a second flight point for design analysis within this region. Following is a second exclusion zone where no data points are selected and is defined to mitigate biased selection of flight points that could be in close range of the second flight selection segment region. A third region for $c_{l_3}^T$ selection follows over an interval range [0.77, 0.86], followed by a third exclusion zone for design robustness. The final flight point selection envelope is from a defined $c_{l_4}^T$ range of [0.96, 1.05].

The flight points within the defined inclusion zones (Fig. 6.11), are re-selected every $\mathcal{K}^{th}$ iteration for the purposes of modeling the scope of $\mathcal{S}$ over the defined flight c_l^T interval envelope. Constant re-selection of flight points facilitates the convergence to a global region due to the extension of the measuring location of the objective function within the solution search space. A comprehensive DoE analysis was undertaken to define the following parameters within the robust airfoil design methodology: **a)** The frequency rate of flight point re-selection over $\mathcal{K}$ design iterations; **b)** The intervals of the flight point selection and exclusion zones; and **c)** The magnitude of the weights for emphasis on flight segment importance (Eqn. 6.13).

The frequency of flight point re-selection of $\bar{c_l^T}$ was set to every ten design iterations based on the findings of the DoE analysis. The population size of the sampling points $\mathcal{N}$ was set at four. The corresponding c_l^T envelope for flight point selection and exclusion interval zones are evenly partitioned in the defined search envelope in Figure 6.11. The importance of flight segments by the definition of weights in the objective function are incrementally increased from the lower ($c_l^T = 0.40$) to the maximum modeled ($c_l^T = 1.05$) flight envelope (Eqn. 6.14). Weighting terms are further imposed to the constraints including c_{lmax}, $\frac{d_{cp}}{d_x}$ and c_{m0}. The search principles of the swarm in $\mathcal{S}$ will be influenced by low drag airfoils that concurrently satisfy the user-defined constraints. The mean of the objective function and the constraints with weights is defined as follows:

$$\mathcal{J}_{min} = \frac{1}{\mathcal{N}=4} \cdot \underbrace{[(c_{d_1} \times 10) + (c_{d_2} \times 20) + (c_{d_3} \times 30) + (c_{d_4} \times 40)]}_{\textbf{Objectives}}$$
$$+ \frac{1}{\mathcal{N}=4} \cdot \underbrace{[(c_{lmax_{pen.}} \times 10) + \left(\frac{d_{cp}}{d_x} pen. \times 10\right) + (t/c_{pen.}) + (c_{m0_{pen.}} \times 10)]}_{\textbf{Constraints}} \tag{6.14}$$

The defined problem formulation in Equation 6.14 with the integration of the AM-PSO algorithm aims to isolate a constraint satisfied airfoil with the lowest mean drag performance over the user-defined c_l^T range. The settings of the AM-PSO algorithm from Section 6.4 are applied in the robust design approach with exception of the shape parameterisation function type. The robust approach is limited to airfoil modeling by the PARSEC-Modified method with a full set of 13 design variables only. The impact of variable elimination based on the defined pre-screening analysis on solution convergence is not modeled.

A parallel computing architecture is applied in the design process. As the swarm size is 30 (Sec. 6.4), each particle will solve the objective function (Eqn. 6.14) at 4 unique c_l^T flight points. As XFOIL is applied in the design process, the computing time required to solve the aerodynamics is negligible. The demand on computing resources for the defined case is attributed to the size of the swarm and not the fidelity of the flow solver. To accelerate the computational process, each particle is concurrently solved on a local node within a parallel computing architecture. The total number of processors applied in the design cycle is equal to the size of the swarm with an additional parent node. Following the aerodynamic analysis, the data from each node is transferred to the host machine to simulate the AM-PSO algorithm. The parallel computing structure operates in iteration until AM-PSO convergence is achieved.

The optimal profile by the robust design approach is evaluated against the benchmark and the multi-point design method in Figure 6.12.

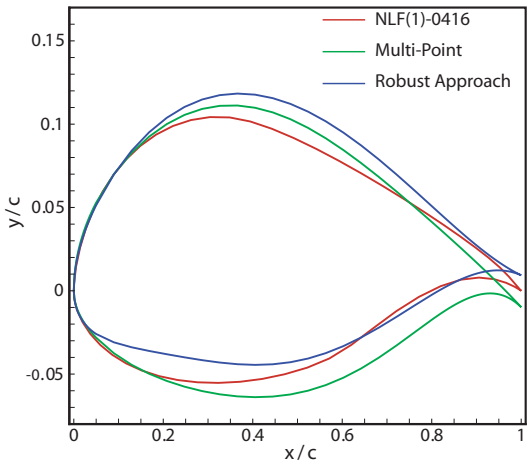

FIGURE 6.12: Airfoil Profile Comparison of the Multi-Point & Robust Design Approach Method with Baseline NLF(1)-0416

The optimal airfoil derived by the robust approach has a highly-cambered nose on the lower surface in comparison to the other shapes modeled in Figure 6.12. The nose contour on airfoil upper surface matches the geometry features of the benchmark and the multi-point based profiles. At the trailing edge, the airfoil is characterised by a minimal trailing edge wedge angle and direction contour features. The optimal shape by the robust method will impose manufacturing challenges. The limited internal wedge angle is representative of an unrealistic result from a design development perspective. As in the case for multi-point designs in Figure 6.9(a), the limited internal wedge angle issue can be addressed by the integration of structural constraints to the design problem including the re-definition of the search variables that control the internal wedge geometry. This will facilitate the development of a realistic profile as a result of the shape optimisation process for ease-of-manufacturing.

The thickness of the robust profile matches the benchmark and the multi-point profile at $t/c \approx 0.16$. Despite a similar thickness distribution, the robust design based profile has a thinner pressure surface relative to the chord plane, hence a low magnitude of variable y_l in comparison to the modeled shapes. The thickness on airfoil suction surface relative to the chord plane is the largest of all the shapes modeled with an extended magnitude for variable y_u. The impact of shape variance between the presented airfoils on drag polar is modeled in Figure 6.13.

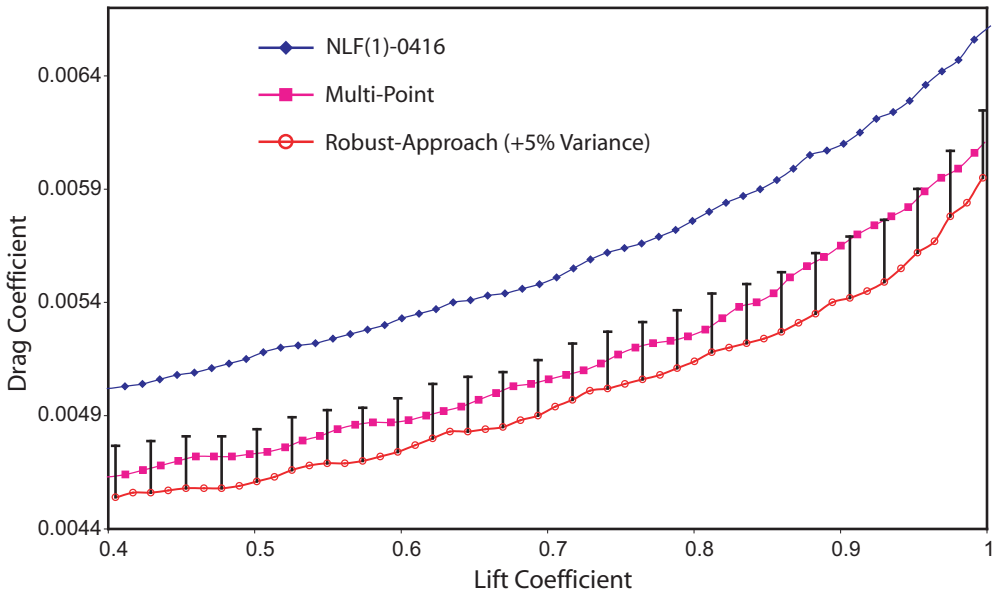

FIGURE 6.13: Airfoil Drag Polar Comparison of the Multi-Point & Robust Design Approach Method with Baseline NLF(1)-0416 at Mach=0.10 & $R_n = 4.0 \times 10^6$

The benchmark profile is characterised by the highest drag performance in comparison to airfoils modeled by the respective optimisation strategy in Figure 6.13. The merits of the robust design approach for drag minimisation is evaluated. The drag polar disparity between the multi-point and robust method as a function of the defined c_l^T flight envelope is modeled. The drag polar by the robust approach is integrated with error bars with a maximum variance of +5% for ease of data interpretation. Comparison of the drag performance between the multi-point and robust design method validates the achievement of low drag performance by the robust approach. The variance between the two datasets is within the 5% threshold for the defined c_l^T flight test envelope. To confirm the viability of the optimal airfoil by the robust method, the state of design constraints is evaluated and compared with the single and multi-point design methods in Table 6.9.

TABLE 6.9: HALE Airfoil Optimisation Comparison of Constraints Measure by the AM-PSO Method with XFOIL & Full Set PARSEC-Modified Shape Function for Single, Multi & Robust Design Approach

Design Approach	c_{lmax} $R_n = 3 \times 10^6$	$\%c_{lmax}$ Gain*	$\frac{d_{cp}}{d_x}$	c_{m0}
NLF(1)-0416	1.7500	——	0.2493	-0.0994
Single-Point	1.7717	+↑1.22	0.0542	-0.0639
Multi-Point	1.7440	-↓0.34	0.3056	-0.0901
Robust Approach	1.6688	-↓4.64	0.2947	-0.0800

* **Relative to the benchmark NLF(1)-0416 Airfoil**

The results confirm the optimal profile by the robust approach satisfies two of the three constraints in Table 6.9. The maximum chord location of the extent of favorable pressure gradient on airfoil upper surface must be less than 0.30 and the defined requirement is satisfied in the design. The zero lift moment coefficient must be ≥ -0.10 and the defined constraint is also achieved. The condition

of maximising the c_{lmax} such that $c_{lmax} > 1.76$, is not achieved by the robust profile. The c_{lmax} performance variance between the benchmark and established optima is -↓4.64%.

The robust design approach yields favorable drag performance in comparison to the current off-the-shelf NASA NLF airfoil. The drag performance is lower than the multi-point solution in Figure 6.13. Constraint definition of the optimal profile with the robust approach represents a design compromise between minimum drag at the expense of lower c_{lmax} in comparison to the benchmark and multi-point airfoil. The results will require designer interpretation to confirm the merits of the compromise between drag and c_{lmax} from mission operation perspective. If c_{lmax} is weighted heavily in terms of importance to the defined mission profile, then the results to the multi-point based approach are valid. This will be at the expense of increased drag performance over the defined c_l^T flight envelope to compensate for an increased maximum lift performance. Else, if drag minimisation is a primary design objective relative to c_{lmax}, the solution by the robust design approach is viable.

6.5 Validation of AM-PSO Optimisation Results

The accuracy of the AM-PSO optimisation results from Sections 6.4.1 and 6.4.2) is validated with the resolution of the variables about the optima confirmed. The shape coefficients of the converged airfoil are perturbed one-factor-at-a-time within an identified test envelope over set user-defined increments. The flow solver is simulated and the aerodynamic and constraint data stored. A data-mining technique is applied to qualitatively represent the solution topology about the optima region by SOMs [136] using the Viscovery SOMine software package [139]. A two-dimensional representation of the multi-dimensional data from the maps is established. The solution topology with minimum drag performance conforming to the user-defined constraints about the established optima is qualitatively modeled. A comparative analysis between c_{dmin} by the AM-PSO and the perturbation approach is performed to assess the validity of the solution for the defined problem type.

The aerodynamic and constraint performance in the maps are ordered by the Kohonen algorithm [136] where data clustering is assigned by prioritising important user-assigned shape and flow parameters. In airfoil optimisation the objective function c_d, with constraint on c_{lmax} is prioritised. The corresponding PARSEC-Modified shape variables are clustered based on the similarity of the attribute values to the important design features. The parameters c_d and c_{lmax} influence the clustering of c_p, c_{m0} and flow transition on upper and lower surfaces. The constraint violation magnitudes are also grouped accordingly. The SOMs will qualitatively represent regions with minimum c_d and high c_{lmax} relative to the identified flow features.

The feasibility of the AM-PSO solution is further evaluated by a hybrid optimisation process. The solution by the AM-PSO method is integrated as search initialisation into a gradient optimiser. Minimum drag performance by the hybrid approach is assessed and compared to the stand-alone AM-PSO simulation. The optimal solution by the hybrid approach is re-validated by the proposed data-mining technique to further verify the feasibility of the converged solution.

6.5.0.1 AM-PSO Single-point Design Solution Validation

A. Qualitative Representation of AM-PSO Results

The PARSEC-Modified variables to the single-point design simulation from Tables 6.4 and 6.5 are applied in the perturbation methodology. Since low-fidelity solvers are applied, a large population of test airfoils are examined with acceptable computation turn-over. A test matrix of 9,261 airfoils are generated by independently perturbing each coefficient over 21 intervals within the mapped search limits defined in Section 4.2.2.1. Non-converged simulations are excluded to avoid misinterpretation of the search topology. The clustering of c_d and c_{lmax} relative to the shape parameters x_u and y_{xxu} are qualitatively represented in Figure 6.14.

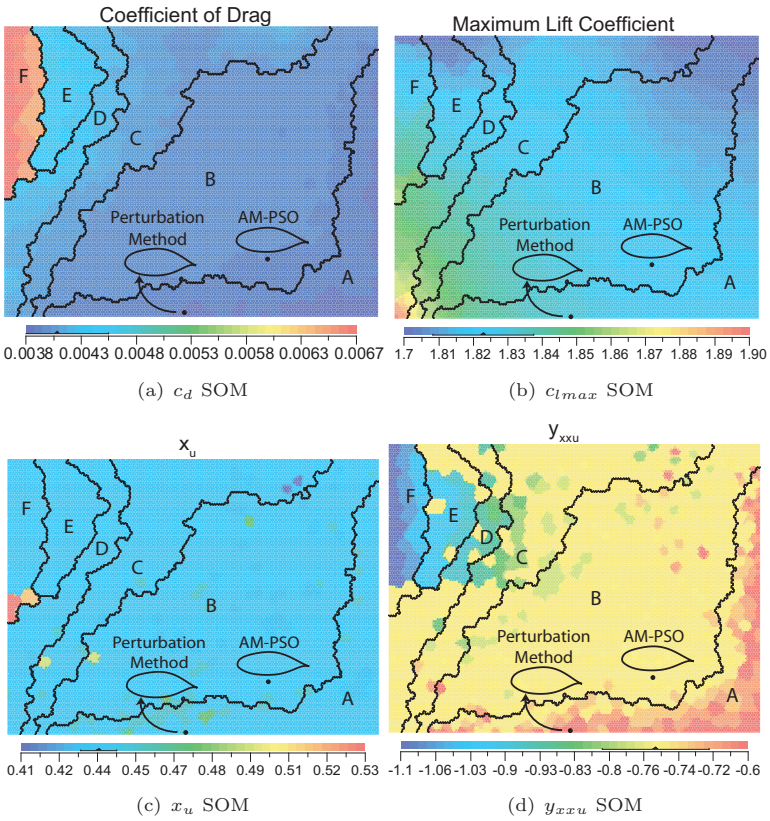

(a) c_d SOM (b) c_{lmax} SOM

(c) x_u SOM (d) y_{xxu} SOM

FIGURE 6.14: Single-point AM-PSO Solution topology by SOMs

The maps are clustered by partitioning c_d of the test airfoils into 6 groups (A-F) in Figure 6.14. Airfoils in cluster A are characterised with low minimum / maximum drag performance in Figure 6.14(a). The magnitude of the lower and upper limits of c_d increases as the data spans from the lower right (cluster A) to the upper left (cluster F) of the map. The relationship of c_d in the clusters to c_{lmax} and shape variables x_u and y_{xxu} is represented in Figures 6.14(b), 6.14(c) and 6.14(d) respectively. The solution of the AM-PSO method to single-point design (Tabs. 6.4 and 6.5) is in cluster B. The drag SOM confirms the solution in cluster B by AM-PSO is not the true optimal as airfoils with lower c_d are present in cluster A. The variables of the AM-PSO require further validation to address this issue.

The perturbation method confirms solution region with lower c_d (cluster A) which have not been exploited by the AM-PSO. The airfoil with the lowest c_d by the perturbation method is represented in cluster A. Airfoil contour variations between the AM-PSO generated solution and the profile in cluster A is isolated to changes in x_u and y_{xxu} (Figs. 6.14(c) and 6.14(d) respectively). The profile in cluster A has lower drag due to an extended x_u which has the affect of delaying flow transition, thus maintaining extended regions of laminar flow on the upper surface in comparison to the shape in cluster B. The variable y_{xxu} has also not converged to the true optima in the AM-PSO simulations. Low drag airfoil in cluster A corresponds to an increase in y_{xxu} in comparison to the shape in cluster B where y_{xxu} is lower (Fig. 6.14(d)). Sensitivity analysis confirmed that y_{xxu} is highly ranked on the level-of-importance scale in the contribution to c_d. The non-convergence of y_{xxu} results in high drag performance in the AM-PSO solution in cluster B relative to the profile in cluster A. The analysis has validated that acceptable variable convergence is needed so that an optimal shape can be established.

B. Results Validation by Hybrid Optimisation

Qualitative representation of the AM-PSO results from Section 6.5.0.1 indicates the solution is within a search topology bounded by low c_d performance. The global search method does not converge to the true optima with airfoils in cluster A missed by the AM-PSO algorithm during the optimisation process (cluster A in Fig. 6.14(a)). Gradient methods are applied to address this issue. A constrained minimisation algorithm using the trust region method is applied. The AM-PSO single-point result is integrated into the gradient algorithm for search initialisation. Airfoil aerodynamic performance by the AM-PSO, perturbation of the AM-PSO solution (Sec. 6.5.0.1) and the hybrid optimisation approach with AM-PSO and GM, including constraint definition is presented in Tables 6.10 and 6.11 respectively.

TABLE 6.10: HALE Single-Point Airfoil Optimisation Objective Measure by the AM-PSO, AM-PSO Perturbation & Hybrid Optimisation Approach with XFOIL

Design Approach	t/c	Max Camber	c_l	AoA(°)	c_d	% c_d Gain*
NLF(1)-0416	0.16	0.025	0.40	-0.695	0.00502	—
AM-PSO	0.16	0.014	0.40	0.203	0.00390	-↓22.31
AM-PSO Perturbation	0.16	0.015	0.40	0.016	0.00376	-↓25.00
Hybrid AM-PSO / GM	0.16	0.019	0.40	0.495	0.00362	-↓28.88

* **Relative to the benchmark NLF(1)-0416 Airfoil**

TABLE 6.11: HALE Single-Point Airfoil Optimisation Constraints Measure by the AM-PSO, AM-PSO Perturbation & Hybrid Optimisation Approach with XFOIL

Design Approach	c_{lmax} $R_n = 3 \times 10^6$	$\%c_{lmax}$ Gain*	$\frac{d_{cp}}{d_x}$	c_{m0}
NLF(1)-0416	1.7500	—	0.2493	-0.0994
AM-PSO	1.7717	+↑1.22	0.0542	-0.0639
AM-PSO Perturbation	1.7804	+↑1.71	0.0658	-0.0697
Hybrid AM-PSO / GM	1.7467	-↓0.20	0.0978	-0.0969

* **Relative to the benchmark NLF(1)-0416 Airfoil**

The hybrid optimisation approach represents a ≈7% reduction in c_d (0.00362) from the stand-alone AM-PSO method (0.00390) and ≈4% reduction from the AM-PSO perturbation method (0.00376) in Table 6.10. The c_{lmax} by the hybrid approach ($c_{lmax} = 1.7467$) is compromised by ≈1% from the AM-PSO method ($c_{lmax} = 1.7717$), but is comparable to the baseline NLF(1)-0416 profile ($c_{lmax} = 1.75$) with a percentage difference of ≈0.20% considered negligible in Table 6.11. The constraints relating to $\frac{d_{cp}}{d_x}$ and c_{m0} are satisfied by the hybrid-based design optimisation algorithm. The benefits of incorporating a global with local search optimisation methodology for drag minimisation is validated.

The feasibility of the converged airfoil design coefficients with the hybrid optimisation approach is verified by the perturbation method. The data is clustered with priority to drag to determine if lower c_d solution regions exist about the hybrid optima shape. The impact on c_{lmax} and sample shape coefficients are presented in Figure 6.15.

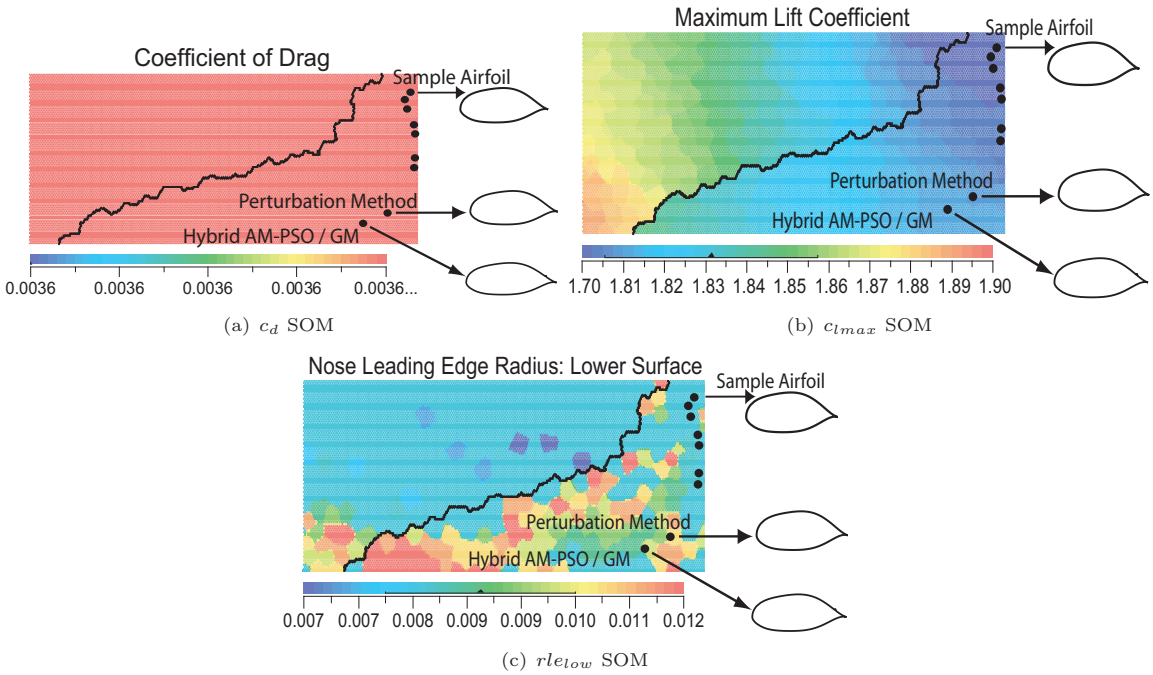

(a) c_d SOM (b) c_{lmax} SOM

(c) rle_{low} SOM

FIGURE 6.15: HALE Single-point Solution topology Validation by SOMs

The lowest c_d performance by the validation of the hybrid AM-PSO/GM data with the perturbation approach in Figure 6.15(a) matches the optimal magnitude by the hybrid optimisation process ($c_d = 0.00362$) from Table 6.10. The solution by the hybrid approach is within a validated search topology. In the drag SOM solution region, nine airfoils with $c_d = 0.00362$ are identified and match the performance by the hybrid approach. The shapes are comparable with variations restricted to the nose radius curvature only on the lower surface in Figure 6.15(c).

If the drag performance between the airfoils is the same, preference to a shape with higher c_{lmax} subject to all design constraints satisfied is defined. The variation in c_{lmax} between the nine profiles in Figure 6.15(b) indicates the hybrid optimisation derived solution with the highest c_{lmax} that is ≈0.50% greater than the perturbation shape. The c_{lmax} decreases as the search topology shifts towards the top-right corner of the SOM. The sample airfoil is modeled with the lowest c_{lmax} but the variation is restricted to ≈1% less than the established optimal shape. Thus, airfoil design coefficients

by the hybrid optimisation approach for single-point design analysis are validated by the qualitative representation of the solution topology.

6.5.0.2 AM-PSO Multi-point Design Solution Validation

The verification of the multi-point optima profile is confirmed by the developed post-processing method. Airfoil performance by the stand-alone AM-PSO algorithm (Sec. 6.4.2), perturbation of the defined AM-PSO solution, hybrid design method by the integration of the AM-PSO and GM methods and the post-processing of the hybrid solution with SOMs by independent variable modifications is examined. The aerodynamic and constraint definition for the defined problem case types is presented in Tables 6.12 and 6.13 respectively for cruise $c_l^T = 0.40$. The aerodynamic performance at the climb profile $c_l^T = 1.00$ by the respective design methodologies is presented in Table 6.14.

TABLE 6.12: HALE Multi-Point Airfoil Optimisation Objective Measure by the AM-PSO, AM-PSO Perturbation, Hybrid Optimisation & Perturbation of the Hybrid Approach with XFOIL at Cruise $c_l^T = 0.40$

Design Approach	t/c	Max Camber	c_l	AoA(°)	c_d	% c_d Gain*
NLF(1)-0416	0.16	0.025	0.40	-0.695	0.00502	—
AM-PSO	0.175	0.027	0.40	-1.396	0.00464	-↓7.57
AM-PSO Perturbation	0.166	0.028	0.40	-0.885	0.00466	-↓7.17
Hybrid AM-PSO / GM	0.166	0.033	0.40	-2.220	0.00463	-↓7.77
Hybrid Perturbation	0.174	0.030	0.40	-2.270	0.00472	-↓5.97

* **Relative to the benchmark NLF(1)-0416 Airfoil**

TABLE 6.13: HALE Multi-Point Airfoil Optimisation Constraints Measure by the AM-PSO, AM-PSO Perturbation, Hybrid Optimisation & Perturbation of the Hybrid Approach with XFOIL at Cruise $c_l^T = 0.40$

Design Approach	c_{lmax} $R_n = 3 \times 10^6$	% c_{lmax} Gain*	$\frac{d_{cp}}{d_x}$	c_{m0}
NLF(1)-0416	1.7500	—	0.2493	-0.0994
AM-PSO	1.7440	-↓0.34	0.3056	-0.0901
AM-PSO Perturbation	1.7725	+↑1.27	0.2913	-0.0902
Hybrid AM-PSO / GM	1.7605	+↑0.60	0.295	-0.0984
Hybrid Perturbation	1.7738	+↑1.34	0.2931	-0.0988

* **Relative to the benchmark NLF(1)-0416 Airfoil**

TABLE 6.14: HALE Multi-Point Airfoil Optimisation Objective Measure by the AM-PSO, AM-PSO Perturbation, Hybrid Optimisation & Perturbation of the Hybrid Approach with XFOIL at Climb $c_l^T = 1.00$

Design Approach	Max Camber	c_l	AoA(°)	c_d	% c_d Gain*
NLF(1)-0416	0.025	1.00	4.479	0.00661	—
AM-PSO	0.027	1.00	3.677	0.00612	-↓7.41
AM-PSO Perturbation	0.028	1.00	4.187	0.00610	-↓7.72
Hybrid AM-PSO / GM	0.033	1.00	2.820	0.00590	-↓10.74
Hybrid Perturbation	0.030	1.00	2.763	0.00604	-↓8.62

* **Relative to the benchmark NLF(1)-0416 Airfoil**

The hybrid AM-PSO / GM optimisation approach yields a lower c_d at $c_l^T = 0.40$ and $c_l^T = 1.00$ than the stand-alone AM-PSO method in Tables 6.12 and 6.14 respectively. The validation analysis confirms airfoil variables by the AM-PSO did not converge to a global optima. The optimal airfoil by the hybrid optimisation approach reduces drag by ≈8% and ≈11% at cruise and climb c_l^T respectively in comparison to the benchmark profile. The constraints definition by the integration of the gradient-method to the AM-PSO algorithm resulted in an increase in c_{lmax} by ≈1.00% relative to the NLF airfoil (Tab. 6.12). The remaining constraint parameters are achieved.

Validation of the hybrid design profile by the perturbation approach yielded no design performance improvements in c_d at the defined cruise and climb lift coefficients. The c_{lmax} by the perturbation approach is marginally greater than the hybrid shape optimisation profile ($c_{lmax} = 1.7738$ versus $c_{lmax} = 1.7605$ in Tab. 6.13), but at the expense of higher drag ($c_d = 0.00472$ versus $c_d = 0.00463$ at $c_l^T = 0.40$ & $c_d = 0.00604$ versus $c_d = 0.00590$ at $c_l^T = 1.00$) at the two flight conditions examined. Hence, a design compromise is required to balance between minimum drag performance and the maximisation of c_{lmax}.

The variance of airfoil variables $r_{le_{up}}$, $r_{le_{low}}$, y_{te}, $t_{eg_{up}}$, $t_{eg_{low}}$, $t_{ew_{up}}$, $t_{ew_{low}}$, x_u, y_u, y_{xxu}, x_l, between the hybrid optimisation and the perturbation of the hybrid solution are limited to ≈< 0.50%. The variance is ≈1% for the parameters y_l and y_{xxl}. The convergence of y_l and y_{xxl} by the AM-PSO, perturbation of the AM-PSO, hybrid AM-PSO / GM and the corresponding perturbation approach are compared in Figure 6.16.

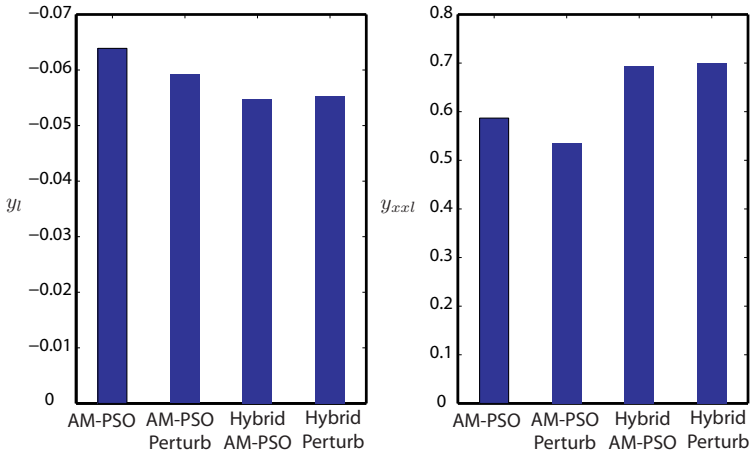

FIGURE 6.16: Multi-Point HALE PARSEC-Modified Coefficients y_l & y_{xxl} by Disparate Optimisation Design Methods

Design variable magnitude differences of y_l and y_{xxl} between the stand-alone AM-PSO and the hybrid AM-PSO / GM optimisation approach are significant in Figure 6.16. Relatively the variances between the AM-PSO / GM method and the corresponding airfoil with the lowest drag established by the perturbation post-processing analysis is minimal for the defined shape coefficients. Drag performance improvement between the AM-PSO and the hybrid design approach is attributed to the convergence of y_l and y_{xxl} design parameters to a global minima solution region. In accordance to the defined problem formulation, it is concluded that the airfoil by the hybrid optimisation approach with the multi-point design analysis has converged to a global minima.

6.5.0.3 Post-Processing of Optimisation Results Summary

The post-processing of the AM-PSO solutions by SOMs confirmed the requirement for further design analysis to achieve convergence to an optima region. The integration of a gradient method with the solution from the AM-PSO algorithm applied as the starting point for search initialisation addressed this requirement. A post-processing analysis to interrogate the convergence of the airfoil variables by the hybrid optimisation approach confirmed the feasibility of search convergence to a global point in the search space.

The application of the hybrid design approach was validated for solution optimality for single (Sec. 6.5.0.1) and multi-point (Sec. 6.5.0.2) airfoil design simulations. The analysis confirmed that the developed AM-PSO method converges to a valid solution region for complex and multi-modal search topologies. The application of the gradient method finalises the search process by converging to a global minima about the initially defined search region mapped by the AM-PSO.

The solution search space for the developed robust design approach is complex and multi-modal. The results by the robust design method are based on the stand-alone AM-PSO algorithm in the design process (Fig. 6.13 & Tab. 6.9). The validation analysis of the AM-PSO simulations on single and multi-point design simulations confirmed the requirement of integrating a gradient search process to attain further performance benefits. The results of the robust design approach are preliminary and

a sub-set of the overall global solution. To attain the expected performance benefits, a gradient design simulation by the integration of the AM-PSO solution as the search initialisation point is needed.

6.6 HALE Single-Point Airfoil Optimisation Architecture Set Up for Flow Analysis by a High-Fidelity Solver

Airfoil design for HALE performance is presented with the integration of a high-fidelity solver in the DNO architecture. The flow solver setup from Section 5.4.3 is applied in the design process. Airfoil design with RANS equations does not involve the computation of the c_{lmax}. Accurate high-lift flow analysis requires the integration of a finer mesh resolution with increased solver fidelity including turbulence modeling in the form of Detached Eddy Simulations (DES). The computational time required for high-lift analysis is intense and is not considered in the thesis.

The airfoil design results with high-fidelity solvers can not be compared with benchmark NLF(1)-0416 airfoil due to the exclusion of the c_{lmax} constraint. The application of the developed DNO structure with a high-fidelity solver is restricted to a single-point design at cruise $c_l^T = 0.40$ only. The viability of the developed optimisation process for multi-point and robust design processes was confirmed with low-fidelity solver simulations, hence is not considered with RANS based solvers.

Prior to the application of the RANS based solvers for airfoil design, the setup of the DNO structure needs to be confirmed with XFOIL. The rapid computational turn-over time from XFOIL facilitates an extensive DoE process to evaluate the sensitivity of the user-defined parameters in the DNO structure to attain feasible search simulations by computationally intensive RANS based solvers. The following points are addressed in the analysis:

1. **Sensitivity of Airfoil Shape Function Type**

   The effect of airfoil shape function type and the dimension search space, on the objective function needs to be defined. A balance between the shape function type with minimal design variable population size and solution feasibility is a design requirement. The results will be used to define airfoil design problem by the high-fidelity solver.

2. **Sensitivity of Swarm Population Size**

   The impact of swarm population size on solution convergence needs to be defined. The population size of the particles must be low to facilitate a computationally efficient design process without compromising the search performance. A DoE analysis is required to address this requirement for application into the DNO process with a high-fidelity solver.

The impact of the shape parameterisation model as a function of problem dimensionality including swarm population size on fitness is evaluated with XFOIL. The single-point design from Equation 6.9 is modeled with the AM-PSO algorithm as part of the DoE process. The constraints integrated into the problem include $\frac{d_{cp}}{d_x}$ (Eqn. 6.5), t/c (Eqn. 6.7) and c_{m0} (Eqn. 6.8). The requirement of maximising the c_{lmax} is not integrated in the DoE analysis as it will not be used for shape design by the high-fidelity solver. The exclusion of the c_{lmax} from the DoE simulations with XFOIL will yield

a valid representation of the optimisation structure required to facilitate shape design simulations by RANS equations.

The swarm population size tested is 20, 30 and 40 particles. The shape functions examined include:

1. CST with BP of order 2 = 9 Design Variables
2. CST with BP of order 3 = 11 Design Variables
3. CST with BP of order 4 = 13 Design Variables
4. CST with BP of order 5 = 15 Design Variables
5. PARSEC Shape Function = 10 Design Variables
6. PARSEC-Modified Shape Function with Full set of Design Variables = 13 Design Variables
7. PARSEC-Modified Shape Function with $t_{eg_{low}}$ eliminated as a Design Coefficient (Sec. 4.2.2.2 - Fig. 4.23) = 12 Design Variables

In each case study the AM-PSO is simulated over five independent trials due to the randomness of the search process. In total there are 105 simulations in the DoE analysis to verify the relationship between the defined parameters. The mean of the fitness (Eqn. 6.10) from the trials for each case is established and reported for analysis. The sensitivity of the BP order in the CST shape function on fitness with the AM-PSO method is presented in Figure 6.17.

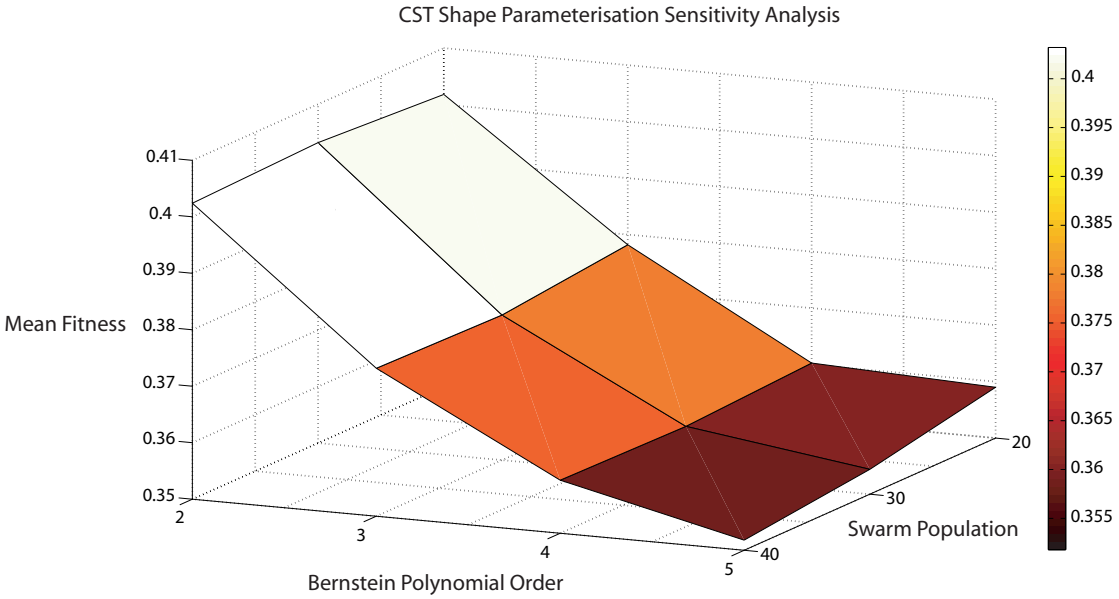

FIGURE 6.17: CST Solution Search Space Convergence for HALE Airfoil Design by the Single-Point Design Approach with AM-PSO & XFOIL

An increase in the BP order of the CST function results in a decrease in the average fitness for single-point airfoil design in Figure 6.17. The results validate the merits of increasing the dimensionality of the airfoil shape function on solution convergence. The effect of an extended swarm population size on fitness minimisation is further verified. The average fitness magnitude for the respective order

of the BP function is lower with 40 particles in comparison to 20 search agents. The mean fitness over the five independent trials for a BP of order five is 0.345, 0.342 and 0.341 for a swarm size of 20, 30 and 40 particles respectively with a standard deviation of 0.0021. It is hypothesised that the standard deviation as a function of swarm population size can be reduced. This is to be achieved by the integration of a gradient-based optimisation method to the analysis. The viability of the proposed methodology will be verified.

The inclusion of the PARSEC and PARSEC-Modified method with the full and reduced set of design variables on solution convergence is presented in Figure 6.18.

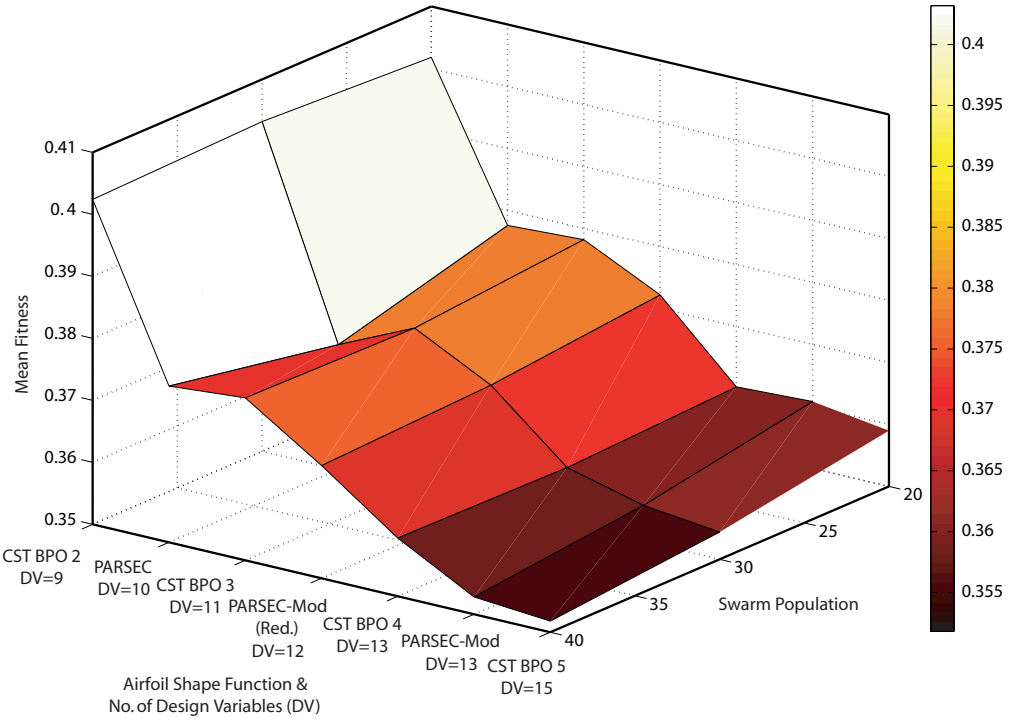

FIGURE 6.18: Solution Search Space Convergence by Disparate Airfoil Shape Parameterisation Function Types as a Function of Swarm Population for HALE Airfoil Design with AM-PSO

The results confirm the merits of increasing the problem dimension search space on fitness minimisation in Figure 6.18. As the number of design variables applied for airfoil parameterisation is increased, the mean fitness convergence decreases proportionally for the respective swarm population size. In each shape function, an increase in swarm population size results in a decrease in mean fitness.

The viability of the developed PARSEC-Modified method with the inclusion of three additional shape variables for independent modeling of airfoil suction and pressure contours is validated. The mean fitness by the original PARSEC method over the five independent trials for a swarm population size of 20, 30 and 40 is 0.378, 0.370 and 0.375 respectively with a standard deviation of 0.00404. The mean fitness by the PARSEC-Modified method is less than the original function at 0.374, 0.366 and 0.363 with a standard deviation of 0.00567 for the represented swarm population size.

The impact of reducing the scope of the problem search space from 13 to 12 variables has a minor impact on the mean fitness. The PARSEC-Modified method with $t_{eg_{low}}$ set to the baseline value

of the NLF(1)-0416 airfoil (DV=12), the average fitness is 0.372, 0.370 and 0.368 with a standard deviation of 0.002. The fitness mean and spread measure is comparable to the PARSEC-Modified method with the full set of 13 design variables. The exclusion of a single shape coefficient from the design optimisation process results in an efficient design process without compromising solution feasibility.

The results in Figure 6.18 confirm the non-convergence of the modeled solution topology as a function of problem dimensionality by the AM-PSO method. The fitness contour carpet plot represents a downward transition, hence fitness minimisation as a function of problem dimensionality. The disparity in mean fitness between the PARSEC-Modified with 13 design variables and the CST function at 15 variables confirms the non-convergence of the solution search space. If the variance in mean fitness between the PARSEC-Modified (DV=13) and CST BPO5 (DV=15) functions was evenly distributed for the respective swarm population size, then convergence could be assumed. The carpet results do not represent this pattern.

To address the non-convergence of the solution search space, a gradient-based optimisation method is integrated into the design process. The theoretical principles in support of this view is based on the hypothesis that the optima by the AM-PSO method has converged to a solution region bounded about the global point. Due to the limited local search capabilities of the AM-PSO algorithm, the swarm method does not converge to the absolute minima. The solution is within a valley of data points that are in an area-of-interest. Theoretically the integration of a gradient search method with the application of the AM-PSO solution as the starting point will facilitate a local search process and shift the initial point into the minima solution valley. A gradient optimisation simulation is performed on each of the 5 AM-PSO trials modeled for the respective shape function and swarm population size in the derivation of the mean fitness from Figure 6.18. The mean fitness of the gradient simulations is modeled in Figure 6.19.

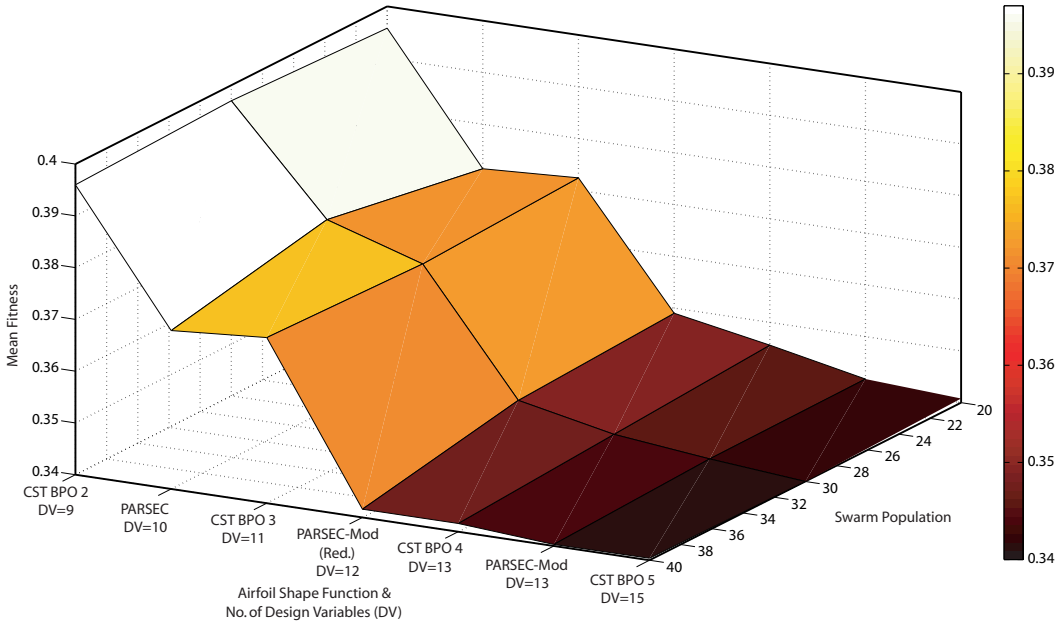

FIGURE 6.19: Solution Search Space Convergence by Disparate Airfoil Shape Parameterisation Function Types as a Function of Swarm Population for HALE Airfoil Design with AM-PSO & Gradient Optimisation Methods

The fitness magnitude by the integration of the gradient method in Figure 6.19 is lower than the respective data modeled by the stand-alone AM-PSO algorithm only from Figure 6.18. The results confirm the viability of applying a gradient optimisation method for fitness minimisation with a well-defined starting point from the AM-PSO method. The data further verifies the solution by the AM-PSO method is about a global minima region and is not representative of the true minima point. The application of a gradient optimisation method address this issue. The fitness converges to a consistent magnitude with negligible variances despite the application of different starting points for each of the five trials from the AM-PSO results. The data confirms the AM-PSO fitness from each independent trial is bounded about the global solution region and the gradient optimisation exploits this point to achieve convergence at the global minima in Figure 6.19.

The viability of increasing the dimensionality of the problem on solution convergence is also confirmed. The fitness landscape represents a downward transition, hence minimisation of drag with an increase in design variable population size in Figure 6.19. The magnitude of fitness variance for a dimensional search space bounded between the PARSEC-Modified method with 12 variables and the maximum limit with CST BPO5 at 15 variables as a function of swarm population size is minimal. The carpet plot in the defined region is 'flat' and the fitness is evenly distributed. The mean fitness for a swarm size of 20, 30 and 40 particles with the PARSEC-Modified with 12 variables is 0.349, 0.347 and 0.342 respectively with a standard deviation of 0.0036. At 15 variables the mean fitness is lower at 0.341, 0.340 and 0.340 for a swarm size of 20, 30 and 40 particles respectively, with a standard deviation of 0.00058. The disparity in mean fitness for the modeled swarm population between 12 and 15 variables is minimal. The impact of integrating a larger swarm search size from 20 to 40 particles has a negligible impact on solution convergence within the defined 'flat' and evenly distributed carpet fitness region.

The application of three fewer design variables by the PARSEC-Modified method with reduced function dimensionality ($t_{eg_{low}}$ not applied) in comparison to the CST model with BPO5 at 15 variables will correspond to significant computational time benefits. A swarm population size of 20 particles in comparison to 40 will further facilitate efficient design simulations. The results map an acceptable balance between problem dimensionality including swarm size on solution feasibility and computational efficiency. The defined setup will ensue search performance benefits for airfoil design simulations with a high-fidelity flow solver in the DNO loop.

6.6.1 Airfoil Optimisation by the Stand-Alone AM-PSO Algorithm with FLUENT

Airfoil design for HALE performance with the validated, high-fidelity flow solver from Section 5.4.3 is applied. The results to the DNO structure development process from Section 6.6 are used to define the setup of the AM-PSO algorithm. The optimisation process is defined based on the AM-PSO principles outlined in Section 6.4 with exception to the following:

- Swarm population size of 20 particles (validated in Fig. 6.19)
- The integration of the PARSEC-Modified shape function in the DNO process with:

  - Full 13 design variables;
  - Elimination of shape coefficient $t_{eg_{low}}$, hence 12 design variables
  - Elimination of shape coefficients $t_{eg_{low}}$ and $t_{ew_{low}}$, hence 11 design variables

- Search termination to a global optima is achieved when:
  - A maximum iteration count of 800 search evolutions is reached; or
  - The following termination measuring units yield an inactive search history (process validated in Sec. 6.4.1 in Figs. 6.8 & 6.10) over 100 consecutive iterations:
    * $pbestg$
    * p_f
    * σ_t

- The solution to the AM-PSO method is integrated as the initialisation point for analysis by the gradient-method for convergence to a global optima (validated in Fig. 6.19)

The AoA required to attain a cruise $c_l^T = 0.40$ on the NLF(1)-0416 airfoil was estimated by FLUENT [153] with the developed trimming methodology. The solver performance variance between low and high-fidelity methods is verified on the defined AoA trimming process. The c_l from FLUENT at the estimated AoA is used as a solver input to XFOIL to establish the corresponding AoA. The AoA disparity and the resulting aerodynamic coefficients between low and high-fidelity solvers is presented in Table 6.15.

TABLE 6.15: Validation of the AoA Trimming Methodology by Performance Evaluation at $c_{l_{cruise}}$ of the NLF(1)-0416 Airfoil with Low and High-Fidelity Solvers

Solver	AoA(°)	c_l	c_d	c_m	$\frac{d_{cp}}{d_x}$
FLUENT [153]	-0.691	0.4029	0.0053	-0.0930	0.2961
XFOIL [78]	-0.672	0.4029	0.0050	-0.1066	0.2506

The results confirm performance similarity between XFOIL and FLUENT at the defined $c_l^T = 0.40$ flight point in Table 6.15. The estimated AoA by FLUENT converges about the defined target c_l^T with a minor miss-match. The integration of $c_l^T = 0.4029$ from FLUENT to XFOIL results in a AoA of $-0.672°$ which offsets the magnitude estimated by the trimming process with FLUENT ($-0.691°$ versus $-0.672°$ in Tab. 6.15 for FLUENT & XFOIL respectively). The impact of a miss-match in the AoA by the two solvers, results in a miss-match in c_d with a percentage difference of $\approx 6\%$. The constraint on c_{m0} is violated by XFOIL in comparison to the analysis by FLUENT. The constraint on $\frac{d_{cp}}{d_x}$ is satisfied by the two methods. The analysis confirms the eligibility of applying XFOIL to model the setup of the DNO structure for HALE analysis at cruise $c_l^T = 0.40$. The design development will be filtered with errors due to the incorrect estimation of the AoA for the user-defined c_l^T which can incorrectly represent a shape with violated or non-violated constraints.

The c_p distribution at the defined AoA from FLUENT ($-0.691°$ in Tab. 6.15) and XFOIL ($-0.672°$ in Tab. 6.15) is modeled in Figure 6.20.

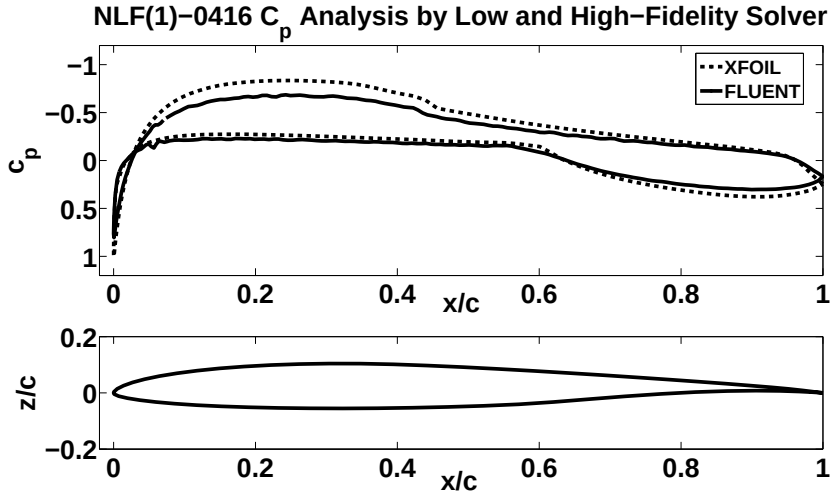

FIGURE 6.20: NLF(1)-0416 c_p distribution with XFOIL & FLUENT at the estimated trimming-based α for $c_l^T \approx 0.40$

The c_p at the defined AoA by low and high-fidelity solvers respectively represents an acceptable match between the two datasets in Figure 6.20. The region of favorable pressure gradient on airfoil upper surface is extended with FLUENT in comparison to XFOIL. The c_p on airfoil upper surface by XFOIL is underestimated in comparison to FLUENT up to the trailing edge region. The variance in c_p performance is minimal. The computation of the boundary layer transition point by the two solvers is in close agreement at $x_{tr_{UP}} \approx 0.41$.

The variances in c_d by the two solvers is limited. On airfoil lower surface, both solvers model an acceptable c_p agreement. The boundary layer transition point by FLUENT is estimated at $x_{tr_{low}} \approx 0.56$ compared to $x_{tr_{low}} \approx 0.60$ by XFOIL. The identified disparity results in a miss-match in c_p performance aft of the transition points between the two solvers. The difference in c_p performance is minimal with XFOIL representing an aft loaded profile, hence a lower c_m compared to FLUENT (Tab. 6.15 & Fig. 6.20).

The results to the single-point airfoil design process with FLUENT are presented. The application of the developed probability of particle mutation process is first demonstrated. Mutation is applied to initiate search diversity as a function of the distance metric d_s, computed from the fitness difference of the worst and best performing particle *pbestg* in the swarm during the optimisation process (Sec. 3.4 - Step 1, Fig. 3.3). The probability of particle mutation pr_M is established from the measure of d_s in Equation 3.10. The history evolution of the two mutation governing parameters from an airfoil design simulation with the PARSEC-Modified method with a full set of 13 design variables is modeled in Figure 6.21.

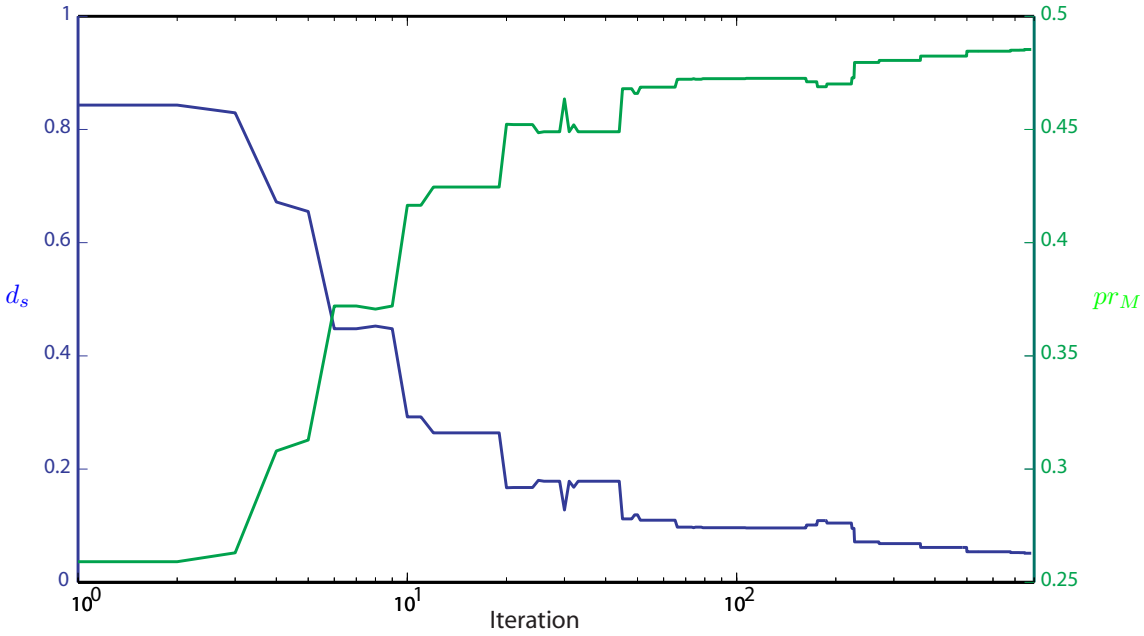

FIGURE 6.21: Probability of Mutation as a Function of Particle Extremity Distance Metric for HALE Airfoil Design with FLUENT & PARSEC-Modified Method with 13 Shape Variables

The deviation of the Euclidean distance between the best and worst performing particle (*pbestg*) influences the magnitude of the probability of mutation pr_M during the optimisation cycle. At search initialisation the Euclidean distance between the two extreme particles d_s is high, hence pr_M is low in Figure 6.21. As the particles are initialised with LHS through the defined solution landscape, a diminished search diversity at search commencement between the swarm population is not an issue, hence pr_M is low. As the search progresses, the particles initiate convergence to a common region due to the information sharing methodology between the swarm in regards to the position of the global solution. Accordingly the d_s decreases and to initiate search diversity to mitigate convergence to a local minima, pr_M increases concurrently (Fig. 6.21 & Eqn. 3.10). At the concluding stages of the optimisation cycle, d_s is at its lowest due to the agreed consensus of convergence to a global solution between the particles in the swarm. Concurrently the pr_M is at its highest to avoid a false convergence.

The developed mutation methodology is applied to induce search diversity only when the swarm indicates convergence to a common solution region which can be to a sub-optimal solution topology. The mapping of the worst (highest fitness) and *pbestg* is an indication of swarm convergence to a solution topology area-of-interest. The defined rate-of-mutation principles are based on the mitigation of the swarm to a local solution by monitoring the position of d_s. By inducing mutation, hence search diversity the identified issues are addressed.

The convergence of the swarm to a global fitness solution region during the design optimisation process is modeled in Figure 6.22

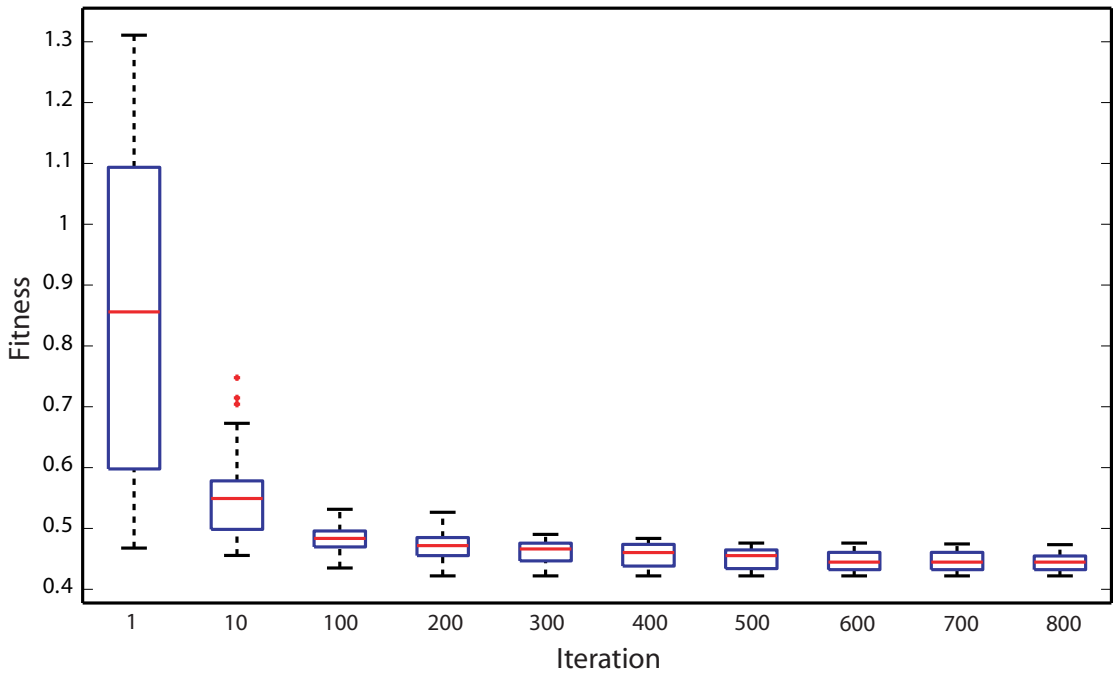

FIGURE 6.22: Swarm Fitness Convergence for HALE Airfoil Design with FLUENT & PARSEC-Modified Method with 13 Shape Variables

The fitness distribution of the 20 particles in the swarm over the defined iteration cycle is modeled in Figure 6.22. As the search progresses, the convergence of the swarm to a fitness minima region in the solution space is identified. At search initialisation, the integration of the LHS methodology for particle dispersion results in a high variance in swarm fitness and the intervals of the boxplot data is high. As the search progresses, the theoretical principles of the developed AM-PSO algorithm shift the particles to an area-of-interest. The information sharing methodology between the particles facilitates the transition of the swarm to a minima fitness region. The collective fitness of the particles reaches a consensus and the data intervals of the boxplots decreases proportionally over the modeled search envelope. The mean fitness of the swarm also stabilises as the search progresses, hence validating a swarm convergence. The application of the developed mutation factor ensures a non-convergence of the particles to a local solution region.

The aerodynamic and geometric data of the optima airfoils is modeled in Table 6.16. The variance in problem dimensionality by the respective shape function type and the corresponding impact on airfoil aerodynamics and geometry features of the established solution is modeled.

TABLE 6.16: HALE Single-Point Airfoil Optimisation Results by the AM-PSO Method with FLUENT

Airfoil	t/c	Max Camber	AoA(°)	c_l	c_d	$\frac{d_{cp}}{d_x}$	c_{m0}
PARSEC-Modified (13 Design Variables)	0.1696	0.0171	1.0137	0.4173	0.004220	0.1028	-0.0629
PARSEC-Modified (12 Design Variables)	0.1737	0.0210	-0.1425	0.4178	0.004267	0.2900	-0.0776
PARSEC-Modified (11 Design Variables)	0.1650	0.0175	0.1638	0.4165	0.004227	0.1315	-0.07710

The optima airfoils by the respective shape function dimensionality size satisfy the c_l^T constraint in Table 6.16. The trimming process applied to estimate the AoA for a user-defined $c_l^T = 0.40$ demonstrates viability with each profile conforming to the defined minimum lift requirement. To further demonstrate the c_l distribution of the population of airfoils analysed by each particle by the trimming process during the optimisation cycle, a boxplot is presented in Figure 6.23.

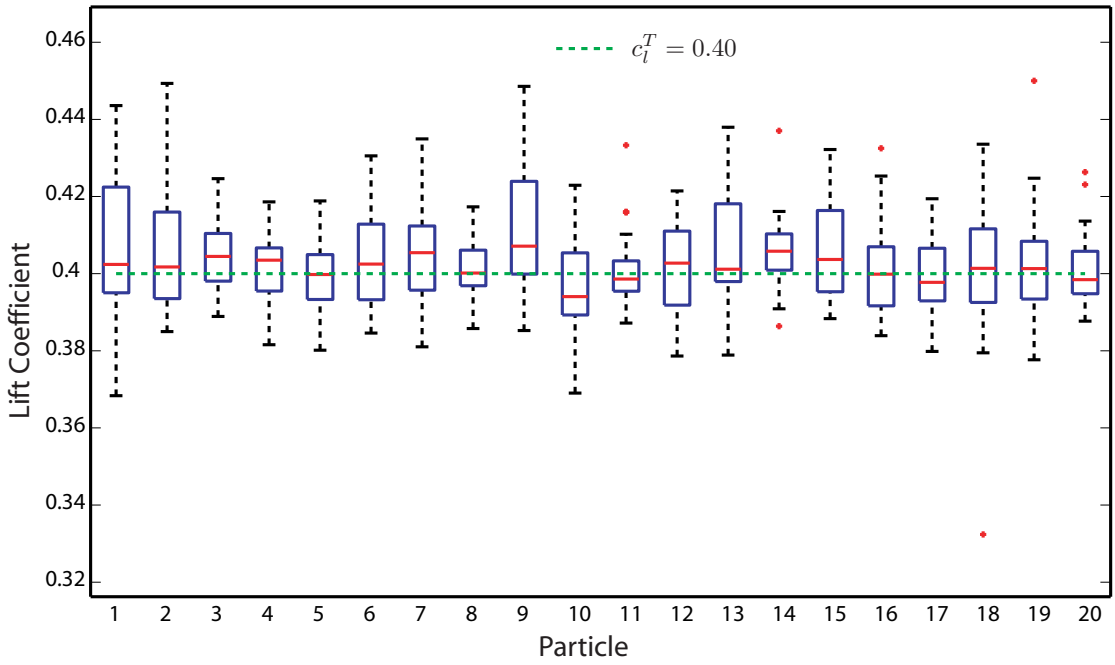

FIGURE 6.23: HALE Airfoil Design Boxplot Analysis of the Computed c_l^T of each Airfoil Modeled by a Particle in the Swarm

The c_l boxplot distribution yields an acceptable convergence of the candidate airfoils in the swarm during the iteration cycle that converge to the user-defined target $c_l^T = 0.40$. The mean c_l in each boxplot is about the user-defined target. To further represent the convergence of airfoil c_l^T, a histogram is modeled to represent the distribution and variance of c_l established by the trimming process for select particles during the design cycle in Figure 6.24.

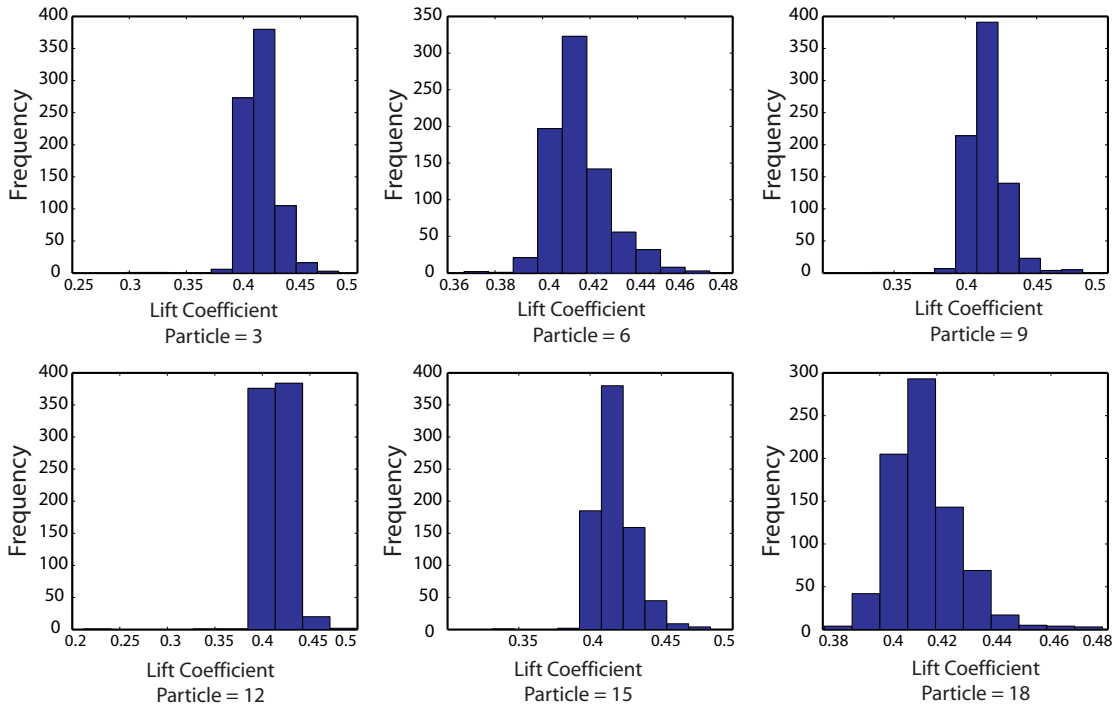

FIGURE 6.24: HALE Airfoil Design Histogram Analysis of the $c_l^T = 0.40$ Distribution For Select Particles in the Swarm

The c_l of the candidate airfoils modeled by the respective search particles during the design process with boxplot and histogram analysis confirms a data variance about the theoretical target $c_l^T = 0.40$. The extended search intervals of each boxplot represents the extremity of c_l modeled during the optimisation process. The histogram analysis confirms the majority of airfoils for the respective search particle are within the target threshold of $c_l^T = 0.40$ in Figure 6.24. There are a select few shapes that are characterised by extreme c_l performances, hence data outliers relative to the defined target in the boxplots (Fig. 6.23). The data deviations are representative of a non-linear lift curve slope and due to source errors in the developed trimming process. A penalty magnitude (Eqn. 6.3) as a summation to the fitness function (Eqn. 6.9) is integrated in the design process to penalise airfoils that violate the lift constraint design requirement.

The results in Table 6.16 conform to the user-defined constraints. The variance in airfoil t/c between the modeled shape functions is minimal. The constraints $\frac{d_{cp}}{d_x}$ (Eqn. 6.5) and c_{m0} (Eqn. 6.8) are achieved, hence validating the feasibility of the design simulation process. The convergence of the optima c_d for the three case studies modeled is similar. Hence, a variance in problem dimensionality size between 11 and 13 variables has a negligible impact on the c_d of the optima airfoil.

The aerodynamic results validate the feasibility of the single-point design process in Table 6.16. The second DNO performance measure is assessed. The computational efficiency as a function of the number of design iterations to achieve convergence to the optima shapes is presented in Table 6.16. Solution termination is based on the defined measures from Section 6.4.1 and is activated when the three units represent an idle search process over 100 consecutive iterations. The evolution when the last of the three units conform to this requirement is achieved, the AM-PSO simulation terminates. The iteration that de-activates the search process is recorded. The measure of search convergence by

the number of design iterations, for the respective shape function dimensionality size is presented in Table 6.17.

TABLE 6.17: HALE Single-Point Airfoil Optimisation Convergence Assessment by the AM-PSO Method with FLUENT

Shape Function Type	*pbestg*	p_f	σ_t	$\therefore$ Convergence
PARSEC-Modified (13 Design Variables)	800	800	800	800
PARSEC-Modified (12 Design Variables - $t_{eg_{low}}$ not used)	704	736	741	741
PARSEC-Modified (11 Design Variables - $t_{eg_{low}}$ & $t_{ew_{low}}$ not used)	514	604	698	698

The optimisation algorithm with a full set of 13 design variables does not converge within the maximum 800 design iteration limit in Table 6.17. The termination measures represent an active search process and do not conform to the required 100 idle search evolutions rule at the point of reaching the maximum allowed limit. The design case study with the elimination of $t_{eg_{low}}$ from the problem represents a converged state as a function of the three defined search termination measuring units. The last of the three parameters to converge in accordance to an idle search process is the fitness standard deviation of the swarm at the 741^{st} iterate. The 12 variable design problem instead of 13 required 59 fewer design evolutions to convergence. As each design iteration carries the probability of additional flow solver calls due to mutation, there is an increased demand on the computing resources. The problem definition with 59 fewer iterations results in a significant time savings in comparison to the full set for the outlined reasons. A computational time benefit of $\approx$ 29 hours was achieved despite the application of a parallel computing architecture.

Further computational time savings are attained with the elimination of two variables from the design problem relative to the shape function with a full set of 13 shape coefficients. The integration of the PARSEC-Modified method without $t_{eg_{low}}$ and $t_{ew_{low}}$ as shape coefficients, results in the search termination at the 698^{th} design iterate in Table 6.17. Corresponding the number of design iterations to computational wall-time results in significant savings in comparison to the simulation with $t_{eg_{low}}$ eliminated only. The integration of 11 design variables required 43 fewer design iterations in comparison to the case with 12 PARSEC-Modified variables. Computational time savings in excess of $\approx$ 21 hours was achieved. Comparison of the 11 variable test problem with the full set of shape coefficients corresponds to a significant time savings without affecting solution feasibility. The elimination of two shape variables represents 102 fewer design iterations in comparison to the full variable population set. This translates to a significant computational wall-time savings of $\approx$ 50 hours.

The aerodynamic data including constraints definition in Table 6.16 and the computational resources required to achieve convergence in Table 6.17, with varying degree-of-problem dimensionality, validated the merits of a pre-screening study to assess and eliminate shape variables that have a minor impact on c_d. The feasibility of the optima solution is not compromised by the design variable elimination. Instead significant computational time savings are achieved.

Effect of Solver Fidelity on Airfoil Optimisation

It was hypothesised that despite the accuracy of the solver as a function of model fidelity, the nature of the solution landscape for the defined test problem will be mapped. To verify this, the optima airfoil from a trial simulation by the AM-PSO algorithm with XFOIL and the PARSEC-Modified method at 11 design variables from Figure 6.18 is compared to the shape design solution by FLUENT in the design process in Figure 6.25.

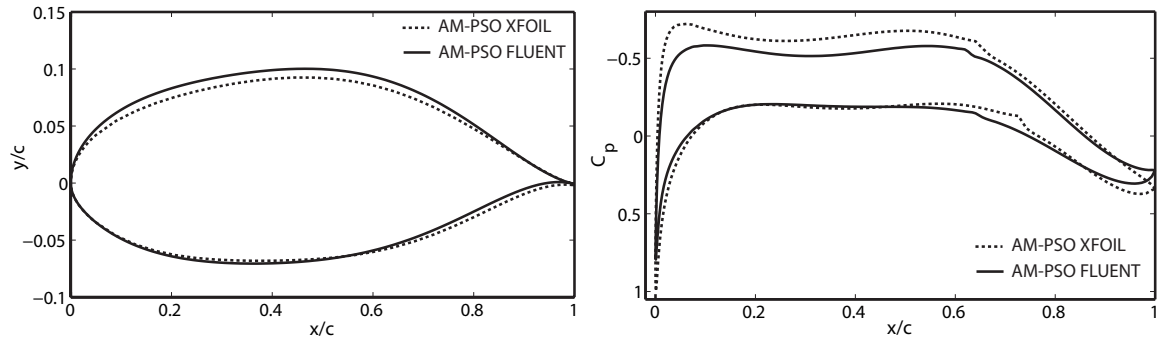

(a) Airfoil Profile

(b) Airfoil c_p

FIGURE 6.25: HALE Single-Point Optima Airfoil Profile by XFOIL & FLUENT in the DNO Structure

The two shapes with a low and high-fidelity solver in the DNO process yield similar geometry features in Figure 6.25(a). The FLUENT derived profile to the optimisation process has a larger t/c in comparison to the XFOIL based solution. The larger thickness is attributed to an extended upper profile contour by the high-fidelity solver relative to XFOIL. The thickness variance on the upper surface by FLUENT in comparison to XFOIL extends from airfoil leading to trailing edge. On the lower surface, the thickness distribution between the two shapes is modeled with negligible variance. The overall t/c disparity between the two profiles is minimal.

It is worth acknowledging that despite the application of a high-fidelity solver in the optimisation structure, the ongoing issue of a limited internal wedge angle at the trailing edge zone for the established optima remains in Figure 6.25(a). This was also evident for shape designs with low-fidelity solvers. The shape convergence results confirm the merits of the developed optimisation algorithm and further re-enforces the need to impose appropriate structural and geometry constraints to ensure unrealistic shapes from a manufacturing perspective are not generated by the shape optimisation process.

The c_p distribution of the XFOIL and FLUENT derived shapes is modeled in Figure 6.25(b). There is a miss-match in the peak negative pressure coefficient about the airfoil nose leading edge between the two solvers. The low-fidelity simulation with XFOIL underestimates the peak c_p in comparison to FLUENT. The c_p performance variance between the two solvers extends from airfoil nose to boundary layer flow transition point at $x_{tr_{up}} \approx 0.61$ which is estimated with agreement by the two solvers. Forward of the transition point, the variance in c_p between the two solvers is minimal. On airfoil lower surface, the disparity in c_p between XFOIL and FLUENT is minimal. The high-fidelity solver estimates flow transition at $x_{tr_{low}} \approx 0.60$ compared to $x_{tr_{low}} \approx 0.70$ by XFOIL. The variance in

flow transition prediction points results in a c_p distribution difference between the two solvers which extends from the estimated transition point, toward the trailing edge region.

The results confirm the scope of the solution topology by the AM-PSO algorithm for HALE single-point design has been mapped. The converged optima airfoils by the high and low-fidelity solvers in the DNO structure yield comparable results. The application of a high-fidelity solver is needed to enhance the accuracy of the aerodynamic coefficients for detail shape design. The feasibility of applying the low-fidelity solver during the conceptual design stage to define the DNO methodology is justified. The results from the DNO design definition phase are applicable for detail shape design with a high-fidelity solver for the purposes of improving the accuracy of the aerodynamic analysis.

6.6.2 Optimisation by Hybrid AM-PSO & Gradient Method Algorithm

The results to the DNO development process validated the merits of integrating a gradient search algorithm in the shape design process for convergence to a true optima region in Section 6.6. The solution from the stand-alone AM-PSO with FLUENT (Sec. 6.6.1) is applied in the hybrid design process. To model the impact of applying disparate starting points from the solution topology on search convergence, the AM-PSO derived optima shapes with the PARSEC-Modified function with 13, 12 and 11 design variables from Table 6.16 are used as search initialisation points in the hybrid design approach. The aerodynamic and geometrical data from the design analysis is presented in Tables 6.18 and 6.19 respectively.

TABLE 6.18: HALE FLUENT-Based Single-Point Airfoil Optimisation Aerodynamic Performance Definition by the AM-PSO & AM-PSO/Gradient Method

Optimal Airfoil By	Design Method	AoA(°)	c_l	c_d
PARSEC-Modified	AM-PSO	1.0137	0.4173	0.00422
(13 Design Variables)	AM-PSO/GM	0.5458	0.4002	0.00395
PARSEC-Modified	AM-PSO	-0.1425	0.4178	0.004267
(12 Design Variables)	AM-PSO/GM	1.0860	0.4007	0.00398
PARSEC-Modified	AM-PSO	0.1638	0.4165	0.004227
(11 Design Variables)	AM-PSO/GM	0.7800	0.4001	0.00399

The simulations by the hybrid-optimisation approach for the respective problem dimensional size conform to the design constraint on $c_l^T = 0.40$ in Table 6.18. The c_d is minimised with a local search process initiated about the AM-PSO derived solution as the starting point. The magnitude in drag reduction relative to the stand-alone AM-PSO algorithm is similar. Minimal c_d variances between the respective case studies is identified. The aerodynamic performance results confirm the convergence of the hybrid search process to a true optima region.

The feasibility of the search starting points from the AM-PSO algorithm is verified. The simulations in Table 6.18 validate that the initialisation points are well-defined and are in a solution topology bounded by the global optima. The data confirms the validity of the AM-PSO search principles. The population-based algorithm converges to a valley of solutions about the global minima, but not to

the true optima. The integration of a gradient optimisation algorithm facilitates convergence to a feasible solution. The c_d of the global minima point is modeled with negligible variances as a function of disparate search starting points. The theoretical advantages of the optimisation approach with the AM-PSO coupled to a GM method is verified.

The geometrical and aerodynamic constraints of the respective shapes from Table 6.18 are presented in Table 6.19.

TABLE 6.19: HALE FLUENT-Based Single-Point Airfoil Optimisation Constraint Definition by the AM-PSO & AM-PSO/Gradient Method

Airfoil	Design Method	t/c	Max Camber	$\frac{d_{cp}}{d_x}$	c_{m0}
PARSEC-Modified	AM-PSO	0.1696	0.0171	0.1028	-0.0629
(13 Design Variables)	AM-PSO/GM	0.1632	0.0142	0.2617	-0.0454
PARSEC-Modified	AM-PSO	0.1737	0.0210	0.2900	-0.0776
(12 Design Variables)	AM-PSO/GM	0.1709	0.0212	0.2580	-0.0485
PARSEC-Modified	AM-PSO	0.1650	0.0175	0.1315	-0.0771
(11 Design Variables)	AM-PSO/GM	0.1619	0.0125	0.1191	-0.0505

The t/c by the hybrid design approach for the respective problem dimensional search size conforms to the defined constraint (Eqn. 6.7) in Table 6.19. The application of the gradient method has the affect of minimising the thickness of the optimal profile relative to the AM-PSO starting point for the defined case studies. The constraints on $\frac{d_{cp}}{d_x}$ (Eqn. 6.5) and c_{m0} (Eqn. 6.8) are satisfied by the hybrid optimisation simulations for the respective problem types presented.

The variance in optima profile AoA and constraints modeled by the different airfoil shape parameterisation dimensional sizes with the hybrid approach, validates a multi-modal solution topology. The AoA required to achieve the $c_l^T = 0.40$ is different for each solution. Accordingly the camber distribution of the respective optimal profile is unique in Table 6.19. The extent of the favorable pressure coefficient gradient on airfoil upper surface is also different for each solution due to the variance in shape AoA and camber distribution required to achieve the target lift coefficient. An increased c_{m0} performance by the hybrid approach relative to the stand-alone AM-PSO method validates an aft loaded shape. The minor variances in the aerodynamic performance between the modeled data for the respective airfoil function dimensional size in Table 6.18 confirms a multi-modal solution topology. The optima profiles by the hybrid design approach are modeled in Figure 6.26 which further confirms the multi-modal characteristics of the HALE airfoil design problem.

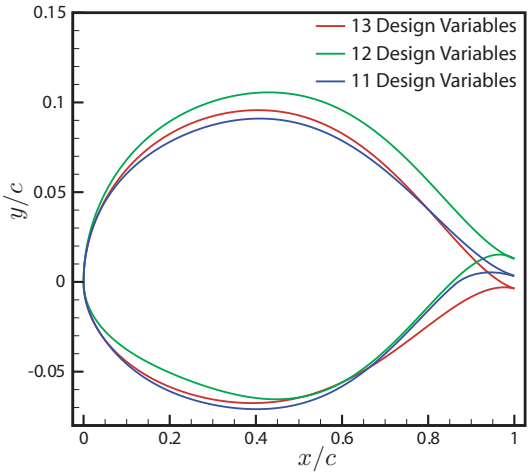

FIGURE 6.26: HALE FLUENT-Based Single-Point Airfoil Optima Profile at Convergence by the AM-PSO/Gradient Method with Variance in Shape Parameterisation Dimensionality Size

The disparity between the converged optimal profiles in Figure 6.26 for the respective hybrid-optimisation test case from Tables 6.18 and 6.19, confirms the existence of multiple airfoil types for the defined test problem, hence a multi-modal solution topology. The application of additional design objectives and/or constraints are needed to isolate the search to one global optima. A multidisciplinary design problem by the integration of additional design disciplines will further address this requirement.

The results to HALE airfoil design with low and high-fidelity solvers confirms the performance merits of the optima airfoil in accordance to the defined goals of the MM-UAV platform. As drag minimisation is a performance objective over an extended user-defined c_l^T flight envelope, the single-point methodology does not achieve this requirement. The multi-point method addressed the disadvantages of the single-point process. Despite the benefits, it is limited due to the ambiguity in flight design point selection process. The developed robust method addressed this limitation as the flight points for optimisation were intelligently selected by the novel AM-PSO algorithm. The fundamental principles of the design approach resulted in favorable drag performance in comparison to the multi-point method. The generated profile by the robust approach with acceptable drag performance, will yield performance gains for the intended MM-UAV platform relative to the NLF(1)-0416 airfoil. The modeled design principles are confirmed from an aerodynamic design optimisation view point for HALE shape design simulations.

6.7 Transonic Airfoil Design

The DNO methodology is applied for airfoil design to govern transonic operations within the mapped MM-UAV flight profile from Figure 6.1. The flexibility of the AM-PSO algorithm for aerodynamic shape optimisation applications is further verified. Transonic airfoil design processes have been examined in the literature and validation data exists for solution performance verification purposes. The objectives and constraints representative of a high-speed operation are directly integrated into the AM-PSO method. The results of the optimisation process are compared against published data. The feasibility of the solution is assessed relative to the user-defined objectives and constraints. The

computational resources required to convergence is compared with data from the literature to verify the efficiency of the design process relative to current off-the-shelf design systems.

Airfoil optimisation architecture development at transonic flight envelopes has several issues and challenges which must be addressed. The aerodynamics at a transonic flight regime is complicated by the transition of local surface Mach numbers from subsonic to supersonic speeds. The development of surface induced shock waves with an increase in wave drag complicates the optimisation process due to the sensitivity of airfoil surface perturbations to shock wave development. Airfoil variables must be intelligently defined to ensure the aerodynamic integrity of the profile is not compromised by excessive wave drag.

The performance of the Gradient optimisation method for transonic airfoil design was verified by Namgoong [41]. The convergence to a solution by the GM with several well-defined initialisation points including the NASA Supercritical profile was verified. It was shown that GM methods generate a local optima about the base starting airfoils. Profile contour comparisons between initial and final shapes indicated minimal deviations, thus verifying a local search process. The drag performance of the established optima was directly related to the initialisation point. The disparity in drag magnitudes for the separate initialisation points validated the limitation of the GM method for transonic airfoil design. It was established that the flight envelope at transonic Mach Numbers is multi-modal. The sensitivity of shock development as a function of airfoil surface modifications results in the generation of local minima regions in the solution topology. The limitation of the GM methods to exploit an acceptable optimal shape from the defined region was identified.

The GA was used to address the disadvantages of the GM in [41]. The drag performance of the optima profile was significantly lower than GM simulations. The feasibility of a global optimisation method for transonic airfoil design was verified. Despite the acceptable results by the GA, it was acknowledged that the established solution may not be global. This is attributed to the definition of the shape parameterisation model type applied in the design process. An analytical approach with the Hicks-Henne shape functions was used to mathematically represent the candidate airfoils. The search intervals of the participating coefficients which act as multipliers to the shape function and are linearly added to a baseline shape were arbitrary defined. The search bounds of the shape variables were fixed for each base airfoil. The solution search space envelope was dependent on the selection of the base airfoil and variations to the starting profile resulted in a different optima. The definition a well-defined starting point was not defined and the optimality of the airfoil can not be confirmed.

The novel optimisation architecture developed is applied to address the shortcomings identified by Namgoong [41]. The following points are covered:

1. The analytical shape parameterisation approach is not applied, hence avoiding the selection of a base airfoil from the analysis. The scope of the solution topology will not be limited by the ambiguous selection of a user-defined starting point. The aerodynamics of the global optima will be governed by the intelligent search mechanisms of the AM-PSO and will not be limited by an ill-defined search space envelope due to the false definition of a search starting point.

2. The search intervals of the shape variables are mapped to attain a solution topology that facilitates an optimisation process toward a global point.

3. Validate the feasibility of the optima against:
   (a) A current off-the-shelf airfoil [9]; and
   (b) The optima airfoil established in literature with the GA by Namgoong [41].
4. Assess the computational efficiency of the developed DNO process with published data [41]

The comparative analysis of the results by the AM-PSO method and the data by Namgoong [41] is performed to verify the viability of the developed optimisation approach for transonic airfoil design. Consideration to the variances in solver accuracy between the two studies is considered. Due to the disparity in solver type and accuracy of the fitness function evaluator, the drag performance of the optima is not used in the comparative analysis. The computational domain mesh size and type and solver setup are different, hence variances in airfoil aerodynamics of the optima by the two methods is expected. Boundary layer flow transition are also treated differently and the drag between the GA and AM-PSO solutions will be different. To affectively assess the performance of the two airfoil design strategies, the overall percentage drag reduction of the optima shape relative to an identified off-the-shelf shape is used in the analysis. The benchmark airfoil used by Namgoong [41] for performance measure purposes is also applied in the presented analysis to facilitate the defined comparative analysis study.

The computational efficiency of the GA [41] and AM-PSO is also verified. The number of solver calls required to achieve convergence is examined to assess the efficiency of the design structure. Despite the variances in solver fidelity and types in the two studies examined, the optimisation algorithms will model the scope of the solution topology. The negligible affect of solver fidelity on the optimisation process was validated by Ray et al. [170] and Hacioglu [150]. The comparative performance analysis between the GA and AM-PSO will verify the feasibility and the computational efficiency of the developed DNO structure. The validity of the DNO approach relative to off-the-shelf systems in literature for transonic airfoil design is confirmed.

6.8 Transonic Single-Point Airfoil Optimisation Architecture Set Up for Flow Analysis by a High-Fidelity Solver

Airfoil design for the MM-UAV platform at transonic flight envelope is based on the principles of a single-point design approach. The initial sizing of the MM-UAV platform based on missions definitions for the Australian industry requirements, resulted in the definition of an accelerated dash-segment for SEAD operations at Mach=0.74 with constraints on minimum target lift and geometry thickness. The RAE 2822 airfoil was integrated into the platform for initial sizing. The identified shape exhibits acceptable aerodynamic performance at the defined $c_l^T = 0.733$ and transonic Mach flight conditions. The problems associated with surface induced wave shocks limit the aerodynamic performance of the airfoil for the intended platform.

The developed DNO process is applied to further minimise airfoil c_d at the transonic flight envelope. The validity of the design process is confirmed by comparison of the established optima with published

data by the Royal Aircraft Establishment [9] with respect to the design goals of the RAE 2822 airfoil. The results are further evaluated against the design efforts by Namgoong [41].

The shape design problem is defined as follows:

$$\begin{aligned} &\text{At } R_n = 2.7 \times 10^6 \text{ \& Mach=0.74} \\ &\text{minimise } c_d \\ &\text{Subject to:} \\ &\Rightarrow c_l^T(x) = 0.733 \\ &\Rightarrow t/c_{max}(x) \geq 0.12 \end{aligned} \tag{6.15}$$

Where: x is the vector of airfoil shape function design variables

The defined aerodynamic optimisation simulations are presented with focus on mission-segment based airfoils only. The problem definition does not focus on the design of a mission profile-based shape which will result in a drag compromise between the different flight segments at HALE and transonic Mach numbers. The results presented are designed to exploit the advancements in material and structural design disciplines for morphing technologies. The design of a mission-segment airfoil will generate a shape with optimal aerodynamic efficiency for a specific operating envelope. The performance metric of the mission-segment airfoil will not compromised by the conflicting design goals from separate operating segments. Shape morphing will be required to transform the airfoil from one performance segment to another to achieve optimal aerodynamic efficiency for the defined operating profile. The analysis into morphing concepts is beyond the scope of this thesis.

Constraints are applied in the design process by the inclusion of a penalty function from Equation 6.3. The cost of the penalty magnitude to the fitness for the defined constraints are presented in Equations 6.16 - 6.17.

- Constraint: c_l^T

$$\begin{aligned} &\text{if } c_l^T < 0.733 \\ &c_{c_l^T} = 0.933 \\ &c_{c_{l\ pen}^T} = \frac{|c_l^T - 0.733|}{c_{c_l^T}} \end{aligned} \tag{6.16}$$

- Constraint: t/c

$$\begin{aligned} &\text{if } t/c < 0.12 \\ &c_{t/c} = 0.0310 \\ &c_{t/c_{pen}} = \frac{|t/c - 0.12|}{c_{t/c}} \end{aligned} \tag{6.17}$$

The parallel computing architecture developed for HALE airfoil design in Section 6.3.1 is used to enhance the computational time to convergence. A comprehensive DoE analysis is needed to define the DNO model for solution feasibility and computational efficiency. The low-fidelity solver TSFOIL

[148] is applied in the DNO design development process due to rapid computational turn-over time. The following systems are examined in the DoE analysis for transonic airfoil design.

1. Sensitivity of Airfoil Shape Function Type; and
2. Sensitivity of Swarm Population Size

The sub-set to each DoE test involves modeling the affect of the swarm population size and airfoil shape function type on solution convergence. The single-point design objective from Equation 6.9 is used in the analysis. The constraints in Equations 6.16 and 6.17 are further integrated into the design problem to achieve an aerodynamically and geometrically viable solution. Due to the randomness in the AM-PSO search process, each sub-set is examined over 5 independent simulations. The inclusion of TSFOIL facilitates a comprehensive design analysis due to the computational efficiency of the solver.

The setup of the AM-PSO algorithm for the DoE analysis follows the definition from Section 6.4.1. The following modifications are imposed:

- **Shape Function Type**:
  - CST - BP of order 2 = 9 Design Variables;
  - CST - BP of order 3 = 11 Design Variables;
  - CST - BP of order 4 = 13 Design Variables;
  - CST - BP of order 5 = 15 Design Variables;
  - Original PARSEC Model (without Δz_{te})= 10 Design Variables;
  - PARSEC-Modified with full 13 design variables; and
  - PARSEC-Modified at 12 variables with $t_{eg_{low}}$ eliminated as a design variable (Fig. 4.24) and set to the baseline value of the RAE 2822 airfoil
- **Swarm Population Range**: 20, 30 & 40 Particles

A carpet plot is generated to represent the results of the DoE analysis for DNO structure development. As each test sub-set is simulated over five independent simulations, the mean fitness of the trials is modeled. The affect of airfoil shape function type and the swarm population size on mean fitness is presented in Figure 6.27.

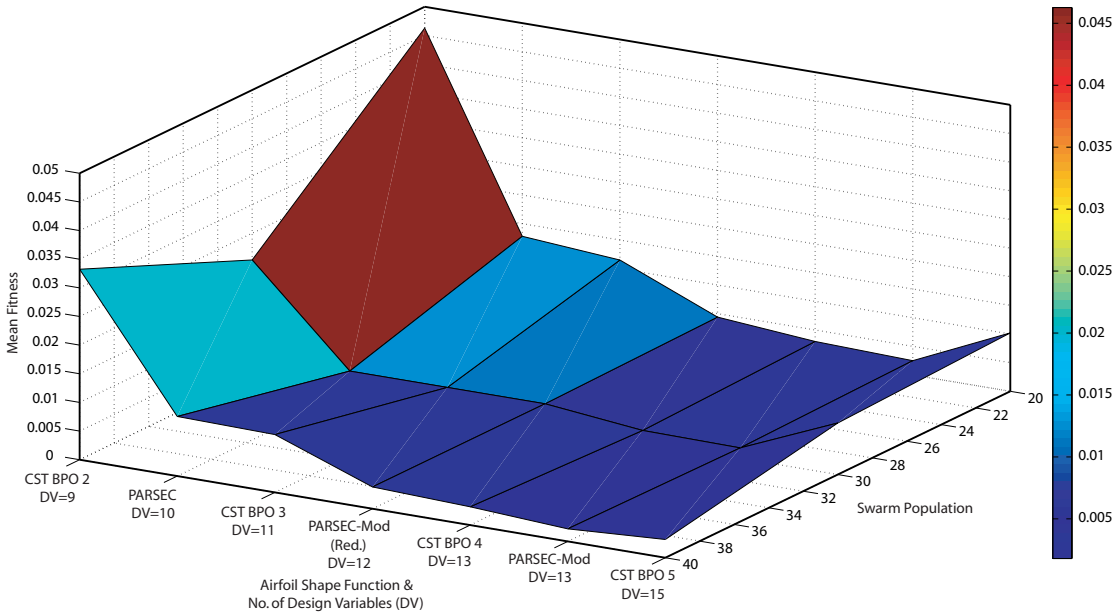

FIGURE 6.27: Solution Search Space Convergence by Disparate Airfoil Shape Parameterisation Function Types as a Function of Swarm Population for Transonic Airfoil Design with AM-PSO

The benefits of increasing the dimensionality of the shape function on mean fitness is validated in Figure 6.27. As the number of design variables applied to parameterise the airfoil increases, the mean fitness decreases. The modeled affect is limited to a threshold of 13 shape variables. The mean fitness at 15 design variables increases in comparison to the use of 13 design variables only. Further analysis into the simulation trials with 15 design coefficients confirms the non-convergence of the defined optimisation termination measuring units (Sec. 6.4.1) within the maximum 800 iteration limit. The mean fitness of the CST method with BPO 5 is representative of solutions with a non-convergence state. The affect of increasing the maximum iteration limit for the defined test sub-set beyond 800 evolutions was not examined.

The merits of increasing the swarm population size on fitness minimisation is further verified in Figure 6.27. The mean fitness convergence is sensitive to the swarm population size for a dimensional size with nine to eleven design variables by the CST method spanning BPO 2 to BPO 3 and including the original PARSEC model. An increase in swarm population from 20 to 40 particles in the defined dimensional search region has the affect of minimising the mean fitness.

Beyond the identified particle population size induced sensitivity region zone, the effect of swarm size on mean fitness has a negligible impact. The solution region between 12 to 13 design variables modeled by the PARSEC-Modified method with reduced modeling, including the CST with BPO4 and the PARSEC-Modified function with the full set of shape coefficients, the impact of particle population size on fitness is minimal. The 'flat' carpet topology spanning the defined test region validates the limited impact of swarm size on mean fitness. At the non-converged solution region with 15 design variables, the sensitivity of swarm population size on mean fitness is established. The maximum iteration limit needs to be increased to achieve a converged search simulation state such that the true effect of swarm size on fitness can be correctly resolved.

The affect of applying the gradient optimisation algorithm with the AM-PSO algorithm on transonic airfoil design is verified. A DoE analysis is established by the application of the AM-PSO solution from each experimental trial in Figure 6.27 as the search starting point for a GM analysis. The mean converged fitness by the hybrid approach is presented for the respective shape function and swarm population size in Figure 6.28.

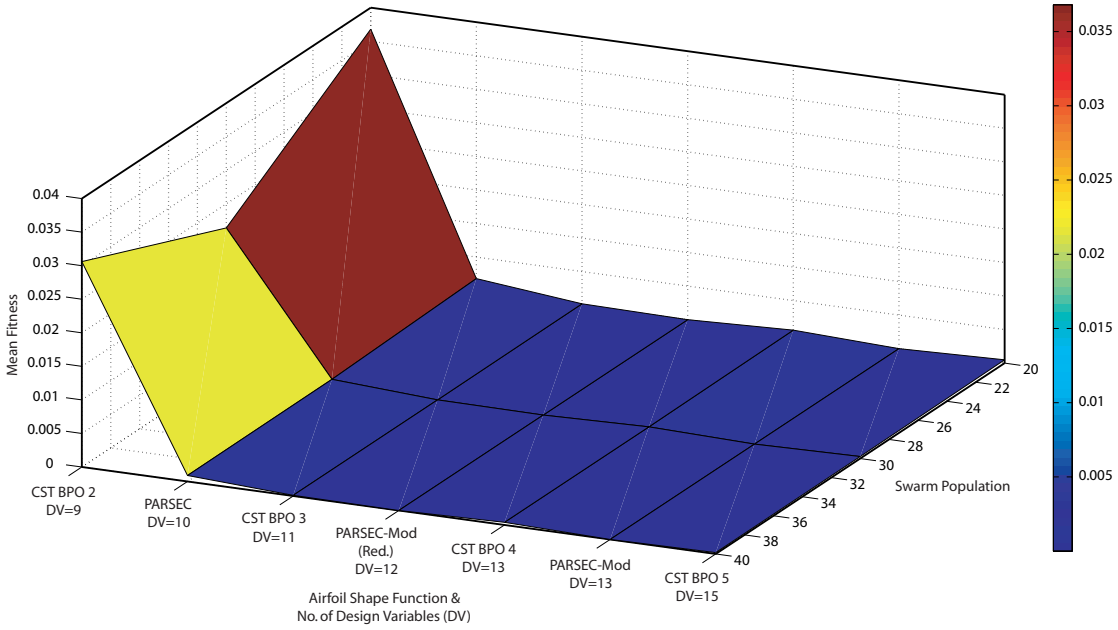

FIGURE 6.28: Solution Search Space Convergence by Disparate Airfoil Shape Parameterisation Function Types as a Function of Swarm Population for Transonic Airfoil Design with AM-PSO & Gradient Optimisation Methods

The data confirms the validity of the hybrid design approach for fitness minimisation in Figure 6.28. The scale of the fitness magnitude is lower than the relative measure by the stand-alone AM-PSO method from Figure 6.27. The comparative analysis of the fitness difference between the two design methodologies validates the performance of the hybrid optimisation approach.

The benefits of the hybrid optimisation approach are not significant for the solution region generated by the CST function with BPO 2 at 9 design variables. The fitness magnitude at the defined test sub-set is lower than the convergence with the AM-PSO in Figure 6.27. The degree-of-fitness reduction at 9 variables by the hybrid approach is not at the same scale relative to the mapped region spanning 10 to 15 design variables in comparison to the AM-PSO algorithm. The 'flat' mean fitness topology region in the hybrid approach in Figure 6.28 for shape functions spanning 10 to 15 variables as a function of swarm population size represent fitness convergence to a common solution point. The standard deviation of the mean fitness at 11 design variables by the CST BPO 3 as a function of swarm population size is 2.8×10^{-4}. Comparably with an additional shape coefficient by the PARSEC-Modified method with reduced modeling, the mean fitness standard deviation for the represented swarm population envelope reduces to 1.15×10^{-5}. The standard deviation beyond 12 shape coefficients, up to the maximum limit of 15 variables remains stable. Hence, solution search space convergence is achieved at 12 variables by the PARSEC-Modified function with $t_{eg_{low}}$ eliminated as a shape coefficient from the analysis in Figure 4.24.

The results by the DoE analysis confirmed the affect of shape parameterisation type, hence problem dimensionality and swarm population size on solution feasibility. The application of the hybrid design approach is warranted to aid convergence to a true search space region. The measure of computational efficiency was implicitly modeled. As the maximum iteration count was set at 800 evolutions and with no other termination criterion applied, the computational time to convergence was consistent for the modeled DoE test envelope. Interrogation of swarm search traits was undertaken to detect the initiation of an idle search process, hence state-of-convergence. The analysis confirmed the onset of an in-active search process is activated earlier as the dimensionality of the problem scope is reduced.

The application of a shape function with 12 instead of 15 variables will theoretically result in a computationally efficient design simulation. The expected time benefits will follow with the application of a high-fidelity, fitness function solver in the design loop. The knowledge gained from the DNO optimisation architecture development process will be applied for transonic airfoil design with the high-fidelity flow solver in the DNO structure.

6.9 Transonic Optimisation by Stand-Alone AM-PSO Algorithm

The results to the DNO structure development process for transonic airfoil design from Section 6.8 will be applied to formulate the optimisation architecture for flow analysis by a high-fidelity solver in the design loop. The optimisation model follows the principles used in HALE shape design simulations with FLUENT in Section 6.4. The following modifications are incorporated into the design process based on the findings of the DoE analysis:

- Swarm Population Size: Set at 20 particles (validated in Figs. 6.27 & 6.28)
- Shape Function Type:
  - PARSEC-Modified with 13 Design Variables; and
  - PARSEC-Modified with 12 Design Variables, ($t_{eg_{low}}$) set to the RAE 2822 airfoil baseline value
- Search Termination:
  - Maximum 800 iterations; or
  - A concurrent idle search activity over 100 consecutive evolutions for the following three measures (validated in Sec. 6.4.1 in Figs. 6.8 & Fig. 6.10)
    - $pbestg$
    - p_f
    - σ_t
- The gradient optimisation method is applied to initiate a local search process about the AM-PSO derived solution.

The results in the DoE analysis for transonic airfoil design simulations with TSFOIL, validated the solution search space convergence at 12 design variables in Figure 6.28. There were no performance improvements in drag by the expansion of the solution search scope with additional shape variables. To further confirm the validity of the mapped solution topology in Figures 6.27 and 6.28, airfoil design simulations are presented with 12 and 13 shape coefficients with the PARSEC-Modified and the reduced variant of the model function with FLUENT as the flow solver. The results will verify the validity of the established solution topology by TSFOIL and further confirm the benefits of the design variable pre-screening process to identify and eliminate shape coefficients that have a negligible impact on the objective function from Section 4.2.2.2. Comparison of results between low and high-fidelity solvers will validate the assumption that the scope of the solution topology for single-point designs is not sensitive to solver fidelity.

The aerodynamic and geometric data by the defined problem definition with FLUENT is presented. The results are compared against the benchmark RAE 2822 airfoil and the design simulations by Namgoong [41] in Table 6.20.

TABLE 6.20: Transonic Single-Point Airfoil Optimisation Results by the AM-PSO Method with FLUENT

Airfoil	t/c	Max Camber	AoA(°)	c_l	c_d	% c_d Gain*	c_{m0}
RAE 2822 [9]	0.121	0.060	3.19	0.733	0.0196	—	-0.0831
Literature [41]	—	—	—	0.733	0.02238⋆	-↓33.20⋆	—
PARSEC-Modified (13 Design Variables)	0.121	0.0240	1.52	0.834	0.0158	-↓20.20	-0.0558
PARSEC-Modified (12 Design Variables)	0.120	0.0350	-0.62	0.745	0.0144	-↓27.27	-0.0701

* **Relative to the benchmark RAE 2822 Airfoil**

⋆ The drag reduction measure is relative to the c_d performance of the RAE 2822 airfoil at the defined flight conditions. The percentage drag reduction by the AM-PSO will be compared to the GA in literature [41]. The drag of the optima shape between the two design methods is not compared as the flow solvers used in the respective studies are different. Instead the performance comparison between the AM-PSO and GA is restricted to the measure of drag minimisation relative to the identified benchmark by the two optimisation algorithms.

The results in Table 6.20 for the respective shape function conform to the user-defined constraints on $c_l^T = 0.733$ (Eqn. 6.16) and minimum airfoil thickness $t/c > 0.12$ (Eqn. 6.16). The converged airfoil and the c_p of the respective shapes relative to the defined benchmark are presented in Figure 6.29.

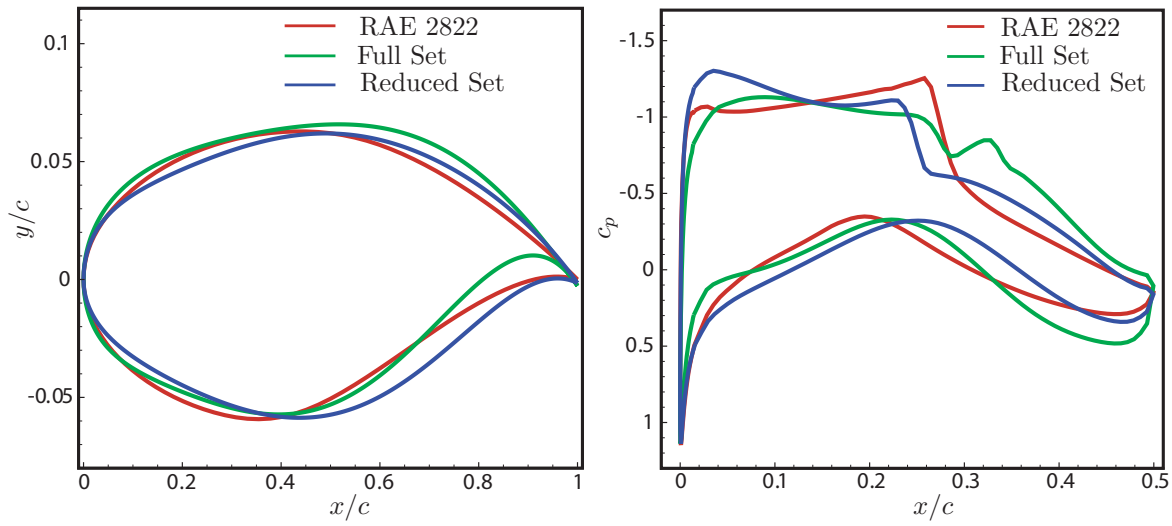

(a) Airfoil (b) Coefficient of Pressure

FIGURE 6.29: Transonic Airfoil Optimisation at $c_l^T \approx 0.733$ by the Stand-Alone AM-PSO Algorithm with PARSEC-Modified Full & Reduced Design Variable Set

The chord location of the maximum thickness point x_u, by the PARSEC-Modified method with full (DV=13) and reduced variable sets (DV=12) is greater than the benchmark RAE 2822 airfoil in Figure 6.29(a). Comparatively airfoil upper surface of the established optima by the two shape parameterisation methods is similar. On airfoil lower surface there is a disparity in contour profile between the three airfoils. The PARSEC-Modified with a full set of 13 shape variables is characterised by a DTE contour feature. The chord location of the lower thickness point x_l, by the reduced modeling approach with 12 variables is aft of the baseline shape. At the TE region the reduced variable modeling airfoil converges to the identified benchmark.

The optimal airfoil that is parameterised by the full set of design variables in Figure 6.29(a) is characterised by a small internal wedge angle that is close to zero degrees. This will induce manufacturing issues and is a trait which was previously noted in low-speed airfoil design simulations by the multi-point and robust approach in Section 6.4. The specification of structural constraints coupled with the re-definition of variable search intervals that control the internal wedge angle is needed to address this issue.

The c_p distribution of the optima shapes from Table 6.20 in comparison to the benchmark profile is presented in Figure 6.29(b). Direct comparison of the aerodynamic pressure profile between the baseline and optima shapes, as a function of airfoil parameterisation variable population size, identifies the suppression of surface induced shocks by the AM-PSO algorithm, hence minimisation of wave drag. The established optima by the DNO approach are modeled with subtle and gradual increases in pressure profile aft of airfoil leading edge, which extends up to the established shock chord location. In comparison the benchmark profile exhibits a sudden and rapid increase in c_p followed by an intensified surface induced shock. The optima shapes by the full and reduced variable sets exhibit a weaker shock in comparison, hence a decrease in wave drag (Tab. 6.20).

Direct comparison of the c_p distribution by the full and reduced variable sets identifies performance variances in Figure 6.29(b). A gradual increase in c_p up to the point of surface induced shock, aft of

airfoil leading edge is modeled. The intensity of the shock wave by the two methods is comparable. The variance in airfoil c_d between the full and reduced variable sets ($c_d = 0.0158$ versus $c_d = 0.0144$ respectively in Tab. 6.20) is restricted to the disparity in c_p profile aft of the initial shock location. The optima profile by the full variable function type is characterised by the generation of a second shock wave following the first. In comparison the optima by the reduced variable set is modeled with a single shock only. Despite the second surface shock by the full variable set being weaker in comparison to the initial, the flow pattern corresponds to a higher wave drag in comparison to the airfoil parameterised by the reduced modeling approach.

Due to the variances in drag performance by the full and reduced variable sets relative to the baseline RAE 2822 airfoil (Tab. 6.20), it is hypothesised that the AM-PSO based solutions are in the region bounded about the global optima, but are not reflective of the true minima point. The c_d performance variances by the high-fidelity approach in Table 6.20 do not conform to the carpet plot data with TSFOIL from Figure 6.27. The use of the low-fidelity solver represented a converged solution space at 12 design variables with the PARSEC-Modified function. Further increases in shape coefficient variable set resulted in negligible variances in c_d, hence validating solution search space convergence (Fig. 6.27). The disparity in c_d by the use of FLUENT (Tab. 6.20) does not conform to the defined convergence region mapped by TSFOIL.

The assumption of achieving solution convergence by the AM-PSO to a global region, but not to the true optima was defined in HALE shape design simulations. Gradient optimisation methods were a requirement and used to aid convergence to the true optima. It is concluded that the AM-PSO solutions for transonic flight envelopes in Table 6.20 are in a region bounded about the global point and are not indicative of the true minima. A gradient optimisation simulation will address this issue and yield convergence to the true solution. Consistent drag reduction magnitudes by the modeled shape function types relative to the identified benchmark will be established. The feasibility of the AM-PSO method for transonic shape design simulations requires further design analysis to validate and achieve the expected performance improvements by the defined process.

The fundamentals of the developed AoA trimming process was confirmed in Section 6.6.1 to estimate the α for a user-defined c_l^T at HALE flight envelopes in Figures 6.23 and 6.24. The developed methodology is further confirmed at transonic flight envelopes. The distribution of the established c_l^T of the candidate airfoils (particles), relative to the user-defined target $c_l^T = 0.733$ during the search evolution process is modeled. The results are presented in Appendix J. The mean c_l^T of the particles in the swarm during the search evolution process from the boxplot analysis in Figure J.1 is about the user-defined target $c_l^T = 0.733$. The extended boxplot intervals about the specified target and data outliers are representative of airfoils with a non-linear lift curve slope and/or due to the contribution of errors in the developed trimming methodology. The frequency of airfoils that are about the specified c_l^T threshold during the iterative design process for select particles are further presented by a histogram chart in Figure J.2. The analysis confirms a large population of airfoils by the select particles are grouped about the specified target $c_l^T = 0.733$. The analysis in Appendix J confirms the AoA trimming process can result in an incorrect interpretation of airfoil c_l relative to the defined target due to a false measure of the AoA. The airfoil sample size with the defined errors is minimal.

The aerodynamic and geometrical data from Table 6.20 confirmed the feasibility of the developed AM-PSO method for airfoil design. The viability of the solution is favorable relative to the established benchmark. The computational efficiency, as the second measuring unit of the DNO model is assessed for the case studies presented in Table 6.20. The convergence of the defined AM-PSO termination measures is presented. The computational efficiency is assessed by the measure of the total number of fitness function evaluations required to achieve convergence by the respective optimisation algorithm. The wall-clock time to design termination is not used in the comparative analysis due to the differences in the computing hardware used between the modeled studies. The total number of fitness function evaluations by the AM-PSO model is established from Equation 6.18 and is compared with published data [41] in Table 6.21.

$$\text{Number of Function Evaluations} = (\text{Swarm Population} \times \text{Iterations to Convergence}) + \text{Additional Fitness Evaluations due to Mutation} \quad (6.18)$$

TABLE 6.21: Transonic Single-Point Airfoil Optimisation Convergence Assessment by the AM-PSO Method with FLUENT

Shape Function Type	*pbestg*	p_f	σ_t	$\therefore$ Convergence	Number of Function Evaluations
Literature [41]	—	—	—	—	107,520
PARSEC-Modified (13 Design Variables)	252	800	800	800	$(20 \times 800) + 14,745 = 30,745$
PARSEC-Modified (12 Design Variables - $t_{eg_{low}}$ not used)	448	649	750	750	$(20 \times 750) + 4,742 = 19,742$

The AM-PSO algorithm with the full set of 13 shape variables represents a non-converged state in Table 6.21. The corresponding convergence history plot as a function of the iterative search process is presented in Figure 6.30(a). The convergence of the defined termination measuring units is modeled in Figure 6.30(b).

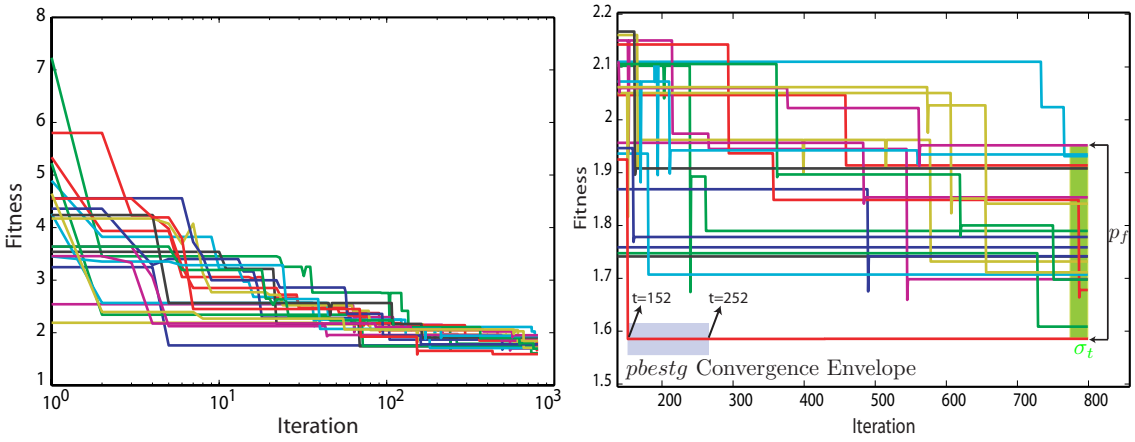

(a) Particles Personal Best Convergence

(b) Representation of Termination Measures applied in the Search Process

FIGURE 6.30: Transonic Airfoil Design Swarm Personal Best Convergence toward Optima as a function of Search Iteration

The personal best fitness of the particles in the swarm during the search evolution process in Figure 6.30(b) represents the convergence of *pbestg* at the 152^{nd} design iterate. The parameter remains idle for the next 100 consecutive iterations and is assumed converged at the 252^{nd} search iterate. Concurrently the termination units p_f and σ_t represent an active search process in the swarm up to the maximum 800^{th} search evolution point despite the convergence of *pbestg*. The optimisation termination parameters do not conform to an idle search pattern spanning 100 iterations at any stage during the search process. As p_f and σ_t do not sustain an idle search activity over 100 consecutive iterations, the search process is assumed to be at a non-converged state at the maximum 800^{th} design iterate.

The PARSEC-Modified shape function with 12 design variables resulted in an efficient search process with convergence at the 750^{th} iterate instead of the maximum 800 by the full variable set in Table 6.21. The last of the three search termination measures to converge was the personal best fitness standard deviation σ_t of the particles in the swarm at the 750^{th} search iterate. The identified measure sustained an idle search activity spanning 100 iterations. Concurrently *pbestg* and p_f also represented an idle search process. By eliminating $t_{eg_{low}}$ as the shape variable from the analysis, an efficient search process ensues in comparison to a model with a full set of 13 design variables. The methodology required $\approx 36\%$ or 11,003 fewer fitness function calls in comparison to the full variable set. This is equivalent to a computational time savings of ≈ 48 hours.

The computational efficiency as a function of the total number of fitness evaluations to convergence by the developed AM-PSO method is confirmed in comparison to the GA for the defined problem type in Table 6.21. The total number of function evaluations is $\approx 71\%$ lower by the AM-PSO method with the PARSEC-Modified shape function at 13 shape variables in comparison to the simulations with GA by Namgoong [41] (30,745 versus 107,520 in Tab. 6.21). The merits of the AM-PSO method is further expanded by the shape function with reduce order modeling in comparison to the GA. The PARSEC-Modified function with 12 variables required $\approx 82\%$ fewer function calls in comparison to the data by Namgoong [41]. The significant reduction in the fitness function evaluation calls between the developed AM-PSO and the GA from the literature confirms the computational efficiency of the novel swarm algorithm for transonic airfoil design simulations.

The application of the novel swarm algorithm has demonstrated the theoretical merits of the optimisation model relative to the GA to sustain efficient design simulations. Despite the validated efficiency of the developed method, the feasibility of the solution requires further design analysis. The established drag reduction relative to the baseline RAE 2822 profile represents a sub-optimal solution. The data in literature [41] for the same problem type with GA, is modeled with drag minimisation that is in excess of $\approx 35\%$. In comparison the solution by the swarm approach with 12 and 13 variables is modeled with a relative drag reduction of $\approx 20\%$ and $\approx 27\%$ respectively in Table 6.20. To address this requirement, the gradient optimisation algorithm is used in the design process.

6.10 Transonic Optimisation by Hybrid AM-PSO & Gradient Method Algorithm

The airfoils by the AM-PSO algorithm from Table 6.20 are applied as the search initialisation point for a gradient-method optimisation analysis. The aerodynamic performance of the derived optima by the defined process is summarised in Table 6.22.

TABLE 6.22: Transonic FLUENT-Based Single-Point Airfoil Optimisation Aerodynamic Performance by the AM-PSO & AM-PSO/Gradient Method

Optimal Airfoil By	Design Method	t/c	AoA(°)	c_l	c_d	$\%c_d$ Gain*
PARSEC-Modified	AM-PSO	0.1210	1.52	0.834	0.0158	—
(13 Design Variables)	AM-PSO/GM	0.1217	2.50	0.7633	0.0128	-↓35
PARSEC-Modified	AM-PSO	0.1200	-0.62	0.745	0.0144	—
(12 Design Variables)	AM-PSO/GM	0.1210	-0.0118	0.734	0.0128	-↓35

* **Relative to the benchmark RAE 2822 Airfoil**

The validity of using a gradient-optimisation method with the AM-PSO algorithm for transonic shape design simulations is confirmed in Table 6.22. The constraint on profile thickness is achieved. The lift performance by the gradient search process results in a decrease in c_l from the initial starting point for the respective shape function type and converges about the user-defined target $c_l^T = 0.733$. Due to the definition of a well-defined starting point from AM-PSO, the c_d performance is minimised relative to the initialisation shape. Drag reduction of $\approx 35\%$ is achieved relative to the benchmark RAE 2822 airfoil and conforms to the solution in literature for the same problem type with GA [41].

The drag of the optima profiles by the hybrid design approach with different starting points is $c_d = 0.0128$, hence convergence to the true solution point is confirmed. The hypotheses defining the convergence of the AM-PSO search process about the global minima region, but not to the true solution is verified. The disparity in drag performance between the starting points from AM-PSO with 13 and 12 PARSEC-Modified shape variables is $\approx 9\%$ ($c_d = 0.0158$ versus $c_d = 0.0144$ respectively in Tab. 6.22). The results of the hybrid design approach confirm the AM-PSO based solutions are about a global minima region. The gradient method facilitates convergence to an airfoil with minima drag performance, hence fitness point by exploiting the feasibility of the well-defined starting points from AM-PSO.

The converged airfoil and corresponding c_p by the AM-PSO and gradient method with the PARSEC-Modified full variable set is presented and compared with benchmark in Figure 6.31.

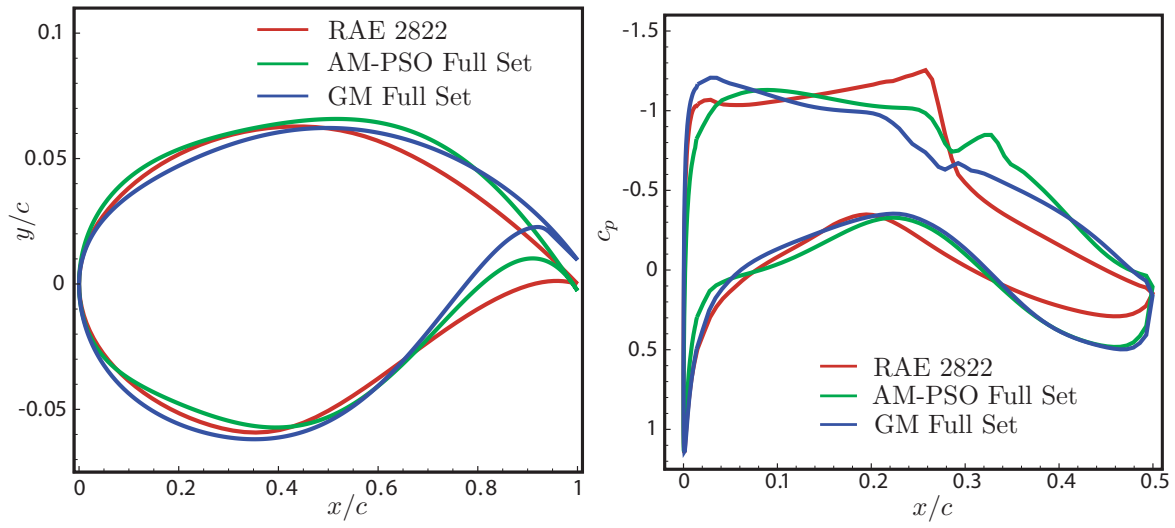

(a) Airfoil (b) Coefficient of Pressure

FIGURE 6.31: Transonic Airfoil Optimisation at $c_l^T \approx 0.733$ by the Stand-Alone AM-PSO & Hybrid Design Approach Method with PARSEC-Modified Full Design Variable Set

The optima airfoil by the gradient method follows the contour profile of the base AM-PSO starting point in Figure 6.31(a). It is modeled with a chord location of the maximum thickness point that is aft of the thickness point of the RAE 2822 airfoil. The disparity in contour profile between the AM-PSO and gradient generated solution is limited to surface modeling at the TE region. The hybrid-based profile is modeled with a DTE contour in comparison to the airfoil by the stand-alone AM-PSO method. The gradient optimisation further shifts the trailing edge ordinate y_{te} upwards $(+y/c)$, in comparison to the stand-alone AM-PSO solution.

The ongoing issue associated with an impractical internal wedge angle that will result in manufacturing issues is evident in the GM full set result in Figure 6.31(a). Additional shape constraints that are localised about the trailing edge region would be needed for future design iterations to address this demerit.

The c_p distribution of the airfoils are modeled in Figure 6.31(b). The impact of the gradient method for minimising airfoil shock on flight performance is validated. On airfoil lower surface the c_p distribution between the AM-PSO and hybrid design method is modeled with negligible variances. The gradient method induces performance benefits by directly modifying c_p performance on upper surface only.

Comparison of pressure profile on airfoil upper surface represents a variance in chord location of the peak c_p point between the two design methods. The hybrid solution peak c_p is about the nose leading edge in comparison to the AM-PSO derived profile which is downstream. The c_p distribution by the hybrid design approach follows a gradual rate-of-change in accordance to the AM-PSO based solution up to the point of shock development. The onset of shock is not sudden or rapid which is a performance trait of the benchmark profile.

Aerodynamic performance analysis of the stand-alone AM-PSO solution validated the minimisation of shock intensity in comparison to the RAE 2822 airfoil in Figure 6.29(b). The integration of the gradient method exploits the benefits of the AM-PSO solution by further reducing the shock

wave intensity in comparison to the AM-PSO derived profile. The AM-PSO solution was modeled with two shock waves with the second just aft of the first and with weaker intensity. The benefits of the gradient process has the affect of diminishing the intensity of the two shock waves. The second wave is almost eliminated to the point where it will have a minor influence on airfoil wave drag. The convergence of the c_p profile by the hybrid optimisation approach in Figure 6.31(b) further validates the hypotheses that AM-PSO based solutions are about a global minima region and are not indicative of the true minima point. The definition of a well-defined starting point that is about an acceptable solution region is exploited by the gradient optimisation method.

The optima airfoil generated by the stand-alone AM-PSO and corresponding hybrid optimisation approach with the PARSEC-Modified function at 12 design variables, represents comparable converged shape and aerodynamic (c_p) flow patterns relative to the presented design methodology with 13 shape coefficients in Figure 6.31. The optima profile and the c_p distribution with reduced problem dimensionality is modeled in Appendix K, Figure K.1.

The evolution of the airfoil design process by the AM-PSO followed by the GM analysis toward an established optima from Figure 6.31(a), is represented by a series of airfoil Mach contour charts in Figure 6.32.

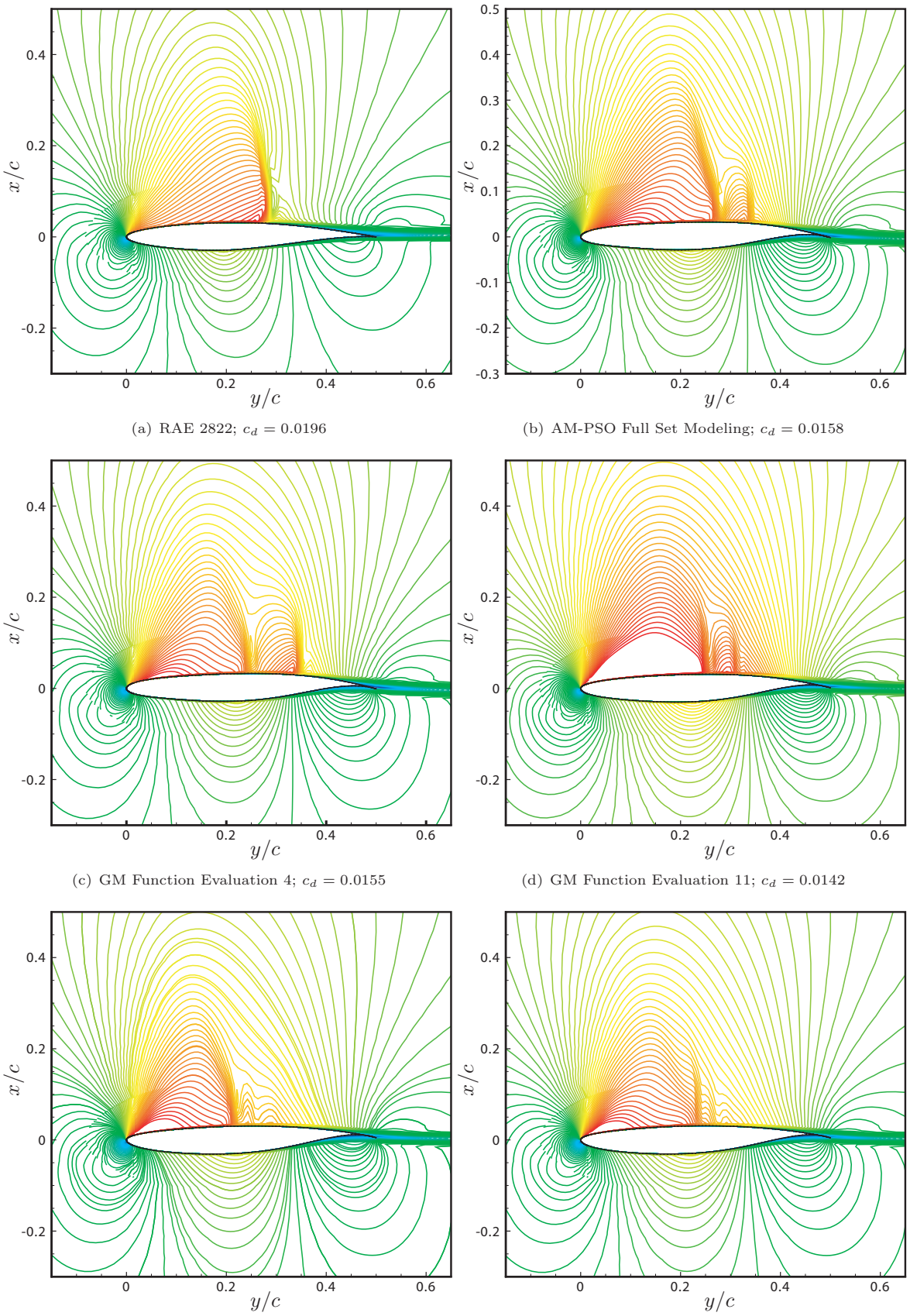

(a) RAE 2822; $c_d = 0.0196$

(b) AM-PSO Full Set Modeling; $c_d = 0.0158$

(c) GM Function Evaluation 4; $c_d = 0.0155$

(d) GM Function Evaluation 11; $c_d = 0.0142$

(e) GM Function Evaluation 17; $c_d = 0.0140$

(f) GM Function Evaluation 37; $c_d = 0.0128$

FIGURE 6.32: Transonic Airfoil Design Convergence toward an Optima by the PARSEC-Modified Full Variable Set Modeling Approach

The benchmark RAE 2822 airfoil is modeled with an intense shock wave and the corresponding drag is high at $c_d = 0.0196$ in Figure 6.32(a). Design optimisation by the developed AM-PSO algorithm has the affect of minimising the shock intensity in comparison to the benchmark profile, hence reducing drag to $c_d = 0.0158$ in Figure 6.32(b). The optima profile is modeled with two shock waves, with the second of weaker intensity than the initial. The gradient process is applied by the use of the AM-PSO profile (Fig. 6.32(b)) as the search initialisation point. The local optimisation process has the affect of further minimising the intensity of the AM-PSO optima derived airfoil surface shocks. The drag is reduced from $c_d = 0.0158$ by the AM-PSO to $c_d = 0.0155$ and $c_d = 0.0142$ at the 4^{th} (Fig. 6.32(c)) and 11^{th} (Fig. 6.32(d)) GM search iterate respectively.

At the concluding stages of the hybrid optimisation process in Figure 6.32(e), the intensity of the initial surface induced shock is further reduced, while the optimiser concurrently minimises the demerit of the second surface shock wave also. This has the affect of reducing drag to $c_d = 0.0140$. At search convergence in Figure 6.32(f), the impact of the second shock wave is eliminated. The intensity of the initial wave is reduced significantly relative to the initial airfoils in Figures 6.32(c) to 6.32(e). The effect of eliminating the second surface induced shock from the AM-PSO solution, while concurrently minimising the demerit of the primary shock on drag, results in a percentage reduction of $\approx 35\%$ in comparison to the defined benchmark RAE 2822 airfoil. The data is in agreement with published results in literature with GA [41].

The impact of the gradient optimisation simulation on airfoil shock with the AM-PSO solution as the search initialisation point is modeled in Appendix K, Figure K.2 for the PARSEC-Modified shape function with 12 design variables. The charts conform to the analysis modeled of the PARSEC-Modified function with full variable set in Figure 6.32. The local search process has the benefits of reducing the shock intensity of the AM-PSO solution over a series of design evolutions. At convergence the impact of surface induced shock has a minor influence on drag (Fig. K.2(f)) relative to the search initialisation phase profile from the stand-alone AM-PSO method (Fig. K.2(a)).

The impact of applying 12 and 13 design variables within the PARSEC-Modified function for hybrid optimisation simulations, resulted in a negligible impact on c_d of the optima profile in Table 6.22. The geometry of the optima and the c_p distribution by the hybrid design approach with 12 (Fig. K.1) and 13 (Fig. 6.31) shape variables represented data disparity between the respective design methods. Despite the identified variances, the drag converged to $c_d = 0.0128$ by the respective parameterisation method as a function of the problem dimensional size. The results re-confirm a multi-modal solution topology exists for the single-point transonic design problem which was also concluded in the analysis by Namgoong [41]. Additional design objectives and/or constraints including a multidisciplinary problem design definition is needed to aid convergence to an operationally viable shape. The presented data validates the feasibility of the developed DNO structure for transonic shape design applications.

6.10.1 Transonic Optimisation by Hybrid AM-PSO & Gradient Method Algorithm: Measure of Computational Efficiency

The results by the high-fidelity, hybrid optimisation approach conform with the corresponding fitness topology mapped by TSFOIL in Figure 6.28. The analysis by the low-fidelity solver confirmed solution

search space convergence at 12 design variables by the PARSEC-Modified method with reduced modeling. The fitness did not decrease with further increases in problem dimensionality. The drag convergence by FLUENT in Table 6.22 with variances in problem dimensionality between 12 and 13 variables, is in agreement with the data by TSFOIL. The importance of integrating the gradient method in the design process is confirmed. An optimisation process with the stand-alone AM-PSO will not result in convergence to the true minima point and is only representative of an airfoil about the minima region. The hybrid design approach exploits the defined region to achieve convergence to the true solution.

The aerodynamic and geometric parameters of the established optima relative to the defined benchmark by the hybrid design approach were confirmed in Table 6.22. The computational efficiency of the optimisation process is assessed. The total number of fitness evaluations needed to achieve convergence is defined as the summation of the solver calls needed by the AM-PSO from Table 6.21, plus function calls by the gradient design simulation. The results are compared with literature [41] in Table 6.23.

TABLE 6.23: Transonic Single-Point Airfoil Optimisation Convergence Assessment by the AM-PSO/GM Method with FLUENT

Data Type	AM-PSO	GM	Total Function Evaluations
Literature [41]	—	—	107,520
PARSEC-Modified (13 Design Variables)	30,745	1,326	32,071
PARSEC-Modified (12 Design Variables - $t_{eg_{low}}$ not used)	19,742	1,209	20,951

The number of solver calls by the GM relative to the AM-PSO is low in Table 6.23. The elimination of $t_{eg_{low}}$ from the gradient design process represents $\approx 9\%$ fewer solver calls in comparison to the full variable set. As the aerodynamics of the optima profile is not compromised by 12 instead of 13 shape variables (Tab. 6.22), the validity of the design variable pre-screening and solution search space mapping analysis (Sec. 4.2.2.2) for transonic airfoil design simulations is confirmed.

The feasibility of the developed DNO architecture in comparison to published data in literature is verified. The hybrid optimisation approach with the full and reduced variable population sets represents $\approx 70\%$ and $\approx 80\%$ fewer solver calls respectively than the GA [41]. The significant savings in computational solver calls confirms the validity of the novel AM-PSO algorithm for airfoil design simulations in comparison to off-the-shelf design systems.

6.11 Summary

To demonstrate the fundamental principles of the developed airfoil design methodology, the DNO model was applied for airfoil design simulations at HALE and transonic flight envelopes. The summary of findings are as follows:

1. **HALE Airfoil Design**

   (a) The solution topology for HALE airfoil design is multi-modal. A gradient optimisation method does not achieve the true optimal solution, hence evolutionary algorithms are needed to address this issue.

   (b) The AM-PSO coupled with the GM algorithm was used in the re-design of the benchmark NLF(1)-0416 airfoil. Favorable drag performances were achieved relative to the defined base profile by the multi-point and robust design methods.

   (c) The convergence of the airfoil shape variables to the established optima were confirmed by a data mining technique. A visual interpretation of the solution topology about the proposed optima point was qualitatively mapped using SOMs. The interpretation of the modeled solution topology by the hybrid optimisation process confirmed airfoil convergence to a true solution based on the defined objective and constraints definition.

2. **Transonic Airfoil Design**

   (a) The DNO approach was used for the re-design of the RAE 2822 airfoil. The fundamental airfoil design principles developed in the thesis were assessed with respect to solution feasibility relative to the defined benchmark [9] and computational efficiency in comparison to the design efforts by Namgoong [41] on the defined problem type.

   (b) The optimal profile by the AM-PSO coupled with the GM converged with $\approx 35\%$ lower drag relative to the identified benchmark RAE 2822 airfoil. The drag reduction was in agreement with the design efforts achieved by Namgoong [41] using the GA.

   (c) The hybrid optimisation approach required $\approx 80\%$ fewer fitness function evaluations than the GA [41] without compromising solution feasibility.

Airfoil design simulations for low-speed and transonic flight envelopes confirmed the generation of unrealistic optima shapes. The trailing edge region was characterised by a small internal wedge angle that was close to zero degrees. Despite the results conforming to an acceptable aerodynamic performance metric relative to off-the-shelf designs, stringent structural constraints are needed to ensure the derived result is acceptable from a manufacturing view point. The re-definition of the design variables that control the wedge angles is needed to remove shapes from the solution space that are representative of airfoils with impractical geometries.

The demonstration of the developed DNO methodology confirmed the design process achieves convergence to the true optima with enhanced computational efficiency relative to off-the-shelf systems. The design principles of shape variable pre-screening including solution search space mapping result in a rapid design optimisation process while maintaining the feasibility of the converged solution relative to the defined design goals. The theoretical principles of the adaptive-mutation swarm algorithm

facilitates an efficient airfoil design simulation. The DNO design measures of solution feasibility and computational efficiency were verified relative to the performance of the GA-based methods from the literature. The test verification process was successfully demonstrated for low and high-speed airfoil design applications.

Chapter 7

Development of a Metamodel Assisted Optimisation Algorithm

7.1 Overview

Engineering shape optimisation simulations are computationally demanding due to the integration of time-intensive, objective function evaluators in the design process. In aerodynamic shape design applications, high-fidelity RANS solvers are needed for solver accuracy. The demerit is an increase in demand of computational resources which limits the computational efficiency of the shape design process. The issue was partially addressed by the design variable sensitivity analysis in Chapter 4. The proposed methodology enhanced the computational efficiency of the design process for test cases with high-fidelity flow solvers in the DNO structure.

A novel design architecture is developed to further minimise the demand on computational resources for shape design simulations. A surrogate-based design structure is proposed to address this requirement. A metamodel is developed by the extraction of fitness from the defined objective function for data points that are within a user-defined solution search space envelope $\mathcal{S}$. The methodology has the potential of solving airfoil flowfield with negligible computational effort in comparison to the application of RANS equations which are computationally exhaustive.

The metamodel assisted optimisation structure is based on the integration of the AM-PSO algorithm into the design process. The validated swarm methodology will exploit the principles of the surrogate model for fitness function evaluations for the intent design problem. Theoretically the proposed methodology has the benefits of enhancing the computational efficiency of the airfoil design process by establishing the state of the objective function with negligible computational effort in comparison to fitness evaluations by the stand-alone flow solver model only as demonstrated in Chapter 6.

The chapter focuses on the design development, validation and application of an accurate surrogate model for design optimisation simulations. The definition of an accurate metamodel has issues and challenges that need to be identified and addressed. The following topics are presented in the chapter:

1. **Related Works**
    - An overview of the current, off-the-shelf surrogate model types applied for engineering design applications are presented. The merits and demerits of each model are defined;
    - A survey of current design optimisation structures with flow solver surrogates for airfoil aerodynamic design simulations; and
    - Definition of online and offline based design algorithms for surrogate-assisted optimisation simulations.
2. **Offline-based Metamodel Assisted Aerodynamic Shape Optimisation**
    - Definition of an offline-based metamodel for airfoil aerodynamic design optimisation analysis;
    - Definition of a comprehensive DoE analysis for the design, development and validation of an offline-based metamodel; and
    - Integration of the developed offline-based metamodel to the AM-PSO algorithm for airfoil aerodynamic optimisation analysis.
3. **Online-based Metamodel for Optimisation Applications**
    - Definition of an online-based metamodel for optimisation simulations;
    - Development of a novel, online-based metamodel assisted design algorithm; and
    - Demonstration and validation of the proposed metamodel assisted design algorithm on benchmark test functions.

In this chapter, the role of surrogate models for optimisation simulations is defined. The development and integration of a metamodel for analysis by a swarm algorithm has not been attempted in the open literature. The merits of the AM-PSO method were demonstrated in Chapter 3 and verified for airfoil design processes in Chapter 6. The fundamental contribution of the proposed work is attributed to the design, development, validation and integration of the surrogate model to the AM-PSO for optimisation simulations. The defined methodology will significantly contribute to the present body-of-knowledge in the related field of study.

7.2 Introduction

Surrogate models are developed to model the objective function for fitness evaluations in design optimisation simulations. Mathematically the methodology is defined as follows (notation adopted from Gorissen et al. [171]): Surrogate modelling is used in the design process to approximate a multivariate function $f\colon \Omega \mapsto \mathbb{C}^n$, in a user-defined domain $\Omega \subset \mathbb{R}^d$, where the corresponding function values $f(x) = [f(x_1), \cdots, f(x_k)] \in \mathbb{C}^n$ are pre-computed measure of fitness of pairwise unique sample points $X = \{x_1, \cdots, x_k\} \subset \Omega$. The development of a metamodel requires the definition of a function s, from approximation space $\mathcal{S}$ such that $s: \mathbb{R}^d \mapsto \mathbb{C}^n \in \mathcal{S}$, where s is closely related to f and the measure of similarity is assessed by the approximation error $\|f - s\|_v$, according to a user-defined norm $\|.\|_v$. The metamodel must be developed to yield acceptable approximation $s^* \in \mathcal{S}$, such that

s^* is in accordance to $\min_{s \in \mathcal{S}} \|f - s\|_v = \|f - s^*\|_v$. It is assumed that the input data is deterministic and noise free, hence facilitating an accurate metamodel where the approximation error between f and s is minimised.

Metamodels have been extensively applied in the literature across various fields of study to evaluate complex and time-intensive reference models [171]. Chaveesuk and Smith [172] applied a Neural Network to model the Economic validation of capital projects. Smith et al. [173] applied an approximate model to estimate the prediction of fibrinogen adsorption onto polymer surfaces. The methodology was further applied in electromagnetic design simulations by De Geest et al. [174] and in Medicine for the estimation of the colon coloration by Hidovic and Rowe [175]. In aerospace applications, surrogate models have been used for high-lift airfoil design [176], including profile definition at HALE [82] and transonic flight envelopes [177]. The approach has further been used for multi-objective airfoil design [178], aircraft engine nacelle shape optimisation [179] and airfoil design operating in uncertain flight conditions for robust design processes by Wang and Yu [180].

7.2.1 Implementation of a Surrogate Model in the DNO Structure

The use of a surrogate model into the DNO architecture facilitates a reduction in time-intensive fitness function calls during an optimisation process. The search algorithm has the flexibility to use an efficient surrogate to model the scope of the objective function in-lieu of using a time-intensive fitness evaluator. The role of a metamodel for airfoil design in the DNO structure is defined in Figure 7.1.

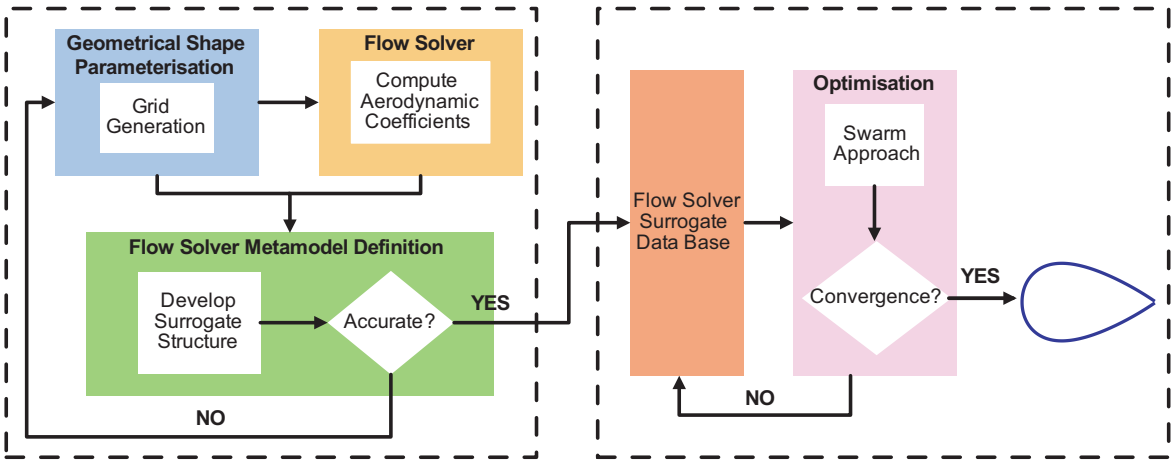

FIGURE 7.1: Definition of Flow Solver Metamodel in the DNO Structure

In a surrogate-assisted design optimisation structure from Figure 7.1, a computational mesh about an airfoil, parameterised by a user-defined shape function is generated. The airfoil is analysed by the flow solver to establish the aerodynamic coefficients. A surrogate model is developed to map the relationship between airfoil geometry as inputs and aerodynamic coefficients as outputs. The development of an accurate surrogate model follows an iterative process from airfoil parameterisation to computational mesh development for flow analysis by a high-fidelity solver. The procedure is repeated until the accuracy of the surrogate model to approximate the aerodynamics for select input airfoils is within a minimum, user-defined threshold.

Once the accuracy of the metamodel is validated, it is integrated into the optimisation structure for airfoil design analysis in Figure 7.1. The dependency on the theoretical flow solver by the optimisation algorithm for fitness measure is relaxed during the design process. Depending on the adopted surrogate-based approach including offline or online strategy (described in Sec. 7.3), the degree-of-dependency on the theoretical flow solver will vary. The optimisation algorithm will operate in iteration with the metamodel for fitness evaluations until convergence is achieved. A DNO structure with a fitness approximation model will result in computational time benefits relative to a design module with a theoretical fitness evaluator only.

7.3 Surrogate Model Type Review of Application

Surrogate models are classified as: **a)** Black-box; or **b)** Physics-based methods. In the black-box approach, a metamodel is established by mapping the relationship between the input and output response variables from the fitness function. The approximation model is developed by solving a subset of input data points from the flow solver and using the defined dataset for metamodel definition. The points sample size for surrogate model development is based on the measure of accuracy of the approximation model relative to theory for respective training points. A black-box surrogate system is developed by the extraction of data directly from the time-intensive fitness function.

In physics-based methods, the underlying principles that govern the scope of the fitness function is modified. The flow solver code is modified to limit the computational time expense for aerodynamic applications. The governing equations are modified with the aim of enhancing the computational time to convergence. The method has issues and challenges. Manipulation of the flow solver code will affect the accuracy of the computational model. The high-fidelity code incorporates fundamental flow theory principles including transport equations to model airfoil performances at HALE and transonic Mach numbers. The simplification of the underlying theory governing the applied turbulence model is a challenge and is not in the scope of this thesis. Hence, black-box surrogate methods are considered instead.

Disparate surrogate model types exist and include: **a)** Polynomial Regression [21, 181]; **b)** Kriging [141]; **c)** Radial Basis Functions (RBF) [182]; **d)** Multiple Adaptive Regression Splines [183]; and **e)** Artificial Neural Network (ANN) [150, 176, 184]. There is no one surrogate model that is valid for all problem types. Gorissen et al. [171] reasons the application of a specific model can be attributed to practical reasons including designer degree-of-expertise, to limitations in computational resources and the overall research tradition within the institution, hence bias on a specific model type. In absence of a supporting theory that can be exploited as *a-priori* knowledge for surrogate model selection, the *No-Free-Lunch* [185] theorem exists. The scope of the problem definition is examined to justify the surrogate selection decision making process.

Box and Draper [186] validated the limitations of low-order regression models for convergence to a feasible optimal when integrated to an optimisation algorithm for complex multi-modal design problems. The sensitivity of airfoil geometry on aerodynamics results in a multi-modal solution topology and the application of a polynomial regression model was not justified.

The Kriging model [141] has been validated to address this issue. The methodology has been applied extensively in literature for airfoil/wing design applications including engine nacelle design [179]. Theoretically the methodology facilitates convergence to an acceptable point in the solution search space for complex multi-modal topologies [187]. Srivastava et al. [188] assessed the effectiveness of the Kriging approach in comparison to the response surface modelling method for High Speed Civil Transport aircraft design. The training sample size required to achieve a valid approximation of the output by the Kriging method was fewer than the response surface model. The Kriging structure followed a computationally time-intensive process for structure definition in comparison to the response surface method, as a function of problem design variable size. The Kriging approach becomes computationally intensive for extended problem dimension search spaces. It was concluded that the choice of surrogate model type required for a specific problem must be based on designer preference with due consideration to the computational time required for surrogate-structure definition, with balance on model level-of-accuracy in accordance to the degree of non-linearity of the system [188].

Joseph et al. [189] acknowledged the importance of assessing the impact of problem scope on the errors by the Kriging method. It was acknowledged that only the variables that have a significant impact on the objective function, hence response of the surrogate model to decision input variables need to be used for surrogate model development. The reported findings conform to the merits of the developed design variable pre-screening analysis from Section 4.2.2.2, where elimination of un-important design variables resulted in efficient design simulations for HALE and Transonic airfoil design applications (Chapter 6). The findings by Joseph et al. [189] confirmed the theoretical benefits of variable mapping-of-importance for surrogate-model development.

Takenaka et al. [190] applied the Kriging approach for the multidisciplinary design of a winglet. The aerodynamic and structural disciplines were integrated in the design process. A Kriging model was developed with variations in winglet shape variables to estimate model aerodynamics, block fuel and the MTOW over 32 sample points distributed by a Latin hypercube sampling sequence. The approximated model was integrated into a multi-objective genetic algorithm to obtain a Pareto front by the minimisation of the block fuel and the maximisation of the takeoff weight. The preliminary results validated the effectiveness of developing surrogate models for multidisciplinary design processes. The established Pareto front provided an overview of the relationship between the conflicting design objectives. The validity of the Kriging approach was verified by the direct comparison of the aerodynamic characteristics between the approximated and Euler results for two sample winglet configurations. The difference between the two models was one drag count and 0.1% for the wing-root bending moment. The negligible differences between computational and approximated solver method are negligible and the application of the Kriging approach was validated [190].

Jeong et al. [177] applied the Kriging approach to develop a relationship between the input design variables and the output objective function of aerodynamic efficiency L/D for multi-element airfoil design simulations. A GA model was applied in the design optimisation process. The approximation model was generated on the performance of 25 sample points that were solved from the high-fidelity solver code. The GA utilised the Kriging model for fitness function estimation and resulted in a computationally efficient design process. The benefits of the approximated data point from Kriging was based on an expected improvement (EI) criterion factor. The measure assessed the probability of the respective input point being an optimum to the design problem. The integrated GA method

used the EI factor instead of L/D to guide the search process to a true solution region in the search topology. The maximisation of EI was applied to improve the robustness of the search process toward the global optimum point. The viability of the applied approach was validated with an increase in L/D in comparison to a baseline NLR 7301 airfoil. The application of the Kriging approach as a surrogate to the high-fidelity flow solver, significantly reduced the computational time for objective function evaluations without affecting the feasibility of the solution [177].

Kanazaki et al. [191] also applied the Kriging approach for high-lift airfoil design based on a multi-objective problem definition. The design goals required the simultaneous maximisation of the lift coefficient at landing and at near-stall conditions. The GA was applied in the design optimisation process. The surrogate model was developed with 90 sample points obtained by the direct computation of the RANS equations. The use of the Kriging method with GA facilitated a computationally efficient optimisation process due to the fitness function evaluations by the proposed surrogate model. The multi-objective design goals were related to the Kriging EI factor and the GA exploited the search volume to maximise the EI performance metric. The results verified the setup of the design module. The converged airfoil element settings corresponded to an increase in lift performance in comparison to the identified benchmark by a computationally efficient design process [191].

The application of the Kriging approach was further applied in the analysis be Keane [178]. Multi-objective design optimisation simulations were performed. A statistical-based Kriging response method was developed and resulted in acceptable solution feasibility and computational time efficiency within a GA optimisation module. Performance improvement factors were introduced in the design process for Pareto front diversity from which an acceptable solution was identified [178].

The Kriging methodology was also applied in the design optimisation of low-speed, HALE airfoils. Wang and Yu [180] applied the surrogate-assisted model to approximate the role CFD for airfoil design operating under uncertain conditions. The optimisation process was defined to incorporate the sensitivity of flight performance by variances in operating c_l, Mach and Reynolds number and the impact of manufacturing errors. The surrogate model was applied in the design process to address the computational expense of modelling shape uncertainty due to the excessive number of function evaluations by the high-fidelity flow solver in the robust design optimisation approach. The GA incorporated with the Kriging-based method was applied in the design process. The results validated the merits of the proposed method. The surrogate-based model generated a feasible and computationally efficient structure for airfoil design optimisation simulations under uncertainties. The analysis was limited as it did not factor the errors of the surrogate model approximations to the CFD solver on the design process. The accuracy of the predicted airfoil performance by the surrogate model due to flight uncertainty was limited [180].

A multi-objective multidisciplinary optimisation of a UAV wing for long-endurance performance was presented by Long et al. [192]. The Kriging approach was used in the design process to reduce the computational costs of the high-fidelity flow solvers, including CFD and Finite Element Methods for aerodynamic and structural analysis respectively. A valid Kriging structure was developed with 75 sample points distributed with stratified-based LHS methodology in the defined search space. Sample points were used to verify the accuracy of the prediction by the Kriging approach and the miss-match between solver and approximated model was limited. The GA was applied for design optimisation and the Kriging used to approximate the aerodynamic and structural performance parameters of

a candidate profile. The results corresponded to aerodynamic performance improvement of 20% in comparison to the baseline wing and a concurrent reduction in structural weight by 43% due to the multidisciplinary design definition. Computational efficiency was achieved by the application of a surrogate-based model for fitness evaluations [192].

Giunta and Watson [193] assessed the accuracy and modelling capabilities of the quadratic-based, Polynomial Response Surface (PRS) method and the Kriging approach on benchmark test functions. The results identified the quadratic polynomial model with acceptable solution feasibility in terms of a reduction in modelling error relative to the Kriging approach. Even for problems that were non-quadratic, the PRS methodology represented a feasible solution in comparison to the Kriging approach. Despite the results established, it was concluded that the data modeled is not representative of an exhaustive design comparison process between the two methods [193] and further design evaluations are needed.

Glaz et al. [21] examined the effectiveness of the Kriging, the radial basis function interpolation method and the polynomial regression process to model helicopter rotor blade vibration. The design analysis validated the merits of the Kriging and the RBF approach to represent the complex, multimodal search topology in the design optimisation of rotor blades with reduced vibration. The analysis identified the demerit of the Kriging approach which was attributed to high approximation errors at specific design points. The average error of a 2^{nd} order polynomial model was the highest of the three models tested and confirmed the limitations of the model for aerodynamic shape design applications. Due to the high rotor blade vibration approximation errors, the Kriging and the RBF approach cannot be used for valid predictions of rotor blade vibrations for an extended design search space [21]. Novel error magnitude control and minimisation techniques are needed to address this requirement.

The Artificial Neural Network approach has also been applied in aerospace applications [194, 195] including aerodynamics [194, 196, 197] for inverse [150] and direct [198] airfoil design simulations. Duvigneau and Visonneau [198] validated the merits of a ANN for airfoil design by the direct approach. A GA was integrated into the design process in parallel with a surrogate model to approximate airfoil aerodynamics. Significant computational time savings were achieved in comparison to a design structure with a GA process coupled to a high-fidelity flow solver. The objective of maximising lift with minimal cruise drag performance was achieved [198].

Prediction of aerodynamic coefficients with ANN by the interaction of airfoil geometry variables as inputs and force coefficients as outputs have been investigated [197, 199–202]. Santos et al. [199] reported a training database of 10,000 airfoils with a multi-layered network consisting of 50 neurons with the two hidden layers is needed for acceptable lift and drag simulations. Ross et al. [197] developed a neural network to model flap deflection parameters as inputs and the aerodynamic coefficients of lift, drag, moment and lift-to-drag as outputs for multi-element airfoils. Wind-tunnel data consisted of 20 flap configurations for network training. Validation results indicated only 50% of available wind-tunnel data was required for training to achieve acceptable network generalisation performance over sample test cases.

Mengistu and Ghaly [203] applied an ANN for the aerodynamic design of turbomachinery blades. The design process was coupled with a GA for single-point aerodynamic optimisation analysis at transonic flow conditions. An ANN was developed by the direct computation of 50 blade profiles

from CFD and applied as the training set for model development (35 cases) and validation (15 cases). The validity of the structure represented errors that were less than 2% for approximately 45% of the test cases. The application of an ANN in the design loop reduced the computational time to design convergence by a factor of 10 in comparison to the use of a stand-alone high-fidelity solver. The optimal blade profile was modeled with enhanced performance efficiency improvements and the feasibility of the applied approach was confirmed. The results validated the merits of integrating an ANN to a population-based optimisation algorithm for aerodynamic applications [203].

Su et al. [204] performed missile aerodynamic shape optimisation simulations using an ANN coupled to a GA and a linearised potential code to establish planform aerodynamics. The shape parameterisation variables were applied as inputs to the neural network and the aerodynamic performance as outputs. The objective function was defined to maximise missile aerodynamic efficiency at high-subsonic Mach numbers with constraints on aerodynamic lift and geometry profile. The design approach resulted in an increase in computational efficiency while maintaining solution feasibility. The presented analysis did not factor the affect of fitness function approximation errors by the ANN on the GA optimisation process. It was confirmed the surrogate-model may mislead the search process [204]. A novel error handling methodology is required to address this requirement (presented in Sec. 7.3.5).

The integration of the neural network with the GA was also applied by Papila et al. [205] for the design optimisation of supersonic turbine blades. The surrogate model development process was enhanced through a design variable pre-screening analysis which limited the scope of the analysis by mapping the problem dimensionality size. As a result, fewer data points were needed to train the ANN and the number of direct CFD calls required in the process were minimised [205]. The importance of the design variable pre-screening analysis to aid an efficient optimisation model was confirmed. The results were in agreement to the findings from Chapter 6, where variable elimination resulted in efficient optimisation simulations in the direct airfoil optimisation approach.

Hacioglu [150] applied a hybrid approach characterised by the integration of a neural network to a GA for inverse airfoil design. The applied methodology was unique such that the neural network was used in parallel with the GA to guide the search process toward an optimal. The population of data points generated by the GA were sequentially used to train the ANN. The results validated the merits of the proposed design approach. Accelerated computational convergence was achieved by the hybrid design process while maintaining solution feasibility. The computational time issues associated with GA-based methods integrated to a high-fidelity fitness function evaluator were addressed [150].

The flexibility of the ANN approach was further verified in the analysis by Vadivelan et al. [206]. The surrogate-based model was applied for inverse airfoil design at transonic flight conditions. Instead of applying the c_p distribution as a surrogate input based on the approach by Hacioglu [150], the aerodynamic coefficients c_l and c_d were used instead. The corresponding model output were the x/c and y/c airfoil coordinates. The training dataset was representative of the NACA 4 digit series airfoils and 78 case data sets were used for network development. The neural network was trained until the accuracy was within an acceptable threshold. The model was then used in the re-design of the NACA 6312 airfoil with the objective of minimising drag, while maintaining a minimum target lift coefficient. Computational efficiency during the shape design process was achieved by the decoupling the CFD solver from the design process. The GA used the trained surrogate to estimate the airfoil contour

for optimisation based on c_l and c_d parameters as inputs. The optimal airfoil was modeled with a 50% reduction in drag while maintaining the lift coefficient of the base NACA 6312 airfoil. Direct analysis of the surrogate optimal aerodynamics with CFD represented differences between the two solvers. The c_l and c_d magnitudes varied by $\approx 2\%$ and $\approx 7\%$ respectively. The issue of approximation errors by the surrogate-based approach will affect the optimisation process and the feasibility of the optimal. A novel design approach is needed and developed accordingly (Sec. 7.3.5) to offset the affect of approximation errors on the design optimisation process.

The review of surrogate model types has verified the application of the Kriging and ANN for airfoil design simulations in the literature. The survey of related works identified the application of the GA as the preferred optimisation method in surrogate-based design structures. There are no set principles that govern the use of either model over the other. The selection of an approximation model type for intended numerical optimisation simulation is based on the findings from the literature.

The review verified the Kriging approach requires fewer training data points for structure development in comparison to the ANN. The drawback was related to structure development which was time consuming for large scale test problems due to the use of multiple matrices operations [207]. The computational costs for large dimensional search space topologies will outweigh the theoretical benefits of the system. The training data point selection process must be intelligently defined. If the points are within a minimum threshold to each other, then the correlation matrix which is the weighted distance between two select training sample points will become singular [207] and result in an ill-defined training process.

The ANN methodology requires a larger training sample size for network development in comparison to the Kriging approach. The computational effort needed to define an accurate surrogate model will be excessive and limit the efficiency of the optimisation structure. The network topology definition process also requires several, user-defined model-dependent parameters and greater computing resources are demanded in comparison to the Kriging method. There are no theoretical principles that define an optimum network structure for specific design problems. Instead a comprehensive DoE analysis is needed to estimate model parameters for intent design problem. The definition of user-defined structure parameters can induce approximation errors if arbitrarily selected and an extensive DoE analysis is needed to address this issue.

7.3.1 Development and Integration Strategies of the Surrogate Model into the DNO Structure

The development and integration principles of a surrogate model into the DNO structure are defined. Regardless of the approximation model used for optimisation simulations, the defined process remains valid. The following points characterise the fundamentals of the development and application stages:

1. **Development Stage**

   (a) The computational effort required to develop a surrogate model is a direct function of the training data sample size. As each sample point is solved by the expensive flow solver, the population of input-output data points must be limited to achieve a balance between

computational efficiency and metamodel accuracy. The development stage facilitates the designer to shift the balance between the two parameters based on user-preference.

(b) The numerical noise in the solution topology due to the non-convergence of the solver flow residuals, hence aerodynamic parameters for ill-defined airfoils complicates the design optimisation process. The metamodel development stage allows the designer to remove false training data points to permit a numerical design process in-lieu of ill-defined data points.

(c) The elimination of ill-defined airfoil geometries as training data points for surrogate development facilitates a valid mapping of the relationship between the input-output parameters. The optimisation algorithm can exploit the surrogate database to aid convergence to the true optimal.

(d) The application of a surrogate model for implementation into the AM-PSO algorithm requires minor code modifications to distinguish fitness function evaluations between the surrogate model and theoretical flow solver for respective search particles.

(e) The AM-PSO coupled to a surrogate-model maintains computational parallelism by distributed computing, hence accelerated and time-efficient simulations are established.

(f) The surrogate model is adaptable to design optimisation in a multidisciplinary field. Design discipline-specific metamodels can be developed and integrated into the optimisation algorithm to define a multidisciplinary design process

2. **Integration Strategies into the DNO Structure**

(a) Offline-based; and

(b) Online-based

In the offline approach, the surrogate model is trained based on a user-defined data population size. A DoE analysis is defined for structure development and validation. The approximation error of the data points that are not directly used for structure training, hence an independent *generalisation* set is used as inputs to the surrogate model to verify structure accuracy. The error between approximated and theoretical fitness magnitude is established to verify the accuracy of the proposed surrogate structure type. The defined DoE process follows an iterative process until the error thresholds of the generalisation dataset is less than a minimum user-defined threshold.

The training dataset is generated by a sampling strategy of the input variables over the defined design space. The corresponding fitness of the sample input training dataset is established from the theoretical function (flow solver for airfoil design processes). Once the surrogate-model is trained with acceptable accuracy, it is used by the optimisation algorithm to evaluate the fitness of the subsequent design evolutions. The theoretical and time consuming fitness function method is decoupled and the optimisation algorithm uses only the surrogate model to estimate solution fitness until convergence is achieved.

There are issues and challenges in the offline surrogate development method. The training dataset may not model the scope of the solution topology with acceptable degree-of-freedom. If the training points are isolated to a restricted solution region in the dimensional search space, then the developed

surrogate model will be representative of data points about a local search region. The integration of the fitness approximation model to the optimisation algorithm will result in a limited search performance for input data points that exceed the scope of the training dataset. The accuracy of the surrogate-model will be affected and the search performance, hence feasibility of the solution will be limited. The definition of an acceptable data sampling strategy is needed to address this issue (Sec. 7.3.3).

In the online approach, the data modeled by the evolutionary optimisation algorithm at each search generation is used for surrogate training and validation. The training data is iteratively introduced to the surrogate model for training. The methodology addresses the issue associated with the offline approach. The training dataset is not restricted to a specific region in the solution topology, but is identified and selected by the search principles of the AM-PSO. Theoretically the online approach will facilitate an accurate surrogate model due to the allocation of training data points that are reflective of the search patterns of the optimiser. The methodology continuously updates the training dataset during the design process. An archive of training data points is established and updated at each iteration to represent the current state of the optimiser. The concurrent development of the surrogate model ensures the fitness approximation model is trained at promising solution regions only.

Unlike the offline-based approach, the online methodology does not require the definition of user-defined sample points for training. Theoretically the online-based method permits an intelligent allocation of training points, instead of arbitrarily defining the scope of the input-outputs with stratified sampling techniques. The online-based approach permits an efficient structure development process as the computing resources are utilised specifically to model the relationship between solution valid data points and not on samples that are randomly selected.

The performance of the online and offline design strategies have been verified for design optimisation simulations in the literature. Husken et al. [208] applied a neural network for fitness function evaluations for structural design optimisation. The feasibility of the surrogate output was estimated by defined quality measuring units. The results validated the merits of the offline approach in comparison to the online method. The limitations of the online method were attributed to an ill-defined neural network structure. The proposed surrogate model was characterised by reduced adaptation handling mechanisms that did not factor the integration of additional design points as inputs from the optimisation algorithm in the online training phase with acceptable accuracy [208].

Giannakoglou et al. [209] further evaluated the principles of the surrogate modelling approach for optimisation problems characterised by computationally time-intensive fitness function evaluators. A novel Inexact Pre-Evaluation (IPE) phase coupled to an EA (EA-IPE) was proposed. The methodology screened the population members in the EA module and restricted the number of exact evaluations per generation to potentially acceptable search members only. The remaining data points were estimated by the approximation model. Data computation phase mechanisms were proposed to distinguish fitness analysis of the respective population members between exact and approximation-based methods. Design optimisation simulations validated the efficiency of the online-based EA-IPE design approach. Drag reduction of 34% and a 75% reduction in computational wall-clock time was noted by EA-IPE in comparison to a stand-alone EA method for transonic shape design. It was shown that the online-based surrogate model has the merits of achieving a feasible solution with enhanced computational efficiency.

Shahrokhi and Jahangirian [210] acknowledged the processes developed by Giannakoglou et al. [209] required the definition of several user-defined parameters to achieve an accurate surrogate-model structure. There were no set guidelines that govern the definition of the identified model parameters. The total number of GA generations required to train the ANN and the partitioning of the evolution search members between exact and approximation based methods were not clarified based on the assessment of the related works of Giannakoglou et al. [209] by Shahrokhi and Jahangirian [210].

A surrogate-assisted design optimisation process was developed by Shahrokhi and Jahangirian [210]. The performance of the proposed design approach was directly evaluated with the findings by Giannakoglou et al. [209] for transonic airfoil design with an ANN as the surrogate model. The reliability of the surrogate approximations for a respective data points were improved by establishing the location of the select data point relative to the defined design space used for ANN training. The design variables in the training set were assumed to be normally distributed. The design variable range between $\mu - \sigma$ and $\mu + \sigma$ was populated with training data points relative to regions exceeding this threshold within the design space. Theoretically data points in the identified region about the mean would exhibit acceptable surrogate-based accuracy in comparison to data points outside of the defined search space window. During the design optimisation process, if 70% of the design variables of a specific search agent were within the acceptable $\mu \pm \sigma$ window, then the surrogate model was used for fitness estimation, otherwise the exact CFD solver was applied instead [210].

The results by the developed methodology in [210] verified the effectiveness of the proposed design optimisation structure in comparison to the approach by Giannakoglou et al. [209] for transonic airfoil design. The computational time to convergence by the two methods was comparable with a reduction of $\approx 40\%$ in comparison to a simulation with a stand-alone GA method with a high-fidelity flow solver as the fitness function evaluator only. The normal distribution method of the design variables to establish the source for fitness function evaluations resulted in a low root-mean-square error of surrogate-based approximations in comparison to the IPE approach by Giannakoglou et al. [209].

Despite the validated merits of the design approach by Shahrokhi and Jahangirian [210], the defined assumptions for model structure development requires verification. The assumption that the search variables are normally distributed about a specific mean value requires clarification. The user-defined parameters applied to induce fitness function evaluation by the theoretical flow solver or by the surrogate-based approximation model requires design validation. The affect of varying the magnitude of 70% of design variables to be within $\mu \pm \sigma$ on optimisation efficiency and feasibility was not defined.

In the analysis by Duvigneau and Visonneau [198] an online-based optimisation simulation with the integration of a GA and an ANN structure for airfoil design was defined. The fitness of a set number of search individuals in the GA from the search population size were evaluated by the neural network which was developed during the initial stages of the design optimisation process and the remaining data points by the flow solver. Exact fitness evaluation data points were added to an archive of training database. The data library was characterised by viable search points that are concentrated about promising regions in the solution topology. The accuracy of the ANN-based approximations increased and a solution valid search process ensued. The search principles of the GA exploited the accuracy of the approximation model to facilitate convergence to a true optima [198].

A DoE analysis was defined to determine the search population size and the minimum number of individuals from the population set that can be used for analysis by the approximation model [198]. The DoE analysis verified a population size of 20 individuals are needed from which ten can be applied for analysis by the ANN. The percentage partitioning of the search population for fitness evaluation between exact and approximation-based methods was also confirmed by Husken et al. [208]. In the analysis 50% of the individuals were evaluated directly by the theoretical function and the remaining rest by the approximation model over the defined evolution stages.

The results by Duvigneau and Visonneau [198] for the proposed online-based optimisation strategy approach was validated. The computational time to convergence was reduced significantly in comparison to a stand-alone GA and flow solver approach. Convergence to a global optimal was attained, hence the viability of the online-based design strategy with an ANN for airfoil design simulations was verified.

Willmes and Jin et al. [211] compared the performances of the Kriging and the neural network surrogate methods for fitness evaluations, hence optimisation of mathematical test functions. The optimisation strategies applied in the verification analysis included the offline and online-based methods. In the online-based approach, ten search individuals from a search population of twenty were used for fitness approximations by the respective surrogate model. The affect of applying the offline (global method) and online (local method) based strategies on surrogate approximation was identified. The results verified the demerits of the offline approach for data approximation of points that are not within an acceptable distance threshold of a closest training point. The online approach indicated acceptable predictions in comparison as the metamodel was generated about solution valid data points only.

It was concluded that the surrogate-based training strategy needed is problem dependent. Test validations on benchmark functions confirmed the viability of the online approach in comparison to the offline method with accurate fitness function predictions. Performance comparisons between the Kriging and the neural network methods did not demonstrate the merits of a specific model over the other for fitness approximations. Hence, no conclusions could be drawn on the viability of a specific metamodel within an evolutionary optimisation structure [211]. The selection of a specific training strategy and surrogate-model type for design optimisation simulations must be examined accordingly for specific problem types.

The review has demonstrated that the definition of an accurate surrogate model is a design challenge based on model accuracy. A balance between the number of flow solver calls required to develop an accurate approximation model and computational efficiency is to be defined. The principle that the computational effort for surrogate architecture development will require excessive number of flow solver simulations, hence the practice will offset the theoretical time merits of the intent metamodel is addressed for the offline and online training strategies from the view point of design:

1. **Offline Strategy - Flexibility:**
   Development of a surrogate model is a one-time investment. The model can be re-used at any design stage where a new measure of fitness is needed due to the re-definition of the problem goal and constraint parameters. An analogy is an airfoil design simulation with a constraint on minimum thickness distribution. The progression of the shape from the conceptual to the detail

design phase may result in a change to the constraint definition that is different from the original design effort. The metamodel developed in the conceptual design stage can be re-applied to establish a new measure of fitness with negligible computational effort due to the re-defined constraint requirement. The surrogate-model design flexibility permits the re-definition of the problem goals and constraints during the design sequence, while maintaining the computational time benefits associated with efficient objective function evaluations. The flexibility will hold true as long as the scope of the problem definition, a function of input variable search intervals that were applied to define the surrogate model are not modified during the re-definition process.

2. **Online Strategy - Solution Search Space Adaptive Model:**
   As outlined, the online based surrogate model is developed in parallel to the EA optimisation simulation process. The input data for metamodel training/development is selected from the mapped solution search space as governed by the select EA method during the iterative design cycle. Data points that are regarded as infeasible to the design objective are identified by user-specified measures and are not used for metamodel development. Instead only solution viable data points are identified and are used for model development. Theoretically the global optimisation algorithm will converge to promising solution regions during the optimisation cycle. The metamodel is established based on the search principles of the EA, hence is adaptive to the defined optimisation process. The computational effort associated with high-fidelity simulations for metamodel definition is justified as only promising sample points are used for model development. The computational resources are intelligently allocated as the number of high-fidelity flow solver calls needed to define the surrogate model are minimised.

7.3.2 Review of Selected Surrogate Model Type for Airfoil Design

The literature review validated the viability of the surrogate-based approach for fitness function evaluations within the DNO structure. Extensive research has also been undertaken for the estimation of airfoil aerodynamic coefficients using neural networks [150, 176, 194, 196, 197, 199–206]. The configuration of the approximation model needed to output an accurate estimation of the aerodynamic coefficients as a relationship to airfoil geometry has been presented in the review of related works [176, 199, 212]. The aerodynamic coefficients from a computational flow solver and wind-tunnel tests have been successfully used as inputs for the design development of an accurate neural network [197, 200, 202]. The affect of varying the user-defined parameters within the surrogate-model on approximation accuracy was examined. Accordingly thumb-of-rule guidelines have been defined to clarify the structure configuration required to map the relationship between airfoil geometry and aerodynamics.

A surrogate model will enhance the computational efficiency of the airfoil design process by simulating the fitness function with negligible computational time. An approximation methodology is needed to estimate the relationship between airfoil shape variables as inputs and the aerodynamic coefficients as outputs. The design application of a GA coupled to an ANN has shown merits for airfoil design processes [209, 210]. The extensive knowledge gained from the review of related works provides an avenue for the design development of a neural network structure for the intended field of study. The novel AM-PSO algorithm is integrated to a surrogate model by the online-training

strategy. Theoretically the design model will further exploit the validated efficiency of the swarm method for aerodynamic shape design simulations in comparison to a design process governed by a GA from the literature.

The fundamentals of the offline and online-based surrogate training strategies are demonstrated on optimisation test problems. Despite the identified limitations of the offline approach in the literature, the methodology is examined to verify the sensitivity of the user-defined parameters within the surrogate model on output accuracy. The knowledge gained from the analysis will be applied to develop an online-training model. The surrogate model development sequence transition from offline to online-based strategy was also undertaken by Husken et al. [208] for the purposes of using the information from the offline analysis to aid in the development of an accurate online model. The following sub-sections address the identified requirements.

7.3.3 Offline-training Global Based Artificial Neural Network

The fundamental steps undertaken for the design development of a neural network structure include:

1. Data generation;
2. Model-structure definition; and
3. Model validation

Data Generation

The data for neural network development needs to be gathered. The source can be from computational and/or experimental processes. Ideally to establish the true scope of the design problem by the surrogate model, training data from experimental setups needs to be used. The errors within the experimental process will limit the performance of the surrogate approximations, thus accurate computational tools are also needed to generate data points for surrogate model definition.

In the presented analysis the data is obtained from deterministic computational algorithms, hence it is noise free. The data is used for network development by training. The training sample size must also be well-defined to attain an accurate representation of the objective function from the proposed surrogate model. If the training population size is minimal then the approximation network will not model the relationship between the defined input-output parameters with acceptable accuracy. If it is excessive, the model will be overfitted as it will memorise the relationship between the parameters instead of generalising a regression function between the datasets.

The definition of training population size and the relative positioning of the points in the design space, which are used as inputs for model training need to be defined. The sample points for network training are representative of the problem scope. The topology of the fitness landscape (unimodal or multi-modal) for the intent design problem is not *a-priori* knowledge. Stratified sampling strategies coupled with an acceptable training population size is needed to map the scope of the solution topology for the user-defined search space envelope. The defined parameters will facilitate a search process to a global solution region by the AM-PSO as the scope of the solution function is well represented by the intent surrogate model.

The data selection and distribution methodologies are classified by two methods: **a)** Global sampling in the offline strategy; and **b)** Local sampling in the online, evolutionary assisted design process. In the offline training approach, a stratified sampling algorithm is used to select the training data points from the solution topology. A DoE is undertaken to evaluate the affect of varying the training population size on surrogate model accuracy. If the accuracy is acceptable, the approximation model is integrated to the optimisation algorithm for design analysis.

In the online approach, the neural network is sequentially trained as a function of the optimisation evolution design stage within the AM-PSO process. The data points are incrementally introduced to the metamodel for training based on the search processes of the swarm. The design optimisation cycle and network training simulation operate in parallel. The coupled methodology solves the intent design problem by the search principles of the swarm while concurrently training the surrogate model based on the collective search pattern of the particles. As the data points for metamodel training are used directly from the iterative search process, the surrogate model will theoretically incorporate the nonlinearities in the input-output parameters and will be inclusive of promising data points for the defined test function.

As the accuracy of the surrogate model increases during the search evolution process due to the continuous update of the training dataset in the online approach, the dependency of the search algorithm for fitness function computation shifts from the time-intensive flow solver to the developed neural network. Significant computational time savings can be achieved as the computational effort is invested at establishing the location of the optimal while concurrently applying the modeled data points for neural network training. Theoretically the surrogate model will exhibit acceptable fitness function accuracy as it has been developed on data points of interest and not at random and poor solution regions that do not reflect the scope of the defined objective function from a global minima perspective.

A sampling strategy is needed for training data generation by the offline approach. Mathematically the sampling point definition process is defined as [171]:

$$\phi\left(X_{i-1}\right) = X_i, i = 1, \cdots, L \tag{7.1}$$

A data hierarchy is constructed in the form [171]:

$$X_0 \subset X_1 \subset X_2 \subset \cdots \subset X_L \subset X \tag{7.2}$$

Where the data is represented by a nested subset of $X = \{x_1, \cdots, x_k\}$, L is the number of levels and X_0 is the initial experimental design modeled by a select algorithm from the Design and Analysis of Computer Experiments (DACE) process [133]. With the selected DACE methodology X_0, the sampling function *phi* is evaluated. At each data point the time-intensive fitness evaluator is used to establish the output to the defined input X. Hence, a constraint on ϕ is to minimise the sample population size $|X_i| - |X_{i-1}|$, while concurrently mapping the scope of the defined solution space with acceptable coverage.

The development of a global surrogate model for offline-based design simulations will result in approximation errors for sample points that are not reflective of the scope of the initial training

population. The search performance of the optimisation algorithm will be affected due to the derivation of false fitness magnitudes. As the scope of the solution landscape is not established prior to design simulations, the training data points must be evenly distributed in the search topology. As the optimisation search space is multi-modal for airfoil design processes, the integration of a global-based surrogate model will require an acceptable stratified sampling approach to map the multi-modal solution landscape.

Sampling techniques include the random distribution and the LHS approach (Sec. 3.4.1, Fig. 3.3). A demerit of the original LHS method was the clustering of data points due to the inclusion of a random operator in the data generation process. The dispersion of training data points within the solution space for offline-based strategies was limited. To address this issue, a variant of the original LHS process is modeled in MATLAB [213] which maximises the minimum distance between the points instead of applying random operators in the distribution process. A uniform space-filling dispersion of data points is generated which enhances the solution search space coverage by the select data points.

The merits of training a neural network with LHS in comparison to the random approach is validated on benchmark test functions. A neural network is developed to map the input-output relationship of the test functions that were used for AM-PSO validation in Section 3.6.1. The performance comparison between the random and LHS approach is assessed. Generalisation data points (points not used in training) are introduced for validation purposes and are evenly distributed in the search space to assess the accuracy of the surrogate model for fitness approximation. The mean-squared-error (MSE) between theoretical and neural network approximated fitness magnitude is established to assess the accuracy of the surrogate model. The neural network structure is not changed in the validation process. The error magnitudes are isolated to variances in the data distribution methods only. The viability of the random and LHS approach for the training data distribution is assessed accordingly.

The test function solution landscape including the generalisation data points for validation purposes are presented in Figure 7.2.

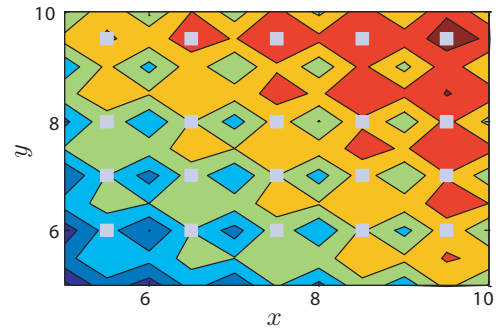

(a) Ackley Function: Representation of Generalisation Points in Solution Topology

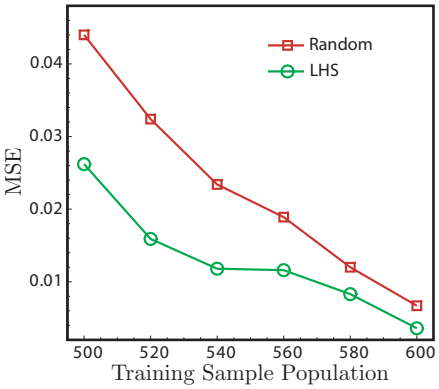

(b) Ackley Function: ANN Generalisation Error Convergence

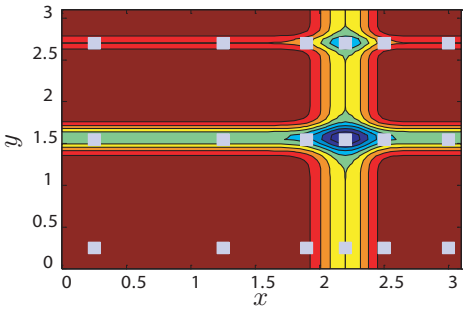

(c) Michalewics Function: Representation of Generalisation Points in Solution Topology

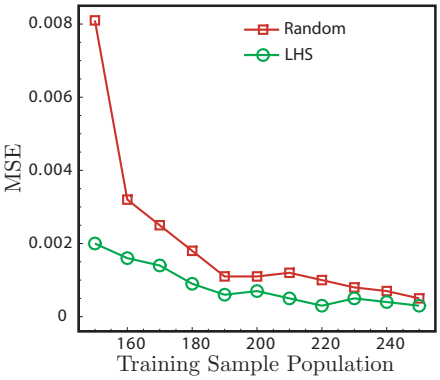

(d) Michalewics Function: ANN Generalisation Error Convergence

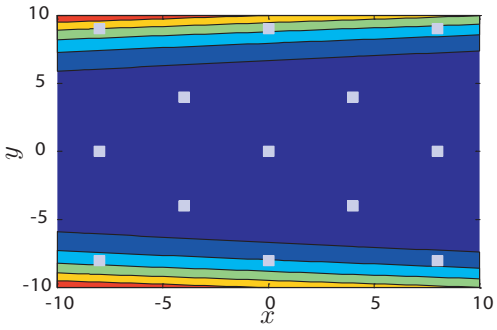

(e) Rosenbrock Function: Representation of Generalisation Points in Solution Topology

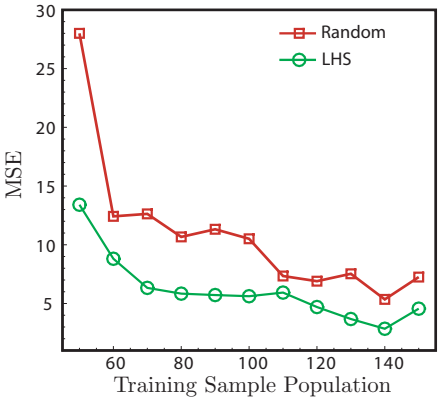

(f) Rosenbrock Function: ANN Generalisation Error Convergence

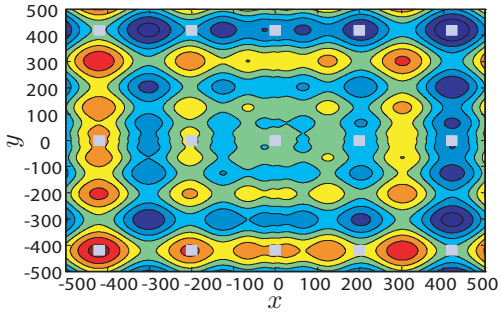

(g) Schwefel Function: Representation of Generalisation Points in Solution Topology

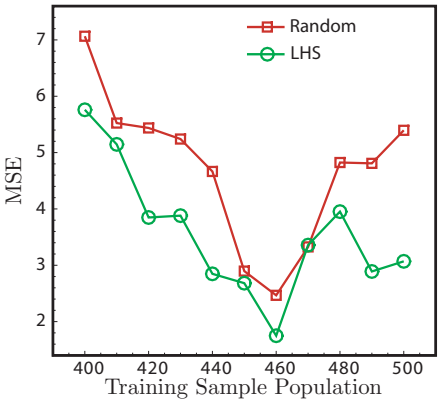

(h) Schwefel Function: ANN Generalisation Error Convergence

FIGURE 7.2: Benchmark Test Functions: Effect of Sampling Strategy on ANN Generalisation Convergence Errors

The MSE distribution validates the merits of the LHS for training data definition by neural networks in comparison to the random approach in Figure 7.2. The LHS exhibits a lower MSE for the modeled training sample size envelope than the random method. The affect of training population size on network accuracy is further confirmed. An increase in network training population size has the affect of enhancing the approximation accuracy of the model at the identified generalisation data points for the respective test function.

The affect of data overfitting on MSE due to network training is evident for the Rosenbrock (Fig. 7.2(f)) and the Schwefel (Fig. 7.2(h)) test functions. If the input training size is excessive, the neural network fails to generalise with acceptable accuracy as it memorises the input-output relationship of the presented data. The corresponding network test validation process for the defined case results in high approximation errors for the identified generalisation dataset. Data overfitting exists for training population size exceeding 140 points for the Rosenbrock test function in Figure 7.2(f) as the MSE increases beyond the defined population size threshold.

The demerit of data overfitting on MSE is evident for the Schwefel test function in Figure 7.2(h). Training data sample size convergence to an optimal low MSE for the defined neural network structure is established at 460 points. Further increases beyond the defined limit results in an increase in MSE by the two sampling methods. The deviations vary sporadically beyond the converged training size limit, hence confirming data overfitting. The results established in Figure 7.2 confirm the viability of the LHS approach for data distribution with low MSE for global-based neural network training processes. The training population size needs to be well-defined to avoid data overfitting.

Model-structure Definition

The definition of a neural network structure M is a complex process. There are no set theoretical principles that define a valid structure topology for specific problem types. A comprehensive DoE analysis is needed to define the topology of the network that yields acceptable approximations. In the development process, there are hyper-parameters that control the complexity of the model, thus the bias-variance trade-off [171]. The definition of a theoretically supported, optimal bias-variance trade-off for the modeled problem is a complex process. In-lieu of a theoretical model supporting the definition of a valid network, a comprehensive DoE analysis is a requirement. The affect of neural network structure definition parameters on approximation accuracy is modeled. The population size of the neurons, hidden layers, transfer function types and training algorithms are varied during the controlled experimental process. The impact of the defined model parameters on surrogate output accuracy by the MSE measure is assessed.

Model Validation

The validity of the developed neural network is assessed by an error measure of the approximation fitness output in comparison to theory (actual fitness target by the derivation of the equations in the objective function). Each neuron generates an output by the computation of the inner product of the input signal to the weight vector. The data is then transferred to a non-linear transfer function [176]. The network development process is defined by a training data set of size $\mathcal{Q}$ with inputs $p_{\mathcal{Q}}$ and targets $t_{\mathcal{Q}}$ as:

$$\{p_1, t_1\}, \{p_2, t_2\}, \cdots, \{p_{\mathcal{Q}}, t_{\mathcal{Q}}\} \tag{7.3}$$

The error of the neural network structure is used as a design objective for data training. Sample off-the-shelf training algorithms from MATLAB [214] are used with the objective of minimising the mse of the represented data pairs from Equation 7.3 as:

$$\begin{aligned} mse &= \frac{1}{\mathcal{Q}} \sum_{k=1}^{\mathcal{Q}} e(k)^2 \\ &= \frac{1}{\mathcal{Q}} \sum_{k=1}^{\mathcal{Q}} [t(k) - a(k)]^2 \end{aligned} \tag{7.4}$$

Where, t and a represent the target and approximated network outputs.

In parallel with the magnitude of the mse, the viability of the surrogate model is also assessed by the measure of the maximum absolute error of a specific data point from the population set. The linear regression r which relates the targets to network approximated outputs for the presented dataset (Eqn. 7.3) is also modeled to represent the goodness of the data fit. The slope of the linear curve r and the $y-$intercept are further established to assess the state-of-the data fit. The slope of the curve r will be one and the $y-$intercept will equal zero for a well-defined data fit between approximated and theoretical solutions ($t = a$ in Eqn. 7.4). The variation in data output relative to the defined target by the $r-$correlation factor will also equal one to represent a perfect correlation between the datasets.

The identified validation measuring units for problem specific neural networks will be defined in the following sub-sections. The merits of the surrogate structure for the modeled test problems is assessed accordingly.

7.3.4 Offline-training: Global Based Artificial Neural Network Development & Application for Airfoil Design

The implementation of a swarm algorithm for airfoil design in the DNO approach is computationally demanding. Each particle represents a candidate solution to the problem. Design optimisation simulations with the swarm algorithm confirmed an acceptable particle population of 20 search agents are needed for convergence to an optimal region in Chapter 6. Mutation operators are further needed to improve search diversity, hence aid convergence to a feasible solution region. The demerit is the additional demand on the computational resources as the particles require fitness evaluations by a time-intensive flow solver.

A neural network will approximate the performance of the RANS solver and address the time-intensive shape design simulations associated with population based optimisation algorithms. An ANN is developed to simulate the scope of the design space for the proposed airfoil design problem. The DNO components defined are applied in the design, development and validation of an ANN structure. The proposed architecture applies the PARSEC-Modified shape coefficients as inputs, which are processed through a structure of neurons, hidden-layers, and transfer functions to estimate the aerodynamic coefficient as an output in Figure 7.3. The network will output a single aerodynamic

coefficient as recommended in the work by Greenman [176] for model accuracy instead of a multiple-output network. Hence, for each aerodynamic coefficient a separate neural network is developed to simulate the shape performance merit.

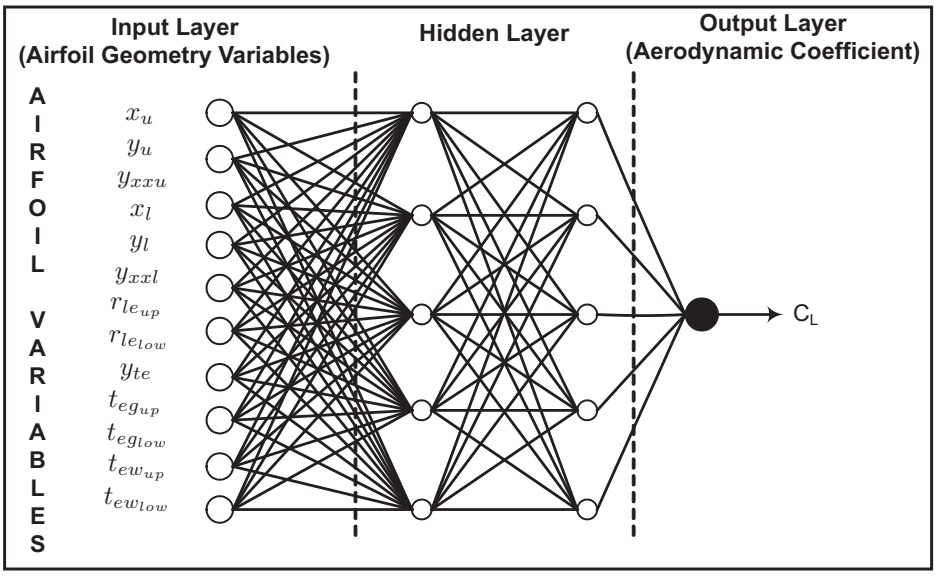

FIGURE 7.3: Offline-Based Neural Network Structure for Airfoil Design

A. Neural Network Structure Development & Validation

A DoE process is established to evaluate the ANN structure type for the proposed test problem. The simulations are performed using MATLABs Neural Networks Toolbox [214]. The following network characteristics are addressed:

- Source of training data (computational and/or experimental);
- Size of training data;
- Number of hidden layers;
- Number of neurons in the hidden layer/s;
- Transfer function type; and
- Generalisation performance of the network to new input data.

A surrogate model with acceptable approximation accuracy is needed. Ideally the training data source for network development should be from experiments. Computational aerodynamic data, although deterministic is modeled with a degree-of-uncertainty due to the errors. Experimental data for airfoils generated with shape functions will signify an accurate representation of the aerodynamic performance. The experimental setup and execution of a large training dataset for neural network development is not possible, thus computational simulations are used.

The affect of integrating a Logarithmic sigmoid transfer function in the hidden layers, including the combination of the Hyperbolic tangent and Logarithmic sigmoid functions for the respective hidden layers, on network accuracy was examined [215, 216]. Test validation simulations confirmed

a network characterised by a Hyperbolic tangent sigmoid transfer function resulted in acceptable approximation accuracy in comparison to the integration of the stand-alone Logarithmic method for airfoil aerodynamic coefficient estimation [215, 216]. The Hyperbolic tangent sigmoid transfer function in the hidden layers coupled with a linear function for model output, resulted in acceptable data agreement between approximated and theoretical solutions.

The application of a low fidelity solver for ANN design definition by a DoE analysis is acceptable due to the rapid computational turn-over time. The low fidelity solver XFOIL [78] is used for ANN design development to approximate the shape aerodynamics at a HALE flight envelope. A DoE process is defined to model the variations in neural network structure type and the impact on network generalisation performance. The high computation time of RANS-based solvers prohibits a comprehensive DoE process. The integration of a high fidelity solver for network development is acceptable when the optimality of the network topology is confirmed based on the findings to the DoE process from low fidelity solvers.

The training dataset for HALE airfoil design is defined. The LHS methodology is used to generate a population of PARSEC-Modified airfoils that are restricted to the mapped design variable solution space defined in Table 4.8. The performance of the network is enhanced by normalising the input and target data into a unit cube between ± 1. A feed-forward backpropagation network with Bayesian Regularisation [217, 218] training algorithm is used. Overfitting of data is mitigated by applying an early stopping condition. The input dataset is distributed into three subsets: 60% training, 20% validation and 20% generalisation. The training process continues as long as the error on the distributed validation vectors decreases at each training simulation. Training termination occurs when there is an increase in error on the validation dataset spanning 50 consecutive iterations. The reported solution is representative of the network structure at the training evolution when data overfitting commenced.

A computational experiment is defined to map the influence of the network structure on surrogate generalisation performance. Airfoil flow analysis is at a Reynolds Number of 4.0×10^6, Mach 0.10 and angle-of-attack of zero degrees. The size of the hidden layers was varied from one to two, neurons 10-50 in increments of ten for a training dataset of 4801, 8011 and 13,493 airfoils. With 60% of the original data distributed for training, the input training vector is reduced to 2880, 4806 and 8095 airfoils respectively from the original dataset. Generalisation is measured over 2,878 airfoils sampled by the LHS methodology. The percentage variance between network output and theoretical aerodynamic coefficient of lift and drag of each airfoil is established as a measure of the generalisation performance. The mean percentage error variance over the generalisation population set is presented for lift in Figure 7.4

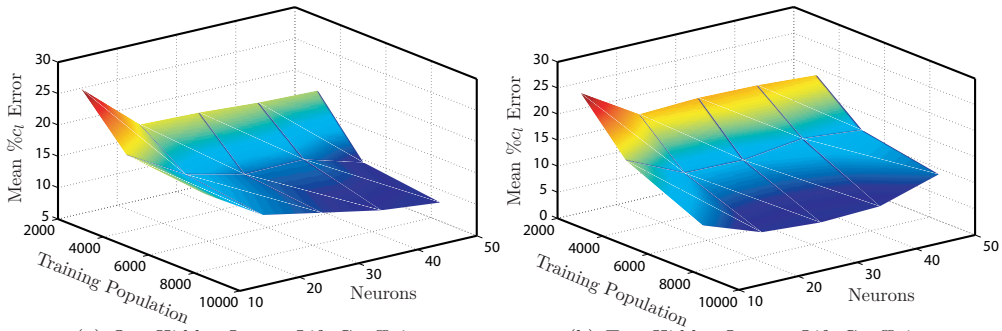

(a) One Hidden Layer: Lift Coefficient (b) Two Hidden Layers: Lift Coefficient

FIGURE 7.4: Affect of Neural Network Structure on Lift Coefficient

The mean error carpet plots with one and two hidden layers for c_l in Figures 7.4(a) and 7.4(b) represent a reduction in error variance with an increase in input training sample size. The maximum error thresholds are associated at the lower spectrum of the training population size. The largest mean error variances are in excess of 25% for the two models for a network with ten neurons. At fewer neurons, the structure is not sufficiently complex to model the c_l at new generalisation input data points. Overfitting of data in a single-layered network in Figure 7.4(a) is not evident despite an increase in neurons. There is a performance stagnation which confirms the convergence of network accuracy to a minimum error threshold.

The double hidden-layered network structure in Figure 7.4(b) represents an overfitted data performance. The point of solution instability is related to the size of the training data. A double hidden-layered network with fewer training vectors is sensitive to premature overfitting than a model with a larger training data set, with minor changes in neuron sample size. A network with 2,880 airfoils is overfitted after 20 neurons compared to 30 for a training size of 4,806 and 40 for 8,095. Hence, network complexity is proportional to the size of the training vector and the underlying structure. The number of hidden layers has a major influence on the over and underfitting of data. Single-layered networks are not sensitive to the identified data fitting demerits even with an extended neuron sample size. In comparison a double-layered network is represented with performance instabilities. From the data modeled, the optimal network structure topology where the affects of under and overfitting are suppressed is identified. An error of 8% for single-layered model is achieved compared to 5% for a doubled hidden-layered network type.

ANN structure development by a DoE analysis for the estimation of c_d is presented in Figure 7.5.

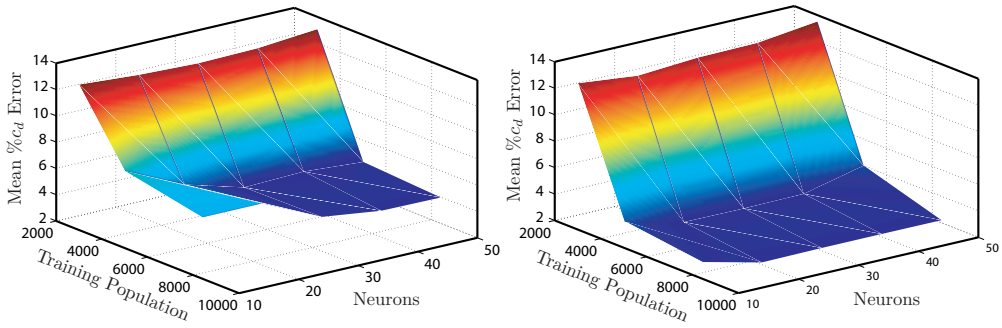

(a) One Hidden Layer: Drag Coefficient (b) Two Hidden Layers: Drag Coefficient

FIGURE 7.5: Affect of Neural Network Structure on Drag Coefficient

The mean error variances for drag approximation in Figure 7.5 represents a similar convergence pattern in comparison to the coefficient of lift analysis. An increase in training sample size results in significant reductions in mean generalisation errors. A single-layered network with 2,880 training airfoils (Fig. 7.5(a)) indicates negligible drag prediction improvements as a function of neuron size. The negligible performance improvement activity is related to the undersized training vector as with further increases in network complexity, performance degradation by overfitting occurs. A training sample size of 4,806 and 8,095 PARSEC-Modified airfoils results in significant performance improvements as a function of neuron size. Overfitting of data which induces generalisation errors is not evident for the identified population sets. A flat plateau region is mapped where errors are stagnant at 4%. Hence, a valid structure type configuration for a single-layered network is established.

The affect of introducing a second hidden-layer on c_d approximations by the neural network is modeled in Figure 7.5(b). The mean error magnitudes are lower for a larger training sample size than for a reduced population set. Network generalisation performance for a training dataset of 2,880 airfoils is similar to a single-layered structure with negligible performance improvements by the introduction of a second hidden-layer. Significant generalisation performance improvements are noted with larger training vectors. A neural network structure with 4,806 input training airfoils represents a consistent error performance at 2.9% between 20-40 neurons, thus representing a converged error tolerance region. By the addition of ten neurons, the error increases to 4.0% due to overfitting. An 8,095 airfoil training configuration represents an in-active performance improvement region between 20-50 neurons with an error of 2.16%. Overfitting is not observed which is attributed to the larger training size. This has an affect of delaying the onset at which model complexity becomes excessive to induce overfitting in comparison to a model with fewer training vectors. If additional neurons were to be added to the database with 8,095 airfoils, model complexity will lead to instabilities and degrade drag prediction accuracy.

The neural network with the lowest mean error distribution between theoretical and generalised dataset is presented in Table 7.1. The data is representative of a network trained with 8,095 airfoils with two hidden-layers. The performance of the developed surrogate model is validated with a regression analysis which correlates network outputs against the corresponding target. The absolute minimum and maximum error magnitude of a select airfoil from the data validation set is further identified. The standard deviation of the error distribution is established to represent the viability of the proposed approximation model for airfoil aerodynamic performance analysis.

TABLE 7.1: Offline Training-based Optimal Neural Network Configuration for Lift and Drag Coefficient

Aerodynamic Coefficient	**Neurons**	**Mean Error Variance**	**Standard Deviation**	**Min. Error %**	**Max. Error %**	**r-value**
Lift	30	4.93%	21.37	0	614.29	0.999
Drag	20	2.16%	3.58	0	53.73	0.995

A mean error of $\approx 5\%$ for lift over the generalisation population set is significant in Table 7.1. Errors in c_l can result in a false optimisation process due to the miss-leading measure of constraint c_l^T and the corresponding aerodynamic efficiency factor L/D for the respective airfoil. An r-correlation

value close to one indicates a strong positive relationship between network output and theory. Due to the extended disparity between the minimum percentage error of zero and the maximum at ≈ 615%, data outliers are evident. The standard deviation identifies the dispersion of the error distribution which is significant for lift relative to drag.

A histogram is presented in Figure 7.6 to model the c_l and c_d error distribution from the measure of the absolute fitness difference between theoretical and approximated data from Table 7.1.

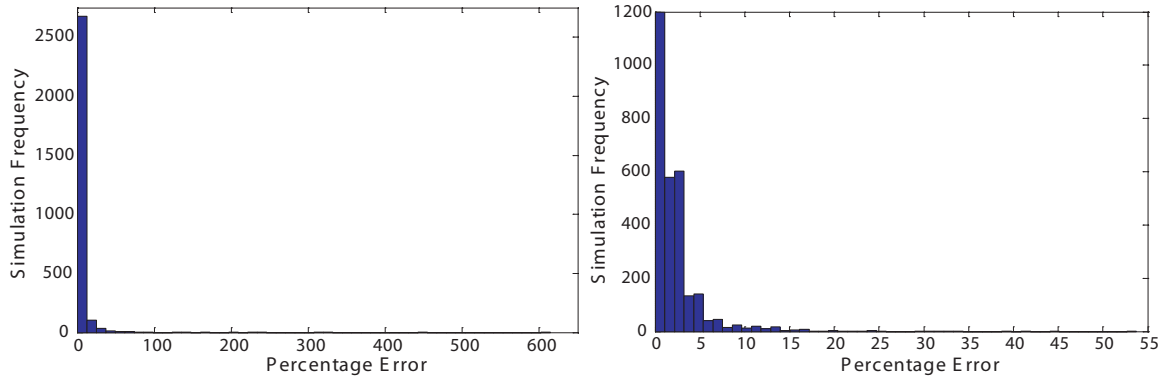

(a) Coefficient of Lift

(b) Coefficient of Drag

FIGURE 7.6: Offline Training-based Neural Network Aerodynamic Coefficient Modelling Histogram of Errors

The assessment of network generalisation performance is over 2,878 airfoils in Figure 7.6. Each histogram error sub-group for c_l spans 12.3% in Figure 7.6(b). There are 2,679 shapes within an error range of 0% - 12.3%. The frequency of airfoils decreases as the errors increase beyond the 12.3% measure. A total of 155 airfoils are approximated by an error measure range of 12.3% - 49.14% with the balance 44 modeled with error magnitudes spanning between 49.14% - 614.29%. The frequency of airfoils with errors in excess of 172% are isolated to one airfoil per error sub-group, up to the maximum miss-match of 614.29%. Hence, despite the low mean error variance of ≈ 5% (Tab. 7.1), the histogram analysis validates regions with poor c_l approximations.

The coefficient of drag approximation needed ten fewer neurons in comparison to the lift coefficient network to achieve accurate surrogate performance in Table 7.1. A mean error variance of ≈ 2% and a low standard deviation validated errors with controlled data dispersion in comparison to the lift coefficient analysis. A minimum error of zero was established with a maximum error percentage of ≈ 54%. An r-correlation of 0.995 confirmed a strong linear relationship between network output with theory.

The histogram of drag errors for the optimal neural network structure in Table 7.1 is presented in Figure 7.6(b). Each histogram bar is categorised by an error of 1.075%. In the first error sub-group, there are 1,199 airfoils which are classified with an error spanning 0% - 1.075%. From the defined population set, 1,081 airfoils have an exact drag approximation relative to theory, hence an error of zero percent. There are 1,456 airfoils classified with error histograms spanning 1.075% - 5.373% and 136 airfoils with errors spanning 5.373% - 10.75%. Population of airfoils with errors in excess of 10% are limited to one shape per error histogram sub-group, with a maximum error of ≈ 54%.

B. Integration of the Developed Neural Network Structure for Airfoil Optimisation

The neural network developed by the offline-training approach for lift and drag coefficient approximations is used for single-point airfoil design by the AM-PSO algorithm. Hence, instead of using XFOIL as the flow solver for fitness evaluations, the surrogate models for the respective aerodynamic coefficient from Table 7.1 are used. The objective function follows the design process defined in Section 6.2, Equation 6.1. The user-defined parameters in the swarm structure follow the test setup applied for shape design simulations in Section 6.2, Table 6.3. Hence, a swarm size of 20 particles is used and the LHS methodology is applied to distribute the swarm in the dimensional search space at optimisation initialisation.

The optimal airfoil by the application of the developed neural network into the AM-PSO algorithm is presented in Figure 7.7(a). The optimal results by the use of the theoretical flow solver in the DNO process as a fitness function evaluator is presented in Figure 7.7(b). The converged shapes are representative of a swarm initiated at different regions of the solution topology by the definition of disparate base airfoils. The converged results by the respective base starting points are superimposed with the optimal by the surrogate model fitness function evaluator from Figure 7.7(a) for a comparative analysis.

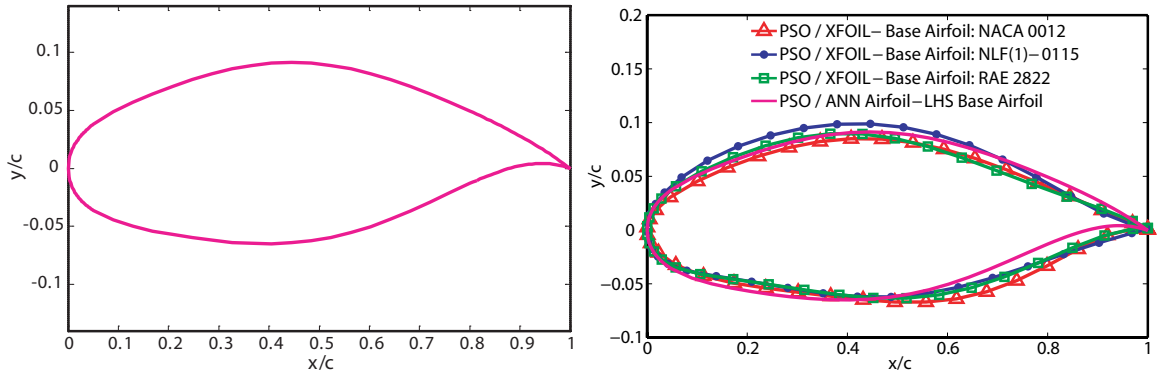

(a) AM-PSO / ANN

(b) AM-PSO / XFOIL & AM-PSO / ANN

FIGURE 7.7: Single-point Airfoil Optimisation by the AM-PSO with ANN developed by an Offline-training Approach

The optimal profile by the AM-PSO/ANN approach in Figure 7.7(a) is comparable to the shape design results with a theoretical flow solver in Figure 7.7(b). The results by the integration of the theoretical flow solver for fitness function evaluations in the DNO architecture with variances in base airfoils, including initial swarm dispersion by the LHS methodology and the data by the offline-trained ANN are comparable, with minor profile deviations only. Hence, solution convergence about a specified region in the design space is evident for the defined problem type. The aerodynamics of the converged PSO/ANN airfoil and the relative measure of accuracy against theory is presented in Table 7.2.

TABLE 7.2: Offline Training-based Optima Airfoil Aerodynamics & Fitness

Base Airfoil	**Method**	**ANN Lift**	**ANN Drag**	**ANN Fitness**	**Theoretical Lift**	**Theoretical Drag**	**Theoretical Fitness**
LHS	AM-PSO/ANN	0.40	0.0046	0.0046	0.3985 (↓ 0.375%)	0.0046 (0%)	0.0061 (↑≈ 25%)

The results in Table 7.2 conform to the defined design objective from Equation 6.1. The constraint on c_l^T is achieved with drag performance comparable to shape design simulations by the AM-PSO/Flow Solver approach, as a function of variances in base airfoil types in Table 6.3. Similarities in airfoil shapes (Fig. 7.7(b)) and aerodynamics (Tabs. 6.3 and 7.2) between the theoretical flow solver and surrogate fitness methods in the DNO structure confirm solution convergence to a common region.

The measure of computational efficiency by the integration of a surrogate model in the airfoil design process is confirmed. The AM-PSO/ANN simulation modeled in Figure 7.7(a) and Table 7.2 converged in 25 seconds on a PC with 1.86GHz CPU with 2.0 GB of RAM. In comparison the use of a theoretical flow solver for airfoil design fitness evaluations on a supercomputing facility spanned hours for low-fidelity methods and weeks with RANS-based solvers. The surrogate-assisted methodology facilitates an efficient shape design process.

The aerodynamics of the ANN assisted optimal shape is confirmed by XFOIL to evaluate the approximation accuracy of the developed surrogate model relative to theory in Table 7.2. Drag is approximated with a zero percent error, hence matches the performance measure by XFOIL. The lift coefficient is underestimated by 0.375% by ANN relative to XFOIL at $c_l = 0.3985$ and is lower than the design target $c_l^T = 0.40$ (Eqn. 6.1). A constraint violated design corresponds to a significantly higher theoretical fitness in comparison to the approximated measure by $\approx 25\%$. The impact of airfoil aerodynamics on fitness convergence by a surrogate-assisted methodology against theory is established. Approximation errors in airfoil aerodynamic computations by the ANN result in fitness errors relative to theory.

The distribution of airfoil aerodynamic approximation errors by the ANN on the shape design process with the AM-PSO must be addressed. Despite the acceptable accuracy of c_l and c_d of the optimal profile by the ANN relative to theory in Table 7.2, residual error distribution by the histogram analysis in Figure 7.6 validated the extremity in error magnitudes that characterise the search space with a surrogate-assisted approximation method. The feasibility of the solution with an ANN is limited due to the accumulation of errors during the search evolution process. This results in significant fitness variances between theory and approximation measure as confirmed in Table 7.2.

The offline-trained surrogate model validated the potential of the proposed ANN for airfoil design simulations. The methodology applied converged to an acceptable optimal with enhanced computational efficiency relative to a design structure with a stand-alone, time-intensive flow solver only. The confirmation of shape convergence to an acceptable solution region by the fitness approximation method was confirmed by a comparative analysis of the ANN-based solution against a design structure with a theoretical flow solver in the DNO process (Fig. 7.7(b)). Minimal shape variances were

established between the identifies shapes. The analysis of airfoil aerodynamics of the ANN-based optimal relative to theory confirmed the viability of a surrogate-assisted design approach (Tab. 7.2). The issue of shape performance approximation errors in Figure 7.6 on the optimisation process must be addressed despite the identified merits of the ANN method for airfoil optimisation.

7.3.5 Design Principles & Merits of an Online-Based Surrogate Model for Optimisation Simulations

The design development of a online training-based surrogate model within the AM-PSO mainframe is needed to address the identified issues associated with offline trained surrogate methods for design optimisation simulations. The fundamentals of the online training method and the direct optimisation approach in-lieu of a surrogate model for airfoil design is compared in Figure 7.8

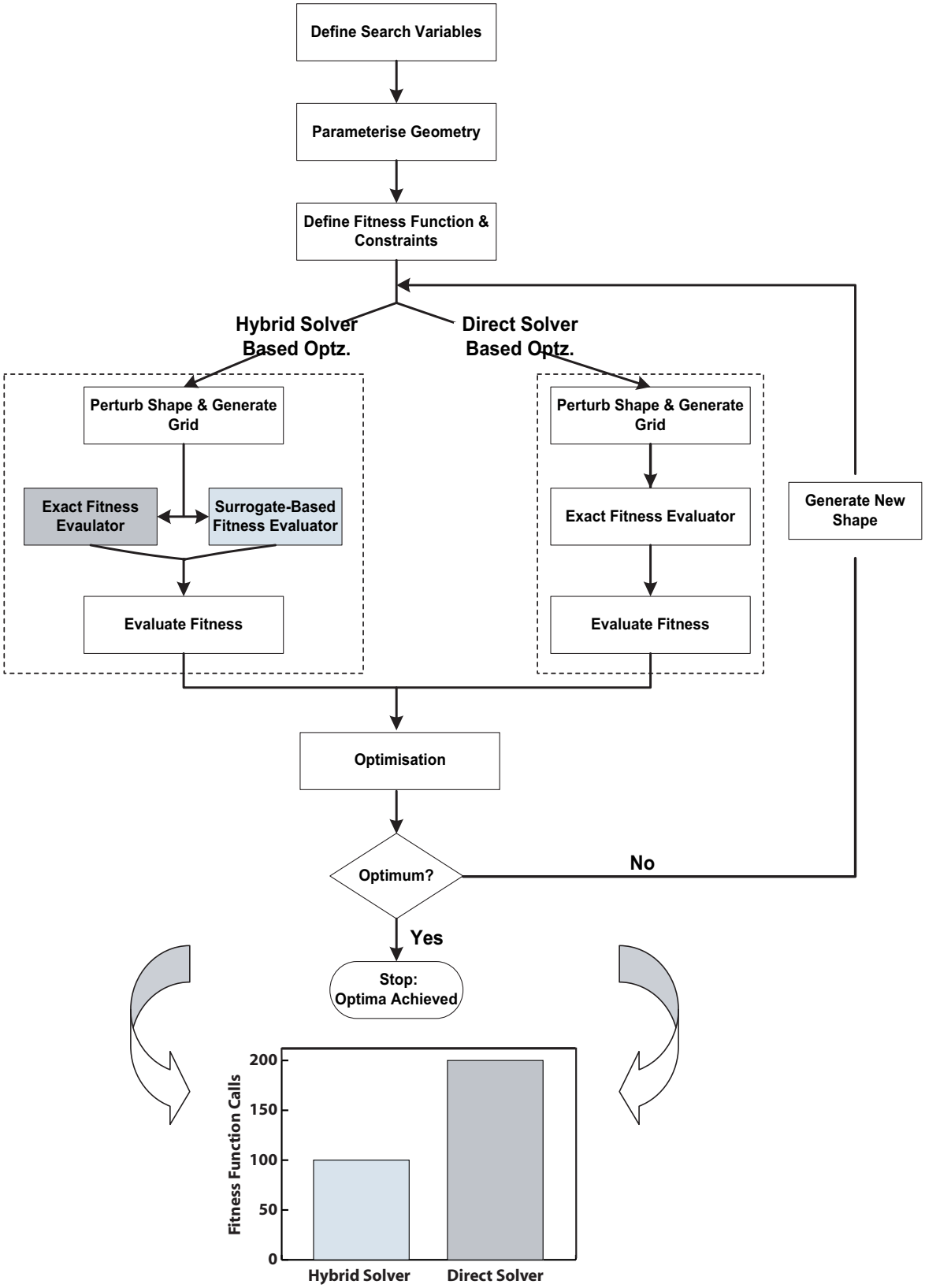

FIGURE 7.8: Flowchart of the Design Process by the Direct & Surrogate-Based Fitness Evaluation Approach

The optimisation process is initiated by the definition of the problem scope in Figure 7.8. The search dimensionality population size and the variable intervals are defined. The airfoil variables are used to parameterise the geometry by the select shape function type. The design goals are defined in accordance to the objectives and constraints. The outlined processes define the pre-processing to the optimisation simulation by the DNO approach with: **a)** Direct solver-based optimisation with fitness computation by the theoretical flow solver; or **b)** A hybrid solver-based optimisation with an integrated online and/or offline-trained surrogate model.

In the direct solver-based optimisation approach for fitness function analysis in Figure 7.8, a computational grid is generated about the parameterised geometry for analysis by the flow solver. The fitness is used for shape optimisation by the novel AM-PSO and the candidate shape is assessed in accordance to the defined objectives and constraints. The feasibility of the respective profile is confirmed. If the design goals are achieved, the optimisation process is terminated and the global best is stored as the optimal to the design problem. Else, an iterative design process follows and a new shape is generated by the perturbation of the airfoil variables. The profile is parameterised by the defined mathematical shape function and the fitness function is computed from the flow solver and assessed relative to the defined goals. The total number of fitness function calls made to the theoretical flow solver by AM-PSO during the design cycle is recorded.

In the hybrid solver-based optimisation approach in Figure 7.8, a computational grid about a candidate shape is first generated. The merits of the respective profile is established by the fitness measure using the pre-defined surrogate model to the flow solver or by the theoretical solver itself. The choice of solver type for fitness evaluations are based on user-defined measures and conditions (Sec. 7.3.5.1). Fitness evaluations by the approximate model require negligible computing resources. The potential of enhancing the computational efficiency of the optimisation process is significant. The fitness from the surrogate and/or theoretical solver is used by the AM-PSO to facilitate the optimisation process. The methodology will operate in iteration until convergence is achieved based on defined objectives and constraints. The number of solver calls by the approximate and theoretical flow solver are recorded for the purposes of a performance-based comparative analysis between the two methods.

The solution feasibility and computational efficiency of the two optimisation approaches modeled in Figure 7.8 is assessed and compared. The convergence of the established optima by the respective optimisation structure is assessed relative to defined benchmark. If a true global minima is achieved, then the total number of fitness function calls evaluated by the time-consuming flow solver within the respective design module (Fig. 7.8) is examined to assess model efficiency. Theoretically the hybrid solver-based fitness approach with an ANN model will be characterised by fewer data points that are analysed by the time-intensive flow solver in comparison to an optimisation methodology without a surrogate model. The defined hybrid solver-based methodology will theoretically induce a computationally efficient optimisation process. The expected performance merit needs to be verified.

The fundamentals of the hybrid solver optimisation approach based on the online training strategy within the AM-PSO structure is defined. The performance merits of the design methodology as a function of solution feasibility and model efficiency is confirmed on benchmark test functions.

7.3.5.1 AM-PSO Based Online-training Surrogate Model Design Definition

To address the limitations of the excessive approximation errors by the offline-training based ANN from Section 7.3.4, an online-training based surrogate model is presented. The ANN is developed in parallel with the search processes of the AM-PSO. The training dataset used for ANN development is from the design evolution of the particles in the swarm during the optimisation process. Hence, only promising data points governed by the AM-PSO principles are integrated for surrogate model definition. The schematic of the proposed methodology is presented in Figure 7.9

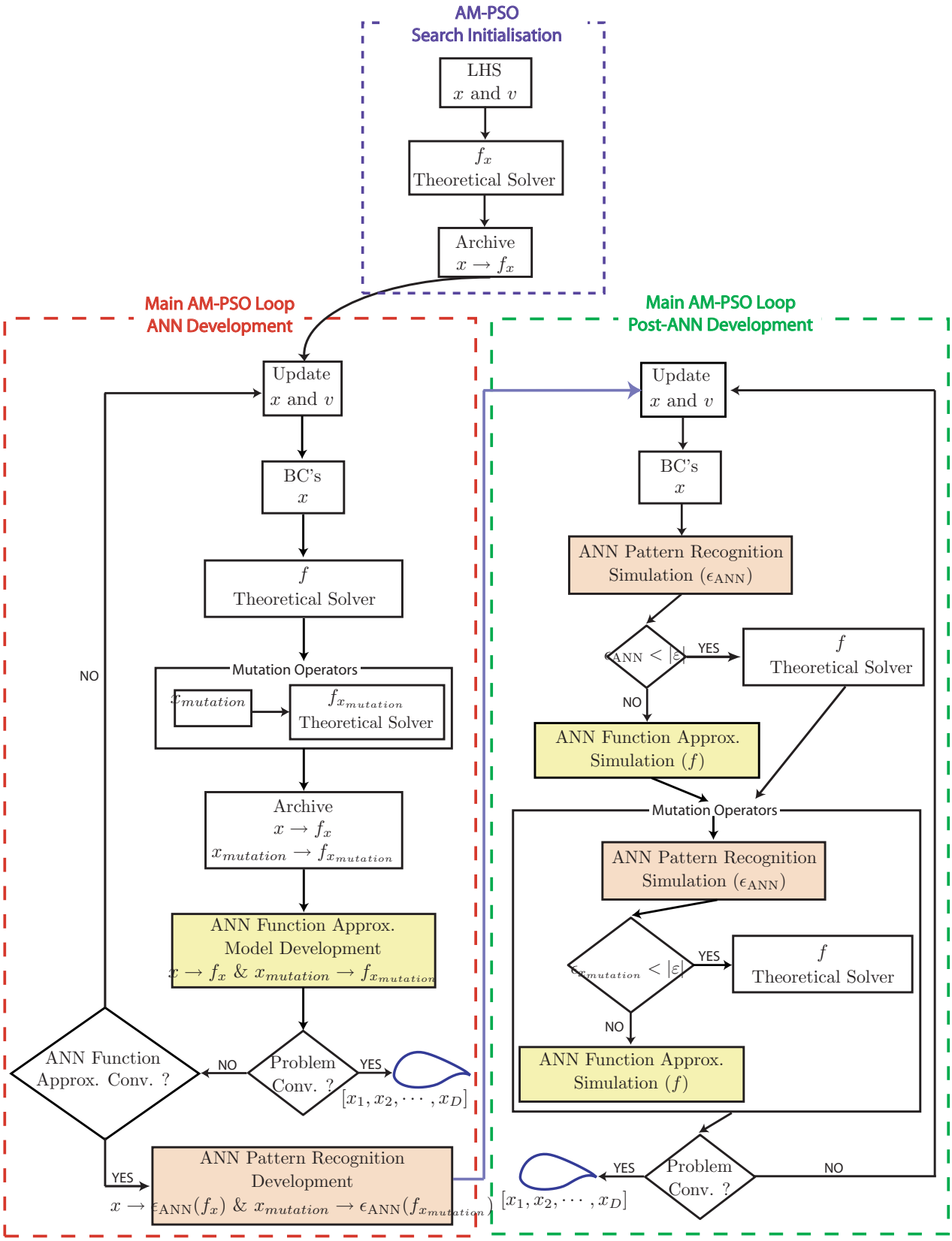

FIGURE 7.9: Optimisation by the AM-PSO Based Online Surrogate Model Development Approach for Fitness Evaluation

The Pseudocode of the methodology in Figure 7.9 is presented in Algorithm 7.

Algorithm 7 Online Artificial Neural Network Training based on AM-PSO Design Principles

1: **for all particles** i **do**
2: Apply AM-PSO operators; Algorithm 4, lines 1-7
3: Archive $x \rightarrow f$; Apply neighborhood Euclidean distance metric
4: **end for**
5: surrogate.status=0
6: **while** termination criteria not satisfied **do**
7: k=0
8: **if** surrogate.status == 0 **then**
9: **for all particles** i **do**
10: AM-PSO operators from Algorithm 4, lines 11-16
11: Evaluate f with theoretical model
12: Apply mutation operators (Alg. 4, lines 23-27)
13: Evaluate fitness of mutated particles $F_{i,m}$ (Alg. 4, line 28) by theoretical model
14: Apply mutation position update rule (Alg. 4, line 29)
15: **end for**
16: Update Archive $x \rightarrow f$; Apply neighborhood Euclidean distance metric
17: **Train** ANN Function Approximation Structure from archive dataset by:
18: **INPUT** $x \rightarrow$ **OUTPUT** f from theoretical solver
19: **if** termination criterion is achieved **then**
20: Output *pbestg* as optima
21: **else**
22: **if** ANN function approximation structure convergence is achieved **then**
23: surrogate.status == 1
24: **Train** ANN pattern recognition structure by:
25: **INPUT** $x \rightarrow$ **OUTPUT** Fitness approximation errors ϵ_{ANN}
26: **else**
27: surrogate.status == 0
28: **end if**
29: **end if**
30: **else**
31: **if** termination criterion not achieved **then**
32: **if** surrogate.status == 1 **then**
33: **for all particles** i **do**
34: AM-PSO operators from Algorithm 4, Lines 13-18
35: **Simulate** ANN pattern recognition structure by:
36: **INPUT** $x \rightarrow$ **OUTPUT** Fitness approximation errors ϵ_{ANN}
37: **if** $\epsilon_{\text{ANN}} <$ user-defined threshold $|\varepsilon|$ **then**
38: Evaluate f with theoretical model
39: **else**
40: **Simulate** f from surrogate model
41: **INPUT** $x \rightarrow$ **OUTPUT** f from ANN function approx. model
42: **end if**
43: Apply mutation operators → lines 12-14
44: **Simulate** ANN pattern recognition structure by:
45: **INPUT** $x_{mutation} \rightarrow$ **OUTPUT** fitness approximation errors ϵ_{ANN}
46: **if** $\epsilon_{mutate} <$ user-defined threshold $|\varepsilon|$ **then**
47: Evaluate f with theoretical model
48: **else**
49: **Simulate** f from surrogate model
50: **INPUT** $x_{\text{mutation}} \rightarrow$ **OUTPUT** f_{mutation} from ANN function approx. model
51: **end if**
52: Update personal best $pbest_i^D(k)$
53: Update global best $pbestg(k)$
54: **end for**
55: **end if**
56: **end if**
57: **end if**
58: k=k+1
59: **end while**

The fundamentals of the novel, online surrogate-based training methodology in Figure 7.9 and the corresponding Pseudocode from Algorithm 7 is defined as follows:

1. **AM-PSO Initialisation**

   (a) The AM-PSO search process is initiated in lines 1-4 in Algorithm 7. The position x and velocity vectors v are distributed in the defined dimensional and speed intervals envelope with the LHS methodology. The fitness f of the data points is computed directly from the function evaluator. The corresponding personal and global best solutions are recorded.

   (b) The position vector and corresponding fitness are stored in array format in archive A_1 (line 3 - Alg. 7). The inclusion of position shared data points as inputs for ANN development will result in an ill-defined training process. To address this issue, an Euclidean neighborhood distance metric E is defined to identify and exclude data points from A_1 that are within a minimum user-defined tolerance of each other. A neighborhood distance metric establishes the positioning of all the particles relative to each other in the swarm over the defined dimensional space D. The Euclidean distance between all corresponding position vectors in A_1 is computed. Position vectors with shared solution regions and the corresponding fitness magnitudes about a specific Euclidean distance computation reference point are identified and eliminated from the archive. The process is defined for a swarm of size $\mathcal{S}$ with a D dimensional position vector x as:

$$\left[\overbrace{\begin{matrix} x_{1,1} & x_{1,2} & x_{1,3} & \cdots & x_{1,\mathcal{S}} \\ x_{2,1} & x_{2,2} & x_{2,3} & \cdots & x_{2,\mathcal{S}} \\ x_{3,1} & x_{3,2} & x_{3,3} & \cdots & x_{3,\mathcal{S}} \\ \vdots & \vdots & \vdots & \vdots & \vdots \\ x_{D,1} & x_{D,2} & x_{D,3} & \cdots & x_{D,\mathcal{S}} \end{matrix}}^{\text{Position Vector } x\text{: } D \times \mathcal{S} \text{ Matrix}}\right] \rightarrow \left[\overbrace{\begin{matrix} E_{[(1,1),(1,2)]} & E_{[(1,1),(1,3)]} & \cdots & E_{[(1,1),(1,\mathcal{S})]} \\ E_{[(2,1),(2,2)]} & E_{[(2,1),(2,3)]} & \cdots & E_{[(2,1),(2,\mathcal{S})]} \\ E_{[(3,1),(3,2)]} & E_{[(3,1),(3,3)]} & \cdots & E_{[(3,1),(3,\mathcal{S})]} \\ \vdots & \vdots & \vdots & \vdots \\ E_{[(D,1),(D,2)]} & E_{[(D,1),(D,3)]} & \cdots & E_{[D,1),(D,\mathcal{S})]} \end{matrix}}^{\text{Euclidean Distance between } D \times \mathcal{S} \text{ Matrix Points}}\right] \tag{7.5}$$

   The column data in the Euclidean distance matrix is assessed to evaluate the proximity of the respective position vector (particle) from measure D, relative to the other particles in the swarm. From a DoE analysis, if each entry E in a specific column, hence particle over D rows is $\leq 10^{-2}$, then the position vector is assumed to be within a minimum distance metric tolerance relative to the measuring reference position vector point. The identified position vector and the corresponding fitness is not stored in the archive. The methodology will facilitate an accurate ANN development process.

2. **Main AM-PSO Loop - ANN Development**

   (a) The main search loop from Figure 7.9 is initiated. The AM-PSO search operators for velocity and position update rules are applied. The random initialisation wall boundary condition is induced to transfer dimensional search space violated particles into the search domain (line 10 - Alg. 7). The fitness of the updated position vectors is established from the theoretical model (line 11 - Alg. 7).

   (b) The novel mutation operators developed and validated in Chapter 3 are applied for search diversity (line 12 - Alg. 7). Modified position vector points $x_{mutation}$ are generated. The

corresponding fitness $f_{mutation}$ of $x_{mutation}$ is established from the theoretical function evaluator (line 13 - Alg. 7).

(c) The data points as a function of particle position in the search space and the corresponding fitness $x \rightarrow f$ are collated from: **a)** AM-PSO search initialisation phase; **b)** Position update rule in the main AM-PSO loop during the ANN development process; and **c)** Position points due to mutation for search diversity. The data points from stages **b & c** are added to the initial archive A_1 from the initialisation phase. The defined neighborhood distance measure methodology from matrix 7.5 is applied for the identification and exclusion of similarity-based position and corresponding fitness data arrays. The archive is updated accordingly and is represented by A_2 in Algorithm 7, line 15.

(d) An ANN function approximation structure is developed to model the relationship between the position vector points as inputs and the fitness as surrogate output from archive A_2. The defined process is modeled in Algorithm 7 by lines 16-17. The input-output dataset is scaled in the interval $[-1, 1]$. A comprehensive DoE analysis confirmed that a two hidden-layered model with 15 neurons in each layer is initially required. The hyperbolic tangent sigmoid transfer functions are applied in the hidden layers and a linear transfer function for model output. The number of neurons in the hidden layers increases proportionally as the population of the archive, hence training dataset increases during the AM-PSO search cycle. The input dataset in A_2 is randomly partitioned into three subsets with the following ratios: **a)** 60% for training; **b)** 30% for validation; and **c)** 10% for general testing. The following parameters further define the network training process:

- The Levenberg-Marquardt [219] in MATLAB's Neural Network toolbox [214] is applied as the training algorithm;
- Training convergence occurs when one of the following is achieved:
  - Maximum training epoch equals 500 iterations; or
  - The generalisation errors of the validation dataset equals 5.0×10^{-6}; or
  - The minimum gradient between subsequent iterations equals 1.0×10^{-100}; or
  - The Marquardt adjustment parameter equals 1.0×10^{50}; or
  - The generalisation error of the validation dataset during network training does not improve over 50 consecutive iterations. The methodology avoids approximation errors due to data overfitting. The ANN structure just prior to the point when network instabilities are initiated by overfitting is acknowledged as the optimal surrogate topology setup.
- Network performance post-processing measures are used to evaluate the accuracy of the developed model as a function of the approximation errors on the training, validation and test datasets.

The subsequent step within the defined methodology in Figure 7.9 assesses the convergence of the AM-PSO based on user-defined conditions for the defined test problem in line 19 of Algorithm 7 as:

- If the user-defined termination criterion is achieved then the corresponding position vector $[x_1, x_2, \cdots, x_D]$ for *pbestg* is denoted as the global optimal and the design optimisation cycle is terminated (line 20); else

- Convergence to the global optimal has not been achieved and the following operators are defined accordingly:
  - The state-of-convergence of the developed ANN function approximation model from lines 17-18 (Alg. 7) is verified in line 22. The performance is assessed on the validation dataset which comprises of 30% of the archive population. Theoretically as the population size of the training data increases, the approximation errors will decrease, hence validity of the ANN will be enhanced. At each design evolution, newer data points are applied for ANN training due to the updated archive as a result of the search processes of the particles in the swarm. The scope of the position vectors are directly related to the search principles of the particles which are guided to a specific solution region in the defined search space. The archive will be saturated by position vectors which are concentrated to a specific solution region. An increase in training sample size population, for a concentrated solution topology region in the defined dimensional search space will enhance the approximation accuracy of the ANN model. The convergence of the proposed ANN function approximation model is defined when the approximation accuracy on the validation dataset has converged to a specific tolerance. The following measuring units verify when this occurs where the convergence measures are based on a comprehensive DoE analysis:
    i. A linear regression analysis between network output and the theoretical targets is generated on the validation dataset. The parameters computed are the slope, y-intercept and the correlation coefficient (r-value) of the regression curve. The slope of the curve will be one and the y-intercept will equal zero for a perfect fit between the datasets. The variation between the two datasets will be represented by a r-correlation of one. The defined parameters are analysed at each archive update sequence, hence during the integration of the newer data points into the ANN for function approximation model development. The DoE analysis confirmed that the slope of the regression curve must be ≥ 0.95, the $y-$intercept needs to be within the intervals $[-0.05, 0.05]$ and the r-value ≥ 0.90, to verify ANN performance accuracy convergence.
  - If the ANN function approximation model defined to map the input position vectors to the theoretical fitness does not converge in accordance to the defined measuring parameters, the iterative AM-PSO design process ensues. The design algorithm is transferred to the original AM-PSO search operators within the design loop and the next design iterate follows (Fig. 7.9). The parameter 'surrogate.status' is introduced and is set at zero to represent the non-convergence of the ANN model in the defined algorithm architecture (line 27, Alg. 4). The application of the surrogate.status to zero and the non-convergence of the fundamental AM-PSO problem to the defined objective has the affect of bypassing the operators in lines 33-57, hence re-instating the design algorithm to line 9 for the following design evolution within the scope of the AM-PSO iterative design cycle.
  - Alternately if the ANN function approximation model converges in accordance to the defined parameters in line 22, the surrogate.status is set to one (line 23). A second ANN structure is introduced based on a pattern recognition methodology

(Fig. 7.9). The input position vectors in the archive A_2, which constitutes to data points from the AM-PSO operators x and the search process due to particle mutation for diversity $x_{mutation}$ are simulated as inputs to the developed ANN function approximation model. The respective fitness approximates f_x and $f_{x_{\text{mutation}}}$ are obtained accordingly for the AM-PSO and mutation-based position vectors respectively. The absolute fitness approximation error ϵ_{ANN}, between the estimated and theoretical target in A_2 is established:

$$\epsilon_{\text{ANN}} = |f_{\text{Theoretical}} - f_{\text{ANN}}| \tag{7.6}$$

The fitness approximation errors ϵ_{ANN} in Equation 7.6 are representative of the accuracy of the developed and converged ANN function approximation model. The approximation errors are used as outputs for the corresponding position vectors as inputs (lines 23-24) to train the proposed pattern recognition model. The defined surrogate will map the viability of estimating the fitness of a candidate position vector as a function of the output error, by the developed and converged ANN function approximation model. As the archive population set will be saturated by position vectors that are isolated to a specific solution topology region due to the fundamental search processes of the AM-PSO algorithm, the approximation errors of the ANN model for fitness estimation will be low at the archive dominated position vector region. Relatively data point simulation by the ANN function approximation model that is not in the scope of the population set A_2, will be modeled with higher approximation errors.

Due to the degree-of-randomness in the AM-PSO search process including the application of mutation operators, the generation of erroneous data points will occur. Theoretically these data points will exceed the scope of the solution topology mapped by the AM-PSO in A_2. Since the scope of the ANN function approximation model is specific to an isolated solution region only from A_2, simulation of data points that exceed the isolated design envelope will constitute to high approximation errors relative to data points that are solution region specific. High error data points simulated by the ANN function approximation model are assumed to be the offset of the search randomness in the AM-PSO and are in reference to a solution region that is not representative of a promising point for the defined test problem.

To aid a computationally efficient search optimisation process with the AM-PSO structure, a novel methodology is needed to distinguish the fitness computation of a candidate data point based on the fitness approximation error between the developed surrogate model and the theoretical solver. A histogram of errors for the library of data points in A_2 from Equation 7.6 is generated. Approximation fitness errors of the ANN model that are in the solution dominated region based on the scope of the data points in A_2 is established. From the histogram of approximation error analysis, a user-defined parameter ε is defined that distinguishes between low to high fitness error for the corresponding position vector. The measure relates solution feasibility by the identification of the respective data point to be within

an solution valid to in-valid search regions within the scope of A_2.

Accordingly the fitness outputs are transformed into a binary format of 0's and 1's based on the magnitude of the approximation error relative to ε in Equation 7.6. An ANN pattern recognition model is developed to distinguish fitness computation of a respective position vector between the two solvers as: **a)** Low approximation errors are promising data points and are represented with marker one for fitness analysis by the theoretical solver; and **b)** High approximation errors are denoted with marker zero and are assumed to be erroneous position vectors relative to the defined design goals. The corresponding fitness is established by the surrogate model.

The input of the pattern recognition model is the archive of position vectors in A_2. The output is in binary format based on the user-defined parameter ε. This is relative to the data established by the histogram analysis of ϵ_{ANN} (Eqn. 7.6), which is a measure of ANN fitness function approximation accuracy for solution topology dominated and offset data points accordingly. A post-processing analysis of the ANN pattern recognition model follows to measure the viability, hence success of the trained model for the defined problem scope. An example of the proposed design development and validation process is presented on a benchmark test function in Section 7.3.5.2.

Once the ANN pattern recognition model has been developed in absence of a non-converged problem state (line 31, Alg. 7), the surrogate.status flag is activated and set to one accordingly (line 32). The fundamental steps of the AM-PSO algorithm with the integration of the developed ANN function and pattern recognition models, hence post-ANN development stage is schematically presented by a sequence of logical steps in Figure 7.5. The Pseudocode of the process is presented by lines 31-57 in Algorithm 7. The methodology is defined in the following sub-section.

3. **Main AM-PSO Loop - Post ANN Development**

   (a) The fundamental AM-PSO search operators including velocity and position update rules are applied (line 34, Alg. 7). The random wall boundary condition is used to re-model dimensional search space violated particles.

   (b) The developed ANN pattern recognition model is simulated to estimate the state-of-the fitness error of the respective particle position if it were to be analysed by the ANN function approximation model. The position vector x is simulated as an input and ϵ_{ANN} is the output to the pattern recognition model (lines 35-36).

   (c) If the estimated ϵ_{ANN} is less than the user-defined threshold $|\varepsilon|$ from the error histogram analysis, the candidate position vector is assumed to be a promising data point. The fitness of the respective particle is established from the theoretical solver (lines 37-38).

   (d) If the estimated ϵ_{ANN} is greater than the user-defined threshold $|\varepsilon|$, the position of the respective particle is assumed to be at an adverse region in the solution topology. Hence, computational resources are not exhausted on non-promising data points and the fitness is estimated by the developed ANN function approximation model. The input to the structure is x and the estimated f is the model output due to surrogate simulation (lines

40-41). The output is established with negligible computational effort in comparison to the direct fitness evaluation by the theoretical solver.

(e) AM-PSO developed mutation operators are applied to induce search diversity (line 43).

(f) The viability of establishing the fitness of x_{mutation} is evaluated in accordance to the principles outlined for x and corresponding f, based on the standard AM-PSO search process (lines 35-42). The pattern recognition model is simulated with x_{mutation} applied as an input and the corresponding $\epsilon_{\text{mutation}}$ established as model output (lines 44-45). If $\epsilon_{\text{mutation}}$ is less than $|\varepsilon|$, the fitness is established by the theoretical solver (lines 46-47). Else, a non-dominant point to the defined objective function is assumed and the fitness is simulated from the developed function approximation surrogate model (lines 49-50). The vector x_{mutation} is used as an input and the corresponding f_{mutation} is estimated.

(g) The $pbest_i^D(k)$ and $pbestg(k)$ at the respective design evolution k, is updated due to the simulation of the AM-PSO and novel mutation search operators (lines 52-53 respectively).

(h) The evolution of the personal and global best particle positions are factored to evaluate the convergence of the swarm toward an acceptable optimal. If the developed AM-PSO search termination measuring units defined in Section 3.6 and demonstrated in Figures 6.8 and 6.10 are achieved, search convergence is assumed and *pbestg* is the output to the optimisation process.

(i) Else, if convergence is not achieved, the optimisation algorithm follows an iterative process and is re-instated to the fundamental AM-PSO search operators (line 9 and Fig. 7.5). As the flag in reference to the development of the ANN function approximation model, surrogate.status is set to one, the defined processes in lines 9-30 are by-passed within the '$IF - ELSE$' statement. The AM-PSO search process is initiated at line 31 and the subsequent design iterations post ANN function approximation development stage, cycle between lines 31 and 58 until search termination is achieved at line 59.

7.3.5.2 Design Definition & Demonstration of the AM-PSO Based Online Surrogate Model

A. Design Definition

The fundamentals of the proposed online-training surrogate development methodology is demonstrated. The principles of the defined approach from Figure 7.9 and Algorithm 7 is verified for design optimisation on benchmark functions. The Ackley, Michalewics, Rosenbrock and the Schwefel test functions are used in the verification process from Chapter 3. The feasibility of the proposed design algorithm is measured by: **a)** Solution feasibility for convergence to the theoretical minima; and **b)** Computational efficiency by the measure of the total number of fitness function calls to the theoretical function evaluator during the optimisation cycle.

The computational process of the surrogate-assisted design optimisation algorithm (Alg. 7) is demonstrated for the Rosenbrock test function. Following the standard AM-PSO search operators, the updated archive characterised by position vector points and fitness magnitudes are applied for surrogate model development. The ANN training process is defined to proceed at every 200^{th} search

iterate until the performance of the ANN function approximation model is within user-defined tolerances. The training of the ANN at the point where approximation performance convergence is achieved is presented in Figure 7.10.

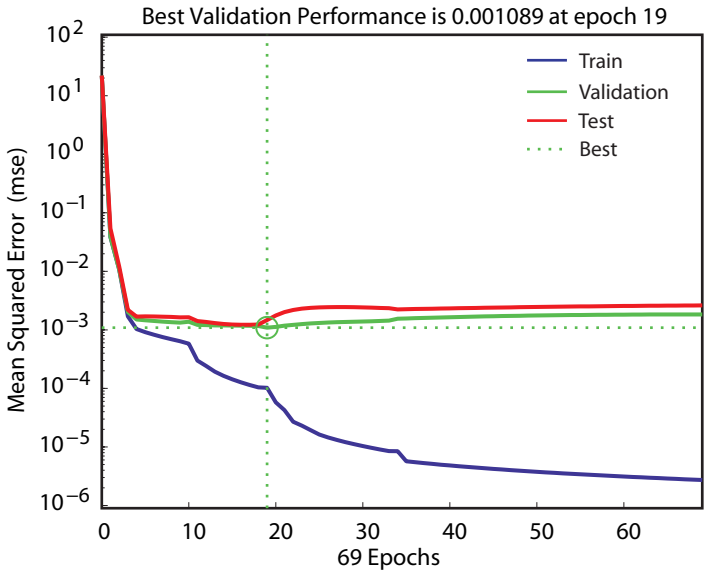

FIGURE 7.10: Rosenbrock Function ANN Approximation Training Performance

The training dataset is modeled with the lowest MSE through the surrogate development evolution stage in Figure 7.10. The validation dataset is introduced and is critical for ANN model development. The defined generalisation points are not used for ANN training. Instead they are used to assess the performance of the ANN. The methodology is applied to measure data overfitting. This occurs when the ANN memorises the pattern between the presented inputs and outputs in the training population instead of approximating a valid function between the defined data. By introducing an independent validation dataset to the training population, ANN overfitting is monitored and is used to evaluate the approximation performance of the surrogate model. At each training evolution, the ANN approximates the fitness of the data points in the validation dataset. The estimated output is compared with theory and the MSE between the datasets is established. One of the ANN training termination criteria is defined accordingly. If the MSE on the validation dataset decreases, the training simulation continues. If the MSE between iterate k and $k+1$ increases, the state of the ANN at k is stored as the optimal setup. The training process terminates if the MSE continues to increase over 50 successive evolutions. In Figure 7.10 the optimal setup of the ANN is achieved at iterate 19. The MSE of the validation dataset does not decrease further and training termination occurs at iterate 69.

The test dataset is further independent to the training and validation points. It has no impact on the ANN development process as a function of model training and in the subsequent termination criteria definition. The test data points are independently simulated by the ANN at each training evolution to further assess the feasibility of the surrogate model. The MSE of the output fitness relative to theory is established. In Figure 7.10 the MSE of the test and validation datasets is comparable. Relative to the training population, the MSE of the respective datasets is higher. To represent the population of input vectors with the corresponding MSE for the training, validation

and test population sets, an histogram of error as a measure of the fitness difference between theory and surrogate-based output is presented in Figure 7.11.

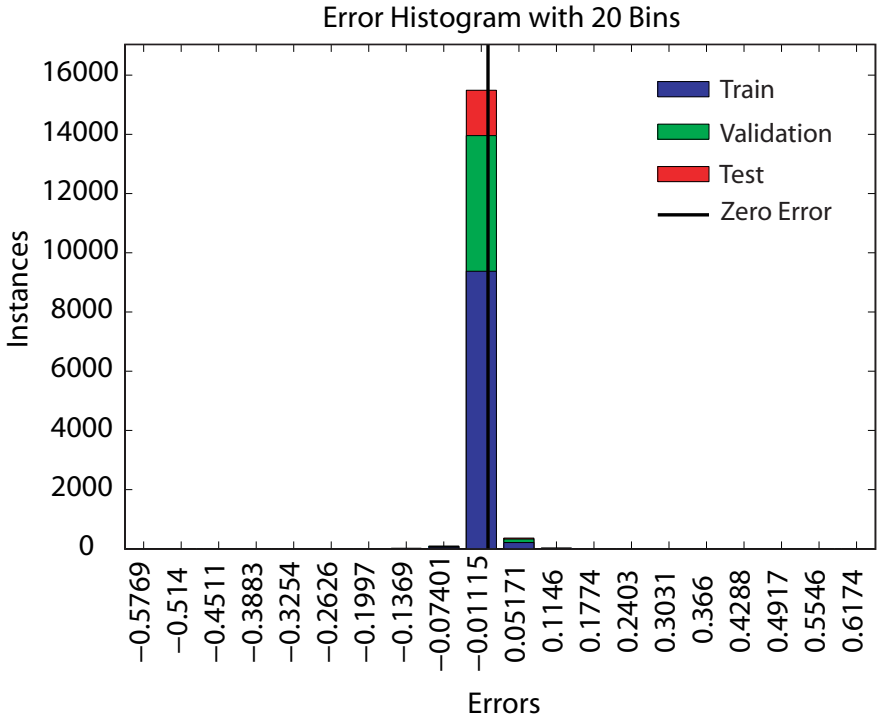

FIGURE 7.11: Rosenbrock Function ANN Approximation Training Error Histogram

The histogram of error analysis in Figure 7.11 represents the MSE on the respective data distribution libraries by the ANN training process. The majority of data points are approximated with a minimal fitness error and are characterised by magnitudes in the range of $[-0.031, \approx 10^{-5}]$. In comparison significantly fewer data points are modeled in a larger fitness error threshold of range $[0.001, 0.05]$. The distribution of the error population decreases spanning from the lowest error classification to the larger error category. At the highest error thresholds of ≈ -0.58 and ≈ 0.62, one data point from the $\approx 16,000$ population set are modeled in the defined error extremes. The error histogram in Figure 7.11 which is representative of the data for a converged ANN at epoch 19 in Figure 7.10, confirms the fitness approximation error for $\approx 98\%$ of data points is in the interval $[-0.031, \approx 10^{-5}]$.

To confirm the convergence of the ANN function approximation model to aid accurate fitness evaluations (line 22, Alg. 7), a regression analysis between the theoretical target and network output for the defined population set in the archive is presented. The linear regression for the training, validation, test and the compilation of the three is presented in Figure 7.12.

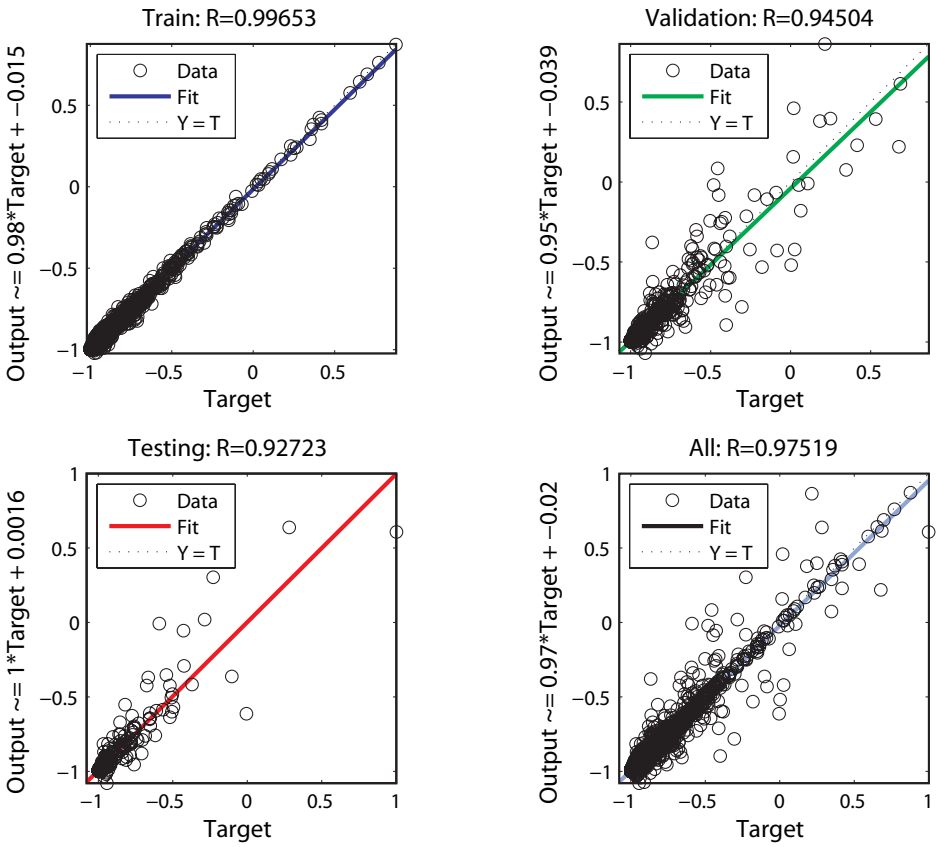

FIGURE 7.12: Rosenbrock Function ANN Approximation Regression Analysis

The network outputs are modeled versus the theoretical targets as open circles in Figure 7.12 for the respective data distribution library set. The best linear fit between network output relative to defined target is represented by a solid line. A dashed line represents a perfect fit where the output equal target for a comparative analysis of network performance against theory. The r-correlation factor, as measure of the variation in surrogate output versus defined target for the training dataset is ≈ 1, hence represents a near perfect fit between the datasets. Relative to the training population, the $r-$correlation factor decreases, yet still represents an acceptable correlation for the validation and testing data points at 0.95 and 0.93 respectively.

To confirm the merits of the ANN function approximation model, the regression analysis on the complete archive population set is modeled. An acceptable measure-of-goodness fit with an $r-$coefficient of 0.98 is established. The line of data fit (solid segment) is almost superimposed by the perfect fit segment (dashed). The analysis confirms that the developed ANN function approximation model will estimate the fitness of a candidate position vector with acceptable accuracy relative to the defined theoretical target.

The linear regression parameters of the developed ANN are used to evaluate the convergence of the surrogate model to yield acceptable fitness approximation performance. Recalling from Figure 7.9 the AM-PSO design simulation process operates in iteration with the coupled theoretical fitness solver until the performance of the ANN model converges to an acceptable state as a function of surrogate accuracy. At every 200^{th} design evolution, the ANN is re-designed with the updated data points from the archive due to the AM-PSO design cycle. The linear regression parameters are evaluated

to assess the approximation accuracy of the surrogate function and include the slope, $y-$intercept, $r-$correlation factor and the MSE of the training, validation and test datasets. The convergence of the defined parameters during the iterative AM-PSO/ANN development process (Fig. 7.9) is presented in Figure 7.13.

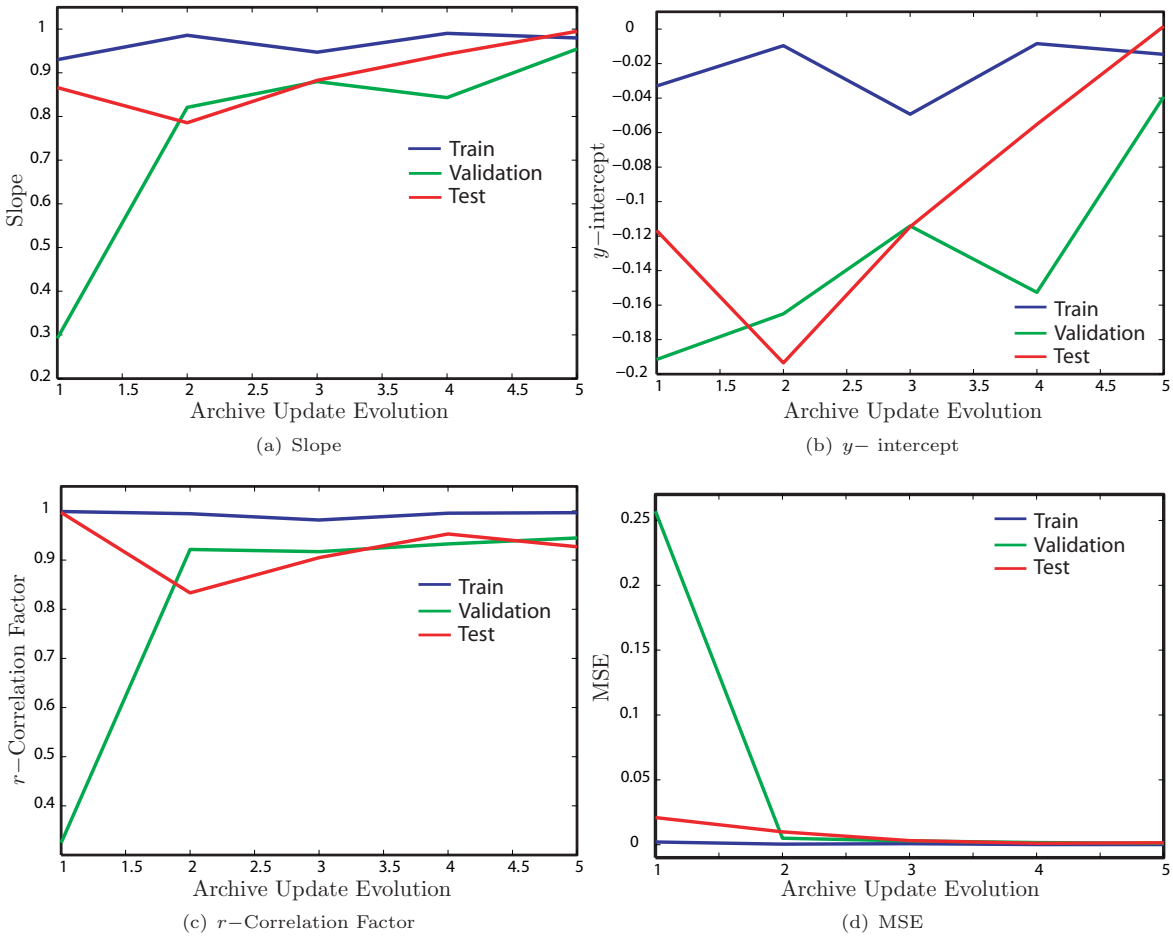

(a) Slope (b) $y-$ intercept

(c) $r-$Correlation Factor (d) MSE

FIGURE 7.13: Rosenbrock Function ANN Training Regression Curve & Error Performance

The ANN was developed over five independent instances spanning 200 design iterations within the main AM-PSO design loop (left flow chart model in Fig. 7.9). The convergence of the linear regression parameters over the five development cases is modeled in Figure 7.13. As anticipated the training dataset yields favorable approximation performance in comparison to the validation and test datasets for the defined regression-based parameters. At $k = 200$ for the first archive update evolution stage, the slope of the best linear regression is low relative to the converged state at $k = 1,000$ (at archive update evolution of five) for the respective datasets in the archive in Figure 7.13(a). Through the AM-PSO design iteration cycle with an update and increase in archive population size, the slope of the respective data increases and at ANN performance convergence it is ≈ 0.95 at $k = 1,000$ for the validation set.

The convergence of the $y-$intercept in Figure 7.13(b) is related to the slope of the linear regression. As $slope \rightarrow 1$ the $y - int \rightarrow 0$. At convergence the $y-$intercept of the respective data is ≈ 0 relative

to the state at $k = 200$ where $y - int < 0$. As the archive is updated with an increase in training population size, the $y - int \rightarrow 0$ through the AM-PSO design evolution stage.

The variation in surrogate output relative to theory by the development of the ANN during the AM-PSO simulation process is presented in Figure 7.13(c). The variance in the $r-$correlation factor as a function of the archive update evolution stage is modeled. As the ANN is trained on an independent dataset, the corresponding r factor of the respective population set is consistently greater than the validation and test points over the defined archive update stage. A perfect fit between regression output and defined theory is achieved for the training set with an r factor that is ≈ 1 at each archive update sequence step. As the training population size in the archive is increased, the generalisation performance of the surrogate model for accurate fitness approximation on new data points is enhanced. The converged validation r factor is ≈ 0.95. The linear regression coefficient for the test population dataset exhibits performance oscillations during the archive update process. At $k = 200$ for ANN development initialisation, the archive population size is limited and a near perfect correlation between network approximate and established theory is achieved. As the archive is updated, the r factor of the test case oscillates before converging to an acceptable correlation factor of ≈ 0.92 at $k = 1,000$.

The MSE convergence of the ANN fitness approximation performance during the AM-PSO evolution stage is modeled in Figure 7.13(d). As the population size of the data archive is increased, the MSE of the training, validation and test data points reduces proportionally. The MSE of the training data is not sensitive to the population size relative to the validation and test points. Acceptable convergence to a low MSE, hence the merits of the ANN is confirmed for the validation and test data points at $k = 1,000$.

The presented data confirms the validity of the ANN to yield acceptable fitness approximations based on the user-defined ANN performance-based convergence parameters (defined in Sec. 7.3.5.1, sub-section 2). At each archive update evolution stage ($k = 200$ iterations), the MSE and the regression analysis parameters are computed and compared to the user-defined convergence measures to assess surrogate performance. The results in Figure 7.13 confirm the state of the regression parameters at $k = 1,000$ are within the defined performance threshold limits as: **a)** The MSE of the respective data is less than the defined magnitude of 10^{-2} (Fig. 7.13(d)); **b)** The slope of the regression curves is ≥ 0.95 (Fig. 7.13(a)); **c)** The $y-$intercepts are within the defined tolerance of $[-0.05, 0.05]$ (Fig. 7.13(b)); and **d)** The $r-$coefficient of the linear regression curves is ≥ 0.90 for the defined data population sets (Fig. 7.13(c)). The regression parameters at $k = 1,000$ are in agreement to the defined convergence performance tolerances, hence verifying ANN accuracy.

Following convergence of the ANN function approximation model, the established archive dataset is used to generate a pattern recognition surrogate model (Fig. 7.9 and Alg. 7, lines 22-25). The position vectors in the archive are simulated with the developed ANN function approximation model and a fitness estimate is established. The error approximation by the absolute difference between theoretical and estimated fitness from Equation 7.6 is computed. The proposed pattern classification model is defined to map the relationship between the position vector x as input and the established approximation error, as a performance measure of the ANN function approximation model for fitness evaluations as output.

The aim of the pattern recognition model is to distinguish the fitness analysis of promising position vector points relative to off-design search agents for computation by the theoretical fitness solver. The analogy is based on the principles of the AM-PSO algorithm. As the archive of position vectors is updated during the AM-PSO design cycle, the library of data points will be dominated by promising search agents that are potential solutions to the defined problem. In comparison the data population size of respective search particles that are not in the region bounded about the global minima will be limited. The development of an ANN function approximation model will yield superior fitness approximation performance at a solution region which is modeled with an extended training sample size, hence promising data points from the AM-PSO. Relatively non-promising solution topologies will be represented by fewer search agents within the archive as the AM-PSO has concluded the respective off-design points to be non-feasible to the defined problem. Due to the limited training sample population size at the defined non-dominated search region, the ANN fitness approximations will be limited.

The pattern recognition model is defined to identify promising position vector points from the expected measure of fitness approximation error by the respective ANN model. If the estimated fitness error is less than a user-defined minimum threshold, the fitness of the respective data point is established directly by the theoretical solver. Else, the data point is assumed to be an off-design point to the defined problem and the corresponding fitness is estimated by the ANN function approximation model. Theoretically the defined methodology will enhance the computational efficiency of the design optimisation process as fitness evaluations are partitioned between time-intensive and computationally efficient solvers.

The input position vectors for the pattern recognition model development/training process are scaled in the interval [-1,1]. The outputs are in binary format of zeros and ones as a function of the estimated fitness approximation error, to represent fitness evaluation by the surrogate and exact method respectively. From a DoE analysis, a three-layered model is defined with 15 neurons in each layer. The hyperbolic tangent sigmoid transfer functions are used in the hidden-layers and a linear transfer function defined for model output. The archive population in A_2 is randomly partitioned into three subsets as: **a)** 70% for training; **b)** 25% for validation; and **c)** 5% for testing.

The Levenberg-Marquardt [219] training algorithm is used for model development. The training performance measure is by the MSE of the respective data subset and is presented in Figure 7.14.

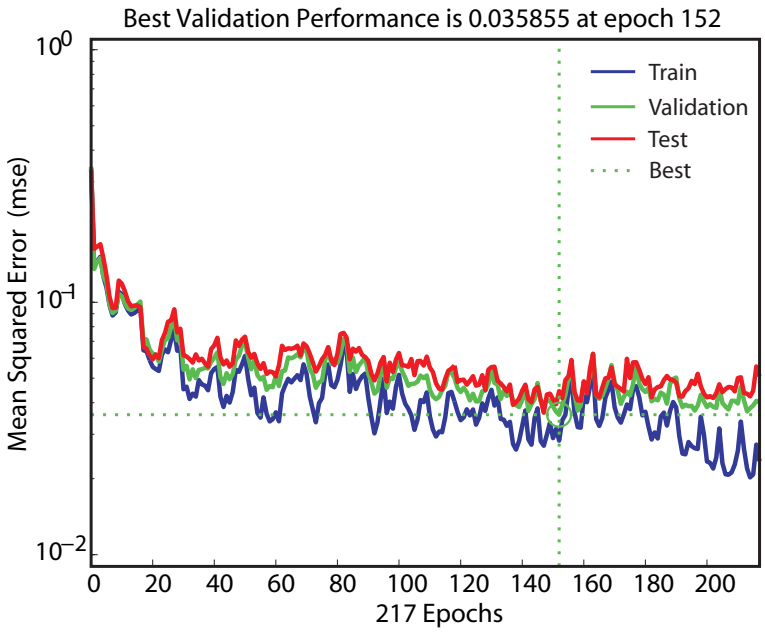

FIGURE 7.14: Rosenbrock ANN Pattern Recognition Surrogate Model Development Training Performance

The training performance of the proposed surrogate model as a function of the MSE is lower for the training data subset, relative to the validation and test data points in Figure 7.14. Surrogate model development is defined to mitigate data overfitting and this condition in enforced by monitoring the MSE on the validation dataset. Training termination will occur if the MSE of the validation dataset does not improve over 65 successive iterations. The lowest MSE on the validation set is at epoch 152. The weights and biases in the hidden-layers at the converged minima MSE state are identified to yield valid model approximations over arbitrarily defined inputs.

The approximation performance of the developed pattern recognition model is evaluated by a confusion matrix plot. The methodology models actual versus predicted classifiers for defined input sets. The general format of the data matrix is presented in Figure 7.15.

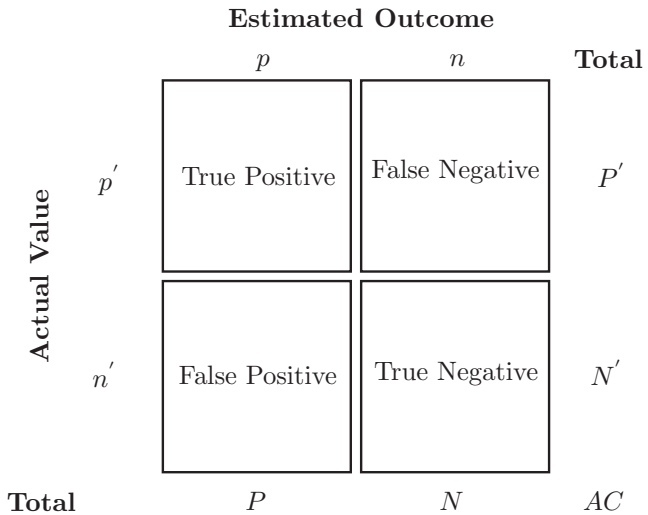

FIGURE 7.15: General Representation of a Confusion Matrix

The entries in the confusion matrix in Figure 7.15 are defined as follows:

- *True Positive (TP):* Number of **correct** predictions classified as positive;
- *False Negative (FN):* Number of **incorrect** predictions classified as negative that are positive;
- *False Positive (FP):* Number of **incorrect** predictions classified as positive that are negative;
- *True Negative (TN):* Number of **correct** predictions classified as negative;
- $P^{'}$*:* Ratio of TP to FN;
- $N^{'}$*:* Ratio of TN to FP;
- P*:* Ratio of TP to FP;
- N*:* Ratio of TN to FN; and
- AC*:* Overall accuracy rate of the developed pattern recognition model.

The equations applied to establish the entries in the confusion matrix from Figure 7.15, as a percentage proportion of the total number of data entries T_c are defined as:

$$\%TP = \left(\frac{TP}{T_c}\right) \times 100 \tag{7.7}$$

$$\%FN = \left(\frac{FN}{T_c}\right) \times 100 \tag{7.8}$$

$$\%FP = \left(\frac{FP}{T_c}\right) \times 100 \tag{7.9}$$

$$\%TN = \left(\frac{TN}{T_c}\right) \times 100 \tag{7.10}$$

$$\%P^{'} = \left(\frac{\text{TP}}{TP+FN}\right) \times 100 \tag{7.11}$$

$$\%N^{'} = \left(\frac{\text{TN}}{TN+FP}\right) \times 100 \tag{7.12}$$

$$\%P = \left(\frac{\text{TP}}{TP+FP}\right) \times 100 \tag{7.13}$$

$$\%N = \left(\frac{\text{TN}}{TN+FN}\right) \times 100 \tag{7.14}$$

$$\%AC = \left(\frac{\text{TP+TN}}{TP+FN+FP+TN}\right) \times 100 \tag{7.15}$$

The confusion matrix of the developed pattern recognition model at the converged training state from Figure 7.14, for the Rosenbrock test function is presented in Figure 7.16. The green matrix cells represent true classification cases, red represent false classifications, gray define the relative data ratio and the blue cell is the representation of the overall accuracy of the model. In the data ratio and AC cells, the green entries denote to correctly classified patterns and the red entries are the total percent of misclassified cases relative to the size of T_c. The matrix data defines the accuracy of the developed model to yield accurate selection of the fitness function solver for the defined input position vector (particle) dataset.

FIGURE 7.16: Rosenbrock ANN Pattern Recognition Confusion Matrix Analysis

The proportion of $\%AC$ relative to the overall size T_c in Figure 7.16 is used to assess the accuracy of the defined model to achieve true classifications for the respective data distribution subsets. Overall $\approx 96\%$ of the classifications are correctly estimated by the surrogate model from the training sample size of 9,636 points. The validity of the developed pattern recognition model is confirmed by the confusion matrices for the validation and test data libraries. The T_c in the validation set equals 4,817 position vector points. The surrogate model correctly generalises the outputs for $\approx 96\%$ of the defined sample size. The testing sample size which is independent to the training and validation sets for model development, is characterised by a sample size of $T_c = 1,605$ points. Pattern classification of the data points by the developed surrogate model yields accurate data representation for $\approx 96\%$ of the overall test sample size. The accuracy of the network is assessed by the compilation of the training, validation and test data points into one confusion matrix. From the overall sample size of $T_c = 16,058$ points, $\approx 96\%$ are correctly generalised by the defined model. The confusion matrix confirms the validity and feasibility of the developed surrogate model to yield true pattern recognition classifications.

An histogram of the approximation error distributions by the surrogate model on the respective data subsets is presented in Figure 7.17.

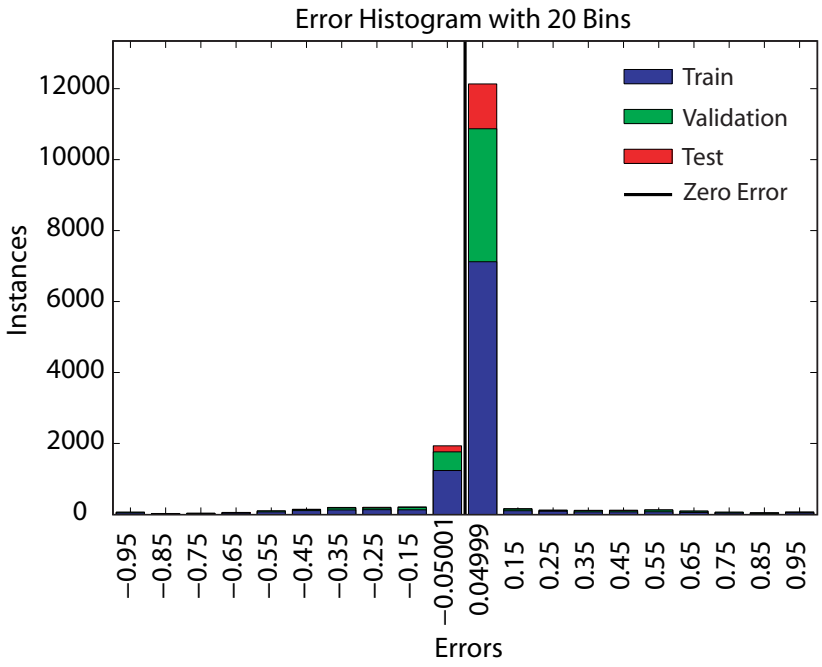

FIGURE 7.17: Rosenbrock ANN Pattern Recognition Training Error Histogram

The error distribution as a measure of the difference in classifications between theory and approximated data of the pattern recognition model is presented in Figure 7.17. There are $\approx 12,000$ points from a total of $16,058$ which are modeled within an error interval of $[0.001, 0.055]$. The remaining test points are distributed by higher error intervals that are offset to the identified minima range. At the highest error magnitude of $\approx \pm 0.95$, the number of data points at this region are minimal relative to the overall population sample size.

The relationship between the true positive (TPR) and false positive rates (FPR) of the approximated classifications relative to theory for the presented dataset T_c is needed. The methodology will map the scope of the classification errors for the defined problem by the developed approximation model. A receiver operating characteristic (ROC) curve developed by Zweig and Campbell [220] is used to model the defined relationship between the defined parameters.

The ROC curve is characterised by the FPR on the x and TPR on the y axes in Figure 7.18. The TPR is a measure of the correct positive classifications of the model during training relative to all theory-based positive classifiers in the data. The FPR is a measure of all incorrect positive classifications for corresponding negative classifiers in the sample population. The ROC curve distinguishes the relative trade-offs between true positive and false positive classifications.

The ROC space is modeled by a line of non-discrimination (diagonal line in Fig. 7.18). Data points that are above the diagonal are representation of true classification results and points that are below are poor classifiers. The validity of the model classification estimations are based on the topology of the ROC curve. A perfect model will be represented by 100% sensitivity with no false negatives. The sensitivity and specificity parameters will equal one. The corresponding ROC curve will originate at (0,0), it will then be generalised about (0,1) and transit to point (1,1). As the ROC curve approaches the optimal point (OP) at (0,1), which is indicative of a high true positive and a

low false positive rate, the model will output acceptable classifications to distinguish between cases and non-cases for the defined problem type.

The ROC curve defines the validity of the modeled relationship between data sensitivity by the TPR versus specificity as a function of FPR for binary-based classification problems. The analysis is addressed by integrating each data entry from the confusion matrix to a point in the ROC space. The representation of the generated ROC curve will yield:

- An alternate data representation approach to the confusion matrix to confirm the validity of model classification predictions of the developed network. The area under the ROC curve (AUC) will provide a measure of the goodness-of-test. The larger the AUC the greater the accuracy of model classifications that result in no false positives and no false negatives.
- The OP of the ROC curve for the respective data subset within A_2 is established. The location of the OP relative to a model with perfect classifications at (0,1) is evaluated.
- The ROC curve further defines the probability threshold (P_t). The term is a decision point threshold in reference to the minimum predicted positive class probability that corresponds to a true positive class estimation. The default P_t of a specific class outcome is 50% for binary classifications. If $P_t < 0.50$ class zero is classified, else class one is activated. The problem specific ROC curve is analysed to establish the exact P_t measure for the modeled data classifications.

The ROC curve for the Rosenbrock test function is presented to confirm the accuracy of the developed pattern recognition model to achieve true classifications in Figure 7.18. The classifier is related to the choice of solver within a binary format definition. It distinguishes between a fitness analysis by the developed ANN function approximation model or by the theoretical solver.

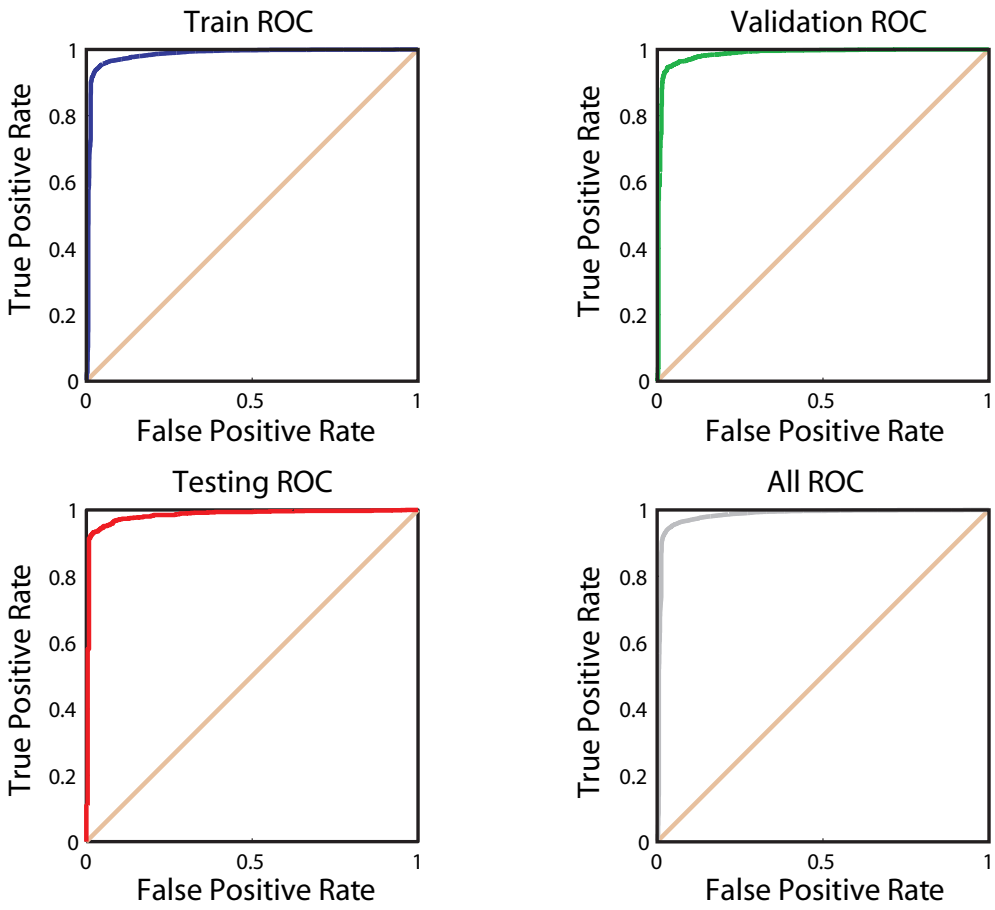

FIGURE 7.18: Rosenbrock ANN Pattern Recognition Receiver Operating Characteristic

The classification performance of the developed pattern recognition model is confirmed in Figure 7.18. The optimal points of the ROC curve for the defined population subsets are about (0,1) which is indicative of an accurate model. The performance measure of the ROC curve for the training, validation, test and the compilation of the tree data subsets as a function of the AUC including the OP is presented in Table 7.3.

TABLE 7.3: Rosenbrock Function - ANN Pattern Recognition Classification Accuracy Measure by ROC Curve Representation

Performance Measure	**Train**	**Validation**	**Testing**	**All**
AUC	0.9832	0.9851	0.9831	0.9837
OP	(0.0713, 0.9646)	(0.1194, 0.9778)	(0.1076, 0.9734)	(0.0777, 0.9654)

The AUC of the respective data subsets is ≈ 1 such that the classifications are near perfect in Table 7.3. The classification accuracy is verified by the AUC of the validation and test data population subsets. Recalling that the validation set is applied to avoid data overfitting during training and the test sample is used to independently verify the classification performance accuracy of the developed surrogate model. The defined population sets are independent of the training points. The generalisation performance of the validation and test points as a function of the AUC is ≈ 1 and

accordingly the accuracy of the developed model is confirmed. The classification performance of all data subsets from the developed pattern recognition model is verified with an AUC that is ≈ 1.

The OP of the ROC curve for the respective data subsets further confirms the validity of the surrogate model to yield accurate classifications in Table 7.3. The OP of the training set is about the perfect classification region of (0,1) at (0.0713, 0.9646). The OP of the ROC curves for the validation and test data subsets is (0.1194, 0.9778) and (0.1076, 0.9734) respectively which further confirms the accuracy of the developed surrogate model. The OP that is representative of the points in A_2, hence the collation of the complete data population set is (0.0777, 0.9654). The measure is about the perfect classification area (0,1), hence is representative of a model that will output accurate classifications.

To classify the boundary between the binary-based classes of zero and one for fitness function analysis by the approximate or the theoretical-based solver respectively, an operating threshold value is established. By default a classification threshold of 0.50 is defined as the boundary between the two classes. To model the exact data intersection region, the ensemble accuracy of the classification model by the TPR against the threshold of the classifier scores is presented.

The classifier scores are in reference to the FPR and TPR. The number of TP count observations with scores greater or equal to the reference threshold are identified for each threshold. Similarly the FP observations and the corresponding classifier scores that are greater or equal to the reference value are identified. The negative counts for TN and FN are defined by the process outlined. The established thresholds are arranged in a descending order that is equivalent to the ascending arrangement of the positive counts. The first threshold in the data array is representative of the highest 'reject all' threshold and the corresponding FPR and TPR for TP=0 and FP=0 are established. The last threshold value is in reference to the lowest 'accept all' threshold for which TN=0 and FN=0.

The ensemble accuracy versus the established data thresholds for the Rosenbrock test function is modeled in Figure 7.19.

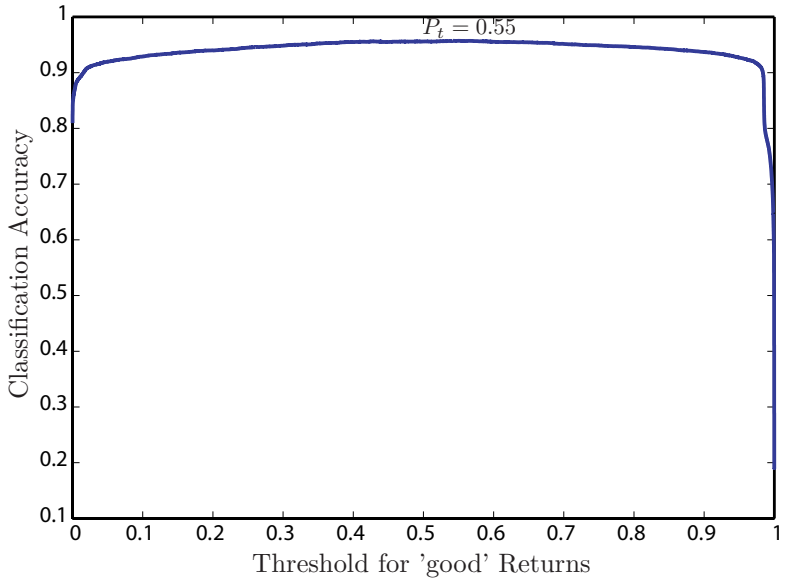

FIGURE 7.19: Rosenbrock ANN Pattern Recognition Classification Ensemble Accuracy

A data plateau extending between thresholds ≈ 0.40 and ≈ 0.60 is evident in Figure 7.19. The exact optimal threshold corresponds to the point with maximum classification accuracy. The established boundary for the Rosenbrock test function is 0.55. Hence, an output classification from the developed pattern recognition model that is less than 0.55 will represent a fitness analysis of the candidate input point by the surrogate model. The fitness for position vectors with classifiers that are ≥ 0.55 will be established by the theoretical solver.

The performance charts presented in this section in reference to the Rosenbrock test function to define the design definition of the ANN function approximation model, is further presented for the Ackley, Michalewics and Schwefel test functions in Appendix L. The design definition of the novel pattern recognition model and the corresponding performance charts to classify between the solver types for fitness analysis is also presented in Appendix L for the identified benchmark test functions.

B. Design Demonstration on Benchmark Test Functions

The principles of the novel process is demonstrated. The results by the developed online-based surrogate training approach coupled with the AM-PSO is presented in Table 7.4 for design optimisation simulations on benchmark test functions. The data is compared to the AM-PSO simulations with the theoretical fitness function evaluator from Table 3.6. The benefits of the defined, surrogate-assisted approach for design optimisation is verified.

TABLE 7.4: Validation of the online-based ANN Training Methodology with AM-PSO Algorithm for Design Optimisation

Function	**Ackley**	**Michalewics**	**Rosenbrock**	**Schwefel**
Converged Fitness				
Literature	3.75e-015 [116]	-9.66e+000 [114]	6.98e-001 [116]	0 [116]
AM-PSO (Chapter 3, Tab. 3.6)	4.44e-015	-9.66e+000	2.15e-001	1.55e-004
AM-PSO / ANN (Alg. 7)	4.44e-015	-9.66e+000	2.50e-003	1.94e-004
Flow Solver Evaluations				
Literature	30,000 [116]	20,000 [114]	30,000 [116]	30,000 [116]
AM-PSO (Chapter 3, Tab. 3.6)	18,459	6,257	28,623	6,164
AM-PSO / ANN (Alg. 7)				
• Exact Solver	14,878	5,760	21,212	5,431
• ANN Solver	1,862	352	3,447	268
• Total Evaluations	16,740	6,112	24,659	5,699
Computational Efficiency*	($\downarrow$) $\approx 20\%$	($\downarrow$) $\approx 8\%$	($\downarrow$) $\approx 26\%$	($\downarrow$) $\approx 12\%$

* **Reduction in exact solver evaluation by the AM-PSO / ANN method relative to the AM-PSO simulations with exact solver only from Chapter 3, Tab. 3.6**

The feasibility and computational efficiency of the novel, online-training surrogate development process within the AM-PSO structure is validated in Table 7.4. The optimisation simulations converge to the established theoretical minima for the respective test function type. Hence, fitness evaluations by a surrogate to the exact model does not affect convergence to a true solution region. The design principle of establishing the fitness of non-dominating data points in the swarm by an approximation model to the exact solver is verified.

As the convergence to a true optimal point is confirmed in Table 7.4, the benefits of the surrogate-assisted optimisation process is measured as a function of the computational efficiency of the design process relative to the implementation of an exact fitness evaluator only in the design process. From the total fitness evaluations by the AM-PSO / ANN approach for the respective test function type, solver calls to the approximation model are limited relative to the analysis by the theoretical model. This is based on the setup of the computational algorithm, where data points for analysis by the exact or surrogate model are selected based on the expected, impact-of-importance of the candidate position vector on the design goal. A limited number of fitness calls to the surrogate model represents a swarm to be in a region bounded about a global optimal, hence a large population of particles are a potential solution to the design problem. To maintain fitness function integrity, the analysis of the respective and promising search particles is established by the theoretical solver. Erroneous data points are accordingly identified and the fitness is estimated by the surrogate model.

The integration of the ANN function approximation model into the optimisation process reduces the total fitness function calls made to the exact solver relative to the design approach with a theoretical fitness evaluator only from Table 3.6. Reductions of $\approx 20\%, \approx 8\%, \approx 26\%$ and $\approx 12\%$ are achieved for the Ackley, Michalewics, Rosenbrock and Schwefel test functions respectively in Table 7.4 in comparison to the presented data with a stand-alone theoretical solver only. The integrity of the developed surrogate-assisted design model in Algorithm 7 for implementation into the DNO process is verified.

The validity of the developed online-training surrogate development process within the AM-PSO structure has been verified on benchmark test functions. In Chapter 3 the validity of the AM-PSO algorithm was confirmed on the identified test problems. It was hypothesised that the design simulation results, to confirm the validity of the AM-PSO algorithm on the defined test functions will be transferable to airfoil design simulations. The assumption was based on the similarity in problem scope between the test functions and airfoil design problem. The following criterion were considered to verify the merits of the defined assumption:

- The problem dimensionality as a function of the number of design variables applied to define the test functions is comparable to airfoil design simulations. The dimensional size of the test functions for validation purposes is set at $D = 10$. The problem dimensionality of HALE and transonic design simulations is based on the airfoil shape parameterisation function used. Since the PARSEC-Modified method is integrated into the design process with reduced modelling by the elimination of the least contributing variable to the objective function, the dimensional size becomes $D = 12$ (Sec. 4.2.2.2). The size of D applied for validation simulations is comparable to the underlying aerodynamic shape design problem within the scope of this thesis.

- The solution topology of the Ackley, Michalewics and Schwefel test functions is comparable to HALE and transonic design problems. The defined test functions are multi-modal. Namgoong [41] verified a multi-modal solution topology exists for transonic airfoil design problems. The analysis in Section 6.2 verified a multi-modal solution landscape for HALE shape design problems. Hence, with the confirmation of the similarity in solution topology landscape type between the test functions and airfoil design processes, the performance of the AM-PSO algorithm for convergence to the theoretical minima for the modeled test functions was validated (Tab. 3.6).

Hence, it was assumed that the validity of the AM-PSO method will be transferable to airfoil design problems also.

- The validity of the AM-PSO algorithm to facilitate acceptable airfoil design simulations at HALE and transonic flight envelopes was confirmed in Chapter 6. The performance of the established optimal by the developed DNO approach was superior to the findings reported in the literature. The assumption of validating the AM-PSO algorithm on mathematical test functions to yield acceptable airfoil design simulations was confirmed.

As the design principles of the online-training based ANN method with the integration of the AM-PSO algorithm have been validated on the test functions, it is assumed that the identified design merits will be applicable to airfoil design simulations at HALE and transonic flight envelopes also. Based on the defined similarity of problem dimensionality and the solution topology type between the test functions and airfoil design problems, performance validations on the benchmark test functions by the novel surrogate-assisted optimisation approach will be compatible to airfoil design simulations. The hypothesis was confirmed during the AM-PSO algorithm design development and validation process. The confirmed merits of solution feasibility and computational efficiency of the AM-PSO method on the benchmark test functions were also evident on airfoil design simulations. As the scope of the two optimisation problems was similar, the performance merits of the AM-PSO method was applicable across the design processes examined. Similarly the confirmed performance merits of the developed online-training based ANN algorithm on benchmark test function will be applicable to airfoil design simulations. Further improvements in computational efficiency are expected by the application of the novel surrogate-assisted methodology into the DNO process relative to a design structure with a stand-alone, time-intensive high-fidelity flow solver only for airfoil design.

7.4 Summary

The fundamentals of the surrogate-assisted design and development approach for optimisation applications was presented. An approximation model for optimisation simulations was used to estimate the fitness with negligible time relative to the computation of the theoretical equations in the objective function. Aerodynamic shape optimisation simulations require the use of high-fidelity and time-consuming flow solvers for enhanced flight performance accuracy. Solving the RANS equations with a turbulence model increases the demand on computational resources. The development of an accurate surrogate model to the flow solver will address this issue and facilitate efficient shape design simulations.

The offline and online ANN training processes were defined and principles demonstrated on select design optimisation problems. A surrogate model developed by the offline-training approach was characterised by a maximum generalisation error on a select airfoil for lift and drag by $\approx 614\%$ and $\approx 54\%$ respectively (Tab. 7.1). The use of the offline-based ANN model for airfoil optimisation resulted in a false measure of fitness of the converged optimal profile relative to theory (Tab. 7.2). This was attributed to the high generalisation errors within the surrogate model.

A novel online-training ANN methodology within the context of the AM-PSO optimisation process was developed to address the demerits of the offline-training approach. The results obtained by

using the developed method consistently converged to the theoretical minima for a number of select benchmark test functions. The computational efficiency of the novel approach further confirmed the merits of the surrogate-assisted structure. Computational time savings in excess of $\approx 26\%$ were achieved relative to a design structure with a stand-alone theoretical fitness function evaluator only. It should be recalled that the performance of the AM-PSO algorithm was validated in Chapter 3. It was shown that the developed optimisation method achieved solution feasibility (convergence to the theoretical optimal) and required significantly fewer design iterations to convergence than the algorithms in the literature. The development of a surrogate model in parallel to the AM-PSO optimisation cycle further enhanced the computational efficiency of the search process relative to the established performance of the AM-PSO from Chapter 3. The computational efficiency of the optimisation structure with a surrogate-assisted model was further enhanced by the use of the novel surrogate-assisted algorithm while maintaining solution feasibility.

Chapter 8

Concluding Remarks

8.1 Research Summary

The aim of this thesis was to develop an airfoil design optimisation architecture for a MM-UAV. The design of a mission adaptive platform by shape morphing will address the issues and challenges of high acquisition costs and limited operating efficiency over extended flight envelopes. A MM-UAV is to exploit the benefits of a uni-mission UAV by performing dull and dirty missions over extended periods of time. By morphing the wings of a MM-UAV to mission-specific flight regimes, the platform will exhibit optimal operating efficiency over extended Reynolds and Mach number flight envelopes. Hence, acceptable flight performances at low-speed HALE and high-speed SEAD sorties is achievable.

Design methodologies in aeronautics follow a multidisciplinary process by the integration of several engineering disciplines. The design principles presented in this thesis addressed the airfoil aerodynamic requirements of the MM-UAV platform for operation at HALE and transonic flight envelopes. The optimal airfoils at the defined flight conditions were established by novel design processes. The aim of the research within the scope of the defined MM-UAV design project was to develop novel aerodynamic design and optimisation algorithms that yield considerable performance benefits relative to present design methodologies that are used in the open literature for the intent design problem. A comprehensive review of related works confirmed the merits of the algorithms developed relative to present off-the-shelf design systems by the measure of solution feasibility and computational efficiency.

8.2 Contributions

The thesis has demonstrated the following contributions to the present body-of-knowledge:

1. **Adaptive-Mutation Particle Swarm Optimisation Algorithm**
   A novel optimisation algorithm was developed. The methodology was characterised by hybrid local and global search mechanisms. At search initialisation a global search phase follows. As the search converged to a promising region, a local search process is activated. To mitigate

convergence to a sub-optimal solution region, adaptive-mutation operators were developed and applied to increase search diversity. A probability function was used to control the rate-of-mutation for population diversity, hence to maintain a low fitness function evaluator count due to the introduction of mutation operators.

The theoretical merits of the developed AM-PSO algorithm were evaluated against the Standard-PSO (S-PSO) and published Adaptive Inertia Weight PSO (AIWPSO) method [8] on benchmark test functions. It was shown that the AM-PSO method consistently converged to a lower fitness than the S-PSO and AIWPSO with fixed search iteration count (Sec. 3.6.1). The theoretical benefits of the novel adaptive inertia weight function (Eqn. 3.8) which balanced the search phase between local and global phases was confirmed. The scope of the DoE process further evaluated the affect of the scalar step on fitness which is related to the particle minimum and maximum speed as a percentage of the dimensional search space. The results were presented by a contour based SOM process which mapped the relationship between the design parameters over four validation test functions. The results confirmed the scalar step length was problem dependent and needs to be defined for the specific design problem type. The parameter cannot be arbitrarily set as practiced in the published literature as this resulted in a sub-optimal design performance.

The validation of the AM-PSO on benchmark test functions was extended and confirmed relative to several off-the-shelf PSO algorithm types including the local-best model [112]. Test function optimisation simulations by the AM-PSO for verification purposes was defined with an extended termination criteria based on the settings used in the literature [114, 116] to facilitate a valid performance comparative analysis between the different methods. The impact of wall-boundary conditions on fitness convergence was evaluated (Sec. 3.6.2.2). The test simulations confirmed that the random wall boundary condition exhibited the lowest fitness magnitude in comparison to the absorbing and reflecting methods for multi-modal solution topologies.

Performance comparison of the AM-PSO with published data verified the merits of the developed algorithm (Sec. 3.6.2.2: Part B) as it consistently outperformed the methods reported in the literature [114, 116]. The AM-SPO converged to the theoretical minima with a perfect success rate of 100% over 30 independent simulations for the three functions and a 97% success measure for the remaining model as part of the design validation process on benchmark test functions. The success rate matched the performance of the best reported algorithms in the open literature, hence confirmed the merits of the developed search operators in the AM-PSO architecture. The true benefits of the AM-PSO algorithm were related to the measure of efficiency to convergence. Over the four benchmark test functions evaluated, the AM-PSO converged to the theoretical minima with significantly lower fitness function calls than the reported published data (Sec. 3.6.2.2: Part B). Computational fitness function call reduction in excess of 98% was established with the average saving in excess of 80% over the four test functions relative to the best reported algorithms in the literature.

Demonstration of the AM-PSO algorithm for validation purposes confirmed the computational merits of the novel optimisation process. The fundamental design principles developed facilitated solution convergence to the theoretical optimal. The computational iterations needed to achieve convergence were significantly less than off-the-shelf algorithms in the literature, hence algorithm efficiency was validated while achieving solution feasibility.

2. **Definition of Airfoil Design Solution Search Space**

   The following sub-components were developed to facilitate valid airfoil design simulations:

   (a) **Development and Application of a Variant, Off-the-Shelf Shape Parameterisation Function**

   A novel PARSEC-Modified airfoil shape function was developed to maximise shape generation flexibility and accuracy (Sec. 4.2.1.3). The methodology was based on the fundamentals of the original PARSEC model as developed by Sobieczky [28]. Airfoil upper and lower surfaces were independently parameterised to enhance the flexibility and accuracy of the proposed shape function. The AM-PSO algorithm would theoretically model infinite airfoil geometry types that are applicable to HALE and transonic flight envelopes during the iterative design process. These included highly cambered nose shapes and divergent trailing edge (DTE) profiles that are representative of low and high speed flight operations respectively.

   (b) **Evaluation of Shape Parameterisation Function Validity**

   The theoretical merits of the PARSEC-Modified airfoil shape function were assessed against several off-the-shelf methods including the Hicks-Henne, Wagner, Legendre, Bernstein, NACA and the CST approach developed by Kulfan [36, 50, 60]. A novel inverse shape fitting optimisation process (Fig. 4.1) was formulated by a least-squares formulation to assess the flexibility and accuracy of the shape function types. The AM-PSO algorithm was integrated in the verification process and the objective function was defined to minimise the shape difference between a user-defined benchmark and the approximating airfoil parameterised by the respective shape function type. Several target airfoils were used in the inverse shape fitting process. The airfoils selected were based on the intended design goal of the respective shape such that the flexibility and accuracy of the shape functions could be verified across different airfoil types that operate under disparate flight conditions. The operating conditions of the target airfoils were based on the following categories (Tab. 4.7): **a)** HALE: HRN; **b)** HALE: MRN; **c)** NACA; **d)** LRN; and **e)** HRN: High-Speed. The analysis confirmed the developed PARSEC-Modified method is characterised by superior flexibility and accuracy in comparison to off-the-shelf systems (Sec. 4.2.1.3).

   (c) **Design Variables Pre-screening Analysis**

   The impact of the PARSEC-Modified function airfoil shape variables on the objective function of drag was quantitatively evaluated by Morris's [146] pre-screening technique at HALE and transonic flight envelopes. The variable $t_{eg_{low}}$ was identified with the lowest contribution to drag (Tabs. 4.10 and 4.11 at low and high-speed operations respectively). Theoretically by setting $t_{eg_{low}}$ to a base value that is representative of an off-the-shelf airfoil with similar operating conditions to the design specification, the computational efficiency of the design optimisation process will be enhanced. The search space of the objective function, hence the scope of the solution topology is reduced by the elimination of un-important design variables. It was confirmed that by the elimination of the least significant design variable does not compromise the obtainable optima, hence feasibility yet it reduces the computing cost significantly.

   (d) **Definition of Airfoil Solution Search Space Envelope for HALE and Transonic Flight Designs**

The developed inverse shape fitting methodology was used to map the dimensional search space of the specified design problem. The magnitude of the design variables were established by the AM-PSO algorithm for the identified off-the-shelf airfoils which were representative of an operating profile over an extended flight range envelope. The shape parameters were modeled in a solution space mapping chart as a function of the airfoil characteristics from Equation 4.4. The results validated the assumption that the magnitude of the shape variables are limited to specific regions in the solution topology as a function of the operating conditions of the respective airfoil type. Transonic-based airfoils were characterised by sharper leading edge radii (Fig. 4.22 and Tab. 4.9) in comparison to HALE-based profiles (Fig. 4.21 and Tab. 4.8). The search intervals of the design variables were mapped accordingly. Theoretically the methodology will facilitate an efficient optimisation process. The AM-PSO will limit the search to solution viable topologies only, instead of wasting computational resources modelling shapes that are not related to the design goals.

3. **Validation of the Developed Optimisation Approach by Airfoil Design Simulations**

   (a) **Assessment of Airfoil Solution Search Space Convergence**

   The solution topology for HALE and transonic airfoil designs was multi-modal. The application of a stand-alone gradient optimisation algorithm for shape design was not a viable design approach. The gradient optimisation process leads to convergence about the design starting point and not the global optimal. Evolutionary design algorithms were used to address this issue.

   The AM-PSO was not sensitive to the selection of solution search starting point for airfoil design optimisation simulations. The definition of a well-defined search initialisation point, a necessity in gradient-based methods was not needed in the swarm search process. Design optimisation simulations on a simplified airfoil design objective definition (Eqn. 6.1) verified swarm convergence to a specific point in the solution topology regardless of the state of the initial swarm at initialisation (Tab. 6.3).

   A comprehensive DoE analysis was undertaken to validate the developed optimisation structure for airfoil design simulations. The results confirmed that a swarm size of 20 particles, with the PARSEC-Modified shape function mapped with 11 design variables for HALE (Tab. 6.18) and 12 for transonic (Tab. 6.22) would be sufficient for single-point design simulations.

   The airfoil design simulations by the AM-PSO algorithm confirmed that the solutions obtained are not the true optimal. Instead convergence about a region bounded about the true minima point was established. A gradient-method with the definition of the AM-PSO solution as the search starting point exploited the benefits of a well-defined search starting point to aid convergence to the true minima.

   The design development and integration of three disparate search termination units as a function of the collective search behavior of the swarm, provided an acceptable measure of search termination measure. The novel measures mitigated premature termination by the assessment of each particles personal search experiences. Convergence was assessed based on the collective consensus by the swarm with regards to the feasibility of the examined solution region over an extended user-defined design cycle.

The merits of the developed optimisation structure was verified for HALE airfoil design. The elimination of the least-important design variable $t_{eg_{low}}$ as identified by the proposed pre-screening analysis resulted in significant computational time savings, hence enhanced computational efficiency. The shape variables screening process resulted in 113 fewer design iterations to convergence in comparison to the integration of the full set of thirteen, PARSEC-Modified shape variables. The affect of eliminating $t_{eg_{low}}$ from the shape design analysis for a swarm size of 20 particles and with the assumption that 50% of the particles are mutated at each design evolution, resulted in 3,390 fewer fitness function evaluations by the high-fidelity solver than a shape design process with full thirteen variables. The performance of the solution obtained was shown not to be compromised by the use reduced variable modelling, when compared to the benchmark NLF(1)-0416 airfoil. Drag reduction of 7.41% and 7.26% was achieved relative to the defined benchmark with the full and reduced variable set modelling respectively.

Assessment of airfoil solution search space convergence at transonic flight envelope was confirmed. The data to the DoE analysis validated a swarm size of 20 particles was needed to facilitate converged shape design simulations in Figure 6.28. Solution search space convergence as a function of the objective fitness was obtained by the PARSEC-Modified function with 12 variables in Table 6.22.

The developed DNO approach was used for airfoil design at transonic Mach numbers with a high-fidelity flow solver for fitness evaluations. The solution feasibility and computational efficiency was evaluated against published data [9, 41]. The optimal profile represented a 35% reduction in drag in comparison to the benchmark RAE 2822 airfoil at the specified flight condition. The magnitude in drag reduction of the optimal airfoil, relative to the identified base shape was in agreement with the published results of Namgoong [41] using the GA. The developed AM-PSO method converged to the solution with significantly fewer solver calls in comparison to the reported data in the literature [41]. The hybrid design approach required approximately 80% fewer fitness function evaluations than that acquired in the design methodology used by Namgoong [41].

Despite the establishment of optimal results based on an aerodynamic shape design problem formulation for HALE and transonic case studies, the feasibility of the converged shape was not acceptable. The limited internal wedge angles for both low-and-high speed airfoils were limited to approximately zero degrees. From an manufacturing view point, the trailing edge topology was not practical. The definition of structural constraints are needed to address this issue.

(b) **Development of a Robust Airfoil Design Methodology**

In-lieu of a multi-objective problem formulation, a robust airfoil design approach was developed. The methodology has performance merits over multi-point design formulations. The robust approach intelligently selects flight points for drag minimisation through a randomised, stratified sampling approach. The results were validated in comparison to published data for the NLF(1)-0416 airfoil. The results showed a drag reduction of 5% over a user-defined c_l^T flight envelope in comparison to the multi-point design method in Figure 6.13. On the other hand, the c_{lmax} performance was compromised and was 5%

lower than the identified benchmark in Table 6.9, as would be expected from the "No free lunch" theory.

(c) **Data-mining for Optimisation Post-Processing**

A novel post-processing of optimisation results test methodology was developed. A data mining technique with Self-Organising Maps yields a visual interpretation of the search topology about the identified solution. The SOMs qualitatively modelled the scope of the solution topology about the identified minima point from a local and/or global optimisation search process. The convergence of the design variables about an optimal region was confirmed for single-point airfoil design simulations in Figure 6.15. A visual inspection of the solution fitness region as a function of the user defined objectives and constraints facilitated an efficient and valid approach to verify the viability of the obtained solution.

4. **Development of a Novel Surrogate-assisted Design Optimisation Methodology**

(a) **Offline-training Surrogate Model Development coupled with AM-PSO for Optimisation Simulations**

A DoE analysis was defined to model the sensitivity of the ANN parameters on model approximation accuracy for airfoil design simulations. The affect of training population size, including the number of hidden-layers and neurons and transfer function types between the hidden-layers on the accuracy of the ANN for lift (Fig. 7.4) and drag (Fig. 7.5) coefficient estimation was modeled. It was confirmed that with a well-defined training population size and ANN structure topology, the accuracy of the aerodynamic parameters was within an acceptable threshold for 98% of the airfoil sample size that was tested in Figure 7.6. There remained select few airfoils that were modeled with excessive approximation errors in Table 7.1. Airfoil design optimisation by the application of the offline-training based ANN for fitness evaluations resulted in a false measure of converged shape fitness due to the excessive aerodynamic performance estimation errors for select airfoils in the solution space.

The results did confirm the computational efficiency of the shape design process is enhanced considerably by a surrogate-assisted design model. Due to the excessive approximation errors on select airfoils, the methodology was regarded infeasible for airfoil design simulations. Hence, an ANN that is developed by the online-training approach within the AM-PSO algorithm was proposed to address the identified limitations. The results of the DoE analysis which mapped the relationship between the ANN structure parameters on model accuracy were used to define an accurate surrogate model within the online-training architecture.

(b) **Online-training Surrogate Model Development coupled with AM-PSO for Optimisation Simulations**

A novel online-training ANN model that operates within the AM-PSO design structure was developed. The training points used for ANN definition were based on the search processes of the AM-PSO algorithm. Only the most promising data points in reference to the defined problem type were used for model development. An archive of position vector points and corresponding fitness values was generated and updated at select search evolution stages. They were then used to train an ANN function approximation model by

mapping the relationship between the position vectors as inputs and the corresponding fitness as output. The ANN training simulations operated in parallel to the search processes of the AM-PSO. The generalised performance of the ANN model was evaluated. The error, as the difference in fitness between theory and approximated magnitude was established.

A second pattern recognition ANN model was defined to model the relationship between the position vectors as inputs and the established fitness estimation error of the ANN function approximation model as output. If the approximation error for a respective input position vector was below a minimum user-defined threshold, a promising data point was assumed and the fitness was computed directly by the theoretical solver. Else, the fitness was estimated by the ANN function approximation model.

The principles of the defined test methodology was verified on benchmark test functions. Convergence to the theoretical minima was achieved, hence model feasibility was verified. The integration of the surrogate-model further enhanced the computational efficiency of the proposed DNO architecture in comparison to a design structure with a theoretical fitness solver only within the AM-PSO algorithm. The verified merits of the novel design approach are suggested to be applicable for airfoil design simulations as well.

The measure of computational efficiency of the developed surrogate-assisted design approach was confirmed on mathematical test functions. The integration of a surrogate model to the theoretical fitness function solver resulted in a reduction of $\approx 20\%, \approx 8\%, \approx 26\%$ and $\approx 12\%$ for the Ackley, Michalewics, Rosenbrock and Schwefel test functions respectively in Table 7.4, in comparison to applying the stand-alone fitness function evaluator only.

8.3 Future Research

1. **Further Application Testing of the AM-PSO Algorithm**
   In this work, the developed AM-PSO algorithm has demonstrated the advantages of the methodology over the variants of the original PSO method presented in the literature for optimisation simulations. The validity of the AM-PSO method for airfoil design simulations was confirmed. The novel algorithm presented performance merits of solution feasibility and computational efficiency over traditional GA-based methods. The test cases presented were limited to select applications. The validity of the developed design algorithm should be examined for complex problems. Design optimisation of aerospace components involving 3D wing designs to nacelle planform configuration must be performed to further confirm the viability of the developed method for aerospace design applications. The sensitivity of the AM-PSO method to yield acceptable shape design configurations over transonic, supersonic and hypersonic flows cases needs to be evaluated.

2. **Extension of the AM-PSO algorithm**
   In the framework of applying the AM-PSO method over disparate problem types, the fundamentals of the design algorithm must be extended. The underlying principles of the developed, adaptive-based mutation principles for search diversity will remain valid. Instead the methodology must be modified from a single-objective to a multi-objective formulation. Hence, multiple objectives can be defined and a Pareto front of the defined design goals can be generated from

which a design compromise is identified. The multi-objective design formulation will not have performance issues that characterise single-objective designs. The definition of arbitrarily defined weight terms, which act as multipliers to the conflicting design goals within the fitness function definition will not be an issue. The sensitivity of the weight terms on the feasibility of the established optima will not be a design issue with multi-objective problem formulations.

The principles of the AM-PSO method must be extended to facilitate optimisation convergence to the theoretical solution for design problems with extended dimensional sizes. The present design algorithm yields acceptable optimisation performances for search topologies limited to $D < 14$. Design modifications may be required to extend the viability of the optimisation method for a search space exceeding $D > 30$.

The flexibility of the AM-PSO method must be extended to facilitate computation by an asynchronous parallel setup. The synchronous approach is not viable within a parallel computing structure as all the design points must be evaluated first before transiting to the next search evolution. The potential to exploit the theoretical speedup that is made available by a parallel computing network is not achieved by the setup used in the thesis, hence computing performance is compromised. An asynchronous evaluations-based AM-PSO algorithm is needed to address this issue. The development process can follow the principles proposed by Venter and Sobieski [221] where a parallel swarm algorithm within an asynchronous evaluations-based structure was developed. Enhanced computing efficiency was achieved in comparison to a swarm architecture centered about a synchronous process. It is expected that a asynchronous-based parallel AM-PSO computing methodology will significantly improve the efficiency of the optimisation simulations in comparison to the synchronous approach.

3. **Extension and Improvement of the Surrogate-assisted Optimisation Methodology**
The convergence to the theoretical optimal by the novel, online-training based ANN methodology within the AM-PSO structure was validated over the presented test functions with enhanced computational efficiency. In comparison the integration of the stand-alone AM-PSO method coupled to the theoretical fitness function evaluator resulted in an extended design iteration process. An AM-PSO algorithm coupled to a surrogate model that is developed based on the online-training approach needs to be evaluated for airfoil aerodynamic shape optimisation simulations at HALE and transonic flight envelopes. The merits of the novel surrogate-assisted approach for aerospace design applications needs to be verified.

   Despite the validated merits of the novel surrogate-assisted design approach for optimisation simulations, the methodology has limitations which must be addressed. The ANN function approximation model will simulate fitness magnitudes for select input position vector points with excessive errors. The developed methodology in this thesis identified expected position vector points that are sensitive to erroneous fitness magnitudes. Despite the expectation that the output of the respective data point will generate a false measure of fitness, the ANN function approximation model was still be used to obtain an estimate of the fitness. Alternate design strategies need to be investigated to formulate the best course of action for data points with excessive fitness approximation errors during the optimisation design cycle.

4. **Application of Kriging-based Surrogate-assisted Optimisation Methodology**
The ANN was used in the thesis as the methodology has been successfully applied in the

literature for aerodynamic coefficient estimation. The Kriging approach has also been used with success for aerodynamic applications. The viability of the Kriging approach for surrogate-assisted, shape optimisation simulations within the AM-PSO structure needs to be explored. A comprehensive performance-based comparative analysis between the two surrogate model types is required to explore the merits and demerits of each method for aerodynamic shape optimisation simulations.

5. **Application of the Adjoint-based Design Optimisation Framework**
   The Adjoint-based optimisation method has been validated in the literature for aerodynamic shape design simulations. The efficiency of the design algorithm is not restricted by problem dimensionality. The methodology has the potential to yield a global optimal for complex solution topologies. Further research analysis is needed to examine the viability of applying the AM-PSO method to establish an initial estimate of the global best followed by the integration of the adjoint solver for gradient estimations (design sensitivities) for a localised optimisation sequence. The coupled AM-PSO / Adjoint-based design formulation has the potential to further enhance the computational feasibility and efficiency of the shape design process for a wide range of problems. The theoretical merits of the hybrid design approach must be demonstrated and validated.

6. **Variable Fidelity Solvers within the Optimisation Structure**
   An overview into the affect of using low and high-fidelity solvers within a shape optimisation simulation needs to be verified. In this thesis, it was shown that a single-point HALE airfoil design process with the AM-PSO coupled to a low and high-fidelity solver resulted in similar profiles at convergence by the two independent simulations with separate fidelity solvers in Figure 6.25. The use of a low-fidelity solver within the AM-PSO for the defined problem is not a design issue. In comparison a high-fidelity code for the respective design application required days of computation time to achieve search convergence. As the comparison of optimal shapes at convergence between the two solver approaches validated solution similarities, the affect of applying variable fidelity codes during specific design optimisation stages for the respective problem needs to be verified. A design structure where a low-fidelity solver is used for time-intensive AM-PSO simulations, followed by a gradient analysis to the AM-PSO derived airfoil by the high-fidelity code needs to be examined. The proposed variable fidelity shape design approach will theoretically enhance the computational time to convergence. The validity of the defined assumption needs to be verified.

7. **Extension of the Presented Optimisation Methodology to Industry Applications**
   The design principles developed in this thesis must be extended for application in real-life problems within the industry. Despite the validation of the developed methodology on 2D problems, the merits of the established approach for design problems with greater degrees-of-freedom ($D > 100$) for complex engineering applications must be explored. It is suggested that the processes applied in this thesis including the shape parameterisation function, design variable pre-screening and definition of solution search space mapping will hold true irrespective of the complexity of the defined problem type.

   Modelling airfoil flow with two/three transport equation turbulence models is not a time-intensive process in comparison to solving the flowfield over 3D geometries, including CFD

simulations for supersonic and/or hypersonic specific flight platforms. Airfoil flow analysis on 2D geometries is resolved in minutes compared to days for a complete aircraft configuration that is coupled with sophisticated turbulence models. The true benefits of the AM-PSO process to yield efficient optimisation simulations in comparison to current off-the-shelf systems is not realised on simplistic, 2D airfoil design processes. It is expected that the merits of the AM-PSO method as confirmed on airfoil design processes will be transferable to shape optimisation simulations of 3D bodies that require complex turbulence models to resolve the flowfield. The computational time savings by the AM-PSO method will be directly proportional to the complexity of the flow solver, hence fitness function evaluator. Time savings in excess of days is achievable for 3D shape design geometries. The validity of the proposed assumption needs to be examined.

The viability of the design principles developed in this thesis must be explored from a multidisciplinary aircraft design view point. Aerospace engineering design disciplines must be integrated to formulate a valid aircraft design process. Each discipline is defined by a set of goals and constraints that must be achieved which results in a design conflict. An analogy is the design of a supersonic business jet with the goal of minimising the sonic boom with low drag at cruise and acceptable performance at off-design conditions. Aircraft geometry constraints are imposed based on minimum volume requirements. The coupling of the design objectives from a multidisciplinary design perspective with the definition of planform constraints may result in a design conflict. The novel design algorithms developed in this thesis need to be applied from an aircraft design perspective. The results will provide an avenue for further design refinement.

Appendix A

Analytical Approach Shape Functions

A.1 Hicks-Henne Functions

$$y(x) = y_0(x) + \sum_{i=1}^{5} x_i f_i(x) \tag{A.1}$$

$$f_i(x) = sin^{\alpha_i}(\pi x^{\beta_i}) \tag{A.2}$$

$$\beta_i = \frac{ln(0.50)}{ln(\pi_i)} \tag{A.3}$$

i	1	2	3	4	5	6	7	8	9	10	11	12	13	14
π	0.025	0.05	0.10	0.15	0.20	0.30	0.40	0.50	0.60	0.70	0.80	0.85	0.90	0.95
α_i	2	2	2	3	3	3	3	3	3	3	3	2	2	1
$\lambda_{i=1,\ldots,14}$	0	1e-4	2e-4	3e-4	4e-4	5e-4	6e-4	7e-4	8e-4	9e-4	1e-3	1.1e-3	1.2e-4	1.3e-4

Table A.1: Convergence to Target Airfoil NACA 0012 by the Hicks-Henne Functions

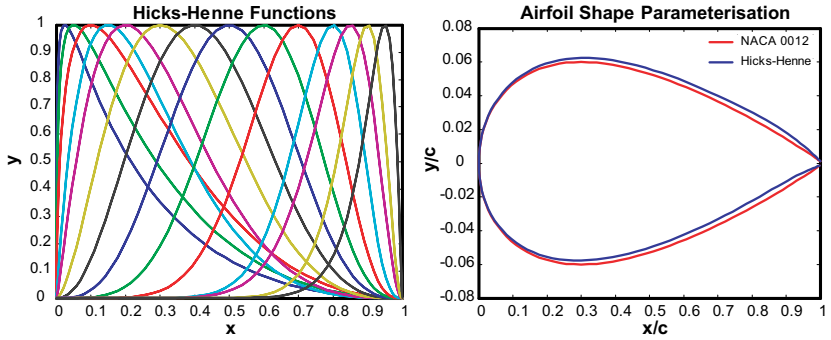

(a) Hicks-Henne Polynomials

(b) Convergence to Target Airfoil NACA 0012 by the Hicks-Henne Functions

FIGURE A.1: Airfoil Shape Parameterisation by the Hicks-Henne Approach

A.2 NACA Functions

$$f_1(x) = \sqrt{x} - x \tag{A.4}$$

$$f_2(x) = x(1-x) \tag{A.5}$$

$$f_{k+1}(x) = x^k(1-x), \text{for } k = 2,3,4,5 \tag{A.6}$$

$$f_7(x) = \sqrt[3]{x} - \sqrt{x} \tag{A.7}$$

$$f_8(x) = \sqrt[4]{x} - \sqrt[3]{x} \tag{A.8}$$

$$f_9(x) = \sqrt[5]{x} - \sqrt[4]{x} \tag{A.9}$$

$$f_{10}(x) = \sqrt[6]{x} - \sqrt[5]{x} \tag{A.10}$$

$$y(x) = y_0(x) + \sum_{i=1}^{5} x_i f_i(x) \tag{A.11}$$

i	1	2	3	4	5	6	7	8	9	10
$\lambda_{i=1,\ldots,10}$	0	1e-4	2e-4	3e-4	4e-4	5e-4	6e-4	7e-4	8e-4	9e-4

TABLE A.2: Convergence to Target Airfoil NACA 0012 by the NACA Shape Functions

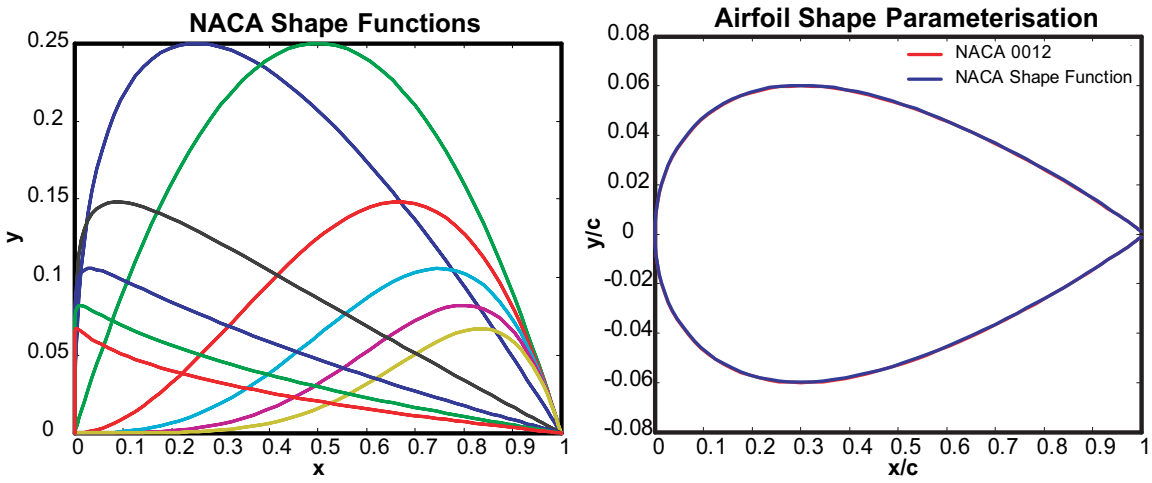

(a) NACA Functions

(b) Convergence to Target Airfoil NACA 0012 by the NACA Functions

FIGURE A.2: Airfoil Shape Parameterisation by the NACA Functions

A.3 Wagner Functions

$$f_1(x) = \frac{\theta + sin(\theta)}{\pi} - sin^2(\frac{\theta}{2}) \tag{A.12}$$

$$f_k(x) = \frac{sin(k\theta)}{k\pi} + \frac{sin[(k-1)\theta]}{\pi} \text{ for } k > 1 \tag{A.13}$$

$$\text{Where } \theta = 2sin^{-1}(\sqrt{x}) \tag{A.14}$$

i	1	2	3	4	5	6	7	8	9	10	11	12	13	14
$\lambda_{i=1,\ldots,14}$	0	1e-4	2e-4	3e-4	4e-4	5e-4	6e-4	7e-4	8e-4	9e-4	1e-3	1.1e-3	1.2e-4	1.3e-4

TABLE A.3: Convergence to Target Airfoil NACA 0012 by the Wagner Functions

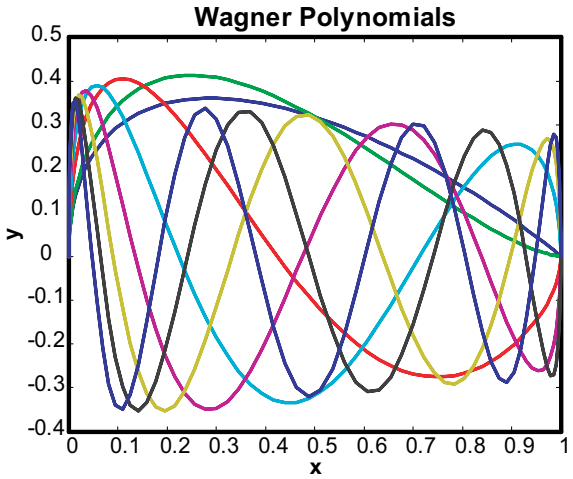

(a) Wagner Functions

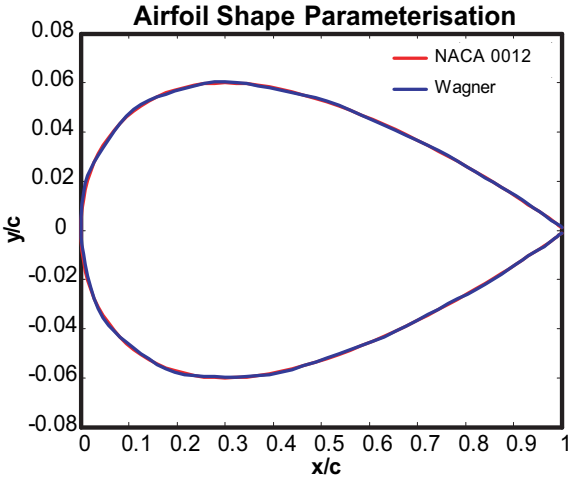

(b) Convergence to Target Airfoil NACA 0012 by the Wagner Functions

FIGURE A.3: Airfoil Shape Parameterisation by the Wagner Functions

A.4 Bernstein Polynomials

$$F_{n,i}(x) = \binom{n}{i} x^i (1-x)^{n-i} \tag{A.15}$$

$$\text{Where, } n = \text{Design Variable Population} \tag{A.16}$$

$$\binom{n}{i} = \frac{n!}{i!(n-i)!}, i = 0, ..., n \tag{A.17}$$

i	1	2	3	4	5	6	7	8	9	10	11	12	13	14
$\lambda_{i=1,...,14}$	0	1e-4	2e-4	3e-4	4e-4	5e-4	6e-4	7e-4	8e-4	9e-4	1e-3	1.1e-3	1.2e-4	1.3e-4

TABLE A.4: Convergence to Target Airfoil NACA 0012 by the Bernstein Polynomials

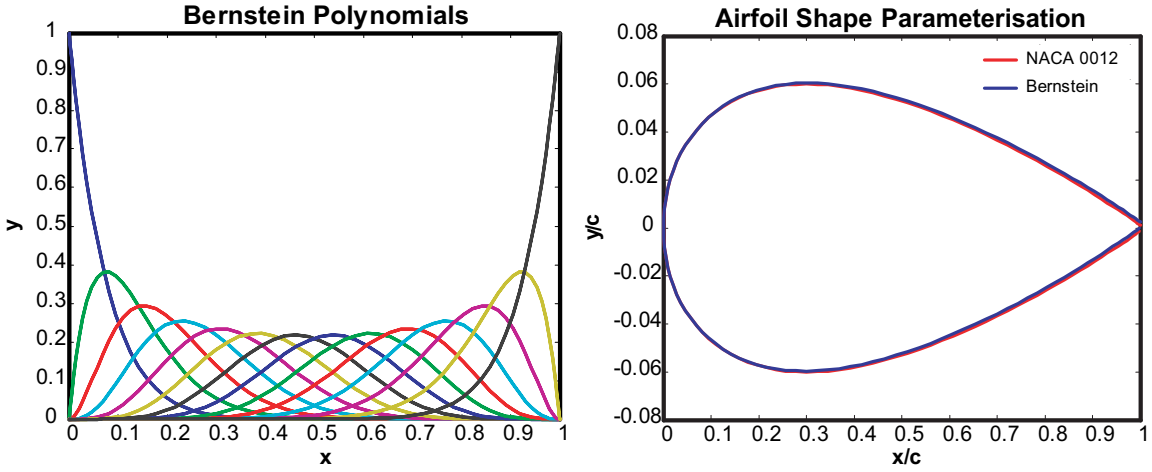

(a) Bernstein Functions

(b) Convergence to Target Airfoil NACA 0012 by the Bernstein Functions

FIGURE A.4: Airfoil Shape Parameterisation by the Bernstein Functions

A.5 Legendre Polynomials

Generated with Rodrigues' formula [222]:

$$P_n(x) = \frac{1}{2^n n!}\left(\frac{d}{dx}\right)^n (x^2-1)^n; \text{ Where, } n = \text{Design Variable Population} \tag{A.18}$$

i	1	2	3	4	5	6	7	8	9	10	11	12	13	14
$\lambda_{i=1,\ldots,14}$	0	1e-4	2e-4	3e-4	4e-4	5e-4	6e-4	7e-4	8e-4	9e-4	1e-3	1.1e-3	1.2e-4	1.3e-4

TABLE A.5: Convergence to Target Airfoil NACA 0012 by Legendre Polynomials

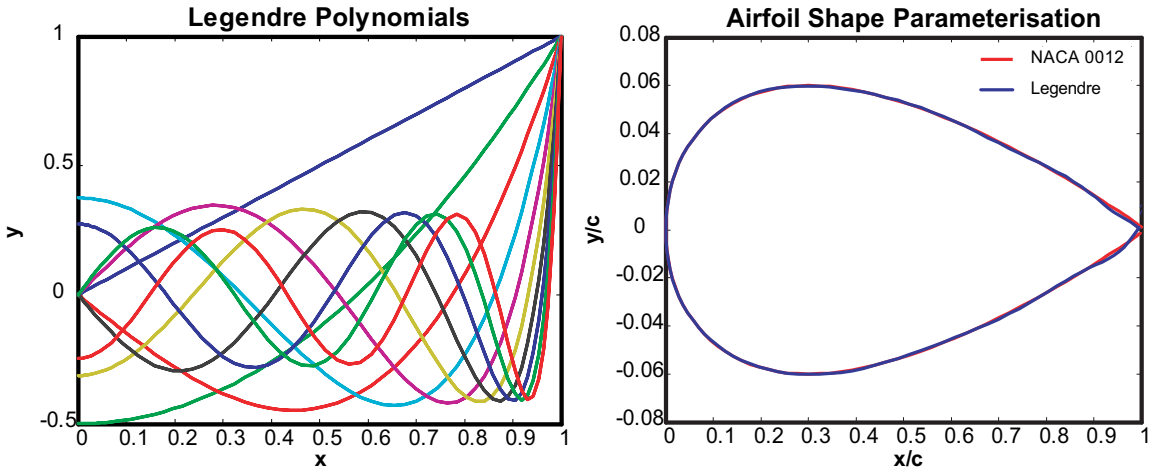

(a) Legendre Functions

(b) Convergence to Target Airfoil NACA 0012 by the Legendre Functions

FIGURE A.5: Airfoil Shape Parameterisation by the Legendre Functions

Appendix B

PSO Test Validation Fitness Contour Plots

B.1 Rosenbrock Function: Fitness Distribution as a function of Particle Population & Maximum Velocity for $D = 10, 20, 30$

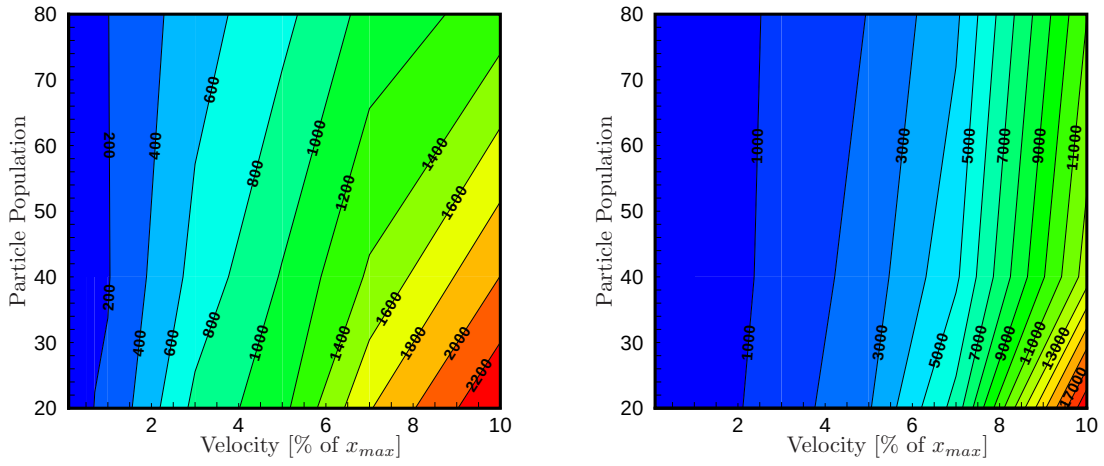

(a) $D = 20$ (b) $D = 30$

FIGURE B.1: Rosenbrock Function: Effect of Particle Population & Velocity on Fitness by the AMPSO Algorithm

B.2 Ackley Function: Fitness Distribution as a function of Particle Population & Maximum Velocity for $D = 10, 20, 30$

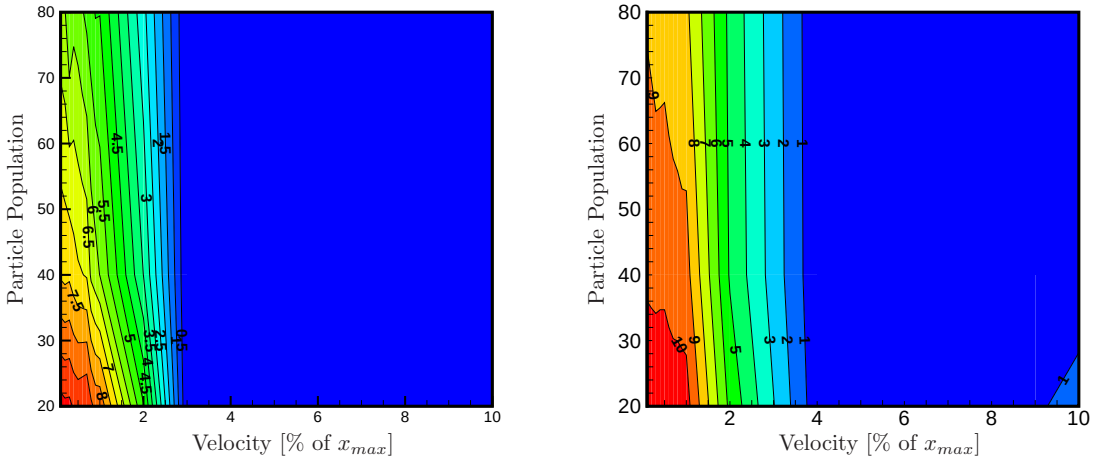

(a) $D = 10$

(b) $D = 20$

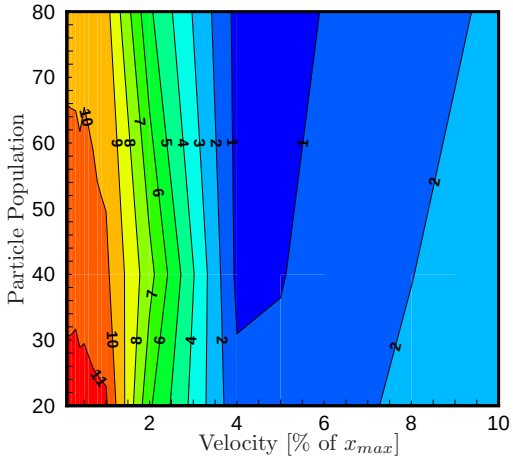

(c) $D = 30$

FIGURE B.2: Ackley Function: Effect of Particle Population & Velocity on Fitness by the AMPSO Algorithm

B.3 Michalewics Function: Fitness Distribution as a function of Particle Population & Maximum Velocity for $D = 10, 20, 30$

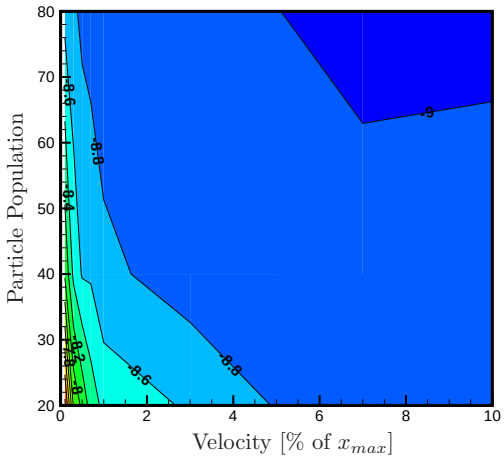

(a) $D = 10$

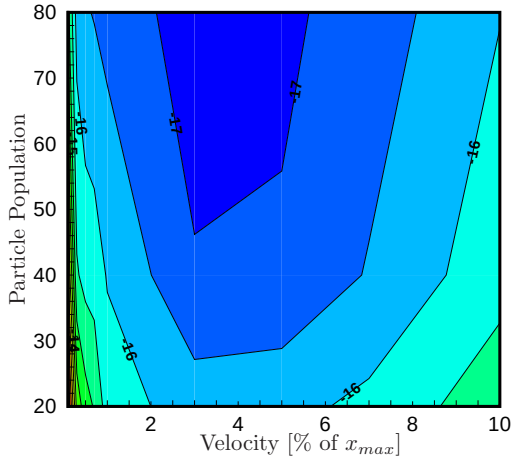

(b) $D = 20$

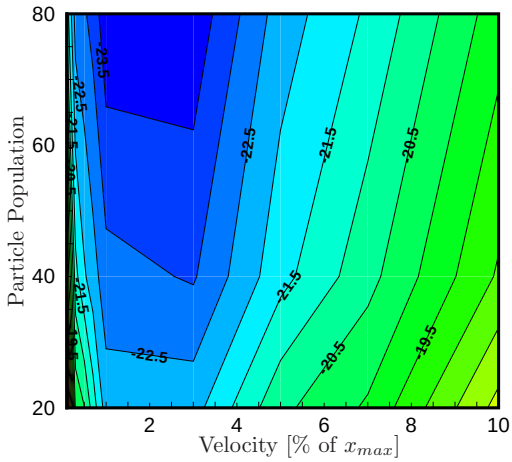

(c) $D = 30$

FIGURE B.3: Michalewics Function: Effect of Particle Population & Velocity on Fitness by the AMPSO Algorithm

B.4 Schwefel Function: Fitness Distribution as a function of Particle Population & Maximum Velocity for $D = 10, 20, 30$

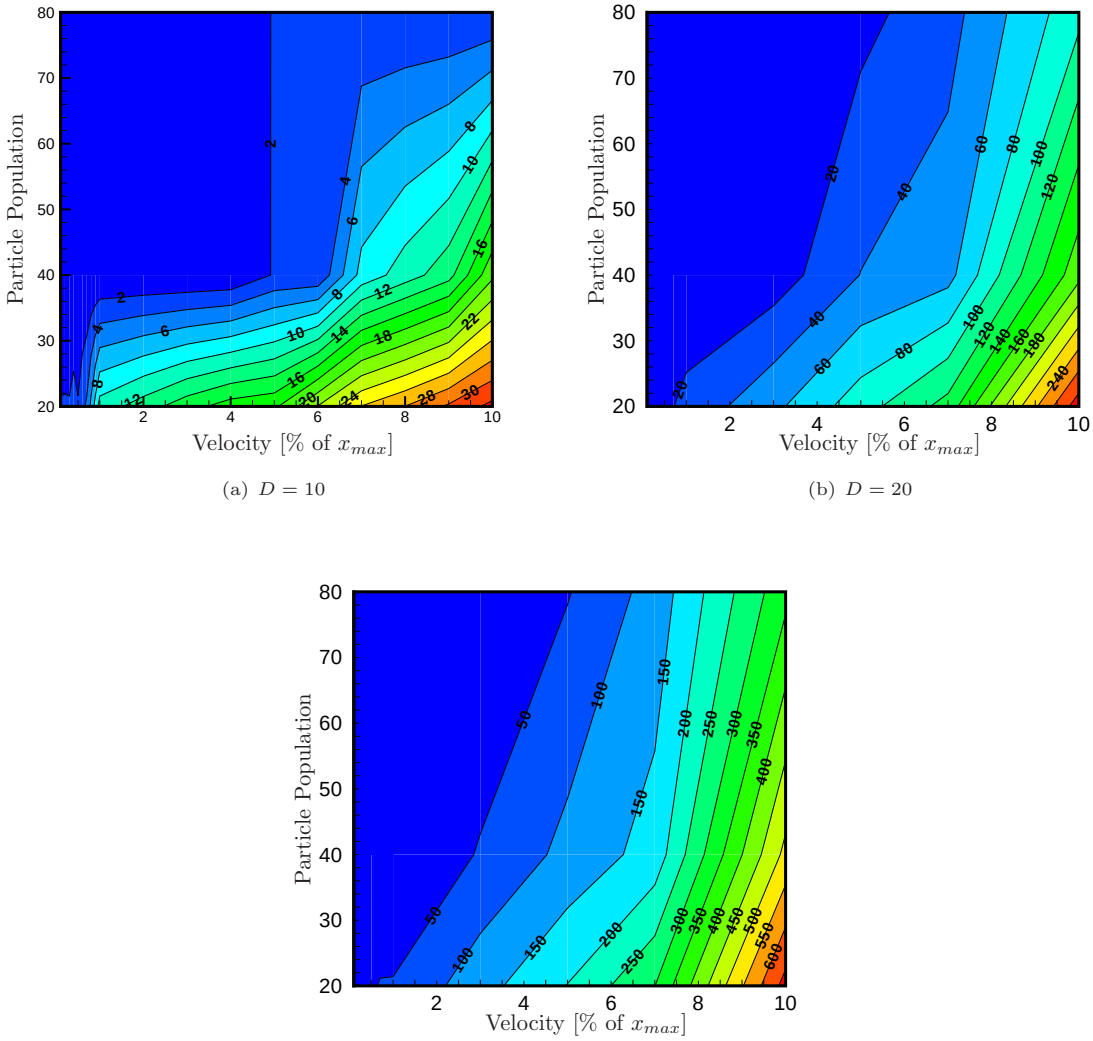

(a) $D = 10$

(b) $D = 20$

(c) $D = 30$

FIGURE B.4: Schwefel Function: Effect of Particle Population & Velocity on Fitness by the AMPSO Algorithm

Appendix C

Demonstration of Swarm Search Process

C.1 Ackley Function: Swarm Convergence to Minima Solution Region by the AM-PSO Algorithm

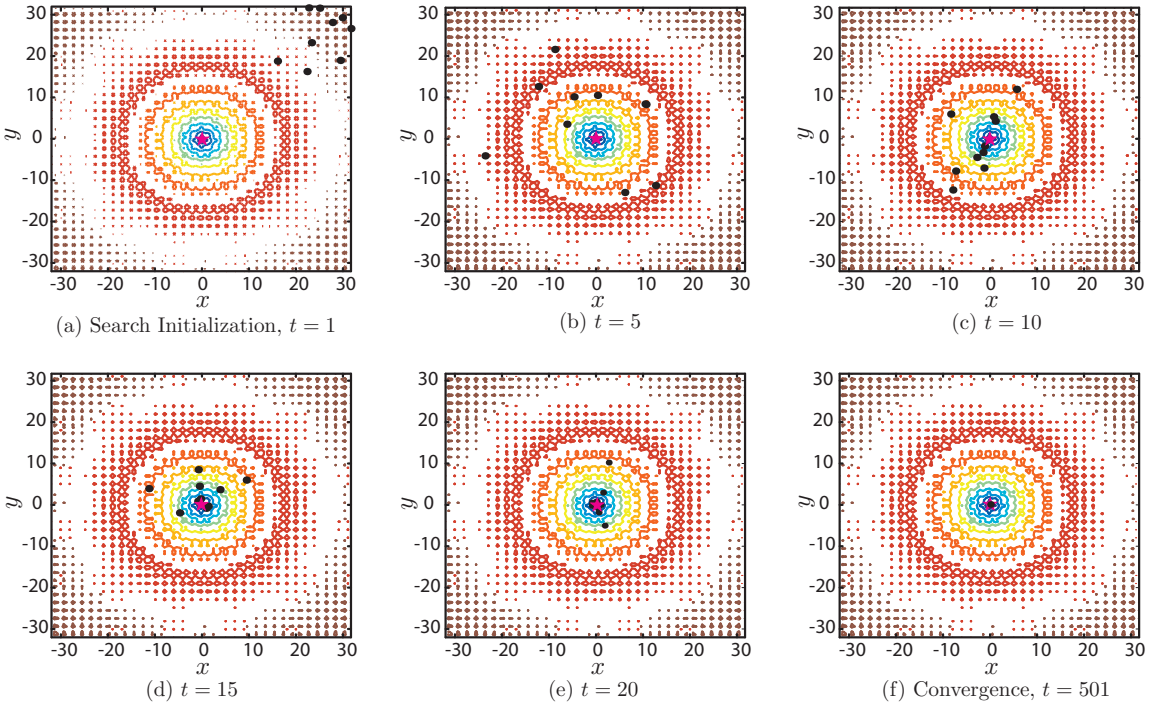

(a) Search Initialization, $t = 1$ (b) $t = 5$ (c) $t = 10$

(d) $t = 15$ (e) $t = 20$ (f) Convergence, $t = 501$

FIGURE C.1: Ackley Function: Demonstration of Swarm Search Progress to Global Point

C.2 Michalewics Function: Swarm Convergence to Minima Solution Region by the AM-PSO Algorithm

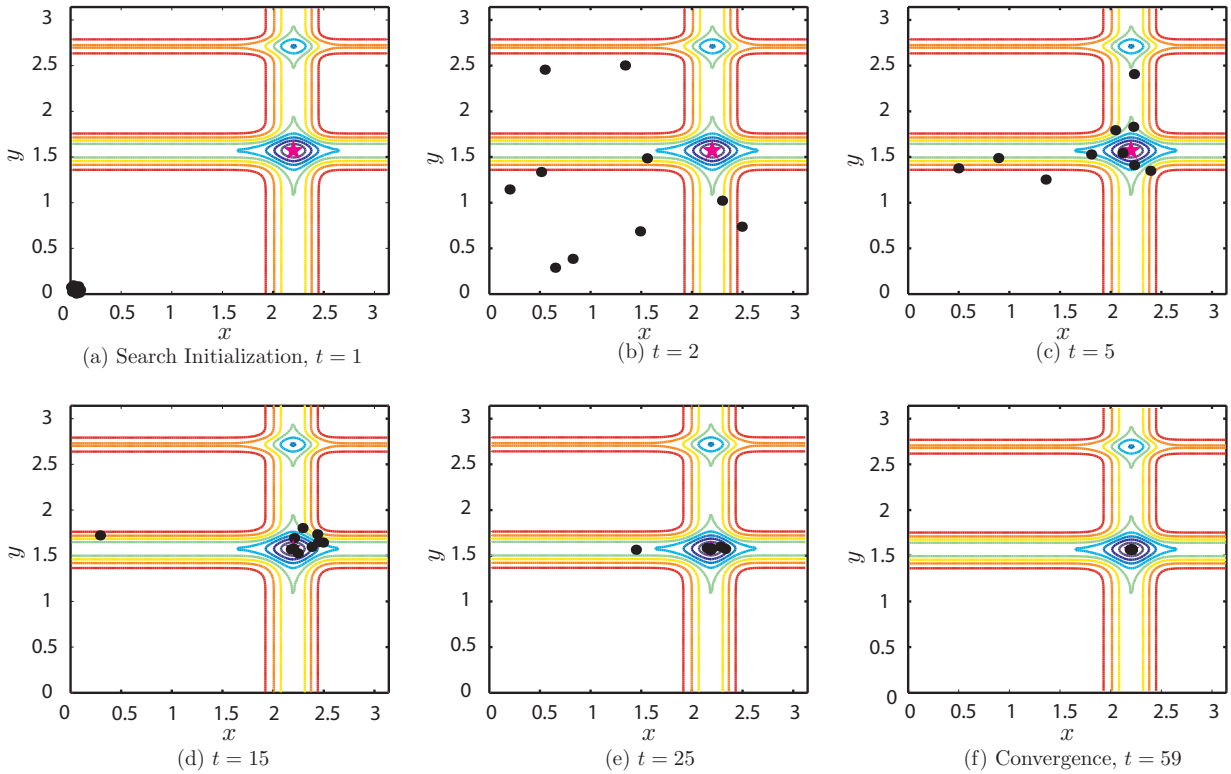

(a) Search Initialization, $t = 1$ (b) $t = 2$ (c) $t = 5$

(d) $t = 15$ (e) $t = 25$ (f) Convergence, $t = 59$

FIGURE C.2: Michalewics Function: Demonstration of Swarm Search Progress to Global Point

C.3 Rosenbrock Function: Swarm Convergence to Minima Solution Region by the AM-PSO Algorithm

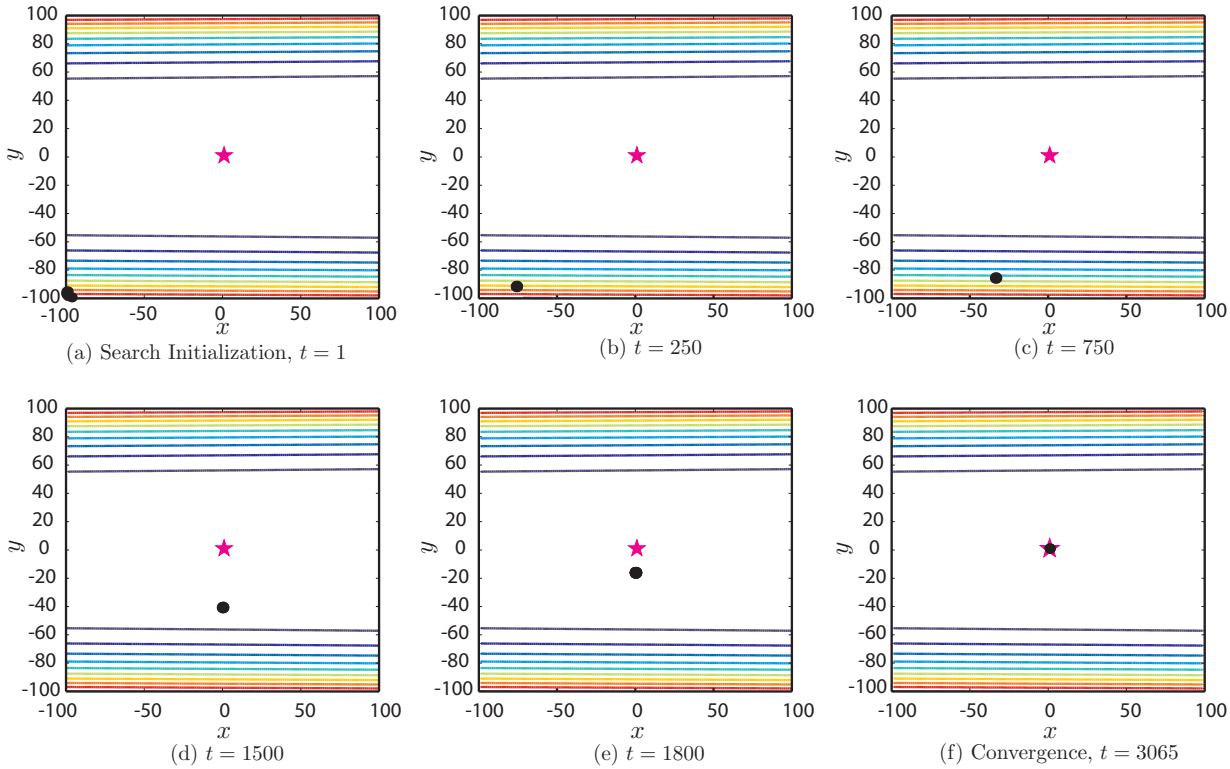

(a) Search Initialization, $t = 1$ (b) $t = 250$ (c) $t = 750$

(d) $t = 1500$ (e) $t = 1800$ (f) Convergence, $t = 3065$

FIGURE C.3: Rosenbrock Function: Demonstration of Swarm Search Progress to Global Point

Appendix D

Impact of PARSEC Shape Variables by Visualisation on Airfoil Aerodynamics & Geometry

D.1 PARSEC Variable: y_{te}

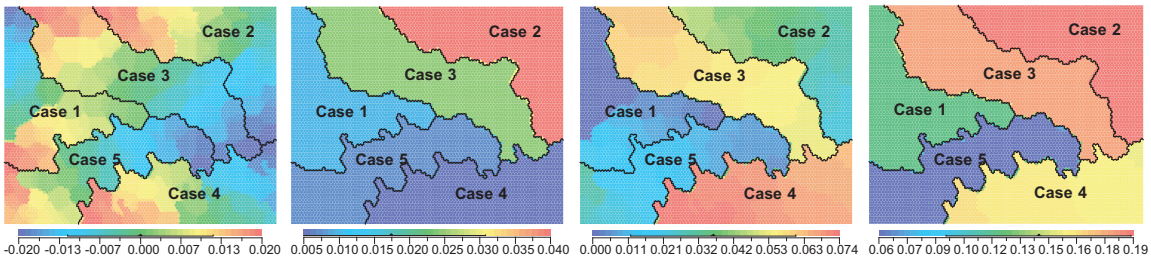

(a) y_{te} (b) r_{le} (c) Camber (d) t/c

FIGURE D.1: Effect of y_{te} on Airfoil Geometry

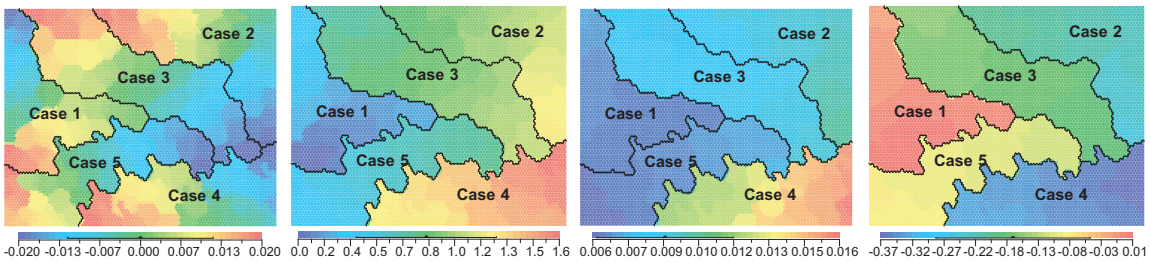

(a) y_{te} (b) c_l (c) c_d (d) c_m

FIGURE D.2: Effect of y_{te} on Airfoil Aerodynamics

D.2 PARSEC Variable: t_{eg}

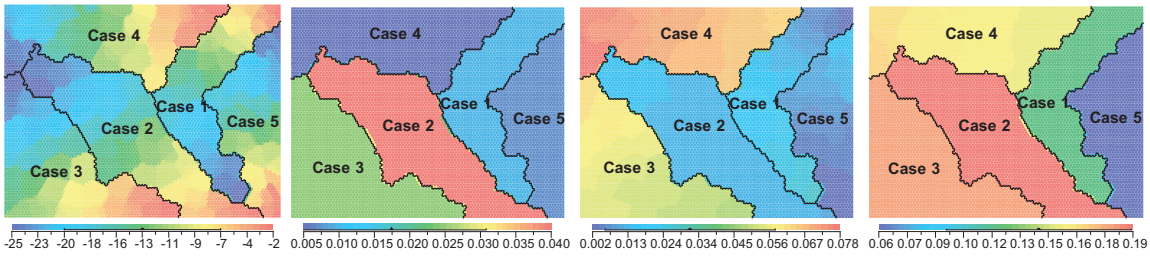

(a) t_{eg} (b) r_{le} (c) Camber (d) t/c

FIGURE D.3: Effect of t_{eg} on Airfoil Geometry

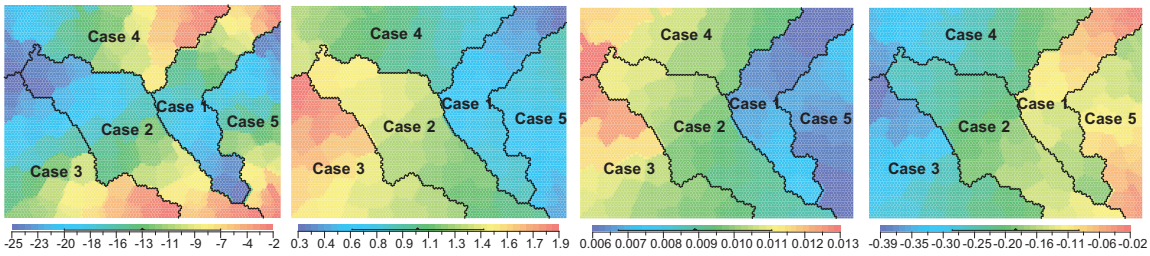

(a) t_{eg} (b) c_l (c) c_d (d) c_m

FIGURE D.4: Effect of t_{eg} on Airfoil Aerodynamics

D.3 PARSEC Variable: t_{ew}

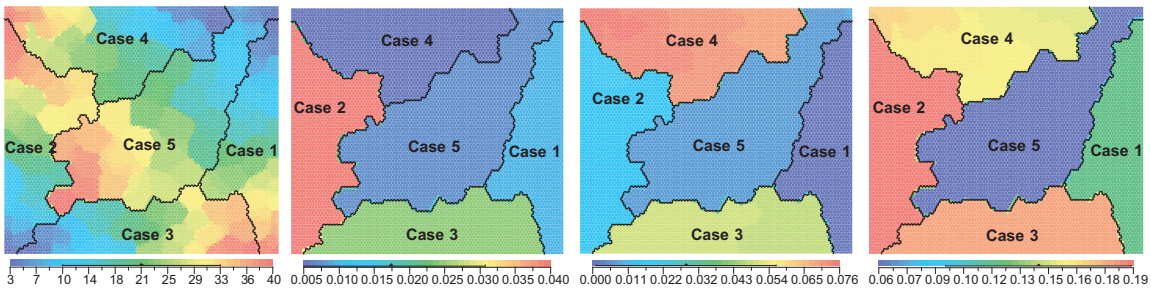

(a) t_{ew} (b) r_{le} (c) Camber (d) t/c

FIGURE D.5: Effect of t_{ew} on Airfoil Geometry

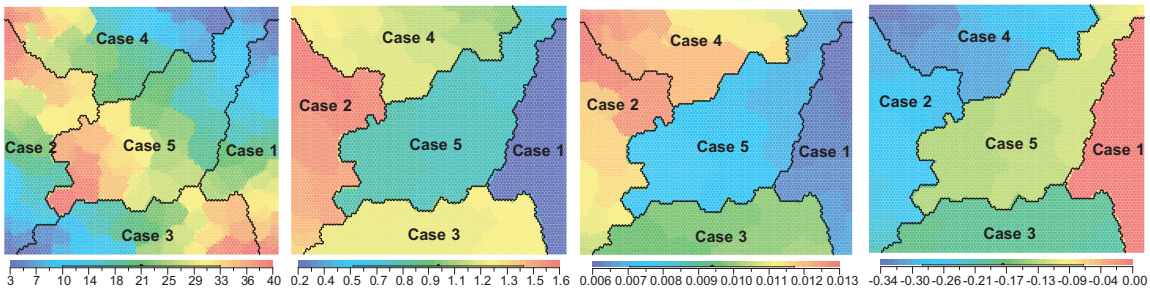

(a) t_{ew} (b) c_l (c) c_d (d) c_m

FIGURE D.6: Effect of t_{ew} on Airfoil Aerodynamics

D.4 PARSEC Variable: x_u

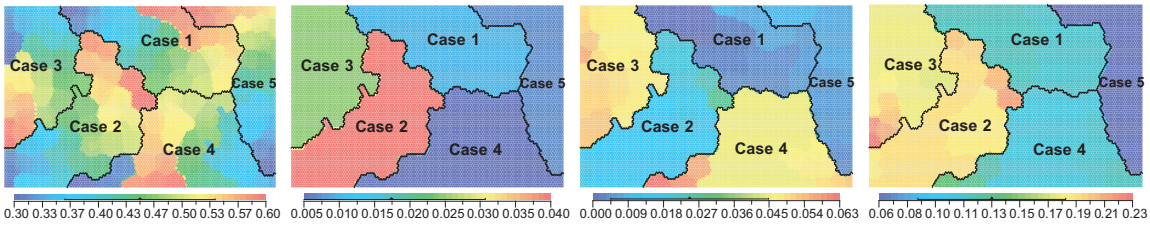

(a) x_u (b) r_{le} (c) Camber (d) t/c

FIGURE D.7: Effect of x_u on Airfoil Geometry

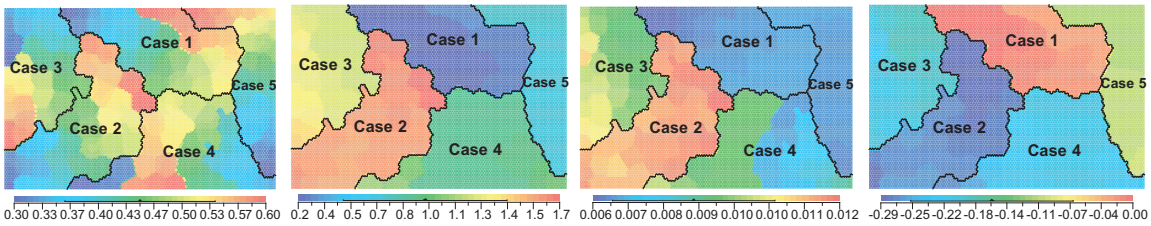

(a) x_u (b) c_l (c) c_d (d) c_m

FIGURE D.8: Effect of x_u on Airfoil Aerodynamics

D.5 PARSEC Variable: y_{xxu}

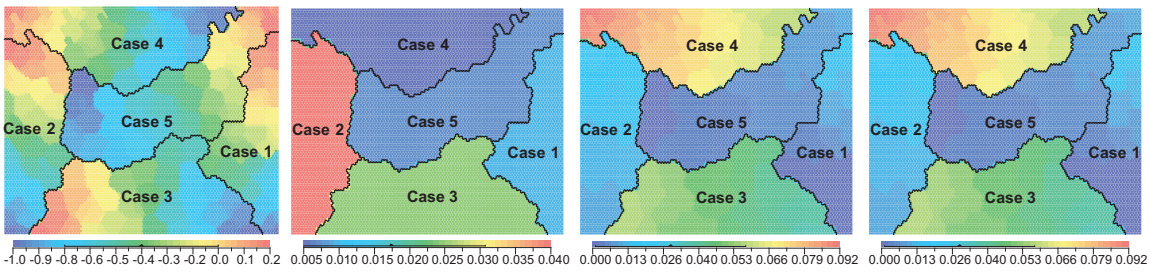

(a) y_{xxu} (b) r_{le} (c) Camber (d) t/c

FIGURE D.9: Effect of y_{xxu} on Airfoil Geometry

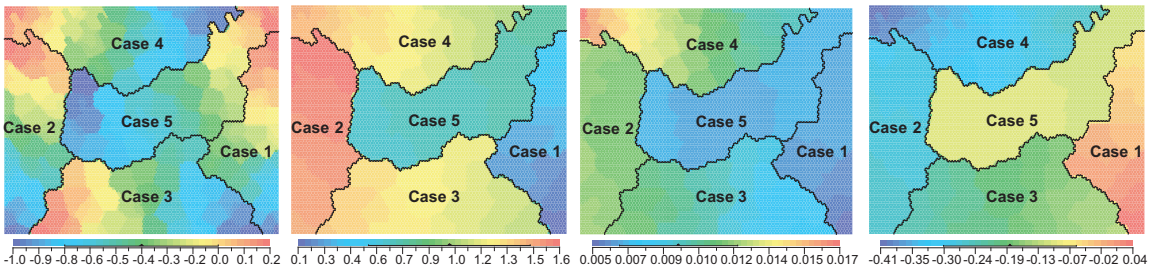

(a) y_{xxu} (b) c_l (c) c_d (d) c_m

FIGURE D.10: Effect of y_{xxu} on Airfoil Aerodynamics

D.6 PARSEC Variable: x_l

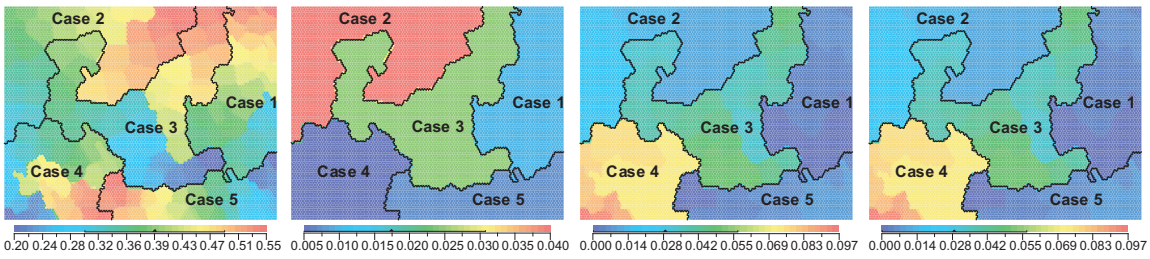

(a) x_l (b) r_{le} (c) Camber (d) t/c

FIGURE D.11: Effect of x_l on Airfoil Geometry

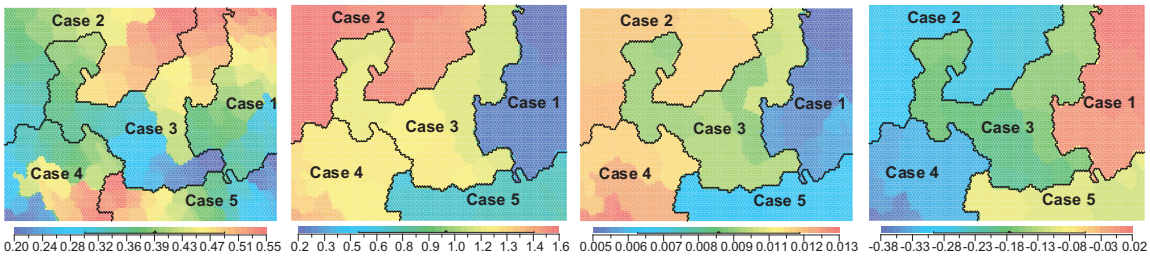

(a) x_l (b) c_l (c) c_d (d) c_m

FIGURE D.12: Effect of x_l on Airfoil Aerodynamics

D.7 PARSEC Variable: y_l

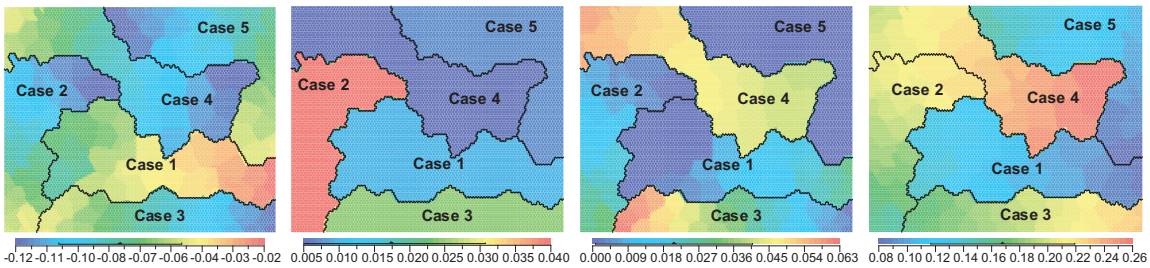

(a) y_l (b) r_{le} (c) Camber (d) t/c

FIGURE D.13: Effect of y_l on Airfoil Geometry

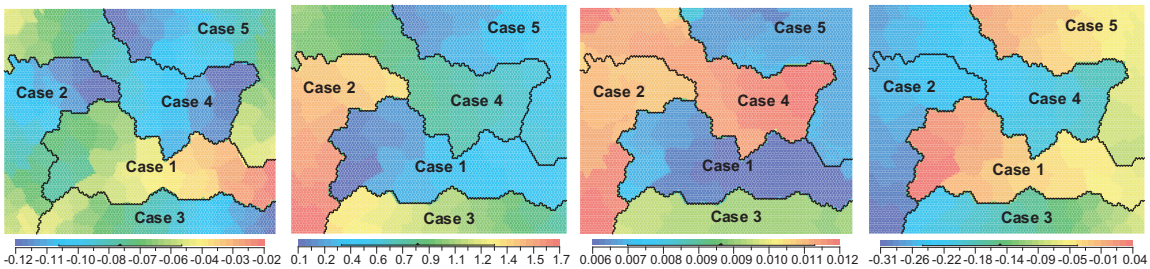

(a) y_l (b) c_l (c) c_d (d) c_m

FIGURE D.14: Effect of y_l on Airfoil Aerodynamics

D.8 PARSEC Variable: y_{xxl}

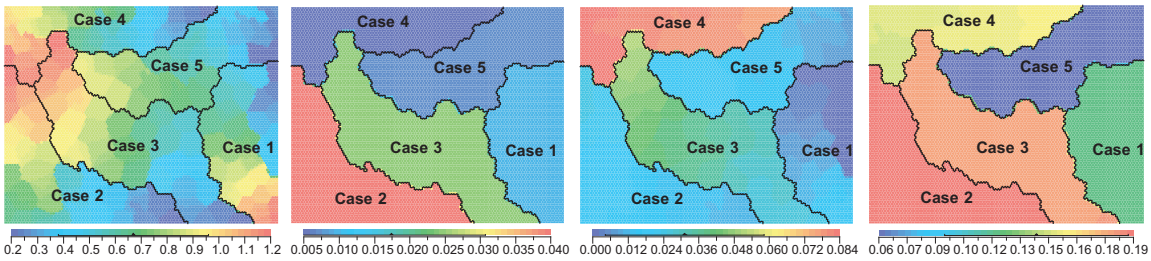

(a) y_{xxl} (b) r_{le} (c) Camber (d) t/c

FIGURE D.15: Effect of y_{xxl} on Airfoil Geometry

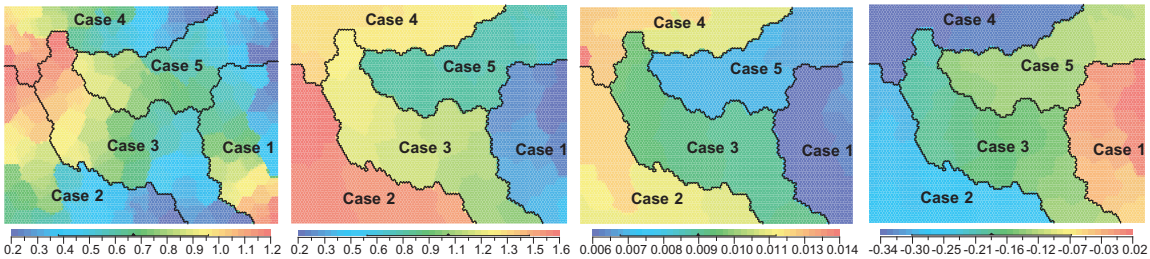

(a) y_{xxl} (b) c_l (c) c_d (d) c_m

FIGURE D.16: Effect of y_{xxl} on Airfoil Aerodynamics

Appendix E

Airfoil Design Variables Solution Space Mapping

E.1 PARSEC Solution Space Mapping at HALE Mach Numbers

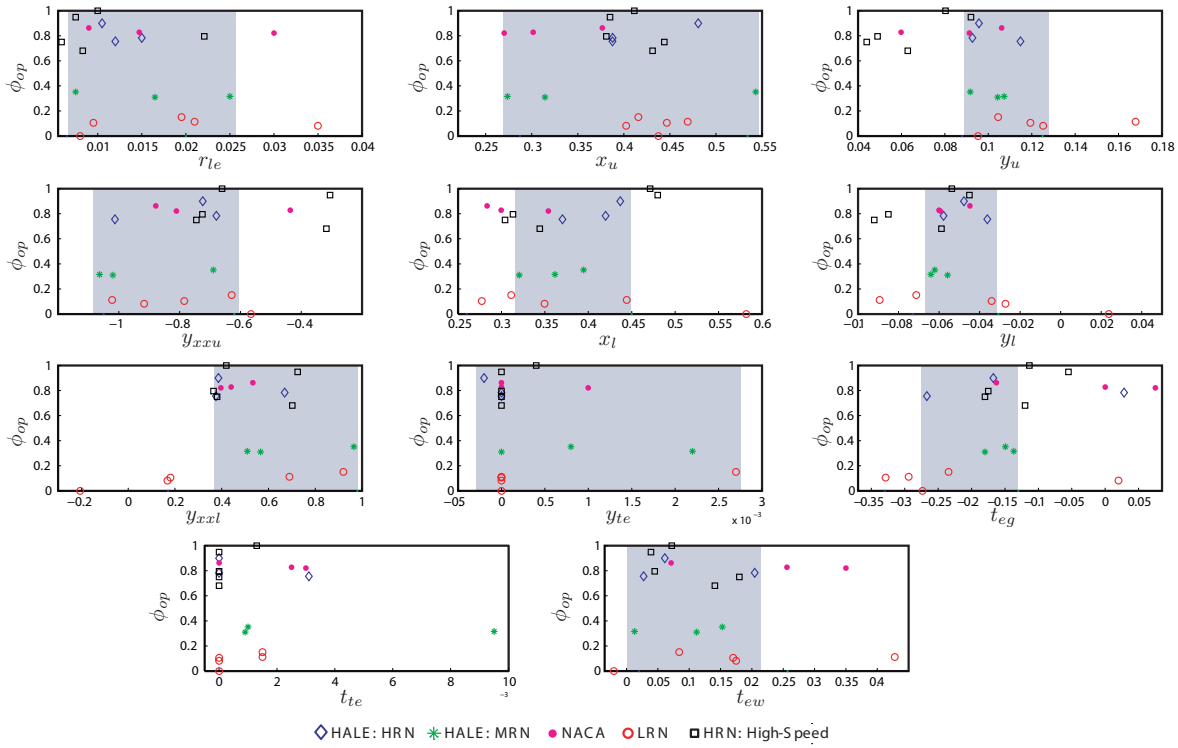

FIGURE E.1: PARSEC Variables Solution Space Mapping for Airfoil Design at HALE Mach Numbers

TABLE E.1: PARSEC Variables Solution Space Mapping for Airfoil Design at HALE Mach Numbers

	Shape Parameter	Minimum	Maximum
r_{le}	: Leading edge radius	0.0065	0.0230
x_u	: Crest of upper surface's x abscissa	0.2873	0.5343
y_u	: Crest of upper surface's y ordinate	0.088	0.125
y_{xxu}	: Curvature at the crest of upper surface	-1.05	-0.620
x_l	: Crest of lower surface's x abscissa	0.310	0.450
y_l	: Crest of lower surface's y ordinate	-0.073	-0.0307
y_{xxl}	: Curvature at the crest of lower surface	0.370	0.980
y_{te}	: Trailing-edge ordinate	-0.020	0.020
t_{eg}	: Trailing-edge direction (degrees)	-16.04°	-6.88°
t_{te}	: Thickness at trailing-edge	0	0.0030
t_{ew}	: Trailing-edge wedge angle (degrees)	1.15°	14.73°

E.2 PARSEC Solution Space Mapping at Transonic Mach Numbers

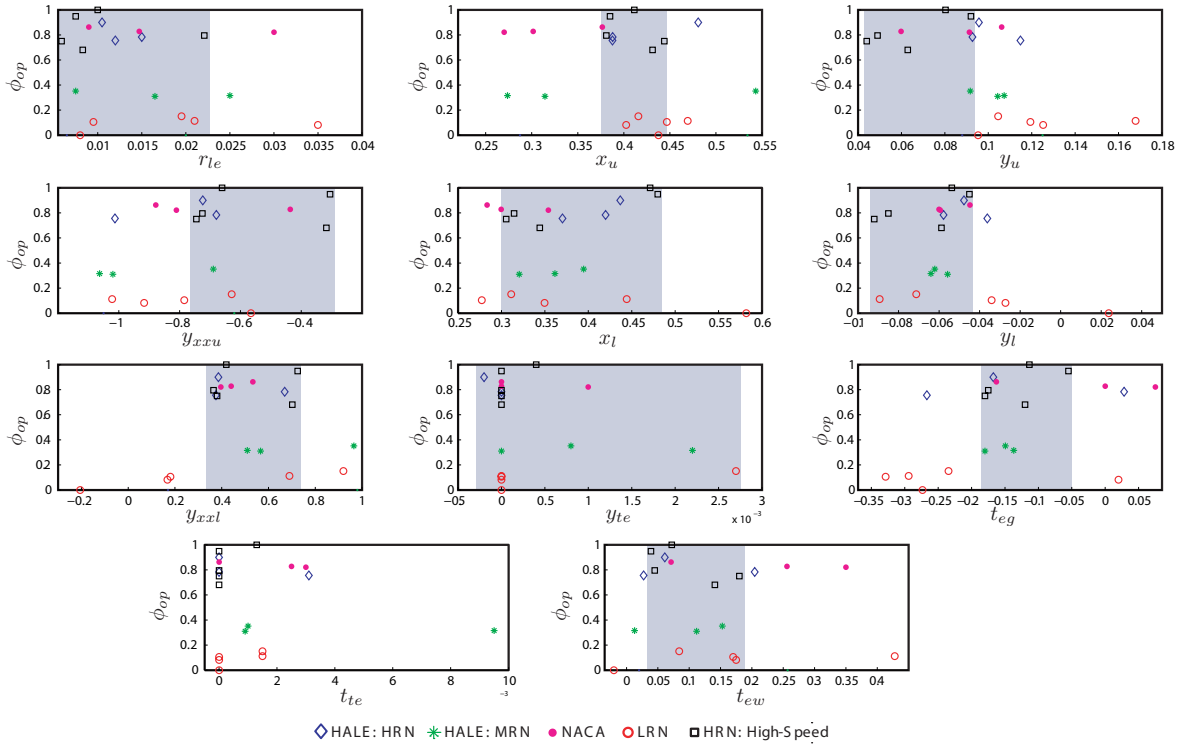

FIGURE E.2: PARSEC Variables Solution Space Mapping for Airfoil Design at Transonic Mach Numbers

TABLE E.2: PARSEC Variables Solution Space Mapping for Airfoil Design at Transonic Mach Numbers

	Shape Parameter	Minimum	Maximum
r_{le}	: Leading edge radius	0.0060	0.0220
x_u	: Crest of upper surface's x abscissa	0.380	0.4443
y_u	: Crest of upper surface's y ordinate	0.044	0.095
y_{xxu}	: Curvature at the crest of upper surface	-0.750	-0.320
x_l	: Crest of lower surface's x abscissa	0.300	0.490
y_l	: Crest of lower surface's y ordinate	-0.093	-0.0430
y_{xxl}	: Curvature at the crest of lower surface	0.385	0.730
y_{te}	: Trailing-edge ordinate	-0.020	0.020
t_{eg}	: Trailing-edge direction (degrees)	-10.90°	-2.87°
t_{te}	: Thickness at trailing-edge	0	0.0030
t_{ew}	: Trailing-edge wedge angle (degrees)	2.87°	10.71°

E.3 CST BPO2 Solution Space Mapping at HALE Mach Numbers

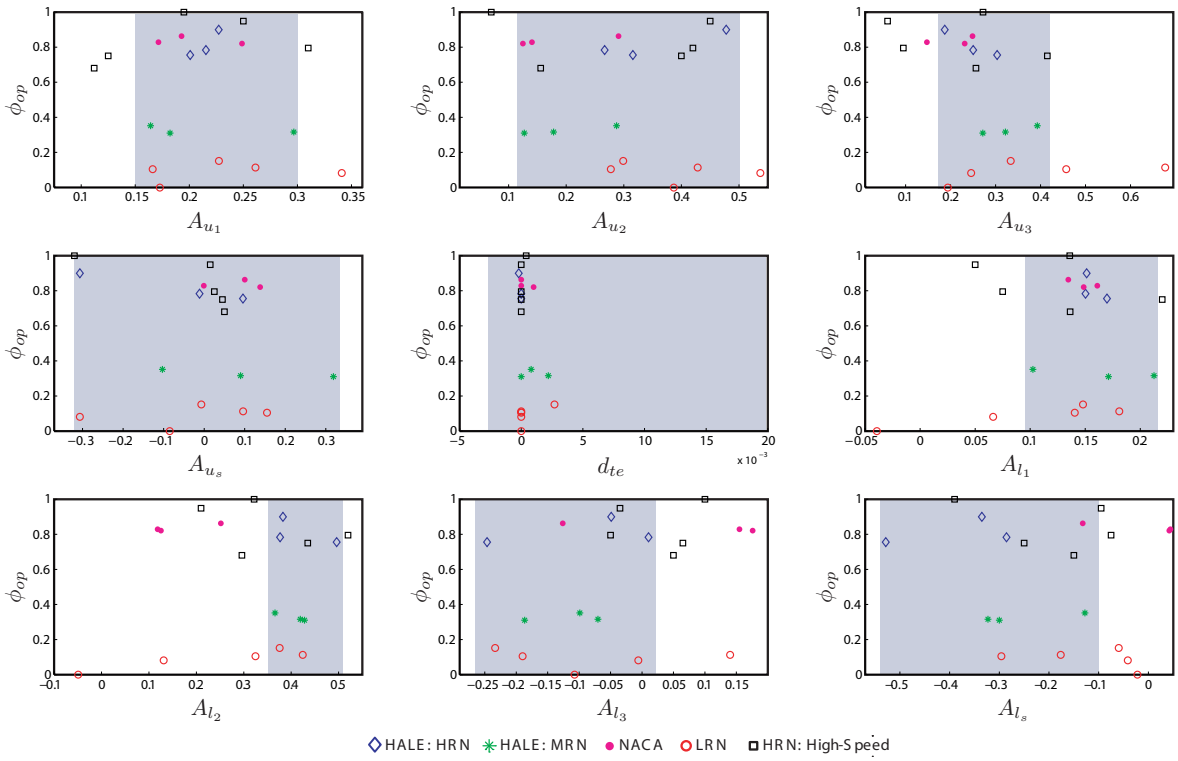

FIGURE E.3: CST BPO2 Variables Solution Space Mapping for Airfoil Design at HALE Mach Numbers

	Shape Parameter	Minimum	Maximum
A_{u_1}	: Upper Surface Coefficient 1	0.150	0.310
A_{u_2}	: Upper Surface Coefficient 2	0.115	0.495
A_{u_3}	: Upper Surface Coefficient 3	0.175	0.415
A_{u_s}	: Upper Surface Nose Slope	-0.315	0.330
d_{te}	: Trailing Edge Ordinate	-0.020	0.020
A_{l_1}	: Lower Surface Coefficient 1	0.095	0.225
A_{l_2}	: Lower Surface Coefficient 2	0.350	0.515
A_{l_3}	: Lower Surface Coefficient 3	-0.260	0.025
A_{l_s}	: Lower Surface Nose Slope	-0.530	-0.100

TABLE E.3: CST BPO2 Variables Solution Space Mapping for Airfoil Design at HALE Mach Numbers

E.4 CST BPO2 Solution Space Mapping at Transonic Mach Numbers

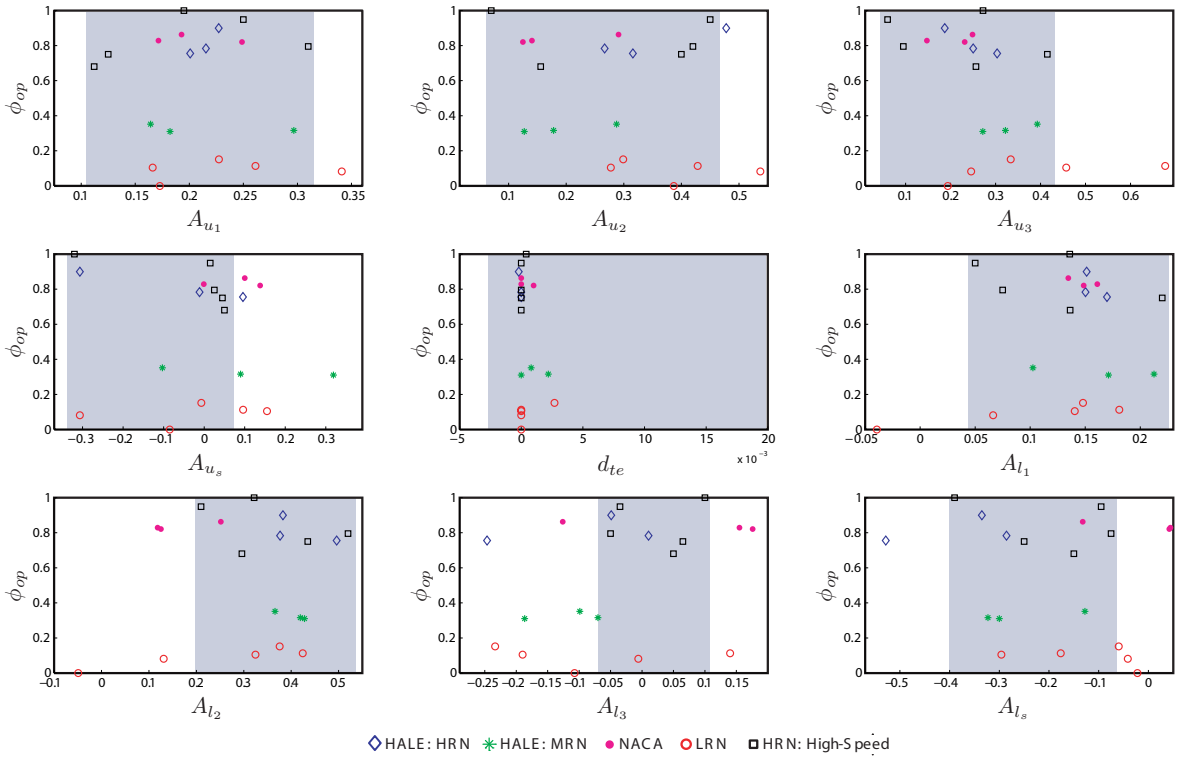

FIGURE E.4: CST BPO2 Variables Solution Space Mapping for Airfoil Design at Transonic Mach Numbers

	Shape Parameter	Minimum	Maximum
A_{u_1}	: Upper Surface Coefficient 1	0.110	0.325
A_{u_2}	: Upper Surface Coefficient 2	0.060	0.460
A_{u_3}	: Upper Surface Coefficient 3	0.050	0.420
A_{u_s}	: Upper Surface Nose Slope	-0.330	0.060
d_{te}	: Trailing Edge Ordinate	-0.020	0.020
A_{l_1}	: Lower Surface Coefficient 1	0.040	0.230
A_{l_2}	: Lower Surface Coefficient 2	0.200	0.530
A_{l_3}	: Lower Surface Coefficient 3	-0.070	0.105
A_{l_s}	: Lower Surface Nose Slope	-0.400	-0.0650

TABLE E.4: CST BPO2 Variables Solution Space Mapping for Airfoil Design at Transonic Mach Numbers

E.5 CST BPO3 Solution Space Mapping at HALE Mach Numbers

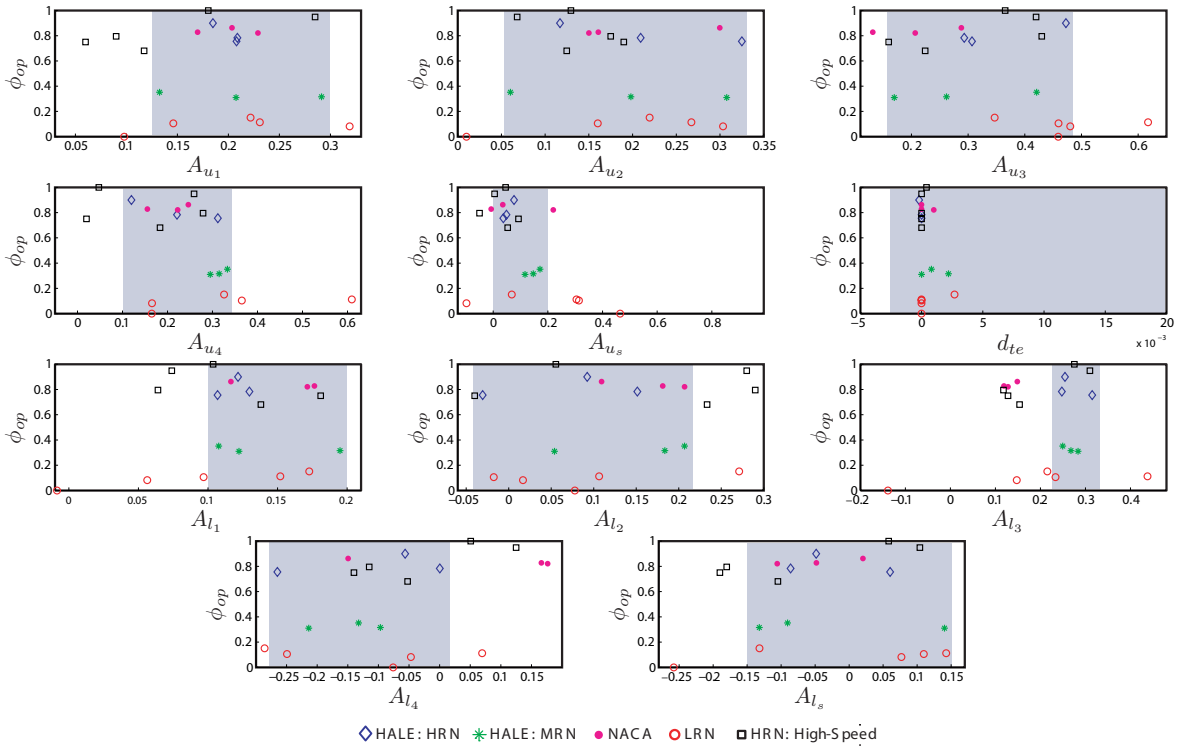

FIGURE E.5: CST BPO3 Variables Solution Space Mapping for Airfoil Design at HALE Mach Numbers

	Shape Parameter	Minimum	Maximum
A_{u_1}	: Upper Surface Coefficient 1	0.130	0.2995
A_{u_2}	: Upper Surface Coefficient 2	0.055	0.3350
A_{u_3}	: Upper Surface Coefficient 3	0.145	0.485
A_{u_4}	: Upper Surface Coefficient 4	0.100	0.335
A_{u_s}	: Upper Surface Nose Slope	0	0.200
d_{te}	: Trailing Edge Ordinate	-0.020	0.020
A_{l_1}	: Lower Surface Coefficient 1	0.100	0.200
A_{l_2}	: Lower Surface Coefficient 2	-0.045	0.215
A_{l_3}	: Lower Surface Coefficient 3	0.215	0.325
A_{l_4}	: Lower Surface Coefficient 4	-0.265	0.025
A_{l_s}	: Lower Surface Nose Slope	-0.150	0.150

TABLE E.5: CST BPO3 Variables Solution Space Mapping for Airfoil Design at HALE Mach Numbers

E.6 CST BPO3 Solution Space Mapping at Transonic Mach Numbers

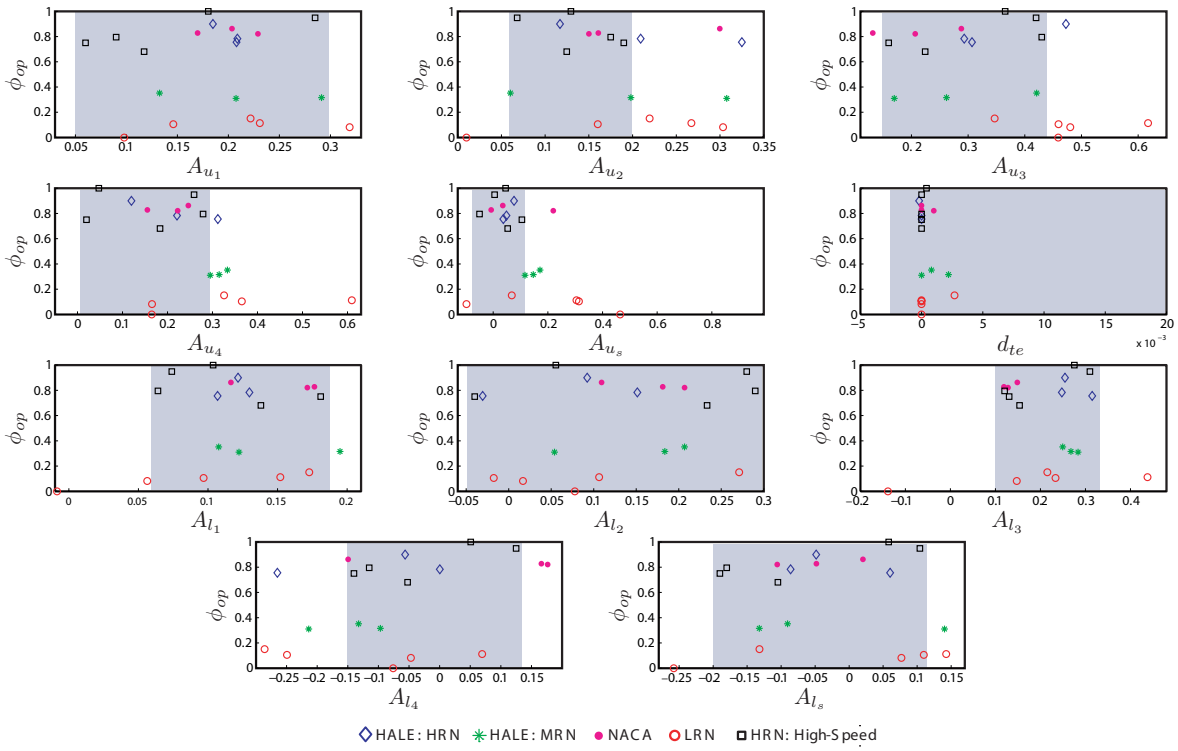

FIGURE E.6: CST BPO3 Variables Solution Space Mapping for Airfoil Design at Transonic Mach Numbers

	Shape Parameter	Minimum	Maximum
A_{u_1}	: Upper Surface Coefficient 1	0.050	0.2950
A_{u_2}	: Upper Surface Coefficient 2	0.0580	0.200
A_{u_3}	: Upper Surface Coefficient 3	0.150	0.440
A_{u_4}	: Upper Surface Coefficient 4	0.010	0.2890
A_{u_s}	: Upper Surface Nose Slope	-0.0150	0.090
d_{te}	: Trailing Edge Ordinate	-0.020	0.020
A_{l_1}	: Lower Surface Coefficient 1	0.0540	0.1910
A_{l_2}	: Lower Surface Coefficient 2	-0.050	0.300
A_{l_3}	: Lower Surface Coefficient 3	0.100	0.3210
A_{l_4}	: Lower Surface Coefficient 4	-0.150	0.135
A_{l_s}	: Lower Surface Nose Slope	-0.200	0.1140

TABLE E.6: CST BPO3 Variables Solution Space Mapping for Airfoil Design at Transonic Mach Numbers

E.7 CST BPO4 Solution Space Mapping at HALE Mach Numbers

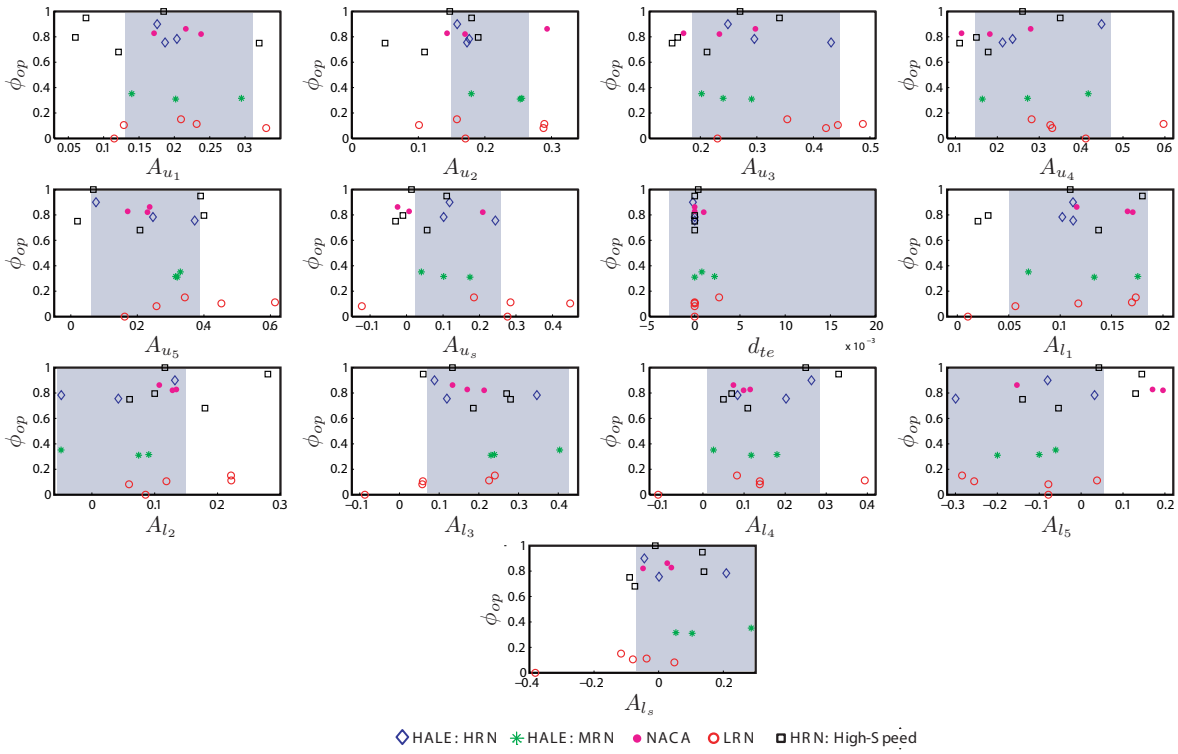

FIGURE E.7: CST BPO4 Variables Solution Space Mapping for Airfoil Design at HALE Mach Numbers

	Shape Parameter	Minimum	Maximum
A_{u_1}	: Upper Surface Coefficient 1	0.130	0.310
A_{u_2}	: Upper Surface Coefficient 2	0.150	0.260
A_{u_3}	: Upper Surface Coefficient 3	0.190	0.450
A_{u_4}	: Upper Surface Coefficient 4	0.150	0.460
A_{u_5}	: Upper Surface Coefficient 5	0.060	0.380
A_{u_s}	: Upper Surface Nose Slope	0.030	0.260
d_{te}	: Trailing Edge Ordinate	-0.020	0.020
A_{l_1}	: Lower Surface Coefficient 1	0.050	0.180
A_{l_2}	: Lower Surface Coefficient 2	-0.300	0.150
A_{l_3}	: Lower Surface Coefficient 3	0.070	0.420
A_{l_4}	: Lower Surface Coefficient 4	0.020	0.280
A_{l_5}	: Lower Surface Coefficient 5	-0.400	0.050
A_{l_s}	: Lower Surface Nose Slope	-0.060	0.300

TABLE E.7: CST BPO4 Variables Solution Space Mapping for Airfoil Design at HALE Mach Numbers

E.8 CST BPO4 Solution Space Mapping at Transonic Mach Numbers

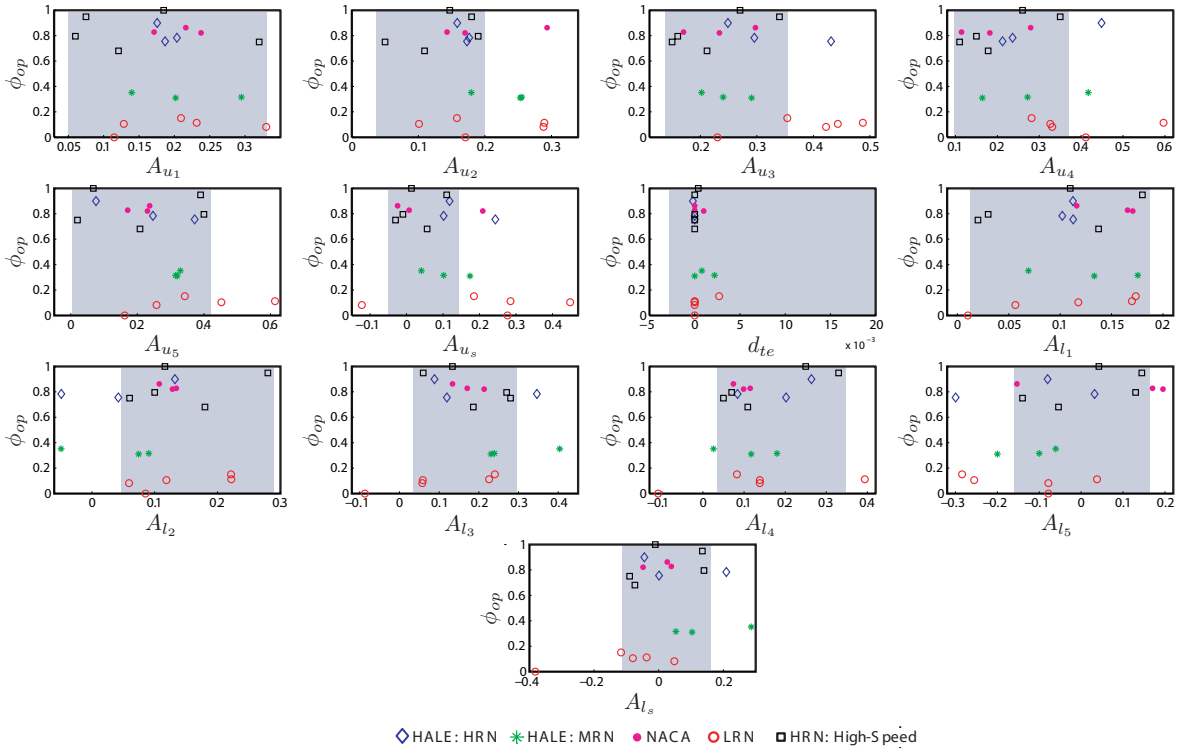

FIGURE E.8: CST BPO4 Variables Solution Space Mapping for Airfoil Design at Transonic Mach Numbers

	Shape Parameter	Minimum	Maximum
A_{u_1}	: Upper Surface Coefficient 1	0.050	0.330
A_{u_2}	: Upper Surface Coefficient 2	0.040	0.200
A_{u_3}	: Upper Surface Coefficient 3	0.140	0.350
A_{u_4}	: Upper Surface Coefficient 4	0.100	0.360
A_{u_5}	: Upper Surface Coefficient 5	0.010	0.410
A_{u_s}	: Upper Surface Nose Slope	-0.040	0.120
d_{te}	: Trailing Edge Ordinate	-0.020	0.020
A_{l_1}	: Lower Surface Coefficient 1	0.010	0.190
A_{l_2}	: Lower Surface Coefficient 2	0.050	0.290
A_{l_3}	: Lower Surface Coefficient 3	0.050	0.290
A_{l_4}	: Lower Surface Coefficient 4	0.040	0.350
A_{l_5}	: Lower Surface Coefficient 5	-0.150	0.150
A_{l_s}	: Lower Surface Nose Slope	-0.100	0.150

TABLE E.8: CST BPO4 Variables Solution Space Mapping for Airfoil Design at Transonic Mach Numbers

E.9 CST BPO5 Solution Space Mapping at HALE Mach Numbers

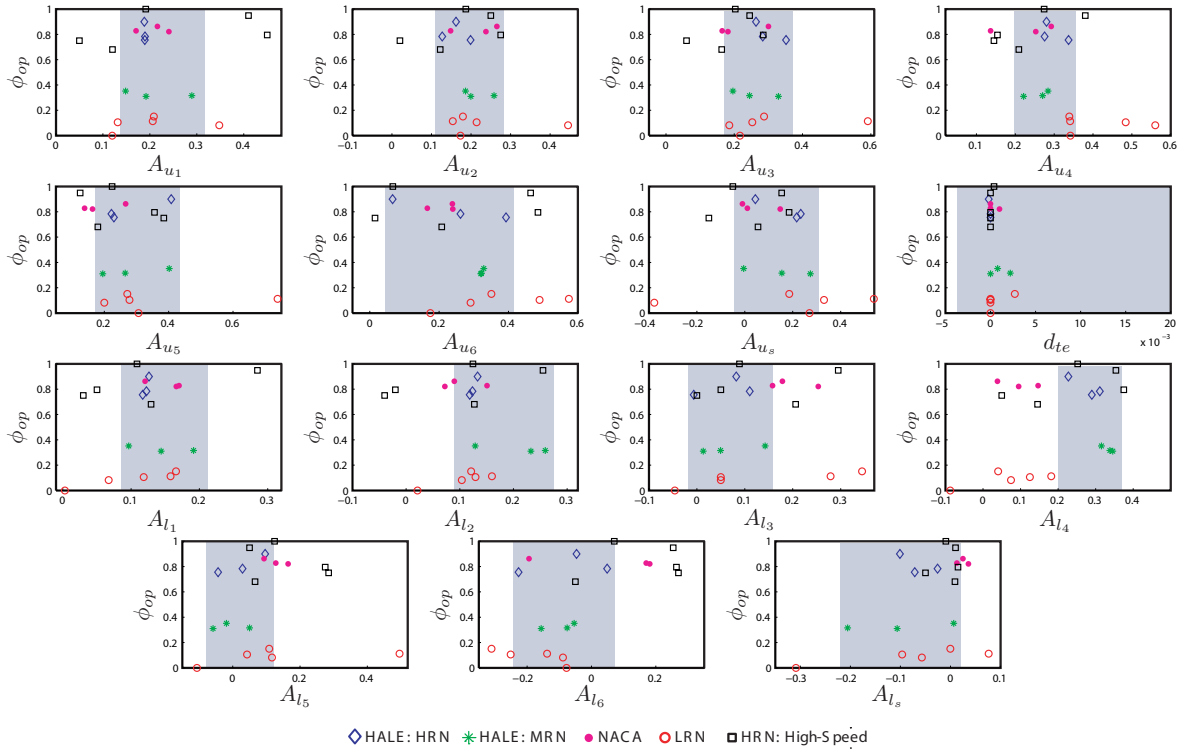

FIGURE E.9: CST BPO5 Variables Solution Space Mapping for Airfoil Design at HALE Mach Numbers

	Shape Parameter	Minimum	Maximum
A_{u_1}	: Upper Surface Coefficient 1	0.130	0.310
A_{u_2}	: Upper Surface Coefficient 2	0.110	0.2650
A_{u_3}	: Upper Surface Coefficient 3	0.180	0.3850
A_{u_4}	: Upper Surface Coefficient 4	0.200	0.350
A_{u_5}	: Upper Surface Coefficient 5	0.180	0.420
A_{u_6}	: Upper Surface Coefficient 6	0.050	0.410
A_{u_s}	: Upper Surface Nose Slope	-0.020	0.290
d_{te}	: Trailing Edge Ordinate	-0.020	0.020
A_{l_1}	: Lower Surface Coefficient 1	0.080	0.210
A_{l_2}	: Lower Surface Coefficient 2	0.090	0.270
A_{l_3}	: Lower Surface Coefficient 3	-0.010	0.160
A_{l_4}	: Lower Surface Coefficient 4	0.200	0.370
A_{l_5}	: Lower Surface Coefficient 5	-0.070	0.120
A_{l_6}	: Lower Surface Coefficient 6	-0.240	0.060
A_{l_s}	: Lower Surface Nose Slope	-0.220	0.010

TABLE E.9: CST BPO5 Variables Solution Space Mapping for Airfoil Design at HALE Mach Numbers

E.10 CST BPO5 Solution Space Mapping at Transonic Mach Numbers

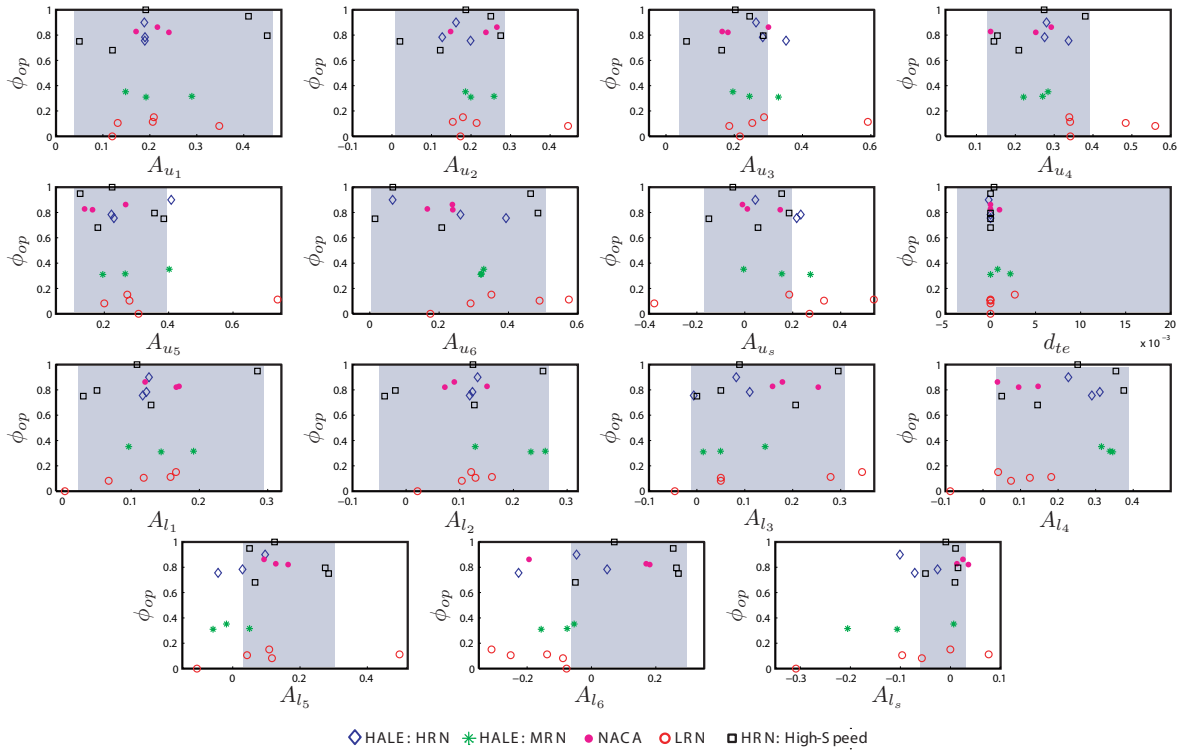

FIGURE E.10: CST BPO5 Variables Solution Space Mapping for Airfoil Design at Transonic Mach Numbers

	Shape Parameter	Minimum	Maximum
A_{u_1}	: Upper Surface Coefficient 1	0.040	0.460
A_{u_2}	: Upper Surface Coefficient 2	0.010	0.2850
A_{u_3}	: Upper Surface Coefficient 3	0.050	0.2950
A_{u_4}	: Upper Surface Coefficient 4	0.135	0.390
A_{u_5}	: Upper Surface Coefficient 5	0.115	0.395
A_{u_6}	: Upper Surface Coefficient 6	0.005	0.495
A_{u_s}	: Upper Surface Nose Slope	-0.200	0.195
d_{te}	: Trailing Edge Ordinate	-0.020	0.020
A_{l_1}	: Lower Surface Coefficient 1	0.020	0.295
A_{l_2}	: Lower Surface Coefficient 2	-0.05	0.265
A_{l_3}	: Lower Surface Coefficient 3	-0.010	0.305
A_{l_4}	: Lower Surface Coefficient 4	0.030	0.385
A_{l_5}	: Lower Surface Coefficient 5	0.005	0.295
A_{l_6}	: Lower Surface Coefficient 6	-0.0070	0.280
A_{l_s}	: Lower Surface Nose Slope	-0.080	0.0195

TABLE E.10: CST BPO5 Variables Solution Space Mapping for Airfoil Design at Transonic Mach Numbers

Appendix F

Shape Variables Qualitative Measure of Sensitivity on Aerodynamics

F.1 PARSEC Sensitivity at HALE Flight Envelope - Aerodynamic Coefficients

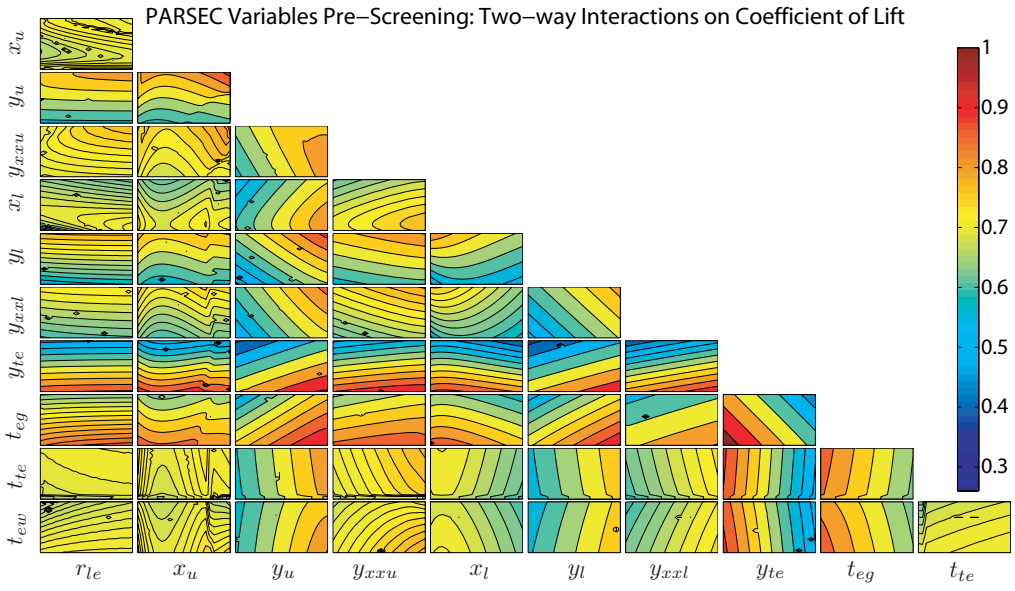

(a) c_l

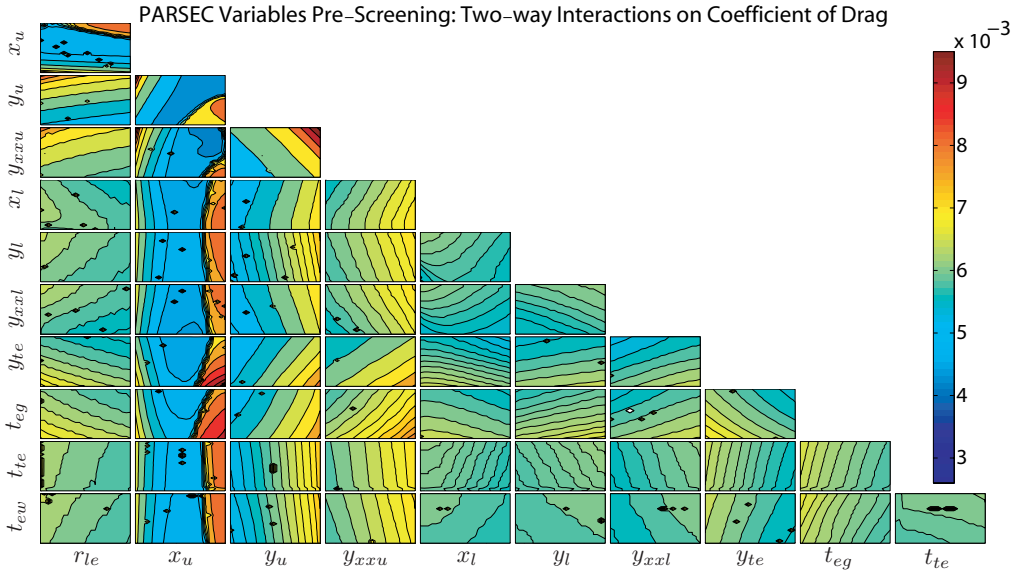

(b) c_d

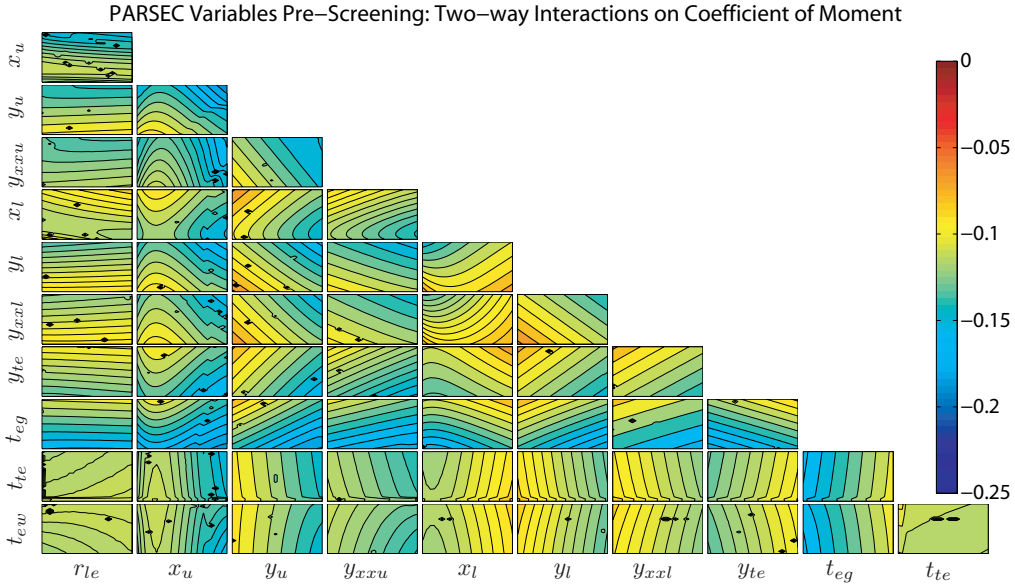

(c) c_m

FIGURE F.1: Qualitative Representation of the Relationship of PARSEC Airfoil Design Variables on c_l, c_d & c_m

F.2 PARSEC Sensitivity at HALE Flight Envelope - Boundary Layer Transition

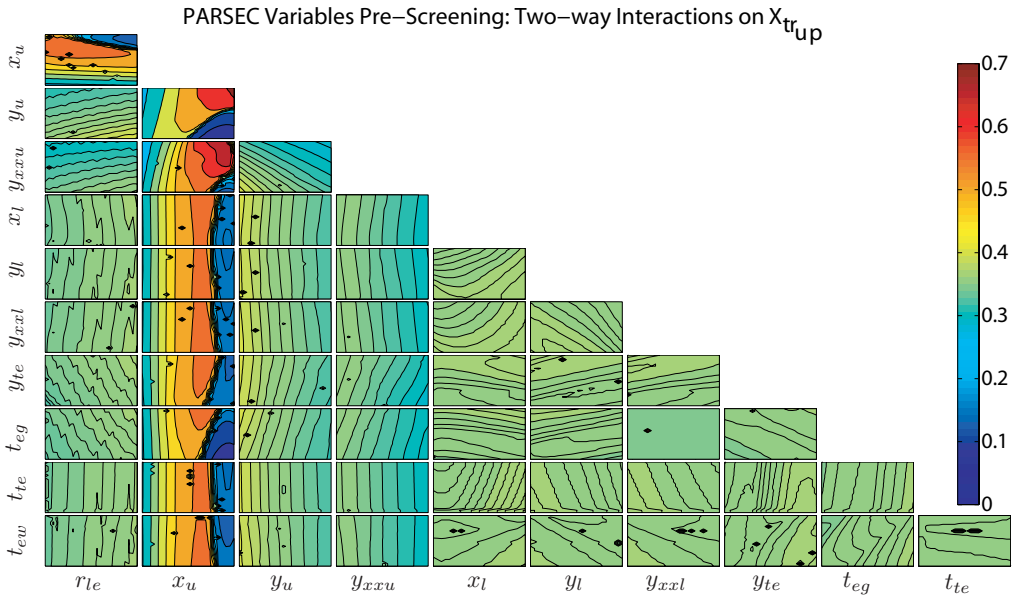

(a) $X_{tr_{Up}}$

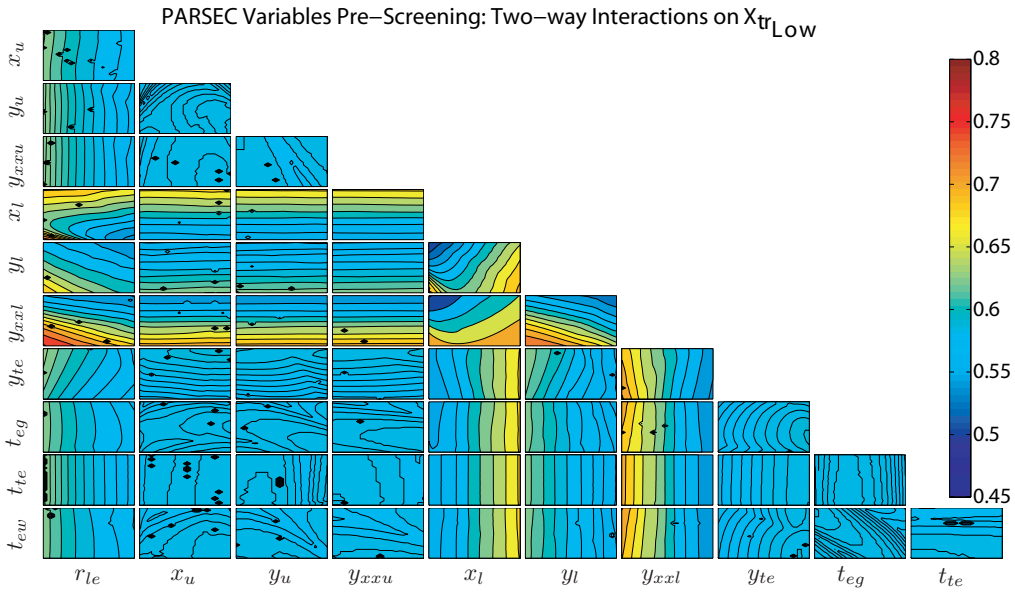

(b) $X_{tr_{low}}$

FIGURE F.2: Qualitative Representation of the Relationship of PARSEC Airfoil Design Variables on Airfoil Boundary Layer Transition

F.3 PARSEC-Modified Sensitivity at Transonic Flight Envelope - Coefficient of Drag

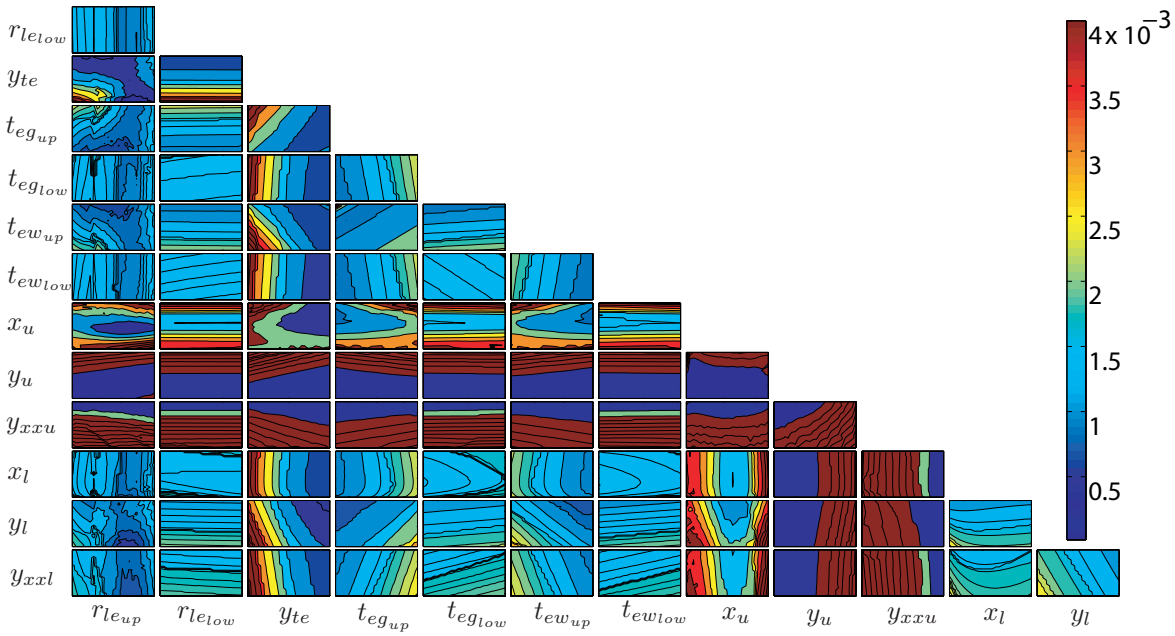

FIGURE F.3: PARSEC-Modified Variables Pre-Screening: Two-Way Interactions on Coefficient of Drag at Transonic Flight Envelope

F.4 PARSEC-Modified Sensitivity at Transonic Flight Envelope - Shock Wave One

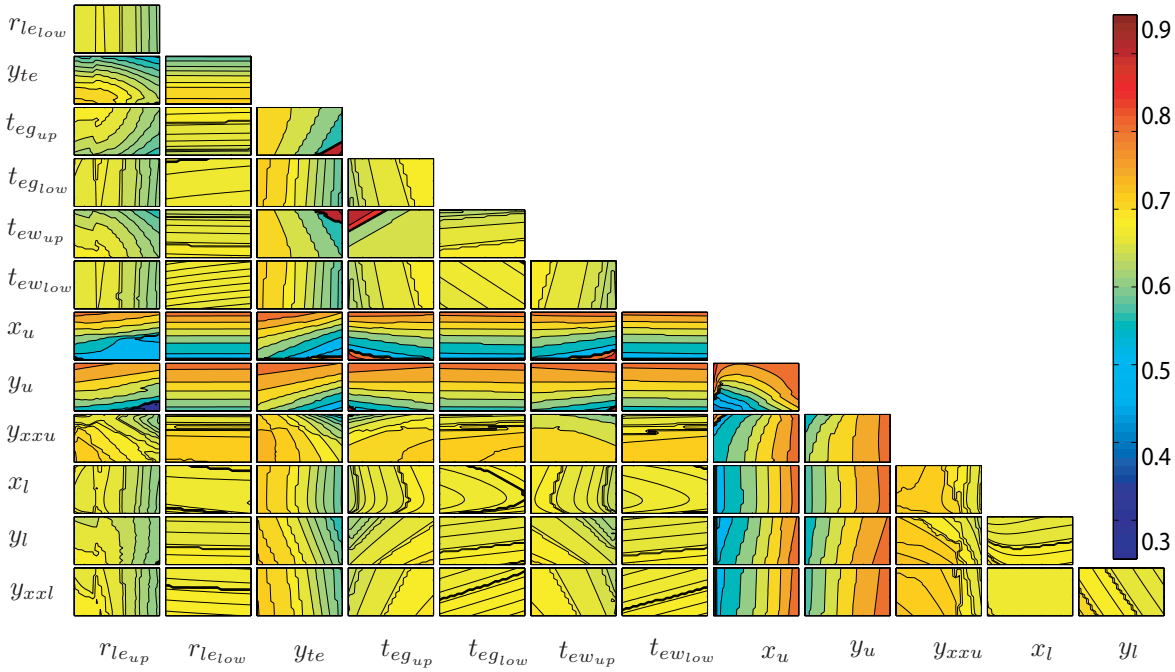

FIGURE F.4: PARSEC-Modified Variables Pre-Screening: Impact of Two-Way Interactions on Airfoil Upper Surface Shock Wave One Chord Location at Transonic Flight Envelope

F.5 PARSEC-Modified Sensitivity at Transonic Flight Envelope - Shock Wave Two

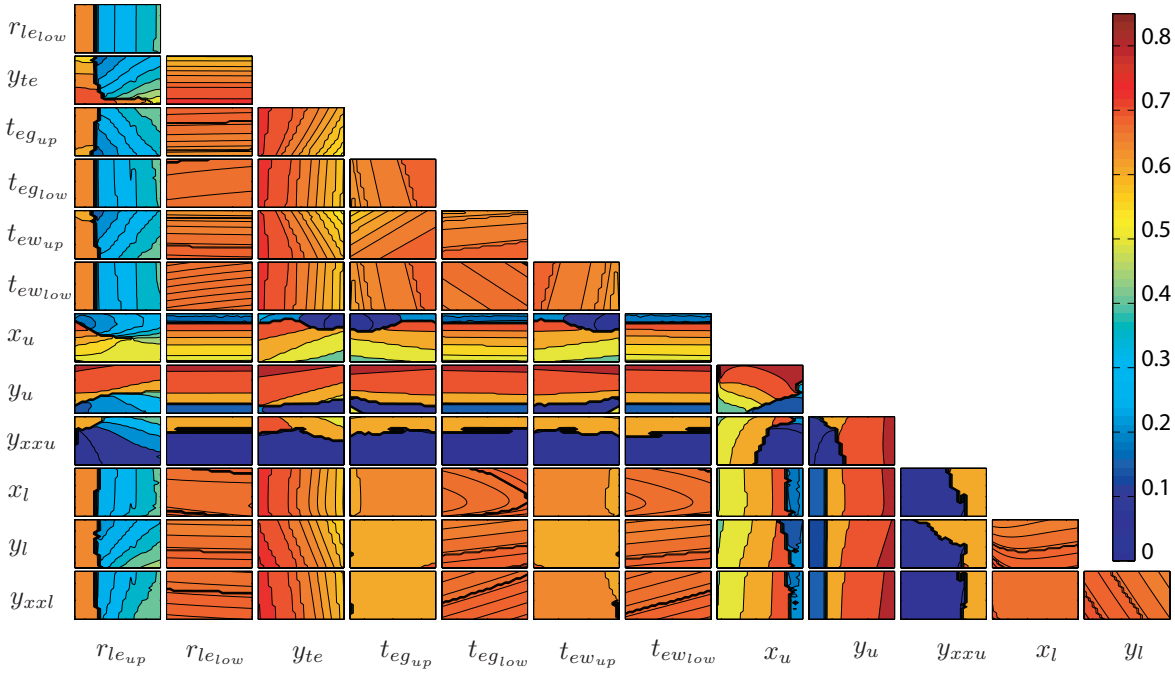

FIGURE F.5: PARSEC-Modified Variables Pre-Screening: Impact of Two-Way Interactions on Airfoil Upper Surface Shock Wave Two Chord Location at Transonic Flight Envelope

F.6 PARSEC-Modified Sensitivity at Transonic Flight Envelope - Coefficient of Moment

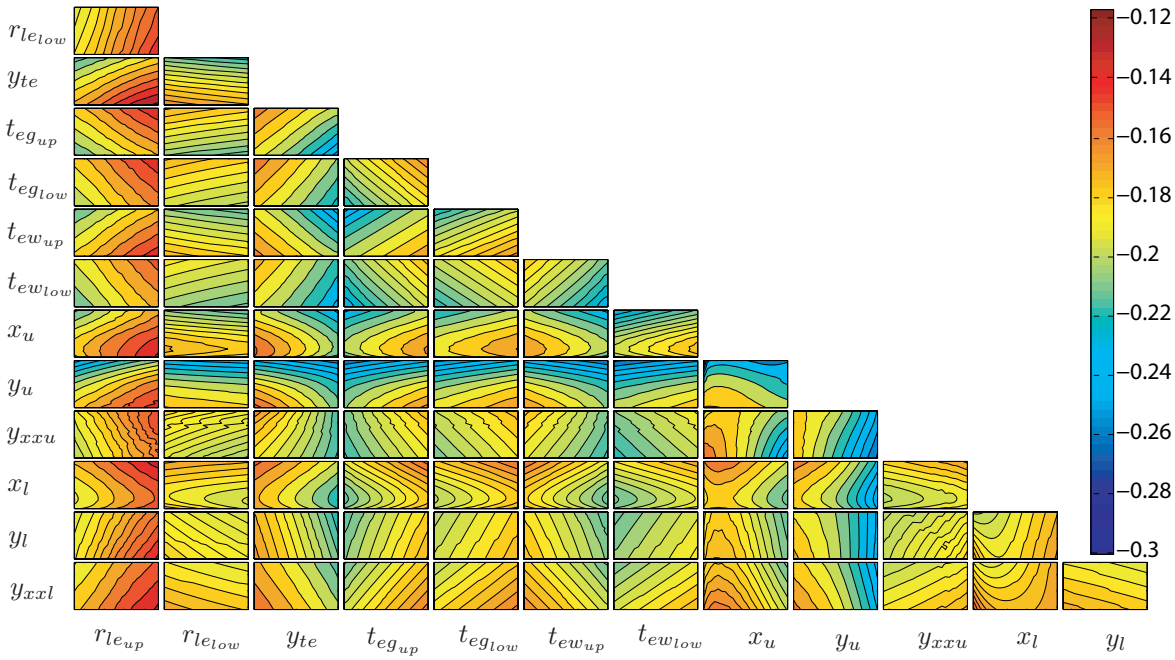

FIGURE F.6: Two-Way Interactions on Coefficient of Moment; $R_n = 2.76 \times 10^6$, Mach=0.74 & $c_l^T = 0.733$

F.7 PARSEC-Modified Sensitivity at Transonic Flight Envelope - Minimum Coefficient of Pressure Airfoil Chord Location

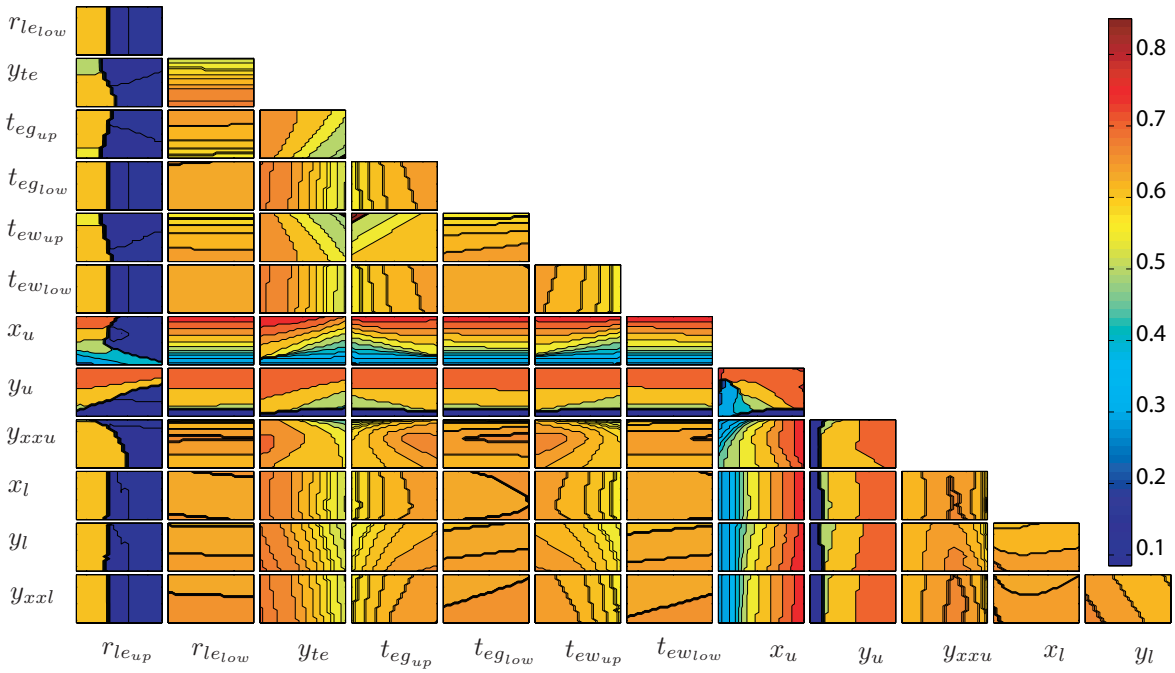

FIGURE F.7: Two-Way Interactions on Minimum c_p Airfoil Chord Location; $R_n = 2.76 \times 10^6$, Mach=0.74 & $c_l^T = 0.733$

Appendix G

Airfoil Shape Variables Quantitative Measure of Sensitivity on Aerodynamics

G.1 HALE Flight Performance - PARSEC Shape Function

G.2 HALE Flight Performance - PARSEC Shape Function Contribution to c_d & $c_{l_{max}}$

G.3 HALE Flight Performance - PARSEC-Modified Shape Function

G.4 Transonic Flight Performance - PARSEC-Modified Shape Function

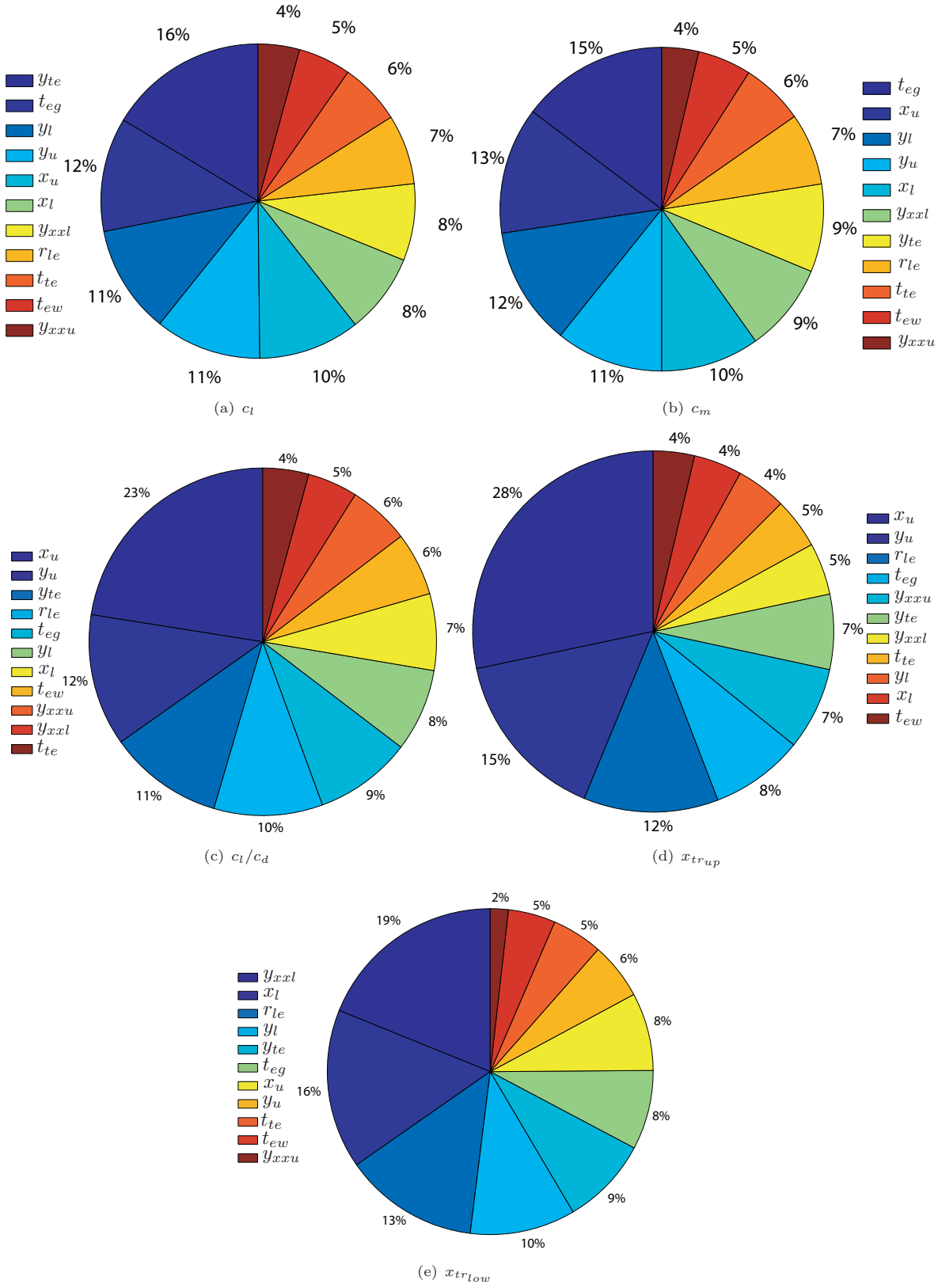

(a) c_l (b) c_m

(c) c_l/c_d (d) $x_{tr_{up}}$

(e) $x_{tr_{low}}$

FIGURE G.1: PARSEC Variables Contribution to Airfoil Aerodynamics at HALE Flight Envelope

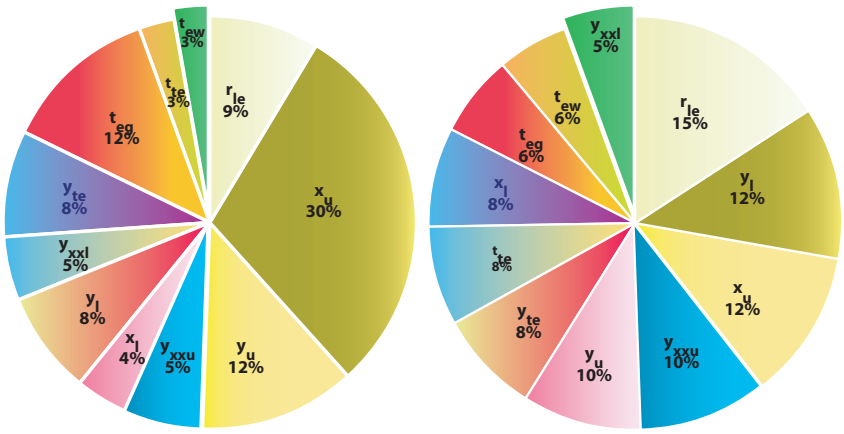

(a) c_d; Mach=0.10, $R_n = 4.00 \times 10^6$, $\alpha = 2°$ (b) $c_{l_{max}}$; Mach=0.10, $R_n = 3.00 \times 10^6$ & $\alpha = \alpha_{c_{l_{max}}}$

FIGURE G.2: PARSEC Variables Contribution to c_d & $c_{l_{max}}$ at HALE Flight Envelope

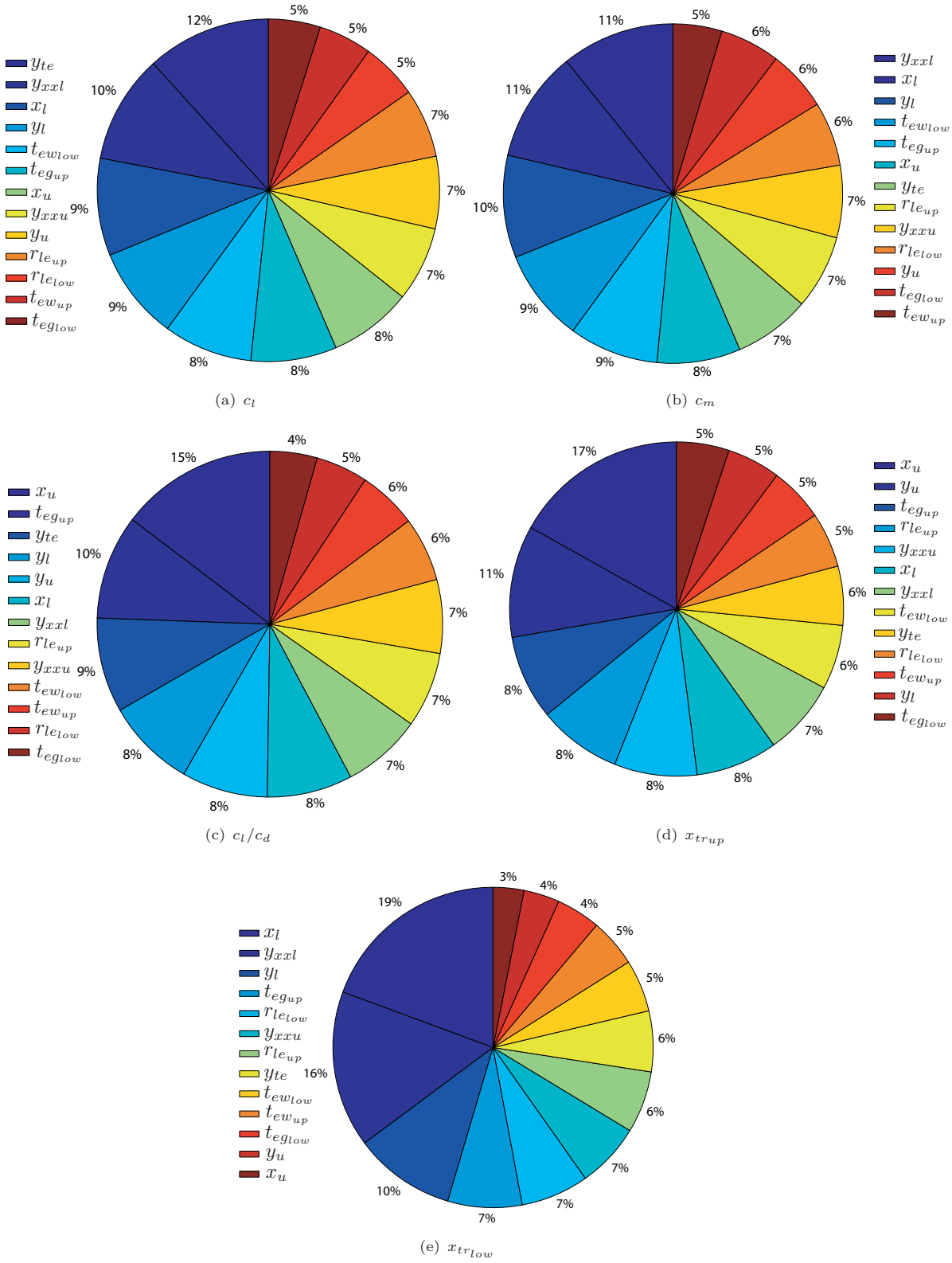

FIGURE G.3: PARSEC-Modified Variables Contribution to Airfoil Aerodynamics at HALE Flight Envelope

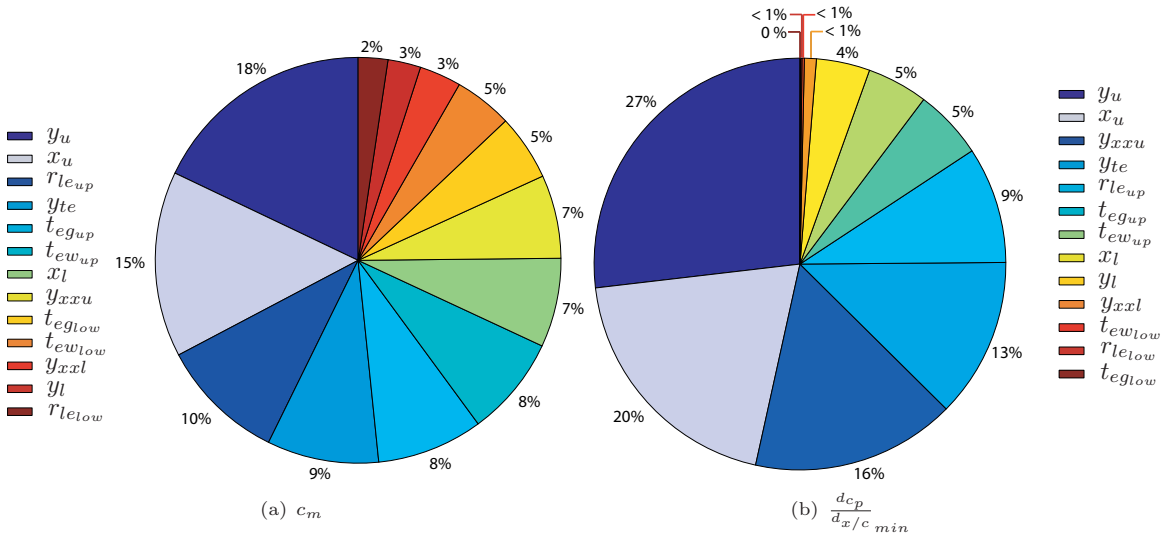

(a) c_m (b) $\frac{dc_p}{d_{x/c}}_{min}$

FIGURE G.4: PARSEC-Modified Variables Contribution to Airfoil Aerodynamics at Transonic Flight Envelope

Appendix H

Low-Fidelity Solver TSFOIL Validation for Transonic Design

H.1 TSFOIL Airfoil Node Population Convergence

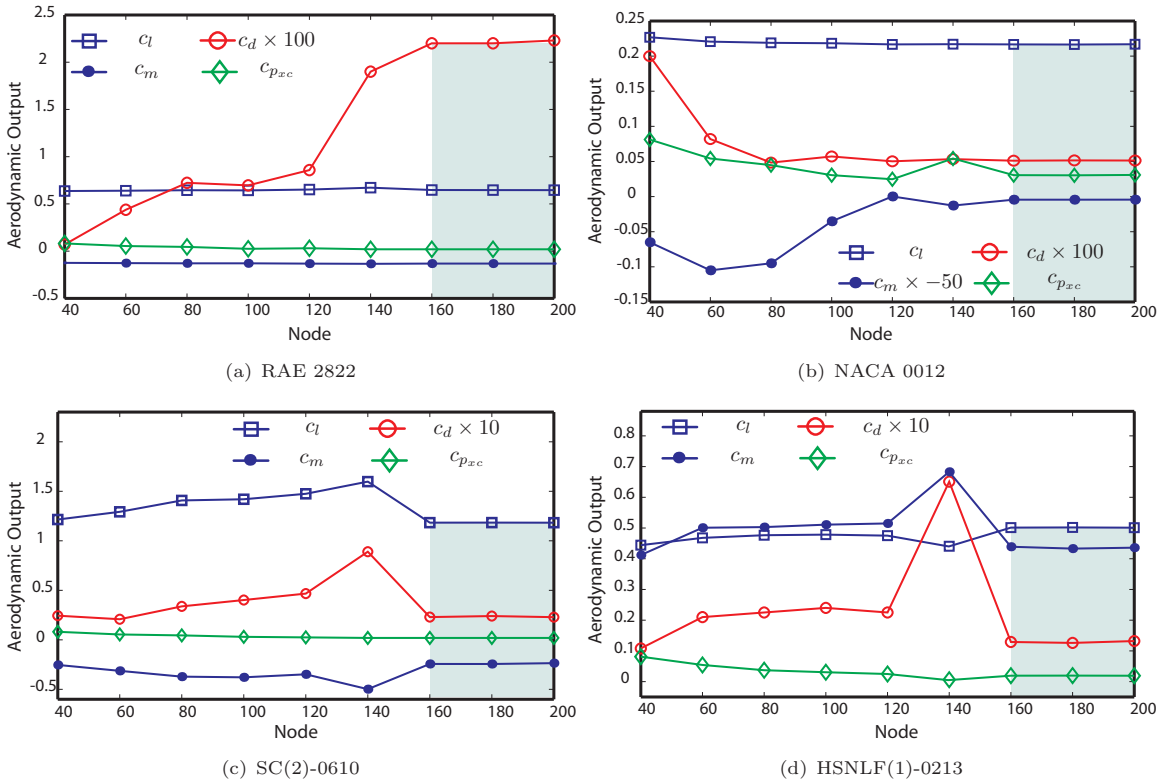

(a) RAE 2822

(b) NACA 0012

(c) SC(2)-0610

(d) HSNLF(1)-0213

FIGURE H.1: Effect of TSFOIL Node Distribution on Aerodynamic Convergence at Transonic Conditions; Mach=0.74, $R_n = 2.70 \times 10^6$ & $\alpha = 2^\circ$

Appendix I

Angle-of-Attack Trimming Analysis at Transonic Flight Envelope

I.1 RAE 2822 Angle-of-Attack Trimming Analysis

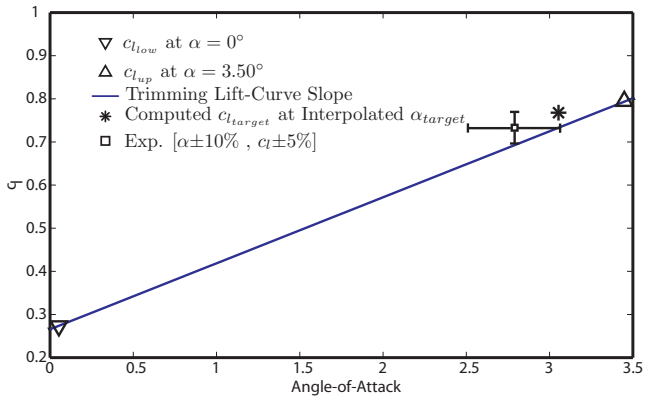

FIGURE I.1: RAE 2822 Lift-Curve Slope Estimation by α_{trim} for c_l^T Estimation Approach

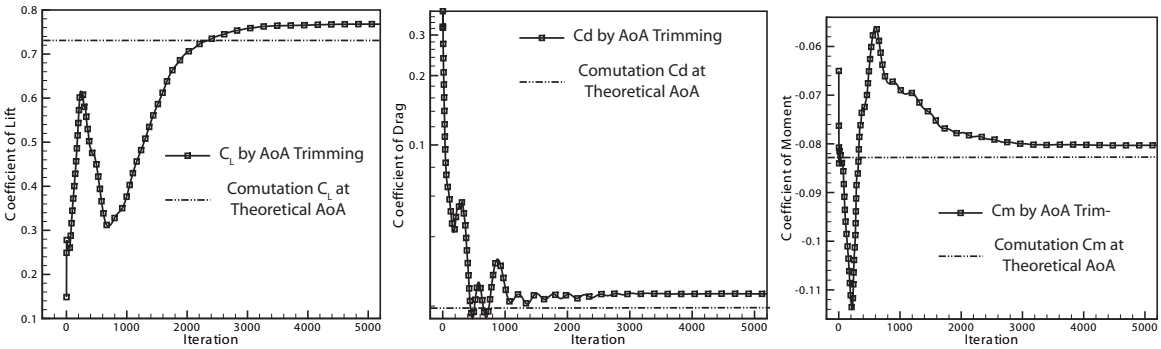

(a) RAE 2822 Convergence to $c_{l_{target}} = 0.733$ by α_{trim}

(b) RAE 2822 Convergence to $c_{d_{target}} = 0.0197$ by α_{trim}

(c) RAE 2822 Convergence to $c_{m_{target}} = -0.0833$ by α_{trim}

FIGURE I.2: RAE 2822 Aerodynamic Coefficients at Target Lift by α_{trim} Approach

Appendix J

AoA by Trimming at Transonic Flight Envelope

The data is representative of the PARSEC-Modified method with 13 design variables from Table 6.20.

J.1 Boxplot Representation of the Established c_l^T Distribution

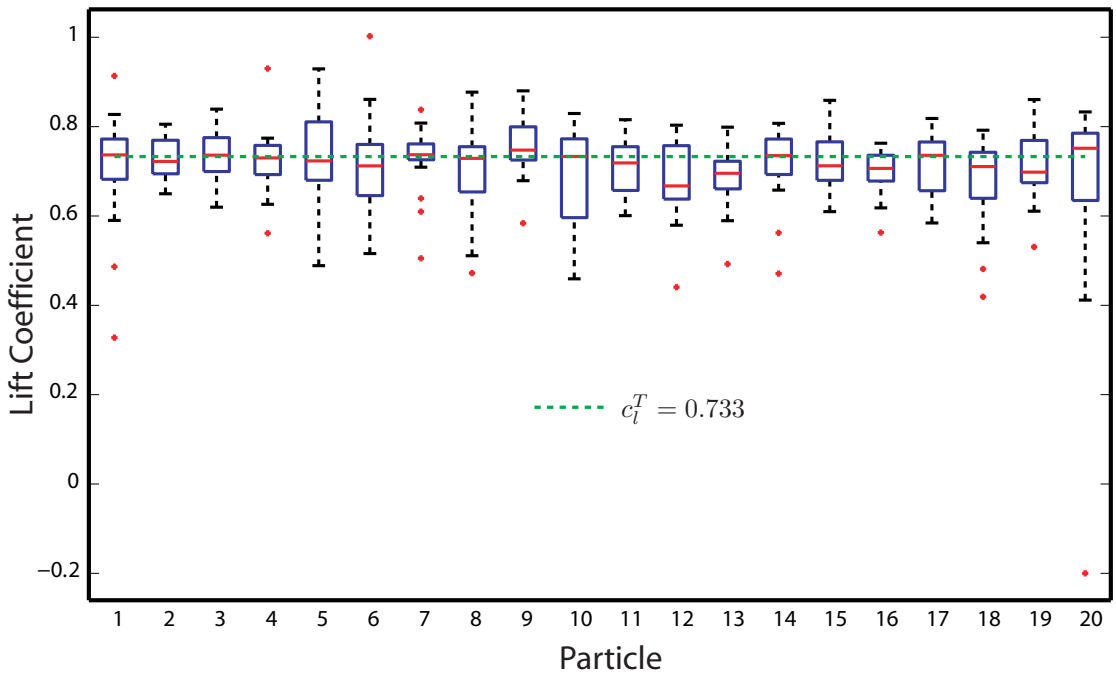

FIGURE J.1: Transonic Airfoil Design Boxplot Analysis of the Computed c_l^T of each Airfoil Modeled by a Particle in the Swarm

J.2 Histogram Representation of the Established c_l^T Distribution

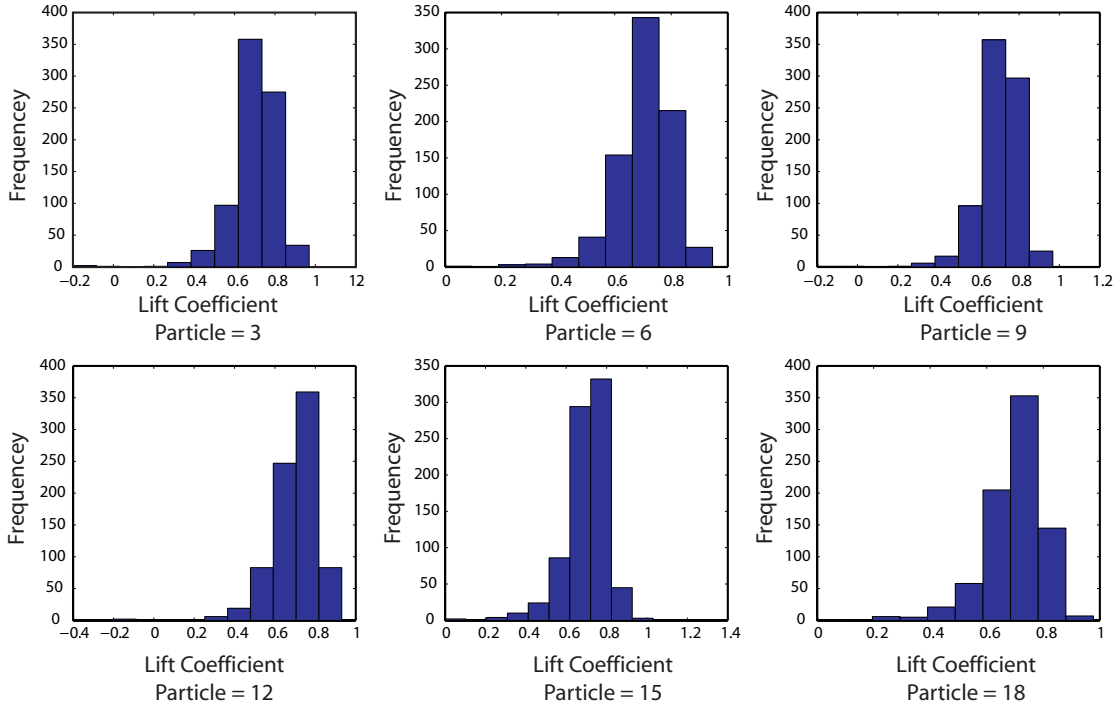

FIGURE J.2: Transonic Airfoil Design Histogram Analysis of the $c_l^T = 0.733$ Distribution For Select Particles in the Swarm

The c_l^T for the majority of airfoils in the swarm during the design evolution process are about the specified target $c_l^T = 0.733$. The sample size of the airfoils decreases proportionally for groupings that are offset to the target range $c_l^T \approx 0.733$. Few Airfoils with c_l^T that are at the boundary of the mapped performance zone are evident and are attributed to errors in the developed methodology.

Appendix K

Transonic Airfoil Design Aerodynamic Optimisation Analysis

K.1 Airfoil Optima & Equating Coefficient of Pressure by the PARSEC-Modified Reduced Modeling Shape Function & Hybrid Optimisation Approach

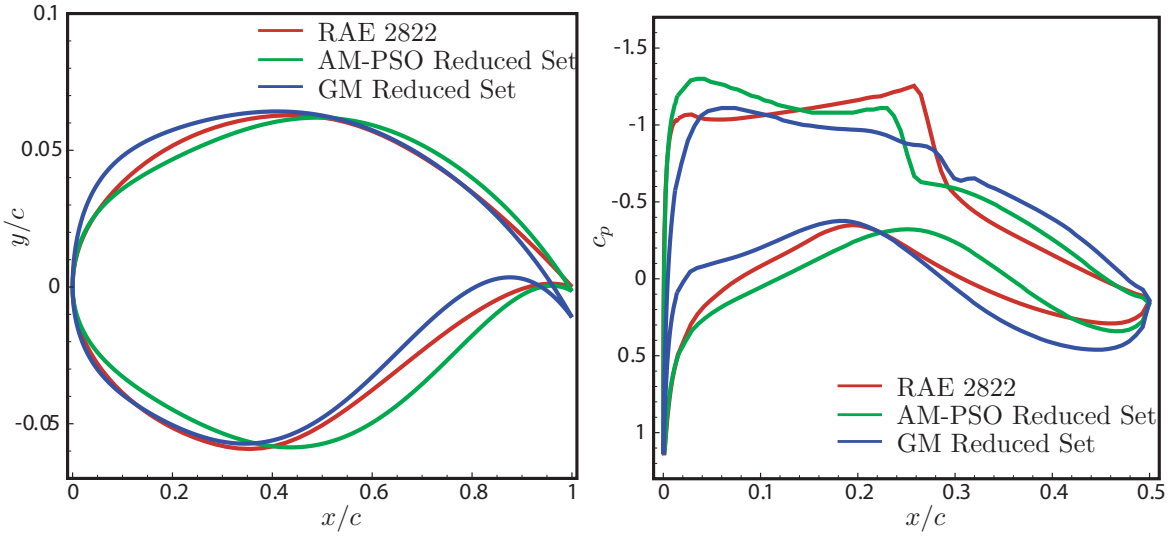

(a) Airfoil

(b) Coefficient of Pressure

FIGURE K.1: Transonic Airfoil Optimisation at $c_l^T \approx 0.733$

K.2 Transonic Airfoil Design Convergence to Optima by PARSEC-Modified Reduced Modeling Shape Function & Hybrid Optimisation Approach

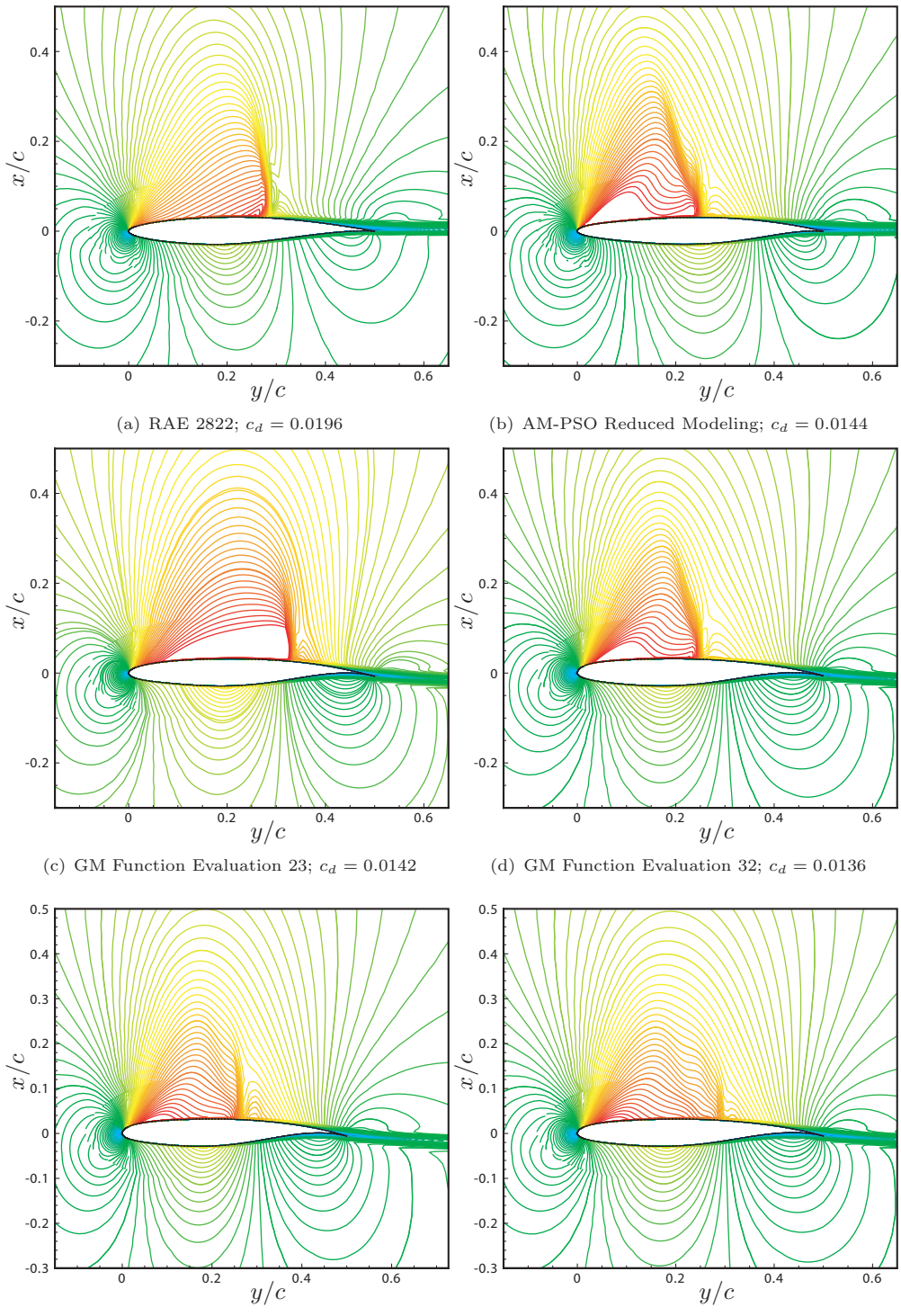

(a) RAE 2822; $c_d = 0.0196$

(b) AM-PSO Reduced Modeling; $c_d = 0.0144$

(c) GM Function Evaluation 23; $c_d = 0.0142$

(d) GM Function Evaluation 32; $c_d = 0.0136$

(e) GM Function Evaluation 36; $c_d = 0.0130$

(f) GM Function Evaluation 43; $c_d = 0.0128$

FIGURE K.2: Transonic Airfoil Design Convergence toward an Optima by the PARSEC-Modified Reduced Variable Set Modeling Approach

Appendix L

Online-Training ANN Model Development Performance Charts

L.1 Ackley Test Function

L.1.1 ANN Function Approximation Model

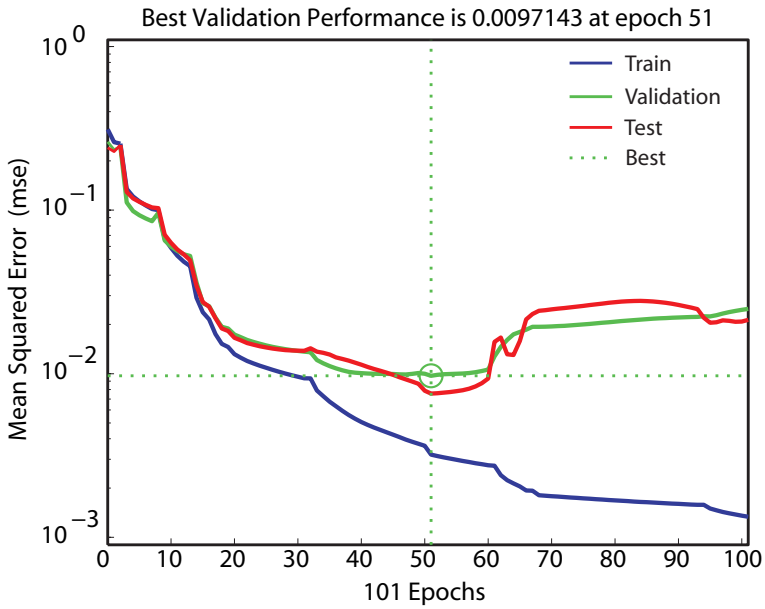

FIGURE L.1: Ackley Function ANN Approximation Training Performance

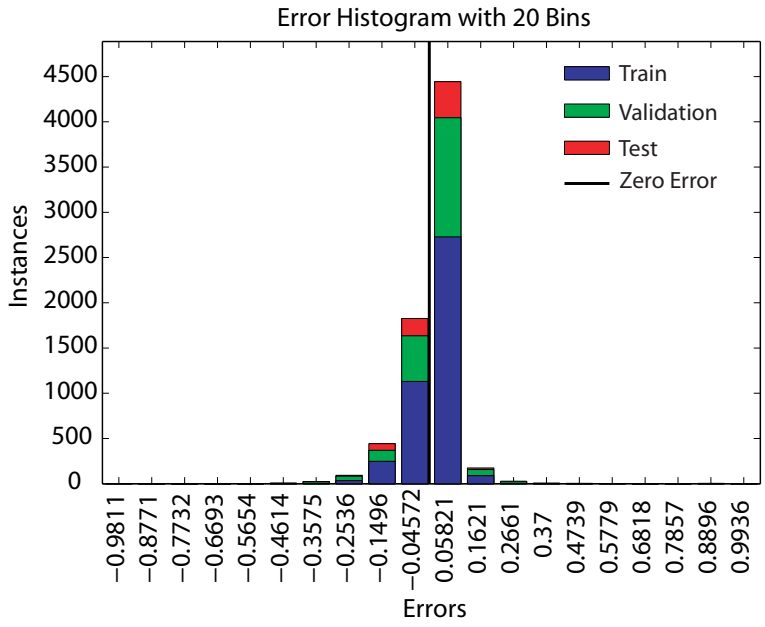

FIGURE L.2: Ackley Function ANN Approximation Training Error Histogram

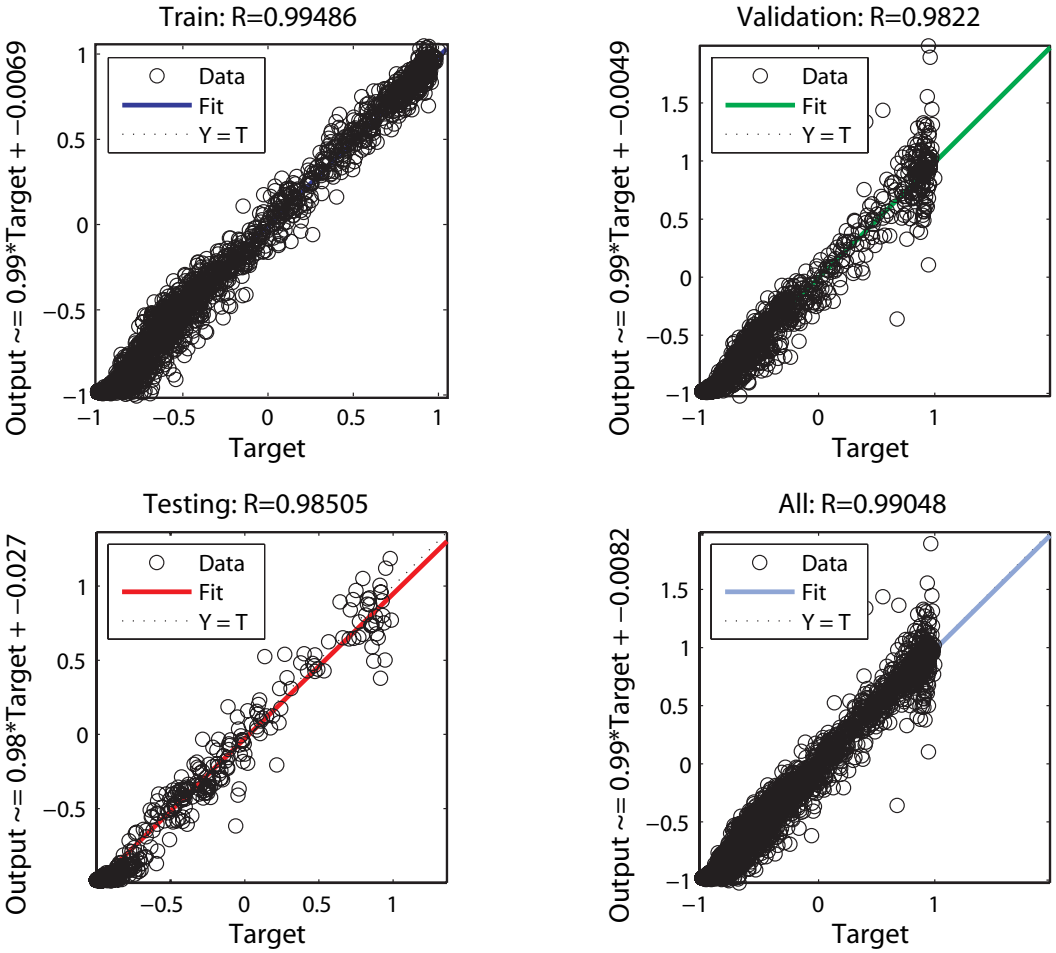

FIGURE L.3: Ackley Function ANN Approximation Regression Analysis

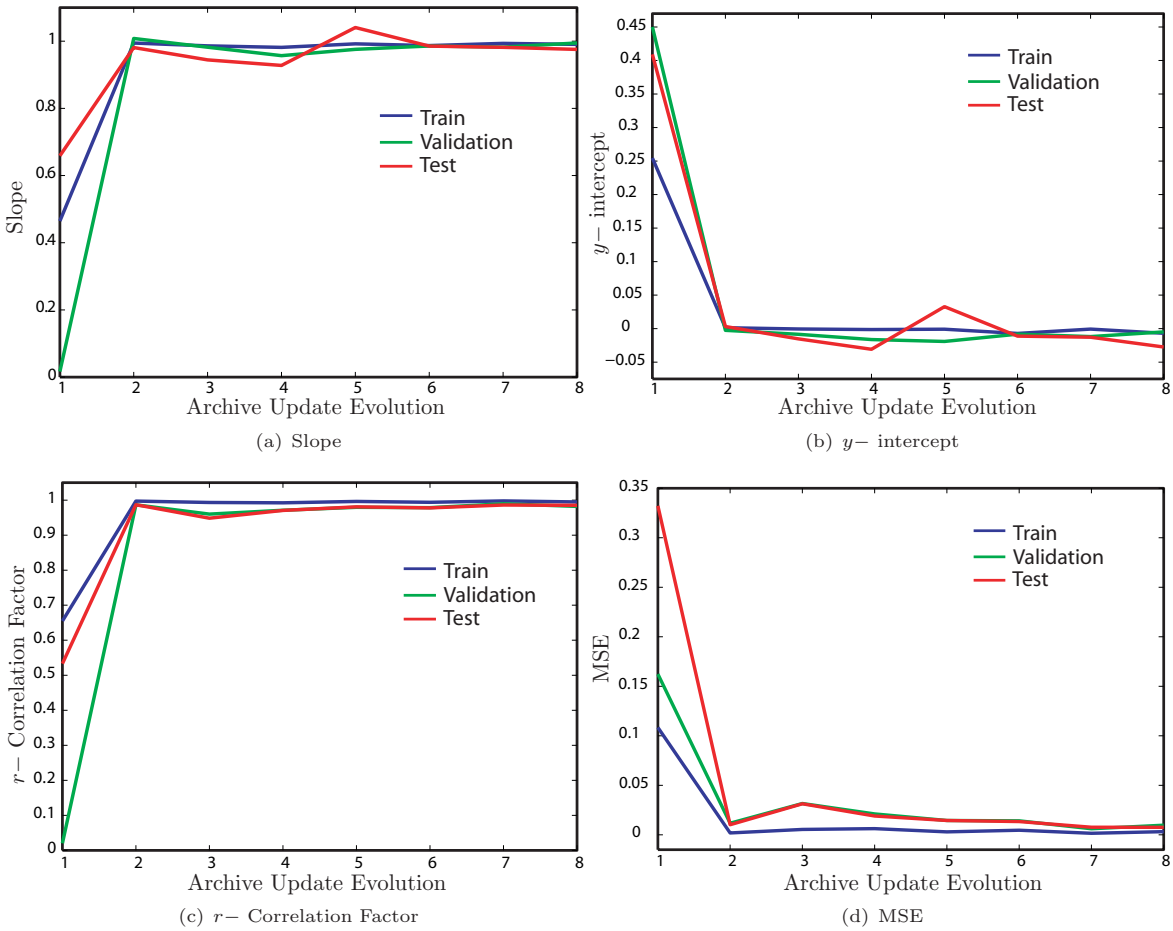

(a) Slope

(b) $y-$ intercept

(c) $r-$ Correlation Factor

(d) MSE

FIGURE L.4: Ackley Function ANN Training Regression Curve & Error Performance

L.1.2 ANN Pattern Recognition Model

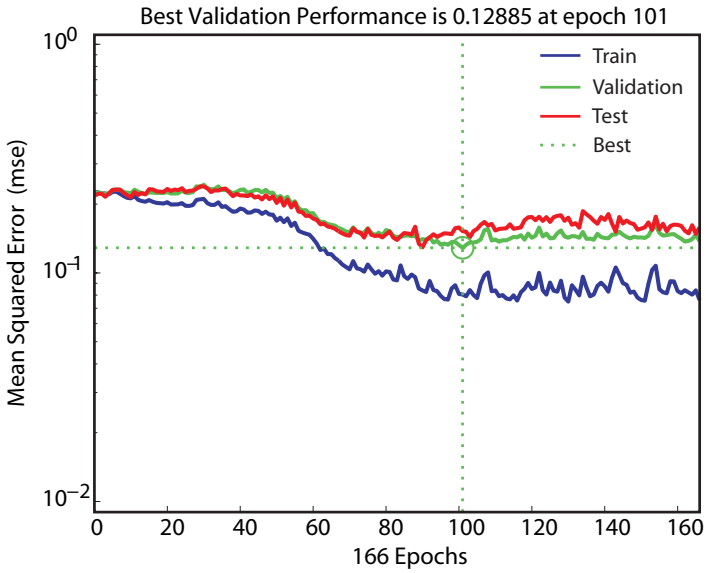

FIGURE L.5: Ackley ANN Pattern Recognition Training Performance

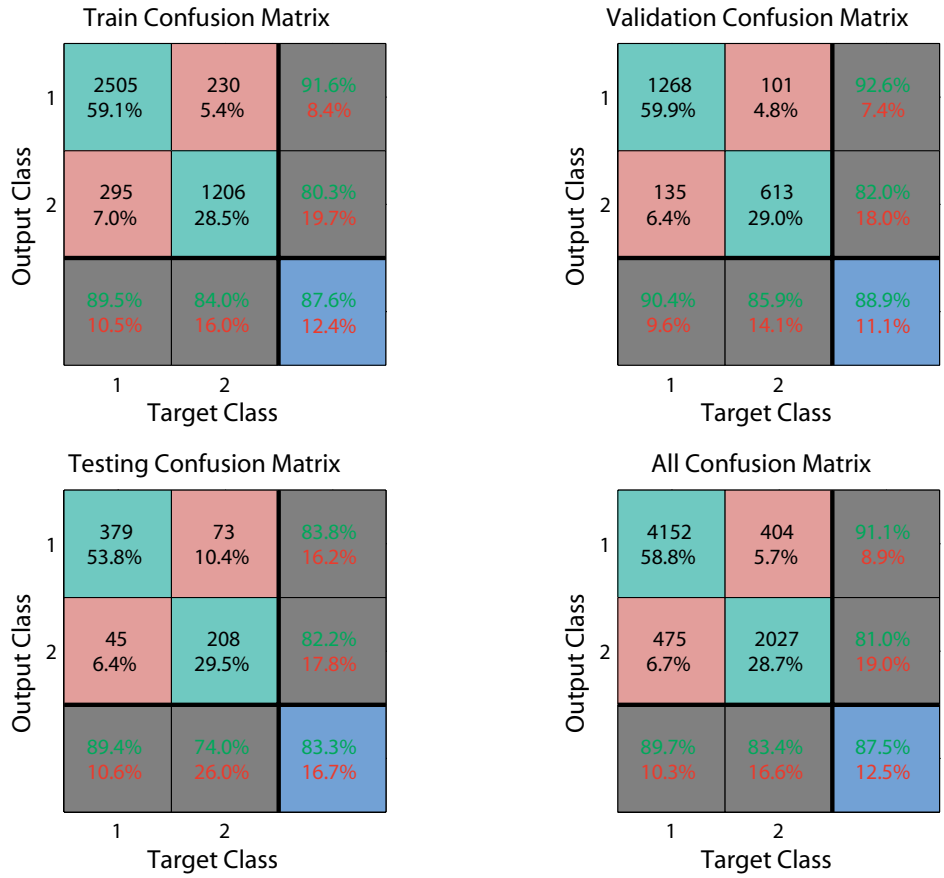

FIGURE L.6: Ackley ANN Pattern Recognition Confusion Analysis

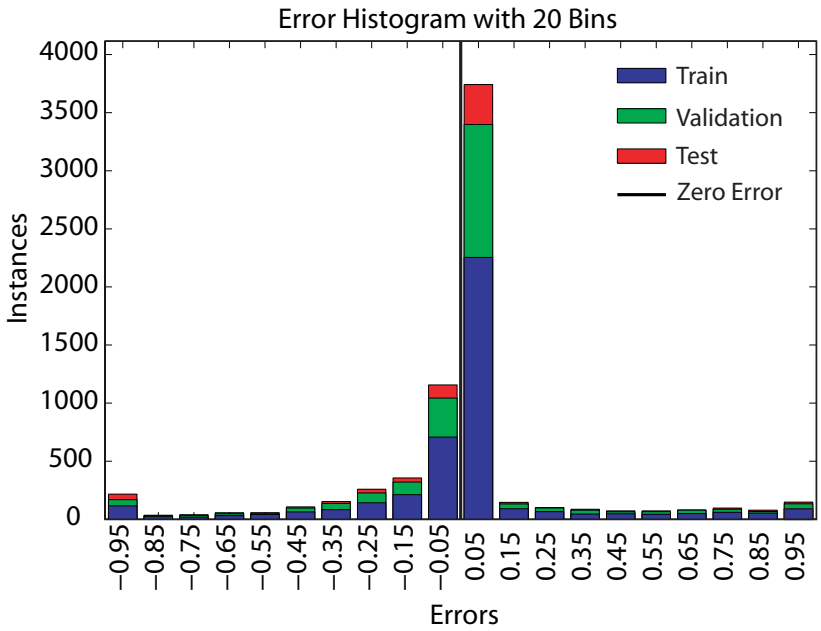

FIGURE L.7: Ackley ANN Pattern Recognition Training Error Histogram

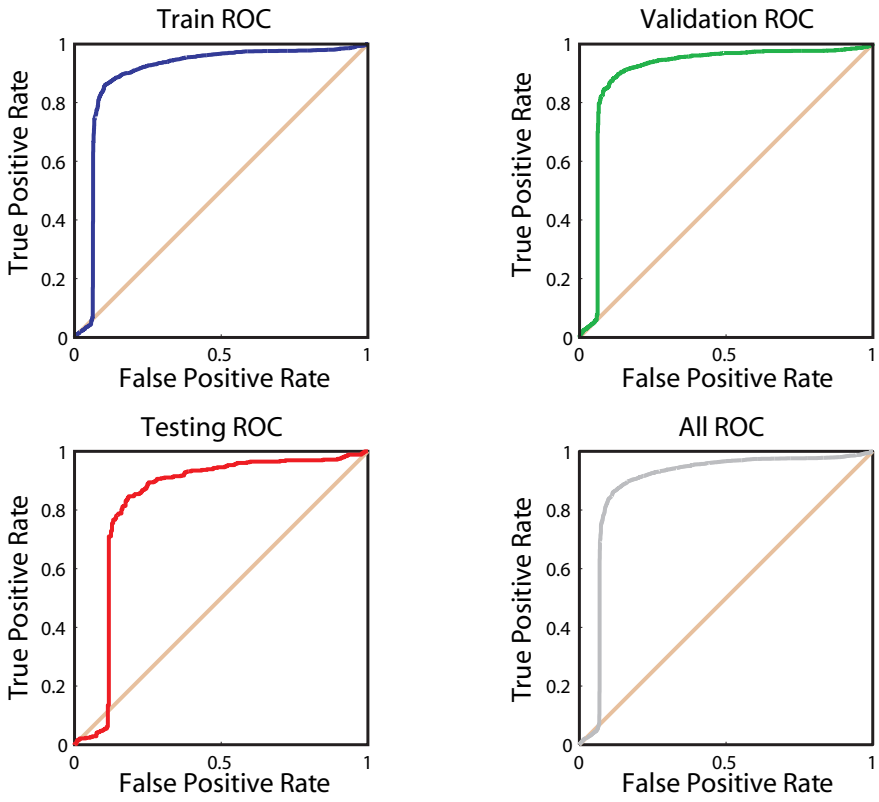

FIGURE L.8: Ackley ANN Pattern Recognition Receiver Operating Characteristic

TABLE L.1: Ackley Function - ANN Pattern Recognition Classification Accuracy Measure by ROC Curve Representation

Performance Measure	Train	Validation	Testing	All
AUC	0.8922	0.8985	0.8279	0.8942
OP	(0.1407, 0.8854)	(0.1415, 0.9052)	(0.2527, 0.8939)	(0.1540, 0.8984)

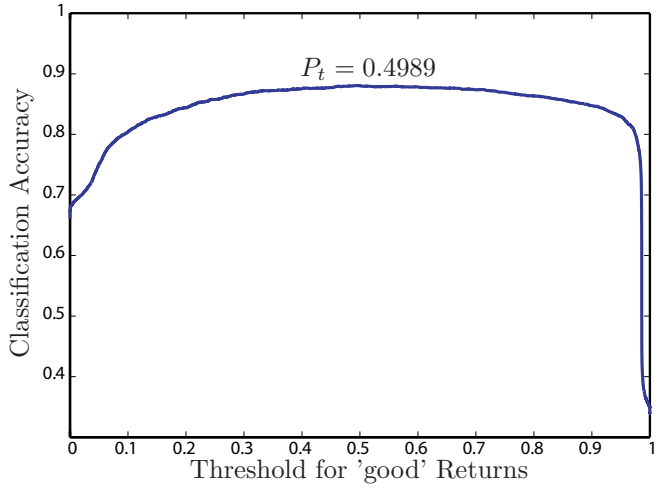

FIGURE L.9: Ackley ANN Pattern Recognition Classification Ensemble Accuracy

L.2 Michalewics Test Function

L.2.1 ANN Function Approximation Model

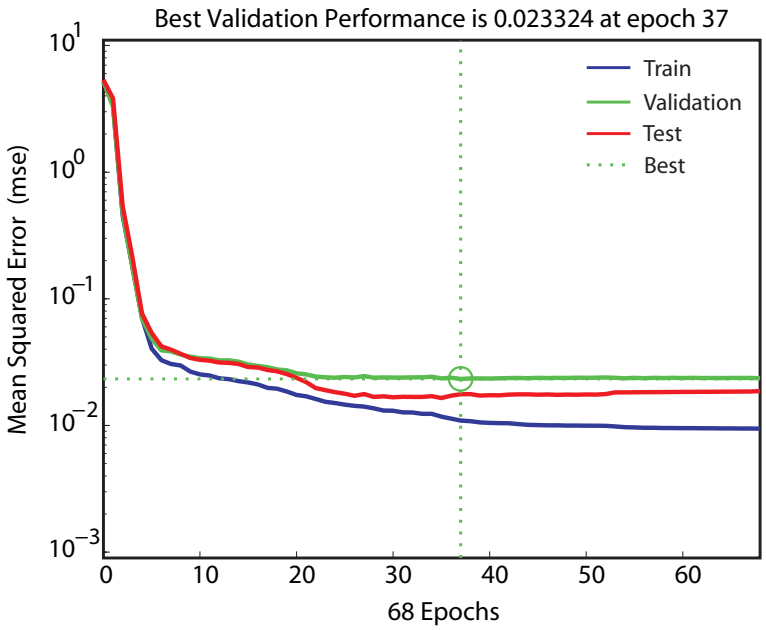

FIGURE L.10: Michalewics Function ANN Approximation Training Performance

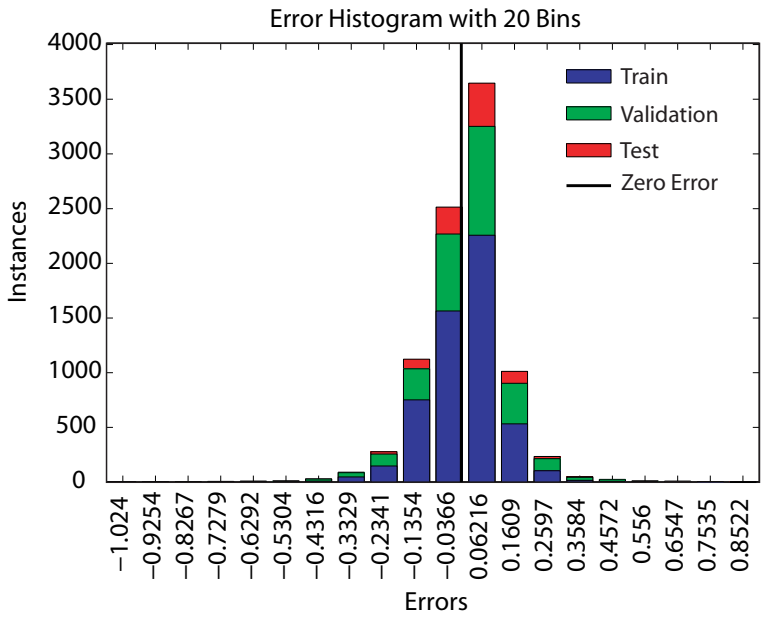

FIGURE L.11: Michalewics Function ANN Approximation Training Error Histogram

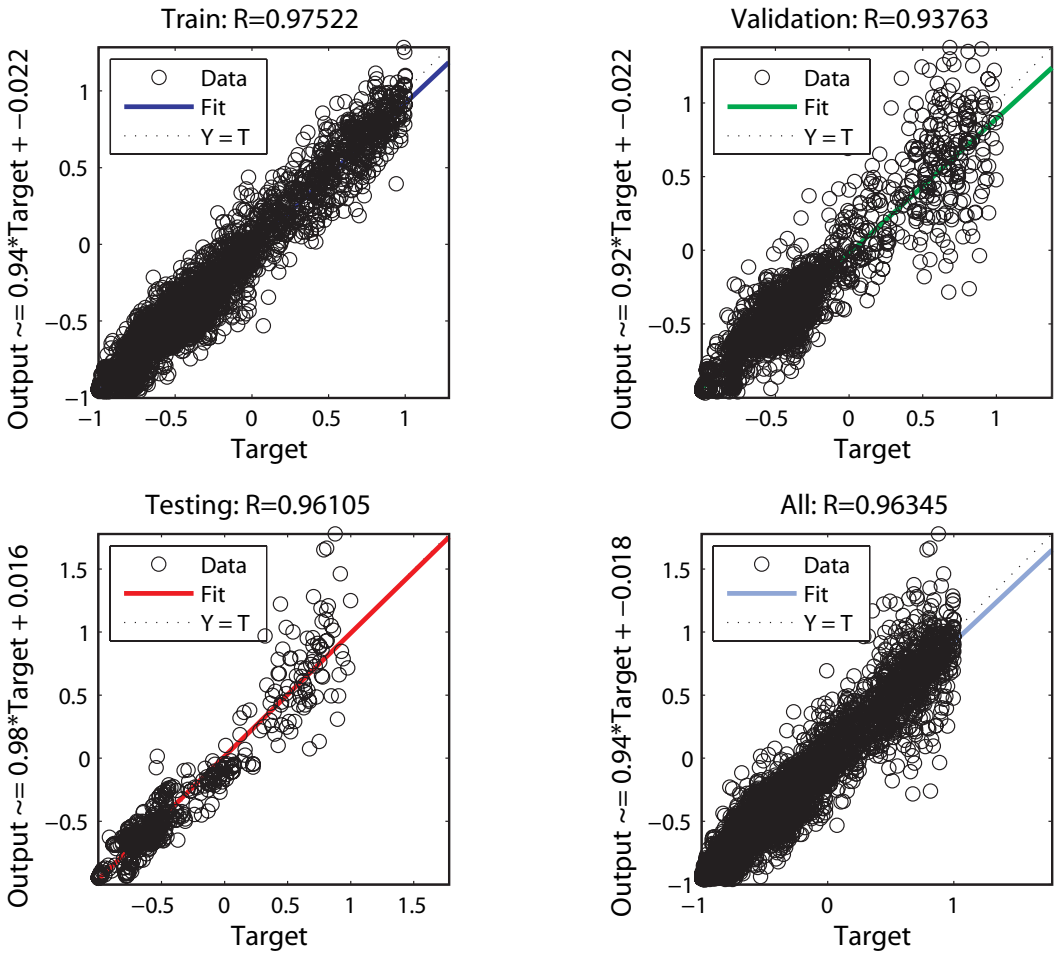

FIGURE L.12: Michalewics Function ANN Approximation Regression Analysis

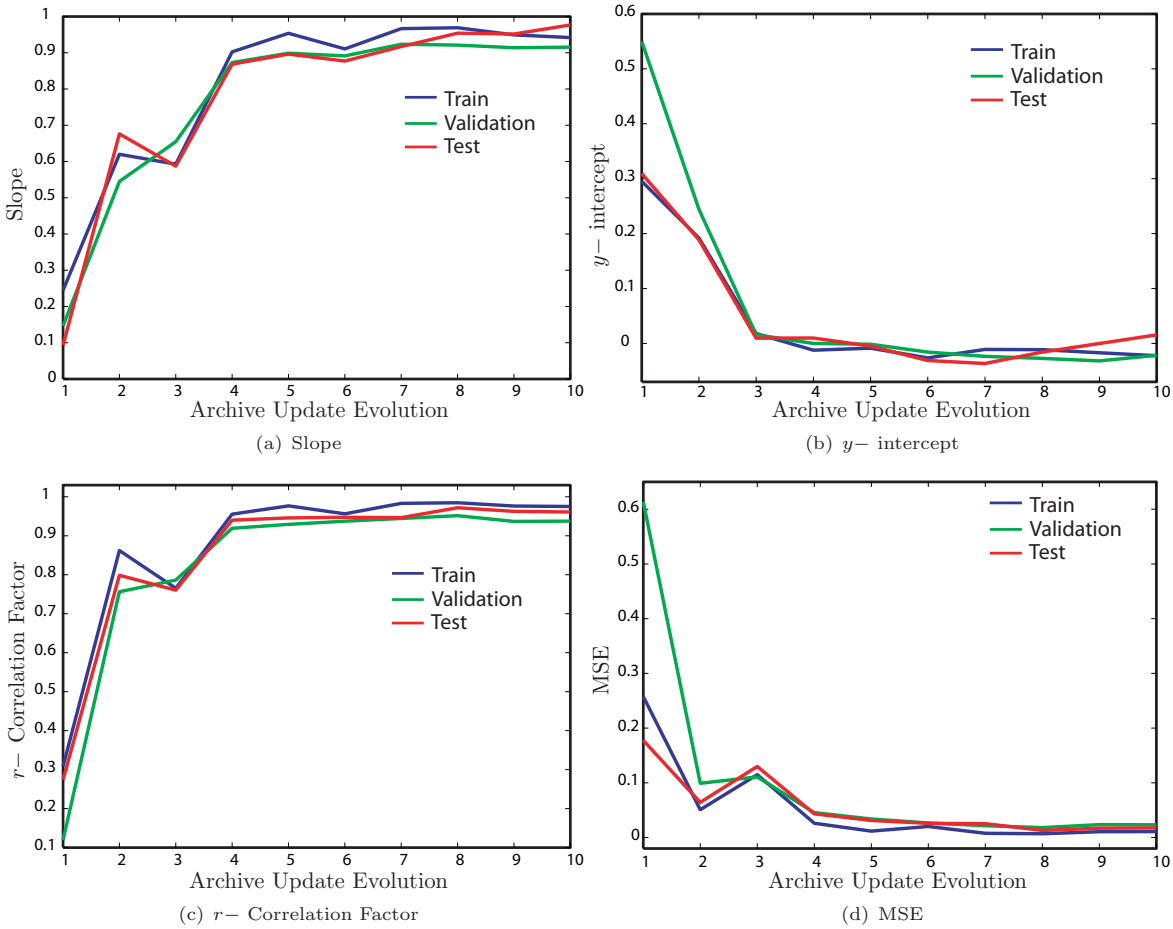

FIGURE L.13: Michalewics Function ANN Training Regression Curve & Error Performance

L.2.2 ANN Pattern Recognition Model

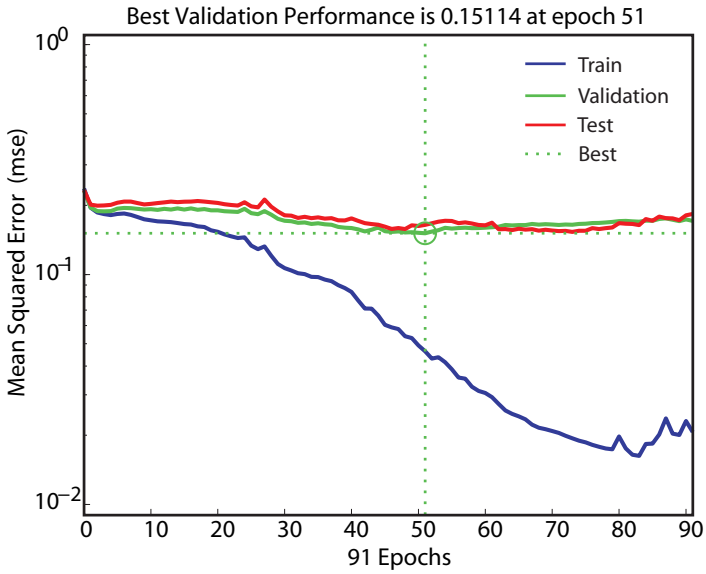

FIGURE L.14: Michalewics ANN Pattern Recognition Training Performance

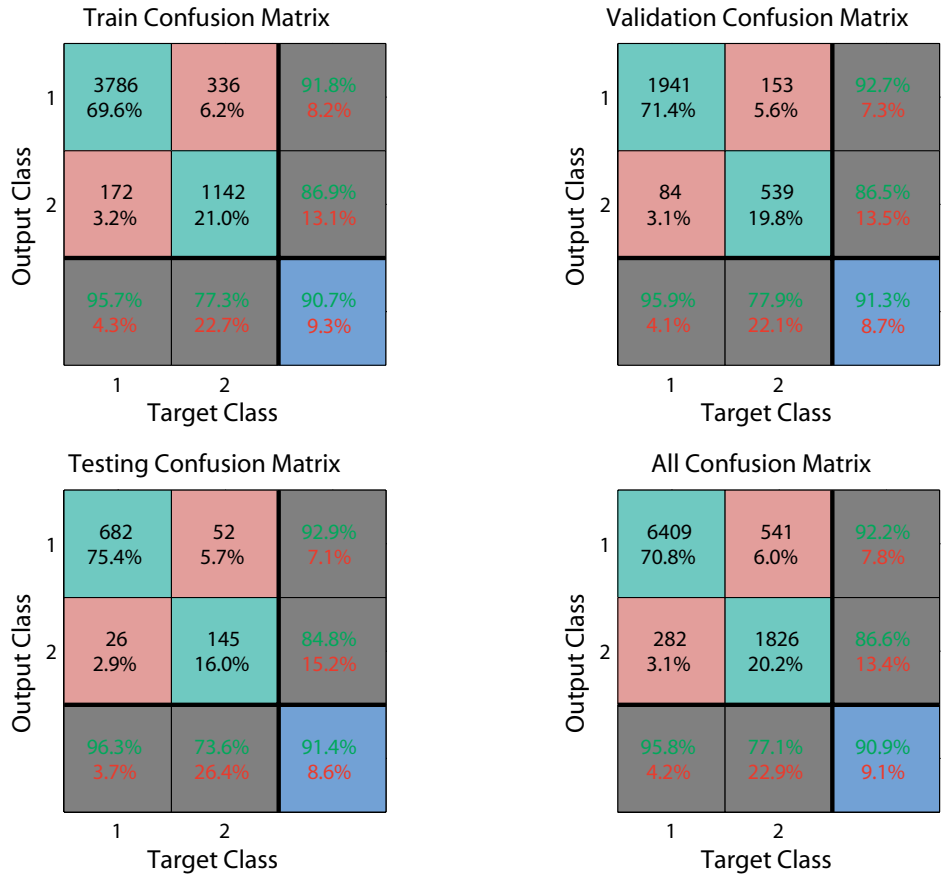

FIGURE L.15: Michalewics ANN Pattern Recognition Confusion Analysis

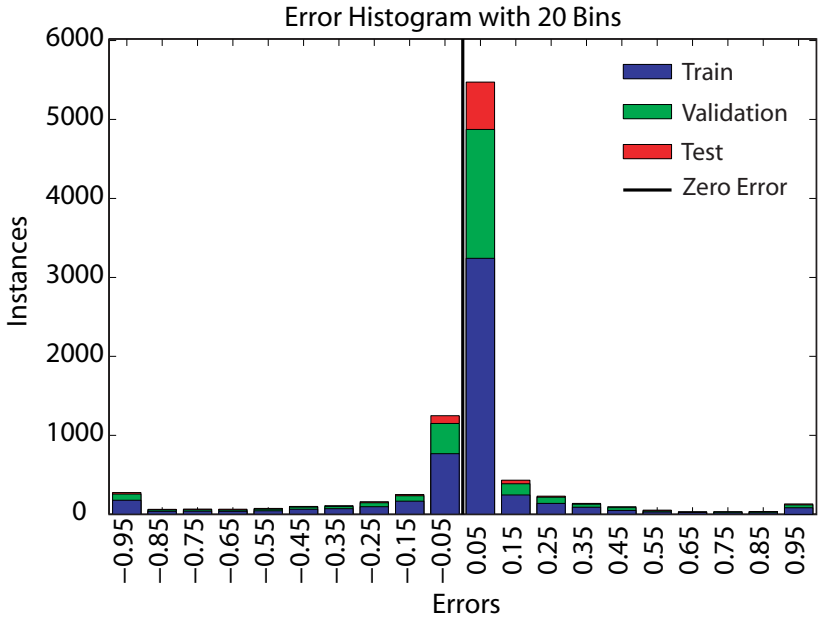

FIGURE L.16: Michalewics ANN Pattern Recognition Training Error Histogram

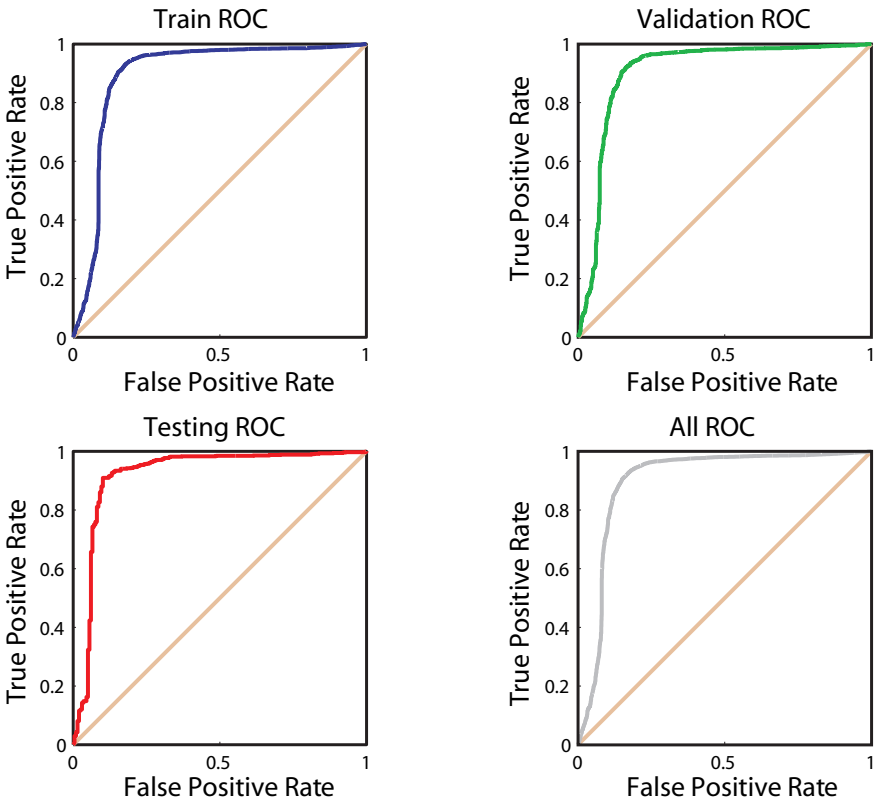

FIGURE L.17: Michalewics ANN Pattern Recognition Receiver Operating Characteristic

TABLE L.2: Michalewics Function - ANN Pattern Recognition Classification Accuracy Measure by ROC Curve Representation

Performance Measure	Train	Validation	Testing	All
AUC	0.7987	0.8250	0.8260	0.8993
OP	(0.3019, 0.8746)	(0.3060, 0.8926)	(0.3075, 0.9192)	(0.2286, 0.9579)

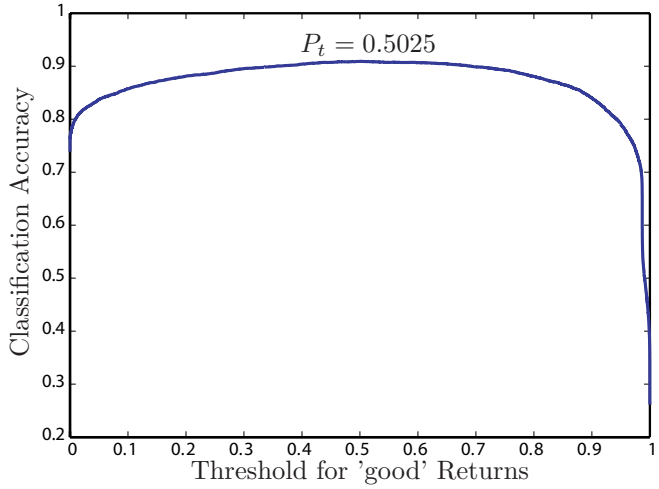

FIGURE L.18: Michalewics ANN Pattern Recognition Classification Ensemble Accuracy

L.3 Schwefel Test Function

L.3.1 ANN Function Approximation Model

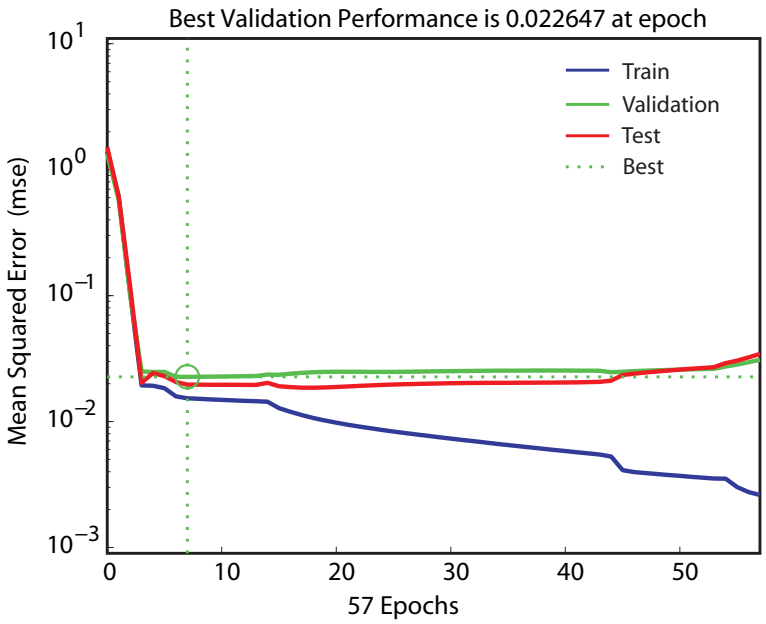

FIGURE L.19: Schwefel Function ANN Approximation Training Performance

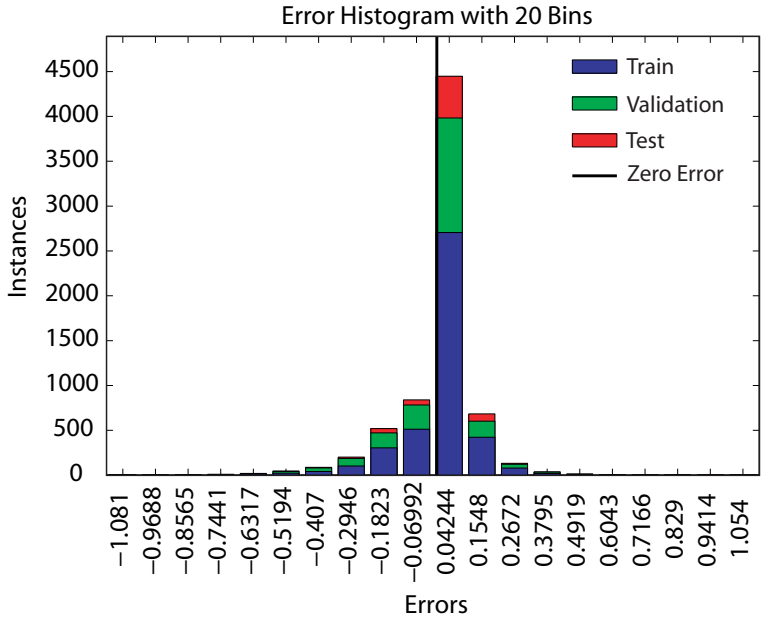

FIGURE L.20: Schwefel Function ANN Approximation Training Error Histogram

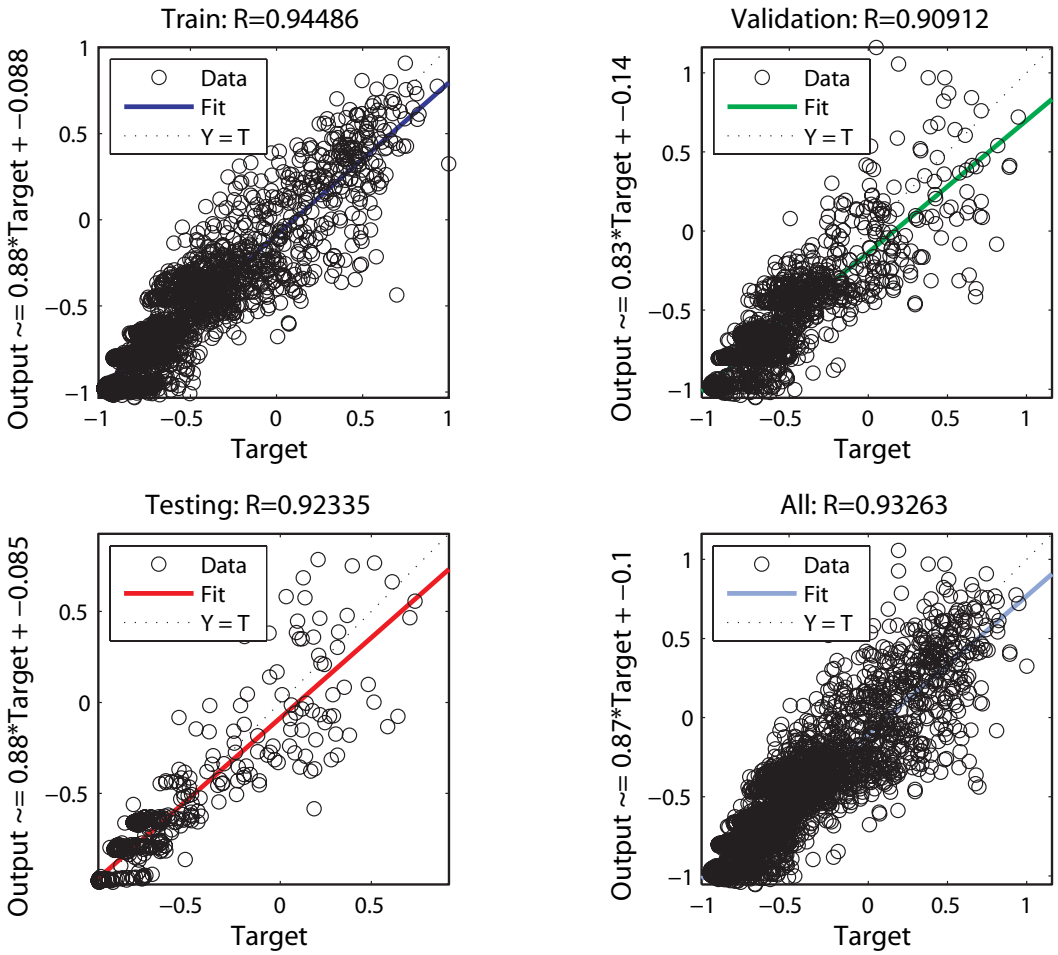

FIGURE L.21: Schwefel Function ANN Approximation Regression Analysis

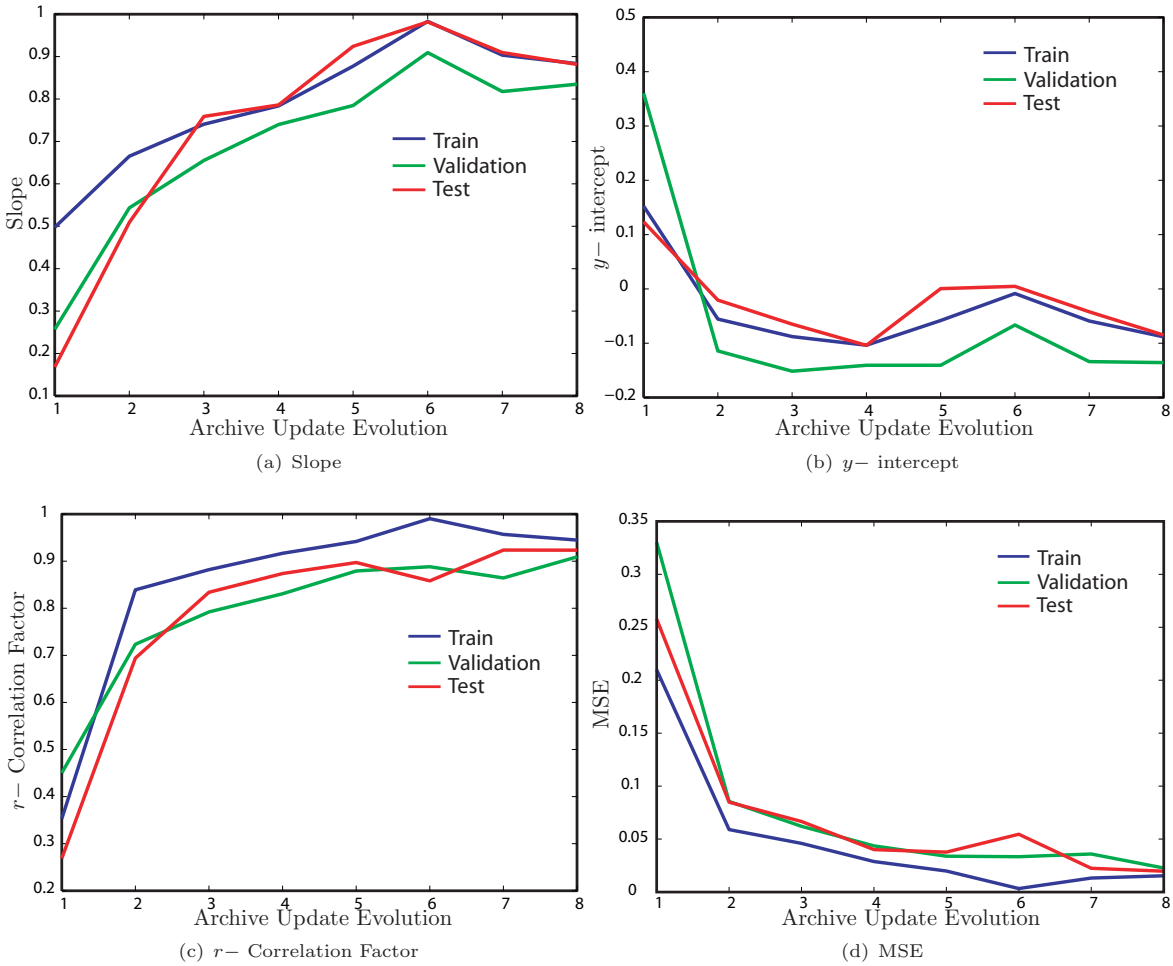

(a) Slope (b) $y-$ intercept

(c) $r-$ Correlation Factor (d) MSE

FIGURE L.22: Schwefel Function ANN Training Regression Curve & Error Performance

L.3.2 ANN Pattern Recognition Model

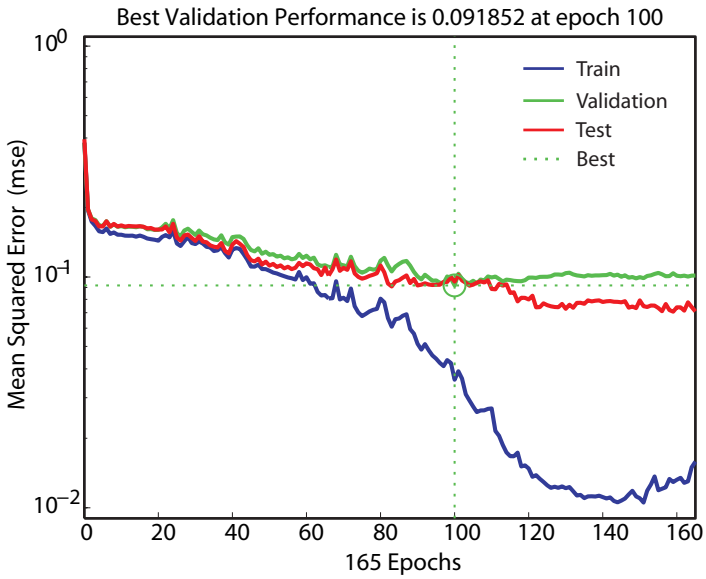

FIGURE L.23: Schwefel ANN Pattern Recognition Training Performance

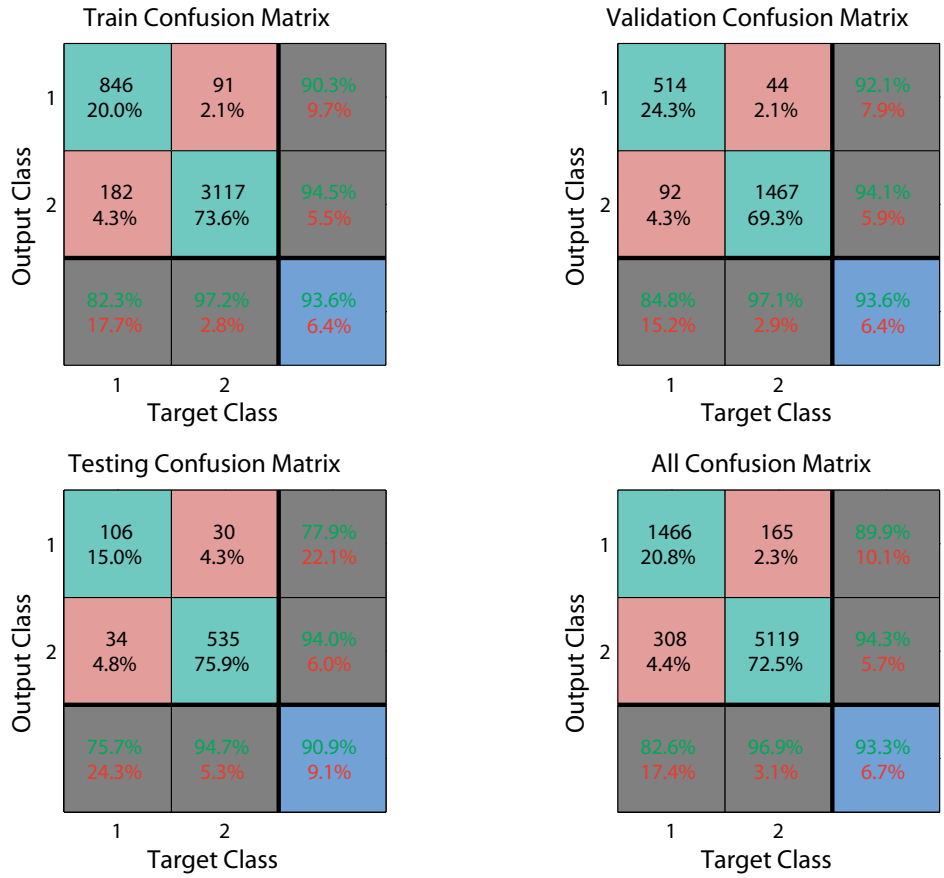

FIGURE L.24: Schwefel ANN Pattern Recognition Confusion Analysis

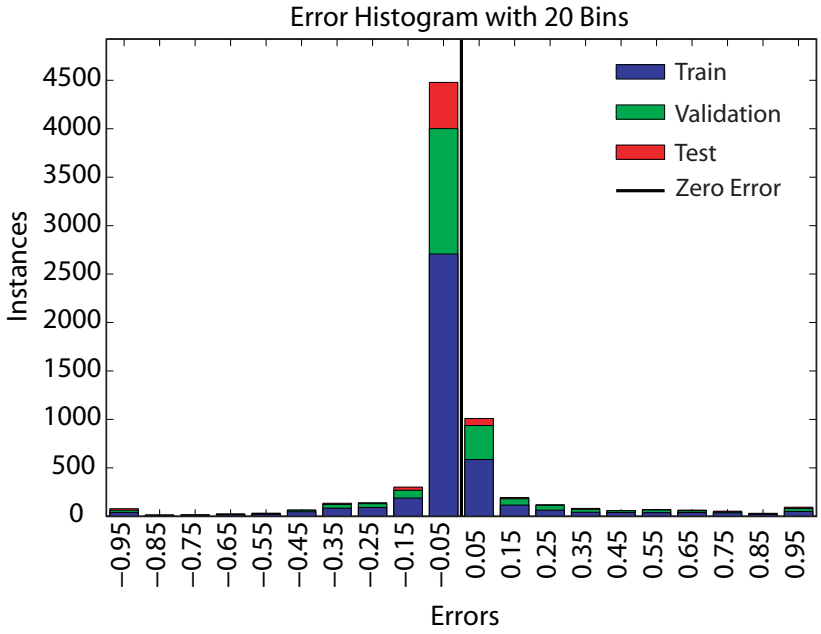

FIGURE L.25: Schwefel ANN Pattern Recognition Training Error Histogram

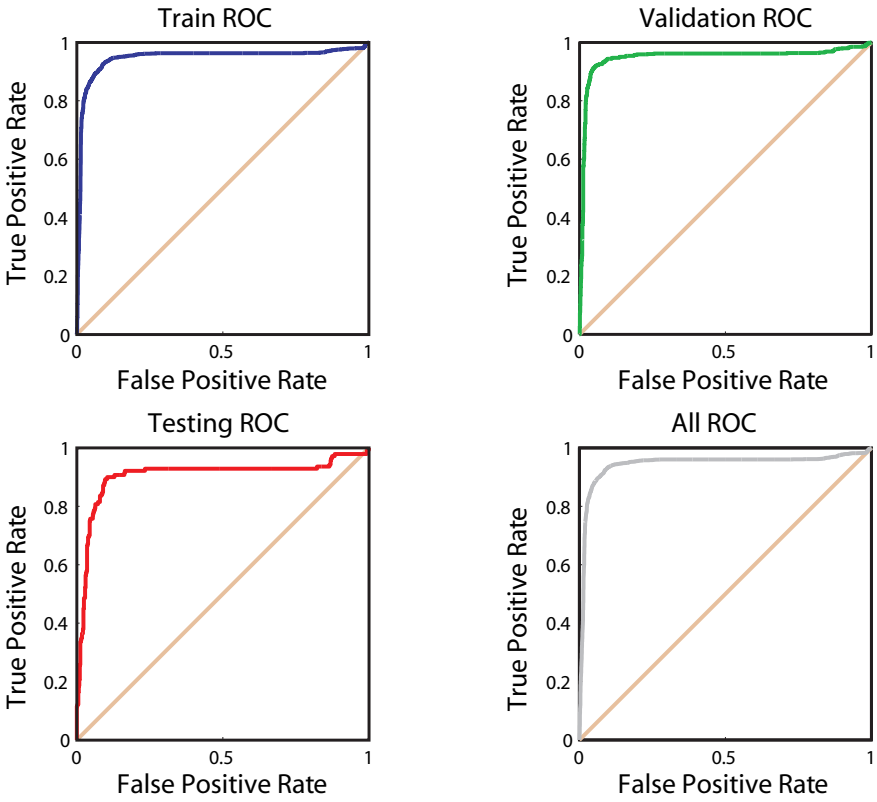

FIGURE L.26: Schwefel ANN Pattern Recognition Receiver Operating Characteristic

TABLE L.3: Schwefel Function - ANN Pattern Recognition Classification Accuracy Measure by ROC Curve Representation

Performance Measure	**Train**	**Validation**	**Testing**	**All**
AUC	0.9464	0.9477	0.9042	0.9470
OP	(0.0334, 0.8414)	(0.0397, 0.8977)	(0.0442, 0.7500)	(0.0335, 0.8501)

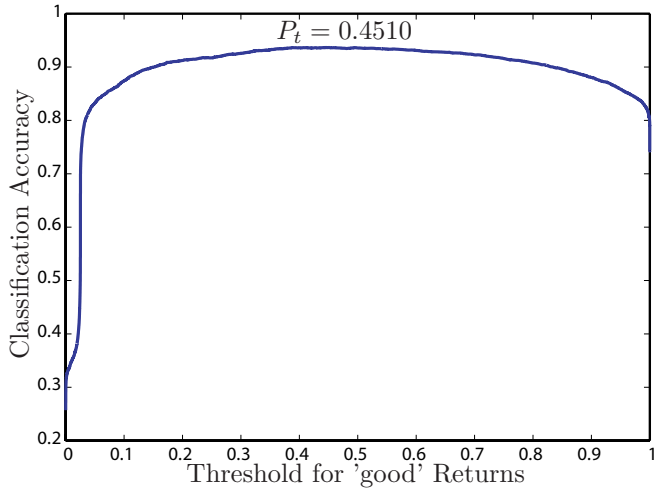

FIGURE L.27: Schwefel ANN Pattern Recognition Classification Ensemble Accuracy

Bibliography

[1] Axel Schauenburg. Conceptual design of a multi-mission re-configurable unmanned aerial vehicle for australian operations. Undergraduate Thesis Project, RMIT University, Australia, June 2004.

[2] Brian D. Roth and William A. Crossley. Application of optimization techniques in the conceptual design of morphing aircraft. In *AIAA* 3^{rd} *Annual Aviation Technology, Integration and Operations (ATIO) Tech, Denver, Colorado*. AIAA, 17-19 November, 2003.

[3] Peter Phleps. Conceptual wing design for a multi-mission re-configurable unmanned aerial vehicle for australian operations. Undergraduate Thesis Project, RMIT University, Australia, October 2005.

[4] Hanno Hessen. Conceptual fuselage design of a multi-mission re-configurable unmanned aerial vehicle. Undergraduate Thesis Project, RMIT University, Australia, September 2005.

[5] Eva-Kristin Roth. Mission simulation of different wing design concepts for a multi mission reconfigurable unmanned aerial vehicle. Undergraduate Thesis Project, RMIT University, Australia, April 2006.

[6] Dan M. Somer. Design and experimental results for a natural-laminar-flow airfoil for general aviation applications. Technical report, NASA Langley Research Center, 1981.

[7] Tom Nguyen and Adrian Stafford. A systems approach to the conceptual design of a multimission re-configurable unmanned air vehicle. Undergraduate Thesis Project, RMIT University, Australia, November 2002.

[8] Zheng Qin, Fan Yu, Zhewen Shi, and Yu Wang. Adaptive inertia weight particle swarm optimization. In Leszek Rutkowski, Ryszard Tadeusiewicz, Lotfi Zadeh, and Jacek Zurada, editors, *Artificial Intelligence and Soft Computing ICAISC 2006*, volume 4029 of *Lecture Notes in Computer Science*, pages 450–459. Springer Berlin / Heidelberg.

[9] M.A. McDonald P.H. Cook and M.C.P. Firmin. Aerofoil rae 2822 - pressure distributions and boundary layer and wake measurements. AGARD Advisory Report 138, Royal Aircraft Establishment, Farnborough, Hants, United Kingdom, 1979.

[10] J.E. Green. Air travel - greener by design, mitigating the environmental impact of aviation: Opportunities and priorities. Technical report, Design Science and Technology Sub-Group.

[11] Jason E. Hicken and David W. Zingg. Aerodynamic optimization algorithm with integrated geometry parameterization and mesh movement. *AIAA Journal*, 48:400–413, 2010.

[12] Advanced aviation fuels: a look ahead via a historical perspective.

[13] J. Lee and J. Kim. Kriging-based approximation optimization of high-speed train nose shape for reducing micropressure wave. *Journal of Rail and Rapid Transit*, 221:263 – 270.

[14] T. Sato Bienz C. Larsson and B. Ullbrand. In front of the grid - cfd at sauber petronas f1 leading the aerodynamic development. In 1^{st} *European Automotive CFD Conference, Bingen, GERMANY*. EACC, 25-26 June, 2003.

[15] Kalle Kaups George Tzong Hamid Hefazi Orhan Kural Hsun Chen Eric Besnard, Adeline Schmitz and Tuncer Cebeci. Hydrofoil design and optimization for fast ships. In *ASME International Congress and Exhibition, Anaheim, CA, USA*, 1998.

[16] National Aeronautics and Space Administration. *Wings in Orbit: Scientific and Engineering Legacies of the Shape Shuttle 1971-2010: Scientific and Engineering Legacies of the Space Shuttle*. United States Government Print, USA, 2005.

[17] Mark D. Maughmer. The design of winglets for low-speed aircraft. Technical report, The Pennsylvania State University, University Park, Pennsylvania, USA, 2001.

[18] Kavita Srinivas Doug Auld Dong-Seop Lee, Luis F. Gonzalez and Kee Chon Wong. Multiobjective and multidisciplinary design and optimisation of blended wing body uav via advanced evolutionary algorithms. In 2^{nd} *Australasian Unmanned Air Vehicles Conference*. AIAC, 19-22 March, 2007.

[19] Boeing. Boeing quiet noise technology initiatives. Technical report, Boeing Commercial Airplanes, Seattle, Washington, USA.

[20] Raymond W. Prouty. *Helicopter Performance, Stability and Control*. Krieger Publishing Company, Inc., Malabar, Florida, USA, 1995.

[21] Peretz P. Friedmann Bryan Glaz and Li Liu. Surrogate based optimization of helicopter rotor blades for vibration reduction in forward flight. In *47th AIAA/ASME/ASCE/AHS/ASC Structures, Structural Dynamics, and Materials Conference, Newport, Rhode Island*. American Institute of Aeronautics and Astronautics, 1-4 May, 2006.

[22] Dr. K. C. Wong. Aerospace industry opportunities in australia - unmanned aerial vehicles (uavs) - are they ready this time? are we? Technical report, Department of Aeronautical Engineering, University of Sydney, NSW, 1997.

[23] The Hon. Dr Brendan Nelson. Defence capability plan 2006 - 2016. Technical report, Australian Government - Department of Defence, Canberra, 2006.

[24] D. P. Raymer. *Aircraft Design: A Conceptual Approach, 2nd ed.* AIAA Education Series, Washington, DC, USA, 1992.

[25] D. J. Roskam. *Airplane Design - Part 1: Preliminary Sizing of Airplanes, vol. 1.* Design, Analysis and Research Corporation, 1440 Wakarusa Drive, Suite 500, Lawrence, Kansas, USA, 1985.

[26] M.L. Scott A.K. Sinha, R. Kusumo. A systems approach to issues and challenges of uav systems. In *16th Bristol International UAV Systems Conference, Bristol, UK*, 3-5 April, 2001.

[27] Michael Hembera. Re-design of a multi-mission re-configurable unmanned aerial vehicle. Undergraduate Thesis Project, RMIT University, Australia, 2005.

[28] H. Sobieczky. Parametric airfoils and wings. *Numerical Fluid Dynamics*, 68:71–88, 1998.

[29] F.J. Torres I.-C. Chang and C. Tung. Geometric analysis of wing sections. Technical report, NASA Technical Memorandum, 1995.

[30] R. Eppler. Airfoil design and data. *Springer-Verlag*, 1990.

[31] D. M. Somers. Subsonic airfoil design. Website: Access Date - 7th October 2009. http://www.airfoils.com/design.pdf.

[32] T. E. Labrujere and J.W. Slooff. Computational methods for the aerodynamic design of aircraft components. *Annual Reviews of Fluid Mechanics*, 25:183–214, 1993.

[33] Neil W. Bressloff Thomas R. Barrett and Andy Keane. Airfoil shape design and optimization using multifidelity analysis and embedded inverse design. *AIAA Journal*, 44:2051–2060, 2006.

[34] Manas Khurana and Hadi Winarto. Development and validation of an efficient direct numerical optimisation approach for aerofoil shape design. *The Aeronautical Journal*, 114:611–628, 2010.

[35] R. M. Hicks and P. A. Henne. Wing design by numerical optimisation. *Journal of Aircraft*, 15: 407–413, 1977.

[36] Brenda M. Kulfan and John E. Bussoletti. 'fundamental' parametric geometry representations for aircraft component shapes. In *in* 11^{th} *AIAA/ISSMO Multidisciplinary Analysis and Optimization Conference, Portsmouth, Virginia*. American Institute of Aeronautics and Astronautics, 6-8 September, 2006.

[37] A. J. Keane and P.B. Nair. *Computational Approaches for Aerospace Design: The Pursuit of Excellence*. John Wiley & Sons, Ltd, West Sussex, England, 2005.

[38] V. Braibant and C. Fleury. Shape optimal design using b-splines. *Computer Methods in Applied Mechanics and Engineering*, 44:247–267, 1984.

[39] J. A. Samareh. A survey of shape parameterization techniques. In *CEAS/AIAA/ICASE/NASA Langley International Forum on Aeroelasticity and Structural Dynamics*, pages 333–343, 1999.

[40] A. Jameson and J. C. Vassberg. Computational fluid dynamics for aerodynamic design: Its current and future impact. In *39th AIAA Aerospace Sciences Meeting & Exhibit*, Reno, NV, 2001.

[41] H. Namgoong. *Airfoil Optimization of Morphing Aircraft*. PhD thesis, Aerospace Engineering, Purdue, Indiana, 2005.

[42] M. S. Gallart. Development of a design tool for aerodynamic shape optimization of airfoils. Master's thesis, Department of Mechanical Engineering, University of Victoria, 2002.

[43] A. Vicini and D. Quagliarella. Inverse and direct airfoil design using a multiobjective genetic algorithm. *AIAA Journal*, 35:1499–1505, 1997.

[44] M. E. Topliss C. A. Toomer and D.P. Hills. Aerodynamic optimization using analytic descriptions of the design space. *Journal of Aircraft*, 35:882–890, 1998.

[45] S. Peigin B. Epstein. Efficient approach for multipoint aerodynamic wing design of business jet aircraft. *AIAA Journal*, 45:2612–2621, 2007.

[46] S. D'Angelo and E.A. Minisci. Multi-objective evolutionary optimization of subsonic airfoils by kriging approximation and evolutionary control. *The 2005 IEEE Congress on Evolutionary Computation*, 2:1262–1267, 2005.

[47] Francois Guibault Anas Bentamy, Jean-Yves Trepanier. Wing shape optimization using a constrained nurbs surface geometrical representation. In *ICAS 2002 Congress*, 2002.

[48] W. Ghaly and T. Mengistu. Optimal geometric representation of turbomachinery cascades using nurbs. *Journal of Inverse Methods in Engineering*, 2003.

[49] Jean-Yves Trepanier Simon Painchaud-Ouellet, Christophe Tribes and Dominique Pelletier. Airfoil shape optimization using a nonuniform rational b-splines parameterization under thickness constraint. *AIAA Journal*, 44:2170–2178, 2006.

[50] B.M. Kulfan. Recent extensions and applications of the cst universal parametric geometry representation method. In *7th AIAA Aviation Technology, Integration, and Operations (ATIO), Belfast, Northern Ireland*, 2007.

[51] A. Sinha M. Khurana, H. Winarto. Airfoil geometry parameterization through shape optimizer and computational fluid dynamics. In *46th AIAA Aerospace Sciences Meeting and Exhibit, Reno, Nevada, USA*, 2008.

[52] G.S. Dwarakanath P. Ramamoorthy and C.L. Narayana. Wagner functions. Technical report, National Aeronautical Laboratory, 1969.

[53] MATHWORKS. Optimization toolbox user's guide, 2005. Help File, MATHWORKS, Inc.

[54] H. Fuhrmann. Design optimisation of a class of low reynolds, high mach number airfoils for use in the martian atmosphere. In *23rd AIAA Applied Aerodynamics Conference*, 2005.

[55] T. Winnemoller and C.P.V. Dam. Design and numerical optimization of thick airfoils. In *44th AIAA Aerospace Sciences Meeting and Exhibit*, 2006.

[56] Armando Vavalle and Ning Qin. Iterative response surface based optimization scheme for transonic airfoil design. *Journal of Aircraft*, 44:365–376, 2007.

[57] Shigeru Obayashi Shinkyu Jeong and Kazuomi Yamamoto. A kriging-based probabilistic optimization method with an adaptive search region. *Engineering Optimization*, 38, July, 2006.

[58] Kazuhisa Chiba Shinkyu Jeong and Shigeru Obayashi. Data mining for aerodynamic design space. *Journal of Aerospace Computing, Information and Communication*, 2, November, 2005.

[59] M. Klein and H. Sobieczky. Sensitivity of aerodynamic optimization to parameterized target functions. In *International Symposium on Inverse Problems in Engineering Mechanics*. Elsevier Science, 2001.

[60] B.M. Kulfan and J.E. Bussoletti. Fundamental parametric geometry representations for aircraft component shapes. In *11th AIAA/ISSMO Multidisciplinary Analysis and Optimization Conference, Portsmouth, Virginia, USA*, 2006.

[61] Patrice Castonguay Arash Mousavi and Siva Nadarajah. Survey of shape parameterization techniques and its effects on three-dimensional aerodynamic shape optimization. In *18th AIAA Computational Fluid Dynamics Conference*. American Institute of Aeronautics and Astronautics, June 2007.

[62] David Bogue and Nick Crist. Cst transonic optimization using tranair. In *46th AIAA Aerospace Sciences Meeting and Exhibit*. Calmar Research, 2008.

[63] S. Obayashi and Y. Yamaguchi. Multiobjective genetic algorithm for multidisciplinary design of transonic wing planform. *Journal of Aircraft*, 34:690–692, 1997.

[64] D. Quagliarella and A. Vicini. Viscous single and multicomponent airfoil design with genetic algorithms. *Finite Elements in Analysis and Design*, pages 365–380, 2001.

[65] G.H. Klopfer and D. Nixon. Nonisentropic potential formulation for transonic flows. *AIAA Journal*, 22:770–776, 1984.

[66] A.Iollo and M. Salas. *Fast Design of Transonic Airfoil Using the Euler Equations*, pages 322–327. Springer-Berlin/Heidelberg, 1997.

[67] S. Ta'asan. Pseudo-time methods for constrained optimization problems governed by pde. Technical report, Carnegie Mellon Univeristy, Hampton, VA, USA, 1995.

[68] L. Huyse and R.M. Lewis. Aerodynamic shape optimization of two-dimensional airfoils under uncertain conditions. Technical report, NASA Langley Research Center, 2001.

[69] Pedro Paglione F.d. Sousa, Fernando Manuel Ramos and Roberto M. Girardi. New stochastic algorithm for design optimization. *AIAA Journal*, 41:1808–1818, 2003.

[70] B. Chaouat. Reynolds stress transport modelling for high-lift airfoil flows. *AIAA Journal*, 44: 2390–2402, 2006.

[71] A. Hellsten. New advanced k-w turbulence model for high lift aerodynamics. *AIAA Journal*, 43:1857–1869, 2005.

[72] U.Scholz J. Windte and R. Radespiel. Validation of the rans-simulation of laminar seperation bubbles on airfoils. *Aerospace Science and Technology*, 10:484–494, 2005.

[73] S. Choi and O. Kwon. Aerodynamic characteristics of elliptic airfoils at high reynolds numbers. *Journal of Aircraft*, 45:641–650, 2008.

[74] S. Kern. Evaluation of turbulence models for high-lift military airfoil flowfields. In *34th Aerospace Sciences Meeting & Exhibit*, Reno, NV, 1996. American Institute of Aeronautics and Astronautics.

[75] A. Hellsten. New advanced $k - w$ turbulence model for high lift aerodynamics. *AIAA Journal*, 43:1857–1869, 2005.

[76] F.R. Menter. Two equations eddy-viscosity turbulence models for engineering applications. *AIAA Journal*, 32:1598–1605, 1994.

[77] J. Windte U. Scholz and R. Radespiel. Validation of the rans-simulation of laminar separation bubbles on airfoils. *Aerospace Science and Technology*, 10:484–494, 2005.

[78] Mark Drela. *XFOIL: An Analysis and Design System for Low Reynolds Number Airfoils*, volume 54, chapter Low Reynolds Number Aerodynamics, pages 1–12. Lecture Notes in Engineering, Springer-Verlag, New York, 1989.

[79] H.W. Stock. Airfoil validation using coupled navier-stokes and e^N transition prediction methods. *Journal of Aircraft*, 39:51–58, 2002.

[80] Rui Hu. *SUPERSONIC BIPLANE DESIGN VIA ADJOINT METHOD*. PhD thesis, Department of Aeronautics and Astronautics, Stanford University, California, 2009.

[81] K.Nakahashi S. Takahashi, S. Obayashi. Inverse design optimization of transonic wings based on multi-objective genetic algorithms. *AIAA Journal*, 37:1656–1662, 1999.

[82] A. Sinha M. Khurana, H. Winarto. Airfoil optimisation by swarm algorithm with mutation and artificial neural networks. In *47th AIAA Aerospace Sciences Meeting, Victoria, Orlando, USA*, 2009.

[83] Kasidit Leoviriyakit. *WING PLANFORM OPTIMIZATION VIA AN ADJOINT METHOD*. PhD thesis, Department of Aeronautics and Astronautics, Stanford University, California, 2005.

[84] Sangho Kim. *DESIGN OPTIMIZATION OF HIGH-LIFT CONFIGURATIONS USING A VISCOUS ADJOINT-BASED METHOD*. PhD thesis, Department of Aeronautics and Astronautics, Stanford University, California, 2001.

[85] A. Jameson. Optimum aerodynamic design using cfd and control theory. In *AIAA 12th Computational Fluid Dynamics Conference and Open Forum*, pages 926–949. American Institute of Aeronautics and Astronautics, 1995.

[86] Kyriakos C. Giannakoglou and Dimitrios I. Papadimitriou. Adjoint methods for shape optimization. Technical report, School of Mechanical Engineering, National Technical University of Athens, Greece.

[87] S. Nadarajah and A. Jameson. A comparison of the continuous and discrete adjoint approach to automatic aerodynamic optimization. In 38^{th} *Aerospace Sciences Meeting & Exhibit, Reno, NV, USA*. AIAA, January, 2000.

[88] G. W. Burgreen and O. Baysal. Three-dimensional aerodynamic shape optimization of wings using sensitivity analysis. In 32^{nd} *Aerospace Sciences Meeting & Exhibit, Reno, NV, USA*. AIAA, January, 1994.

[89] W. K. Anderson and V. Venkatakrishnan. Aerodynamic design optimization on unstructured grids with a continuous adjoint formulation. In 35^{th} *Aerospace Sciences Meeting & Exhibit, Reno, NV, USA*. AIAA, January, 1997.

[90] K.C. Giannakoglou & D.I. Papadimitriou. *Adjoint Methods for Shape Optimization*, chapter 4, pages 79–108. Springer-Verlag Berlin/Heidelberg, 2008.

[91] J. Holland. *Adaption in Natural and Artificial Systems.* University of Michigan Press, Ann Arbor, Michigan, USA, 1974.

[92] C.D. Gelatt S. Kirkpatrick and M.P.Vecchi. Optimization by simulated annealing. *Science. New Series*, 220:671–680, 1983.

[93] A. Colorni and V. Maniezzo. Distributed optimization by ant colonies. In *European Conference on Artificial Life, Paris, France*, pages 134–142, 1991.

[94] J. Kennedy and R. Eberhart. Particle swarm optimization. In *IEEE International Conference on Neural Networks, Perth, Australia*, pages 1942–1948, 1995.

[95] Ava Shahrokhi and Alireza Jahangirian. Optimization of airfoil flow control using a genetic algorithm with diversity control. *Journal of Aircraft*, 44:1337–1349, 2007.

[96] Terry L. Holst and Thomas H. Pulliam. Aerodynamic shape optimization using a real-number-encoded genetic algorithm. In *19^{th} AIAA Applied Aerodynamics Conference, Anaheim, CA, June 11-14*. American Institute of Aeronautics and Astronautics, 2001.

[97] W.A. Crossley H. Namgoong and A.S. Lyrintzis. Aerodynamic optimization of a morphing airfoil using energy as an objective. *AIAA Journal*, 45:2113–2124, 2007.

[98] T. Winnemoller and C.P.v. Dam.

[99] D. D'Ambrosio D. Quagliarella and A. Iollo. Airfoil design using navier-stokes equations and hybrid evolutionary optimization techniques. In *Proceedings of the RTO AVT Course on Intelligent Systems for Aeronautics, Rhode-Saint-Genese, Belgium*, 13-17 May, 2002.

[100] M. Damodaran X. Wang and S.L. Lee. Inverse transonic airfoil design using parallel simulated annealing and computational fluid dynamics. *AIAA Journal*, 40:791–794, 2002.

[101] X. Wang and M. Damodaran. Aerodynamic shape optimization using computational fluid dynamics and parallel simulated annealing algorithms. *AIAA Journal*, 39:1500–1508, 2001.

[102] N. Sinha and B. Purkayastha. Pso embedded evolutionary programming technique for non-convex economic load dispatch. In *Proceedings of the Power Systems Conference and Exposition, IEEE*, pages 66–71, 2004.

[103] G.E. Fainekos and K.C. Giannakoglou. Inverse design of airfoils based on novel formulation of the ant colony optimisation method. *Inverse Problems in Engineering*, 11:21–38, 2003.

[104] M. Dorigo A. Colorni and V. Maniezzo. Distributed optimization by ant colonies. In *Proceedings of the European Conference on Artificial Life, Paris, France*, pages 134–142. Elsevier Publishing, 1991.

[105] J. Robinson and Y. Rahmat-Samii. Particle swarm optimization in electromagnetics. *IEEE Transactions on Antennas and Propagation*, 52:397–407, 2004.

[106] Somayyeh Koohi Mehdi Kamal and Shaahin Hessabi. *A Novel Partitioned Encoding Scheme for Reducing Total Power Consumption of Parallel Bus*, chapter Advances in Computer Science and Engineering: 13^{th} International CSI Computer Conference, pages 90–97. Springer-Berlin/Heidelberg, March 9-11, 2008.

[107] V. Chudacek M. Macas J. Bernardes G. Georgoulas, C. Stylios and L. Hotska. Classification of fetal heart rate signals based on features selected using the binary particle swarm algorithm. *World Congress of Medical Physics and Biomedical Engineering*, 2:1156–1159, 2006.

[108] Yun Chen and Hanhong Zhu. Pso heuristics algorithm for portfolio optimization. In Ying Tan, Yuhui Shi, and Kay Tan, editors, *Advances in Swarm Intelligence*, volume 6145 of *Lecture Notes in Computer Science*, pages 183–190. Springer Berlin / Heidelberg.

[109] T. Shinkyu Jeong K. Shimoyama, Kazuya Seo Nishiwaki and S. Obayashi. Material design optimization for a sport shoe sole by evolutionary computation and fem analysis. In *IEEE Congress on Evolutionary Computation (CEC), Barcelona, Spain*, pages 1–7. IEEE, 27 September 2010.

[110] Y. Shi and R. Eberhart. A modified particle swarm optimizer. In *IEEE World Congress on Computation Intelligence*, pages 69–73, 1998.

[111] R.C. Eberhart and Y. Shi. Particle swarm optimization: Developments, application, and resources. In *IEEE Congress on Evolutionary Computation CEC2001*, pages 81–86, 2001.

[112] Daniel Bratton and James Kennedy. Defining a standard for particle swarm optimization. In *in Proceedings of the 2007 IEEE Swarm Intelligence Symposium*. IEEE, 2007.

[113] S. K. Halgamuge A. Ratnaweera and H. C. Watson. Self-organizing hierarchical particle swarm optimizer with time-varying acceleration coefficients. *IEEE Transactions on Evolutionary Computation*, 8:240–255, 2004.

[114] Q. Luo M.R. Chen, Y.Z. Lu. A novel hybrid algorithm with marriage of particle swarm optimization and external optimization. Technical report, Shanghai Jiaotong University.

[115] J. Fu L. Wang, X. Wang and L. Zhen. A novel probability binary particle swarm optimization algorithm and its application. *Journal of Software*, 3:28–35, 2008.

[116] A.K. Qin J.J. Liang. Comprehensive learning particle swarm optimizer for global optimization of multimodal functions. *IEEE Transactions on Evolutionary Computation*, 10:281–295, 2006.

[117] G. Lambert-Torres abd G.B. Alvarenga A.A.A Esmin. Hybrid evolutionary algorithm based on pso and ga mutation. In *Proceedings of the Sixth International Conference on Hybrid Intelligent Systems (HIS '06), Auckland, New Zealand*, 2006.

[118] M. Jancic A. Stacey and I. Grundy. Particle swarm optimization with mutation. In *Evolutionary Computation, Canberra, Australia*, pages 1425–1430, 2003.

[119] N. Higashi and H. Iba. Particle swarm optimization with gaussian mutation. In *Swarm Intelligence Symposium, Indianapolis, Indiana, USA*, pages 72–79, 2003.

[120] D. Srinivasan and T.H. Seow. Particle swarm inspired evolutionary algorithm (ps-ea) for multicriteria optimization problems. In *Proceedings of Evolutionary Computation, Canberra, Australia*, pages 147–165, 2003.

[121] R.C. Eberhart Y. Shi. Fuzzy adaptive particle swarm optimization. In *Proceedings of Evolutionary Computation, Seoul, Korea*, pages 101–106, 2001.

[122] L.H. Ma Y.l. Zheng and J.X. Qian. Empirical study of particle swarm optimizer with an increasing inertia weight. Technical report, Shanghai Jiaotong University, 2003.

[123] J. Zheng Z. Cui and H. Sun. *Adaptive Velocity Threshold Particle Swarm Optimization*, pages 327–332. Springer-Berlin/Heidelberg, 2006.

[124] S.K.S. Fang and J.M. Chang. *A Modified Particle Swarm Optimizer Using an Adaptive Dynamic Weight Scheme*, pages 56–65. Springer-Berlin/Heidelberg, 2007.

[125] J.J. Robinson and Y. Rahmat-Samii. Particle swarm optimization in electromagnetics. *IEEE Transactions on Antennas and Propagation*, 52:397–407, 2004.

[126] J. Wei and Y. Wang. A dynamical particle swarm algorithm with dimension mutation. *IJCSNS International Journal of Computer Science and Network Security*, 6:221–224, 2006.

[127] T.K. Rasmussen M. Lovbjerg and T. Krink. Hybrid particle swarm optimizer with breeding and subpopulations. In *Proceedings of Genetic and Evolutionary Computing Conference, San Francisco, California, USA*, pages 469–476, 2001.

[128] W.J. Zhang X.F. Xie and Z.L. Yang. A dissipative particle swarm optimization. In *Congress on Evolutionary Computation, Hawaii, USA*, pages 1456–1461, 2002.

[129] F. Bergh and A.P. Engelbrecht. A cooperative approach to particle swarm optimization. *IEEE Transactions on Evolutionary Computation*, 8:225–239, 2004.

[130] H.Y. Fan and Y. Shi. Study on vmax of particle swarm optimization. In *in Proc. Workshop Particle Swarm Optimization, Indianapolis, IN, USA*, 2001.

[131] P.J. Angeline. Using selection to improve particle swarm optimization. In *Proceedings IEEE Congress of Evolutionary Computing, Anchorage, AK, USA*, pages 84–89, 1998.

[132] Y. Liu X. Yao and G. Lin. Evolutionary programming made faster. *IEEE Transactions on Evolutionary Computation*, 3:82–102, 1999.

[133] D.M. McKay R.J. Beckman and W.J.Conover. A comparison of three methods for selection values of input variables in the analysis of output from a computer code. *Technometrics*, 21: 239–245, 1979.

[134] P.S. Andrews. An investigation into mutation operators for particle swarm optimization. In *IEEE Congress on Evolutionary Computation, Vancouver, BC, Canada*, pages 1044–1051, 2006.

[135] Peter Angeline. Evolutionary optimization versus particle swarm optimization: Philosophy and performance differences. In V. Porto, N. Saravanan, D. Waagen, and A. Eiben, editors, *Evolutionary Programming VII*, volume 1447 of *Lecture Notes in Computer Science*, pages 601–610. Springer Berlin / Heidelberg, 1998. URL http://dx.doi.org/10.1007/BFb0040811. 10.1007/BFb0040811.

[136] T. Kohonen, M. R. Schroeder, and T. S. Huang, editors. *Self-Organizing Maps*. Springer-Verlag New York, Inc., Secaucus, NJ, USA, 3rd edition, 2001. ISBN 3540679219.

[137] Masahiro Takatsuka and Michael Bui. *Parallel Batch Training of the Self-Organizing Map Using OpenCL*, volume 6444, chapter Lecture Notes in Computer Science, pages 470–476. Springer-Berlin/Heidelberg, March 2010.

[138] R.D. Lawrence, G.S. Almasi, and H.E. Rushmeier. A scalable parallel algorithm for self-organizing maps with applications to sparse data mining problems. *Data Mining and Knowledge Discovery*, 3:171–195, 1999. ISSN 1384-5810. URL http://dx.doi.org/10.1023/A:1009817804059. 10.1023/A:1009817804059.

[139] Viscovery. Viscovery somine 5.1. http://www.viscovery.net, last access on February 18, 2010.

[140] Shigeru Obayashi Kazuhisa Chiba and Kazuhiro Nakahashi. High-fidelity multidisciplinary design optimization of aerostructural wing shape for regional jet. In *23rd AIAA Applied Aerodynamics Conference, Toronto, Canada*, pages 1–24. American Institute of Aeronautics and Astronautics, 6-9 June, 2005.

[141] A.I.J. Forrester, A. Sóbester, and A.J. Keane. *Engineering design via surrogate modelling: a practical guide*. Progress in astronautics and aeronautics. J. Wiley, 2008. ISBN 9780470060681. URL http://books.google.com.au/books?id=ulMHmeMnRCcC.

[142] L. Blasi and G.D. Core. Particle swarm approach in finding optimum aircraft configuration. *Journal of Aircraft*, 44:679–682, 2007.

[143] P. Sriyanyong. A hybrid particle swarm optimization solution to ramping gate constrained dynamic economic dispatch. In *Proceedings of World Academy of Science, Engineering and Technology*, pages 991–996, 2008.

[144] I. Gregg P.A. Henne and D. Robert. Patent application for a.

[145] Andras Sobester. Exploiting patterns in the kulfan transformations of supercritical airfoils. In *9th AIAA Aviation Technology, Integration and Operations Conference, Hilton Head, South Carolina*, 2009.

[146] M.D. Morris. Factorial sampling plans for preliminary computational experiments. *Technometrics*, 33:161–174, 1991.

[147] F. Campolongo A. Saltelli, S. Tarantola and M. Ratto. *Sensitivity Analysis in Practice*. John Wiley & Sons, Ltd, Ispra, Italy, 2004.

[148] F.R. Bailey E.M. Murman and M.L. Johnson. Tsfoil - a computer code for two-dimensional transonic calculations, including wind-tunnel wall effects and wave drag evaluation, March 1975. NASA SP-347.

[149] J. Carboni F. Campolongo and A. Saltelli. An effective screening design for sensitivity analysis of large models. *Environmental Modelling & Software*, 22:1509–1518, 2007.

[150] Abdurrahman Hacioglu. Fast evolutionary algorithm for airfoil design via neural network. *AIAA Journal*, 45:2196–2203, 2007.

[151] W.H. Mason. Tsfoil2 manual, December 2003. Virginia Tech Aircraft Design Software.

[152] FLUENT Academic Research. Modeling turbulence guide, chapter 12, September 2006. Release 6.3, Help System, FLUENT, Inc.

[153] ANSYS FLUENT Academic Research, January 2009. Release 12.0, ANSYS, Inc.

[154] J. Driver and D.W. Zingg. Optimized natural-laminar-flow airfoils.

[155] Mark Drela. Design and optimization method for multi-element airfoils. In *AIAA, AHS and ASEE, Aerospace Design Conference*, page 12, Irvine, CA, USA, 16-19 Feb, 1993. American Institute of Aeronautics and Astronautics.

[156] Wassim A. Basha and Wahid S. Ghaly. Drag prediction in transitional flow over airfoils. *Journal of Aircraft*, 44:824–832, 2007.

[157] ANSYS FLUENT. Turbulence, chapter 4, 29 January 2009. Release 12.0, ANSYS FLUENT Theory Guide, ANSYS Inc.

[158] F. R. Menter, R. B. Langtry, S. R. Likki, Y. B. Suzen, P. G. Huang, and S. Volker. A correlation-based transition model using local variables—part i: Model formulation. *Journal of Turbomachinery*, 128(3):413–422, 2006. doi: 10.1115/1.2184352. URL http://link.aip.org/link/?JTM/128/413/1.

[159] ANSYS FLUENT. Solver theory, chapter 18, 29 January 2009. Release 12.0, ANSYS FLUENT Theory Guide, ANSYS Inc.

[160] MATHWORKS. Parallel computing toolbox, 2010. MATHWORKS, Inc.

[161] Mark Drela. *Pros & Cons of Airfoil Optimization*, chapter Frontiers of Computational Fluid Dynamics, pages 363–381. World Scientific, Singapore, 1998.

[162] R.M. Lewis L. Huyse, S.L. Padula and W. Li. Probabilistic approach to free-form airfoil shape optimization under uncertainty.

[163] L. Huyse W. Li and S. Padula. *Robust Airfoil Optimization to Achieve Drag Reduction Over a Range of Mach Numbers*, volume 24, chapter Industrial Applications and Design Case Studies - Structural Multidisciplinary Optimisation, pages 38–50. Springer-Verlag, 2002.

[164] Luc Huyse. Free-form airfoil shape optimization under uncertainty using maximum expected value and second-order second-moment strategies. Technical Report ICASE Report No. 2001-18, NASA Langley Research Center, June, 2001.

[165] Luc Huyse Wu Li and Sharon Padula. Robust airfoil optimization to achieve consistent drag reduction over a mach range. Technical Report ICASE Report No. 2001-22, NASA Langley Research Center, August, 2001.

[166] Wu Li and Sharon Padula. Using high resolution design spaces for aerodynamic shape optimization under uncertainty. Technical Report NASA/TP-2004-213003, NASA Langley Research Center, March, 2004.

[167] Wu Li. Profile optimization method for robust airfoil shape optimization in viscous flow. Technical Report NASA/TM-2003-212408, NASA Langley Research Center, May, 2003.

[168] Sang Wook Lee and Oh Joon Kwon. Robust airfoil shape optimization using design for six sigma. *Journal of Aircraft*, 43:843–846.

[169] L.B. Lurati. Robust airfoil design under uncertain operation conditions using stochastic collocation. In *46th AIAA Aerospace Sciences Meeting and Exhibit, Reno, Nevada, USA*. American Institute of Aeronautics and Astronautics, 2008.

[170] H.M. Tsai T. Ray and C.M. Tan. Effects of solver fidelity on a parallel search algorithm's performance for airfoil shape optimization problems. In *9th AIAA/ISSMO Symposium on Multidisciplinary Analysis and Optimization, Atlanta, Georgia, USA*. American Institute of Aeronautics and Astronautics, 2002.

[171] Ivo Couckuyt Dirk Gorissen, Karel Crombecq and Tom Dhaene. Automatic approximation of expensive functions with active learning. Technical report, Department of Information Technology, Ghent University, Belgium.

[172] R. Chaveesuk and A. Smith. Economic valuation of capital projects using neural network metamodels. *The Engineering Economist*, 48:1–30, 2003.

[173] J. Kohn K. Rasheed N. Weber V. Kholodovych JR Smith, D. Knight and WJ Welsh. Using surrogate modeling in the prediction of fibrinogen absorption onto polymer surfaces. *Journal of Chemical Information and Computer Science*, 44:1088–1097.

[174] N. Fache J. De Geest, T. Dhaene and D. De Zutter. Adaptive cad-model building algorithm for general planar microwave structures. *IEEE Transactions on Microwave Theory and Techniques*, 47:1801–1809, 1999.

[175] D. Hidovic and J. Rowe. *Validating a model of colon colouration using an evolution strategy with adaptive approximations*, volume 3103, chapter Proceedings of GECCO, Part 2 - Lecture Notes in Computer Science, pages 1005–1016. Springer-Verlag, 2004.

[176] Roxana M. Greenman. *Two-Dimensional High-Lift Aerodynamic Optimization Using Neural Networks*. PhD thesis, NASA Ames Research Center, Moffett Field, California, USA, June 1998.

[177] M. Murayama S. Jeong and K. Yamamoto. Efficient optimization design method using kriging model. In *AIAA Aerospace Sciences Meeting and Exhibit, Reno, NV, USA*, pages 413–420, 2004.

[178] A.J. Keane. Statistical improvement criteria for use in multiobjective design optimization. *AIAA Journal*, 44:879–891, 2006.

[179] Wenbin Song and Andy J. Keane. Surrogate-based aerodynamic shape optimization of a civil aircraft engine nacelle. *AIAA Journal*, 45:2565–2574.

[180] Yu Wang and Xiongqing Yu. Surrogate-based aerodynamic optimization under uncertainty. In *The Fourth China-Japan-Korea Joint Symposium on Optimization of Structural and Mechanical Systems, Kunming, China*, November 6-9, 2006.

[181] Andrew R. Conn, Katya Scheinberg, and Luis N. Vicente. *Introduction to Derivative-Free Optimization*. Society for Industrial and Applied Mathematics, Philadelphia, PA, USA, 2009. ISBN 0898716683, 9780898716689.

[182] M. D. Buhmann. *Radial Basis Functions: Theory and Implementations*. Cambridge University Press, 2003.

[183] Jerome H. Friedman. Multivariate adaptive regression splines. *Annals of Statistics*, 19:1–67, 1991. doi: 10.1214/aos/1176347963.

[184] Daniel Graupe. *Principles of artificial neural networks*. World Scientific Publishing Co., Inc., River Edge, NJ, USA, 1997. ISBN 981-02-2516-4.

[185] D. Wolpert. The supervised learning no-free-lunch theorems. In *Proceedings of the 6th Online World Conference on Soft Computing in Industrial Applications*, 2001.

[186] G.E.P Box and N.R. Draper. *Empirical Model-Building and Response Surfaces*. Wiley Series in Probability and Mathematical Statistics, New York, USA, 1987.

[187] Neil W. Bressloff Alexander I.J. Forrester and Andy J. Keane. Optimization using surrogate models and partially converged computational fluid dynamics simulations. *The Royal Aeronautical Society*, 462:2177–2204, 2006.

[188] Kemper Lewis Timothy Simpson Amit Srivastava, Kurt Hacker. Development of a kriging based surrogate approximation method for large-scale systems. Technical report, State University of New York & Pennsylvania State University.

[189] Ying Hung V. Roshan Joseph and Agus Sudjianto. Blind kriging: A new method for developing metamodels. Technical report, Georgia Institute of Technology, Atlanta, GA.

[190] Wataru Yamazaki Keizo Takenaka, Keita Hatanaka and Kazuhiro Nakahashi. Multidisciplinary design exploration for a winglet. *Journal of Aircraft*, 45:1601–1611.

[191] Shinkyu Jeong Masahiro Kanazaki, Kentaro Tanaka and Kazuomi Yamamoto. Multi-objective aerodynamic exploration of elements' setting for high-lift airfoil using kriging model. *Journal of Aircraft*, 44:858–864.

[192] Jiabo Wang Sida Zhou Teng Long, Li Liu and Lingtao Meng. Multi-objective multidisciplinary optimization of long-endurance uav wing using surrogate models in modelcenter. In *12th AIAA/ISSMO Multidisciplinary Analysis and Optimization Conference, Victoria, British Columbia, Canada*. American Institute of Aeronautics and Astronautics, 10-12 September, 2008.

[193] Anthony A. Giunta and Layne T. Watson. A comparison of approximation modeling techniques: Polynomial versus interpolating models, 1998.

[194] Man Mohan Rai and Nateri K. Madavan. Application of artificial neural networks to the design of turbomachinery airfoils. In *36th Aerospace Sciences Meeting & Exhibit,Reno, NV,USA*. American Institute of Aeronautics and Astronautics, 1998.

[195] Salvatore D'Angelo and Edmondo Minisci. Multi-objective evolutionary optimization of subsonic airfoils by meta-modeling and evolution control. *Proceedings of the Institution of Mechanical Engineers, Part G: Journal of Aerospace Engineering*, 221:805–814, 2007.

[196] Man Mohan Rai and Nateri K. Madavan. Aerodynamic design using neural networks. *AIAA Journal*, 38:173–182.

[197] Charles C. Jorgenson James C. Ross and Magnus Norgaard. Reducing wind tunnel data requirements using neural networks. Technical report, NASA Technical Memorandum, Moffett Field, CA, USA, May.

[198] R. Duvigneau and M. Visonneau. Hybrid genetic algorithms and neural networks for fast cfd-based design. In *9th AIAA/ISSMO Symposium on Multidisciplinary Analysis and Optimization, Atlanta, Georgia, USA*, pages 633–643. American Institute of Aeronautics and Astronautics, 4-6 September, 2002.

[199] Bento Silva de Mattos Mailema Celestino dos Santos and Roberto da Mota Girardi. Aerodynamic coefficient prediction of airfoils using neural networks. In *46th AIAA Aerospace Sciences Meeting and Exhibit, Reno, Nevada, USA*. American Institute of Aeronautics and Astronautics, 2008.

[200] Charles C. Jorgensen Magnus Norgaard and James C. Ross. Neural network prediction of new aircraft design coefficients. Technical report, NASA Ames Research Center, Moffett Field, California, USA, May.

[201] L.S. Miller S.Y. Huang and J.E. Steck. An exploratory application of neural networks to airfoil design. In *32nd Aerospace Sciences Meeting and Exhibit, Reno, Nevada, USA*. American Institute of Aeronautics and Astronautics, 1994.

[202] T. Rajkumar and Jorge Bardina. Training data requirements for a neural network to predict aerodynamic coefficients. In *Independent Component Analysis, Wavelets, and Neural Networks, Orlando, USA*. SPIE Digital Library, 2003.

[203] Temesgen Mengistu and Wahid Ghaly. Aerodynamics optimization of turbomachinery blades using evolutionary methods and ann-based surrogate models. *Springer - Optimisation Engineering*, 9:239–255, 2008.

[204] Zhenghong Gao Wei Su, Yingtao Zuo. Preliminary aerodynamic shape optimization using genetic algorithm and neural network. In 11^{th} *AIAA/ISSMO Multidisciplinary Analysis and Optimization Conference, Portsmouth, Virgina, USA*. American Institute of Aeronautics and Astronautics, 6-8 September, 2006.

[205] Lisa Griffin Nilay Papila, Wei Shyy and Daniel J. Dorney. Shape optimization of supersonic turbines using response surface and neural network methods. In 39^{th} *AIAA Aerospace Sciences Meeting & Exhibit, Reno, NV, USA*. American Institute of Aeronautics and Astronautics, 8-11 January, 2001.

[206] Dominic Denver C. Vadivelan and John Chandar. Transonic airfoil design using artificial neural networks. In 8^{th} *Annual CFD Symposium, Bangalore, India*, 11-13 August, 2005.

[207] M. Y. M. Ahmed and N. Qin. Surrogate-based aerodynamic design optimization: Use of surrogates in aerodynamic design optimization. In 13^{th} *AEROSPACE SCIENCES & AVIATION TECHNOLOGY ASAT- 13, Kobry Elkobbah, Cairo, Egypt*, May 2628, 2009.

[208] Yaochu Jin Michael Husken and Bernhard Sendhoff. Structure optimization of neural networks for evolutionary design optimization. *Soft Computing: Special Issue on Approximation and Learning in Evolutionary Computation*, 9:21–28, 2005.

[209] Marios K. Karakasis Kyriakos C. Giannakoglou and Ioannis C. Kampolis. Evolutionary algorithms with surrogate modeling for computationally expensive optimization problems. In *ERCOFTAC 2006 Design Optimization International Conference, Gran Canaria, Spain*, pages 85–96. ERCOFTAC, 5-7 April, 2006.

[210] Ava Shahrokhi and Alireza Jahangirian. A surrogate assisted evolutionary optimization method with application to the transonic airfoil design. *Taylor & Francis - Engineering Optimization*, 42:497–515.

[211] Lars Willmes and Yaochu Jin. Comparing neural networks and kriging for fitness approximation in evolutionary optimization. In *The 2003 Congress on Evolutionary Computation*, pages 663–670. IEEE, 8-12 December, 2003.

[212] Roberto da Mota Girardi Marcelo Curvo Ricardo Wallach, Bento S. Mattos. Aerodynamic coefficient prediction of a general transport aircraft using neural network. In 44^{th} *AIAA Aerospace Sciences Meeting and Exhibit, Reno, Nevada, USA*. American Institute of Aeronautics and Astronautics, 2006.

[213] MATHWORKS. Statistics toolbox user's guide, 2005. Help File, MATHWORKS, Inc.

[214] MATHWORKS. Neural networks toolbox user's guide, 2005. Help File, MATHWORKS, Inc.

[215] A. Sinha M. Khurana, H. Winarto. Application of swarm approach and artificial neural networks for airfoil shape optimization. In *12th AIAA/ISSMO Multidisciplinary Analysis and Optimisation, Victoria, British Columbia, Canada*, 2008.

[216] Manas S. Khurana. Application of an hybrid optimization approach in the design of long endurance airfoils. In 26^{th} *INTERNATIONAL CONGRESS OF THE AERONAUTICAL SCIENCES, Anchorage, Alaska, USA*. ICAS, 2008.

[217] D.J.C. MacKay. Neural computation: Bayesian interpolation. *Neural Computation*, 4:415–447, 1992.

[218] F. Dan Foresee and Martin T. Hagan. Gauss-newton approximation to bayesian learning. In *International Conference on Neural Networks, Houston, TX, USA*, pages 1930–1935. IEEE, 1997.

[219] M. T. Hagan and M. Menhaj. Training feedforward networks with the marquardt algorithm. *IEEE Transactions on Neural Networks*, 5:989–993, 1994.

[220] Mark H. Zweig and Gregory Campbell. Receiver-operating characteristic (roc) plots: a fundamental evaluation tool in clinical medicine. *Clin Chem*, 39:561 – 577, April.

[221] Gerhard Venter and Jaroslaw Sobieszczanski-Sobieski. Parallel particle swarm optimization algorithm accelerated by asynchronous evaluations. *Journal of Aerospace Computing, Information, And Communication*, 3:123–137.

[222] MATHWORKS. Curve fitting toolbox, 2005. Help File, MATHWORKS, Inc.